frontiers | Research Topics

Wave propagation in complex environments

Edited by
Leilei Chen, Pei Li, Elena Atroshchenko and Yilin Qu

Published in
Frontiers in Physics

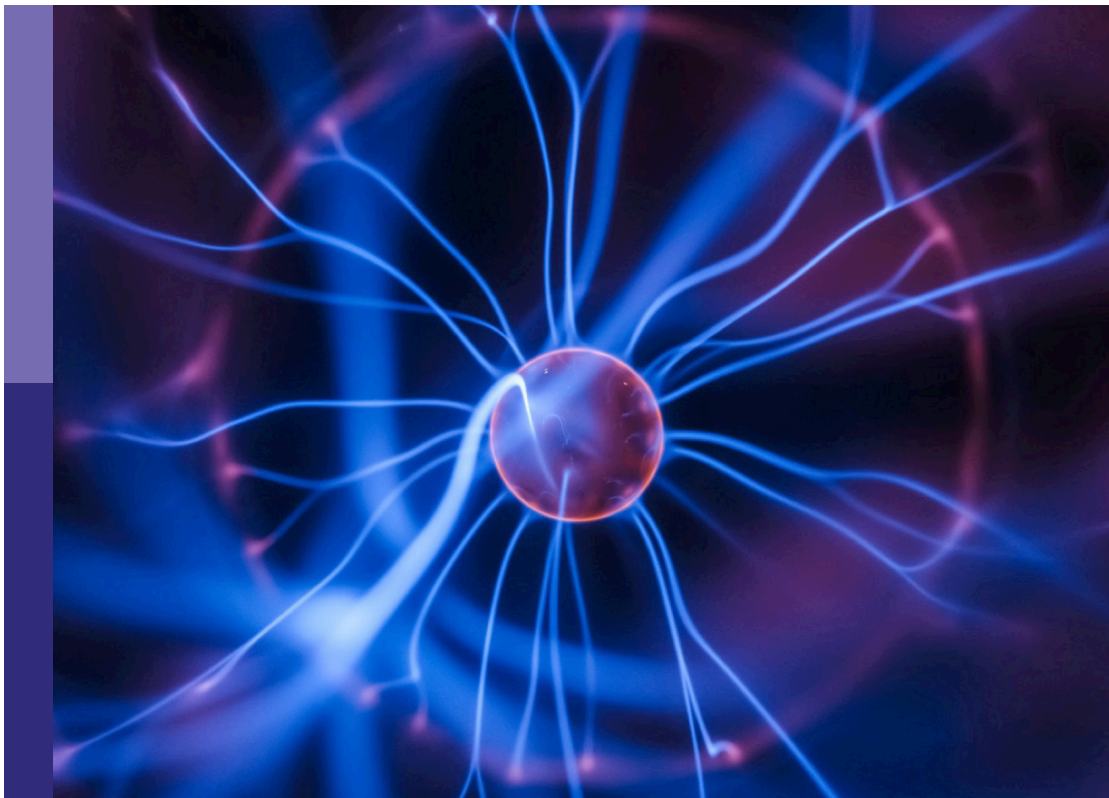

ISSN 1664-8714
ISBN 978-2-8325-5752-5
DOI 10.3389/978-2-8325-5752-5

About Frontiers

Frontiers is more than just an open access publisher of scholarly articles: it is a pioneering approach to the world of academia, radically improving the way scholarly research is managed. The grand vision of Frontiers is a world where all people have an equal opportunity to seek, share and generate knowledge. Frontiers provides immediate and permanent online open access to all its publications, but this alone is not enough to realize our grand goals.

Frontiers journal series

The Frontiers journal series is a multi-tier and interdisciplinary set of open-access, online journals, promising a paradigm shift from the current review, selection and dissemination processes in academic publishing. All Frontiers journals are driven by researchers for researchers; therefore, they constitute a service to the scholarly community. At the same time, the *Frontiers journal series* operates on a revolutionary invention, the tiered publishing system, initially addressing specific communities of scholars, and gradually climbing up to broader public understanding, thus serving the interests of the lay society, too.

Dedication to quality

Each Frontiers article is a landmark of the highest quality, thanks to genuinely collaborative interactions between authors and review editors, who include some of the world's best academicians. Research must be certified by peers before entering a stream of knowledge that may eventually reach the public - and shape society; therefore, Frontiers only applies the most rigorous and unbiased reviews. Frontiers revolutionizes research publishing by freely delivering the most outstanding research, evaluated with no bias from both the academic and social point of view. By applying the most advanced information technologies, Frontiers is catapulting scholarly publishing into a new generation.

What are Frontiers Research Topics?

Frontiers Research Topics are very popular trademarks of the *Frontiers journals series*: they are collections of at least ten articles, all centered on a particular subject. With their unique mix of varied contributions from Original Research to Review Articles, Frontiers Research Topics unify the most influential researchers, the latest key findings and historical advances in a hot research area.

Find out more on how to host your own Frontiers Research Topic or contribute to one as an author by contacting the Frontiers editorial office: frontiersin.org/about/contact

Wave propagation in complex environments

Topic editors

Leilei Chen — Huanghuai University, China

Pei Li — University of Southern Denmark, Denmark

Elena Atroshchenko — University of New South Wales, Australia

Yilin Qu — Northwestern Polytechnical University, China

Citation

Chen, L., Li, P., Atroshchenko, E., Qu, Y., eds. (2024). *Wave propagation in complex environments*. Lausanne: Frontiers Media SA. doi: 10.3389/978-2-8325-5752-5

Table of contents

frontiers | Frontiers in Physics

TYPE Original Research
PUBLISHED 04 December 2023
DOI 10.3389/fphy.2023.1325930

OPEN ACCESS

EDITED BY
Pei Li,
Xi'an Jiaotong University, China

REVIEWED BY
Xiaowei Shen,
Hohai University, China
Chuang Lu,
University of Science and Technology of China, China

*CORRESPONDENCE
Ruijin Huo,
huoruijin0117@163.com

RECEIVED 22 October 2023
ACCEPTED 13 November 2023
PUBLISHED 04 December 2023

CITATION
Yang Y, Huo R, Yuan X and Wu W (2023), A generalized isogeometric boundary element method for the uncertain analysis of infinite domain two-dimensional acoustic problems. *Front. Phys.* 11:1325930. doi: 10.3389/fphy.2023.1325930

A generalized isogeometric boundary element method for the uncertain analysis of infinite domain two-dimensional acoustic problems

Yan Yang[1,2], Ruijin Huo[3,4]*, Xiaohui Yuan[3] and Wenbo Wu[5]

[1]College of Architectural and Civil Engineering, Huanghuai University, Zhumadian, China, [2]Henan International Joint Laboratory of Structural Mechanics and Computational Simulation, Huanghuai University, Zhumadian, China, [3]College of Architecture and Civil Engineering, Xinyang Normal University, Xinyang, China, [4]Henan Unsaturated Soil and Special Soil Engineering Technology Research Center, Xinyang Normal University, Xinyang, China, [5]School of Mechanical and Electric Engineering, Guangzhou University, Guangzhou, China

The key aim of this paper is to provide a new *n*th generalized order perturbed isogeometric fast multistage technique of boundary elements to compute the propagation of time harmonics in an infinite region. Structural geometry and boundary integral equations are constructed by using non-uniform rational B-splines. The source of system uncertainty is believed to be the incident plane wave number's unpredictability. The actual field, depending on the input random variables, is simulated using the extended *n*th-order perturbation method. The field and kernel values for boundary integral formulas are generated via the *n*th-order generalized series of Taylor expansions using perturbation parameters. The fast multipole method (FMM) is utilized to speed up the process. The effectiveness and correctness of the proposed algorithm are verified by Monte Carlo simulations (MCs) with numerical examples.

KEYWORDS

uncertainty analysis, isogeometric boundary element method, perturbation method, Helmholtz formula, finite difference method

1 Introduction

Numerous areas are affected practically by wave propagation in an unlimited domain [1–8]. Although a lot of efforts have been put into modeling this issue, it focuses on deterministic systems. The parameters obtained from laboratory experiments and measurements are essentially random. In order to take into account the influence of these uncertainties on the system response, it is advisable to incorporate some uncertainty analysis techniques into various theoretical and computational methodologies, such as Monte Carlo simulation (MCs) [9–11], the stochastic spectrum methods [12, 13], and the perturbation technique [14–18]. Among them, MCs is the most common and simplest method, but its accuracy is largely based on the quantity of samples, resulting in high-level computational costs [19–21]. Therefore, MCs is often used as a reference solution to validate other probabilistic methods [22–24]. The stochastic spectrum method is more efficient and takes advantage of generality, but it is still difficult to apply to large-scale problems. Perturbation is the most effective method, but it is mainly limited to linear problems.

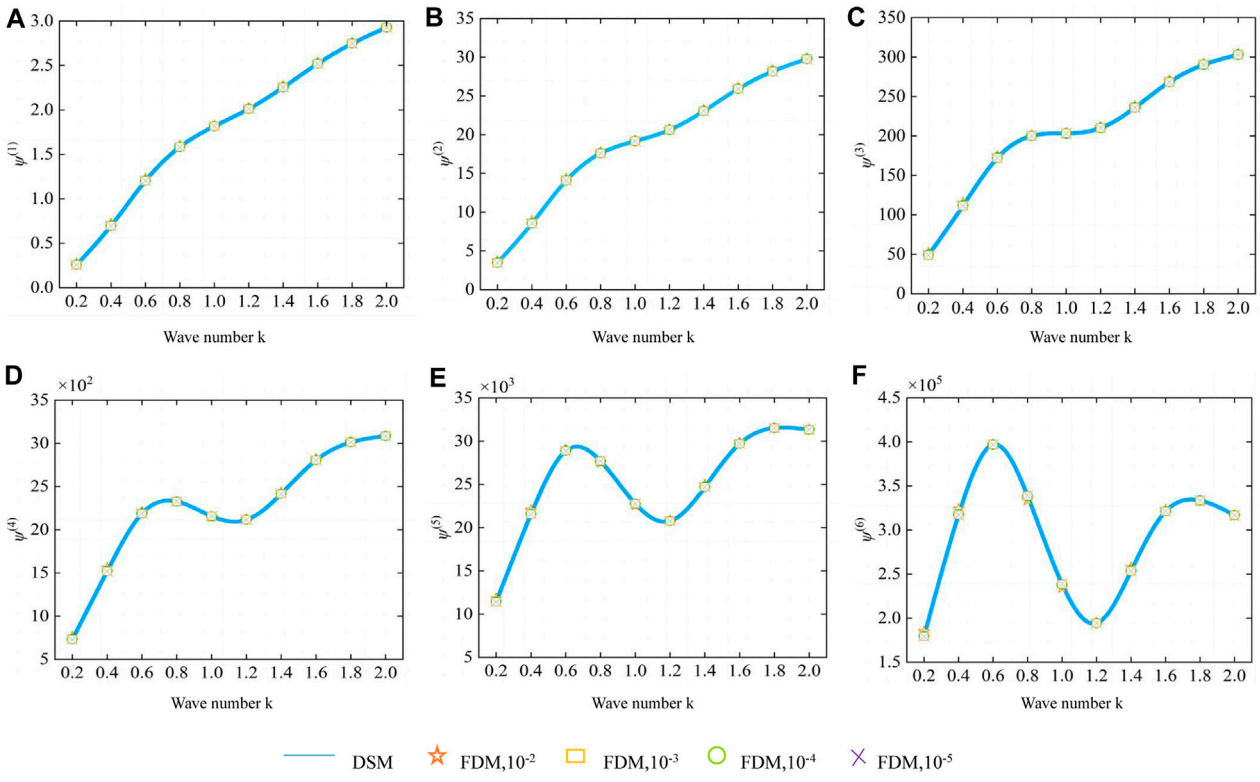

FIGURE 1
Curve of the amplitude of the field function of an infinite cylinder with a wave number *k*: **(A)** first-order, **(B)** second-order, **(C)** third-order, **(D)** fourth-order, **(E)** fifth-order, and **(F)** sixth-order derivatives.

TABLE 1 Relative errors ε_{err} in first- and second-order derivatives of the field function of an infinite cylinder.

Wave number	First-order derivative			Second-order derivative		
	$\Delta x = 10^{-2}$	$\Delta x = 10^{-3}$	$\Delta x = 10^{-4}$	$\Delta x = 10^{-2}$	$\Delta x = 10^{-3}$	$\Delta x = 10^{-4}$
0.2	0.06243	0.00650	0.00065	0.05555	0.00577	0.00058
0.4	0.03560	0.00367	0.00037	0.03297	0.00339	0.00034
0.6	0.01883	0.00193	0.00019	0.01641	0.00168	0.00017
0.8	0.00906	0.00092	0.00009	0.00632	0.00065	0.00006
1.0	0.00528	0.00053	0.00005	0.00312	0.00031	0.00003
1.2	0.00533	0.00053	0.00005	0.00466	0.00046	0.00005
1.4	0.00587	0.00059	0.00006	0.00620	0.00062	0.00006
1.6	0.00498	0.00050	0.00005	0.00507	0.00051	0.00005
1.8	0.00360	0.00036	0.00004	0.00322	0.00033	0.00003

Because numerical analysis frequently uses the finite element method (FEM), stochastic analysis with FEM is extensively studied. For example, spectral stochastic FEM is investigated by [12]. The stochastic FEM with the perturbation method is presented in [14–17]. Kamiński puts forward the generalized second-order and *n*th-order stochastic perturbation techniques [25, 26], which provide results with high computational accuracy. A smoothed finite element approach based on generalized perturbation for stochastic analysis is proposed in [22] to effectively maintain accuracy and withstand mesh distortion, especially in irregular mesh.

Despite its versatility, the finite element method is not easy to use when simulating wave scattering in unbounded media. A significant issue arises because the unbounded domain must be truncated into a sizable bounded domain enclosed by an artificial border using the finite element method. In addition, there are

TABLE 2 Relative errors ε_{err} in third- and fourth-order derivatives of the field function of an infinite cylinder.

Wave number	Third-order derivative			Fourth-order derivative		
	$\Delta x = 10^{-2}$	$\Delta x = 10^{-3}$	$\Delta x = 10^{-4}$	$\Delta x = 10^{-2}$	$\Delta x = 10^{-3}$	$\Delta x = 10^{-4}$
0.2	0.05188	0.00539	0.00054	0.04482	0.00462	0.00046
0.4	0.02973	0.00306	0.00031	0.02651	0.00272	0.00027
0.6	0.01311	0.00135	0.00014	0.00917	0.00096	0.00010
0.8	0.00261	0.00028	0.00003	0.00213	0.00020	0.00002
1.0	0.00015	0.00001	0.00000	0.00393	0.00040	0.00004
1.2	0.00395	0.00039	0.00004	0.00338	0.00032	0.00003
1.4	0.00696	0.00070	0.00007	0.00848	0.00085	0.00008
1.6	0.00526	0.00053	0.00005	0.00553	0.00056	0.00006
1.8	0.00266	0.00027	0.00003	0.00178	0.00018	0.00002

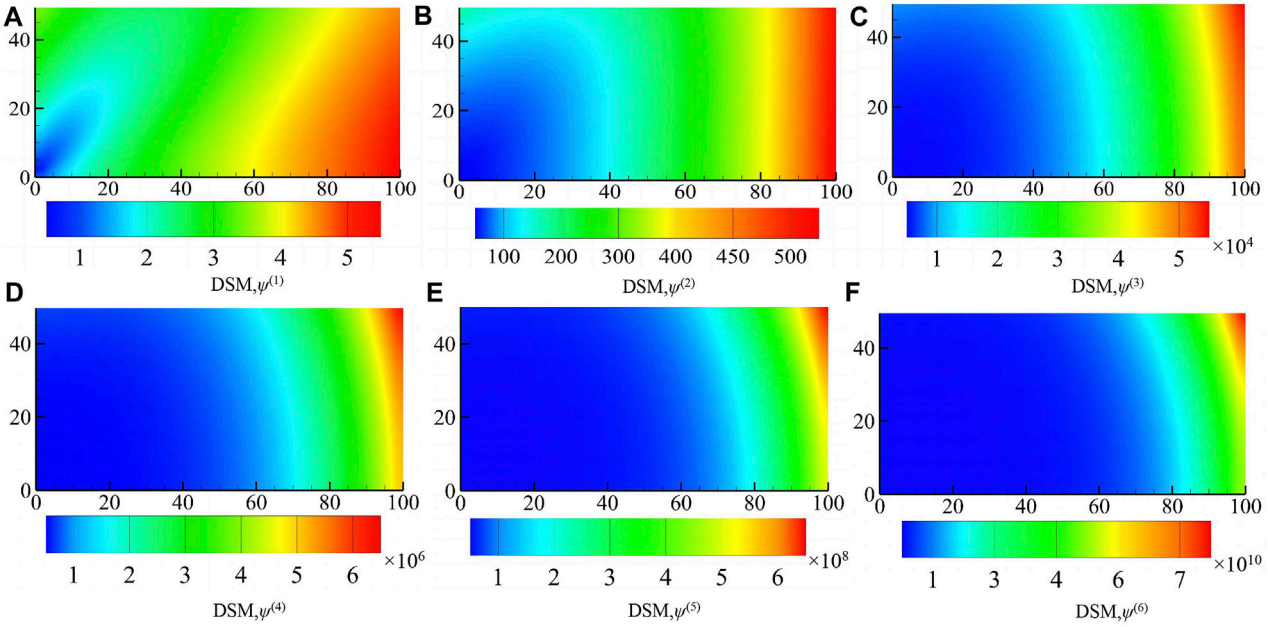

FIGURE 2
Infinite cylindrical field function derivative distribution cloud: **(A)** first-order, **(B)** second-order, **(C)** third-order, **(D)** fourth-order, **(E)** fifth-order, and **(F)** sixth-order derivatives.

specific methods that must be used to estimate the boundary conditions at infinity. In contrast, known alternatively as the method of moments (MOM) in electromagnetic fields [27, 28], the boundary element method (BEM) is preferred for infinite domain problems [29–34]. Boundary element method has advantages such as reduced dimensionality calculation, and boundary element method only discretizes the surface of the structure and naturally satisfies the boundary conditions at infinity. The creation of an asymmetrical, thick coefficient matrix, resulting in higher memory needs and processing complexity, is a common drawback of the boundary element approach. Some fast-solving algorithms are proposed, such as the fast direct solution method [35], adaptive cross approximation method [36], and fast multipole method (FMM) [37]. Another unavoidable disadvantage of the boundary element method is the need to precisely calculate the singular integral. The singularity subtraction technique is successfully utilized to remove the boundary integrals' singularity [38].

Isogeometric analysis (IGA), first suggested by Hughes and others [39], has developed into a key numerical approach in recent years. In traditional numerical analysis, grids must be constructed using computer-aided design (CAD), which is time-consuming and necessitates a sizable amount of human involvement. The basis functions that have given rise to CAD are

TABLE 3 Expectation of the field function of an infinite cylinder with different coefficients of variation.

Order	Coefficient of variation (γ)					
	0.05	0.07	0.09	0.11	0.13	0.15
2	0.19735	0.22034	0.25100	0.28932	0.33531	0.38897
4	0.19903	0.22681	0.26868	0.32879	0.41229	0.52542
6	0.19911	0.22740	0.27133	0.33759	0.43629	0.58204
8	0.19911	0.22744	0.27163	0.33909	0.44198	0.59991
10	0.19911	0.22744	0.27167	0.33939	0.44358	0.60661
MCSs	0.19911	0.22744	0.27167	0.33939	0.44358	0.60661

used by IGA to solve systems of partial differential equations, such as PHT-splines, which are hierarchy T-meshes over quadratic splines [40], and non-uniform rational B-splines (NURBS) [41, 42]. IGA eliminates the need for gridding while maintaining geometric precision. IGA has been widely employed in numerous domains, including uncertainty analysis, since its beginnings. A *n*th-order generalized perturbation isometric approach that is a steady-state heat transfer analysis simulation with material uncertainties was created by Rojas et al. [43]. Ding et al. [24] studied the *n*th-order perturbation method based on IGA to simulate the geometric uncertainty of shell structure. Cao et al. [44] used uncertainty analysis to solve the equi-geometric bi-reciprocal finite element for non-Fourier transient heat transfer problems. Chen et al. [45, 46] proposed an effective deep learning method based on IGA samples for the quantification of multivariable uncertainty issues with the interplay of vibration and sound. IGA was first put forth in relation to finite element methods before being expanded to boundary element method [47]. Boundary units and CAD are compatible since they both employ boundary notation. The boundary element also satisfies the boundary criteria at infinity, making it highly accurate and efficient for modeling the spread of waves across infinite domains, such as the sound [27] and electromagnetic field [48].

The generalized *n*th-order perturbation based on the isogeometric boundary element method (IGABEM) is proposed to assess the uncertainty of the propagation of time harmonics in an infinite region. The fact that the coefficient matrix in the boundary element system is an asymmetric complete matrix, which raises computing complexity and storage needs, is a characteristic drawback of the boundary element system. Therefore, we avoid directly calculating the coefficient matrix in the equation of boundary integrals of components of the *n*th order; instead, we apply the fast multipole method suggested in [37] to quicken the computation of multiplication of vectors in matrices. As a result, uncertainty analysis using isogeometric boundary elements is more effective. This increases how well uncertainty analysis works based on isogeometric border elements. Another disadvantage of the boundary element is the existence of singular integrals in the equation, which requires careful calculation. In order to address this issue, the singularity of the boundary integral is generally eliminated using the singular subtraction approach suggested in [38].

The remainder of this paper is organized as follows: a technique of extending *n*th order perturbation is introduced in Section 2 that

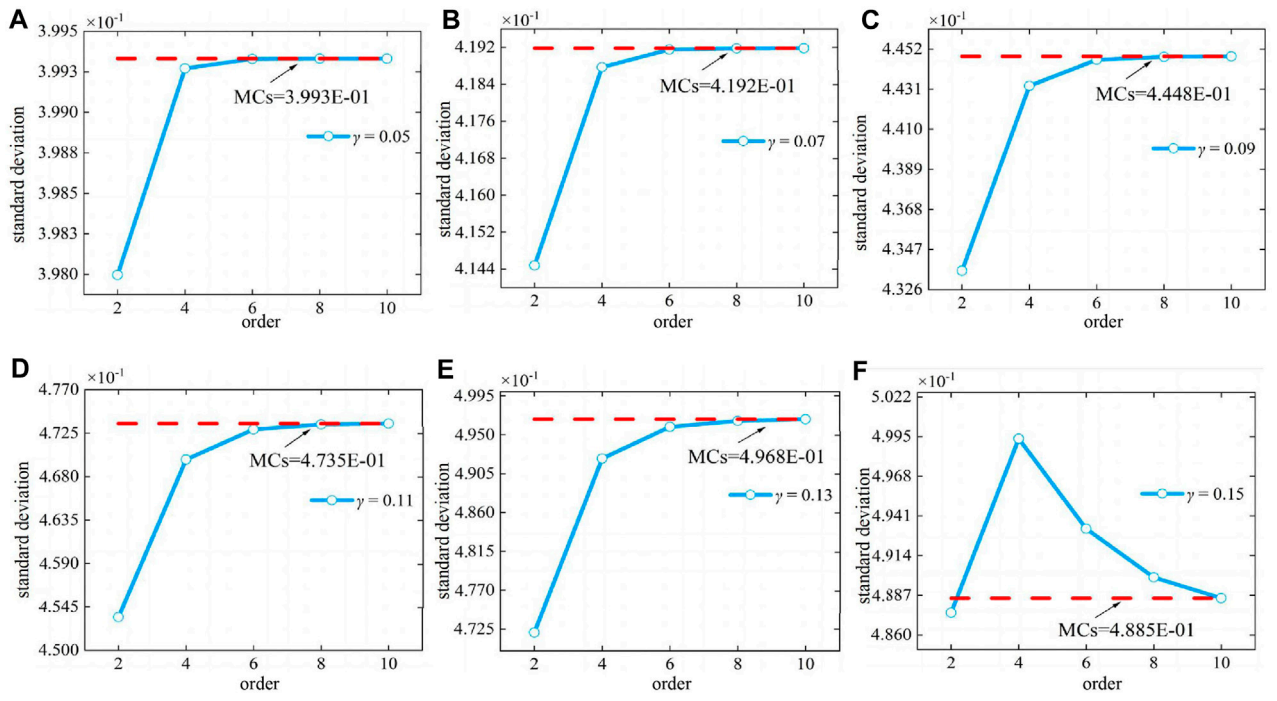

FIGURE 3
Curve of the standard deviation of the field function with derivatives for an infinite cylinder: **(A)** $\gamma = 0.05$, **(B)** $\gamma = 0.07$, **(C)** $\gamma = 0.09$, **(D)** $\gamma = 0.11$, **(E)** $\gamma = 0.13$, and **(F)** $\gamma = 0.15$.

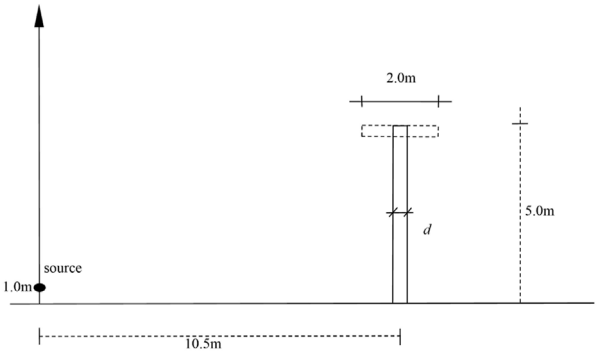

FIGURE 4
The apical shape is a cross-sectional view of the upright and T-shaped acoustic barriers.

employs equations for boundary integrals using random coefficients from the Taylor series. The equal geometric boundary element approach is described in Section 3. Section 4 provides three numerical instances that might be used to verify the suggested uncertainty analysis technique, followed by the conclusions in Section 5.

2 2D acoustic scattering using an isogeometric BEM based on perturbation method

Consider a two-dimensional domain enclosed by a boundary Γ. The symbol Ω represents the limitless domain outside the structural surface. Within Ω, the medium is a uniform ideal fluid. So the sound pressure satisfies the following wave equation:

$$\nabla^2 P(m,t) - \frac{1}{c_f^2}\frac{\partial^2 P(m,t)}{\partial t^2} = 0, \forall m \in \Omega, \tag{1}$$

where ∇^2 represents the Laplacian operator, $P(m, t)$ represents the sound pressure at point m in the middle of the sound field at time t, and c_f^2 represents the wave velocity. The sound pressure is expressed as

$$P(m,t) = p(m)e^{-i\omega t}, \tag{2}$$

where $p(m)$ represents the sound pressure value independent of time, $i = \sqrt{-1}$ represents an imaginary number, $2\pi f$ represents the circular frequency, and $e^{-i\omega t}$ represents the time-dependent terms. Then, the Helmholtz governing differential equation based on the sound pressure is obtained as follows:

$$\nabla^2 p(m) + k^2 p(m) = 0, \forall m \in \Omega, \tag{3}$$

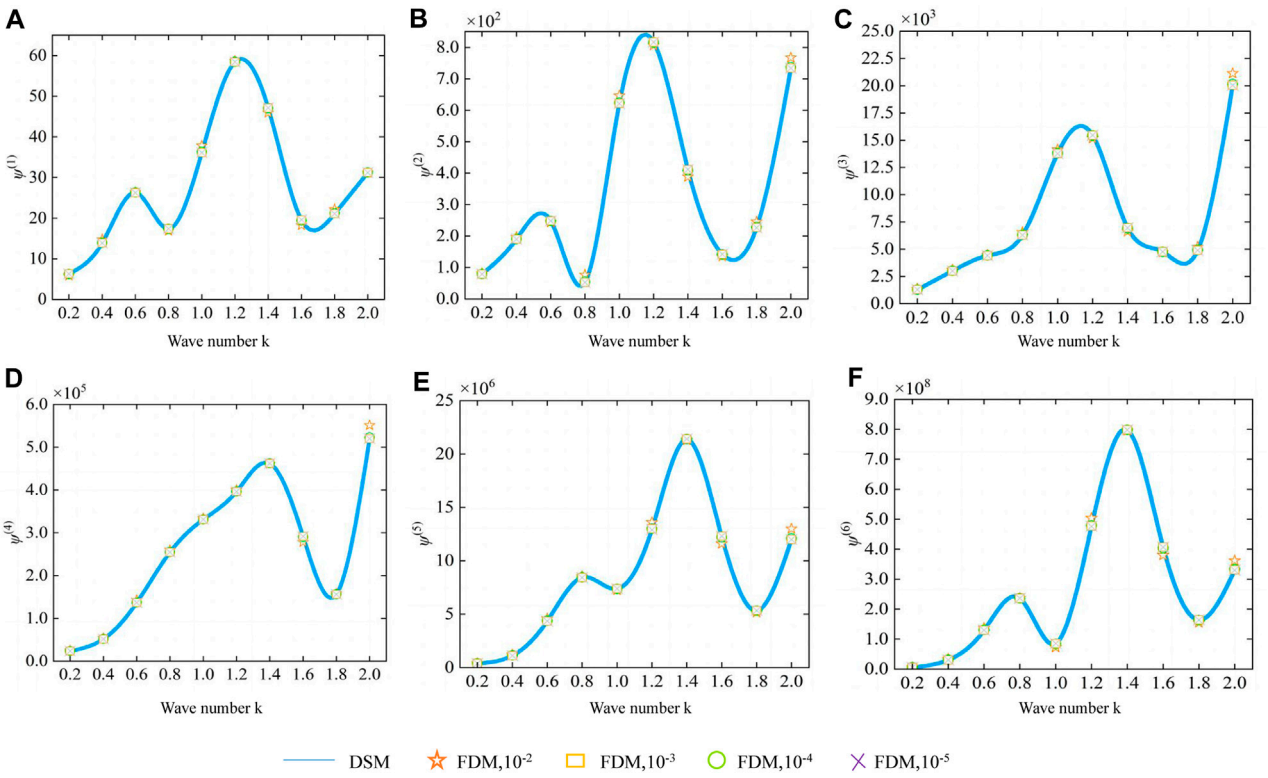

FIGURE 5
Curve plot of the amplitude of the rectangular field function oscillations as a function of the wave number k: **(A)** first-order, **(B)** second-order, **(C)** third-order, **(D)** fourth-order, **(E)** fifth-order, and **(F)** sixth-order derivatives.

TABLE 4 Relative errors ε_{err} of the first- and second-order derivatives of the rectangular field function.

Wave number	First-order derivative			Second-order derivative		
	$\Delta x = 10^{-2}$	$\Delta x = 10^{-3}$	$\Delta x = 10^{-4}$	$\Delta x = 10^{-2}$	$\Delta x = 10^{-3}$	$\Delta x = 10^{-4}$
0.2	0.06702	0.00649	0.00065	0.02994	0.00282	0.00028
0.4	0.05976	0.00632	0.00064	0.03453	0.00359	0.00036
0.6	0.00376	0.00049	0.00005	0.01789	0.00158	0.00016
0.8	0.03049	0.00324	0.00033	0.31533	0.04217	0.00436
1.0	0.04514	0.00473	0.00048	0.03853	0.00407	0.00041
1.2	0.00351	0.00043	0.00004	0.01186	0.00107	0.00011
1.4	0.02602	0.00251	0.00025	0.05911	0.00569	0.00057
1.6	0.07236	0.00691	0.00069	0.04941	0.00476	0.00047
1.8	0.04845	0.00512	0.00052	0.07659	0.00809	0.00081

TABLE 5 Relative errors ε_{err} of the third- and fourth-order derivatives of the rectangular field function.

Wave number	Third-order derivative			Fourth-order derivative		
	$\Delta x = 10^{-2}$	$\Delta x = 10^{-3}$	$\Delta x = 10^{-4}$	$\Delta x = 10^{-2}$	$\Delta x = 10^{-3}$	$\Delta x = 10^{-4}$
0.2	0.05134	0.00527	0.00053	0.04413	0.00460	0.00046
0.4	0.02880	0.00297	0.00030	0.04405	0.00444	0.00044
0.6	0.01015	0.00104	0.00010	0.04222	0.00436	0.00044
0.8	0.03797	0.00377	0.00038	0.01865	0.00192	0.00019
1.0	0.02573	0.00269	0.00027	0.00963	0.00097	0.00010
1.2	0.01860	0.00173	0.00017	0.00983	0.00098	0.00010
1.4	0.05031	0.00503	0.00050	0.00214	0.00014	0.00001
1.6	0.01398	0.00132	0.00013	0.04818	0.00464	0.00046
1.8	0.05969	0.00585	0.00058	0.01217	0.00092	0.00009

where $k = \omega\sqrt{\epsilon\mu}$ denotes the wave number of the medium Ω. The boundary integral formula of the scalar Helmholtz formula can be obtained as

$$c(\mathbf{m})p(\mathbf{m};k) + \int_{\Gamma} R(\mathbf{m},\mathbf{y};k)p(\mathbf{y};k)d\Gamma(\mathbf{y}) = \int_{\Gamma} G(\mathbf{m},\mathbf{y};k)q(\mathbf{y};k)d\Gamma(\mathbf{y}) + p_{\text{inc}}(\mathbf{m};k). \tag{4}$$

If the source point is represented by $\mathbf{m}$ and the field point is represented by $\mathbf{y}$, the coefficient $c(\mathbf{m})$ is determined by the geometric features at point $\mathbf{m}$. $c(\mathbf{m})$ equals 1/2 when the boundary is smooth at $\mathbf{m}$. The symbol $\int$ in Eq. 4 represents the integral in the sense of Cauchy principal value. It implies that the integral does not include the case where $\mathbf{m} = \mathbf{y}$. $q(\mathbf{y};k) = \frac{\partial p(\mathbf{y};k)}{\partial n(\mathbf{y})}$ represents the acoustic flux, and $p_{\text{inc}}(\mathbf{m};k)$ is the sound pressure present at location $\mathbf{m}$ of the incident wave. The Green functions in media are defined as $G(\mathbf{m},\mathbf{y};k)$ and are expressed as

$$G(\mathbf{m},\mathbf{y};k) = \frac{\mathrm{i}}{4}H_0^{(1)}(k\mathbf{r}), \tag{5}$$

where $H_n^{(1)}$ is the first kind of the nth-order Hankel function and $\mathbf{r} = \|\mathbf{m} - \mathbf{y}\|$ is the Euclidean distance between the source location and the field point. $R(\mathbf{m},\mathbf{y};k)$, representing the variations of the Green's functions G($\mathbf{m}$, $\mathbf{y}$; k) with regard to the standard $n(\mathbf{y})$, is given by

$$R(\mathbf{m},\mathbf{y};k) = \frac{\partial G(\mathbf{m},\mathbf{y};k)}{\partial n(\mathbf{y})} = -\frac{ik}{4}H_1^{(1)}(k\mathbf{r})\frac{[\mathbf{r}]\cdot\hat{\mathbf{n}}(\mathbf{y})}{\mathbf{r}}. \tag{6}$$

It is important to note that the non-uniqueness issue arises when solving outer boundary-value issues using Eq. 4. This issue may be solved using the Burton–Miller formulation [49, 50]; it is derived by combining Eq. 4 with its standard derivation while considering the outside standard at the location specified in Eq. 4. This secondary formulation is written as

$$c(\mathbf{m})q(\mathbf{m};k) + \int_{\Gamma} \frac{\partial R(\mathbf{m},\mathbf{y};k)}{\partial n(\mathbf{m})}p(\mathbf{y};k)d\Gamma(\mathbf{y}) = \int_{\Gamma} \frac{\partial G(\mathbf{m},\mathbf{y};k)}{\partial n(\mathbf{m})}q(\mathbf{y};k)d\Gamma(\mathbf{y}) + \frac{\partial p_{\text{inc}}(\mathbf{m};k)}{\partial n(\mathbf{m})}, \tag{7}$$

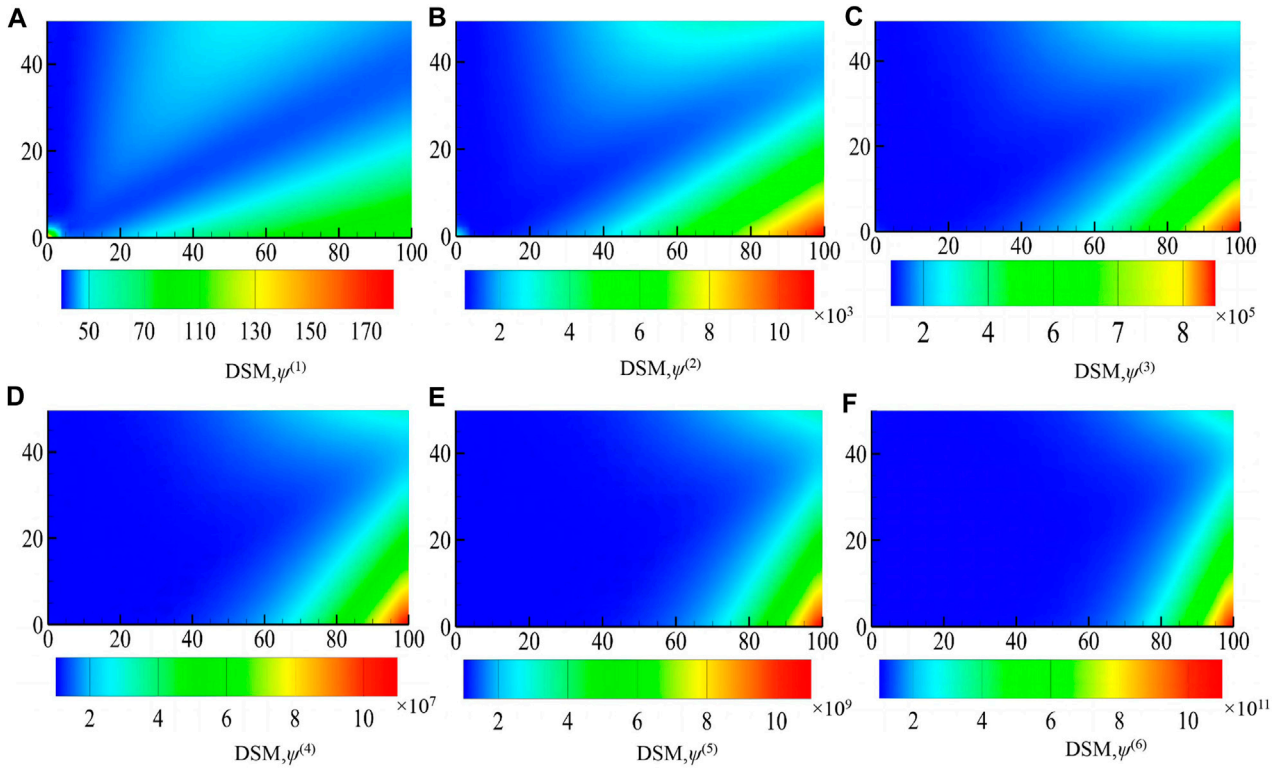

FIGURE 6
Rectangular field function derivative distribution cloud image: **(A)** first-order, **(B)** second-order, **(C)** third-order, **(D)** fourth-order, **(E)** fifth-order, and **(F)** sixth-order derivatives.

TABLE 6 Expectation of the rectangular field function with different coefficients of variation.

Order	Coefficient of variation (γ)					
	0.05	0.07	0.09	0.11	0.13	0.15
2	2.51572	2.72498	3.00399	3.35274	3.77126	3.89473
4	2.61297	3.09856	4.02484	5.63080	5.85923	5.87458
6	2.64064	3.30692	4.96601	5.92546	6.43758	6.58376
8	2.64658	3.31456	4.96826	5.92549	6.48424	6.58479
10	2.66128	3.31625	3.31625	5.92634	6.51458	6.58342
MCs	2.66128	3.31625	3.31625	5.92634	6.51458	6.58342

where

$$\begin{cases} \dfrac{\partial G(\mathbf{m},\mathbf{y};k)}{\partial n(\mathbf{m})} = -\dfrac{ik}{4}H_1^{(1)}(k\mathbf{r})\dfrac{[\mathbf{r}]\cdot\hat{\mathbf{n}}(\mathbf{m})}{\mathbf{r}}, \\ \dfrac{\partial R(\mathbf{m},\mathbf{y};k)}{\partial n(\mathbf{m})} = \dfrac{ik}{4\mathbf{r}}H_1^{(1)}(k\mathbf{r})[\hat{\mathbf{n}}(\mathbf{m})\cdot\hat{\mathbf{n}}(\mathbf{y})] - \\ \dfrac{ik^2}{4}H_2^{(1)}(k\mathbf{r})\dfrac{[\mathbf{r}\cdot\hat{\mathbf{n}}(\mathbf{m})][\mathbf{r}\cdot\hat{\mathbf{n}}(\mathbf{y})]}{\mathbf{r}^2}. \end{cases} \tag{8}$$

The linear mixture formulas of Eqs 4, 7 are generated as

$$\begin{aligned} & c(\mathbf{m})\left(p(\mathbf{m};k)+\alpha q(\mathbf{m};k)\right) \\ & +\int_\Gamma\left[R(\mathbf{m},\mathbf{y};k)+\alpha\frac{\partial R(\mathbf{m},\mathbf{y};k)}{\partial n(\mathbf{m})}\right]p(\mathbf{y};k)d\Gamma(\mathbf{y}) \\ & =\int_\Gamma\left[G(\mathbf{m},\mathbf{y};k)+\alpha\frac{\partial G(\mathbf{m},\mathbf{y};k)}{\partial n(\mathbf{m})}\right]q(\mathbf{y};k)d\Gamma(\mathbf{y})+q_{\text{inc}}(\mathbf{m};k), \end{aligned} \tag{9}$$

where $q_{\text{inc}}(\mathbf{m};k) = p_{\text{inc}}(\mathbf{m};k) + \alpha\frac{\partial p_{\text{inc}}(\mathbf{m};k)}{\partial n(\mathbf{m})}$. Its coupling coefficient $\alpha = \mathrm{i}/k$ for $k \geqslant 1$, and $\alpha = \mathrm{i}$ for $k < 1$.

2.1 *n*th-order generalized perturbation

In this work, the wave number k is used as a random input parameter. Given the unpredictability of this input parameter k, every variable and functions of state are extended using a Taylor series to approximate to their expected values. This is done by expanding the Taylor series around the point k_0, which serves as the expected value of k. The expansion of p, q, G, and R functions with $\Delta k = k - k_0$ can be written as

$$\begin{cases} p(k) = p(k_0) + \varepsilon p^{(1)}(k_0)\Delta k + \frac{1}{2}\varepsilon^2 p^{(2)}(k_0)[\Delta k]^2 + \cdots + \frac{1}{n!}\varepsilon^n p^{(n)}(k_0)[\Delta k]^n, \\ q(k) = q(k_0) + \varepsilon q^{(1)}(k_0)\Delta k + \frac{1}{2}\varepsilon^2 q^{(2)}(k_0)[\Delta k]^2 + \cdots + \frac{1}{n!}\varepsilon^n q^{(n)}(k_0)[\Delta k]^n, \\ G(k) = G(k_0) + \varepsilon G^{(1)}(k_0)\Delta k + \frac{1}{2}\varepsilon^2 G^{(2)}(k_0)[\Delta k]^2 + \cdots + \frac{1}{n!}\varepsilon^n G^{(n)}(k_0)[\Delta k]^n, \\ R(k) = R(k_0) + \varepsilon R^{(1)}(k_0)\Delta k + \frac{1}{2}\varepsilon^2 R^{(2)}(k_0)[\Delta k]^2 + \cdots + \frac{1}{n!}\varepsilon^n R^{(n)}(k_0)[\Delta k]^n. \end{cases} \tag{10}$$

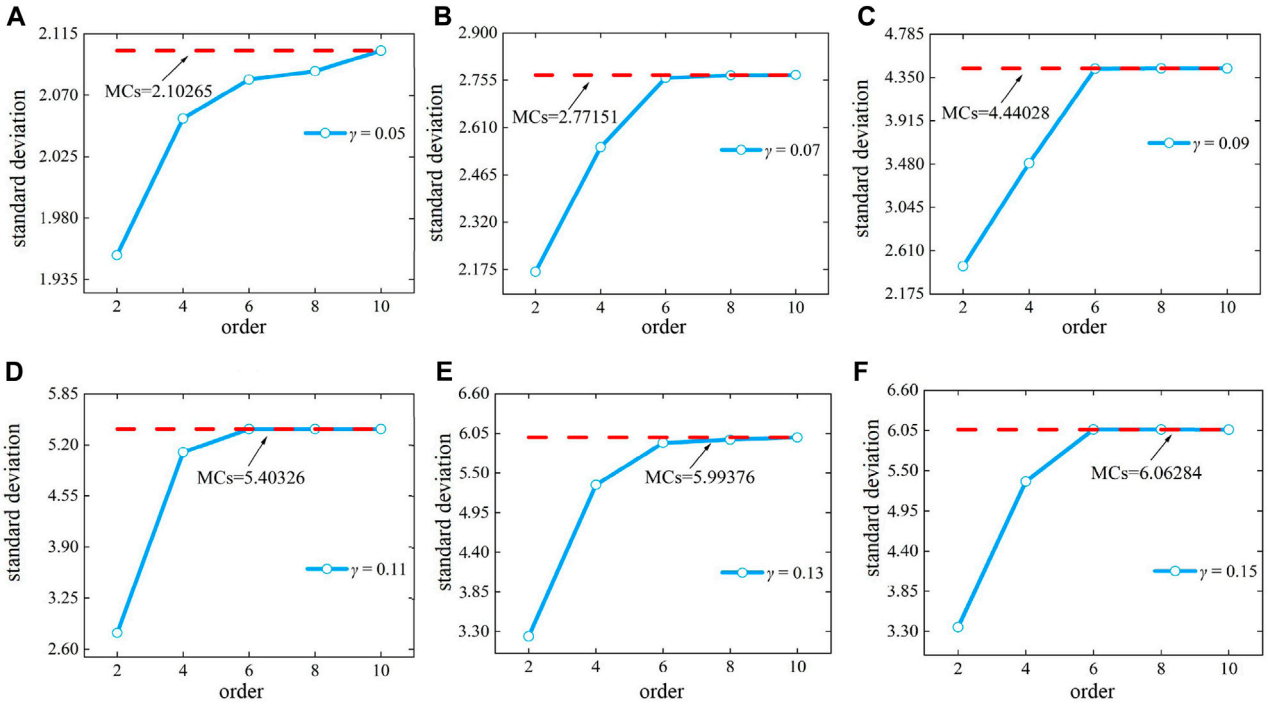

FIGURE 7
Plot of amplitude and standard deviation of the rectangular field function with different derivatives: **(A)** $\gamma = 0.05$, **(B)** $\gamma = 0.07$, **(C)** $\gamma = 0.09$, **(D)** $\gamma = 0.11$, **(E)** $\gamma = 0.13$, and **(F)** $\gamma = 0.15$.

The derivation of the boundary integral in Eq. 9 involves a nth-order expansion, which is written as

$$\begin{aligned} &c(\mathbf{m})\left[p^{(n)}(\mathbf{m}) + \alpha\hat{q}^{(n)}(\mathbf{m})\right] \\ &= \sum_{s=0}^{n}\binom{n}{s}\int_{\Gamma}\left[G^{(s)}(\mathbf{m},\mathbf{y})\hat{q}^{(n-s)}(\mathbf{y}) - R^{(s)}(\mathbf{m},\mathbf{y})p^{(n-s)}(\mathbf{y})\right]d\Gamma(\mathbf{y}) \\ &+ \alpha\sum_{s=0}^{n}\binom{n}{s}\int_{\Gamma}\left[\frac{\partial G^{(s)}(\mathbf{m},\mathbf{y})}{\partial n(\mathbf{m})}\hat{q}^{(n-s)}(\mathbf{y}) - \frac{\partial R^{(s)}(\mathbf{m},\mathbf{y})}{\partial n(\mathbf{m})}p^{(n-s)}(\mathbf{y})\right]d\Gamma(\mathbf{y}) \\ &+ \hat{p}_{\mathrm{inc}}^{(n)}(\mathbf{m}). \end{aligned} \tag{11}$$

To obtain a clear and simple expression corresponding to the sth-order derivative of the kernel function, as given in Eq. 11, we must first compute the product of the Hankel function. The Hankel function exhibits the following recursive feature:

$$\frac{\mathrm{d}H_n^{(1)}(z)}{\mathrm{d}z} = \frac{n}{z}H_n^{(1)}(z) - H_{n+1}^{(1)}(z). \tag{12}$$

The Hankel function's formula corresponding to the sth-order derivatives can be derived by repeatedly differentiating the aforementioned equation with respect to the variable z, as follows:

$$\left[H_n^{(1)}(z)\right]^{(s)} = \sum_{\ell=1}^{s}\left[H_n^{(1)}(z)\right]^{(s-\ell)}\frac{(-1)^{\ell+1}(s-1)!}{z^{\ell}(s-\ell)!} - \left[H_{n+1}^{(1)}(z)\right]^{(s-1)}. \tag{13}$$

Additionally, the functions $zH_1^{(1)}(z)$ and $z^2H_2^{(1)}(z)$ that define the kernel's sth-order derivative are obtained as

$$\begin{aligned} \left[zH_1^{(1)}(z)\right]^{(s)} &= s\left[H_1^{(1)}(z)\right]^{(s-1)} + z\left[H_1^{(1)}(z)\right]^{(s)}, \\ \left[z^2H_2^{(1)}(z)\right]^{(s)} &= \begin{cases} s(s-1)\left[H_2^{(1)}(z)\right]^{(s-2)} + 2sz\left[H_2^{(1)}(z)\right]^{(s-1)} + z^2\left[H_2^{(1)}(z)\right]^{(s)}, & s>1 \\ 2z\left[H_2^{(1)}(z)\right]^{(s-1)} + z^2\left[H_2^{(1)}(z)\right]^{(s)}, & s=1. \end{cases} \end{aligned} \tag{14}$$

Assuming $z = k\|\mathbf{m}-\mathbf{y}\|$ and $z_0 = k_0\|\mathbf{m}-\mathbf{y}\|$, the kernel operations for the sth-order derivative in Eq. 11 are deduced using Eqs 13, 14.

$$\begin{aligned} G^{(s)}(\mathbf{m},\mathbf{y};k_0) &= \frac{\mathrm{i}r^s}{4}\left[H_0^{(1)}(z_0)\right]^{(s)}, \\ R^{(s)}(\mathbf{m},\mathbf{y};k_0) &= -\frac{\mathrm{i}r^{(s-1)}}{4}\frac{\partial r}{\partial n(\mathbf{y})}\left[z_0H_1^{(1)}(z_0)\right]^{(s)}, \\ \frac{\partial G^{(s)}(\mathbf{m},\mathbf{y};k_0)}{\partial n(\mathbf{m})} &= -\frac{\mathrm{i}r^{(s-1)}}{4}\frac{\partial r}{\partial n(\mathbf{m})}\left[z_0H_1^{(1)}(z_0)\right]^{(s)}, \\ \frac{\partial R^{(s)}(\mathbf{m},\mathbf{y};k_0)}{\partial n(\mathbf{m})} &= \underbrace{\frac{\mathrm{i}r^{(s-2)}}{4}\left[\hat{\mathbf{n}}(\mathbf{m})\cdot\hat{\mathbf{n}}(\mathbf{y})\right]\left[z_0H_1^{(1)}(z)\right]^{(s)}}_{R_1^{(s)}} \\ &\quad \underbrace{-\frac{\mathrm{i}r^{(s-2)}}{4}\frac{\partial r}{\partial n(\mathbf{m})}\frac{\partial r}{\partial n(\mathbf{y})}\left[z_0^2H_2^{(1)}(z)\right]^{(s)}}_{R_2^{(s)}}, \end{aligned} \tag{15}$$

where $r = \|\mathbf{m}-\mathbf{y}\|$, $\frac{\partial r}{\partial n(\mathbf{m})} = \frac{[\mathbf{m}-\mathbf{y})\cdot\hat{\mathbf{n}}(\mathbf{m})}{\|\mathbf{m}-\mathbf{y}\|}$, and $\frac{\partial r}{\partial n(\mathbf{y})} = \frac{[\mathbf{m}-\mathbf{y})\cdot\hat{\mathbf{n}}(\mathbf{y})}{\|\mathbf{m}-\mathbf{y}\|}$.

3 BEM with isogeometric fast multipole

3.1 Irrational B-splines which is not uniform

In isogeometric analysis, geometric and physical fields are approximated using NURBS basis functions. A knot vector,

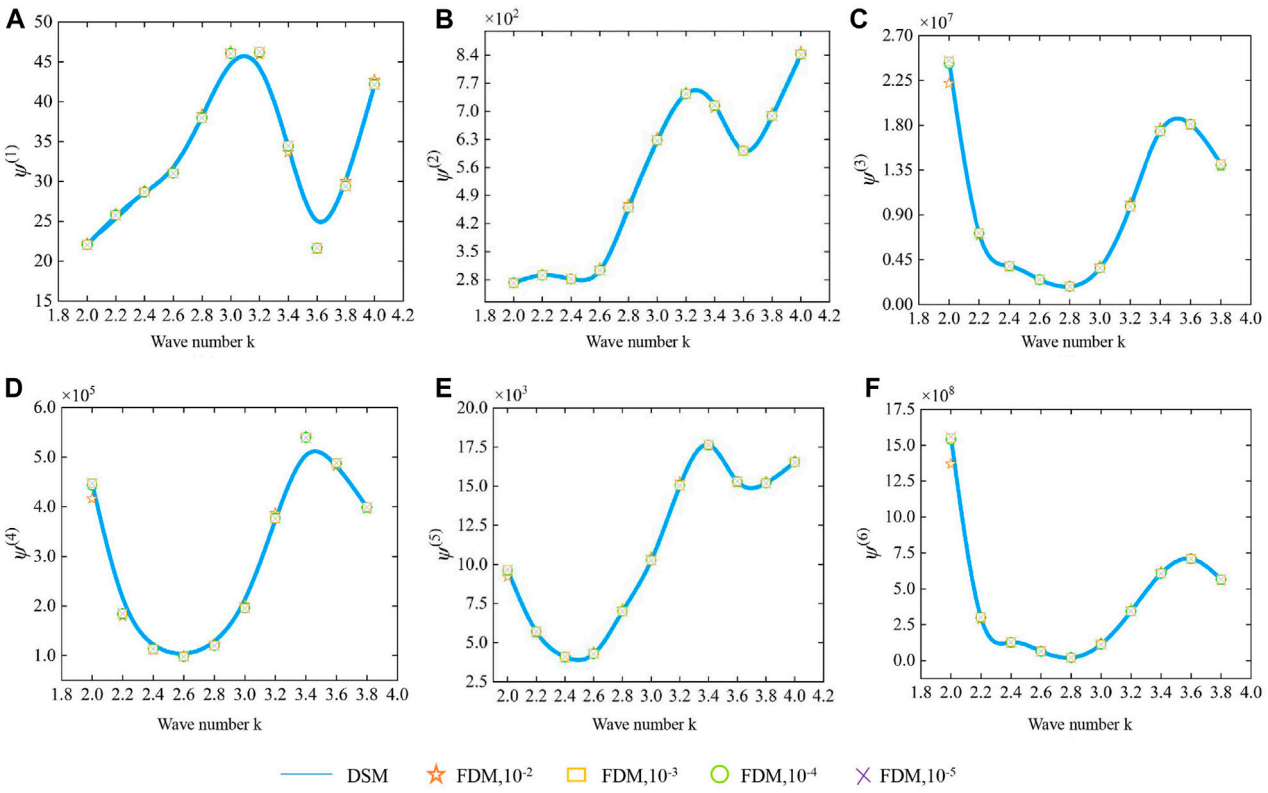

FIGURE 8
Plot of the amplitude of the T-shaped field function as a function of the wave number *k*: **(A)** first-order, **(B)** second-order, **(C)** third-order, **(D)** fourth-order, **(E)** fifth-order, and **(F)** sixth-order derivatives.

TABLE 7 Relative errors ε_{err} of the third- and fourth-order derivatives of the T-shaped field function.

Wave number	First-order derivative			Second-order derivative		
	$\Delta x = 10^{-2}$	$\Delta x = 10^{-3}$	$\Delta x = 10^{-4}$	$\Delta x = 10^{-2}$	$\Delta x = 10^{-3}$	$\Delta x = 10^{-4}$
2.0	0.007834	0.000783	0.000078	0.001723	0.000232	0.000024
2.2	0.007082	0.000717	0.000072	0.002750	0.000295	0.000030
2.4	0.003411	0.000347	0.000035	0.004442	0.000450	0.000045
2.6	0.006644	0.000647	0.000065	0.016573	0.001619	0.000161
2.8	0.011907	0.001199	0.000120	0.019420	0.001978	0.000198
3.0	0.005590	0.000582	0.000059	0.011636	0.001184	0.000119
3.2	0.006634	0.000628	0.000062	0.004184	0.000443	0.000045
3.4	0.024425	0.002377	0.000237	0.008932	0.000865	0.000086
3.6	0.005213	0.000675	0.000068	0.001565	0.000209	0.000021
3.8	0.021712	0.002208	0.000221	0.011006	0.001105	0.000111

which is a collection of non-decreasing real values, generates a non-uniform rational B-splines (NURBS) curve as follows: $\Xi = [\xi_0, \xi_1, \ldots, \xi_{n+p+1}]$with $\xi_a \in \mathbb{R}$, where p is the rank of the polynomial, n is the basic function or control point count, and a is the node index. The recursive formulation of the B-spline basis function $N_{a,p}$ is written as

$$N_{a,0}(\xi) = \begin{cases} 1 & \text{if} \quad \xi_a \le \xi < \xi_{a+1}, \\ 0 & \text{otherwise,} \end{cases} \tag{16}$$

and for $p = 1, 2, 3, \ldots$,

$$N_{a,p}(\xi) = \frac{\xi - \xi_a}{\xi_{a+p} - \xi_a} N_{a,p-1}(\xi) + \frac{\xi_{a+p+1} - \xi}{\xi_{a+p+1} - \xi_{a+1}} N_{a+1,p-1}(\xi). \tag{17}$$

TABLE 8 Relative errors ε_{err} of first- and second-order derivatives of the T-shaped field function.

Wave number	Third-order derivative			Fourth-order derivative		
	$\Delta x = 10^{-2}$	$\Delta x = 10^{-3}$	$\Delta x = 10^{-4}$	$\Delta x = 10^{-2}$	$\Delta x = 10^{-3}$	$\Delta x = 10^{-4}$
2.0	0.046993	0.004742	0.000475	0.074230	0.007397	0.000740
2.2	0.015218	0.001519	0.000152	0.028162	0.002809	0.000281
2.4	0.016825	0.001702	0.000170	0.019696	0.001991	0.000199
2.6	0.024099	0.002391	0.000239	0.005452	0.000510	0.000051
2.8	0.020400	0.002077	0.000208	0.015680	0.001545	0.000154
3.0	0.019244	0.001935	0.000194	0.032066	0.003234	0.000324
3.2	0.015844	0.001623	0.000162	0.027878	0.002859	0.000287
3.4	0.002134	0.000170	0.000016	0.004899	0.000550	0.000056
3.6	0.006509	0.000677	0.000068	0.011701	0.001157	0.000116
3.8	0.004120	0.000407	0.000041	0.006975	0.000710	0.000071

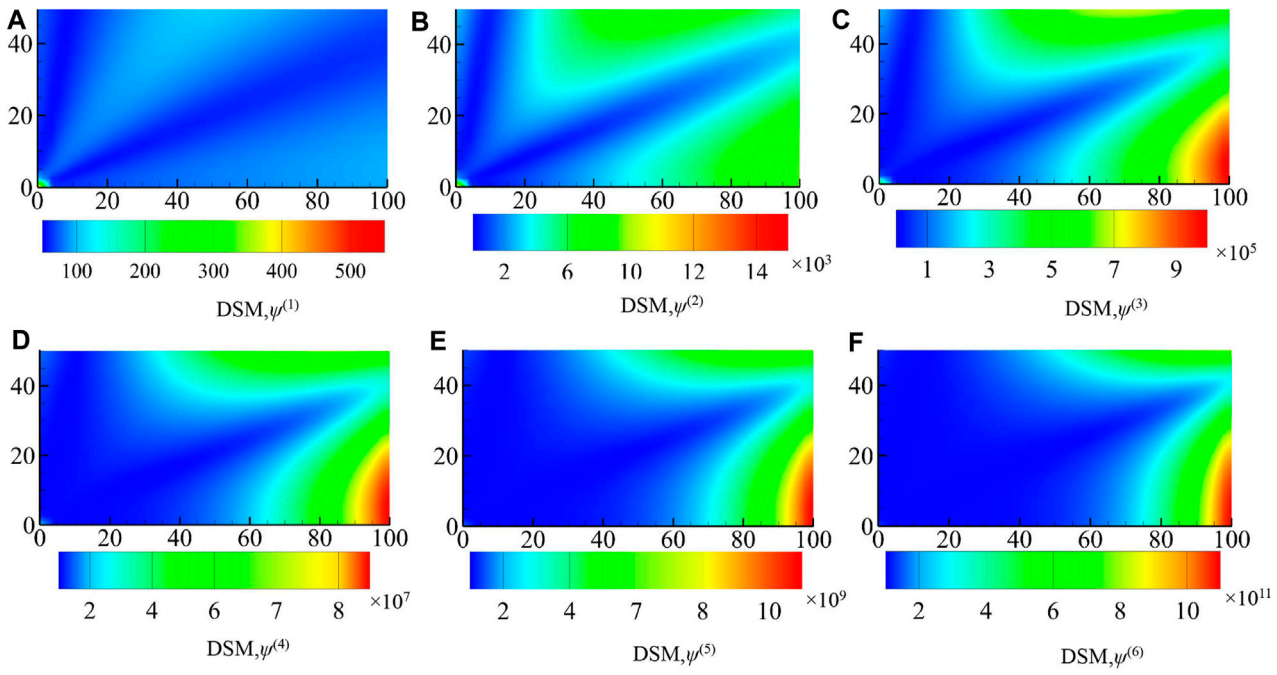

FIGURE 9
Distribution of T-shaped field functions under different derivatives: **(A)** first-order, **(B)** second-order, **(C)** third-order, **(D)** fourth-order, **(E)** fifth-order, and **(F)** sixth-order derivatives.

The basis functions for B-splines exhibit some advantageous characteristics, including locality, point non-negativeness, linear independence, and simplicity of numerical analysis. NURBS is created using a B-spline and control point weights:

$$B_{a,p}(\xi) = \frac{N_{a,p}(\xi) w_a}{W(\xi)}, \tag{18}$$

with

$$W(\xi) = \sum_{a=0}^{n} w_a N_{a,p}(\xi), \tag{19}$$

where w_a stands for a weight connected to each control point and $B_{a,p}(\xi)$ stands for NURBS basis functions. Consequently, the NURBS curve point $\mathbf{x}(\xi)$ is calculated as

$$\mathbf{x}(\xi) = \sum_{a=0}^{n} B_{a,p}(\xi) \mathbf{P}_a, \tag{20}$$

TABLE 9 Expectation of the T-shaped field function with different coefficients of variation.

Order	Coefficient of variation (γ)					
	0.05	0.07	0.09	0.11	0.13	0.15
2	1.56901	1.79665	2.10017	2.47957	2.93485	3.46601
4	1.58434	1.85556	2.26115	2.83879	3.63561	4.70813
6	1.58523	1.86226	2.29143	2.93976	3.91071	5.35732
8	1.58588	1.87181	2.30270	2.94463	3.92112	5.36010
10	1.58599	1.87181	2.30270	2.94463	3.92112	5.36010
MCs	1.58599	1.87181	2.30270	2.94463	3.92112	5.36010

where $\mathbf{P}_a$ refers to the ath command point.

3.2 Discretizations

The coefficients of the derivative of the pressure of sound and flux fields on the boundary, as given in Eq. 11, have been interpolated applying NURBS basis functions utilizing the IGA technique, as follows:

$$p^{(n)}(\xi) = \sum_{a=0}^{n_f} B_{a,p_f}(\xi) p_a^{(n)}, \qquad q^{(n)}(\xi) = \sum_{a=0}^{n_f} B_{a,p_f}(\xi) q_a^{(n)}, \tag{21}$$

where n_f indicates the amount of integration points, p_f denotes the order of the polynomial, and $p_a^{(n)}$ and $q_a^{(n)}$ represent the worldwide derivative sound pressure and flow characteristics associated with the ath control point, respectively.

Because the Kronecker delta condition is not satisfied with NURBS basis functions, $p_a^{(n)}$ and $q_a^{(n)}$ do not represent a field and flux within the boundary's derivative values. As a result, the collocation points must be rebuilt. In this study, the Greville abscissa method is utilized, and collocation points are created in the parameter space, as demonstrated in the following equation:

$$\widehat{\xi}_a = \frac{\xi_{a+1}^f + \xi_{a+2}^f + \cdots + \xi_{a+p_f}^f}{p_f}, \quad a = 0, 1, \ldots, n_f. \tag{22}$$

The discretized versions of isogeometric BEM are obtained by substituting Eq. 21 into Eq. 11.

$$\begin{aligned} & c\left(\mathbf{x}\left(\widehat{\xi}_a\right)\right) \sum_{\kappa=0}^{n_f} B_\kappa\left(\widehat{\xi}_a\right)\left(p_\kappa^{(n)} + \alpha q_\kappa^{(n)}\right) \\ &= \sum_{s=0}^{n} \frac{n!}{s!(n-s)!} \sum_{e=1}^{N_e} \sum_{\kappa=0}^{n_f} \left[\int_{\xi_e}^{\xi_{e+1}} G^{(s)} B_\kappa(\xi) J(\xi) d\xi \right] q_\kappa^{(n-s)} \\ &\quad - \sum_{s=0}^{n} \frac{n!}{s!(n-s)!} \sum_{e=1}^{N_e} \sum_{\kappa=0}^{n_f} \left[\int_{\xi_e}^{\xi_{e+1}} R^{(s)} B_\kappa(\xi) J(\xi) d\xi \right] p_\kappa^{(n-s)} \\ &\quad + \alpha \sum_{s=0}^{n} \frac{n!}{s!(n-s)!} \sum_{e=1}^{N_e} \sum_{\kappa=0}^{n_f} \left[\int_{\xi_e}^{\xi_{e+1}} \frac{\partial G^{(s)}}{\partial n(\mathbf{x})} B_\kappa(\xi) J(\xi) d\xi \right] q_\kappa^{(n-s)} \\ &\quad - \alpha \sum_{s=0}^{n} \frac{n!}{s!(n-s)!} \sum_{e=1}^{N_e} \sum_{\kappa=0}^{n_f} \left[\int_{\xi_e}^{\xi_{e+1}} \frac{\partial R^{(s)}}{\partial n(\mathbf{x})} B_\kappa(\xi) J(\xi) d\xi \right] p_\kappa^{(n-s)} \\ &\quad + q_{\text{inc}}^{(n)}\left(\mathbf{x}\left(\widehat{\xi}_a\right)\right), \end{aligned} \tag{23}$$

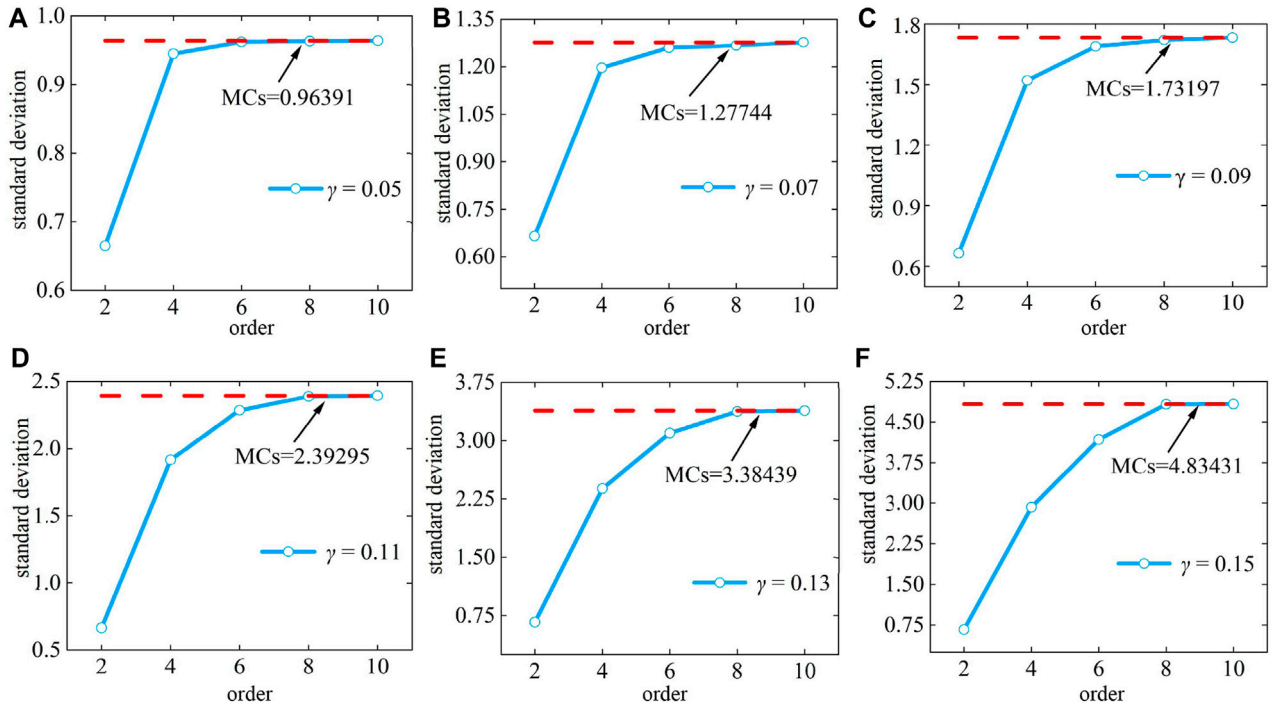

FIGURE 10
The curve where the standard deviation of a T-shaped field function changes with the derivative: **(A)** $\gamma = 0.05$, **(B)** $\gamma = 0.07$, **(C)** $\gamma = 0.09$, **(D)** $\gamma = 0.11$, **(E)** $\gamma = 0.13$, and **(F)** $\gamma = 0.15$.

where $a = 0, 1, \ldots, n_f$. The period of time between two non-repeating intersections is represented by the NURBS element $[\xi_e, \xi_{e+1}]$, N_e indicates the number of NURBS elements, and $J(\xi)$ indicates the Jacobian.

The matrix representation of the discretization of the boundary value integral equations using the nth-order derivative is as follows:

$$\sum_{s=0}^{n} \frac{n!}{s!(n-s)!}\left[\bar{\mathbf{R}}^{(s)}\boldsymbol{p}^{(n-s)} - \bar{\mathbf{G}}^{(s)}\boldsymbol{q}^{(n-s)}\right] = \boldsymbol{q}_{\text{inc}}^{(n)}. \tag{24}$$

By rearranging each term and applying the boundary conditions, the equations can be solved as follows:

$$\mathbf{Ax} = \mathbf{B}. \tag{25}$$

Taking the incident wave into consideration, $\mathbf{x} = \boldsymbol{p}^{(n)}$ is an unknown quantity on the boundary of the matrix. $\mathbf{A} = \bar{\mathbf{R}}^0$, which is an asymmetrical dense matrix. $\mathbf{B}$ is a known vector obtained by the matrix multiplication of vector operations.

$$\mathbf{B} = \sum_{s=0}^{n} \frac{n!}{s!(n-s)!}\bar{\mathbf{G}}^{(s)}\boldsymbol{q}^{(n-s)} - \sum_{s=1}^{n} \frac{n!}{s!(n-s)!}\bar{\mathbf{R}}^{(s)}\boldsymbol{p}^{(n-s)} + \boldsymbol{q}_{\text{inc}}^{(n)}. \tag{26}$$

Eq. 25 can be solved with $n = 0$ to obtain the field vector $\boldsymbol{p}^0$ result. Next, the field's initial derivative value concerning the random number is determined by substituting $\boldsymbol{p}^0$ into Eq. 25 with $n = 1$. By analogy, it is possible to determine the value of a field derivative for any order. Finally, the following two equations can be used to determine the expectation and variance of the field at these border points:

$$E(u(k)) = \int_{-\infty}^{+\infty} u(k)\rho(k)\,\mathrm{d}k \tag{27}$$

and

$$V(u(k)) = \int_{-\infty}^{+\infty} [u(k) - E(u(k))]^2\rho(k)\,\mathrm{d}k. \tag{28}$$

Where $\rho(k)$ represents the probability density function, and the field variable of is represented by u of p, q, G or R, and $u(k)$ represents the k-fold density of probability function.

It is crucial to remember that the kernel functions' derivatives of the boundary integral, as given in Eq. 11, are singular. Singular integrals of this nature require special treatment. Such integrals may be explicitly and directly derived utilizing the Hadamard finite-part integral and Cauchy principal value methods.

The singularity of Eq. 24 is up to the second order. Therefore, a numerical instance of spline order 2 can thus be accepted.

3.3 Accelerating using the fast multipole method

Applying the FMM will accelerate the matrix–vector product of isogeometric finite elements in Eq. 11. The key core of FMM is to form a tree structure and delineate the boundary integrals. The original boundary integral is divided into a near-field part and a far-field part, and the near-field part is generally calculated using conventional BEM, while the far-field part is calculated using accelerated FMM-based BEM. In the stochastic analysis involved in this work, the presence of higher-order derivatives of the Green's function can make the fast algorithm more complex and difficult to implement. The detailed calculation procedure is as follows:

$$G(\mathbf{x},\mathbf{y}) = \frac{\mathrm{i}}{4}\sum_{\tilde{m}=-\infty}^{+\infty} O_{\tilde{m}}(\overrightarrow{\mathbf{y}_c\mathbf{x}})I_{-\tilde{m}}(\overrightarrow{\mathbf{y}_c\mathbf{y}}), \tag{29}$$

where $\mathbf{y}_c$ is the unfolding point around $\mathbf{y}$ and the functions $O_{\tilde{m}}$ and $I_{\tilde{m}}$ are defined as

$$\begin{aligned} O_{\tilde{m}}(\mathbf{z}) &= \mathrm{i}^{\tilde{m}}H_{\tilde{m}}^{(1)}(kr)e^{\mathrm{i}\tilde{m}\theta}, \\ I_{\tilde{m}}(\mathbf{z}) &= (-\mathrm{i})^{\tilde{m}}J_{\tilde{m}}(kr)e^{\mathrm{i}\tilde{m}\theta}, \end{aligned} \tag{30}$$

where $J_{\tilde{m}}$ denotes a Bessel function of order $\tilde{m}$ and (r, θ) is the polar coordinate of the vector $\mathbf{z}$. The random input variable is repeatedly used to distinguish Eq. 29 from the following equation.

$$G^{(s)}(\mathbf{x},\mathbf{y}) = \frac{\mathrm{i}}{4}\sum_{\ell=0}^{s}\left[\frac{s!}{\ell!(s-\ell)!}\sum_{\tilde{m}=-\infty}^{+\infty} O_{\tilde{m}}^{(\ell)}(\overrightarrow{\mathbf{y}_c\mathbf{x}})I_{-\tilde{m}}^{(s-\ell)}(\overrightarrow{\mathbf{y}_c\mathbf{y}})\right]. \tag{31}$$

Substituting Eq. 31 into Eq. 11, the integral equation can be expressed as follows:

$$\begin{aligned} &\int_{\Gamma_{\text{far}}}\left[G^{(s)}(\mathbf{x},\mathbf{y})\Phi^{(n-s)}(\mathbf{y}) - R^{(s)}(\mathbf{x},\mathbf{y})\psi^{(n-s)}(\mathbf{y})\right]d\Gamma(\mathbf{y}) \\ &\quad= \sum_{\ell=0}^{s}\left[\frac{s!}{\ell!(s-\ell)!}\sum_{\tilde{m}=-\infty}^{+\infty} O_{\tilde{m}}^{(\ell)}(\overrightarrow{\mathbf{y}_c\mathbf{x}})M_{\tilde{m},s-\ell}(\mathbf{y}_c)\right], \\ &\int_{\Gamma_{\text{far}}}\left[\frac{\partial G^{(s)}(\mathbf{x},\mathbf{y})}{\partial n(\mathbf{x})}\Phi^{(n-s)}(\mathbf{y}) - \frac{\partial R^{(s)}(\mathbf{x},\mathbf{y})}{\partial n(\mathbf{x})}\psi^{(n-s)}(\mathbf{y})\right]d\Gamma(\mathbf{y}) \\ &\quad= \sum_{\ell=0}^{s}\left[\frac{s!}{\ell!(s-\ell)!}\sum_{\tilde{m}=-\infty}^{+\infty} \frac{\partial O_{\tilde{m}}^{(\ell)}(\overrightarrow{\mathbf{y}_c\mathbf{x}})}{\partial n(\mathbf{x})}M_{\tilde{m},s-\ell}(\mathbf{y}_c)\right], \end{aligned} \tag{32}$$

where Γ_{far} stands for a subsection of the structural boundary located away from the source point $\mathbf{x}$ and $M_{\tilde{m},j-\ell}(\mathbf{y}_c)$ is the multipole moment of $(j - \ell)$ at the expansion point $\mathbf{y}_c$, which is denoted as follows:

$$M_{\tilde{m},s-\ell}(\mathbf{y}_c) = \frac{\mathrm{i}}{4}\int_{\Gamma_{\text{far}}}\left[I_{-\tilde{m}}^{(s-\ell)}(\overrightarrow{\mathbf{y}_c\mathbf{y}})\Phi^{(n-s)}(\mathbf{y}) - \frac{\partial I_{-\tilde{m}}^{(s-\ell)}(\overrightarrow{\mathbf{y}_c\mathbf{y}})}{\partial n(\mathbf{y})}\psi^{(n-s)}(\mathbf{y})\right]d\Gamma(\mathbf{y}). \tag{33}$$

Substituting Eq. 21 into Eq. 33, the discrete formula for the multipole moment is expressed as follows:

$$\begin{aligned} M_{\tilde{m},s-\ell}(\mathbf{y}_c) = \frac{\mathrm{i}}{4}\sum_{e=1}^{N_e}\sum_{\kappa=0}^{n_f}\Bigg[&\int_{\xi_e}^{\xi_{e+1}} I_{-\tilde{m}}^{(s-\ell)}B_\kappa(\xi)J(\xi)d\xi\Phi_\kappa^{(n-s)} \\ &-\int_{\xi_e}^{\xi_{e+1}} \frac{\partial I_{-\tilde{m}}^{(s-\ell)}}{\partial n(\mathbf{y}(\xi))}B_\kappa(\xi)J(\xi)d\xi\psi_\kappa^{(n-s)}\Bigg]. \end{aligned} \tag{34}$$

The calculation of the residual coefficients and translations, such as local-to-local, multipole-to-local, and multipole-to-multipole translations, is independent of the geometric representation and approximation of the field variables. So we can refer to [51] to

establish the continuum formulation of FMM for BEM, and the far-field integral equation could be written as

$$\begin{aligned}
&\int_{\Gamma_{\text{far}}}\left[G^{(s)}(\mathbf{x},\mathbf{y})\Phi^{(n-s)}(\mathbf{y})-R^{(s)}(\mathbf{x},\mathbf{y})\psi^{(n-s)}(\mathbf{y})\right]d\Gamma(\mathbf{y})\\
&\quad=\sum_{\ell=0}^{s}\left[\frac{s!}{\ell!(s-\ell)!}\sum_{\tilde{m}=-\infty}^{+\infty}I_{-\tilde{m}}^{(\ell)}(\overrightarrow{\mathbf{x}_1\mathbf{x}})L_{\tilde{m},s-\ell}(\mathbf{x}_1)\right],\\
&\int_{\Gamma_{\text{far}}}\left[\frac{\partial G^{(s)}(\mathbf{x},\mathbf{y})}{\partial n(\mathbf{x})}\Phi^{(n-s)}(\mathbf{y})-\frac{\partial R^{(s)}(\mathbf{x},\mathbf{y})}{\partial n(\mathbf{x})}\psi^{(n-s)}(\mathbf{y})\right]d\Gamma(\mathbf{y})\\
&\quad=\sum_{\ell=0}^{s}\left[\frac{s!}{\ell!(s-\ell)!}\sum_{\tilde{m}=-\infty}^{+\infty}\frac{\partial I_{-\tilde{m}}^{(\ell)}(\overrightarrow{\mathbf{x}_1\mathbf{x}})}{\partial n(\mathbf{x})}L_{\tilde{m},s-\ell}(\mathbf{x}_1)\right],
\end{aligned}\tag{35}$$

where $L_{\tilde{m},s-\ell}(\mathbf{x}_1)$ is the local moment of $(s-\ell)$ of the unfolding point $\mathbf{x}_1$, as detailed in [51].

It is important to note that the number of terms $\tilde{m}$ used in Eq. 31 should be truncated. An increase in the number of expansion terms usually not only results in higher precision but also consumes more memory and time. The formula $\tilde{M}=kd+c\cdot\log(kd+\pi)$ is provided in [52], where the parameter $\tilde{M}$ is the number of truncations, c is a constant, and d is the size of the cell. When $c=5$, there is a good balance between precision and performance, and it will be used in the following calculations [52]. The solution summary of geometric boundary element methods was studied in detail by [53]. The results of the study show that the solution time is improved when a corresponding higher order of convergence is reached in geometric boundary element methods. Therefore, it is the key parameter of the fast multipole isogeometric boundary element method.

4 Scattering by an infinite cylinder

Uncertainty analysis is used in this section using an example of acoustic dispersion from an endless cylinder. The existing direct uncertainty analysis approaches are first used to compare the derivative values with arbitrary ordering, and the global finite difference method (FDM) is established by

$$\psi'(x)=\frac{\psi(x+\Delta x)-\psi(x)}{\Delta x},\tag{36}$$

where Δx represents the minor disruption connected to x.

Several scenarios are taken into consideration in order to research the impact of perturbation Δx on the values of derivatives of field functions of every order, as illustrated in Figure 1. The image contrasts the magnitude of the field function's sixth-order derivative at various wave numbers k. Even for high-order derivatives, FDM and direct uncertainty analysis are trustworthy methods. The derivative value increases under a particular wave number as the field function's derivative number increases. Additionally, this behavior can be observed in real-world engineering applications.

Their relative errors under various Δx values are given to further analyze FDM and the accuracy of the initial uncertainty analysis. The estimated findings are shown in Tables 1, 2, which compare the relative errors ε_{err} of the direct uncertainty analysis method (DSM) and FDM.

$$\varepsilon_{err}=\frac{\left|\psi_{(DSM)}-\psi_{(FDM)}\right|}{\left|\psi_{(FDM)}\right|},\tag{37}$$

where $\psi_{(DSM)}$ and $\psi_{(FDM)}$ indicate the direct calculation approach and the finite difference method of solving the problem, respectively.

Tables 1, 2 show that, as the disturbance Δx reduces, the relative inaccuracy gradually diminishes. The relative errors of the various field function derivatives are typically limited to a relatively low number, which confirms the algorithm's accuracy.

Subsequently, the infinite cylinder's field function sensitivity distribution, as shown in Figure 2, facilitates a straightforward check of the algorithm's accuracy at a wave number $k=1$. The fact is that the distributions resulting from applying DSM and FDM were substantially consistent, as shown in Figure 2, confirming the accuracy of the algorithm used in this work once more.

The uncertainty of an infinite cylinder model is then examined using the perturbation method, where the value of the random variable k is set to be the wave number with a Gaussian distribution. The standard deviation is set in the range of $\sigma\in[0.05,0.15]$, the corresponding disruption parameter ε is 1, and the wave number k's average value μ is 1. The perturbation method with various order expansion terms is used to compare the first two probability moments of the field function at a position (10,0) with those of MCs. Here, the control group for MCs consists of 500 sample points produced utilizing a random number generator. The responses of 500 sampling points were obtained by repeatedly solving 500 inferior geometric fast multipole BEM equations using the isogeometric fast multipole BEM group. In actuality, this phase is time-consuming.

The predicted value of the field function for various $\gamma=\sigma/\mu$ coefficients of variation is shown in Table 3. The table shows that as the order of expansion increases, the perturbation method's output approaches that of MCs. The field function's standard deviation is shown in Figure 3 along with several coefficients of variation. Similar to this, the closer the outcome of the perturbation method is to MCs, the higher the order. We can also discover that this affects the perturbation method's computational convergence. The Taylor expansion's restriction causes the convergence to decline as the γ value increases.

4.1 Sound barrier structure

This section presents the noise distribution in the sound shadow area under two simple top shapes. The top shape is an upright rectangle, where the height of the linear sound source from the ground is 1 m, the distance from the sound barrier is 10.5 m, the width of the bottom of the sound barrier is 0.2 m, and the vibration frequency of the sound barrier is 100 Hz, as shown in Figure 4. All surfaces are assumed to be rigid surfaces, so the amount of attenuation of the diffracted sound waves determines the sound barrier's ability to reduce noise. Due to the total reflection of the ground, this analysis is used to solve a two-dimensional semi-space sound field problem. In the study of the sound barrier structure, the boundary element method only needs to be discretized by a grid instead of discretizing the infinite ground, which shows that the boundary element method has great advantages in calculating the sound field problem in an infinite domain. The vertical sound barrier boundary is discretized into 100 constant boundary units.

4.1.1 Rectangular model

We regard the input parameter as random—the wave number that adheres to the Gaussian distribution. Figure 5 studies the first, second, and third and fourth, fifth, and sixth variations of the field function with respect to random parameters at the position (10, 0). The derivative amplitude of the field function is calculated using FDM DSM. The steps of FDM are set at $\Delta k = 10^{-2}k$, $\Delta k = 10^{-3}k$, $\Delta k = 10^{-4}k$, and $\Delta k = 10^{-5}k$. The results of FDM and the direct uncertainty analysis approach are comparable, as shown in Figure 5.

Their relative errors under various Δx values are given to further investigate the accuracy of FDM and the explicit uncertainty analysis technique. The relative error ε_{err} values of the direct uncertainty analysis approach and FDM are provided in Tables 4, 5. They show that when the disruptions Δx increase, the relative error steadily reduces. The fact that the relative errors of the various field function derivatives are maintained at a relatively low level confirms the algorithm's accuracy.

We look at the sensitivity field function's distribution around the infinite cylinder when the wave number $k = 1$ to more easily ascertain the algorithm's accuracy, as shown in Figure 6. It shows that the distribution generated by the direct technique for uncertainty analysis is essentially consistent with that obtained by FDM, further demonstrating the algorithm's accuracy.

Then, using a rectangular model with the number of waves k considered to be a Gaussian-distributed random quantity, we analyzed uncertainty using the perturbation method. The relevant interference parameter ε is set to 1, the mean value of the number of waves k is set to 1, and the normal deviation is set in the range of $\sigma \in [0.05, 0.15]$. Comparisons are made between the probability moments acquired by MCs and the first two probability moments of the field function at a position (10, 0) generated by the perturbation method with extensions of various orders. The predicted value of the field function for various coefficients of variation $\gamma = \sigma/\mu$ is shown in Table 6. It shows that as the order of expansion increases, the perturbation method's results approach those of the MCs. The predicted value and standard deviation of the field function for the extension are displayed in Figure 7.

The predicted value and standard deviation of the field function for the extension are displayed in Figure 7. The figure illustrates that, as the expansion term lengthens, the results of the two probability moments calculated using this approach closely approximate to those of MCs. In addition, poor convergence results from an increase in the coefficient of variation γ.

4.1.2 T-shaped model

Similar to the aforementioned rectangular model in this paper, we consider the input parameters to be random parameters and treat the computation of the derivative amplitudes of the treated field functions in the same way. That is, the following figure shows the variation in the first- to sixth-order derivative random parameters of the field function for the position point (10, 0), and the comparison of the results of FDM and the direct deterministic analysis method is shown in Figure 8. Then, the accuracy of FDM and direct uncertainty analysis techniques is further analyzed by their relative errors at different Δx. The relative errors, as shown in Tables 7, 8, indicate a decreasing trend with increasing Δx.

We also investigate the distribution of the sensitivity field function around the infinite cylinder when the wave number is 1, as shown in Figure 9. This result further demonstrates the accuracy of the algorithm. Using a T-shaped model with a Gaussian-distributed random quantity with a wave number k, the uncertainty is analyzed using the perturbation method, the relevant disturbance parameter ε is set to 1, the mean value μ is also set to 1, and the normal deviation is set in the range of $\sigma \in [0.05, 0.15]$. By comparing the probability moments obtained under the perturbation method with those obtained by MCs, the predicted values of the field function under different coefficients of variation $\gamma = \sigma/\mu$ are shown in Table 9, and the predicted values and standard deviations of the extended field function are shown in Figure 10.

By analyzing these two numerical examples, Figures 7, 10 illustrate that as the expansion term lengthens, the results of the two probability moments calculated using this approach closely approximate to those of MCs. In addition, poor convergence results from an increase in the coefficient of variation γ.

5 Conclusion

The generalized nth-order perturbation approach is used in this study to analyze the uncertainty around sound wave propagation in an infinite domain. IGABEM enhances the precision and effectiveness of the stochastic perturbation method through the seamless integration of CAD and numerical analysis. Furthermore, it mainly uses NURBS to construct structural geometry and discretize the boundary integral equation. We discover that the isogeometric BEM simulation, which uses an exact geometric representation compared to a traditional Lagrange-based BEM simulation, is often more accurate. The investigation of the immediate uncertainty approach and finite difference method proves accurate for larger derivatives, which confirms the validity of the suggested algorithm. In addition, we compare this method with other derivatives generated by the global finite difference method. Under a specific wave number, the derivative value increases as the field function's derivative order increases. Additionally, this phenomenon can be utilized in real-world engineering applications. The result of uncertainty qualification shows that with the increase in the extended order term, the predicted value of field functions based on this technique is comparable to the anticipated value of MCSs, demonstrating the accuracy of the suggested methodology. The existing strategy has some drawbacks. When the unpredictability of the input random variable is high, capturing its statistical characteristics adequately can be challenging. While improving computation accuracy by modifying the order of the Taylor expansion, it also increases the cost of the calculation. In the future, we can extend the perturbation method to deal with three-dimensional acoustic scattering problems as well as target objects with more complex geometries, which will not only increase the complexity of the problem but also expand its range of applications. Uncertainty analysis of acoustic scattering problems at different frequencies can also be investigated to gain a more comprehensive understanding of the properties of acoustic wave propagation. This is essential for solving multi-frequency acoustic scattering problems and for practical applications.

Data availability statement

The original contributions presented in the study are included in the article/Supplementary material; further inquiries can be directed to the corresponding author.

Author contributions

YY: conceptualization, methodology, and writing–review and editing. RH: formal analysis, software, validation, and writing–original draft. XY: project administration, supervision, and writing–original draft. WW: software and writing–review and editing.

Funding

The author(s) declare that financial support was received for the research, authorship, and/or publication of this article. This research was supported by the Postgraduate Education Reform and Quality Improvement Project of Henan Province under Grant No. YJS2023JD52 and sponsored by the Laboratory of Aerodynamic Noise Control under Grant No. ANCL20220301. This research was supported by the Youth Backbone Teacher Training Program of Henan Province under Grant No. 2019GGJS232 and sponsored by the Key Scientific Research Project of Henan University under Grant No. 23A560015. This research was supported by the school funds of Guangzhou University under Grant No. 202201020134.

Conflict of interest

The authors declare that the research was conducted in the absence of any commercial or financial relationships that could be construed as a potential conflict of interest.

Publisher's note

References

1. Marburg S. Developments in structural-acoustic optimization for passive noise control. *Arch Comput Methods Eng* (2002) 9:291–370. doi:10.1007/bf03041465

2. Liu Y. On the bem for acoustic wave problems. *Eng Anal Boundary Elem* (2019) 107:53–62. doi:10.1016/j.enganabound.2019.07.002

3. Chen L, Lian H, Liu Z, Chen H, Atroshchenko E, Bordas S. Structural shape optimization of three dimensional acoustic problems with isogeometric boundary element methods. *Comp Methods Appl Mech Eng* (2019) 355:926–51. doi:10.1016/j.cma.2019.06.012

4. Chen L, Lu C, Lian H, Liu Z, Zhao W, Li S, et al. Acoustic topology optimization of sound absorbing materials directly from subdivision surfaces with isogeometric boundary element methods. *Comp Methods Appl Mech Eng* (2020) 362:112806. doi:10.1016/j.cma.2019.112806

5. Zhang J, Lin W, Shu X, Zhong Y. A dual interpolation boundary face method for exterior acoustic problems based on the burton–miller formulation. *Eng Anal Boundary Elem* (2020) 113:219–31. doi:10.1016/j.enganabound.2020.01.005

6. Bourlier C, Pinel N, Kubicke G. *Method of moments for the scattering from 2d problems: basic concepts and applications* (2013).

7. Li H, Zhao J, Guo X, Cheng Y, Xu Y, Yuan X. Sensitivity analysis of flexoelectric materials surrogate model based on the isogeometric finite element method. *Front Phys* (2022) 10:1343. doi:10.3389/fphy.2022.1111159

8. Qu Y, Pan E, Zhu F, Jin F, Roy A. Modeling thermoelectric effects in piezoelectric semiconductors: new fully coupled mechanisms for mechanically manipulated heat flux and refrigeration. *Int J Eng Sci* (2023) 182:103775. doi:10.1016/j.ijengsci.2022.103775

9. Xu Y, Li H, Chen L, Zhao J, Zhang X. Monte Carlo based isogeometric stochastic finite element method for uncertainty quantization in vibration analysis of piezoelectric materials. *Mathematics* (2022) 10:1840. doi:10.3390/math10111840

10. Shen X, Du C, Jiang S, Zhang P, Chen L. Multivariate uncertainty analysis of fracture problems through model order reduction accelerated sbfem. *Appl Math Model* (2024) 125:218–40. doi:10.1016/j.apm.2023.08.040

11. Shen X, Du C, Jiang S, Sun L, Chen L. Enhancing deep neural networks for multivariate uncertainty analysis of cracked structures by pod-rbf. *Theor Appl Fracture Mech* (2023) 125:103925. doi:10.1016/j.tafmec.2023.103925

12. Ghanem R, Spanos P. *Stochastic finite elements: a spectral approach* (1991).

13. Honda R. Stochastic bem with spectral approach in elastostatic and elastodynamic problems with geometrical uncertainty. *Eng Anal Bound Elem* (2005) 29:415–27. doi:10.1016/j.enganabound.2005.01.007

14. Liu W, Belytschko T, Mani A. Random field finite elements. *Internat J Numer Methods Engrg* (1986) 23:1831–45. doi:10.1002/nme.1620231004

15. Chen L, Liu C, Zhao W, Liu L. An isogeometric approach of two dimensional acoustic design sensitivity analysis and topology optimization analysis for absorbing material distribution. *Comp Methods Appl Mech Eng* (2018) 336:507–32. doi:10.1016/j.cma.2018.03.025

16. Chen L, Cheng R, Li S, Lian H, Zheng C, Bordas S. A sample-efficient deep learning method for multivariate uncertainty qualification of acoustic–vibration interaction problems. *Comp Methods Appl Mech Eng* (2022) 393:114784. doi:10.1016/j.cma.2022.114784

17. Kamiński M. Stochastic perturbation approach to engineering structure vibrations by the finite difference method. *J Sound Vibration* (2001) 251:651–70. doi:10.1006/jsvi.2001.3850

18. Kamiński M. On generalized stochastic perturbation-based finite elements. *Comm Numer Methods Engrg* (2006) 22:23–31. doi:10.1002/CNM.795

19. Au S, Beck J. Subset simulation and its application to seismic risk based on dynamic analysis. *J ENG Mech* (2003) 129:901–17. doi:10.1061/(asce)0733-9399(2003)129:8(901)

20. Feng Y, Li C, Owen D. A directed Monte Carlo solution of linear stochastic algebraic system of equations. *Finite Elem Anal Des* (2010) 46:462–73. doi:10.1016/j.finel.2010.01.004

21. Ding C, Tamma K, Lian H, Ding Y, Dodwell T, Bordas S. Uncertainty quantification of spatially uncorrelated loads with a reduced-order stochastic isogeometric method. *Comput Mech* (2021) 67:1255–71. doi:10.1007/s00466-020-01944-9

22. Hu X, Cui X, Feng H, Li G. Stochastic analysis using the generalized perturbation stable node-based smoothed finite element method. *Eng Anal Boundary Elem* (2010) 70:40–55. doi:10.1016/j.enganabound.2016.06.002

23. Ding C, Cui X, Deokar RR, Li G, Cai Y, Tamma KK. Modeling and simulation of steady heat transfer analysis with material uncertainty: generalized n-th order perturbation isogeometric stochastic method. *Numer Heat Transfer A Appl* (2018) 74:1565–82. doi:10.1080/10407782.2018.1538296

24. Ding C, Tamma K, Cui X, Ding Y, Li G, Bordas S. An nth high order perturbation-based stochastic isogeometric method and implementation for quantifying geometric uncertainty in shell structures. *Adv Eng Softw* (2020) 148:102866. doi:10.1016/j.advengsoft.2020.102866

25. Kamiński M. Stochastic second-order perturbation approach to the stress-based finite element method. *Int J Sol Structures* (2001) 38:3831–52. doi:10.1016/s0020-7683(00)00234-1

26. Kamiński M. Generalized perturbation-based stochastic finite element method in elastostatics. *Comput Struct* (2007) 85:586–94. doi:10.1016/j.compstruc.2006.08.077

27. Chen L, Lian H, Natarajan S, Zhao W, Chen X, Bordas SPA. Multi-frequency acoustic topology optimization of sound-absorption materials with isogeometric

boundary element methods accelerated by frequency-decoupling and model order reduction techniques. *Comp Methods Appl Mech Eng* (2022) 395:114997. doi:10.1016/j.cma.2022.114997

28. Chen L, Lian H, Liu Z, Gong Y, Zheng CJ, Bordas SPA. Bi-material topology optimization for fully coupled structural-acoustic systems with isogeometric fem–bem. *Eng Anal Boundary Elem* (2022) 135:182–95. doi:10.1016/j.enganabound.2021.11.005

29. Chen L, Wang Z, Peng X, Yang J, Wu P, Lian H. Modeling pressurized fracture propagation with the isogeometric bem. *Geomechanics Geophys Geo-Energy Geo-Resources* (2021) 7:51. doi:10.1007/s40948-021-00248-3

30. Chen L, Zhang Y, Lian H, Atroshchenko E, Ding C, Bordas S. Seamless integration of computer-aided geometric modeling and acoustic simulation: isogeometric boundary element methods based on catmull-clark subdivision surfaces. *Adv Eng Softw* (2020) 149:102879. doi:10.1016/j.advengsoft.2020.102879

31. Chen L, Li H, Guo Y, Chen P, Atroshchenko E, Lian H. Uncertainty quantification of mechanical property of piezoelectric materials based on isogeometric stochastic fem with generalized n th-order perturbation. *Eng Comput* (2023) 1–21. doi:10.1007/s00366-023-01788-w

32. Chen L, Lu C, Zhao W, Chen H, Zheng C. Subdivision surfaces—boundary element accelerated by fast multipole for the structural acoustic problem. *J Theor Comput Acoust* (2020) 28:2050011. doi:10.1142/s2591728520500115

33. Qu Y, Zhang G, Gao X, Jin F. A new model for thermally induced redistributions of free carriers in centrosymmetric flexoelectric semiconductor beams. *Mech Mater* (2022) 171:104328. doi:10.1016/j.mechmat.2022.104328

34. Qu Y, Jin F, Yang J. Temperature effects on mobile charges in thermopiezoelectric semiconductor plates. *Int J Appl Mech* (2021) 13:2150037. doi:10.1142/s175882512150037x

35. Martinsson P, Rokhlin V. A fast direct solver for scattering problems involving elongated structures. *J Comput Phys* (2007) 221:288–302. doi:10.1016/j.jcp.2006.06.037

36. Bebendorf M, Rjasanow S. Adaptive low-rank approximation of collocation matrices. *Computing* (2003) 70:1–24. doi:10.1007/s00607-002-1469-6

37. Chen L, Wang Z, Lian H, Ma Y, Meng Z, Li P, et al. Reduced order isogeometric boundary element methods for CAD-integrated shape optimization in electromagnetic scattering. *Comp Methods Appl Mech Eng* (2024) 419:116654. doi:10.1016/j.cma.2023.116654

38. Guiggiani M, Casalini P. Direct computation of Cauchy principal value integrals in advanced boundary elements. *Int J Numer Methods Eng* (1987) 24:1711–20. doi:10.1002/nme.1620240908

39. Hughes T, Cottrell J, Bazilevs Y. Isogeometric analysis: CAD, finite elements, NURBS, exact geometry and mesh refinement. *Comp Methods Appl Mech Eng* (2005) 194:4135–95. doi:10.1016/j.cma.2004.10.008

40. Qin X, Dong C, Yang H. Isogeometric vibration and buckling analyses of curvilinearly stiffened composite laminates. *Appl Math Model* (2019) 73:72–94. doi:10.1016/j.apm.2019.03.045

41. Dölz J, Kurz S, Schöps S, Wolf F. A numerical comparison of an isogeometric and a parametric higher order raviart–thomas approach to the electric field integral equation. *IEEE Trans Antennas Propagation* (2020) 68:593–7. doi:10.1109/tap.2019.2935778

42. Dölz J, Kurz S, Schöps S, Wolf F. Isogeometric boundary elements in electromagnetism: rigorous analysis, fast methods, and examples. *SIAM J Scientific Comput* (2019) 41:B983–B1010. doi:10.1137/18m1227251

43. Rojas J, Bendaou O, Hami A, Rade D. Stochastic and reliability analysis of fluid-structure interaction problems using finite element models. *Multidiscipline Model Mater structures* (2010) 6:6–22. doi:10.1108/15736101011055248

44. Cao G, Yu B, Chen L, Yao W. Isogeometric dual reciprocity bem for solving non-fourier transient heat transfer problems in fgms with uncertainty analysis. *Int J Heat Mass Transfer* (2023) 203:123783. doi:10.1016/j.ijheatmasstransfer.2022.123783

45. Chen L, Lian H, Xu Y, Li S, Liu Z, Atroshchenko E, et al. Generalized isogeometric boundary element method for uncertainty analysis of time-harmonic wave propagation in infinite domains. *Appl Math Model* (2023) 114:360–78. doi:10.1016/j.apm.2022.09.030

46. Chen L, Zhao J, Lian H, Yu B, Atroshchenko E, Li P. A bem broadband topology optimization strategy based on taylor expansion and soar method—-application to 2d acoustic scattering problems. *Int J Numer Methods Engineering*/(2023) 124:5151–82. doi:10.1002/nme.7345

47. Dölz J, Harbrecht H, Kurz S, Multerer M, Schöps S, Wolf F. Bembel: the fast isogeometric boundary element c++ library for laplace, helmholtz, and electric wave equation. *SoftwareX* (2020) 11:100476. doi:10.1016/j.softx.2020.100476

48. Simpson R, Liu Z, Vázquez R, Evans J. An isogeometric boundary element method for electromagnetic scattering with compatible b-spline discretizations. *J Comput Phys* (2018) 362:264–89. doi:10.1016/j.jcp.2018.01.025

49. Burton A, Miller G. The application of integral equation methods to the numerical solution of some exterior boundary-value problems. *Proc R Soc Lond A. Math Phys Sci* (1971) 323:201–10. doi:10.1098/rspa.1971.0097

50. Marburg S. The burton and miller method: unlocking another mystery of its coupling parameter. *J Comput Acoust* (2016) 24:1550016. doi:10.1142/s0218396x15500162

51. Nishimura N. Fast multipole accelerated boundary integral equation methods. *Appl Mech Rev* (2002) 55:299–324. doi:10.1115/1.1482087

52. Coifman R, Rokhlin V, Wandzura S. The fast multipole method for the wave equation: a pedestrian prescription. *Antennas Propag Mag IEEE* (1993) 35:7–12. doi:10.1109/74.250128

53. Dölz J, Harbrecht H, Kurz S, Schöps S, Wolf F. A fast isogeometric bem for the three dimensional laplace- and helmholtz problems. *Comp Methods Appl Mech Eng* (2018) 330:83–101. doi:10.1016/j.cma.2017.10.020

frontiers | Frontiers in Physics

TYPE Original Research
PUBLISHED 06 December 2023
DOI 10.3389/fphy.2023.1333198

OPEN ACCESS

EDITED BY
Yilin Qu,
Northwestern Polytechnical University, China

REVIEWED BY
Mengxi Zhang,
Tianjin University, China
Xudong Li,
Chinese Academy of Sciences (CAS), China

*CORRESPONDENCE
Yanming Xu,
xuyanming@ustc.edu

RECEIVED 04 November 2023
ACCEPTED 24 November 2023
PUBLISHED 06 December 2023

CITATION
Chen X, Huang Y, Zhou Z and Xu Y (2023), FEM/Wideband FMBEM coupling based on subdivision isogeometry for structural-acoustic design sensitivity analysis.
Front. Phys. 11:1333198.
doi: 10.3389/fphy.2023.1333198

FEM/Wideband FMBEM coupling based on subdivision isogeometry for structural-acoustic design sensitivity analysis

Xiuyun Chen[1], Yajun Huang[2], Zhongbin Zhou[1] and Yanming Xu[1]*

[1]Henan International Joint Laboratory of Structural Mechanics and Computational Simulation, School of Architecture and Civil Engineering, Huanghuai University, Zhumadian, China, [2]College of Intelligent Construction, Wuchang University of Technology, Wuhan, China

A computer simulation approach known as the isogeometric (IGA) method may directly use the surface information of geometric model. In 3D computer graphics, Loop subdivision surfaces are a common method for creating complicated shapes. In this study, we propose a coupling algorithm that utilizes Loop subdivision surfaces and a direct differentiation method for the computation of acoustic-fluid-structure interaction and the performance of structural-acoustic sensitivity analysis. This algorithm combines the finite element method (FEM) and wideband fast multipole boundary element method (FMBEM). Because of that the proposed method is of a great ability of integrating the numerical calculation and computer-aided modeling, the current technique can deliver results quickly and accurately. The numerical prediction of the effects of vibrating structures with arbitrary shape within sound field is made feasible by the FEM/Wideband FMBEM technique. Calculation examples are provided to show the applicability and effectiveness of the suggested method.

KEYWORDS

loop subdivision surfaces, IgA, fluid-structure interaction, design sensitivity analysis, direct differentiation method

1 Introduction

The elastic structures in heavy fluid resulting in acoustic radiation or scattering is a common issue in underwater acoustics. It is possible to give the analytical solutions of the issues with acoustic fluid-structure interaction phenomenon while the structure is with simple boundary conditions and geometry [1,2]. However, as it comes for real-world issues which usually have complex geometries, providing an analytical solution becomes harder and even impossible, thus effective simulation techniques are needed.

FEM is extensively utilized to study the dynamic behavior of issues involving fluid-structure interactions, acoustics, and structures. The FEM has several drawbacks for modeling infinite domains, though. Because it offers good accuracy and simple mesh generation, BEM has been widely employed to calculate acoustic issues. The Sommerfeld radiation condition [3] is met, especially for external acoustic issues. The Galerkin technique has been frequently used in BEM implementation to solve the boundary integral problem numerically [4]. However, the collocation approach, has historically been popular in the engineering field. Hence, the coupled FEM/BEM technique [5,6] is suitable for studying fluid-structure interaction problems. However, the high computational expense remains a challenge when performing coupling analysis of underwater structural-acoustic problems

using the FEM/Conventional BEM (CBEM) algorithm. This is primarily because CBEM generates a dense and non-symmetric coefficient matrix. Many techniques have been used to speed up the integral problem solution, including fast multipole method (FMM), the adaptive cross approximation methodology and fast direct solver. Martinsson and Rokhlin [7,8] introduced the fast direct solver, which works well for issues requiring moderately ill-conditioned matrices and immediately builds a compressed factorization of the matrix inverse. The adaptive cross approximation methodology [9], developed by Bebendorf and Rjasanow, has the capability to generate blockwise low-rank approximations from the BEM matrices. This methodology is particularly suitable for problems that require a large number of iterations. FMM [10–12] has been developed to reduce memory requirements while speeding up the solving of the CBEM system of equations. In reality, the Helmholtz equation has two versions of the Fast Multipole Method (FMM), namely, the original FMM and the diagonal form. However, it is well-known that both of these versions tend to fail outside of their optimal frequency ranges in some manner. On the other hand, the aforementioned issues can potentially be resolved by utilizing wideband FMM [13–18]. This advanced technique combines the original FMM with the diagonal form FMM, leading to more efficient solutions. Therefore, the challenges related to large-scale fluid-structure interaction problems can be effectively resolved through the utilization of the coupling approach based on FEM/fast multipole boundary element method (FEM/FMBEM) [19–23]. Furthermore, this study proposes the utilization of the FEM/Wideband FMBEM coupling method to tackle the intricate problems associated with fluid-structure interactions.

Through the use of appropriate software, FEM and BEM may be implemented—a process known as computer-aided engineering (CAE). Nowadays, industry 4.0 and digital twin technologies are being developed with the use of CAE simulation. The models created by CAD software must, however, be transformed into simulation-ready models as part of the preprocessing stage used by modern CAE. The CAE's most time-consuming manual intervention phase, the geometric model data transfer stage produces geometry inaccuracies. The integration of geometric modeling and numerical simulation using isogeometric analysis [24–26] with boundary element method (IGABEM) [27,28] is suggested as a solution to this issue. By using IGABEM, geometric mistakes and time-consuming preprocessing steps may be avoided and numerical simulation can be carried out straight from the precise models. Since its inception, IGABEM has been used to address a variety of issues, including those related to elastic mechanics [27–30], potential issues [15], wave-resistance [31], fracture mechanics [32,33], electromagnetics [34–39], and structural optimization [40–46].

In addition to the benefits already discussed, IGABEM offers significant benefits for modelling acoustics issues. Numerous engineering fields have found extensive use for acoustics, including noise control, underwater navigation using sonar, ultrasound imaging for medical purposes, seismology, electroacoustic communications, etc. Numerous numerical simulation techniques have significant challenges when it comes to acoustics for that the sound wave may travel through semi-infinite domains. By shifting the acoustic field from a semi-infinite domain to the boundary of the domain, IGABEM can get around this problem. Simpson [16,47] applied IGABEM to acoustics. Acoustic optimization [37,48,49] with IGABEM was studied.

In the framework of the IGABEM, several sorts of geometric modeling approaches have been extensively researched. The ability to build multi-resolution geometries with complex forms and topologies makes the subdivision surface approach among them very promising [51–56]. There are two types of subdivision surfaces: Catmull-Clark and Loop method. Structure-acoustic interaction [1,57,58] and acoustic optimization [59–63] were both addressed using IGABEM based on Loop subdivision surfaces. The goal of the current effort is to merge Loop subdivision surfaces with IGABEM for sensitivity analysis. Additionally, we'll speed up the solution process using wideband FMM.

Designers are increasingly considering passive noise management by altering the geometry of the construction. Particularly for thin shell structures, this structural-acoustic optimization has considerable promise for minimizing radiated noise [64]. Acoustic design sensitivity analysis is a crucial component in the process of acoustic design and optimization, as it allows for understanding the effect of geometry changes on the acoustic performance. In a comprehensive review by Marburg [65], advancements in structural-acoustic optimization for passive noise reduction were discussed. The global finite difference method (FDM) has been extensively employed for structural-acoustic optimization due to its ease of implementation [66–69]. However, this approach doesn't work so well, particularly while considering several design elements simultaneously. To get over this issue, employ the adjoint variable approaches [70,71] or the direct differentiation method [72]. The sensitivity analysis for interaction issues is widely recognized as the most time-consuming step in gradient-based optimization. In our study, we aim to accelerate the calculation process by employing a direct differentiation approach for structural-acoustic sensitivity analysis in the FEM/Wideband FMBEM method.

In this study, we propose the incorporation of wideband FMBEM in the coupling of structural-acoustic sensitivity analysis and present the formulation for sensitivity analysis in the coupled FEM/BEM analysis. We advocate for the adoption of coupled FEM/Wideband FMBEM to address fluid-structure interaction problems and conduct structural-acoustic sensitivity analysis. To eliminate the geometry inaccurices, Loop subdivision scheme is applied to the sensitivity analysis of an underwater fluid-structure coupling problem. Through the computation of various numerical examples, we have demonstrated the accuracy and effectiveness of the proposed strategy.

2 Structural-acoustic coupling deduction

2.1 Subdivision scheme

In computer animation and graphics, it is of great advantages of using Subdivision surfaces [73,74] since their emergence in the 1970s. They may also be accessed in most industrial CAD solid modeling applications. Subdivision surfaces are frequently mentioned as a technique for continually fine-tuning and smoothing a control mesh so a smooth limit surface could be produced. They may also be regarded as the extension of splines to arbitrarily linked meshes for FEM and BEM.

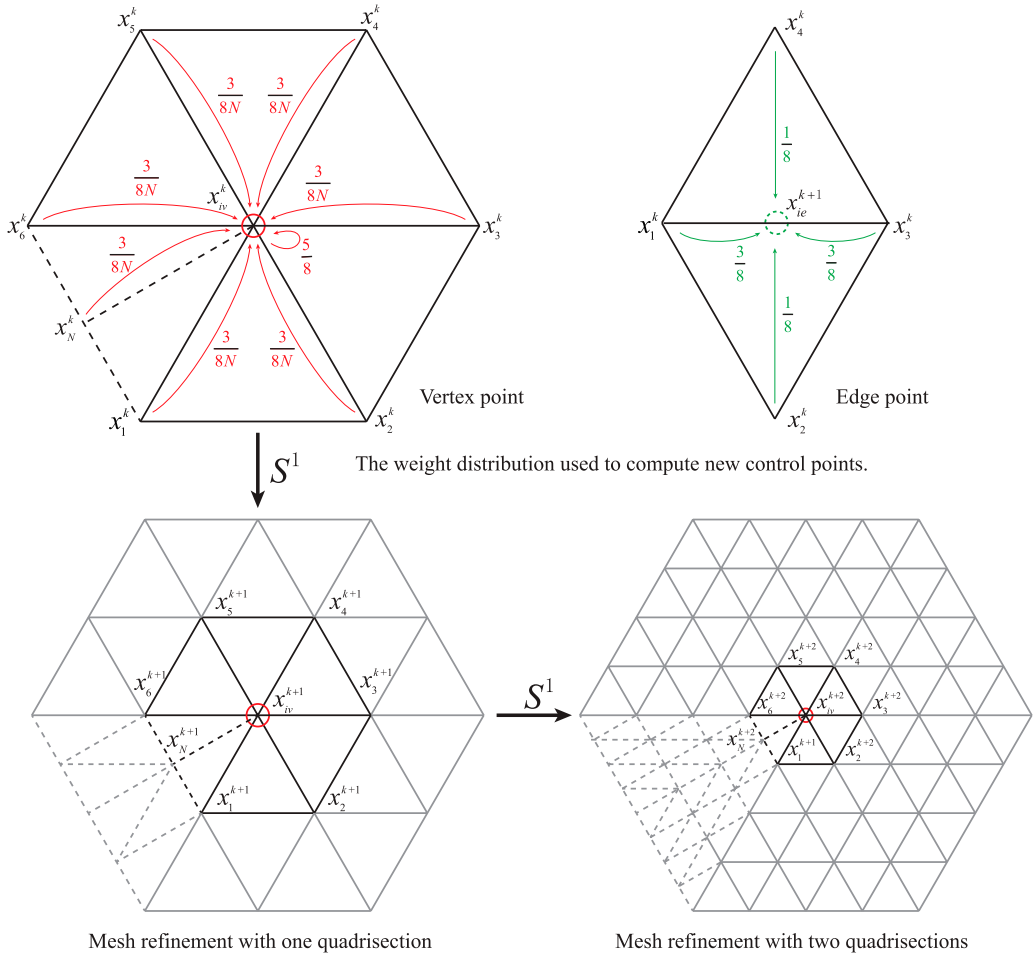

FIGURE 1
Templates for vertex and edge points with regular and irregular shapes.

A rough polygon mesh is transformed into a smooth surface using subdivision techniques. The creation of a smooth surface using subdivision method—which is usually classified as interpolating schemes—involves a constrained, repeating refinement process that starts with an initial control mesh. Due to the refinement characteristic inherited from splines, all control meshes generated during subdivision refinement accurately represent the same spline surface.

The structural-acoustic coupling analysis in this study is carried out utilizing the Loop subdivision scheme [59]. The quadrisection refinement of a triangular mesh in a construction of loop subdivision is shown in Figure 1. A vertex's valence is the edges number that link it. When $N = 6$, a vertex is considered regular, and when $N \neq 6$, it is considered irregular. Each triangle is split into four smaller triangles by adding a new vertex at the middle of each edge. As indicated in Eqs 1, 2, the positions of new vertices and edge points may be determined from the previous level.

$$x_{iv}^{k+1} = \frac{5}{8}x_{iv}^{k} + \frac{3}{8N}\sum_{i=1}^{N} x_i^k, \tag{1}$$

$$x_{ie}^{k+1} = \frac{3}{8}x_1^k + \frac{1}{8}x_2^k + \frac{3}{8}x_3^k + \frac{1}{8}x_4^k, \tag{2}$$

where

iv is the i-th vertex point

$i.e.$, is the i-th edge point

In reality, there are too many nodes, making it impossible to achieve smooth surfaces with few subdivisions. Another method for creating limit surfaces for any degree of refinement is to create an elementwise map using linear combinations of Box-splines basis functions on triangular control meshes. For further details, please refer to Chen et al.[59].

2.2 BEM analysis

$$\nabla^2 p(x) + k^2 p(x) = 0, \tag{3}$$

$$\begin{aligned} p(x) &= \bar{p}(x) \qquad x \in \Gamma_p, \\ q(x) &= \frac{\partial p(x)}{\partial n(x)} = \mathrm{i}\rho\omega\bar{v}(x) \qquad x \in \Gamma_q, \\ p(x) &= zv(x) \qquad x \in \Gamma_z, \end{aligned} \tag{4}$$

where

p is sound pressure

k is wave number

n is external normal direction of the boundary

q is normal derivative of p

i is imaginary unit, $i = \sqrt{-1}$

ρ is structural density

ω is frequency of the incoming force

v is normal velocity

z is acoustic impedance

Γ_p is Dirichlet boundary condition

Γ_q is Neumann boundary condition

Γ_z is Robin boundary condition

$\overline{()}$ is known function given on the border

Equation 3 describes a acoustic wave which is time-harmonic in the Helmholtz equation, and Eq. 4 serves as an expression for the boundary conditions. A boundary integral equation (BIE) specified on the Γ can be created from Eqs 3–5.

$$c(x)p(x) + \int_\Gamma F(x,y)p(y)\mathrm{d}\Gamma(y) = \int_\Gamma G(x,y)q(y)\mathrm{d}\Gamma(y), \quad (5)$$

where

x is source point

y is field point

$c(x)$ is 1/2 if the boundary Γ is smooth in the vicinity of the source point x

$p(x)$ is intensity of the incoming wave at source point x

$p(y)$ is sound pressure at field point y

$G(x, y)$ is Green's function

$q(y)$ is normal derivative of $p(y)$

$F(x, y)$ is normal derivative of $G(x, y)$

Equations 6, 7 gives the expression of Green's function for acoustic problems in two and three dimensional problems, respectively.

$$G(x,y) = \frac{i}{4}H_0^{(1)}(kr), \quad (6)$$

$$G(x,y) = \frac{e^{ikr}}{4\pi r}, \quad (7)$$

$$r = |y - x|.$$

When the boundary Γ is smooth around the source point x, the derivative of the integral representation in Eq. 5 with respect to the outer normal can be expressed as Eq. 8.

$$\frac{1}{2}q(x) + \int_\Gamma \frac{\partial F(x,y)}{\partial n(x)}p(y)\mathrm{d}\Gamma(y) = \int_\Gamma \frac{\partial G(x,y)}{\partial n(x)}q(y)\mathrm{d}\Gamma(y). \quad (8)$$

It is common knowledge that applying a single Helmholtz boundary integral equation to issues involving external boundary values may be challenging due to nonuniqueness. In order to effectively solve the nonuniqueness problem, the Burton-Miller approach [75]—which is a linear combination of Eqs 5, 8—is used in this study. The computation of the singular boundary integrals introduced by Eqs 5, 8 can also be performed directly and efficiently using the Cauchy principal value and the Hadamard finite part integral method [72].

If the boundary Γ is divided into elements, the system can be obtained [76] and can be expressed as Eq. 9 by assembling the equations for collocation points located in the center of each element.

$$\mathbf{Hp} = \mathbf{Gq} + \mathbf{p_i}, \quad (9)$$

where

H is the coefficient matrix of the vector **p**

G is the coefficient matrix of the vector **q**

$\mathbf{p_i}$ is the nodal pressure caused by the incoming wave

2.3 FEM analysis

The complete structural-acoustic simulation approach was described by Fritze et al. [6], and related expressions are supplied here. The structure response is determined by analyzing of frequency-response under the assumption that a harmonic load performs on the structure. Equation 10 derives the linear system of structural-acoustic equation.

$$(\mathbf{K} + i\omega\mathbf{C} - \omega^2\mathbf{M})\mathbf{u} = \mathbf{f} \quad (10)$$

where

K is stiffness matrix

i is imaginary unit, $i = \sqrt{-1}$

ω is excitation frequency of the harmonic load

C is damping matrix

M is mass matrix

u is nodal displacement vector

f is complete excitation

It is crucial to take into account that, because of damping, the steady-state response may have the same frequency as the applied load but a different phase angle. To handle non-harmonic imposed loads, the time-dependent forces can be examined in the frequency domain, enabling the use of Eq. 10. To address the effect of acoustic pressure on structural surfaces, a coupling matrix is introduced. This matrix facilitates the transfer of the structural nodal load from the fluid effect to the fluid nodal pressure. Then, Eq. 11 could be used to express the complete excitation, combining the acoustic load and the structural load.

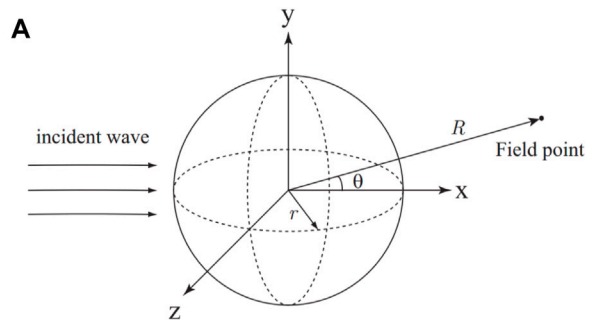

The sphere model.

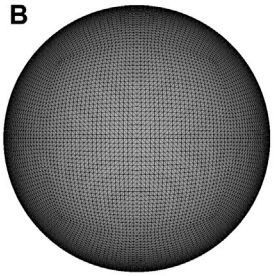

Mesh of the sphere model.

FIGURE 2
The sphere model and its mesh plot. **(A)** The sphere model. **(B)** Mesh of the sphere model.

$$\begin{aligned} \mathbf{f} &= \mathbf{C}_{\mathbf{sf}}\mathbf{p} + \mathbf{f}_{\mathbf{s}}, \\ \mathbf{C}_{\mathbf{sf}} &= \int_{\Gamma_{int}} \mathbf{N}_{\mathbf{s}}^{\mathrm{T}} \mathbf{n} \mathbf{N}_{\mathbf{f}} \mathrm{d}\Gamma, \end{aligned} \tag{11}$$

where

$\mathbf{C}_{\mathbf{sf}}$ is coupling matrix

$\mathbf{p}$ is fluid nodal pressure

$\mathbf{C}_{\mathbf{sf}}\mathbf{p}$ is acoustic load

$\mathbf{f}_{\mathbf{s}}$ is structural load

$\mathbf{N}_{\mathbf{s}}$ is interpolation function for structural domain

$\mathbf{N}_{\mathbf{f}}$ is interpolation function for fluid domain

$\mathbf{n}$ is external normal direction of the structural surface

Γ is interaction surface between the structural and fluid domains

The structural nodal load from the fluid effect is directed to fluid nodal pressure via the coupling matrix $\mathbf{C}_{\mathbf{sf}}$. The nodal displacement could then be obtained from Eq. 10, as shown in Eq. 12.

$$\mathbf{u} = \left(\mathbf{K} + \mathrm{i}\omega\mathbf{C} - \omega^2\mathbf{M}\right)^{-1}\mathbf{f}. \tag{12}$$

2.4 FEM-BEM coupling analysis

The exact formulas of FEM/BEM modeling were published by Fritze et al. [6], and related expressions are supplied in this part. The continuity constraint over the interaction surface—as shown in Eq. 13—connects the governing equations as illustrated in the above section. Then, the normal velocity $\mathbf{v}$ may be written as a function with the displacement $\mathbf{u}$, according to Eq. 14.

$$\mathbf{q} = -\mathrm{i}\omega\rho\mathbf{v}, \tag{13}$$

$$\mathbf{v} = \mathrm{i}\omega\mathbf{S}^{-1}\mathbf{C}_{\mathbf{fs}}\mathbf{u}, \tag{14}$$

$$\begin{aligned} \mathbf{S} &= \int_{\Gamma_{int}} \mathbf{N}_{\mathbf{f}}^{\mathrm{T}} \mathbf{N}_{\mathbf{f}} \mathrm{d}\Gamma, \\ \mathbf{C}_{\mathbf{fs}} &= \mathbf{C}_{\mathbf{sf}}^{\mathrm{T}}. \end{aligned}$$

We can get Eq. 15 by inserting Eqs 13, 14 into Eq. 9.

$$\mathbf{H}\mathbf{p} = \omega^2\rho\mathbf{G}\mathbf{S}^{-1}\mathbf{C}_{\mathbf{fs}}\mathbf{u} + \mathbf{p}_{\mathbf{i}}. \tag{15}$$

Equations 10, 11, 15 can be connected to form a equation system, as shown in Eq. 16.

$$\begin{bmatrix} \mathbf{K} + \mathrm{i}\omega\mathbf{C} - \omega^2\mathbf{M} & -\mathbf{C}_{\mathbf{sf}} \\ -\omega^2\rho\mathbf{G}\mathbf{S}^{-1}\mathbf{C}_{\mathbf{fs}} & \mathbf{H} \end{bmatrix} \begin{Bmatrix} \mathbf{u} \\ \mathbf{p} \end{Bmatrix} = \begin{Bmatrix} \mathbf{f}_{\mathbf{s}} \\ \mathbf{p}_{\mathbf{i}} \end{Bmatrix}. \tag{16}$$

The direct iterations on Eq. 16 converge rather slowly, and directly solving the system equation would demand far more computational power and storage space. We present the following method as an alternative to utilizing an iterative solver to resolve the above non-symmetric linear equation. The coupled boundary element equation (6) shown in Eq. 17 may be obtained by putting Eq. 12 into Eq. 15.

$$\begin{aligned} \mathbf{H}\mathbf{p} - \mathbf{G}\mathbf{W}\mathbf{C}_{\mathbf{sf}}\mathbf{p} &= \mathbf{G}\mathbf{W}\mathbf{f}_{\mathbf{s}} + \mathbf{p}_{\mathbf{i}}, \\ \mathbf{W} &= \omega^2\rho\mathbf{S}^{-1}\mathbf{C}_{\mathbf{fs}}\mathbf{A}^{-1}, \\ \mathbf{A} &= \mathbf{K} + \mathrm{i}\omega\mathbf{C} - \omega^2\mathbf{M}. \end{aligned} \tag{17}$$

By using a sparse direct solver, the equation linear system in Eq. 17 could be solved. To speed up the solution, FMM and the Generalized Minimum Residual (GMRES) iterative solver are used.

In this study, Loop subdivision is introduced in the model discretization in order to realize the FEM-BEM coupling and the ensuing sensitivity analysis.

3 Sensitivity analysis for shape design

Finding the optimum design parameters specifying the intended form of the given structure under specified restrictions is the aim of shape optimization. Calculating the gradients of stated cost functions is done using shape design sensitivity analysis. The direction in which to look for the best values of the design variables may then be decided using the acquired gradients. As a result, the first and most crucial phase in the design and optimization of acoustic shapes is often acoustic form sensitivity analysis [72,77]. The direct method utilizes the chain rule of differentiation to compute the sensitivity of the performance function. This process begins with determining the sensitivity of the variables before proceeding to compute the performance function sensitivity. Because it is so directly tied to the analytical process, this strategy is quite popular.

By differentiating Eqs 5, 8 with respect to any arbitrary design variable, assuming that the boundary Γ is smooth around the source point x, we can derive Eqs 18, 19.

10.3389/fphy.2023.1333198

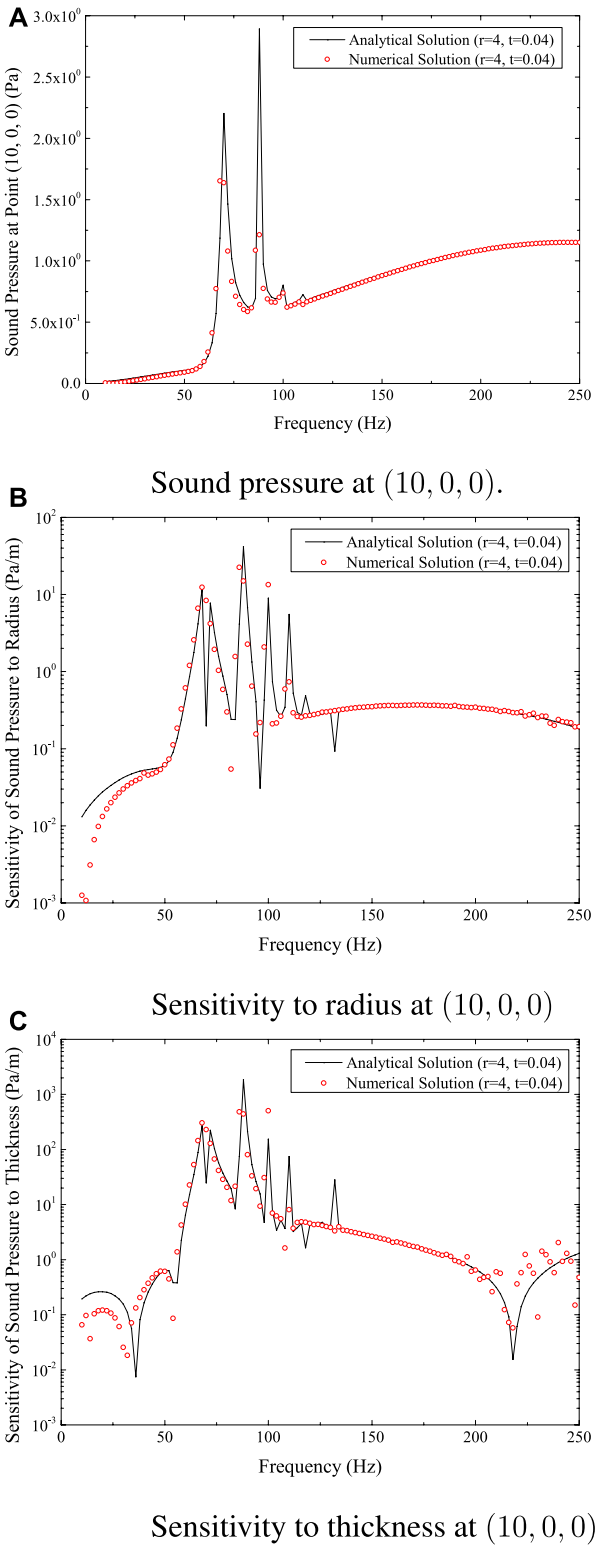

FIGURE 3
Sound pressure and sensitivity at (10,0,0) for spherical shell model. **(A)** Sound pressure at (10,0,0). **(B)** Sensitivity to radius at (10,0,0). **(C)** Sensitivity to thickness at (10,0,0).

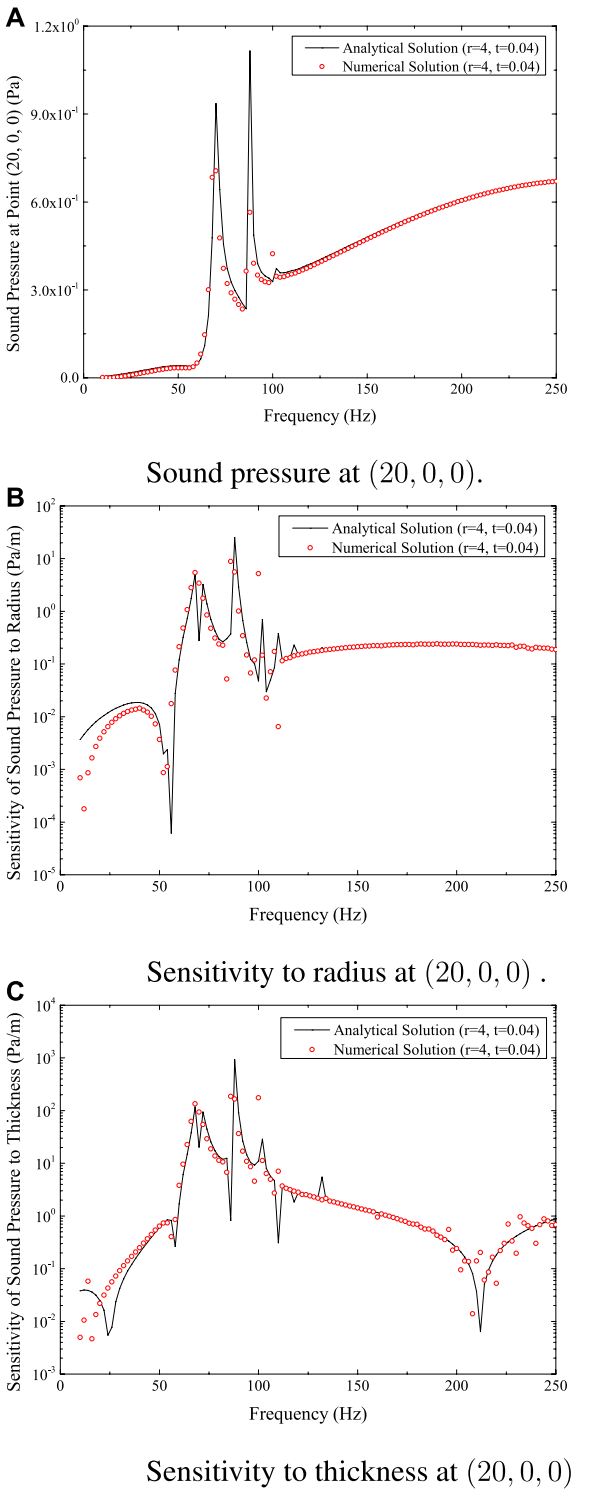

FIGURE 4
Sound pressure and sensitivity at (20,0,0) for spherical shell model. **(A)** Sound pressure at (20,0,0). **(B)** Sensitivity to radius at (20,0,0). **(C)** Sensitivity to thickness at (20,0,0).

10.3389/fphy.2023.1333198

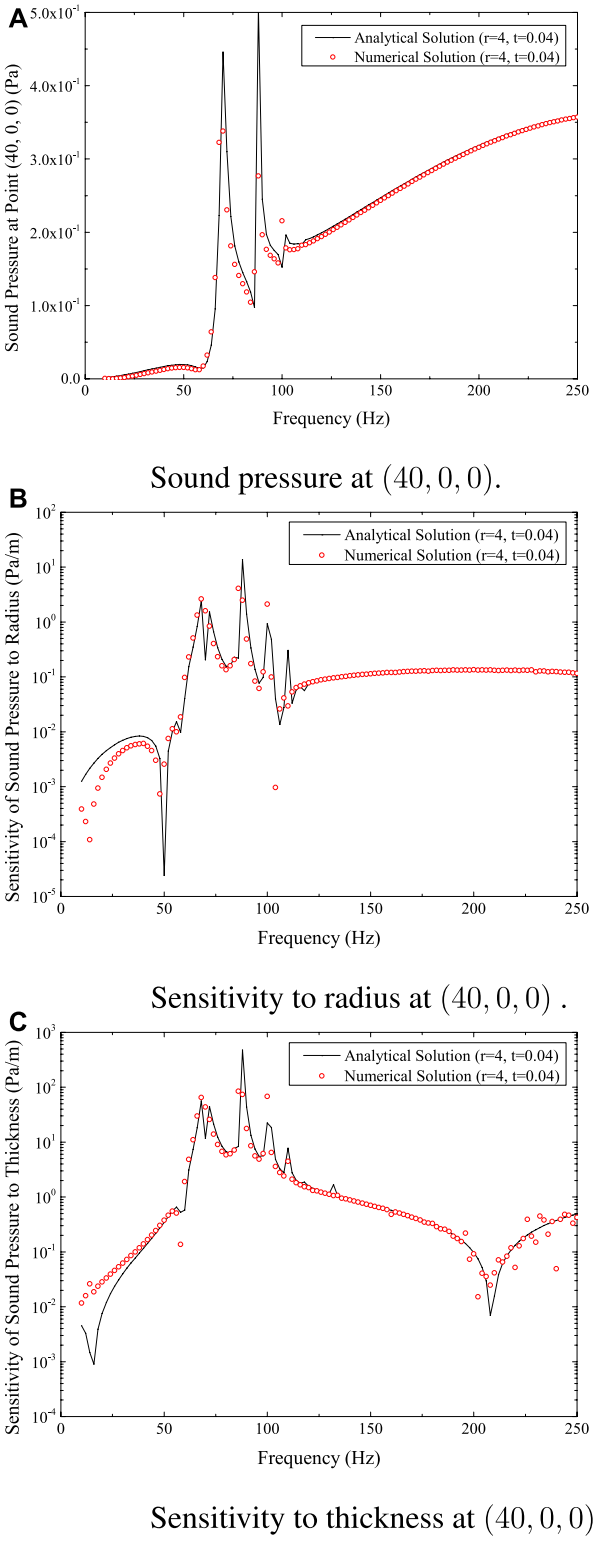

FIGURE 5
Sound pressure and sensitivity at (40,0,0) for spherical shell model. **(A)** Sound pressure at (40,0,0). **(B)** Sensitivity to radius at (40,0,0). **(C)** Sensitivity to thickness at (40,0,0).

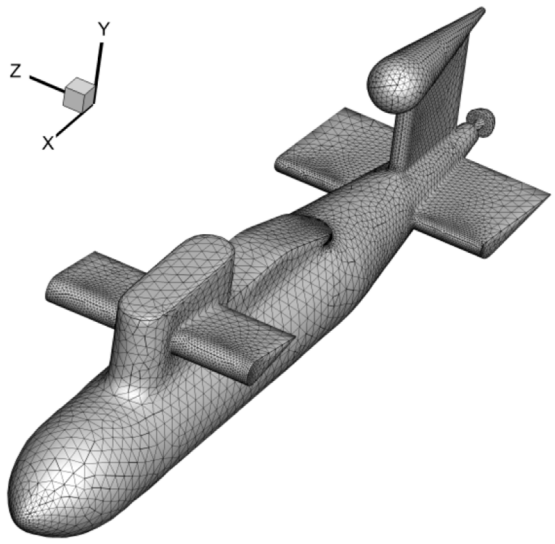

FIGURE 6
The submarine model.

$$\begin{aligned}\frac{1}{2}\dot{p}(x) &= \int_\Gamma \left[\dot{G}(x,y)q(y) - \dot{F}(x,y)p(y)\right]\mathrm{d}\Gamma(y) \\ &+ \int_\Gamma \left[G(x,y)\dot{q}(y) - F(x,y)\dot{p}(y)\right]\mathrm{d}\Gamma(y) \\ &+ \int_\Gamma \left[G(x,y)q(y) - F(x,y)p(y)\right]\mathrm{d}\dot{\Gamma}(y).\end{aligned} \tag{18}$$

$$\begin{aligned}\frac{1}{2}\dot{q}(x) &= \int_\Gamma \left[\frac{\partial \dot{G}(x,y)}{\partial n(x)}q(y) - \frac{\partial \dot{F}(x,y)}{\partial n(x)}p(y)\right]\mathrm{d}\Gamma(y) \\ &+ \int_\Gamma \left[\frac{\partial G(x,y)}{\partial n(x)}\dot{q}(y) - \frac{\partial F(x,y)}{\partial n(x)}\dot{p}(y)\right]\mathrm{d}\Gamma(y) \\ &+ \int_\Gamma \left[\frac{\partial G(x,y)}{\partial n(x)}q(y) - \frac{\partial F(x,y)}{\partial n(x)}p(y)\right]\mathrm{d}\dot{\Gamma}(y).\end{aligned} \tag{19}$$

For two dimensional problems, we have Eq. 20.

$$\begin{aligned}\dot{G}(x,y) &= -\frac{ik}{4}H_1^{(1)}(kr)\dot{r}, \\ \dot{F}(x,y) &= -\frac{ik}{4}H_1^{(1)}(kr)\left[\frac{(\dot{y}_j - \dot{x}_j)n_j(y)}{r} + r_{,j}\dot{n}_j(y)\right] \\ &+ \frac{ik^2}{4}H_2^{(1)}(kr)\dot{r}r_{,j}n_j(y), \\ \dot{r} &= r_{,j}(\dot{y}_j - \dot{x}_j).\end{aligned} \tag{20}$$

For three dimensional problems, we have Eq. 21.

$$\begin{aligned}\dot{G}(x,y) &= -\frac{e^{ikr}}{4\pi r^2}(1-ikr)\frac{\partial r}{\partial y_i}(\dot{y}_i - \dot{x}_i), \\ \dot{F}(x,y) &= \frac{e^{ikr}}{4\pi r^3}\left[(3 - 3ikr - k^2r^2)\frac{\partial r}{\partial n(y)}\frac{\partial r}{\partial y_j} - (1-ikr)n_j(y)\right](\dot{y}_j - \dot{x}_j) \\ &- \frac{e^{ikr}}{4\pi r^2}(1-ikr)\frac{\partial r}{\partial y_i}\dot{n}_i(y), \\ \dot{r} &= r_{,j}(\dot{y}_j - \dot{x}_j).\end{aligned} \tag{21}$$

The singular boundary integrals introduced by Eqs 18, 19 can be computed directly and efficiently using the Cauchy

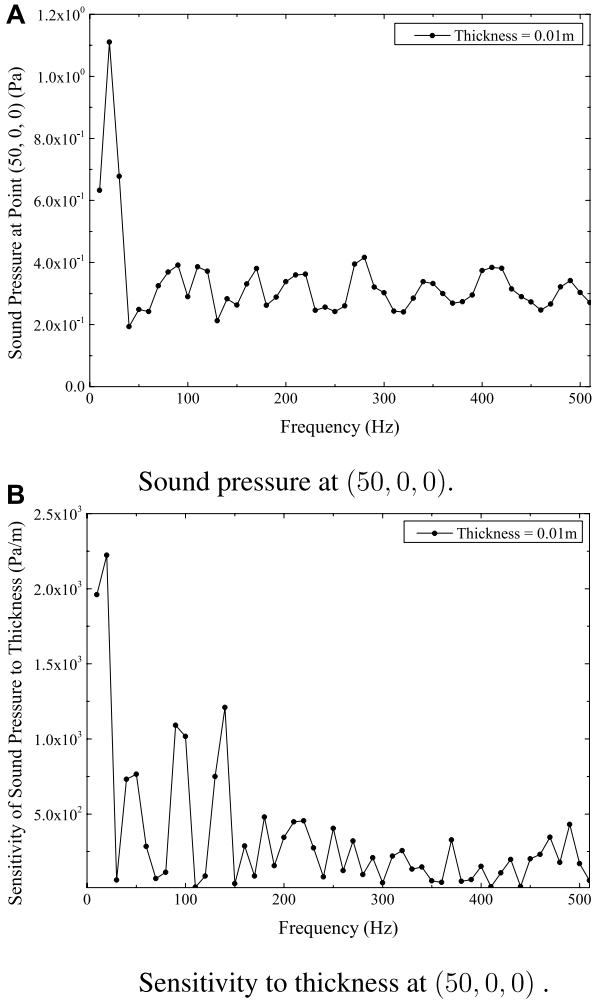

FIGURE 7
Sound pressure and sensitivity at point (50,0,0) for submarine model. **(A)** Sound pressure at (50,0,0). **(B)** Sensitivity to thickness at (50,0,0).

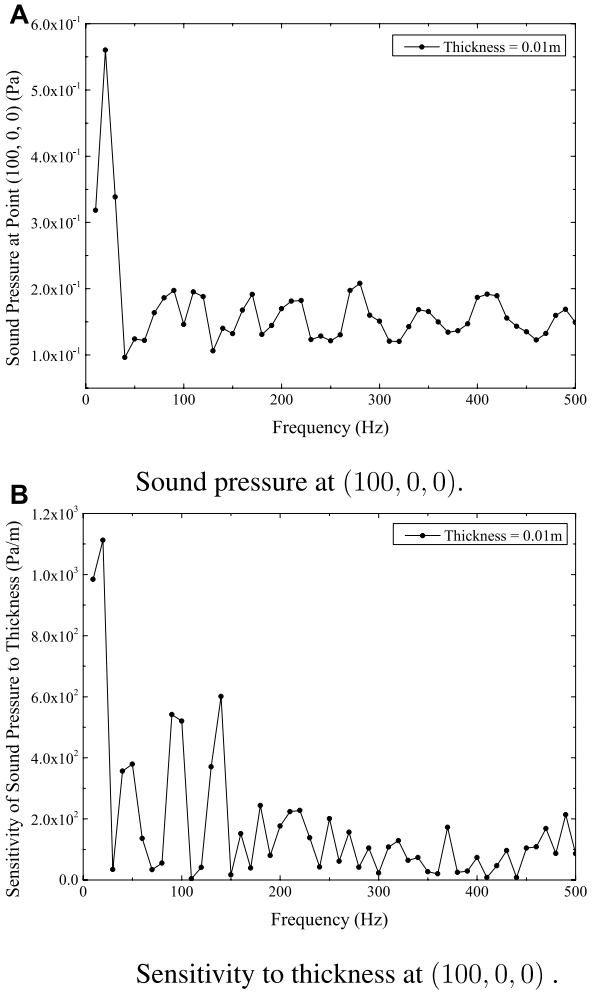

FIGURE 8
Sound pressure and sensitivity at point (100,0,0) for submarine model. **(A)** Sound pressure at (100,0,0). **(B)** Sensitivity to thickness at (100,0,0).

principal value and the Hadamard finite part integral method [72].

By differentiating Eq. 17 with respect to the design variable, the sensitivity analysis for shape design using the coupling FEM-BEM can yield Eq. 22.

$$\begin{aligned} \mathbf{H}\dot{\mathbf{p}} - \mathbf{G}\mathbf{W}\mathbf{C}_{\mathbf{sf}}\dot{\mathbf{p}} &= \dot{\mathbf{G}}\mathbf{X} + \mathbf{G}\mathbf{Y} - \dot{\mathbf{H}}\mathbf{p}, \\ \mathbf{X} &= \mathbf{W}\left(\mathbf{C}_{\mathbf{sf}}\mathbf{p} + \mathbf{f}_{\mathbf{s}}\right), \\ \mathbf{Y} &= \dot{\mathbf{W}}\left(\mathbf{C}_{\mathbf{sf}}\mathbf{p} + \mathbf{f}_{\mathbf{s}}\right) + \mathbf{W}\left(\dot{\mathbf{C}}_{\mathbf{sf}}\mathbf{p} + \dot{\mathbf{f}}_{\mathbf{s}}\right), \\ \dot{\mathbf{W}} &= \omega^2\rho\left(\dot{\mathbf{S}^{-1}}\mathbf{C}_{\mathbf{fs}}\mathbf{A}^{-1} + \mathbf{S}^{-1}\dot{\mathbf{C}}_{\mathbf{fs}}\mathbf{A}^{-1} + \mathbf{S}^{-1}\mathbf{C}_{\mathbf{fs}}\dot{\mathbf{A}^{-1}}\right). \end{aligned} \tag{22}$$

Since the matrices are full and asymmetric, it takes a lot of computing time to directly solve Eq. 22 using conventional BEM. However, it is possible to speed up the computational process using FMM and GMRES. The matrix-vector products in Eqs 17, 22 are accelerated using wideband FMM, and the FEM-BEM coupling formula and the associated sensitivity equation are solved using the iterative solver GMRES.

4 Numerical examples

Several numerical tests are conducted to examine the validity and dependability of the established methodology in this section. In each case, the FEM uses shell elements whereas the discontinuous linear boundary elements are applied for acoustic analysis. All calculations are performed using a customized internal Fortran 95/2003 algorithm.

4.1 Sphere with an incoming sound wave

This section examines the sound field of an thin spherical shell that is centered at location (0, 0, 0), while accounting for an incoming sound wave with an amplitude of 1.0 in positive x direction, as shown in Figure 2. The following are the materials and geometrical elements used in this example.

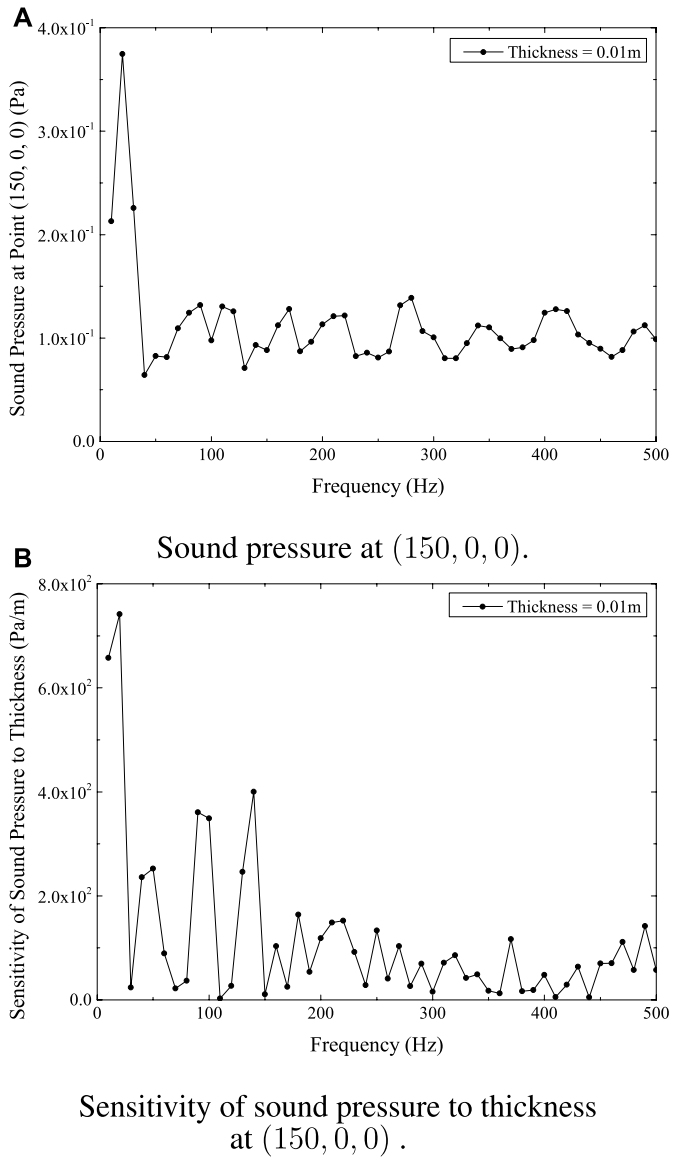

FIGURE 9
Sound pressure and sensitivity at point (150,0,0) for submarine model. **(A)** Sound pressure at (150,0,0). **(B)** Sensitivity of sound pressure to thickness at (150,0,0).

Radius	4.0 m
thickness	0.04 m
elasticity modulus	2.10×10^{11} Pa
Poisson's ratio	0.3
structural density	7.86×10^{3} kg/m^3
fluid density	1.00×10^{3} kg/m^3
sound velocity in water	1.482×10^{3} m/s

Figure 3 gives the results at position (10, 0, 0). Figure 3A displays the analytical and numerical solutions. The GMRES implementation with the wideband FMM technique is employed to accelerate the solution of linear systems without preconditioning. The discretized thin-shell model consists of 25,392 elements. The wideband FMM approach keeps the high accuracy of BEM, as the numerical and analytical answers present the good agreement which can seen in the figure.

Figures 3B, C shows, respectively, how sensitive the structure's surface is to sound pressure in relation to the radius and thickness of the sphere. Basically, these graphs demonstrate a good agreement between the analytical and numerical results. Figure 3 shows that the sound pressure sensitivity grows significantly at resonance peaks, and the lower frequency range is crucial for this spherical shell model because the sound pressure there is substantially higher and more responsive to thickness and radius.

The results are shown in Figures 4, 5, respectively, for the positions (20, 0, 0) and (40, 0, 0). The curves for the same physical quantity at various locations, as shown in Figures 3, 4, 5—Figures 3A, 4A, 5A for sound pressure, Figures 3B, 4B, 5B for sensitivity to radius, and Figures 3C, 4C, 5C for sensitivity to thickness—all show a similar pattern of fluctuation.

4.2 Submarine model under an incoming sound wave

This section focuses on the underwater submarine model's scattering sound field when influenced by an incoming plane wave [78]. The plane wave propagates predominantly along the *x*-axis and has an incidence wave amplitude of 1.0 Pa. The thickness of the submarine model is 0.01 m, and the sub has a length of 9.2 m. The origin of the coordinate is in the middle of the axial length of the submarine, and the *x*-axis is along the axial length of the submarine. The submarine model constructed using Loop subdivision scheme is shown in Figure 6, which has a total of 19,016 elements.

Several calculation points are selected. Figure 7A gives the sound pressure changing with frequency at point (50, 0, 0) and Figure 7B illustrates the changing of its sensitivity to thickness. These two data demonstrate that the lower frequency range, given the existing material and geometrical parameters, is a vital region for this submarine model, as the sound pressure is noticeably greater and more sensitive to thickness there.

The computation of sound pressure at location (100, 0, 0) and (150, 0, 0) is shown in Figures 8A, 9A, respectively. Figures 8B, 9B depicts the sensitivity of sound pressure at point (100, 0, 0) and (150, 0, 0) to shell thickness, respectively. Figures 7A, 8A, 9A show comparable patterns in the sound pressure curves at the places (50, 0, 0), (100, 0, 0), and (150, 0, 0). As seen in Figures 7B, 8B, 9B, the sensitivity of sound pressure at (50, 0, 0), (100, 0, 0), and (150, 0, 0) also demonstrates a similar pattern. Additionally, and in line with predictions, the sound pressure and its sensitivity to thickness both decline with increasing distance from the structure.

5 Conclusion

The simulation of acoustic-structure interaction and sensitivity analysis are conducted using a coupling approach that combines the Finite Element Method (FEM) and Boundary Element Method (BEM). FEM is applied to model structural elements of the issue. To eliminate the need for meshing the acoustic domain, the boundary of the structure being analyzed is discretized using the BEM. FMM is applied to expedite the matrix-vector output. IGABEM enables direct structural-acoustic interaction and sensitivity analysis from CAD models without the requirement for meshing, thereby eliminating any geometric errors. For coupled structural-acoustic systems, equations are derived for the sound pressure sensitivity. To prove the accuracy and practicality of the recommended strategy, calculation examples are given. The recommended method may be used to quantitatively predict how design parameters would affect the sound field in real-world scenarios.

Reduced order isogeometric boundary element methods for CAD-integrated shape optimization of electromagnetic scattering.

Data availability statement

The original contributions presented in the study are included in the article/Supplementary Material, further inquiries can be directed to the corresponding author.

Author contributions

XC: Data curation, Formal Analysis, Writing–original draft. YH: Methodology, Resources, Software, Writing–original draft. ZZ: Investigation, Validation, Visualization, Writing–original draft. YX: Conceptualization, Project administration, Supervision, Writing–original draft.

Funding

The author(s) declare financial support was received for the research, authorship, and/or publication of this article. The authors appreciate the financial support from Henan Provincial Key R&D and Promotion Project under Grant No. 232102220033.

Conflict of interest

The authors declare that the research was conducted in the absence of any commercial or financial relationships that could be construed as a potential conflict of interest.

Publisher's note

All claims expressed in this article are solely those of the authors and do not necessarily represent those of their affiliated organizations, or those of the publisher, the editors and the reviewers. Any product that may be evaluated in this article, or claim that may be made by its manufacturer, is not guaranteed or endorsed by the publisher.

References

1. Chen L, Zheng C, Chen H, Marburg S. Structural-acoustic sensitivity analysis of radiated sound power using a finite element/discontinuous fast multipole boundary element scheme. *Int J Numer Methods Fluids* (2016) 82:858–78. doi:10.1002/fld.4244

2. Junger MC, Feit D. *Sound, structures, and their interaction*, 225. Cambridge, MA: MIT press (1986).

3. Sommerfeld A. *Partial differential equations in Physics*. Academic Press (1949). doi:10.1016/B978-0-12-654658-3.50003-3

4. Engleder O, Steinbach S. Stabilized boundary element methods for exterior Helmholtz problems. *Numerische Mathematik* (2008) 110:145–60. doi:10.1007/s00211-008-0161-y

5. Everstine GC, Henderson FM. Coupled finite element/boundary element approach for fluid-structure interaction. *The J Acoust Soc America* (1990) 87:1938–1947. doi:10.1121/1.399320

6. Fritze D, Marburg S, Hardtke H-J (2005). FEM-BEM-coupling and structural-acoustic sensitivity analysis for shell geometries. *Comput Structures* 83, 143–54. doi:10.1016/j.compstruc.2004.05.019

7. Martinsson P, Rokhlin V. A fast direct solver for boundary integral equations in two dimensions. *J Comput Phys* (2005) 205:1–23. doi:10.1016/j.jcp.2004.10.033

8. Martinsson P, Rokhlin V. A fast direct solver for scattering problems involving elongated structures. *J Comput Phys* (2007) 221:288–302. doi:10.1016/j.jcp.2006.06.037

9. Bebendorf S, Rjasanow M. Adaptive low-rank approximation of collocation matrices. *Computing* (2003) 70:1–24. doi:10.1007/s00607-002-1469-6

10. Greengard L, Rokhlin V. A fast algorithm for particle simulations. *J Comput Phys* (1987) 73:325–48. doi:10.1016/0021-9991(87)90140-9

11. Coifman R, Rokhlin V, Wandzura S. The fast multipole method for the wave equation: a pedestrian prescription. *IEEE Antennas Propagation Mag* (1993) 35:7–12. doi:10.1109/74.250128

12. Rokhlin V. Diagonal forms of translation operators for the Helmholtz equation in three dimensions. *Appl Comput Harmonic Anal* (1993) 1:82–93. doi:10.1006/acha.1993.1006

13. Cheng H, Crutchfield WY, Gimbutas Z, Greengard LF, Ethridge JF, Huang J, et al. A wideband fast multipole method for the Helmholtz equation in three dimensions. *J Comput Phys* (2006) 216:300–25. doi:10.1016/j.jcp.2005.12.001

14. Gumerov NA, Duraiswami R. A broadband fast multipole accelerated boundary element method for the three dimensional Helmholtz equation. *J Acoust Soc America* (2009) 125:191–205. doi:10.1121/1.3021297

15. Takahashi T, Matsumoto T. An application of fast multipole method to isogeometric boundary element method for Laplace equation in two dimensions. *Eng Anal Boundary Elem* (2012) 36:1766–75. doi:10.1016/j.enganabound.2012.06.004

16. Simpson R, Liu Z. Acceleration of isogeometric boundary element analysis through a black-box fast multipole method. *Eng Anal Boundary Elem* (2016) 66:168–82. doi:10.1016/j.enganabound.2016.03.004

17. Chen L, Lian H, Xu Y, Li S, Liu Z, Atroshchenko E, et al. Generalized isogeometric boundary element method for uncertainty analysis of time-harmonic wave propagation in infinite domains. *Appl Math Model* (2023) 114:360–78. doi:10.1016/j.apm.2022.09.030

18. Gao H, Chen L, Lian H, Zheng C, Xu H, Matsumoto T. Band structure analysis for 2d acoustic phononic structure using isogeometric boundary element method. *Adv Eng Softw* (2020) 149:102888. doi:10.1016/j.advengsoft.2020.102888

19. Schneider S. FE/FMBE coupling to model fluid-structure interaction. *Int J Numer Methods Eng* (2008) 76:2137–56. doi:10.1002/nme.2399

20. Liu C, Chen L, Zhao W, Chen H. Shape optimization of sound barrier using an isogeometric fast multipole boundary element method in two dimensions. *Eng Anal Boundary Elem* (2017) 85:142–57. doi:10.1016/j.enganabound.2017.09.009

21. Chen L, Zhao J, Li H, Huang Y, Yuan X. A polynomial chaos expansion method for mechanical properties of flexoelectric materials based on the isogeometric finite element method. *Sustainability* (2023) 15:3417. doi:10.3390/su15043417

22. Cao G, Yu B, Chen L, Yao W. Isogeometric dual reciprocity bem for solving non-fourier transient heat transfer problems in fgms with uncertainty analysis. *Int J Heat Mass Transfer* (2023) 203:123783. doi:10.1016/j.ijheatmasstransfer.2022.123783

23. Chen L, Li H, Guo Y, Chen P, Atroshchenko E, Lian H. Uncertainty quantification of mechanical property of piezoelectric materials based on isogeometric stochastic fem with generalized n th-order perturbation. *Eng Comput* (2023) 1–21. doi:10.1007/s00366-023-01788-w

24. Hughes T, Cottrell J, Bazilevs Y. Isogeometric analysis: CAD, finite elements, NURBS, exact geometry and mesh refinement. *Comput Methods Appl Mech Eng* (2005) 194:4135–95. doi:10.1016/j.cma.2004.10.008

25. Chen L, Lu C, Lian H, Liu Z, Zhao W, Li S, et al. Acoustic topology optimization of sound absorbing materials directly from subdivision surfaces with isogeometric boundary element methods. *Comput Methods Appl Mech Eng* (2020) 362:112806. doi:10.1016/j.cma.2019.112806

26. Shen X, Du C, Jiang S, Sun L, Chen L. *Enhancing deep neural networks for multivariate uncertainty analysis of cracked structures by pod-rbf*. Theoretical and Applied Fracture Mechanics (2023).103925

27. Simpson R, Bordas S, Trevelyan J, Rabczuk T. A two-dimensional isogeometric boundary element method for elastostatic analysis. *Comput Methods Appl Mech Eng* (2012) 209-212:87–100. doi:10.1016/j.cma.2011.08.008

28. Simpson R, Bordas S, Lian H, Trevelyan J (2013). An isogeometric boundary element method for elastostatic analysis: 2D implementation aspects. *Comput Structures* 118, 2–12. doi:10.1016/j.compstruc.2012.12.021

29. Scott M, Simpson R, Evans J, Lipton S, Bordas S, Hughes T, et al. Isogeometric boundary element analysis using unstructured T-splines. *Comput Methods Appl Mech Eng* (2013) 254:197–221. doi:10.1016/j.cma.2012.11.001

30. Liu K, Meng L, Zhao A, Wang Z, Chen L, Li P. A hybrid direct fe2 method for modeling of multiscale materials and structures with strain localization. *Comput Methods Appl Mech Eng* (2023) 412:116080. doi:10.1016/j.cma.2023.116080

31. Ginnis A, Kostas K, Politis C, Kaklis P, Belibassakis K, Gerostathis T, et al. Isogeometric boundary-element analysis for the wave-resistance problem using T-splines. *Comput Methods Appl Mech Eng* (2014) 279:425–39. doi:10.1016/j.cma.2014.07.001

32. Peng X, Atroshchenko E, Kerfriden P, Bordas S. Linear elastic fracture simulation directly from CAD: 2D NURBS-based implementation and role of tip enrichment. *Int J Fracture* (2017) 204:55–78. doi:10.1007/s10704-016-0153-3

33. Peng X, Atroshchenko E, Kerfriden P, Bordas S (2017). Isogeometric boundary element methods for three dimensional static fracture and fatigue crack growth. *Comput Methods Appl Mech Eng* 316, 151–85. doi:10.1016/j.cma.2016.05.038

34. Simpson R, Liu Z, Vázquez R, Evans J. An isogeometric boundary element method for electromagnetic scattering with compatible B-spline discretizations. *J Comput Phys* (2018) 362:264–89. doi:10.1016/j.jcp.2018.01.025

35. Qu Y, Pan E, Zhu F, Jin F, Roy A. Modeling thermoelectric effects in piezoelectric semiconductors: new fully coupled mechanisms for mechanically manipulated heat flux and refrigeration. *Int J Eng Sci* (2023) 182:103775. doi:10.1016/j.ijengsci.2022.103775

36. Qu Y, Zhang G, Gao X, Jin F. A new model for thermally induced redistributions of free carriers in centrosymmetric flexoelectric semiconductor beams. *Mech Mater* (2022) 171:104328. doi:10.1016/j.mechmat.2022.104328

37. Qu Y, Jin F, Yang J. Temperature effects on mobile charges in thermopiezoelectric semiconductor plates. *Int J Appl Mech* (2021) 13:2150037. doi:10.1142/s175882512150037x

38. Xu Y, Li H, Chen L, Zhao J, Zhang X. Monte Carlo based isogeometric stochastic finite element method for uncertainty quantization in vibration analysis of piezoelectric materials. *Mathematics* (2022) 10:1840. doi:10.3390/math10111840

39. Chen L, Wang Z, Ma Y, Lian H, Meng Z, Li P, et al. Reduced order isogeometric boundary element methods for CAD-integrated shape optimization in electromagnetic scattering. *Comput Methods Appl Mech Eng* (2023) 419:116654. doi:10.1016/j.cma.2023.116654

40. Bandara K, Cirak F, Of G, Steinbach O, Zapletal J. Boundary element based multiresolution shape optimisation in electrostatics. *J Comput Phys* (2015) 297:584–98. doi:10.1016/j.jcp.2015.05.017

41. Kostas K, Ginnis A, Politis C, Kaklis P (2015). Ship-hull shape optimization with a T-spline based BEM-isogeometric solver. *Comput Methods Appl Mech Eng* 284, 611–22. doi:10.1016/j.cma.2014.10.030

42. Lian H, Kerfriden P, Bordas S. Shape optimization directly from CAD: an isogeometric boundary element approach using T-splines. *Comput Methods Appl Mech Eng* (2017) 317:1–41. doi:10.1016/j.cma.2016.11.012

43. Xu G, Li M, Mourrain B, Rabczuk T, Xu J, Bordas SP. Constructing IGA-suitable planar parameterization from complex CAD boundary by domain partition and global/local optimization. *Comput Methods Appl Mech Eng* (2018) 328:175–200. doi:10.1016/j.cma.2017.08.052

44. Li S, Trevelyan J, Zhang W, Wang D. Accelerating isogeometric boundary element analysis for 3-dimensional elastostatics problems through black-box fast multipole method with proper generalized decomposition. *Int J Numer Methods Eng* (2018) 114:975–98. doi:10.1002/nme.5773

45. Li S, Trevelyan J, Wu Z, Lian H, Wang D, Zhang W. An adaptive SVD-Krylov reduced order model for surrogate based structural shape optimization through isogeometric boundary element method. *Comput Methods Appl Mech Eng* (2019) 349:312–38. doi:10.1016/j.cma.2019.02.023

46. Lian H, Chen L, Lin X, Zhao W, Bordas SPA, Zhou M. Noise pollution reduction through a novel optimization procedure in passive control methods. *Comput Model Eng Sci* (2022) 131:1–18. doi:10.32604/cmes.2022.019705

47. Simpson R, Scott M, Taus M, Thomas D, Lian H. Acoustic isogeometric boundary element analysis. *Comput Methods Appl Mech Eng* (2014) 269:265–90. doi:10.1016/j.cma.2013.10.026

48. Chen L, Lian H, Liu Z, Chen H, Atroshchenko E, Bordas S. Structural shape optimization of three dimensional acoustic problems with isogeometric boundary element methods. *Comput Methods Appl Mech Eng* (2019) 355:926–51. doi:10.1016/j.cma.2019.06.012

49. Chen L, Lian H, Natarajan S, Zhao W, Chen X, Bordas S. Multi-frequency acoustic topology optimization of sound-absorption materials with isogeometric boundary element methods accelerated by frequency-decoupling and model order reduction techniques. *Comput Methods Appl Mech Eng* (2022) 395:114997. doi:10.1016/j.cma.2022.114997

50. Chen L, Wang Z, Peng X, Yang J, Wu P, Lian H. Modeling pressurized fracture propagation with the isogeometric bem. *Geomechanics Geophys Geo-Energy Geo-Resources* (2021) 7:51. doi:10.1007/s40948-021-00248-3

51. Burkhart D, Hamann B, Umlauf G. Iso-geometric finite element analysis based on catmull-clark: subdivision solids. *Comput Graphics Forum* (2010) 29:1575–84. doi:10.1111/j.1467-8659.2010.01766.x

52. Wei X, Zhang Y, Hughes TJ, Scott MA. Truncated hierarchical Catmull-Clark subdivision with local refinement. *Comput Methods Appl Mech Eng* (2015) 291:1–20. doi:10.1016/j.cma.2015.03.019

53. Wawrzinek A, Polthier K. Integration of generalized B-spline functions on Catmull-Clark surfaces at singularities. *Computer-Aided Des* (2016) 78:60–70. doi:10.1016/j.cad.2016.05.008

54. Pan Q, Xu G, Xu G, Zhang Y. Isogeometric analysis based on extended Catmull-Clark subdivision. *Comput Maths Appl* (2016) 71:105–19. doi:10.1016/j.camwa.2015.11.012

55. Bandara K, Rüberg T, Cirak F. Shape optimisation with multiresolution subdivision surfaces and immersed finite elements. *Comput Methods Appl Mech Eng* (2016) 300:510–39. doi:10.1016/j.cma.2015.11.015

56. Bandara K, Cirak F. Isogeometric shape optimisation of shell structures using multiresolution subdivision surfaces. *Computer-Aided Des* (2018) 95:62–71. doi:10.1016/j.cad.2017.09.006

57. Liu Z, Majeed M, Cirak F, Simpson NR. Isogeometric FEM-BEM coupled structural-acoustic analysis of shells using subdivision surfaces. *Int J Numer Methods Eng* (2018) 113:1507–30. doi:10.1002/nme.5708

58. Chen L, Marburg S, Chen H, Zhang H, Gao H. An adjoint operator approach for sensitivity analysis of radiated sound power in fully coupled structural-acoustic systems. *J Comput Acoust* (2017) 25:1750003. doi:10.1142/s0218396x17500035

59. Chen L, Cheng R, Li S, Lian H, Zheng C, Bordas S. A sample-efficient deep learning method for multivariate uncertainty qualification of acoustic-vibration interaction problems. *Comput Methods Appl Mech Eng* (2022) 393:114784. doi:10.1016/j.cma.2022.114784

60. Chen L, Liu C, Zhao W, Liu L. An isogeometric approach of two dimensional acoustic design sensitivity analysis and topology optimization analysis for absorbing material distribution. *Comput Methods Appl Mech Eng* (2018) 336:507–32. doi:10.1016/j.cma.2018.03.025

61. Zhao W, Chen L, Chen H, Marburg S. An effective approach for topological design to the acoustic–structure interaction systems with infinite acoustic domain. *Struct Multidisciplinary Optimization* (2020) 62:1253–73. doi:10.1007/s00158-020-02550-2

62. Chen L, Marburg S, Zhao W, Liu C, Chen H. Implementation of isogeometric fast multipole boundary element methods for 2d half-space acoustic scattering problems with absorbing boundary condition. *J Theor Comput Acoust* (2019) 27:1850024. doi:10.1142/s259172851850024x

63. Chen L, Zhao J, Lian H, Yu B, Atroshchenko E, Li P. A bem broadband topology optimization strategy based on taylor expansion and soar method—application to 2d acoustic scattering problems. *Int J Numer Methods Eng* (2023) 124:5151–82. doi:10.1002/nme.7345

64. Kim NH, Dong J. Shape sensitivity analysis of sequential structural-acoustic problems using FEM and BEM. *J Sound Vibration* (2006) 290:192–208. doi:10.1016/j.jsv.2005.03.013

65. Marburg S. Developments in structural-acoustic optimization for passive noise control. *Arch Comput Methods Eng* (2002) 9:291–370. doi:10.1007/BF03041465

66. Lamancusa J. Numerical optimization techniques for structural-acoustic design of rectangular panels. *Comput Structures* (1993) 48:661–75. doi:10.1016/0045-7949(93)90260-K

67. Hambric SA. Sensitivity calculations for broad-band acoustic radiated noise design optimization problems. *J Vibration Acoust* (1996) 118:529–32. doi:10.1115/1.2888219

68. Marburg S, Hardtke H-J. Shape optimization of a vehicle hat-shelf: improving acoustic properties for different load cases by maximizing first eigenfrequency. *Comput Structures* (2001) 79:1943–57. doi:10.1016/S0045-7949(01)00107-9

69. Zhao W, Chen L, Chen H, Marburg S. Topology optimization of exterior acoustic-structure interaction systems using the coupled fem-bem method. *Int J Numer Methods Eng* (2019) 119:404–31. doi:10.1002/nme.6055

70. Choi K, Shim I, Wang S. Design sensitivity analysis of structure-induced noise and vibration. *J Vibration Acoust* (1997) 119:173–9. doi:10.1115/1.2889699

71. Wang S. Design sensitivity analysis of noise, vibration, and harshness of vehicle body structure. *Mech Structures Machines* (1999) 27:317–35. doi:10.1080/08905459908915701

72. Zheng C, Matsumoto T, Takahashi T, Chen H. Explicit evaluation of hypersingular boundary integral equations for acoustic sensitivity analysis based on direct differentiation method. *Eng Anal Boundary Elem* (2011) 35:1225–35. doi:10.1016/j.enganabound.2011.05.004

73. Schröder P. Subdivision for modeling and animation. In: *Acm siggraph 1998* (1998).

74. Cirak F, Ortiz M, Schröder P (2000). Subdivision surfaces: a new paradigm for thin-shell finite-element analysis. *Int J Numer Methods Eng* 47, 2039–72. doi:10.1002/(SICI)1097-0207(20000430)47:12¡2039::AID-NME872¿3.0.CO;2–1

75. Burton AJ, Miller GF. The application of integral equation methods to the numerical solution of some exterior boundary-value problems. *Proc R Soc Lond* (1971) 323:201–10. doi:10.1098/rspa.1971.0097

76. Ciskowski RD, Brebbia CA. *Boundary element methods in acoustics*. Springer (1991).

77. Chen L, Lian H, Liu Z, Gong Y, Zheng C, Bordas S. Bi-material topology optimization for fully coupled structural-acoustic systems with isogeometric FEM-BEM. *Eng Anal Boundary Elem* (2022) 135:182–95. doi:10.1016/j.enganabound.2021.11.005

78. Chen L, Lu C, Zhao W, Chen H, Zheng C. Subdivision surfaces - boundary element accelerated by fast multipole for the structural acoustic problem. *J Theor Comput Acoust* (2020) 28:2050011. doi:10.1142/S2591728520500115

frontiers | Frontiers in Physics

TYPE Original Research
PUBLISHED 07 February 2024
DOI 10.3389/fphy.2024.1351018

OPEN ACCESS

EDITED BY
Yilin Qu,
Northwestern Polytechnical University, China

REVIEWED BY
Yun Huang,
Hunan University, China
Zhang Yao,
Southwest Jiaotong University, China

*CORRESPONDENCE
Qingling Du,
duqingling@huanghuai.edu.cn

RECEIVED 06 December 2023
ACCEPTED 25 January 2024
PUBLISHED 07 February 2024

CITATION
Du Q, Pan Y, Zhao K and Gao D (2024), Research examining a spatial autocorrelation imaging method based on stationary characteristics of microtremors.
Front. Phys. 12:1351018.
doi: 10.3389/fphy.2024.1351018

Research examining a spatial autocorrelation imaging method based on stationary characteristics of microtremors

Qingling Du[1,2]*, Yanhui Pan[1], Kuanyao Zhao[1] and Denghui Gao[1]

[1]School of Architectural Engineering, Huanghuai University, Zhumadian, China, [2]Henan International Joint Laboratory of Structural Mechanics and Computational Simulation, Huanghuai University, Zhumadian, China

The spatial autocorrelation method is an important method for extracting the velocity dispersion curve from microtremor data. However, site data typically cannot strictly meet spatial and temporal stationary feature, and this greatly affects the accuracy of the calculation results of this method. Therefore, based on the cosine similarity theory, this study deduces the applicability of the spatial autocorrelation method to unidirectional Rayleigh surface waves and again verifies the applicability of this method to spatially and temporally stationary Rayleigh waves. The numerical simulation results demonstrate that the velocity dispersion curve can be extracted from a one-way Rayleigh wave using the spatial autocorrelation method to obtain an accurate geological profile, whereas the superposition of finite groups of Rayleigh waves in different directions cannot yield an accurate geological profile. In this study, we quantitatively analyzed the impact of the spatial autocorrelation method on the extraction of the velocity dispersion curve when the signal could not meet the characteristics of temporal and spatial stationarity through numerical simulation. The results reveal that the velocity-dispersion curve can be accurately extracted only when the signal satisfies both spatial and temporal stationarity. When a signal is closer to the spatial and temporal stationary characteristics, this indicates that a more accurate velocity dispersion curve can be extracted. These results provide a reference for improving the calculation accuracy of spatial autocorrelation methods.

KEYWORDS

microtremors, Rayleigh wave, numerical simulation, SPAC method, velocity dispersion

1 Introduction

Microtremors are ubiquitous in nature and include various linearly polarized waves (body and longitudinal waves) and elliptically polarized Rayleigh surface waves [1–6]. It has been observed that the Rayleigh surface waves in the far field are dominant, and the spectral characteristics are closely related to the site changes [7]. This study provides a feasible basis for geological exploration using micromotion Rayleigh surface waves. The micro-motion signal contains rich information, including wide-frequency Rayleigh waves from 0.1 Hz to tens of Hz, and the detection depth can also reach from a few meters to several thousand meters. Therefore, researchers have begun to study the application of microtremor Rayleigh wave signals in the context of geological engineering exploration. Seismic exploration using a micromotion signal is termed the micromotion method and is also known as the microtremor method. It is used to deduce the geological structure by studying the

frequency spectrum, velocity dispersion, and particle motion of the wave in the microtremors signal of the surface of the Earth. This enables the micro-motion signal to be widely used in site evaluation, engineering geophysics, and large-scale research examining the crust and mantle such as the frequency wavenumber method (F-K), the spatial correlation method (SPAC), the horizontal and vertical component Purby method (HVSR), and others [8–13].

The spatial autocorrelation method is important for extracting geological structural information using micromotion signals. This method was first proposed by Aki (1957). The basic principle of this method is to assume that the background noise fields incident in different directions around the array possess stationary random characteristics and the same phase velocity at the same frequency. Under this assumption, the cross-correlation of the spatial coordinates of the noise signal (vertical component) is received by two stations at different positions, and the azimuth average of the station pairs at different positions and the same distance is then calculated to obtain the spatial autocorrelation coefficient after the azimuth average. The spatial autocorrelation coefficient was used to fit the zero-order Bessel function of the first type, to calculate the phase velocity at different frequencies, and to obtain the dispersion curve of the surface wave. However, in theory, this method requires that geophones be uniformly distributed around the circumference, and this cannot be achieved in actual data acquisition [3]. In 1983, Okada and Sakajiri studied the collection and arrangement of spatial autocorrelation methods and demonstrated the rationality of a regular triangular arrangement. These research results promote a leap in the spatial autocorrelation method in practical applications [14]. Cho et al. analyzed the feasibility of the spatial autocorrelation method in 2008 and studied the error caused by the influence factors on the correlation coefficient, thus providing a theoretical basis for optimizing the results of the method [15]. In 1973, Cox et al. demonstrated the equivalence relationship between the spatial autocorrelation coefficient and the time-domain cross-correlation spectrum in Aki's spatial autocorrelation formula method [16]. Horike, Matsushima, Okada, Tokimatsu, and others studied the method of spatial autocorrelation to extract the velocity dispersion curve from the microtremor signal [17–22]. Okada introduced a theoretical derivation of microtremor spatial autocorrelation and its application in a literature review published in 2003 [22]. Asten studied the inversion of spatial autocorrelation velocity dispersion and the effects of array mode and signal incidence direction on velocity dispersion [23–25]. Luo studied the application of a spatial autocorrelation method to extract velocity dispersion from one-way Rayleigh surface waves [26]. However, it is difficult to arrange circular arrays in complex terrain sites. To adapt SPAC to more complex site conditions, Ling and Okada proposed the extended spatial auto-correlation (ESPAC) method in 1993, improved the SPAC method geophone array, allowed the diversity of array layouts, and designed linear array, T-type, and L-type geophone arrays [27]. Ohori (2002) and Parolai used the ESPAC method to detect underground structures and achieved good results [28–30]. Although its effect is not as accurate as that of the circular array, it can make the geophone array shape not limited to the circular array and promote further development of the spatial sub-correlation method. Cho et al. used numerical simulations to study the characteristics of the spatial autocorrelation method in the case of a full-wave field. These results imply a possible improvement in the accuracy of the microtremor array survey analysis for velocity-structure interference by applying the full-wave theory to the peak phase velocity [31]. Ikeda et al. corrected the correlation coefficient using the imaginary portion of the signal to improve the accuracy of the velocity dispersion curve and achieved good results in field data applications [32, 33].

Although this method has been extensively studied by many scholars and is widely used in engineering, most of the research focuses on improving the accuracy of the velocity dispersion curve using methods such as virtual spectral density, the number of circular geophones, nested geophones, changing the shape of geophones, joint active source exploration, and further mining of useful information in the microtremor signal. However, many problems remain associated with this method. The fundamental reason for this is that the theoretical assumption of this method is that the micromotion signal possesses the characteristics of space and time stability, and the geophones are densely distributed in the circumference. However, these two preconditions cannot be strictly met in practical applications. Skaji studied the time-stationary characteristics of a microtremor signal using the frequency distribution of the amplitude of the microtremor signal and its autocorrelation coefficient. The research demonstrates that microtremor data with a sampling time of 10 min are stable over time, but stationary characteristics cannot be maintained when the sampling time is greater than 3 hours. Additionally, the noise interference between nearby and other vehicles breaks the stationary state. The spatial stability must consider the spatial interval of data acquisition [7]. Toks et al. (1964) observed that the micromotion signal in the range of 1–6s s contains multiple directional signal sources, and the short-period micromotion signal was unstable for more than 5 or 10 min. It can be observed that the conditions required for the microtremor signals of different frequency bands to meet the stationary characteristics are different [34]. This causes the velocity dispersion curve extracted using this method to be erroneous.

In summary, research examining spatial autocorrelation methods has primarily focused on arrangement, data acquisition, and joint inversion. Although current research focused on spatial autocorrelation is fruitful and has been applied to some practical projects, the problem of the accuracy of the velocity–dispersion curve extraction of this method has still not been perfectly solved. This significantly limits the application of this method in engineering. However, few studies have been conducted examining the influence of the time- and space-stationary characteristics of data on the velocity dispersion curve. Based on the cosine similarity theory and numerical simulations, this study analyzes the influence mechanism of time and space stationarity on the spatial autocorrelation method to extract the velocity dispersion curve from the perspective of theory and simulation, thus providing a reference for further research on the calculation accuracy and application range of this method.

2 Methods

In this study, the spatial autocorrelation method was derived based on the cosine similarity theory that measures the similarity between two vectors using the cosine value of their angle. The

similarity between the two vector directions can be determined using the cosine of the angle between the two vectors. When two vectors possess the same direction, the cosine similarity value is 1, and when the angle between two vectors is 90°, the cosine similarity is zero. When two vectors point in opposite directions, the cosine similarity value is −1. This result is independent of the vector length and is related only to the direction of the vector. This method of measuring the vector similarity is also applicable to multi-dimensional vectors.

As any signal of finite length is discretized into finite points when received, this study addresses each segment of the signal as a multi-dimensional vector, and the cosine similarity of the two vectors can be expressed by formula (1).

$$\boldsymbol{cos}(\boldsymbol{\theta}) = \frac{\sum_{k=1}^{n} \boldsymbol{x}_{1k}\boldsymbol{x}_{2k}}{\sqrt{\sum_{k=1}^{n} \boldsymbol{x}_{1k}{}^2}\sqrt{\sum_{k=1}^{n} \boldsymbol{x}_{2k}{}^2}} \tag{1}$$

The more similar the two vectors, the smaller the angle is between them. The larger the absolute value of the cosine, the more negative is the value, and the two vectors are negatively correlated. The inner product of the vector is expressed as follows:

$$\mathbf{cos}(\boldsymbol{\theta}) = \frac{\mathbf{X} \cdot \mathbf{Y}}{|\mathbf{X}| \cdot |\mathbf{Y}|} \tag{2}$$

Where, $X = (x_{1,}x_{2,}\cdots x_{n,})$ and $Y = (y_{1,}y_{2,}\cdots y_{n,})$.

If vectors X and Y are points on functions $f(t)$ and $g(t)$, respectively, the sampling rate is sufficient. Eq. 1 can be written as:

$$\mathbf{cos}(\boldsymbol{\theta}) = \frac{\sum_{k=1}^{n} f(\mathbf{t_k})\mathbf{g}(\mathbf{t_k})}{\sqrt{\sum_{k=1}^{n} \mathbf{f}(\mathbf{t_k})^2}\sqrt{\sum_{k=1}^{n} \mathbf{f}(\mathbf{t_k})^2}} \tag{3}$$

The definite integral of function $f(x)$ in the definition domain (a, b) can be expressed as follows:

$$\lim_{n\to+\infty} \sum_{i=1}^{n} \boldsymbol{f}\left[\boldsymbol{a} + \frac{\boldsymbol{i}}{\boldsymbol{n}}(\boldsymbol{b}-\boldsymbol{a})\right] \frac{\boldsymbol{b}-\boldsymbol{a}}{\boldsymbol{n}} = \int_{a}^{b} \boldsymbol{f}(\boldsymbol{x})\boldsymbol{dx} \tag{4}$$

According to the definition of the definite integral, when the sampling interval is infinite and the number of sampling points n tends to infinity, the summation formula can be expressed as a definite integral:

$$\begin{aligned}\mathbf{cos}(\boldsymbol{\theta}) &= \frac{\lim_{\mathbf{n}\to+\infty} \frac{\mathbf{T}}{\mathbf{n}}\sum_{\mathbf{k}=1}^{\mathbf{n}} f(\mathbf{t_k})\mathbf{g}(\mathbf{t_k})}{\lim_{\mathbf{n}\to+\infty} \sqrt{\frac{\mathbf{T}}{\mathbf{n}}\sum_{\mathbf{k}=1}^{\mathbf{n}} \mathbf{f}(\mathbf{t_k})^2}\sqrt{\frac{\mathbf{T}}{\mathbf{n}}\sum_{\mathbf{k}=1}^{\mathbf{n}} \mathbf{g}(\mathbf{t_k})^2}} \\ &= \frac{\int_{-\frac{\mathbf{T}}{2}}^{\frac{\mathbf{T}}{2}} \mathbf{f}(\mathbf{t})\mathbf{g}(\mathbf{t})\mathbf{dt}}{\sqrt{\int_{-\frac{\mathbf{T}}{2}}^{\frac{\mathbf{T}}{2}} \mathbf{f}(\mathbf{t})^2\mathbf{dt}}\sqrt{\int_{0}^{\mathbf{T}} \mathbf{g}(\mathbf{t})^2\mathbf{dt}}}\end{aligned} \tag{5}$$

According to the Fourier transform, any seismic wave signal can be obtained by the harmonic superposition of different frequencies and amplitudes. We first assume that $f(t) = cos(\omega t)$, $g(t) = cos(\omega t + \Delta\delta)$ is a function on [-T/2, T/2], We then assume that $f(t) = cos(\omega t)$ and $g(t) = cos(\omega t + \Delta\delta)$ are two functions on the interval [-T/2, T/2]. These two functions are cosine waves with different phases that propagate in the same direction. At this time, the cosine similarity of functions f (t) and g (t) can be rewritten from Formula (5) as follows:

$$\boldsymbol{cos}(\boldsymbol{\theta}) = \frac{\int_{-\frac{T}{2}}^{\frac{T}{2}} \boldsymbol{cos}(\boldsymbol{\omega t})\,\boldsymbol{cos}\,(\boldsymbol{\omega t} + \boldsymbol{\Delta\delta})\boldsymbol{dt}}{\sqrt{\int_{-\frac{T}{2}}^{\frac{T}{2}} \boldsymbol{cos}(\boldsymbol{\omega t})^2\boldsymbol{dt}}\sqrt{\int_{-\frac{T}{2}}^{\frac{T}{2}} \boldsymbol{cos}\,(\boldsymbol{\omega t} + \boldsymbol{\Delta\delta})^2\boldsymbol{dt}}} \tag{6}$$

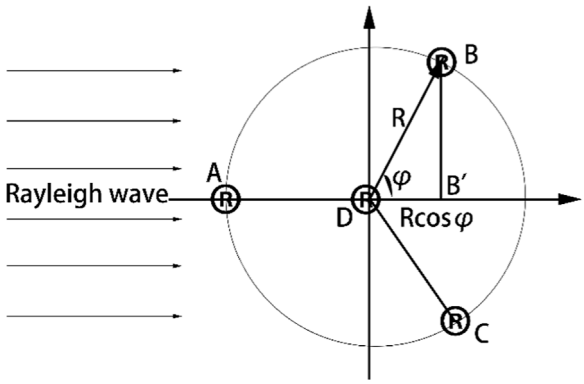

FIGURE 1
Plane wave and circular geophones array.

We can simplify Equation 6 to yield:

$$\begin{aligned}\boldsymbol{cos}(\boldsymbol{\theta}) &= \frac{\int_{-\frac{T}{2}}^{\frac{T}{2}} \boldsymbol{cos}(\boldsymbol{\omega t})\,\boldsymbol{cos}(\boldsymbol{\omega t} + \boldsymbol{\Delta\delta})\boldsymbol{dt}}{\sqrt{\int_{-\frac{T}{2}}^{\frac{T}{2}} \boldsymbol{cos}(\boldsymbol{\omega t})^2\boldsymbol{dt}}\sqrt{\int_{\frac{T}{2}}^{\frac{T}{2}} \boldsymbol{cos}(\boldsymbol{\omega t} + \boldsymbol{\Delta\delta})^2\boldsymbol{dt}}} \\ &= \frac{\boldsymbol{cos}(\boldsymbol{\Delta\delta}) \cdot \left(\frac{t}{2} + \frac{1}{4\omega}\boldsymbol{sin}^2(\boldsymbol{\omega t})\right)\Big|_{-\frac{T}{2}}^{\frac{T}{2}} - \boldsymbol{sin}(\boldsymbol{\Delta\delta}) \cdot \frac{1}{2\omega}\boldsymbol{sin}^2(\boldsymbol{\omega t})\Big|_{-\frac{T}{2}}^{\frac{T}{2}}}{\sqrt{\frac{t}{2} + \frac{1}{4\omega}\boldsymbol{sin}^2(\boldsymbol{\omega t})\Big|_{-\frac{T}{2}}^{\frac{T}{2}}}\sqrt{\frac{t}{2} + \frac{1}{4\omega}\boldsymbol{sin}^2(\boldsymbol{\omega t} + \boldsymbol{\Delta\delta})\Big|_{-\frac{T}{2}}^{\frac{T}{2}}}} \\ &= \boldsymbol{cos}\,(\boldsymbol{\Delta\delta})\end{aligned} \tag{7}$$

The integral in formula (7) is only related to vector θ, specifically:

$$\boldsymbol{cos}(\boldsymbol{\theta}) = \boldsymbol{cos}\,(\boldsymbol{\Delta\delta}) \tag{8}$$

It can be observed from Equation 8 that when the functions $f(t)$ and $g(t)$ are regarded as vectors, θ is the angle of the n-dimensional vector, and $cos(\theta)$ is the vector similarity. If the functions $f(t)$ and $g(t)$ are regarded as two cosine functions, θ is the phase difference between two cosine functions. According to the above conclusion, if the functions $f(t)$ and $g(t)$ are regarded as the signals of cosine waves received by two points A and B on the free surface of a homogeneous half space assuming that the distance between two points A and B is x, the wave propagation velocity in the medium of the half-space is v, and the wave propagates along direction AB. The following equation can be established based on the phase difference:

$$\boldsymbol{\theta} = \frac{\boldsymbol{\omega x}}{\boldsymbol{v}} = \frac{\boldsymbol{2\pi f x}}{\boldsymbol{v}} \tag{9}$$

Any signal in nature can be regarded as a superposition of multiple sinuses or cosines of different frequencies. Eq. 6 represents the similarity of the single-frequency harmonic signals, and $\frac{1}{T}\int_{-\frac{T}{2}}^{\frac{T}{2}} f(t)g(t)dt$ represents the energy spectrum of the two single-frequency signals. The energy of a single frequency is the energy spectral density, and the power is the power spectral density. Therefore, if signals $f(t)$ and $g(t)$ are

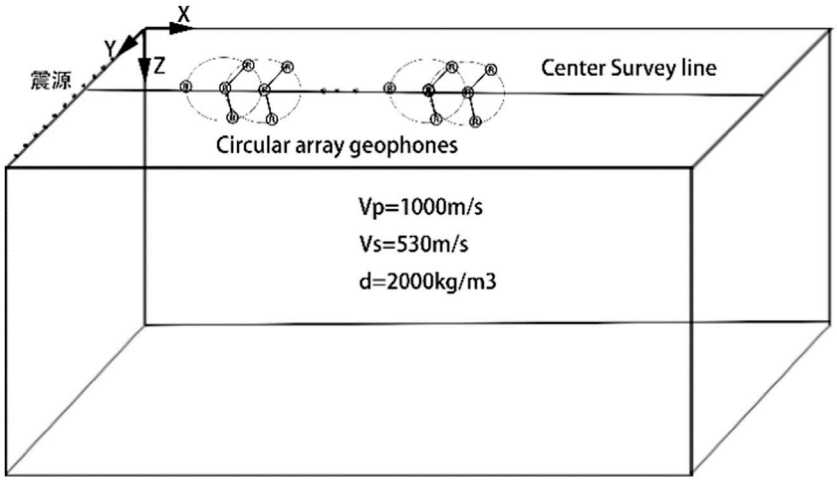

FIGURE 2
Homogeneous half-space model.

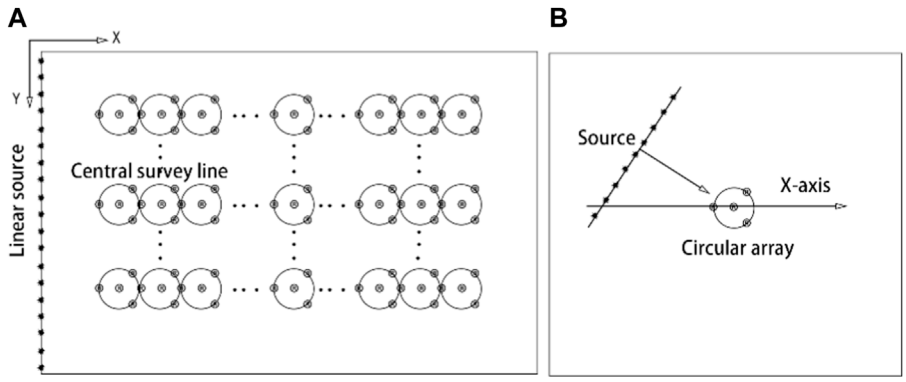

FIGURE 3
Arrangement of source and geophone. **(A)** Arrangement of geophone; **(B)** arrangement of source.

TABLE 1 Elastic parameters of medium.

Media properties	Longitudinal wave velocity VP(m/s)	Shear wave velocity VS(m/s)	Density ρ (g/cm^3)
Media	1,000 m/s	530 m/s	2000 g/cm^3

broadband signals containing more than one frequency, (6) can be rewritten as follows:

$$cos(\theta(f)) = \frac{\int_{-\frac{T}{2}}^{\frac{T}{2}} f(t)g(t)dt}{\sqrt{\int_{-\frac{T}{2}}^{\frac{T}{2}} f(t)^2 dt}\sqrt{\int_{-\frac{T}{2}}^{\frac{T}{2}} g(t)^2 dt}} = \frac{\frac{1}{T}\int_{-\frac{T}{2}}^{\frac{T}{2}} f(t)g(t)dt}{\sqrt{\frac{1}{T}\int_{-\frac{T}{2}}^{\frac{T}{2}} f(t)^2 dt}\sqrt{\frac{1}{T}\int_{-\frac{T}{2}}^{\frac{T}{2}} g(t)^2 dt}} \quad (10)$$

The numerator and denominator correspond to the spectral density functions. The left side of (10) is the correlation coefficient of signals $f(t)$ and $g(t)$. This is also a formula for calculating the velocity of Rayleigh surface waves in one-dimensional arrangement according to the spatial autocorrelation method.

Two-dimensional spatial geophones are arranged in a circular manner, and a triangular arrangement as an example is presented in Figure 1.

When a unidirectional plane Rayleigh surface wave is transmitted, if there are only two AB geophones arranged along the wave propagation direction, the velocity dispersion curve can be calculated according to (11).

$$cos\left(\frac{2\pi f R}{v}\right) = \frac{\int_{-\frac{T}{2}}^{\frac{T}{2}} f(t)g(t)dt}{\sqrt{\int_{-\frac{T}{2}}^{\frac{T}{2}} f(t)^2 dt}\sqrt{\int_{-\frac{T}{2}}^{\frac{T}{2}} g(t)^2 dt}} = \rho(f) \quad (11)$$

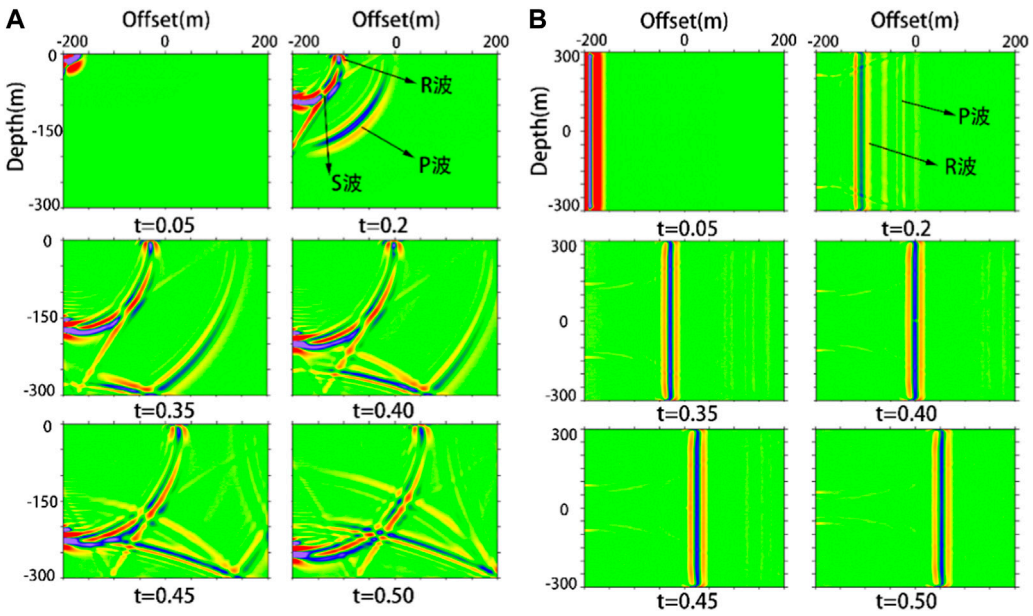

FIGURE 4
Arrangement of source and geophone. **(A)** the vertical section wave field; **(B)** the horizontal section wave field.

As presented in the figure, when AB is not arranged along the wave propagation direction, Eq. 11 cannot accurately provide the velocity dispersion curve. For the plane Rayleigh surface wave signal, the signal received at point B is the same as that at point B Therefore, the following formula can be used to calculate the velocity dispersion curve from the signals at points B and D:

$$\rho_B(f,\varphi) = \cos\left(\frac{2\pi f}{v} R\cos(\varphi)\right) \tag{12}$$

When the geophones are uniformly and densely arranged on the circumference, the data of each point on the circumference can be processed in the same manner as for that of B. The following formula can be obtained by averaging the results of all the points:

$$\rho(f) = \frac{1}{2\pi}\int_0^{2\pi} \rho(f,\varphi)d\varphi = \frac{1}{2\pi}\int_0^{2\pi} \cos\left(\frac{2\pi f}{v} R\cos(\varphi)\right)d\varphi = J_0\left(\frac{2\pi f R}{v}\right) \tag{13}$$

This conclusion is the same as that of the spatial autocorrelation method under the conditions of spatial and temporal stationarity in which the formula for calculating the correlation coefficient is as follows:

$$\rho(r,f) = \frac{\pi}{2}\int_0^{2\pi} \frac{Re[S(r,\theta,f)]}{\sqrt{S_r(r,f)S_0(0,f)}}d\theta, \tag{14}$$

Where $S_r(r,f)$ *and* $S_0(0,f)$ are the self-power spectrum of the seismic record at the circumference and center, respectively, and $S(r,\theta,f)$ is the cross power spectrum of the seismic record on the circumference and the seismic record at the center of the circle.

A single-direction Rayleigh surface wave is calculated using a circular spatial autocorrelation array. When the signal meets the spatial and temporal stationary characteristics, the spatial autocorrelation method can be used to calculate the dispersion curve. However, in actual received signals, it is difficult to meet the requirements of time and space stationarity in many cases. Therefore, this study considers a situation in which the signal does not meet the stationarity characteristics in the later numerical simulation portion of the paper. It is likely that a precise spatial autocorrelation exploration can be realized by combining stationary and nonstationary signals.

3 Numerical simulation

The finite element method has a wide range of applications in the simulation of acoustic and seismic wave propagation [35–38]. This section primarily focuses on three aspects that include the establishment of a numerical model, the extraction of the velocity dispersion curve of a single group of Rayleigh waves in a homogeneous half-space, and the extraction of the velocity dispersion curve of multiple Rayleigh waves.

3.1 Numerical model

First, the numerical models and parameters used in the velocity-dispersion simulation are introduced. Considering the far-field characteristics of the microtremor signal, a plane-wave source was used for numerical simulation. Each plane-wave source is composed of a linear array of point sources. According to Huygens' principle, the wavefront of a Rayleigh wave radiated by a linear array of point sources is of the plane type. In this study, the plane-wave field was simulated in this manner. The model grid was divided into 2m, and the 20 Hz dominant frequency of the Rick wavelet was selected as the source. The circular array radius of the geophones was 2m, and 15 survey lines were set with each side-line

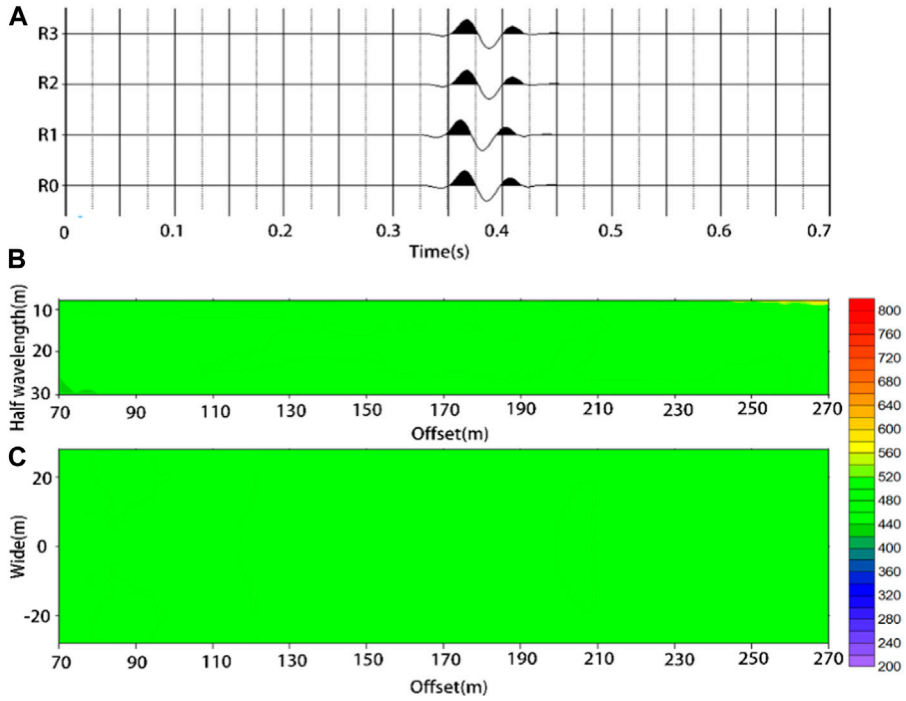

FIGURE 5
Single source simulation results of homogeneous half-space model; **(A)** vertical component seismic records of single circular array; **(B)** the vertical velocity profile of the centerline; **(C)** the velocity horizontal slice at 20m from the free surface.

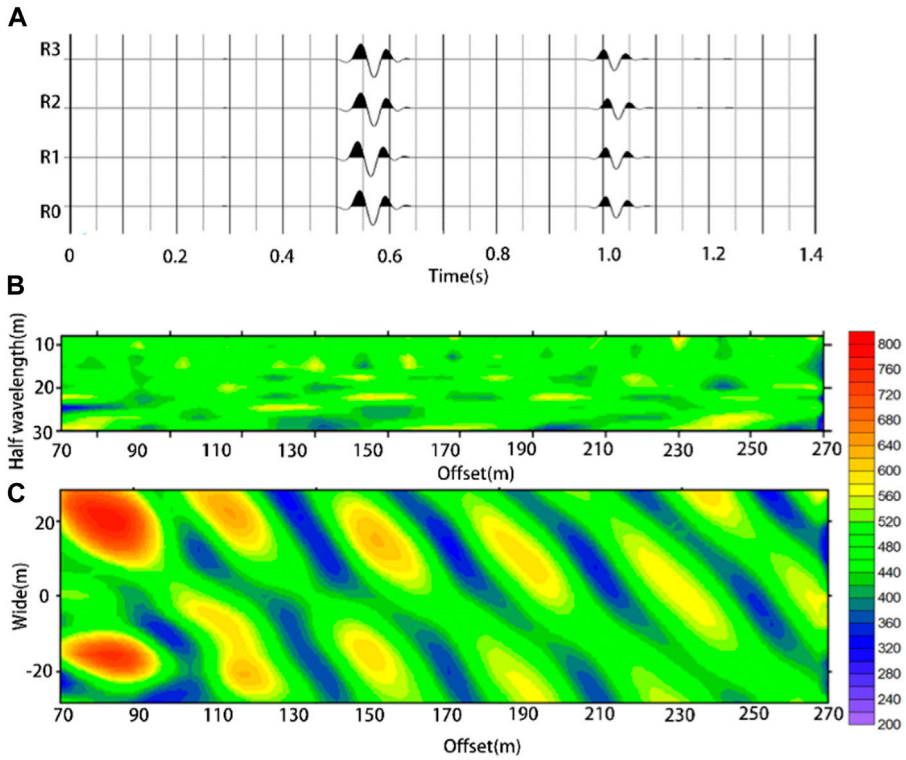

FIGURE 6
Multi-direction Rayleigh surface wave simulation results of the homogeneous half-space model. **(A)** vertical component seismic records of single circular array; **(B)** the vertical velocity profile of the centerline; **(C)** the horizontal velocity profile at 20m from the free surface.

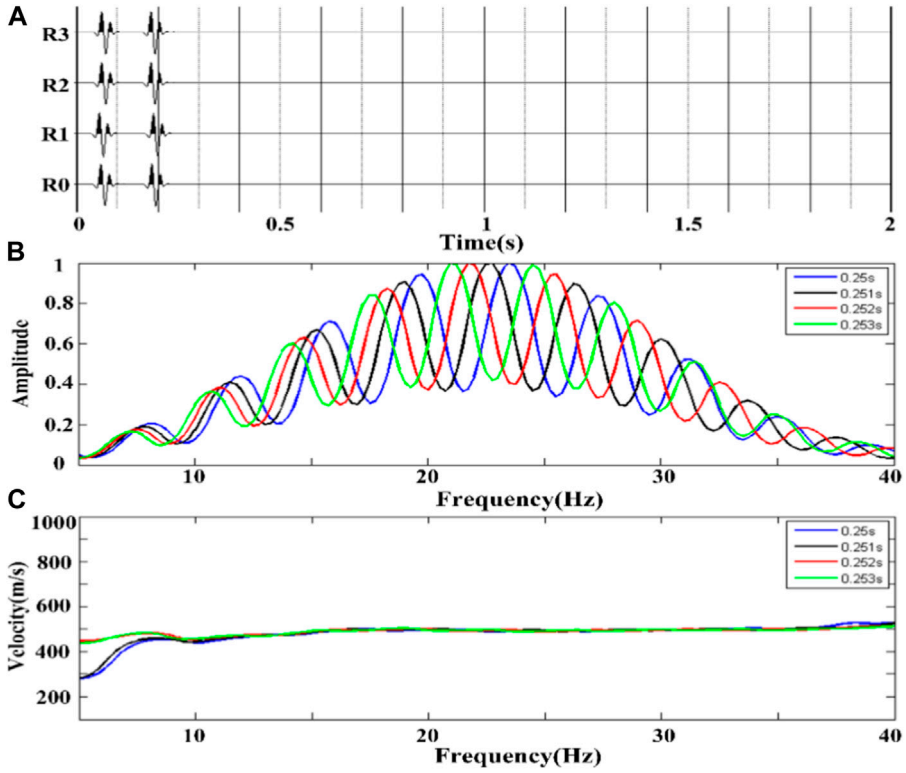

FIGURE 7
Same direction Rayleigh surface wave with different time intervals. **(A)** a single-array Rayleigh wave vertical component seismic record with an interval of 0.253s; **(B)** the spectrum diagram of four groups of seismic records; **(C)** the velocity dispersion curve of each group of seismic records.

4m apart. The basic model is presented in Figure 2 and indicates only a circular geophone array on the central side.

This study primarily focused on two aspects that included the velocity profile characteristics of the half-space model and the influence of the multi-directional Rayleigh surface wave on the spatial autocorrelation method to extract the velocity dispersion curve. According to different research contents, different sources and geophone distributions were set in this study as presented in Figure 3. All of the data related to the velocity profile in this study are derived from the layout in Figure 3A. Among them, Rayleigh surface wave data with two propagation directions were additionally loaded with linear sources as presented in Figure 3A. Relevant research data for the velocity dispersion curve of a single array were derived from the layout presented in Figure 3B. The multi-source data revealed a continuous increase in linear sources around the circular array as presented in Figure 3B. The vertical distance between the linear sources and the circular array was the same. The difference in the wave arrival times was determined by adjusting the shooting time. Table 1 presents the elastic parameters of the half-space model.

3.2 Application analysis of numerical simulation

First, the wave field distribution and velocity dispersion characteristics of a single-source Rayleigh wave inhomogeneous half-space were analyzed. To clearly reveal the distribution of the wave field excited by a plane source in a homogeneous half-space, we extracted snapshots of the vertical wave field along the central line and the horizontal wave field on the free surface as presented in Figure 4. The vertical wave field snapshot (Figure 4A) clearly distinguishes the S wave (shear waves), P wave (longitudinal waves), and R wave (Rayleigh surface waves) after 0.2s. After 0.35s, the reflected wave of P wave reflected from the bottom boundary appears below. To prevent the interference caused by boundary reflection, the operation time was set to be less than the time required for the reflected wave to reach the ground. Figure 4B presents a snapshot of the wave field in the horizontal section. The P and R waves can also be clearly distinguished after 0.2s. As the energy of the P wave is weak, and the diffusion speed is faster than that of the Rayleigh surface wave, the color code in the figure is shallow. The wave field distribution of the plane-wave source in the homogeneous model is clearly presented.

According to the needs of the experiment, the sampling interval of the homogeneous half-space model data was 0.0005s, the sampling time was 0.7s, and the seismic records of 15 survey lines were obtained. Figure 5A presents the data of an array in the central line, whereR1, R2, and R3 are the three vertical component seismic records uniformly distributed on the circumference of the array, and R0 is the vertical component seismic record at the center of the circle. It can be observed from the seismic records that there was no interference (similar to the coda and refraction waves) before and after the primary wave peak.

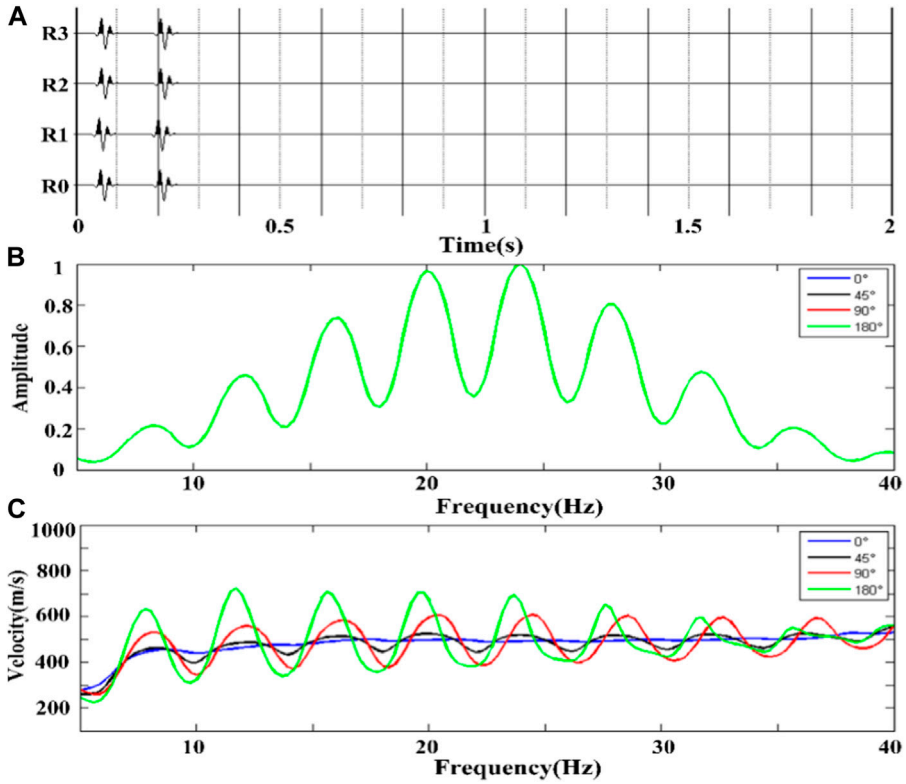

FIGURE 8
Rayleigh surface waves with different propagation directions at the same time interval. **(A)** a single array Rayleigh wave vertical component seismic record with opposite propagation direction; **(B)** frequency spectrum of four groups of seismic records; **(C)** velocity dispersion curve of each group of seismic records.

Next, we analyzed the velocity dispersion of the homogeneous half-space data. According to this theory, the spatial autocorrelation method calculates the velocity dispersion curve using the relationship between the correlation coefficient and the first zero-order Bessel function. A velocity-dispersion curve can be obtained if an accurate correlation coefficient is obtained. The correlation coefficient and velocity dispersion curve were calculated using (13) and 14, respectively.

The spatial autocorrelation method was used to calculate the velocity-dispersion curve of each measuring point in the 15 measuring lines. The corresponding velocity profile was obtained by collecting the dispersion curves. Figure 5B presents the vertical velocity profile obtained from the seismic records of the central line. The depth of the profile was converted to a half wavelength. Figure 5C presents the calculation results of the seismic records of the 15 survey lines and the construction of a horizontal section with a half-wavelength of 20 m. The two sections clearly reflect the homogeneous properties of the half-space. The calculated Rayleigh wave velocity was also consistent with the theoretical Rayleigh wave velocity, where Vs .= 490 m/s. This indicates that the spatial autocorrelation method can be used to calculate the velocity dispersion curve of a single set of Rayleigh waves and that the seismic records obtained by the numerical simulation software and method are reliable.

When the micromotion signal satisfies the spatial and temporal stationary characteristics, the velocity dispersion curve obtained by the spatial autocorrelation method can truly reflect the velocity property of the medium, and the theoretical and practical applications have been verified. The above numerical simulation verified that a single-plane Rayleigh surface wave can also reflect the medium properties of a homogeneous half-space. However, the composition of the surface waves of microtremor signals is complex and typically contains multiple sets of surface waves. Therefore, considering the superposition of two sets of Rayleigh surface waves as an example, this study uses a numerical simulation method to study a situation in which the signal contains two sets of Rayleigh surface waves with mutually perpendicular propagation directions. Two sets of plane sources were set in the homogeneous half-space model with one along the central line direction and the other perpendicular to the central line direction. The simulation results are presented in Figure 6.

Figure 6A presents the vertical component of the seismic record of one of the circular array geophones. Both the vertical (Figure 6B) and horizontal velocity profiles (Figure 6C) exhibit obvious high- and low-velocity anomalies. As the alternation of high- and low-velocity anomalies is relatively evident with frequency, the anomalies in the fixed-frequency wave velocity distribution profile (Figure 6C) were more evident than were those in the vertical profile (Figure 6B). However, regardless of the horizontal or vertical velocity profiles, the velocity distribution was significantly different from the theoretical velocity distribution of the homogeneous half-space model. This also indicates that the

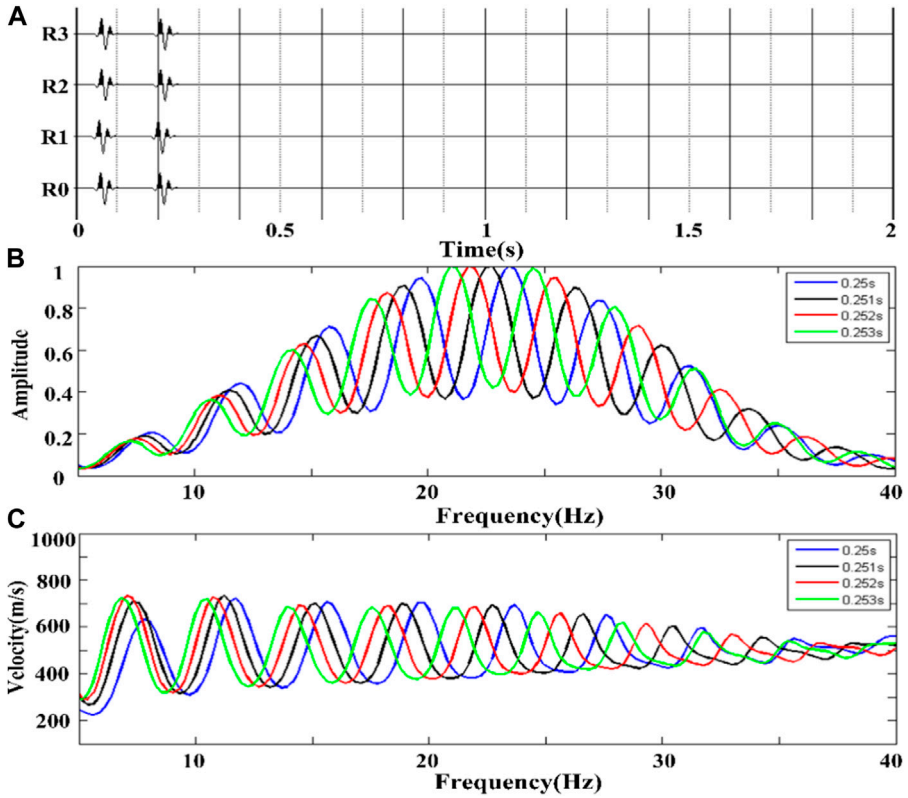

FIGURE 9
Reverse Rayleigh surface wave superposition at different time intervals. **(A)** a single-array Rayleigh wave vertical component seismic record with an interval of 0.253s; **(B)** frequency spectrum of four groups of seismic records; **(C)** velocity dispersion curve of each group of seismic records.

credibility of the velocity dispersion curve extracted by the spatial autocorrelation method is significantly reduced when the Rayleigh surface wave superposition in different directions does not satisfy the stationary condition.

From the above numerical simulation experiment results, it can be observed that a single set of Rayleigh surface waves can accurately extract the velocity dispersion curve through the spatial autocorrelation method, but the nonstationary superposition of multiple sets of Rayleigh surface waves may affect the calculation of the velocity dispersion curve. The following section discusses the influence of nonspatial and time-stationary signals superimposed by multiple groups of surface waves on the velocity dispersion curve of the spatial autocorrelation method.

4 Analysis of influencing factors of the velocity dispersion curve

When the micromotion signal meets the requirements of spatial and temporal stationarity, the spatial autocorrelation method can be used to calculate the velocity dispersion curve, and this has been confirmed by Aki's theory and has been widely applied by many scholars [10]. Concurrently, through the theoretical derivation and simulation results in the previous section, it can be observed that the spatiotemporal autocorrelation method is also valid when only a single-plane Rayleigh wave is accepted by a circular array. However, many scholars have demonstrated that it is difficult for ground pulsation signals to satisfy stationary characteristics in space and time. It is necessary to consider the length and spatial distance of a section of the signal, particularly for surrounding cities and high-speed railways, as some frequency-band signals exhibit obvious directionality. In these cases, the traditional spatial autocorrelation method cannot be used to calculate the velocity-dispersion curve. Specifically, when the Rayleigh surface wave superposition in different directions in the signal does not satisfy the spatial and temporal stationary characteristics, the velocity dispersion cannot accurately analyze the characteristics of the medium.

This section primarily studies the situation in which the signal does not meet the stationary characteristics of space and time and contains multiple sets of Rayleigh surface waves as well as the influence of the non-stationary state of the microtremor signal on the spatial autocorrelation method to extract the velocity dispersion curve. The stationary characteristics of time and space are primarily reflected in the arrival time interval and propagation direction of different waves in the signal. Focusing on these two characteristics, two groups and multiple groups of Rayleigh wave superpositions were discussed. As the purpose of the experiment was to analyze the influence of the characteristics of the signal itself on the velocity dispersion curve, all the experimental data were from the homogeneous model. There was no interference caused by the difference in geological structure, and only the Rayleigh surface wave was retained by filtering when processing the data. The experimental half-space model is presented in Figure 2 and

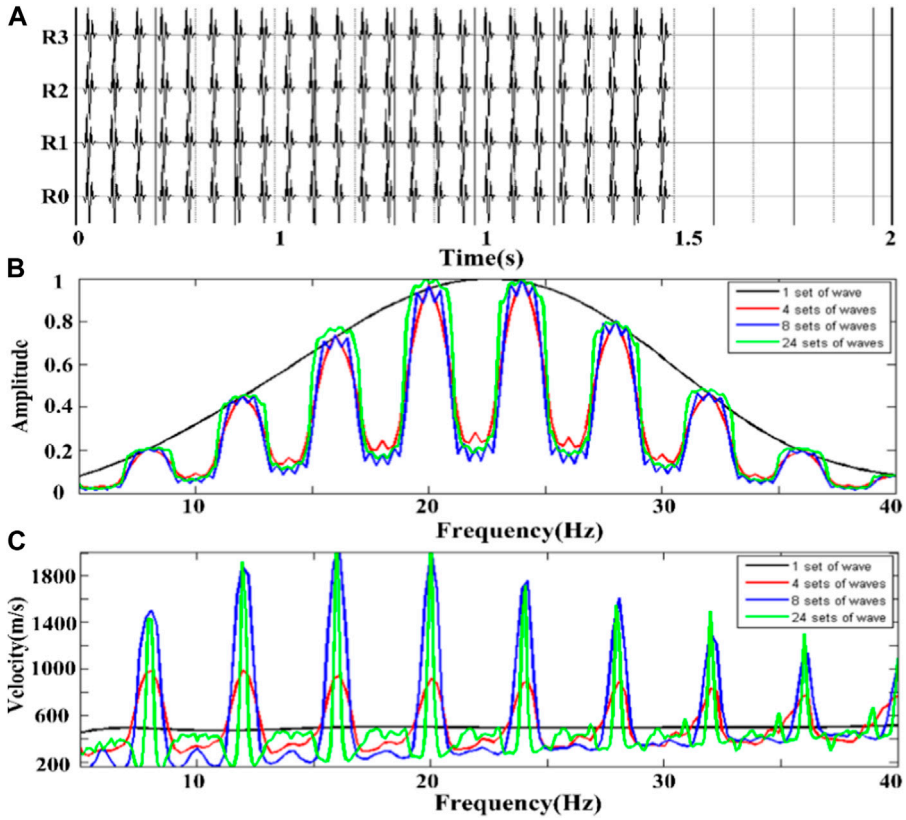

FIGURE 10
Multiple sets of Rayleigh surface waves in different directions with equal time intervals. **(A)** the single array Rayleigh wave vertical component seismic record when 24 groups of waves are superpositioned; **(B)** the spectrum diagram of four groups of seismic records; **(C)** the velocity dispersion curve of each group of seismic records.

Figure 3B As the data were too large, only a single circular array was arranged in the center of the model in this section. The array comprises four sensors. The following describes the numerical experimental analysis process and research results presented in this section.

4.1 Two groups of Rayleigh wave superposition

This section primarily considers the influence of two groups of Rayleigh surface waves superimposed at different time intervals or in different directions on the spatial autocorrelation velocity-dispersion curve. First, the influence of two sets of Rayleigh waves propagating in the same direction on the velocity-dispersion curve was studied. In this study, the same source was used for two consecutive shots within 2s with time intervals of 0.25, 0.251, 0.252, and 0.253s to obtain four sets of data. Each dataset contained two Rayleigh surface waves that propagated in the same direction. One group of seismic records is presented in Figure 7A, and Figure 7B presents the spectral distribution of the seismic records.

Figure 7A presents four vertical-component seismic records of the circular array and center point, including two groups of co-propagating Rayleigh surface waves. It can be observed from Figure 7B that the effective frequency band of seismic records is 10 Hz–30 Hz, and there is a zigzag fluctuation that is caused by the time-shift characteristic of Fourier transform. Coherent phase cancellation occurred when the Rayleigh wave Fourier transform was superimposed. The velocity-dispersion curve was calculated using four sets of data as presented in Figure 7C The blue, black, red, and green curves in the figure correspond to the velocity dispersion curves of the two sets of seismic records with arrival intervals of 0.25, 0.251, 0.252, and 0.253s for the Rayleigh surface waves in the data. It can be observed from the figure that within the effective frequency band, the four curves are almost identical, and this can reflect the Rayleigh surface wave velocity of 490 m/s in the homogeneous half-space model. This also demonstrates that the superposition of two Rayleigh surface waves in the same direction does not affect the spatial autocorrelation method used for calculating the velocity–dispersion curve. The arrival times of the two sets of Rayleigh surface waves did not affect the velocity dispersion.

Next, we studied the influence of the superposition of two sets of Rayleigh surface waves in different directions on the dispersion curve. We fixed a plane source and continuously adjusted the angle between the other source and the fixed source to obtain four groups of seismic records of two Rayleigh surface wave superpositions with the angles of 0°, 45°, 90°, and 180° in the propagation direction.

Figure 8A presents a single array Rayleigh wave vertical component seismic record with the same time interval and

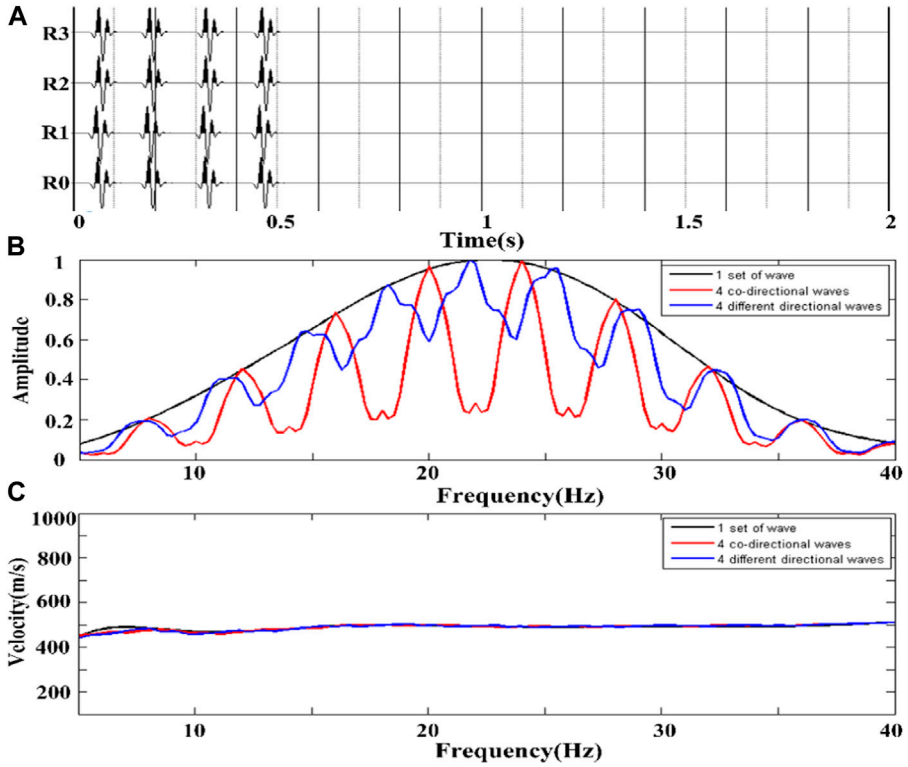

FIGURE 11
Multiple sets of Rayleigh surface waves in the same direction at different time intervals. **(A)** a single array vertical component seismic record with 4 groups of Rayleigh surface wave intervals superimposed at different times; **(B)** the spectrum diagram of three groups of seismic records; **(C)** the velocity dispersion curve of each group of seismic records.

opposite propagation direction, and Figure 8B corresponds to the spectrum of two groups of superimposed Rayleigh wave propagation directions with included angles of 0°, 45°, 90°, and 180°, respectively. It can be observed that the spectrum of four groups of seismic records is completely consistent, thus indicating that the coherent cancellation of the spectrum of Rayleigh wave superposition is only related to the time interval. The four curves (blue, black, red, and green, respectively) represent the velocity dispersion curves when the propagation directions of two groups of Rayleigh surface waves differ by 0°, 45°, 90°, and 180°. Experiments confirmed that the velocity dispersion curve of the superposition of two groups of Rayleigh surface waves in the same direction is consistent with the theoretical velocity. When the propagation directions of the two groups of superimposed Rayleigh surface waves differed, the velocity-dispersion curve periodically fluctuated around the theoretical value. As presented in Figure 8C, the fluctuation became increasingly intense with an increase in the difference in direction. The experimental results demonstrate that Rayleigh surface wave superposition in different directions affects the velocity dispersion curve, and the degree of influence is related to the included angle of the propagation direction.

Taking Rayleigh surface waves with opposite propagation directions as an example, the effect of time interval on the velocity dispersion curve of two groups of Rayleigh surface waves with different propagation directions was studied. The plane sources were set at the left and right ends of the model, and a circular array of geophones was placed in the middle of the model. After the left source was fired, the right source was fired with delays of 0.25, 0.251, 0.252, and 0.253 s. Four groups of seismic records are simulated as presented in Figure 9A Figure 9B presents the spectra of the corresponding seismic records. The spectral curves exhibit periodic fluctuations. With a change in the time interval, fluctuations appear and correspond to translation.

The blue, black, red, and green curves presented in Figure 9C correspond to the velocity dispersion curves extracted from the two sets of seismic records at intervals of 0.25, 0.251, 0.252, and 0.253s for the Rayleigh surface wave in the data, respectively. The figure indicates that the four groups of dispersion curves possess the same fluctuation amplitudes and similar fluctuation trends. The difference in time interval caused the wave to shift along the horizontal direction. The results revealed that when two groups of Rayleigh surface waves with different propagation directions were superimposed, the arrival time interval of the Rayleigh surface waves affected the velocity dispersion curve. Concurrently, it was also observed that a higher frequency resulted in a higher fluctuation frequency of the influence, and the internal influence mechanism requires further study.

The above experimental results reveal that the superposition of Rayleigh surface waves propagating in the same direction does not affect the spatial autocorrelation method to extract the velocity dispersion curve. If the two groups of waves are superimposed by Rayleigh surface waves propagating in different directions, the velocity dispersion curve fluctuates periodically around the theoretical value, and the size of the time interval between the

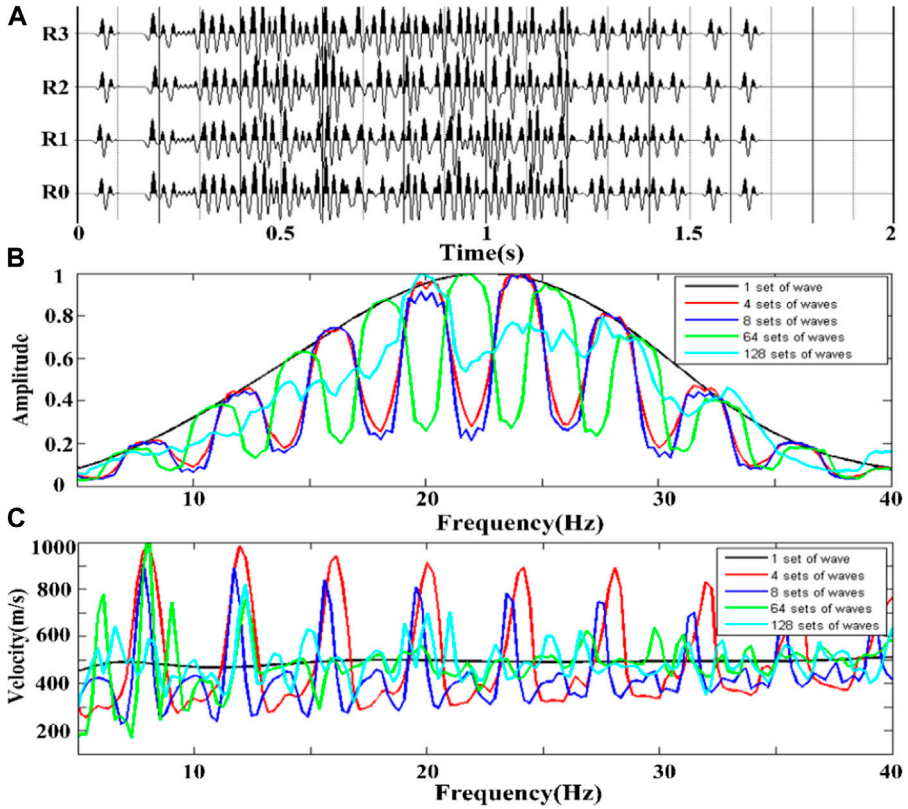

FIGURE 12
Multiple sets of Rayleigh surface waves with different time intervals and directions. **(A)** a single array vertical component seismic record with 4 groups of different Rayleigh wave intervals superimposed; **(B)** the spectrum diagram of five groups of seismic records; **(C)** the velocity dispersion curve of each group of seismic records.

two Rayleigh surface waves also affects the velocity dispersion curve. The wave phase of the dispersion curve changes with a change in the time interval.

4.2 Multi-group Rayleigh surface wave superposition

This section discusses the effects of changing the time interval and spatial distribution of the source on the velocity dispersion curve when multiple groups of Rayleigh surface waves are superpositioned. First, the influence of increasing the number of Rayleigh waves at equal time intervals on the velocity-dispersion curve was analyzed. A circular array of geophones was placed in the middle of the model, and four, eight, and 24 sources were loaded in different directions. The sources are evenly distributed. Each source was shot at equal time intervals of 0.25s. The seismic records of four, eight, and 24 groups of Rayleigh surface wave superposition with uniform distribution in the direction and equal time intervals were obtained. The seismic records of the 24 groups of Rayleigh surface-wave superpositions are presented in Figure 10A Figure 10B presents the spectral distribution of each group of seismic records. The figure indicates that the superposition spectrum of the Rayleigh surface waves in different directions exhibits coherent cancellation, and the effect of coherent cancellation increases with an increase in the number of equally spaced Rayleigh surface waves. This demonstrates that increasing the number of Rayleigh surface wave overlays in different directions at equal time intervals strengthens coherent cancellation in the fixed frequency band.

The four curves presented in Figure 10C (black, red, blue, and green) correspond to the velocity dispersion curves recorded by equal-interval superposition of Rayleigh surface waves in directions 1, 4, 8, and 24, respectively. It can be observed from the figure that by increasing the number of Rayleigh surface waves in different directions, the dispersion curve still fluctuates violently. Specifically, the emphasis on the average of the source direction cannot eliminate the volatility of the velocity dispersion. Additionally, a comparison of the velocity dispersion and spectrum distribution reveals that the fluctuation period of the velocity *versus* dispersion curve is consistent with the period of coherent cancellation, and the underlying reason requires further study.

Next, we studied the effect of the superposition of multiple Rayleigh surface waves at equal intervals and different intervals on the extraction of velocity dispersion curves. First, by simulating four shots of the same plane source at equal time intervals of 2s, we obtained the same direction and equal interval multiple groups of Rayleigh surface wave superposition seismic records. Then, the source shooting time was changed such that the time interval between each shot was different, and the seismic records of multiple groups of Rayleigh surface wave superpositions in the same direction and at different time intervals are presented in

Figure 11A. Figure 11B presents the spectrum distribution diagram. By comparing the spectral distribution in the figure, it can be observed that the coherent cancellation effect of the seismic records at the same interval is significantly stronger than that of the superposition at different intervals for the same four groups of Rayleigh surface waves. When the time interval of the four groups of Rayleigh surface waves was changed, the coherent cancellation effect of the spectrum was significantly weakened, and the effect became more obvious when the number of different interval waves was further increased.

Figure 11C presents the velocity-dispersion curve extracted from the four groups of Rayleigh surface-wave superposition records in the same direction and at different intervals. It can be observed from the figure that the velocity dispersion curve is approximately equal to the theoretical value, regardless of if the time interval is the same. When multiple Rayleigh surface waves in the same direction are superimposed, the frequency distribution is coherently cancelled; however, this does not affect the velocity dispersion curve. Therefore, it cannot be observed that changing the superposition time interval will affect the velocity dispersion curve.

The experimental results of multiple groups of Rayleigh surface wave superposition indicate that increasing the number of Rayleigh surface waves at equal time intervals does not eliminate the influence of Rayleigh surface wave superposition in different directions on the spatial autocorrelation extraction of the velocity dispersion curve. With an increase in the number of Rayleigh surface waves, the fixed-frequency coherence cancellation becomes more severe, and the effect of coherent cancellation will be weakened with the increase in Rayleigh surface waves at different time intervals.

4.3 Analysis of the joint effect of time interval and propagation direction

The influence of Rayleigh surface wave superposition on the spatial autocorrelation velocity dispersion curve was analyzed from the perspective of the Rayleigh surface wave time interval and direction distribution. Different directions led to periodic fluctuations in the velocity dispersion curve, and a change in the time interval led to a shift in the dispersion curve along the frequency direction. Changing only one of the variables cannot eliminate the influence of the Rayleigh wave superposition on the velocity dispersion curve.

This section considers the influence of changes in the time interval and direction distribution on the velocity dispersion curve. The experiment continuously increased the number of uniformly distributed Rayleigh surface waves, changed the time interval of arrival of the two waves, gradually simulated the uniform characteristics of the microtremor signal in the spatial direction and arrival time, and studied the influence of the microtremor signal on the spatial autocorrelation velocity dispersion curve when stationary and non-stationary. The seismic records of 4, 8, 64, and 128 groups of Rayleigh surface wave superpositions were simulated by increasing the number of sources and adjusting the source shooting interval. Figure 12A presents the seismic records of the 128 groups of Rayleigh surface-wave superpositions. These seismic records consider the direction of Rayleigh surface waves and the shooting time interval simultaneously so that the seismic records gradually meet the uniform distribution of source space and time. Figure 12B presents the spectral distributions of the five groups of seismic records. It can be seen from the figure that between 15 Hz and 30 Hz, the spectrum gradually tends to become uniform with the change in the number of superimposed waves and the time interval. This is due to the observation that the signal tends to be stable in space and time with a change in the number of superimposed waves and time interval.

Figure 12C presents the corresponding velocity dispersion curve. The velocity dispersion curve (black) corresponding to the non-stack seismic records is close to the theoretical Rayleigh wave velocity of 490 m/s. From the change trends of the four groups of dispersion curves (red, blue, green, and green), we can see that the fluctuation amplitude of the velocity dispersion curve gradually decreases with an increase in the number of waves and change in time. The velocity dispersion curve gradually approached the theoretical velocity value. This influence gradually increases from low to high frequencies as predicted. An accurate velocity dispersion curve can be obtained when the amount of data increases to a certain amount.

In summary, the superposition of Rayleigh surface waves in the same direction did not affect the extraction of the spatial autocorrelation velocity dispersion curve. Different propagation directions cause periodic fluctuations in the dispersion curve, and the degree of influence changes with changes in the Rayleigh surface wave propagation direction. The arrival time interval of Rayleigh surface waves also affects the dispersion curve. Increasing the number of Rayleigh waves with equal time intervals alone strengthened the coherent cancellation of a fixed frequency but did not eliminate the influence on the dispersion curve. Simultaneously, gradually increasing the number of Rayleigh surface waves in different directions and changing their arrival time interval of Rayleigh surface waves will gradually reduce the periodic fluctuation of the velocity dispersion curve caused by Rayleigh surface wave superposition.

5 Conclusion and discussion

This study focuses on the application of the spatial autocorrelation method to seismic wave exploration from two perspectives that include theory and numerical simulation. First, the spatial autocorrelation method was theoretically deduced based on cosine similarity theory. The results demonstrated that single-group or spatially and temporally stable Rayleigh surface waves can be accurately extracted from the velocity dispersion curve using this method. The spatial autocorrelation method was applied to extract the velocity dispersion curve of a single set of Rayleigh surface-wave seismic data from the homogeneous model. It was observed that the velocity profile of a single set of Rayleigh surface waves clearly reflected the homogeneous property of the half-space, and the calculated velocity was consistent with the theoretical Rayleigh wave velocity. This indicates that the spatial autocorrelation method can use a single set of Rayleigh waves to calculate the velocity dispersion curve. When mutually perpendicular Rayleigh surface waves are superimposed, the velocity distribution of the

velocity dispersion profile is extremely chaotic, and it is unable to accurately distinguish the structural characteristics of the homogeneous half space. Thus, the non-stationary multiple sets of Rayleigh surface waves may not be applicable to the spatial autocorrelation method.

Based on the characteristics of spatial and temporal stationarity, the influence of the superposition of multiple Rayleigh surface waves on the extraction of the spatial autocorrelation velocity dispersion curve was also studied. The results reveal that the calculated velocity-dispersion curve is not affected by the spatial and temporal stationarity characteristics when the Rayleigh surface wave is superimposed in the same direction. When Rayleigh surface waves in different directions are superimposed, they are affected by the propagation direction and time interval of the waves. Increasing the number of Rayleigh surface waves in different directions or at different time intervals in one direction did not reduce their impact on the velocity dispersion curve. With an increase in the direction and different time intervals, the signal gradually satisfies the stationary characteristics, and the velocity dispersion curve returns to the theoretical value. This indicates that the non-stationary microtremor signal cannot be used to accurately calculate the velocity dispersion curve through the spatial autocorrelation method. A more stable microtremor signal results in a more accurate velocity dispersion curve. The conclusions of this study further broaden the application range of the spatial autocorrelation method and improve the accuracy of the velocity dispersion curve extraction method.

Data availability statement

The original contributions presented in the study are included in the article/Supplementary Material, further inquiries can be directed to the corresponding author.

Author contributions

QD: Conceptualization, Data curation, Formal Analysis, Investigation, Methodology, Project administration, Software, Writing–original draft, Writing–review and editing. YP: Data curation, Resources, Software, Investigation, Writing–review and editing. KZ: Funding acquisition, Resources, Visualization, Writing–review and editing. DG: Visualization, Writing–review and editing.

Funding

The author(s) declare financial support was received for the research, authorship, and/or publication of this article. This research is funded by National Natural Science Foundation of China (grant numbers 42207200) and the Science and Technology Project of Henan Province (Project Nos. 222102320451).

Conflict of interest

The authors declare that the research was conducted in the absence of any commercial or financial relationships that could be construed as a potential conflict of interest.

Publisher's note

References

1. Konno K, Ohmachi T. Ground-motion characteristics estimated from spectral ratio between horizontal and vertical components of microtremor. *Bull Soc Am* (1998) 88(1): 228–41. doi:10.1785/bssa0880010228

2. Tokimatsu K, Arai H, Asaka Y. Deep shera-wave structure and earthquake ground motion characteristics in Sumiyoshi area, Kobe city, based on microtremor measurements. *J Struct Constr Engng AIJ* (1997) 491:37–45. doi:10.3130/aijs.62.37-1

3. Nakamura Y. On the H/V spectrum. In: The the 14th world conference on earthquake engineering; Beijing, china (2008).

4. Arai H, Tokimatsu K. Effects of Rayleigh and Love waves on microtremors H/V spectra. In: Proc. 12th World Conf. on Earthquake Engineering (2000). 2232. CD-ROM.

5. Thomson WT. Transmission of elastic waves through a stratified solid medium. *J Appl physocs* (1950) 21:89–93. doi:10.1063/1.1699629

6. Qingling D, Yanhui P, Youyang X. Research and application of Rayleigh wave extraction method based on microtremors signal analysis. *Front Phys* (2023) 11:11. doi:10.3389/fphy.2023.1158049

7. Sakaji K. Temporal variation of the power spectra of microtremors observed at soil and rock site. Graduation thesis. Sapporo, Japan: Hokkaido University (1998). (in Japanese).

8. Capon J. High-resolution frequency-wave number spectrum analysis. *Proc IEEE* (1969) 57(8):1408–18. doi:10.1109/proc.1969.7278

9. Aki K Space and time spectra of stationary stochastic waves, with special reference to microtremors. *Bull Earthq Res Inst* (1957) 35:415–56.

10. Boore DM, Toksöz MN. Rayleigh wave particle motion and crustal structure. *Bull Seismol Soc Am* (1969) 59(1):331–46.

11. Zhao H, Zhang Y. CWT-based method for extracting seismic velocity dispersion. *IEEE Geosci remote sensing Lett* (2022) 19:1–5. doi:10.1109/lgrs.2021.3056610

12. Giulia S, Silvia C. Detecting 1-D and 2-D ground resonances with a single-station approach. *Geophys J Int* (2020) 223(1):471–87. doi:10.1093/gji/ggaa325

13. Asten MW, Hayashi K. Application of the spatial auto-correlation method for shear-wave velocity studies using ambient noise. *Surv Geophys* (2018) 39(4):633–59. doi:10.1007/s10712-018-9474-2

14. Okada H, Sakajili N. Estimation of an S-wave velocity distribution using long-period microtremors. *Geophys Bull* (1983) 42:119–43. Hokkaido University.

15. Cho I, Tada and T, Shinozaki Y. Assessing the applicability of the spatial autocorrelation method: a theoretical approach. *J Geophys Res* (2008) 113:B06307. doi:10.1029/2007jb005245

16. Cox H. Spatial correlation in arbitrary noise fields with application to ambient sea noise. *J Acoust Soc America* (1973) 54(5):1289–301. doi:10.1121/1.1914426

17. Horike M. Inversion of phase velocity of long-period microtremors to the S-wave-velocity structure down to the basement in urbanized areas. *J Phys Earth* (1985) 33: 59–96. doi:10.4294/jpe1952.33.59

18. Matsushima T, Okada H An exploration method using microtremors (2)-anpexperment to identify Love waves in long-period microtremors. In: Proc. The 82nd SEGF Conf (1990). p. 5–8. (in Japanese).

19. Tokimatsu K, Shinzawa K, Kuwayama S Use of short-period microtremors for vs profiling. *J Geotechnical Eng* (1992) 118(10):1544–58. doi:10.1061/(asce)0733-9410(1992)118:10(1544)

20. Zhang H, Kristine P High-resolution Bayesian spatial auto-correlation (SPAC) quasi-3D vs model of Utah FORGE site with a dense geophone array. *Geophys J Int* (2021) 225(3):1605–15.

21. Hayashi K, Asten MW, Stephenson WJ, Cornou C, Hobiger M, Pilz M, et al. Microtremor array method using spatial autocorrelation analysis of Rayleigh-wave data. *J Seismol* (2022) 26:601–27. doi:10.1007/s10950-021-10051-y

22. Cho I Compensating for the impact of incoherent noise in the spatial autocorrelation microtremor array method. *Bull Seismological Soc America* (2018) 109(1):199–211. doi:10.1785/0120180153

23. Okada H, Suto K *The microtremor survey method*. Tulsa, OK: Society of Exploration Geophysicists (2003). p. 1–53.

24. Asten MW, Dhu T, Lam N Optimized array design for microtremor array studies applied to site classification; comparison of results with SCPT logs. In: Proc. 13th Annual World Conf. Earthq. Engineering (2004). 2903.

25. Asten MW On bias and noise in passive seismic data from finite circular array data processed using SPAC methods. *Geophysics* (2006) 71(6):153–62. doi:10.1190/1.2345054

26. Luo S, Luo Y, Zhu L, Xu Y On the reliability and limitations of the SPAC method with a directional wavefield. *J Appl Geophys* (2016) 126:172–82. doi:10.1016/j.jappgeo.2016.01.023

27. Ling S, Okada H An extended use of the spatial autocorrelation method for the estimation of structure using microtremors. *Soc Exploration Geophysicists Jpn* (1993) 44:48.

28. Ohori M, Nobata A, Wakamatsu K A comparison of ESAC and FK methods of estimating phase velocity using arbitrarily shaped microtremor arrays. *Bull.Seismol Soc Am* (2002) 92(6):2323–32. doi:10.1785/0119980109

29. Parolai S, Richwalski SM, Milkereit C, Fäh D. S-Wave velocity profiles for earthquake engineering purposes for the cologne area (Germany). *Bull Earthquake Eng* (2006) 4:65–94. doi:10.1007/s10518-005-5758-2

30. Parolai S, Mucciarelli M, Gallipoli MR Comparison of empirical and numerical site responses at the tito test site. *South. Italy Bull Seismol Soc Am* (2007) 97(5):1413–31.

31. Uebayashi H, Cho I, Ohori M, Yoshida K, Arai H. The effect of body waves on phase-velocity determined by the spatial autocorrelation (SPAC) method, evaluated using full-wave modelling. *Exploration Geophysics* (2020) 51(4): 483–93. doi:10.1080/08123985.2020.1719825

32. Cho I. Two-sensor microtremor SPAC method: potential utility of imaginary spectrum components. *Geophys J Int* (2020) 220(3):1735–47. doi:10.1093/gji/ggz454

33. Ikeda T, Tsuji T, Konishi C, Saito H. Spatial autocorrelation method for reliable measurements of two-station dispersion curves in heterogeneous ambient noise wavefields. *Geophys J Int* (2021) 226(2):1130–47. doi:10.1093/gji/ggab150

34. Toksöz MN Microseisms and an attempted application to exploration. *Geophysics* (1964) 29(2):154–77. doi:10.1190/1.1439344

35. Chen L, Lian H, Natarajan S, Zhao W, Chen X, Bordas SPA. Multi-frequency acoustic topology optimization of sound-absorption materials with isogeometric boundary element methods accelerated by frequency-decoupling and model order reduction techniques. *Comp Methods Appl Mech Eng* (2022) 395:114997. doi:10.1016/j.cma.2022.114997

36. Chen L, Lian H, Liu Z, Gong Y, Zheng CJ, Bordas SPA. Bi-material topology optimization for fully coupled structural-acoustic systems with isogeometric fem–bem. *Eng Anal Boundary Elem* (2022) 135:182–95. doi:10.1016/j.enganabound.2021.11.005

37. Chen L, Wang Z, Lian H, Ma Y, Meng Z, Li P, et al. Reduced order isogeometric boundary element methods for CAD-integrated shape optimization in electromagnetic scattering. *Comp Methods Appl Mech Eng* (2024) 419:116654. doi:10.1016/j.cma.2023.116654

38. Chen L, Lian H, Xu Y, Li S, Liu Z, Atroshchenko E, et al. Generalized isogeometric boundary element method for uncertainty analysis of time-harmonic wave propagation in infinite domains. *Appl Math Model* (2023) 114:360–78. doi:10.1016/j.apm.2022.09.030

frontiers | Frontiers in Physics

TYPE Original Research
PUBLISHED 08 February 2024
DOI 10.3389/fphy.2024.1345581

OPEN ACCESS

EDITED BY
Yilin Qu,
Northwestern Polytechnical University, China

REVIEWED BY
Peng Yu,
Guangxi University, China
Feng Zhu,
Nanjing University of Aeronautics and Astronautics, China

*CORRESPONDENCE
Shuai Li,
lishuai@s.dlu.edu.cn

RECEIVED 28 November 2023
ACCEPTED 29 January 2024
PUBLISHED 08 February 2024

CITATION
Li S, Fu J, Liu G and Zhou J (2024), Research on intrusion and large arch bulge in lining structure for highway's mudstone tunnel.
Front. Phys. 12:1345581.
doi: 10.3389/fphy.2024.1345581

Research on intrusion and large arch bulge in lining structure for highway's mudstone tunnel

Shuai Li[1]*, Jing Fu[2], Gengren Liu[3] and Jinghu Zhou[1]

[1]College of Civil Engineering and Architecture, Dalian University, Dalian, China, [2]Key Laboratory of Geotechnical Mechanics and Engineering of Ministry of Water Resources, Yangtze River Scientific Research Institute, Wuhan, China, [3]CCCC Second Highway Consultants Co., Ltd., Wuhan, China

During the construction of a highway in northwest China, large deformation of mudstone caused severe deformation of and damage to side walls, initial support, and secondary lining to various extents. To reveal the causes of mudstone's large deformation in the tunnels of this highway, a comprehensive study was conducted by using engineering geological survey, on-site monitoring and measurement, indoor rock mechanics test, numerical simulation, and macroscopic analysis. For the problem of large deformation of this highway's tunnel section from YK209 + 500 m to YK210 + 030 m, the 3D finite difference method FLAC^{3D} was used to simulate the large deformation of the wall rock and compare the deformation of the tunnel and the mechanical characteristics of the lining structure under different conditions by means of inverse analysis of the rheological characteristics of the mudstone and simulation of the softening of the mudstone in water. The research results provide a reference and basis for the construction design of similar mudstone tunnel projects. For the management of tunnel deformation, it is recommended to enhance the tunnel's drainage measures, thereby mitigating the intensification of mudstone softening when exposed to water.

KEYWORDS

highway tunnel, Mudstone, viscoelastic plastic, large deformation, intrusion limit, Softening

1 Introduction

The large deformation of tunnel rock has always been a key scientific issue in geotechnical engineering. In recent years, scholars have conducted extensive research on the microscopic and macroscopic mechanisms. Fan et al. [1] investigated the large deformation patterns in multi-sectional tunnels within stratified mudstone. Liu et al. [2] analyzed the large deformation characteristics of Tertiary soft rock tunnels. The impact of groundwater effects on large deformations in deep-buried slate tunnels was explored by Sun et al. [3]. Ma et al. [4] studied the drum failure mechanism in sandstone and shale rock tunnels. The deformation and failure characteristics of weathered sandstone rock tunnels were discussed by Wang et al. [5]. Zhou et al. [6] analyzed the destructive impact of loess mudstone landslides on high-speed rail tunnels. A computational method for large tunnel deformations was proposed by Wang et al. [7]. Chen et al. [8] explored the failure mechanism in single-oblique alternating soft and hard rock tunnels. Meng et al. [9] used D-InSAR monitoring to analyze the causes of large deformations in tunnels. The collapse mechanism of tunnels in soft-hard interlayered rock was investigated by Liu et al. [10]. Chen et al. [11] analyzed the squeezing deformation in high geostress stratified soft

rock tunnels. The nonlinear deformation mechanism in high-stress soft rock roadways was discussed by Zheng et al. [12]. Yang et al. [13] studied the fracturing damage behavior in mudstone. The construction technology for large-span intersections in soft rock was explored by Li et al. [14]. Lastly, Bao et al. [15] analyzed the large deformation mechanism in deep brittle rock tunnels based on the evolution of microcracks. The geometric finite element simulation of crack propagation under pressure by Chen Leilei et al. provided some inspiration for the modeling and simulation of large deformation in this paper [16–30]. Mainly focused on the changes in the mechanical properties and mineral composition of rocks after water exposure, current researches rarely devote themselves to the relationship between soft rock deformation and the surrounding environment to establish models and field experiments for comparison and analysis, and study in a multi-dimensional way to develop a systematic and in-depth research on the relationship between the large deformation mechanism of mudstone and the macroscopic deformation behavior of seepage tunnels. This study extensively investigates the significance of mudstone tunnel lining structures through finite element analysis, particularly emphasizing the understanding and prevention of substantial deformation in tunnels. Such an exploration is vital for ensuring the stability and safety of underground engineering projects. The analysis underscores the criticality of addressing these deformations, which are pivotal in maintaining the integrity of subterranean structures.

In this paper, we take a tunnel section of a highway in northwest China as our research object and carry out on-site monitoring and experiments, data analysis, model building analysis, and conjecture and experiments of tunnel deformation mechanism. We explore the causes of large deformation of wall rock during excavation of this tunnel section and hope to provide references for the planning, survey, design, construction and design of support structures for tunnel in similar geological conditions.

2 Project overview

2.1 Basic geological conditions

The tunnel is located in an area of eroded and accumulated loess with relatively huge variations in altitude as well as outstanding rises and slopes. The elevation of the tunnel is about 1248–1536 m. The attitude of rock is 44°–28°∠30°. Joint planes occur near YK209 + 734. Two groups of relatively smooth planes occur, namely, J1: 7°∠30° and J2: 13°∠86°. Special rock and soil structures in the tunnel area are mainly collapsible loess and expansive rock. According to the statistics of saturated compressive strength in detailed survey, the mudstone in this area is extremely soft rock. Boreholes made in the arch at YK209 + 650 and YK209 + 845 reveal groundwater, while groundwater is not found in other boreholes. The water level revealed by these boreholes shows that the distribution of groundwater in the tunnel is uneven.

2.2 Engineering issues

Large deformation was found in the YK209 + 500-YK210 + 030 section of the tunnel in 2019 as shown in Figure 1.

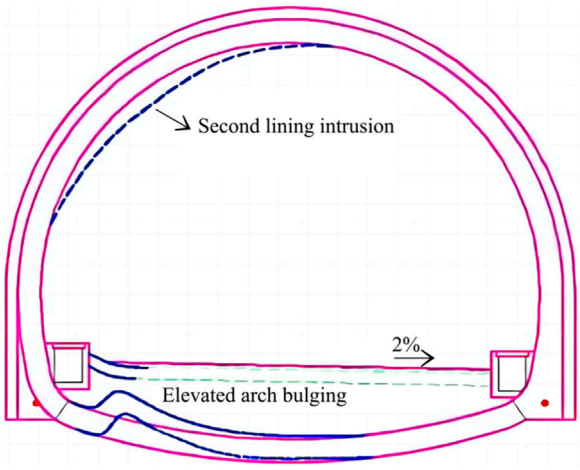

FIGURE 1
Monitoring large deformation sections.

Such large deformation includes: 1) bulges and cracks occur in the left foot of the invert arch. Boreholes in the invert arch found outstanding bulges in the back-filled part of the left half of the arch, separation in the range of 50–100 cm from the side wall, and bending of steel bars inside the invert arch. The maximum height of a bulge of the invert arch exceeds 60 cm. 2) intrusions occur in the lining structure from the left arch foot to the right arch waist. Most intrusions reaches 15 cm. The highest intrusion reaches 26.1 cm, and there are more intrusions on the left side of the line structure than on the right side.

3 Mudstone physical and mechanical tests and ground stress tests

The hydraulic fracturing method was used to test the initial ground stress of the surrounding rock. The hydrofracturing method offers several distinct advantages: It enables deep measurement capabilities; The data compilation process does not necessitate the inclusion of rock elasticity parameters, thereby reducing errors caused by inaccurate parameter estimations; A wide stress distribution on the rock walls, attributed to the lengthy pressurized borehole section, mitigates the limitations associated with point stress conditions and heterogeneous geological factors; The method is characterized by its simplicity of operation and short testing duration. The principle underlying the hydrofracturing method for stress testing involves the use of expandable rubber packers. These packers isolate a borehole section at a predetermined depth, into which a liquid is then pumped to apply pressure. The *in situ* stress is determined by analyzing the characteristic pressure values from the pressure curve during the fracturing process.

The ground stress test was carried out in the section of the tunnel where outstanding deformations occur. In the test area, the maximum horizontal principal stress is 1.0–2.2°MPa, the minimum horizontal principal stress is 0.7–1.8°MPa, and the vertical stress is 5.1–5.9 MPa. On the whole, the stress field shows that the dead-weight stress is larger than the horizontal stress, indicating that the ground stress field in this area is dominated by dead-weight stress.

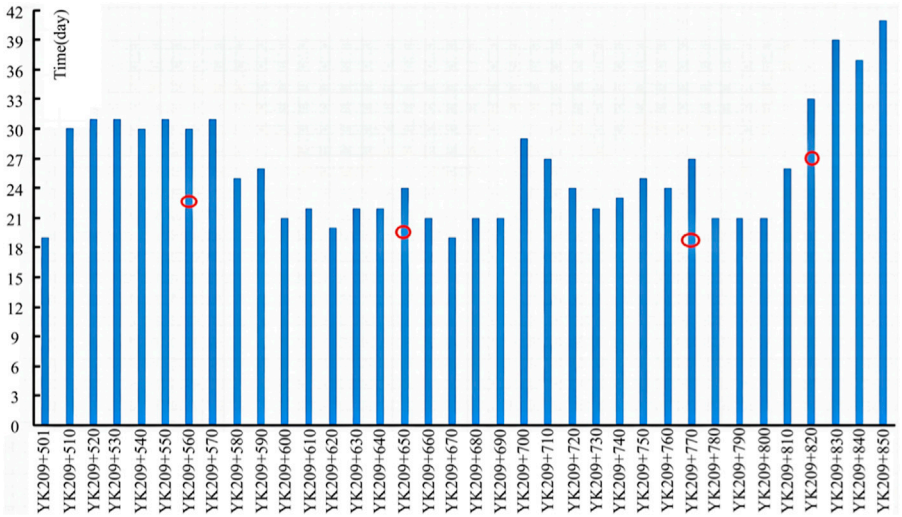

FIGURE 2
Time spent watching various monitoring areas.

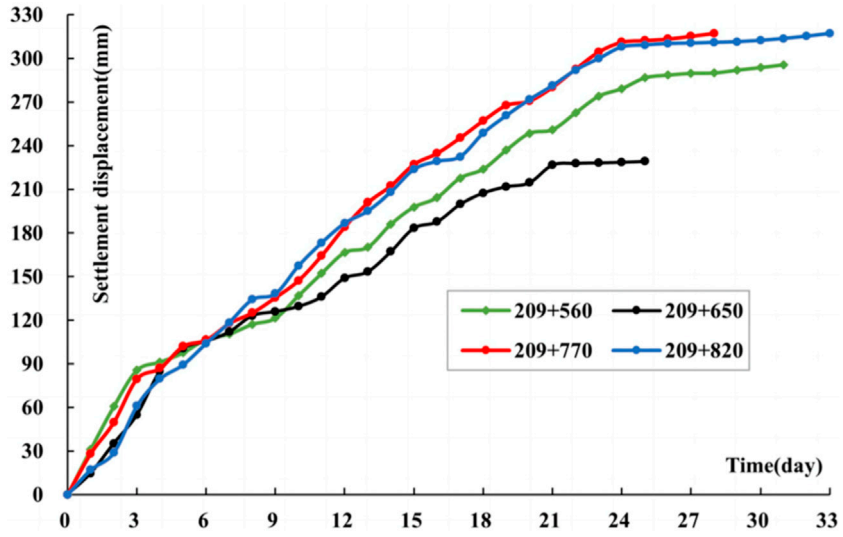

FIGURE 3
Variation curve of average section vault settling movement over time.

4 Analysis of tunnel wall rock deformation monitoring data

As shown in Figure 2, in the YK209 + 500-YK209 + 850 section of the tunnel, 36 observation sections are arranged with an interval of 10 m. The monitoring period commenced upon the completion of the initial lining and ends upon the pre-application of the secondary lining. The monitoring period of a section ranges from 18 days to 41 days.

It can be seen from Figure 3 that the settlement displacement of the arch at a measuring point increases in an nonlinear way with time. When the monitoring starts, the settlement displacement rate is relatively huge. In the first 3 days, the displacement rate is 15–32 mm/d, and the value reduces slightly to about 2.5–20 mm/d between the 4th and 20th days. As the time goes by, the value reduces further. On the 25th day of monitoring, the settlement displacement rate is less than 2.0 mm/d.

As can be seen from Figure 4, 5, during the secondary lining stage, the settlement displacement of the arch top in the YK209 + 511-YK209 + 841 section is mostly between 5 and 40mm, and the average value is about 32.0 mm. Figure 5 reveals that the highest bulges on the invert arch is mostly 300–650°mm, the maximum deformation is 702°mm, the minimum is 28°mm, and the average is 319.5 mm. After the secondary lining is done, the settlement displacement of the arch top is still time-dependent. On the whole, the bulges of the invert arch is larger, and the deformation of the surrounding rock at the bottom shows strong rheological properties. The deformation velocity of the invert arch gradually flattens, and the displacement gradually stabilizes as the time goes by.

10.3389/fphy.2024.1345581

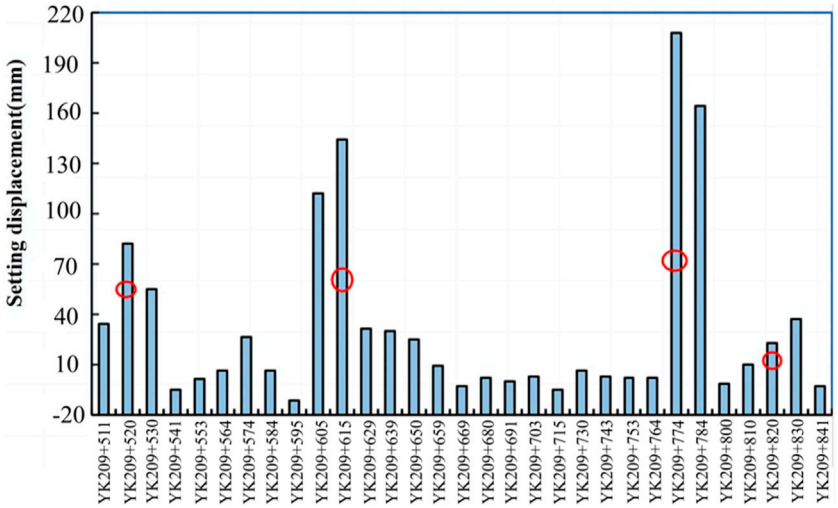

FIGURE 4
Tunnel top arch settlement displacement curve along different pile numbers.

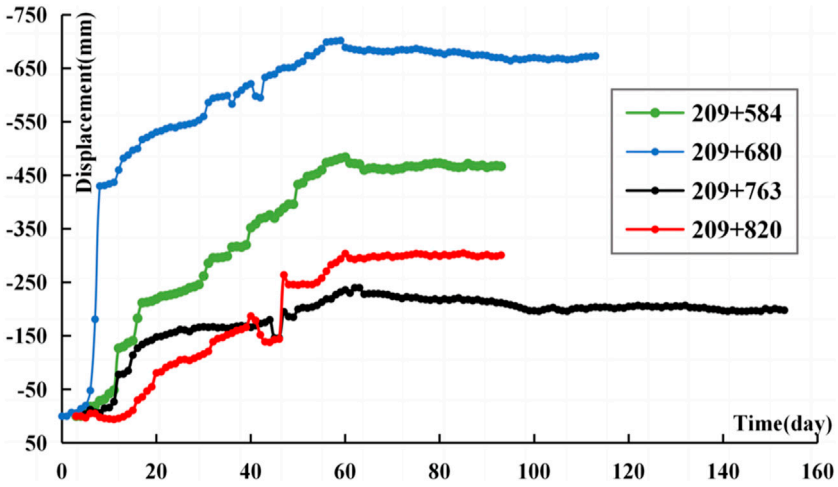

FIGURE 5
The temporal shift of the elevation arch process curve.

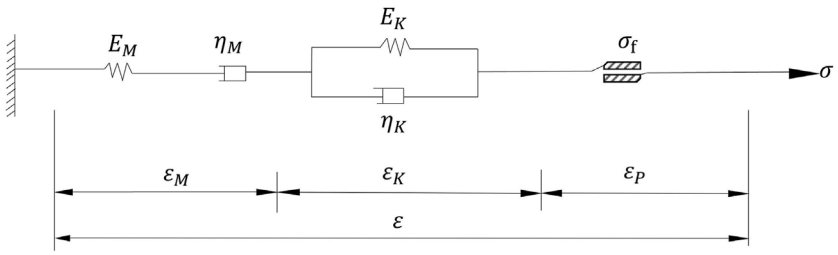

FIGURE 6
Burgers creeping viscoelastic-plastic model σ is the rock stress, E_M, E_K, η_M, and η_K are the rock's elastic modulus, viscoelastic modulus, Maxwell viscosity coefficient, and Kelvin viscosity coefficient, respectively, σ_f is the yield strength of the rock, and ε_M, ε_K, and ε_P are the strain and plastic strain of the Maxwell body and Kelvin body.

5 Study on the mechanism of large deformation damage of mudstone

Considering mudstone's water-softening property and obvious rheological characteristic, we applied the numerical simulation to the tunnel at different support stages by using FLAC^{3D} to study the deformation mechanism, structural stress characteristics and creep development law of the tunnel's surrounding rock, and to explore the mechanism of their large deformation.

5.1 Rock viscous-elastic-plasticity constitutive model

In the study, a creep-viscoplastic model, which comprises the Burgers model and Mohr Coulomb model is used. The former, which simulates the time-dependent creep characteristics of rock and soil, can reflect the attenuating creep stage and stable creep stage of a material after loading. The latter considers viscoelastic-plastic stress deviation characteristics and the elastic-plastic volume change of a material. It is assumed that the viscoelastic strain rate component and plastic strain rate component act together in series. The viscoelastic component corresponds to the Burgers model (composing Kyle style and Magswell body in series), while the plastic component is consistent with the Mohr-Coulomb model. When the stress is less than the yield stress, the viscoelastic deformation of the model equals to the creep equation of the Burgers model, and when the stress is greater than the yield stress, the plastic flow deformation shall also be governed by the Mohr-Coulomb criterion.

To ensure the effectiveness of the finite element model used in this study, a creep-viscoplasticity model was adopted, providing a comprehensive and reliable method for simulating and analyzing the behavior of geotechnical materials, as illustrated in Figure 6. The validity of the model was confirmed by calibrating its parameters using experimental data, thereby ensuring the consistency of the model's predictive results with actual scenarios.

The plasticity criterion uses a composite criterion combining Mohr-Coulomb shear damage and tensile damage, where the yield function of the Mohr-Coulomb criterion is:

$$f^s = \sigma_t - \sigma_3 N_\phi + 2c\sqrt{N_\phi} \tag{1}$$

The maximum tensile stress criterion yield function is:

$$f^t = \sigma_t - \sigma_3 \tag{2}$$

Where c is the cohesive force of the material, φ is the friction angle, $N_\phi = (1 + \sin\phi)/(1 - \sin\phi)$, σ_t is the tensile strength, σ_1 and σ_3 are the minimum and maximum principal stress (pressure is negative).

5.2 Model generalization and calculation conditions

The model's boundary of both tunnels are 68 m away from the center line. Its top is 60 m away from the center of the tunnel and the bottom is 50 m away from the central point. The model's length is 20 m along the axis of the tunnel. In the simulation, the number of units is 151,800 and the number of nodes is 161,637 as shown in Figure 7. The diameter of the excavation in the mudstone is 12.38m, while its inner diameter behind the lining is 10.86m, and its buried depth is about 237 m.

The design lining structure of this tunnel is SVb: I20a steel I-beam, spacing 100cm, 26 cm C25 shotcrete, Φ6 double layer mesh, 3.5 m long R25 hollow grouting anchors, spacing 75 cm × 100 cm, 50 cm C30 reinforced concrete lining and 10.25 m × 5 m design building limit of the main cavern.

The designed lining structure of the tunnel is SVb: I20a I-steel, spacing 100cm; 26 cm-thick C25 shotcrete, Φ6 double-layer steel mesh, 3.5 m-long R25 hollow grouting anchor, spacing 75°cm × 100°cm; 50 cm-thick C30 reinforced concrete lining. The designed limitation of the main tunnel is 10.25°m × 5 m.

With reference to mudstone's laboratory test results and the values of physical and mechanical parameters adopted in tunnel projects in Gansu province contained in previous literature, the values of physical and mechanical parameters of mudstone in natural and saturated states used in this study are as shown in Tables 1–3.

5.3 Inversion of the rheological parameter of mudstone

It is complicated to determine the rheological parameters of the tunnel's surrounding rock. In this paper, the numerical calculation and on-site deformation monitoring data were used for curve fitting to inverse the mudstone's rheological parameters. The inversion results of the rheological parameters of mudstone in natural state are as shown in Table 4.

The time-based curve of mudstone's rheological inversion and monitoring displacement is as shown in Figure 8. The deformation around the tunnel mostly occurs in the initial support. At first, the maximum deformation rate around the tunnel is about 18 mm/d. In the first 10°days, the deformation rate is relatively large, basically in the range of 7.0–18.0 mm/d. As the time elapses, the deformation rate decreases gradually. The rate decreased to 2.0–7.0 mm/d between the 11th and 20th days. By the 40th day, the rate was basically less than 1 mm/d. At this time, the deformation around the hole tends to be stable.

After the initial lining of the tunnel is done, the second lining will be applied after the deformation of the surrounding rock is basically stable. As can be seen from Figure 9, the long-term deformation of the lining structure is about 1.2–1.5 mm. Displacements in all directions are all towards the center of the tunnel, and these displacements and their values on both sides of the vertical line are basically symmetrical. Both the top arch and the invert arch deform downward under the action of dead weight. The lining stress is small. The maximum compressive stress is about 0.6°MPa, the tensile stress is about 0.2°MPa, and the relatively large stress appears in the arch feet on both sides of the arcs.

5.4 Deformation and stress state hole cycle after softening of water seepage in the wall rock

The groundwater was not exposed during tunnel excavation. However, as the time goes by, the groundwater seeped along

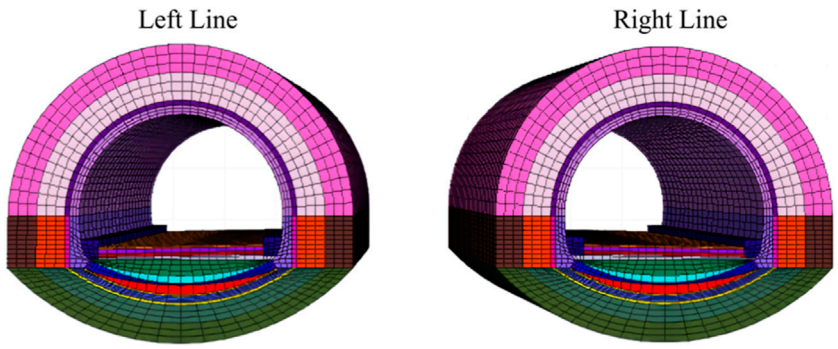

FIGURE 7
Numerical model.

TABLE 1 Laboratory test results of rock physical characteristics.

Sampling depth	Rocks	Particle densityg/cm^3	Water content/%	Water filling rate/%	Porosity/%
5.8 ~ 62.4 m	Mudstone	2.23	7.87	8.62	17.81
		2.22	8.43	9.52	19.45
		2.23	8.80	7.43	15.21
Average value		2.22	8.37	8.52	17.49
8.4 ~ 71.0 m	Mudstone	2.18	9.60	9.46	18.83
		2.28	10.46	7.46	15.40
		2.01	8.83	12.38	22.90
Average value		2.16	9.63	9.77	19.04

TABLE 2 Laboratory test results for rock mechanical properties.

Sampling depth	Rocks	Uniaxial compressive strength/MPa		Modulus of deformation/GPa	Elastic modulus/GPa	Poisson ratio
		Nature	Saturate	Nature	Nature	Nature
5.8 ~ 62.4 m	Mudstone	8.43	1.58	1.41	1.69	0.30
		6.75	0.97	1.13	1.35	0.30
		5.06	0.52	0.84	1.01	0.30
Average value		6.75	1.02	1.13	1.35	0.30
8.4 ~ 71.0 m	Mudstone	8.44	2.23	1.41	1.69	0.30
		6.42	5.42	1.07	1.28	0.30
		3.80	3.35	0.63	0.76	0.31
Average value		6.22	3.67	1.04	1.24	0.30

Mudstone cores from the ground stress test for the tunnel in the project were taken and tested for physical and mechanical properties. The results are as shown as Tables 1 and Table 2.

mudstone cracks after the excavation for invert arch in some sections, and then some unstable deformations occur such as cracks in the invert arch and convergence in the tunnel's wall rock. During the on-site investigation, the groundwater was also found in the boreholes in the problematic sections and in the slots of the invert arch, but the groundwater distribution was uneven. The infiltration of groundwater is the root cause of problems in the tunnel.

The development of structural planes such as joints and cracks in the problematic section leads to the breakage of the rock mass.

TABLE 3 Values of the physical and mechanical characteristics of mudstone.

Mudstone	Modulus of deformation/MPa	Poisson ratio	Gravity kN/m3	Cohesion/ kPa	φ/°	Tensile strength/kPa
Nature	800	0.32	22	200	30	50
Saturate	300	0.35	23	60	25	15

TABLE 4 Mudstone rheological parameters taking values.

Mudstone	EM(GPa)	Ek (GPa)	ηk (GPa.d)	ηm (GPa.d)
Nature	2.4	0.25	0.18	1,000

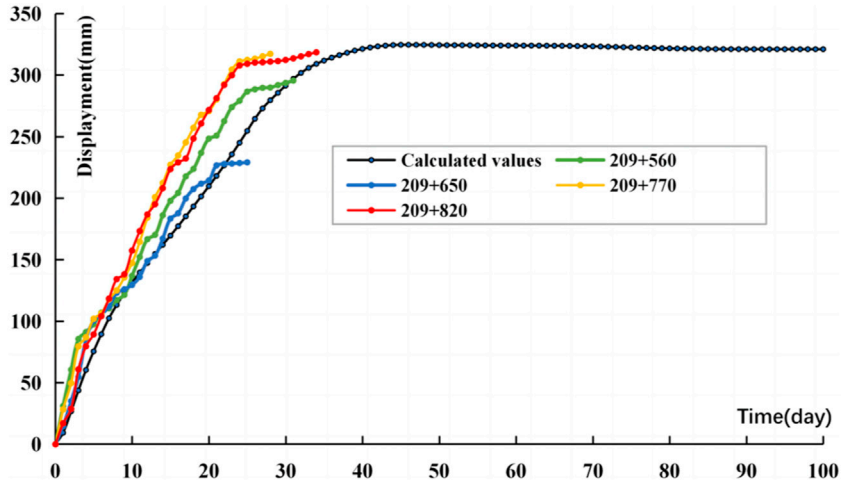

FIGURE 8
Monitoring and inverting the displacement time graph at measurement point A.

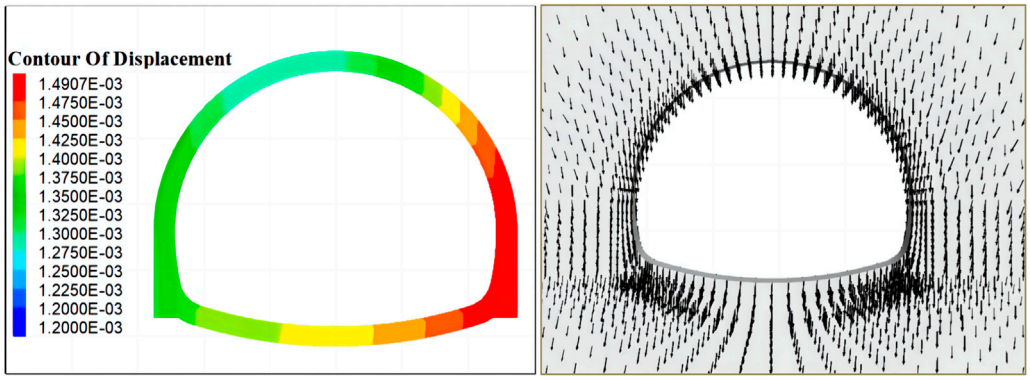

FIGURE 9
Long-term displacement vector of the liner after lining application.

The groundwater in a changed environment slowly seeps into the surrounding rock and results in the gradual immersion and softening of the surrounding rock and its weaker strength, as shown in Figure 10. After the completion of the tunnel structure, the natural discharge of groundwater along the cracks is blocked, and the groundwater is mainly concentrated in the rock pillar area about 30 m between the left and right tunnels and at the bottom of the tunnel. Mudstone is also a kind of rock prone to interact with

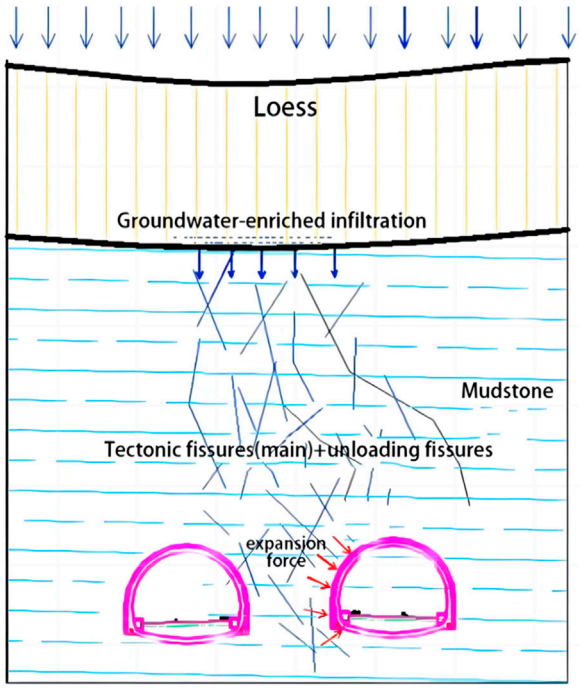

FIGURE 10
Analyzing the mechanisms of tunnel displacement.

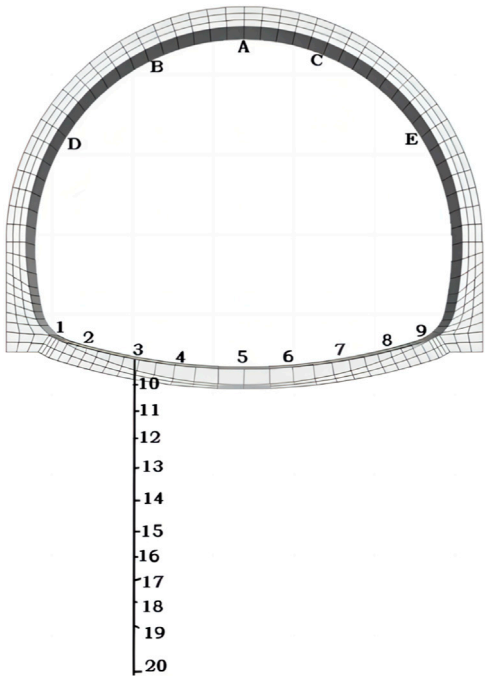

FIGURE 11
Location of tunnel lining measurement points.

water. Under the action of water, the growth and expansion of macroscopic fissures is the main reason for the rapid deterioration of the main physical and mechanical parameters of mudstone. Under the same confining pressure, the higher the water content of mudstone is, the more obvious the aging characteristic is.

In order to accurately express the research results, a number of measuring points are installed in the lining's top arch, arch shoulder, arch waist and invert arch. The measuring points #1 - #9 are evenly distributed on the invert arch. The buried measuring points #10-#20 are on #3's vertical line. The distance between #3, #10 - #19 are in an interval of 2 m while that between #19 and #20 is 5 m. The distance between #3 and #20 is 25 m. The layout of these measuring points are as shown in Figure 11.

The measuring point A, on the top of the lining arch, has a downward displacement of about 58.9 mm. The measuring points B and C has a downward displacement of 140.1 mm and 29.3 mm respectively and a horizontal convergence deformation of about 48 mm. The downward displacements of D and E are 173.4 mm and 23.0 mm respectively while their horizontal convergence deformation is about 95.5 mm. Intrusions on the left side of the second lining of the tunnel is obvious. Most of them are more than 10 cm, and the maximum intrusion is more than 20 cm. The deformation of the tunnel in the problematic section is characterized by the arch's downward displacement, convergence at the waist on both sides, and inclined bulges on the invert arch with the ones on the left higher than those on the right. It can be seen that the plastic flow caused by water-softening of the rock pillar mudstone is the main factor of the large deformation of the tunnel.

As shown in Figure 12, when the mudstone on the left side of the tunnel is saturated with and softened by water, its strength is obviously weakened, and the surrounding rock produces a large squeezing deformation on the left side of the supporting structure. The deformation of the left arch foot and the left arch bottom of the lining is about 250–470°mm, and the deformation of the left arch is about 150–300 mm.

As shown in Figure 13, among the nine measuring points arranged on the bottom of the invert arch, the measuring point #3, which is about 2.0 m away from the left arch foot, has the largest bulge displacement of 383 mm. The bulge displacement of the left arch foot is about 30mm, while the right arch foot sinks slightly, and the downward displacement is about 12 mm. The deformation along the measuring point #3's vertical line shows that the upward displacement of the floor along such line gradually decreases. The rheological effect of the shallow surrounding rock of the invert arch is obvious, and the time-based curve of mudstone softening and creep deformation rate increases at first, and then decreases to zero gradually.

The lining structure as a whole is in a compressed state, and the compressive stress concentration is high at both ends of the arch foot and bottom plate. The maximum compressive stress near the left and right arch feet are 17.0°MPa and 20.0 MPa respective. And it is 2.0–9.0 MPa at the bottom of the arch, 5.0–8.5 MPa at the left arch, about 4.0–11.0 MPa at the right arch, and about 7.0–13.0 MPa at the top of the arch.

The uneven deformation around the tunnel caused by mudstone softening acts on the lining structure. The latter bears large deformation pressure, and the force is unevenly distributed due to the difference of deformation. Looking at the overall stress of the lining structure, the stress on the arch foot and the arch top is larger, and the tension at the lower part of the left arch waist is obvious, which is easy to cause the tension crack and damage of the lining structure in the stress concentration and tension stress area of the arch foot.

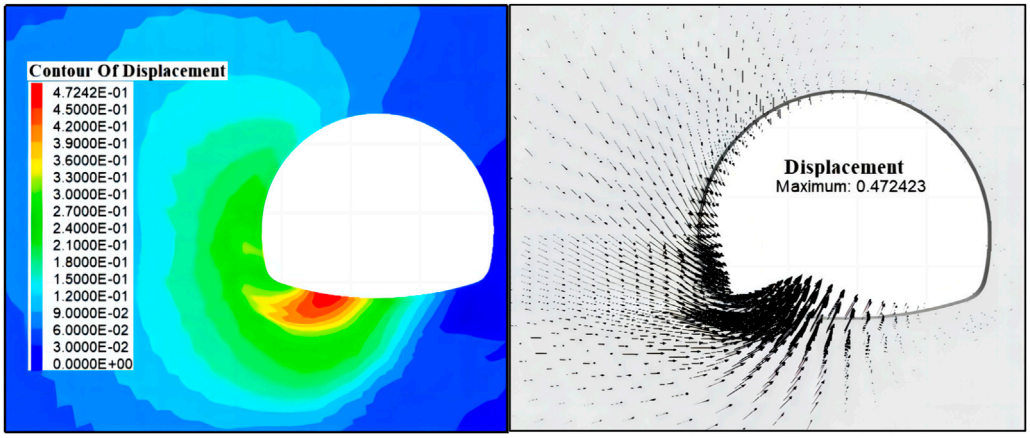

FIGURE 12
Mudstone softening-related tunnel displacement vector.

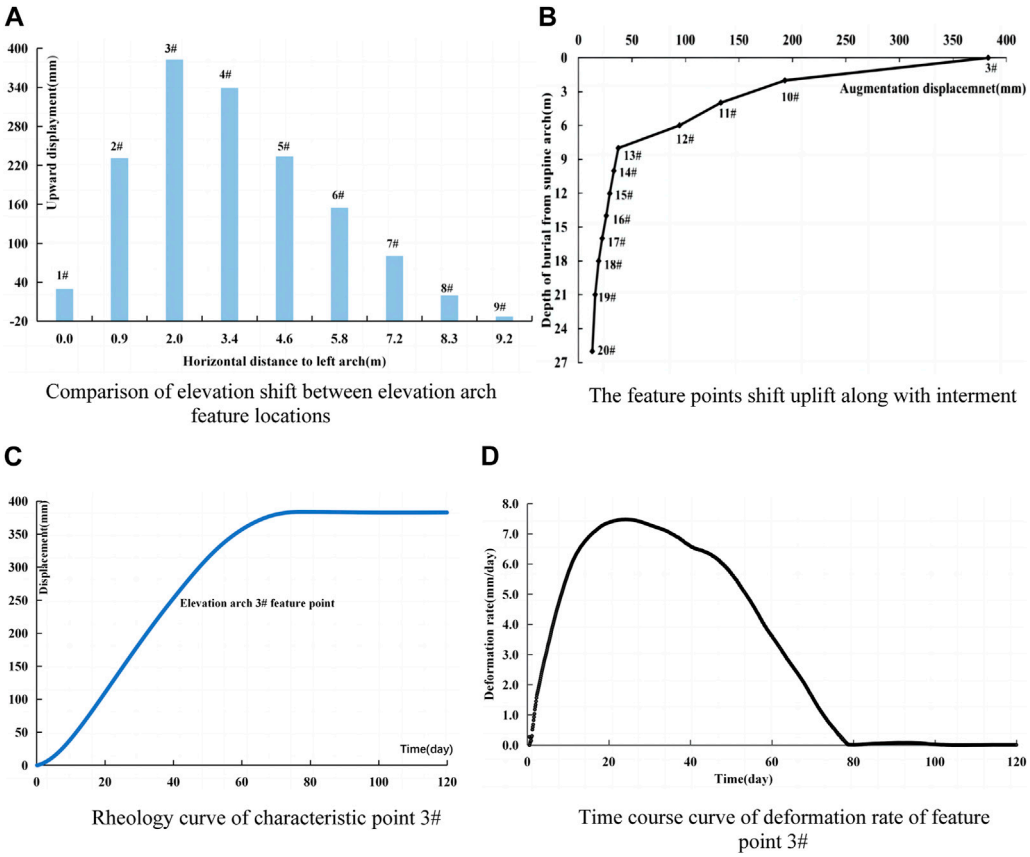

Comparison of elevation shift between elevation arch feature locations

The feature points shift uplift along with interment

Rheology curve of characteristic point 3#

Time course curve of deformation rate of feature point 3#

FIGURE 13
Arch Feature Displacement. **(A)** Elevation Shift Comparison. **(B)** Feature Points Uplift. **(C)** Rheology Curve (Point 3#). **(D)** Deformation Rate Curve (Point 3#).

6 Conclusion

The main results of this paper are as follows:

1) The tunnel's problematic section of large deformation is located in the core of the wide and gentle syncline. Due to the tectonic action, the joints and cracks are developed and the rock mass is broken, and the unloading of tunnel excavation leads to the opening and expansion of the primary cracks in the left and right rock pillars. At the same time, the pore groundwater in the overlying loess seeps down along the

joints and cracks and invades the surrounding rock of the tunnel.

2) Mudstone has strong hydrophilicity and weak expansibility, which will lead to increase and expansion of macroscopic fissures, a sharp decrease in physical and mechanical characteristics. Mudstone's aging deformation characteristics become more obvious as the content of water increases. Further research indicates a close interplay between the softening mechanisms of the surrounding rock and changes in stress distribution. Particularly in water-sensitive rocks such as mudstone, the permeation of moisture leads to a reduction in the strength of the surrounding rock and a redistribution of stress, thereby exacerbating the instability of rock layers around tunnels.
3) Computational comparative analysis reveals that the depth of the tunnel and stress levels exert a relatively significant influence on the unloading deformation of the surrounding rock, the magnitude of time-dependent deformation, and the convergence time. Conversely, the impact of swelling forces is comparatively minor, and they are not the primary controlling factors for substantial deformation and cracking of the lining in the surrounding rock.

When preparing suggestions for the treatment of a tunnel, it is necessary to improve the interception and drainage measures of the tunnel to ensure smooth drainage. It is also necessary to strengthen the weak surrounding rock at a certain depth around the tunnel in order to improve the strength and anti-deformation ability of rock mass. It is also recommended to strengthen the stress and strain monitoring of the tunnel lining and the monitoring of drainage facilities, and dynamically track and analyze the long-term stability of the tunnel by means of real-time monitoring, so as to provide security for the normal operation of the tunnel.

Data availability statement

The original contributions presented in the study are included in the article/Supplementary material, further inquiries can be directed to the corresponding author.

Author contributions

SL: Writing–original draft. FJ: Writing–review and editing. GL: Writing–review and editing. JZ: Writing–review and editing.

Funding

The author(s) declare that no financial support was received for the research, authorship, and/or publication of this article.

Conflict of interest

Author GL was employed by CCCC Second Highway Consultants Co., Ltd.

The remaining authors declare that the research was conducted in the absence of any commercial or financial relationships that could be construed as a potential conflict of interest.

Publisher's note

References

1. Fan S, Song Z, Li X, Zhang Y, Liu L. Investigation into the large deformation mechanism and control technology of variable cross-section tunnel in layered mudstone stratum. *Buildings* (2022) 13(1):110. doi:10.3390/buildings13010110

2. Liu D, Huang S, Ding X, Chi J, Zhang Y. Characteristics and mechanism of large deformation of tunnels in tertiary soft rock: a case study. *Buildings* (2023) 13(9):2262. doi:10.3390/buildings13092262

3. Sun Z, Zhang D, Li M, Guo F. Large deformation characteristics and the countermeasures of a deep-buried tunnel in layered shale under groundwater. *Tunnelling Underground Space Tech* (2024) 144:105575. doi:10.1016/j.tust.2023.105575

4. Ma K, Zhang J, Zhang J, Dai Y, Zhou P. Floor heave failure mechanism of large-section tunnels in sandstone with shale stratum after construction: a case study. *Eng Fail Anal* (2022) 140:106497. doi:10.1016/j.engfailanal.2022.106497

5. Wang K, Xu S, Zhong Y, Han Z, Ma E. Deformation failure characteristics of weathered sandstone strata tunnel: a case study. *Eng Fail Anal* (2021) 127:105565. doi:10.1016/j.engfailanal.2021.105565

6. Zhou S, Tian Z, Di H, Guo P, Fu L. Investigation of a loess-mudstone landslide and the induced structural damage in a high-speed railway tunnel. *Bull Eng Geology Environ* (2020) 79:2201–12. doi:10.1007/s10064-019-01711-y

7. Wang M, Zhang N, Li J, Ma L, Fan P. Computational method of large deformation and its application in deep mining tunnel. *Tunnelling Underground Space Tech* (2015) 50:47–53. doi:10.1016/j.tust.2015.06.006

8. Chen J, Liu W, Chen L, Luo Y, Li Y, Gao H, et al. Failure mechanisms and modes of tunnels in monoclinic and soft-hard interbedded rocks: a case study. *KSCE J Civil Eng* (2020) 24:1357–73. doi:10.1007/s12205-020-1324-3

9. Meng X, Qi T, Zhao Y, Dijkstra T, Shi W, Luo Y, et al. Deformation of the Zhangjiazhuang high-speed railway tunnel: an analysis of causal mechanisms using geomorphological surveys and D-InSAR monitoring. *J Mountain Sci* (2021) 18(7): 1920–36. doi:10.1007/s11629-020-6493-5

10. Liu X, Liu F, Song K. Mechanism analysis of tunnel collapse in a soft-hard interbedded surrounding rock mass: a case study of the Yangshan Tunnel in China. *Eng Fail Anal* (2022) 138:106304. doi:10.1016/j.engfailanal.2022.106304

11. Chen Z, He C, Wang J, Ma C. Time-dependent squeezing deformation mechanism of tunnels in layered soft-rock stratum under high geo-stress. *J Mountain Sci* (2021) 18(5):1371–90. doi:10.1007/s11629-020-6356-0

12. Zheng L, Zuo Y, Hu Y, Wu W. Deformation mechanism and support technology of deep and high-stress soft rock roadway. *Adv Civil Eng* (2021) 2021:1–14. doi:10.1155/2021/6634299

13. Yang SQ, Tian WL, Jing HW, Huang YH, Yang XX, Meng B. Deformation and damage failure behavior of mudstone specimens under single-stage and multi-stage triaxial compression. *Rock Mech Rock Eng* (2019) 52:673–89. doi:10.1007/s00603-018-1622-y

14. Guofeng LI, Manchao HE, Zhang G, Tao Z. Deformation mechanism and excavation process of large span intersection within deep soft rock roadway. *Mining Sci Tech (China)* (2010) 20(1):28–34. doi:10.1016/s1674-5264(09)60156-3

15. Bao H, Liu C, Liang N, Lan H, Yan C, Xu X. Analysis of large deformation of deep-buried brittle rock tunnel in strong tectonic active area based on macro and microcrack evolution. *Eng Fail Anal* (2022) 138:106351. doi:10.1016/j.engfailanal.2022.106351

16. Chen LL, Lian H, Liu Z, Gong Y, Zheng C, Bordas S. Bi-material topology optimization for fully coupled structural-acoustic systems with isogeometric

FEM–BEM. *Eng Anal Boundary Elem* (2022) 135:182–95. doi:10.1016/j.enganabound.2021.11.005

17. Chen L, Li H, Guo Y, Chen P, Atroshchenko E, Lian H. Uncertainty quantification of mechanical property of piezoelectric materials based on isogeometric stochastic FEM with generalized n th-order perturbation. *Eng Comput* (2023) 1–21. doi:10.1007/s00366-023-01788-w

18. Chen LL, Lian H, Natarajan S, Zhao W, Chen X, Bordas S. Multi-frequency acoustic topology optimization of sound-absorption materials with isogeometric boundary element methods accelerated by frequency-decoupling and model order reduction techniques. *Comp Methods Appl Mech Eng* (2022) 395:114997. doi:10.1016/j.cma.2022.114997

19. Chen L, Lian H, Xu Y, Li S, Liu Z, Atroshchenko E, et al. Generalized isogeometric boundary element method for uncertainty analysis of time-harmonic wave propagation in infinite domains. *Appl Math Model* (2023) 114:360–78. doi:10.1016/j.apm.2022.09.030

20. Chen L, Zhao J, Lian H, Yu B, Atroshchenko E. A BEM broadband topology optimization strategy based on Taylor expansion and SOAR method—application to 2D acoustic scattering problems. *Int J Numer Methods Eng* (2023) 124:5151–82. doi:10.1002/nme.7345

21. Chen L, Wang Z, Lian H, Ma Y, Meng Z, et al. Reduced order isogeometric boundary element methods for CAD-integrated shape optimization in electromagnetic scattering. *Comp Methods Appl Mech Eng* (2024) 419:116654. doi:10.1016/j.cma.2023.116654

22. Chen L, Cheng R, Li S, Lian H, Zheng C, Bordas SP. A sample-efficient deep learning method for multivariate uncertainty qualification of acoustic–vibration interaction problems. *Comp Methods Appl Mech Eng* (2022) 393:114784. doi:10.1016/j.cma.2022.114784

23. Chen LL, Zhang Y, Lian H, Atroshchenko E, Ding C, Bordas S. Seamless integration of computer-aided geometric modeling and acoustic simulation: isogeometric boundary element methods based on Catmull-Clark subdivision surfaces. *Adv Eng Softw* (2020) 149:102879. doi:10.1016/j.advengsoft.2020.102879

24. Chen L, Lu C, Lian H, Liu Z, Zhao W, Li S, et al. Acoustic topology optimization of sound absorbing materials directly from subdivision surfaces with isogeometric boundary element methods. *Comp Methods Appl Mech Eng* (2020) 362:112806. doi:10.1016/j.cma.2019.112806

25. Chen LL, Lian H, Liu Z, Chen H, Atroshchenko E, Bordas S. Structural shape optimization of three dimensional acoustic problems with isogeometric boundary element methods. *Comp Methods Appl Mech Eng* (2019) 355:926–51. doi:10.1016/j.cma.2019.06.012

26. Chen L, Liu C, Zhao W, et al. An isogeometric approach of two dimensional acoustic design sensitivity analysis and topology optimization analysis for absorbing material distribution. *Comp Methods Appl Mech Eng* (2018) 336:507–32. doi:10.1016/j.cma.2018.03.025

27. Shen X, Du C, Jiang S, Sun L, Chen L. Enhancing deep neural networks for multivariate uncertainty analysis of cracked structures by POD-RBF. *Theor Appl Fracture Mech* (2023) 125:103925. doi:10.1016/j.tafmec.2023.103925

28. Shen X, Du C, Jiang S, Zhang P, Chen L. Multivariate uncertainty analysis of fracture problems through model order reduction accelerated SBFEM. *Appl Math Model* (2024) 125:218–40. doi:10.1016/j.apm.2023.08.040

29. Lu C, Chen L, Luo J, Chen H. Acoustic shape optimization based on isogeometric boundary element method with subdivision surfaces. *Eng Anal Boundary Elem* (2023) 146:951–65. doi:10.1016/j.enganabound.2022.11.010

30. Cao G, Yu B, Chen L, Yao W. Isogeometric dual reciprocity BEM for solving non-Fourier transient heat transfer problems in FGMs with uncertainty analysis. *Int J Heat Mass Transfer* (2023) 203:123783. doi:10.1016/j.ijheatmasstransfer.2022.123783

frontiers | Frontiers in Physics

TYPE Original Research
PUBLISHED 21 February 2024
DOI 10.3389/fphy.2024.1361605

OPEN ACCESS

EDITED BY
Yilin Qu,
Northwestern Polytechnical University, China

REVIEWED BY
Feng Zhu,
Nanjing University of Aeronautics and Astronautics, China
Zhiqing Zhang,
Wenzhou University of Technology, China

*CORRESPONDENCE
Xiaohui Yuan,
yxh@xynu.edu.cn

RECEIVED 26 December 2023
ACCEPTED 29 January 2024
PUBLISHED 21 February 2024

CITATION
Yuan X, Huo R and Zhang X (2024), Experimental study on flexural mechanical properties of steel fiber reinforced alkali-activated slag concrete beams.
Front. Phys. 12:1361605.
doi: 10.3389/fphy.2024.1361605

Experimental study on flexural mechanical properties of steel fiber reinforced alkali-activated slag concrete beams

Xiaohui Yuan[1,2]*, Ruijin Huo[1,2] and Xin Zhang[3]

[1]College of Architecture and Civil Engineering, Xinyang Normal University, Xinyang, China, [2]Henan New Environmentally-Friendly Civil Engineering Materials Engineering Research Center, Xinyang Normal University, Xinyang, China, [3]Henan International Joint Laboratory of Structural Mechanics and Computational Simulation, Huanghuai University, Zhumadian, China

As an environmentally friendly alternative to ordinary concrete, slag concrete is subject to limitations such as drying shrinkage and micro-cracking during its promotion and application. In order to address these challenges, steel fibers, known for their excellent tensile, shear, crack-resistance, and toughness properties, have been introduced to enhance the ductility of alkali-activated slag concrete. This study utilized steel fiber content as a variable and produced eight steel fiber-reinforced alkali-activated slag concrete beams to investigate their flexural mechanical properties. By exploring the influence of steel fiber content variation on the mechanical behavior of alkali-activated slag concrete beams and conducting validation through finite element analysis, the study unveiled the impact of steel fibers on the performance of alkali-activated slag concrete beams. The research findings demonstrate a significant enhancement in the flexural mechanical properties of alkali-activated slag concrete beams with the addition of steel fibers, leading to a reduction in surface cracking and an improvement in the durability of the elements. The outcomes of this study hold crucial theoretical implications for the widespread application of steel fiber-reinforced alkali-activated slag concrete.

KEYWORDS

alkali-activated slag concrete, steel fiber, flexural mechanical properties, toughness performance, finite element method

1 Introduction

Resource scarcity and environmental pollution have always been prominent concerns in contemporary human society. As a crucial component in the construction process, cement is manufactured and consumed on a substantial scale annually. Traditional cement production, employing the "two grinding and one burning" process, not only depletes considerable energy resources but also generates significant quantities of harmful gases like NO_x, SO_2, and greenhouse gases like CO_2 during clinker calcination, thereby exerting a severe impact on the natural environment [1–3]. According to statistical data provided in 2022 by China's Ministry of Ecology and Environment, the cement industry's emissions of particulate matter and nitrogen oxides account for 20.9% and 17.3% of the total industrial emissions in the country, respectively, while CO_2 emissions constitute approximately 13.0% of the overall national emissions, resulting in substantial environmental consequences. Consequently, the adoption of novel and eco-friendly structural materials as substitutes for

conventional concrete is imperative [4, 5]. Therefore, the development of innovative and sustainable construction materials is not only a leading trend in the field of civil engineering materials but also a critical objective within the current global resource and energy development strategies.

In recent years, alkali-activated slag concrete has emerged as an environmentally-friendly substitute for ordinary Portland cement (OPC) concrete [6–8]. As a novel, energy-efficient, and eco-friendly building material, alkali-activated slag cement maximizes the utilization of industrial waste and by-products, such as fly ash and granulated blast furnace slag, thus achieving optimal secondary utilization of industrial waste. In comparison to ordinary Portland cement, alkali-activated slag cement significantly reduces the energy consumption and environmental pollution associated with raw material production [9, 10]. The raw material production process of alkali-activated slag concrete is straightforward, characterized by low energy consumption and high utilization of industrial solid waste. Relative to ordinary Portland cement concrete, alkali-activated slag concrete demonstrates excellent mechanical and durability properties, including high strength, freeze-thaw resistance, and corrosion resistance [11].

However, alkali-activated slag concrete does have certain drawbacks that limit its widespread adoption and application. These include its sensitivity to environmental factors, short setting time [12], high carbonation rate, and susceptibility to steel bar corrosion [13]. It is also prone to potential alkali-aggregate reaction [14], shrinkage, and the formation of micro-cracks due to significant drying shrinkage [15, 16]. These issues have a significant impact on the promotion and application of alkali-activated slag concrete. The occurrence of micro-cracks caused by drying shrinkage can gradually worsen over time, leading to the corrosion of internal steel bars. This ultimately affects the durability and safety of structural components [17]. Durability is a critical functional requirement for building structures. Therefore, effectively addressing the excessive formation of micro-cracks resulting from the drying shrinkage of alkali-activated slag concrete is crucial for improving the material's durability during use.

Steel fibers, as the most common fiber material, possess excellent tensile, shear, crack resistance, and toughness properties. The addition of steel fibers in concrete matrix materials can enhance the concrete's resistance to permeability, shrinkage, and deformation, as well as reduce the width of cracks during normal structural usage [18]. Therefore, it is possible to incorporate steel fibers into alkali-activated slag concrete to mitigate its drying shrinkage behavior and improve post-cracking behavior, toughness, and ductility [19, 20]. Relevant studies have been conducted in this regard. For instance, Qin et al. [21] found that steel fibers enhance the toughness of alkali-activated slag concrete. However, excessive steel fibers tend to aggregate and do not distribute uniformly in the concrete, leading to increased internal defects. Serdar et al. [22] investigated the influence of steel fiber content and length on the properties of alkali-activated slag mortar. The results showed that with increasing steel fiber content and length, the drying shrinkage decreases gradually, while the compressive and flexural strengths increase. Gülsßan [23] studied the influence of nano-silica and steel fibers on the workability and mechanical performance of self-consolidating geopolymer concrete. The findings suggested that the incorporation of nano-silica and steel fibers negatively affects workability but significantly improves the flexural performance of geopolymer concrete.

Steel fiber alkali-activated slag concrete demonstrates potential applications in the construction industry similar to those of standard Portland cement concrete. However, a comprehensive evaluation of its mechanical and load-bearing performance in structural components necessitates extensive component testing and adherence to applicable regulations. Regrettably, the existing literature on the use of steel fiber alkali-activated slag concrete in structural components is limited, requiring further research to provide theoretical references for its application and promotion. Therefore, the objective of this study is to investigate the flexural mechanical properties of steel fiber alkali-activated slag concrete beams by varying the steel fiber content. This research endeavor will explore the influence of different steel fiber contents on the mechanical performance of steel fiber alkali-activated slag concrete beams and validate these findings through finite element analysis.

2 Experimental

2.1 Materials

Milled steel fibers were selected for use, with a length (L_f) of 36 mm, a width of 2.3 mm, and a thickness of 0.6 mm. The effective diameter d_f is 1.08 mm, and the length-to-diameter ratio (L_f/d_f) is 27.07. The tensile strength is 700 MPa.

The slag is sourced from Xinxing Cement Plant in Henan Province, China. According to the standard "Ground granulated blast furnace slag powder for use in cement and concrete" (GB/T 18046-2000), its physical properties were tested and it was classified as an S95 grade. The density of the slag was determined to be 3.27 g/cm^3 and the specific surface area was calculated to be 434.6 m^2/kg. Scanning electron microscopy revealed that the slag particles were irregularly shaped blocks.

The fly ash is sourced from Yangluo Power Plant in Wuhan, China. According to the standard "Fly ash for use in cement and concrete" (GB/T 1596-2005), its physical properties were tested. The density of the fly ash was determined to be 2.187 g/cm^3. Scanning electron microscopy revealed that the fly ash particles were spherical in shape with a regular structure.

The activator solution is a mixture of sodium hydroxide, water glass (sodium silicate), and water, with a mass ratio of 100 kg/m^3: 10.36 kg/m^3: 90.35 kg/m^3. The modulus of the water glass in the solution was determined to be 2.93 using the titration method. The role of sodium hydroxide is to adjust the modulus of the water glass, which was subsequently adjusted to 1.6. Water, on the other hand, is used to regulate the moisture content of the activator solution, resulting in a final moisture content of 73.5%.

The fine aggregate is sourced from the Xinxiang River in China. Its physical properties were tested according to "Standard for Quality and Testing of Sand and Stone for Ordinary Concrete" (JGJ 52-2006). The apparent density of the sand was determined to be 2,600 kg/m^3, and the fineness modulus was found to be 2.99, belonging to Zone II medium sand.

The coarse aggregate is sourced from the Xinxiang quarry in China, with a particle size less than 20 mm. Its physical properties were tested according to the standard "Standard for Quality and Testing of Sand and Stone for Ordinary Concrete" (JGJ 52-2006). The apparent density of the stone was determined to be 2,700 kg/m^3.

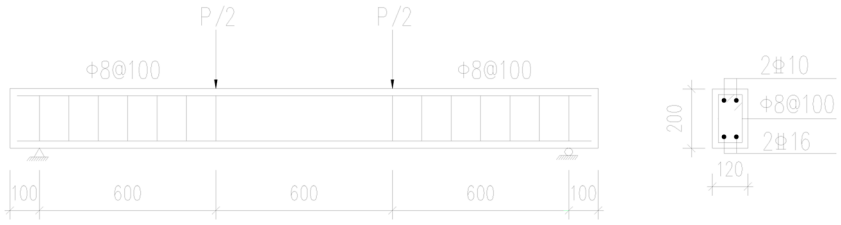

FIGURE 1
Reinforcement diagram of the test beams'.

TABLE 1 Mix proportion design of steel fiber reinforced AASC (kg/m³).

GGBS	Fly ash	Fine aggregate	Coarse aggregate	Activator solution	Steel fiber	Solution to powder ratio	Water to solid ratio
280	120	615	1,260	248	0.00	0.62	0.46

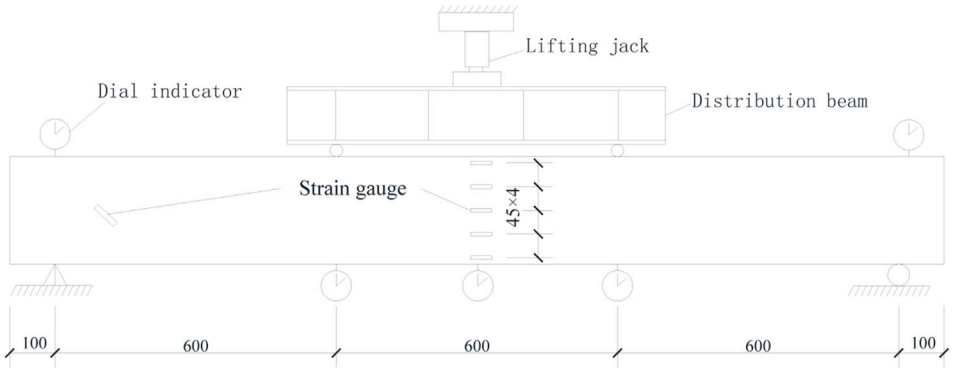

FIGURE 2
Measuring point layout of the test beams'.

2.2 Test beams

A total of 8 steel fiber reinforced alkali-activated slag concrete (SFRASC) beams were produced, with steel fiber dosages (V_f) of 0.0%, 0.5%, 0.9%, 1.0%, 1.1%, 1.2%, 1.3%, and 1.4%, respectively. The test specimens were numbered SFRASC-X (1-8). The cross-sectional dimensions of the test beams were 120 mm × 200 mm, and the beam length was 2000 mm. The bottom reinforcement was $2\Phi16$ with a cross-sectional area of 402 mm² and a reinforcement ratio of 2.0%. The formwork was supported by $2\Phi10$ stirrups and tied with $\Phi8@100$ hoop steel. The thickness of the protective layer was 25 cm, and the shear-to-span ratio of the beam was 3.6. The beams' reinforcement diagram is shown in Figure 1. The concrete mix ratio of the test beam is shown in Table 1.

2.3 Measuring point layout

The displacement was measured using a dial gauge, with a total of 5 displacement measurement points placed at the beams' support top surface, mid-span ($L/2$), and mid-span ($L/3$), respectively. The theoretical value of the mid-span displacement was calculated as the difference between the measured mid-span displacement and the average displacement measured at the supports. Strain gauges of type BE120-5AA were placed on the surface of the bottom reinforcing steel bars, while strain gauges of type BX120-50AA were placed on the surface of the positive cross-sectional side at the mid-span of the beam, with a spacing of 45 mm. The bottom-most strain gauge was situated 10 mm away from the bottom of the beam, and the topmost strain gauge was positioned 10 mm away from the top of the beam. Strain gauges were also placed on the concrete surface in the neutral axis of the support's shear web, aligned in the direction of tensile stress trace, as per the layout indicated in the test specimen arrangement diagram shown in Figure 2. Cracks were tested in the pure bending section and the bending-shear zone using a reading microscope of type MG10085-1.

2.4 Test standards

The test was conducted in accordance with the relevant provisions of the "Standard Test Methods for Concrete

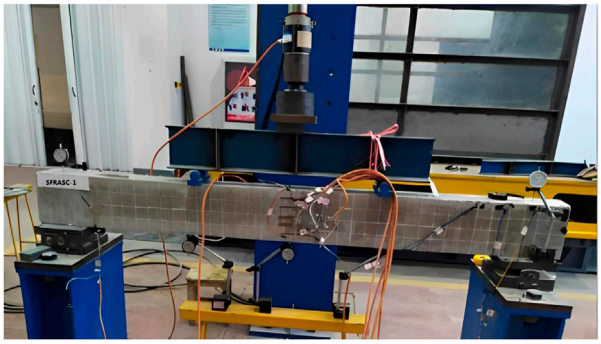

FIGURE 3
Experimental loading device diagram of the beams'.

Structures" (GB/T 50152-2012). Preloading: the specimen was preloaded to 5 kN and then unloaded to 0 kN, repeated twice. Formal loading: the loading was carried out in a stepwise manner, with each load level set at 5 kN. After the completion of each loading stage, the load was held for approximately 5 min, during which data were recorded, and the surface cracks on the beam were marked using a marker pen. As the cracking load value approached, the load increment for each stage was reduced to 1 kN to ensure accurate measurement of the cracking load. Once the specimen cracked, the load for each stage was readjusted to 5 kN. The test was concluded when the measured deflection of the beam reached $L/50$ of the span, indicating the beam had reached its ultimate bearing capacity limit state. Experimental loading device diagram of the beams' is shown in Figure 3.

3 Results and discussion

3.1 Load results and analysis

The results of the tests for the normal section cracking load (P_{cr}), mid span cracking moment ($M_{fcr}{}^{0}$), diagonal section cracking load (P'_{cr}), diagonal section cracking shear force (V_{cr}), ultimate load (P_u), ultimate moment ($M_{fu}{}^{0}$) are presented in Table 2. As shown in the experimental results in Table 2, the addition of steel fibers significantly enhances the load-carrying capacity of the concrete beams. The function of steel fibers in steel fiber-reinforced concrete is to effectively improve the mechanical and durability properties of the concrete by utilizing their high strength and toughness [24]. The addition of steel fibers effectively enhances the tensile stress and crack resistance of the concrete, thereby preventing cracking and fracture [25, 26], and consequently improving the overall flexural performance and load-bearing capacity of steel fiber reinforced alkali-activated slag concrete beams.

The theoretical value of the positive section bending load-bearing capacity of the test beam was calculated according to the formula specified in the "Technical Code for Fiber Reinforced Concrete Structures" (CECS38:2004). The comparison between the theoretical calculation and the test result is shown in Figure 4. From the figure, it is evident that the test results exhibit a reasonable level of agreement with the theoretical calculations. The theoretical calculation curve appears to be smoother in comparison, whereas the test curve shows some fluctuations. These variations can be attributed to multiple factors, including test conditions, the testing process, and the characteristics of the test specimens themselves. The ratio of the average test value to the average calculated value is found to be 1.0218, with a standard deviation of 0.0106 and a coefficient of variation of 0.0104. These results indicate that the calculation formula for determining the positive section bearing capacity of the beam, as specified in the guidelines, is equally applicable to steel fiber alkali slag concrete beams. These values suggest a relatively small deviation from the theoretical calculations, further supporting the reliability and suitability of the formula for this type of concrete beam.

3.2 Deflection results and analysis

The load-deflection curves for the tested beams are presented in Figure 5. The load-deflection curve can be divided into three stages. In Stage I, there is a linear relationship between load and deflection. In Stage II, cracking occurs in the beam, causing the load to transfer abruptly from the concrete to the reinforcing steel bars. This results in a decrease in effective height, stiffness, and an increase in the rate of deflection. A clear inflection point can be observed between Stage I and Stage II. Finally, in Stage III, the load remains constant, but the displacement increases rapidly as the beam reaches its ultimate limit state.

Analysis of the eight load-deflection curves reveals that the difference in stiffness among the beams in Stage I is not significant. In Stage II, it is noticeable that the increase in deflection rate for beams containing steel fibers is lower than that for the non-fiber reinforced specimens. This suggests that

TABLE 2 Test results of the beams.

Test piece number	P_{cr}(kN)	$M_{fcr}{}^{0}$ (kN·m)	P'_{cr} (kN)	V_{cr}(kN)	P_u(kN)	$M_{fu}{}^{0}$ (kN·m)
SFRASC-1	15.8	4.74	45.2	22.6	89.4	26.82
SFRASC-2	19.5	5.85	50.0	25.0	96.4	28.92
SFRASC-3	22.1	6.63	55.2	27.6	100.2	30.06
SFRASC-4	21.2	6.36	57.4	28.7	101.2	30.38
SFRASC-5	22.8	6.84	60.7	30.35	103.8	31.14
SFRASC-6	23.7	7.11	63.1	31.55	107.0	32.10
SFRASC-7	24.4	7.32	65.7	32.85	108.0	32.40
SFRASC-8	25.3	7.59	67.5	33.75	111.5	33.45

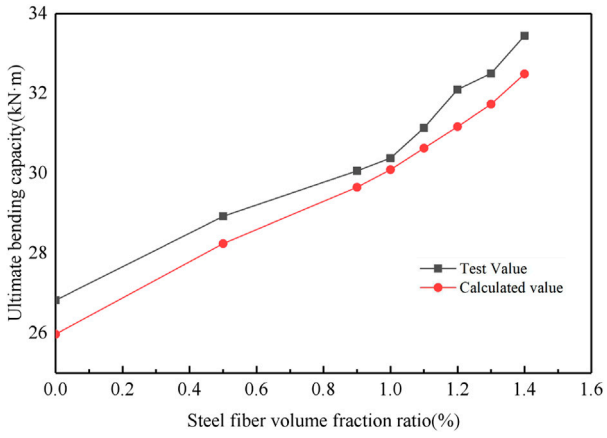

FIGURE 4
Comparative analysis of ultimate bending moment test and theoretical calculation values.

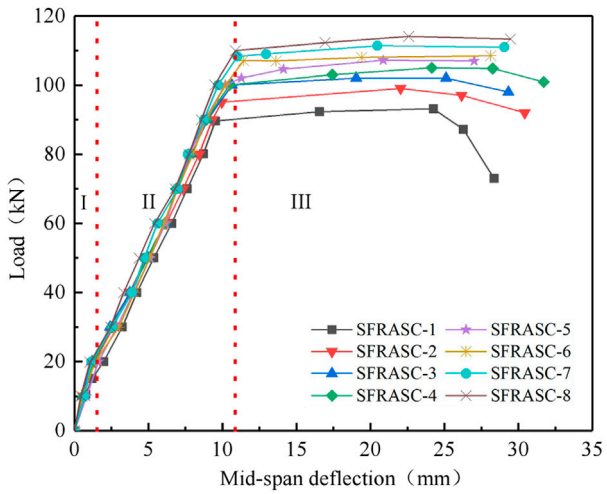

FIGURE 5
Load-deflection curves for the tested beams.

the addition of steel fibers contributes to the ductility of steel fiber alkali slag concrete beams. For instance, at a load of 60kN, the mid-span deflection of the SFRASC-1, SFRASC-2, SFRASC-4, and SFRASC-8 beams were 6.57 mm, 6.21 mm, 6.1 mm, and 5.41 mm, respectively.

Moreover, as the steel fiber content increases, the load capacity gradually increases. For steel fiber content below 1.1%, the deflection curve of the test specimen experiences a horizontal development phase followed by a drop. For steel fiber content greater than 1.1%, the deflection curve is without a downward phase. This provides further evidence of the positive impact of steel fibers on the ductility of steel fiber alkali slag concrete beams.

Overall, the results highlight the potential of steel fibers to enhance the mechanical and structural properties of concrete. The findings also have significant implications for the design and construction of durable infrastructure.

3.3 Crack results and analysis

Figure 6 illustrates the expansion of surface cracks on the lateral side of eight tested beams. The numerical values in the figure correspond to the load conditions at which cracks become noticeable. Observing the figure, it can be seen that once the load reaches the cracking load for the normal section, an initial vertical crack manifests in the middle of the beam span within the normal section. Subsequently, as the load further increases, the vertical crack progressively extends upward while simultaneously widening.

Upon reaching the cracking load for the diagonal section, diagonal cracks emerge in a 45° direction from the neutral axis of the beam's support region. As the load continues to rise, these diagonal cracks gradually propagate towards both the support and loading positions. As the beam approaches failure, the load stabilizes, yet the crack width experiences a rapid expansion.

Analysis of the surface crack distribution reveals that an increase in steel fiber content leads to a significant reduction in beam surface cracks. This positive outcome can be primarily attributed to the beneficial effects of steel fibers, including crack bridging and improved crack resistance [27, 28].

As the bending process of the test beam progresses, the increase in the number of surface cracks corresponds to a continuous increase in both the width and height of each crack. The magnitude of crack width stands out as a pivotal factor influencing the load-bearing capacity of the test beam. During the bending test, cracks predominantly manifest in the pure bending section, particularly in the lower extremity where tensile stress reaches its peak. Consequently, the maximum crack width is chiefly observed in the pure bending section, a phenomenon that becomes particularly conspicuous during the bending failure of a concrete beam. The load versus maximum crack width relationship of the test beam is portrayed in Figure 7 based on the test findings.

Figure 7 illustrates that the inclusion of steel fibers in the test beam delayed cracking and substantially reduced the maximum crack width under equivalent loads. Initially, when the test beam undergoes cracking, the longitudinal tensile steel bars remain unyielding. At this stage, the crack development is constrained not only by the bond strength between the ribbed longitudinal bars and the concrete, but also by the interaction of steel fibers with the concrete on either side of the crack. The subsequent increase in maximum crack width is considerably slower. For instance, at a load of 40 kN, test beams with steel fiber contents of 0% and 1.0% exhibited maximum crack widths of 0.20 mm and 0.16 mm, respectively, marking a 20% reduction. Additionally, the tensile longitudinal reinforcement's effectiveness in restraining crack propagation diminishes drastically in alkali slag concrete beams upon yielding, leading to a notable surge in maximum crack width for SFASC1 beams. However, steel fiber alkali slag concrete beams demonstrate a bridging effect at crack sites, impeding crack propagation and resulting in a slower increase in maximum crack width after tensile longitudinal reinforcement yield. At a load of 80 kN, test beams with steel fiber contents of 0% and 1.0% displayed maximum crack widths of 0.50 mm and 0.30 mm, respectively, representing a 40% reduction.

In accordance with the theoretical calculation method for determining the maximum crack width of beams outlined in the Technical Specification for Fiber Reinforced Concrete Structures

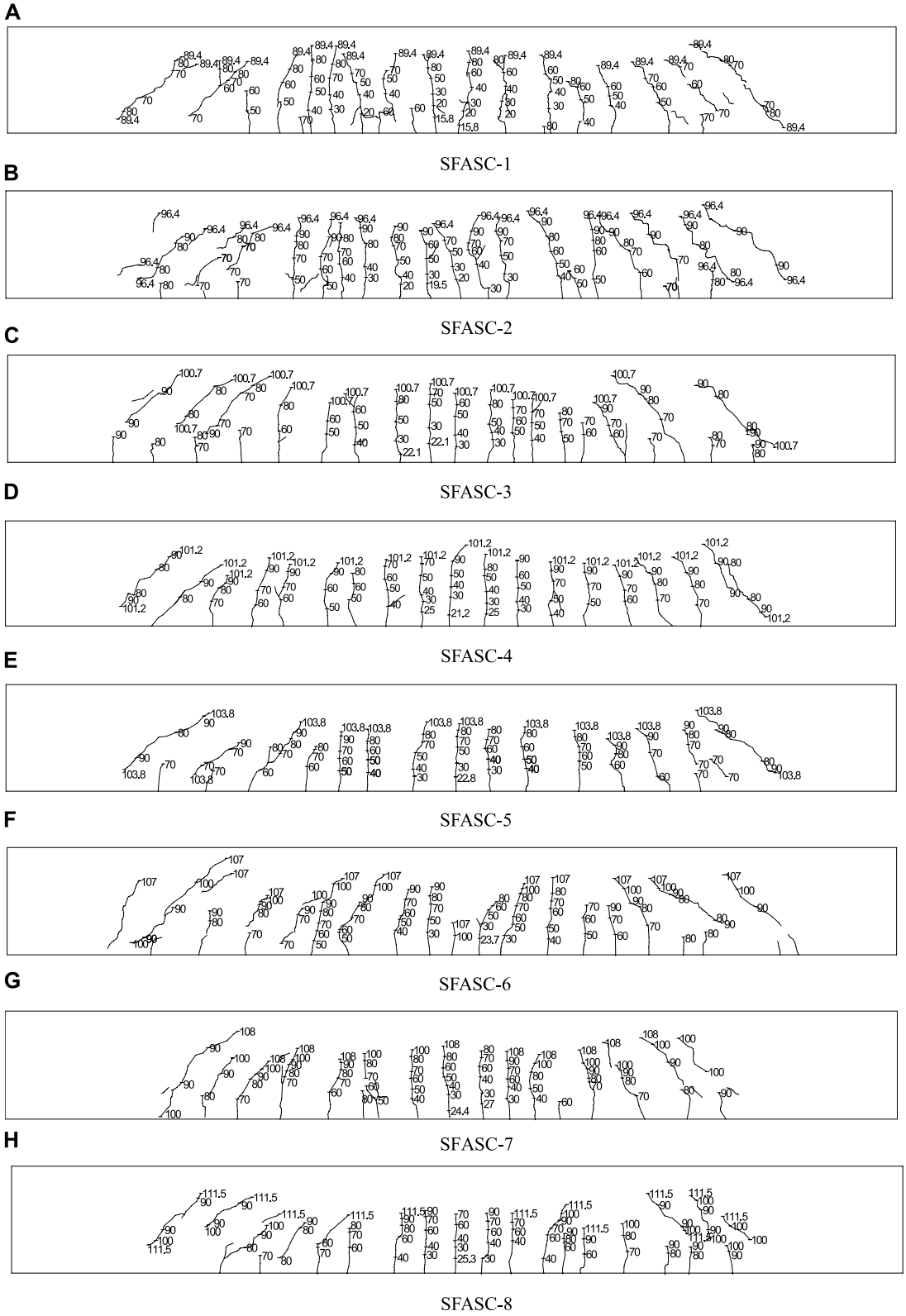

FIGURE 6
Development and distribution of surface cracks during the bending process of SFRASC-1, SFRASC-2, SFRASC-3, SFRASC-4, SFRASC-5, SFRASC-7, and SFRASC-8.

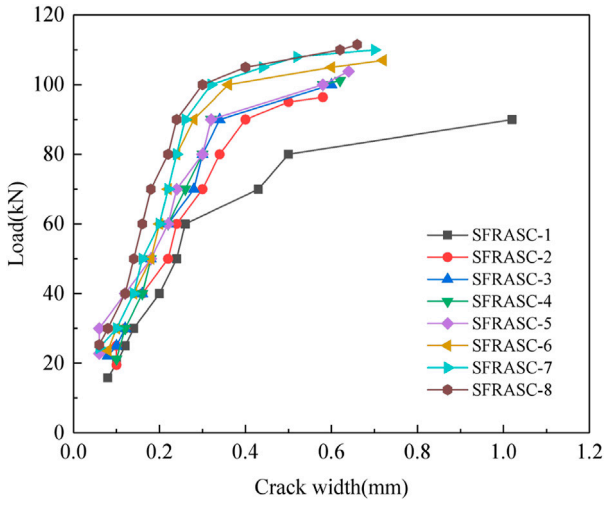

FIGURE 7
Load crack width curve.

(CECS38:2004), the maximum crack widths for each test beam under various load levels were computed. The resulting theoretical and experimental values are presented in Table 3 for comparative analysis. Where the P is the load of the test, ω_{fmax} and $\omega_{fmax}{}^{c}$ is experimental and theoretical values of crack width respective.

Based on the results presented in Table 3, certain disparities exist between the experimental values and the theoretical calculations, primarily due to the influence of steel fiber content on crack width. To account for this effect, the formula for computing the maximum crack width, as specified in the guidelines, is revised with the incorporation of the steel fiber crack reduction coefficient γ. The modified formula is shown as Eq. 1.

$$\omega_{f\,\max} = \gamma\omega_{\max}\left(1 - \beta_{cw}\lambda_f\right) \tag{1}$$

In the revised formula, the symbol ω_{fmax} represents the maximum crack width of the fiber-reinforced concrete beams, while ω_{max} refers to the corresponding calculation formulas provided in the "Code for Design of Concrete Structures" (GB50010-2010). Additionally, λf denotes the characteristic parameters of steel fibers, and β_{cw} represents the coefficient that accounts for the influence of steel fibers on the crack width of structural components. Specifically, for bending components, the value of β_{cw} is set to 0.35. Linear regression is employed to compute the average ratio between the experimental value and the calculated value of the steel fiber crack reduction coefficient γ. The calculation formula is shown as Eq. 2.

$$\gamma = 0.3682V_f + 1.578 \tag{2}$$

Figure 8 displays the comparison curve between the computed results obtained from the modified formula and the experimental data. The figure reveals a high level of concordance between the calculated outcomes and the empirical values, signifying the potential theoretical relevance of these calculations in real-world engineering scenarios.

3.4 Strain results and analysis

The surface strain analysis conducted on the lateral side of the beam demonstrates that the cross-section of the beam adheres to the assumption of having a flat section throughout the stress process. This study exclusively presents the surface strain test results for specimens with 0% and 1% steel fiber content. Figure 9 exhibits the surface strain distribution along the height of the beam cross-section on the normal section side of the specimen. The cracking load of the two test beams is observed to manifest at distances of 6.7 mm and 14.1 mm above the beam's centerline, respectively. The inclusion of steel fibers enhances the tensile strength of alkali slag concrete. By virtue of the static equilibrium principle, beams containing steel fibers exhibit a relatively diminished height for the relative compression zone. This experimental finding aligns with theoretical expectations. With an incremental increase in the applied load, the position of the neutral axis progressively shifts upwards, and the strain on the lateral surface of the beam exhibits a linear descent along the beam's height.

Figure 10 illustrates the relationship between the strain of the longitudinal steel bars at the bottom of the test beam and the applied load. It can be categorized into three distinct stages, analogous to the load-deflection curve. In Stage I, which corresponds to low load levels, a linear relationship between strain and load is observed, indicating the specimen's elastic behavior. Stage II marks the second phase, wherein a clear inflection point manifests at the intersection of Stages I and II. This inflection point signifies the onset of concrete cracking, resulting in the instantaneous transfer of tension from the beam's bottom to the longitudinal steel bars and a redistribution of stress within the beam section. The inclusion of steel fibers mitigates the inflection point phenomenon in specimens, leading to a gradual increase in the strain of the longitudinal steel bars with subsequent load increments. Stage III designates the third phase, where the load reaches its ultimate capacity and remains constant, while the strain of the longitudinal steel bars continues to increase. It is evident from the curve that specimens with added steel fibers exhibit comparatively lower strains in the longitudinal steel bars under the same applied load. Furthermore, the ultimate load of the specimens progressively increases with higher steel fiber content, corroborating the earlier analyzed findings.

Figure 11 displays the relationship curve between the principal tensile strain and load at the oblique section of each specimen. Prior to the occurrence of diagonal section cracking, the concrete and reinforcement primarily bear the shear force in the oblique section. Subsequently, as the main tensile stress in the diagonal section reaches the concrete cracking stress, the shear stress gradually transfers to the reinforcement. It is evident from the figure that the specimen with added steel fibers exhibits lower main tensile strain values compared to the specimen without steel fibers, under the same level of load. Furthermore, as the steel fiber content increases, the test values decrease, indicating that the inclusion of steel fibers enhances the tensile strength of alkali slag concrete. The steel fibers assist in sharing some of the tensile force of the concrete, and this effect becomes more pronounced with higher steel fiber content.

10.3389/fphy.2024.1361605

TABLE 3 Experimental and theoretical values of maximum crack width of the beams.

Specimen number	P (kN)	P/P_u	ω_{fmax} (mm)	$\omega_{fmax}{}^c$ (mm)	$\omega_{fmax}/\omega_{fmax}{}^c$
SFRASC-1	20	0.22	0.10	0.0399	2.500
	30	0.36	0.14	0.0822	1.703
	40	0.44	0.20	0.1244	1.607
	50	0.56	0.24	0.1667	1.440
	60	0.67	0.26	0.2088	1.244
SFRASC-2	20	0.21	0.10	0.0372	2.689
	30	0.31	0.12	0.0765	1.569
	40	0.41	0.16	0.1157	1.382
	50	0.52	0.22	0.1550	1.419
	60	0.62	0.24	0.1942	1.235
	70	0.73	0.30	0.2335	1.284
SFRASC-3	22	0.22	0.08	0.0350	2.289
	30	0.30	0.12	0.0719	1.670
	40	0.40	0.16	0.1087	1.471
	50	0.50	0.18	0.1456	1.235
	60	0.60	0.22	0.1825	1.205
	70	0.70	0.28	0.2194	1.275
SFRASC-4	30	0.30	0.12	0.0707	1.697
	40	0.40	0.16	0.107	1.495
	50	0.50	0.18	0.1433	1.256
	60	0.60	0.22	0.1796	1.224
	70	0.70	0.26	0.2159	1.204
SFRASC-5	30	0.29	0.06	0.0696	0.863
	40	0.39	0.12	0.1053	1.140
	50	0.48	0.18	0.1410	1.276
	60	0.58	0.22	0.1767	1.245
	70	0.67	0.24	0.2124	1.129
SFRASC-6	30	0.28	0.10	0.0684	1.462
	40	0.37	0.14	0.1035	1.352
	50	0.47	0.18	0.1386	1.298
	60	0.56	0.2	0.1738	1.150
	70	0.65	0.22	0.2089	1.053
	80	0.75	0.26	0.2440	1.065
SFRASC-7	30	0.28	0.10	0.0672	1.487
	40	0.37	0.14	0.1018	1.375
	50	0.46	0.16	0.1363	1.173
	60	0.56	0.2	0.1708	1.170
	70	0.65	0.22	0.2054	1.071
	80	0.74	0.24	0.2399	1.000
SFRASC-8	30	0.27	0.08	0.0661	1.210
	40	0.36	0.12	0.1000	1.199
	50	0.45	0.14	0.1340	1.045
	60	0.54	0.16	0.1679	0.952
	70	0.63	0.18	0.2019	0.891
	80	0.72	0.22	0.2358	0.933

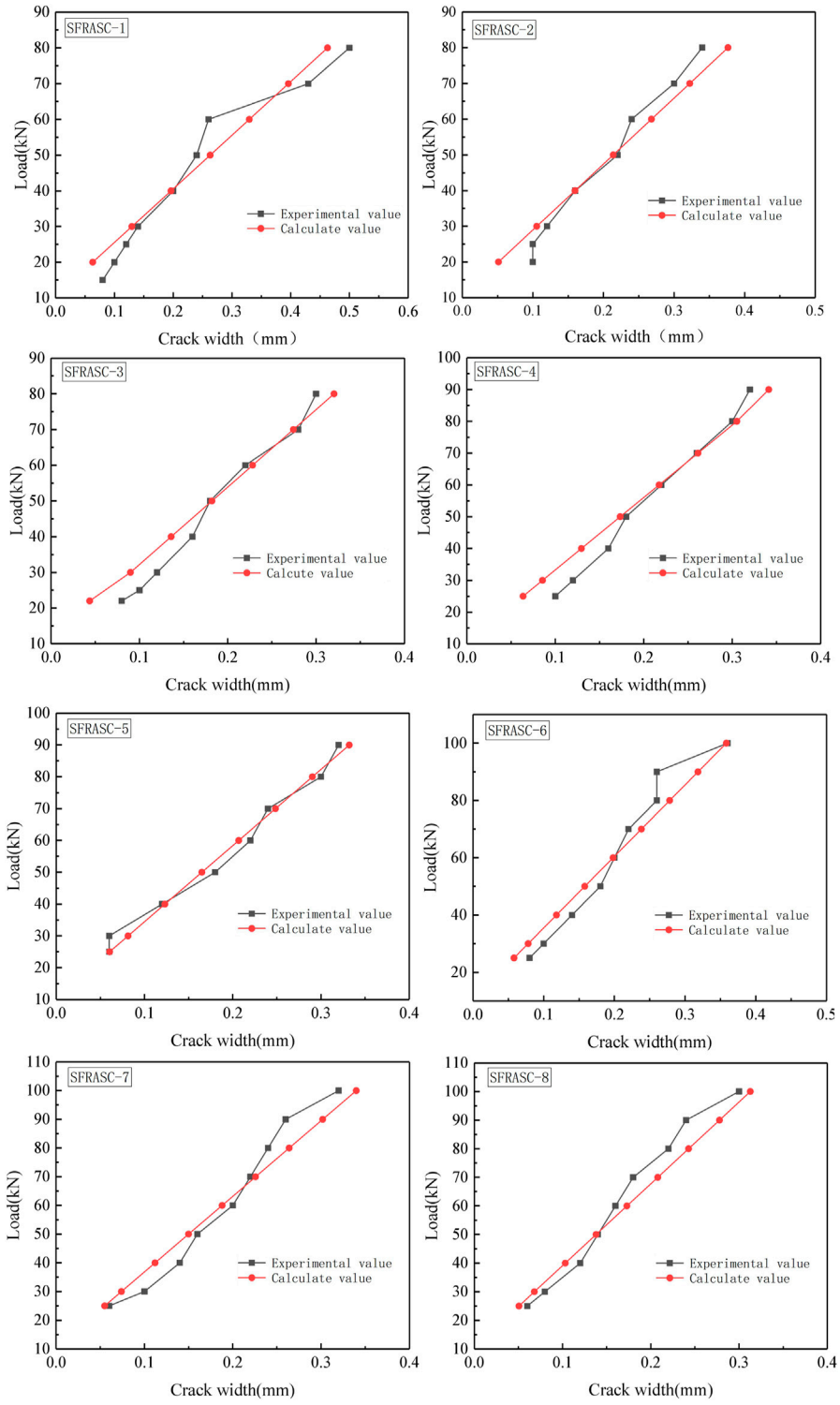

FIGURE 8
Load crack width curve.

4 Analysis of fractal characteristics of SFRASC beams

MATLAB is employed for numerical calculations and analysis and fractal theory is applied to describe the intricate distribution of surface cracks on experimental beams. Initially, the RGB crack image of the experimental beam is transformed into an 8-bit grayscale image utilizing MATLAB. Subsequently, a binary image is generated from the grayscale image by applying a threshold where crack pixels are denoted as 0. The binary image

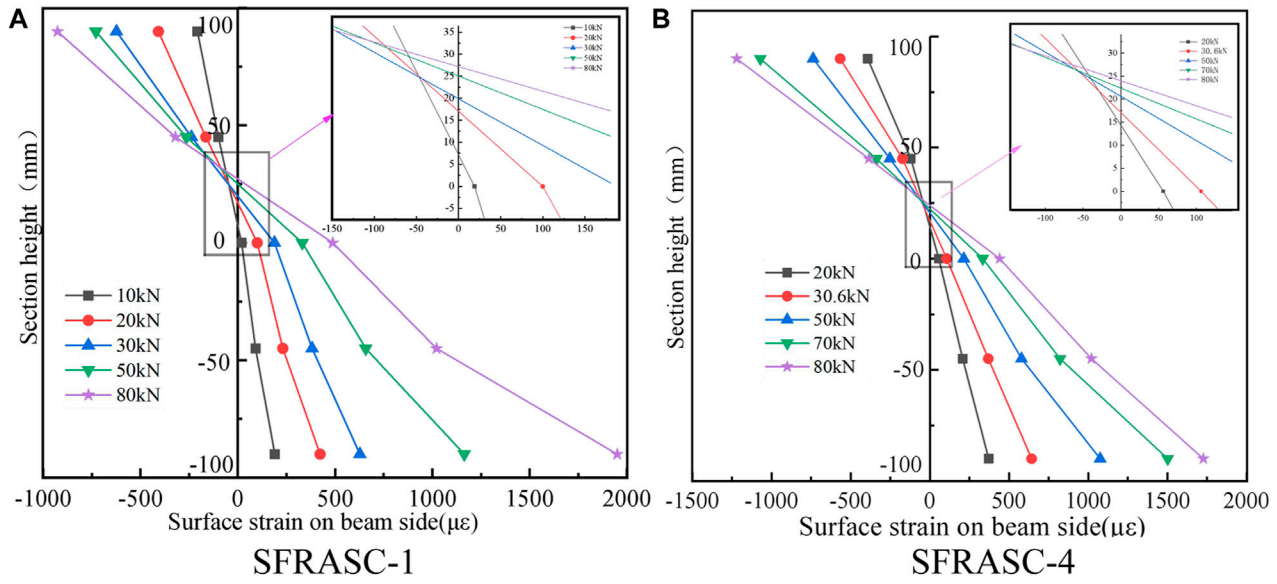

FIGURE 9
Surface strain distribution along the height of the beam cross-section of SFRASC-1 and SFRASC-4.

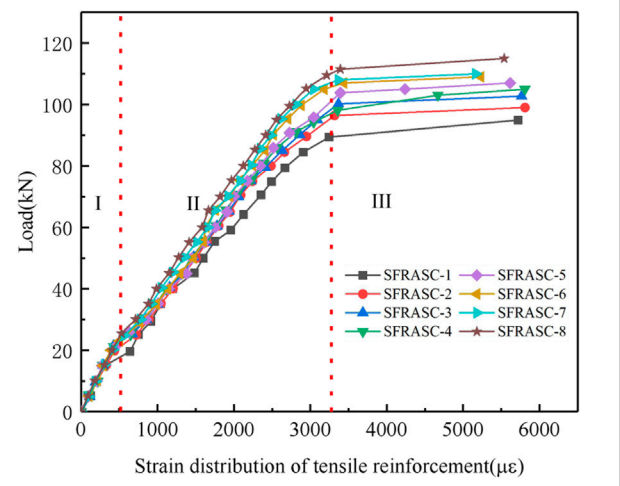

FIGURE 10
Steel bar strain under load.

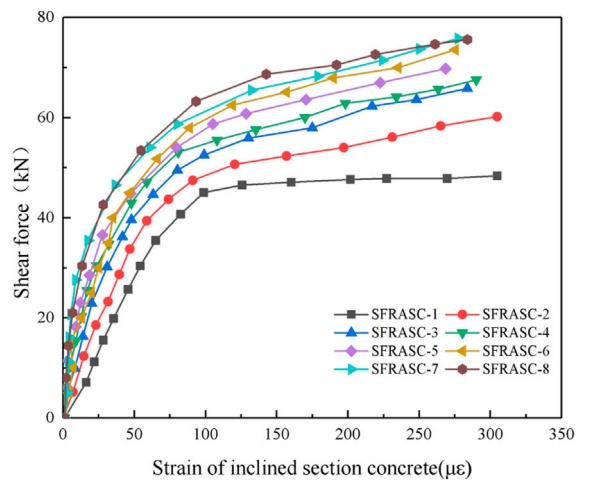

FIGURE 11
Diagonal section concrete strain under load.

is inverted, changing all crack pixels to 1, for subsequent data processing and calculation of the fractal dimension. The adjustment of the coverage network's grid size "r" is managed by modifying the pixel matrix and sub-matrix of the crack image. For each sub-matrix, the sum of its elements is computed and compared to a threshold of 1 in order to identify non-empty regions, i.e., cracks. This process is repeated for various grid densities to determine the count of non-empty regions at different resolutions. These non-empty regions are termed "boxes" and their sizes are correlated with the fractal dimension. The logarithm of the box size and its corresponding number of boxes $N(r)$ are plotted on a logarithmic coordinate graph. Using the least squares method, a logarithmic relationship curve $\ln N(r)$–$\ln(r)$ is derived to describe the change in resolution, where the slope of the curve represents the fractal dimension.

Using specimen SFRASC-1 as a case study, the specific processing procedure is outlined as follows: Firstly, the surface image of the beam is subjected to preprocessing, aiming to eliminate any irrelevant information and focus solely on the test beam, as depicted in Figure 12A. Subsequently, the preprocessed crack image is converted into an 8-bit grayscale image, as displayed in Figure 12B. Binary processing is then applied to the grayscale image, wherein the crack regions are represented in black while the beam surface appears in white, resulting in the binary representation of the crack image shown in

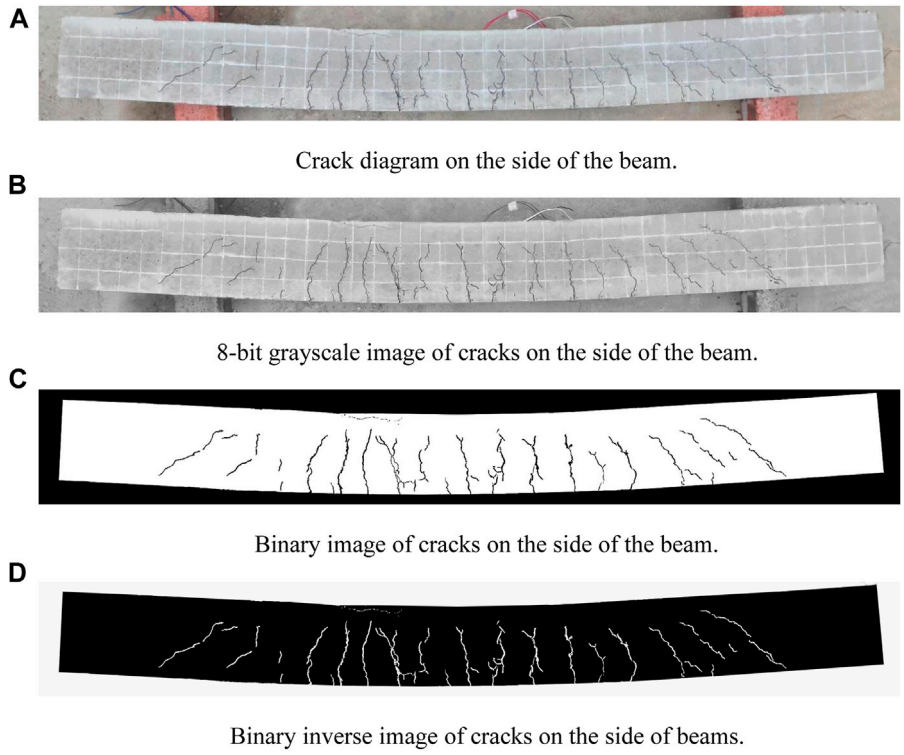

FIGURE 12
SFRASC-1 beam surface crack analysis software workflow.

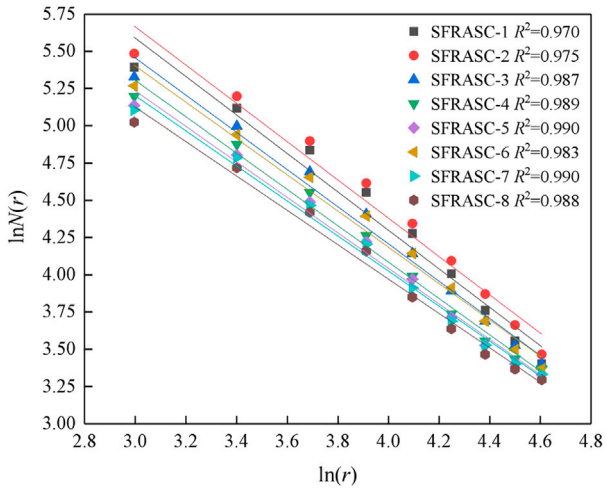

FIGURE 13
Fractal dimension fitting results.

Figure 12C. To obtain the inverse crack image, an inverse operation is performed on the binary image, setting the color of the cracks as white and the beam surface as black, as illustrated in Figure 12D.

Moreover, the binary image of the inverted crack is divided into different network sizes, namely 20 mm, 30 mm, 40 mm, 50 mm, 60 mm, 70 mm, 80 mm, 90 mm, and 100 mm. By overlaying the crack image, the number of non-empty grids $N(r)$ is determined within each network size for subsequent analysis.

For each group, obtain the logarithm of the box sizes r and the corresponding number of non-empty grids $N(r)$, and fit the $\ln N(r)$—$\ln(r)$ relationship curve using the least squares method. The slope of the fitted curve represents the fractal dimension. The fractal dimension of cracks in the test beam under ultimate limit state Fitting results are shown in Figure 13, the correlation coefficient is above 0.9, and the fitting effect is good. The calculation results dimension of different cross-sections during the failure of experimental beams is shown in Table 4.

Upon examination of Table 4, it is evident that there exists a certain degree of variation in the fractal dimension of the pure bending section, bending shear section, and full section across different test beams. This variability indicates distinct differences in crack morphology and distribution among the various test beams. In accordance with fractal theory, smaller fractal dimensions signify more uniform and densely concentrated crack distributions, while larger fractal dimensions indicate more irregular and isolated crack distributions [29]. The larger fractal dimension of the bending shear section for each specimen in the table, in comparison to that of the pure bending section, suggests that the crack distribution in the bending shear section exhibits greater irregularity than that in the pure bending section. This discrepancy can be attributed primarily to the fact that cracks in the pure bending section are predominantly induced by tensile stress in the direction perpendicular to the crack, with parallel shear stress being almost negligible, thereby

TABLE 4 Calculation results of the dimension of different cross-sections during the failure of experimental beams.

Section	Fractal dimension							
	SFRASC-1	SFRASC-2	SFRASC-3	SFRASC-4	SFRASC-5	SFRASC-6	SFRASC-7	SFRASC-8
Pure bending section	1.289	1.280	1.237	1.220	1.194	1.203	1.180	1.150
Bending and shearing section	1.292	1.289	1.257	1.221	1.193	1.228	1.182	1.156
Full cross-section	1.291	1.285	1.249	1.220	1.191	1.217	1.176	1.154

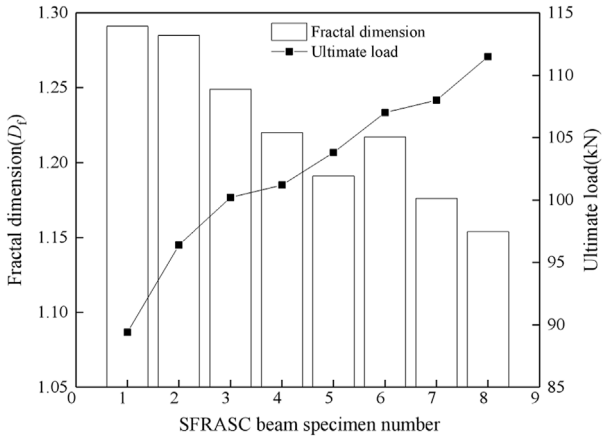

FIGURE 14
Fractal dimension under ultimate load.

precluding the occurrence of shear cracks. In contrast, the bending shear section experiences both bending normal stress and shear stress, resulting in a more intricate interplay and contributing to irregularities in crack formation.

In the pure bending and bending shear sections, the fractal dimension gradually decreases with the increase in steel fiber content. This phenomenon indicates that the inclusion of steel fibers exerts a certain retarding effect on the propagation of pure bending cracks and abdominal shear diagonal cracks, resulting in a more uniform and closely distributed crack pattern. This can be mainly attributed to the ability of steel fibers to impede crack expansion and enhance the material's toughness. Furthermore, the fractal dimension of the entire section also decreases with the rise in steel fiber content, underscoring the positive impact of steel fiber addition in enhancing the crack morphology of the entire section, thereby leading to a more uniform and closely distributed crack pattern.

The fractal dimension of each test beam in the limit state is illustrated in Figure 14. As observed in the figure, the fractal dimension of the cracks in the test beam decreases with an increase in steel fiber content. For instance, the fractal dimension of the cracks in SFASC1 alkali slag concrete measures 1.291, while in the test beam with a steel fiber content of 1.4%, it measures 1.154, indicating a reduction of 10.6%. This implies that the addition of steel fibers effectively mitigates crack occurrence, curbs crack propagation, and enhances the load-bearing capacity of the test beam.

5 Numerical simulation analysis

5.1 Finite element model

The numerical analysis was conducted using ABQUS software. The finite element model of the beam was created with dimensions consistent with the experimental beam, employing C3D8R elements for concrete and T3D2 elements for steel reinforcement. To ensure the calculation results were not influenced by the cushion block, a support pad measuring 120 mm × 50 mm × 50 mm was utilized, with the material properties of the cushion block set as rigid. The finite element model of the beam and the reinforcement bar cage is shown in Figure 15.

The constitutive relationship model of concrete material adopts a two-stage damage constitutive model [30–32], which takes into account the progressive degradation of the material as it undergoes loading and damage. Meanwhile, the reinforcement bars adopt a two-stage double line model, which is a common model used to simulate the behavior of steel subjected to tension and compression. This model accounts for the yielding and hardening of the material under different loading conditions. The interface between steel bars and concrete is assumed to have no relative slip, and a composite model [33–35] is adopted.

5.2 Numeric simulation results and analysis

Table 5 presents a comparative analysis of the numerical simulation results and experimental results for the four selected experimental beams. As shown in the table, the cracking load error ranges from 8.7% to 14.5%, and the ultimate load error ranges from 7.4% to 11.1%. These errors stem from the idealized nature of the finite element simulation. In the simulation, the steel fibers are assumed to be uniformly distributed in the test beam, and the concrete material is tightly bonded with isotropic properties. Additionally, a rigid connection is assumed between the concrete and the steel reinforcement skeleton without any relative slip. However, in real-world scenarios, the uniform distribution of steel fibers in

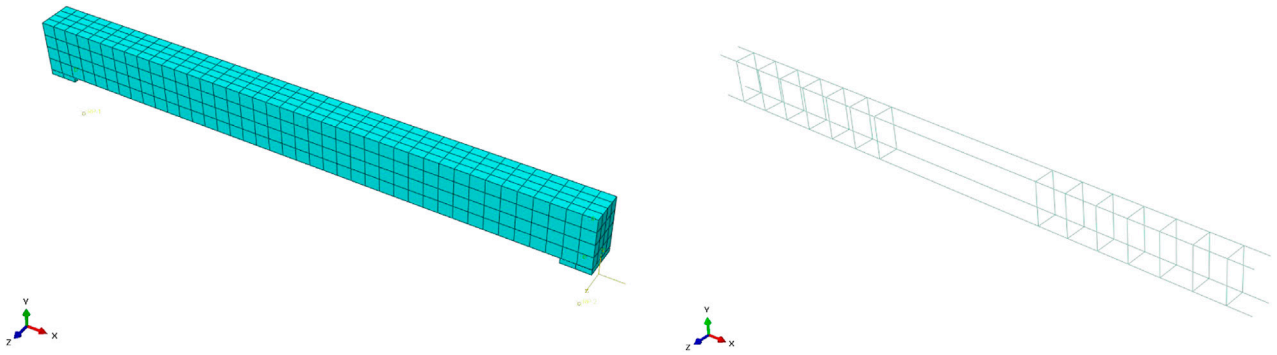

FIGURE 15
The finite element model of the beam and the reinforcement bar cage.

TABLE 5 Comparison between simulated and experimental values.

Specimen number	Cracking load (kN)			Ultimate load (kN)		
	Test value	Analog value	Eerror (%)	Test value	Analog value	Eerror (%)
SFRASC-1	15.8	18.1	14.5	89.4	97.7	9.3
SFRASC-2	19.5	21.7	11.3	96.4	104.3	8.2
SFRASC-4	21.2	24.1	13.4	101.2	112.4	11.1
SFRASC-8	25.3	27.5	8.7	111.5	119.8	7.4

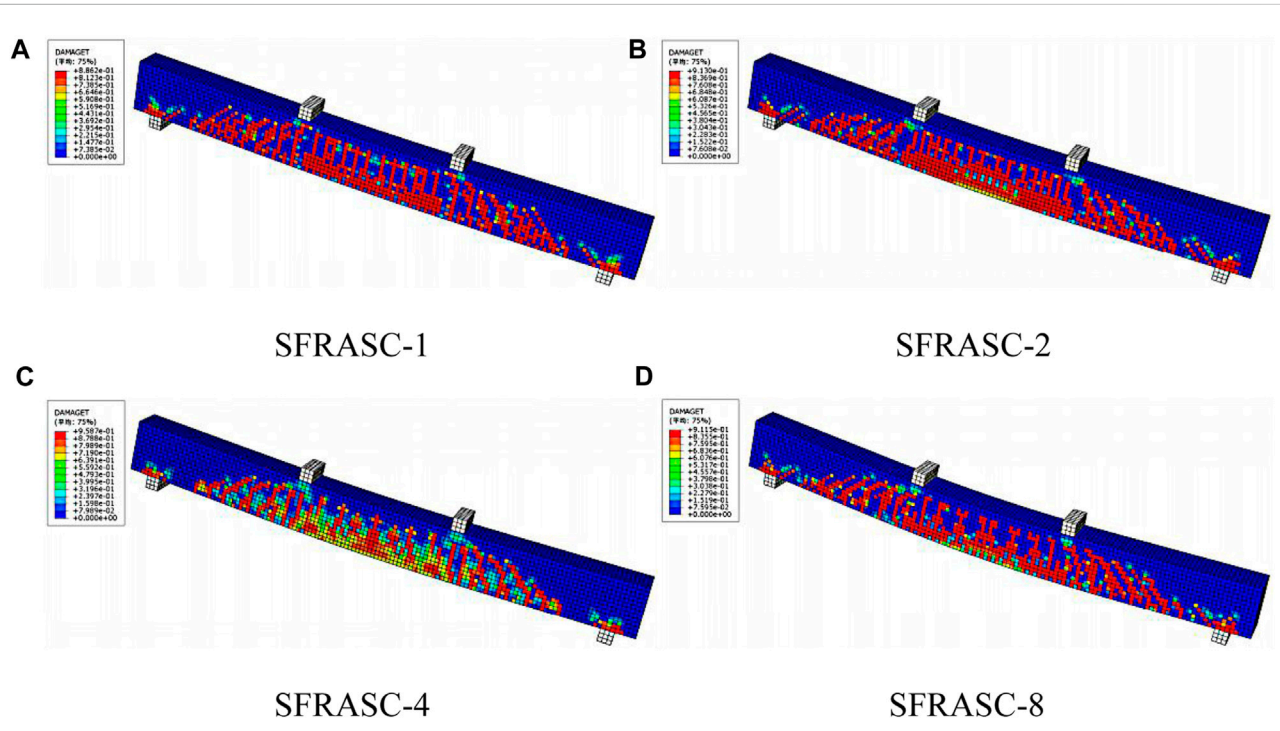

FIGURE 16
Compression damage cloud map of specimen of SFRASC-1, SFRASC-2, SFRASC-4 and SFRASC-8.

concrete beams is challenging to achieve, resulting in non-uniform weak surfaces. Moreover, concrete materials are subject to various factors such as mixing time, methods, and curing techniques, which often lead to the presence of internal microcracks and pores. These differences between the actual conditions and the simulation contribute to the

simulated values being greater than the corresponding experimental values.

Figure 16 shows the damage cloud map of the simulated test beam at ultimate failure under ultimate load, and it can be seen from the figure that the crack distribution pattern is similar to the test results.

6 Conclusion

Adding steel fibers to alkali-activated slag concrete can enhance the tensile stress and crack resistance of the concrete, thereby improving the flexural performance and load-carrying capacity of alkali-activated slag concrete beams. Within the specified range of steel fiber content in this study, an increasing trend is observed in the effectiveness of these enhancements with the increase of steel fiber content.

The existing "Technical Specification for Fiber Concrete Structures" (CECS38: 2004) regarding the calculation formula of beam cross-sectional load-carrying capacity is also applicable to steel fiber-reinforced alkali-activated slag concrete beams.

Both the experimental and fractal analysis results demonstrate the bridging and crack-arresting effect of steel fibers. The addition of steel fibers significantly reduces the number of surface cracks in beams, with this effect becoming more pronounced as the fiber content increases. The given calculation formula for the maximum crack width of fiber concrete beams in the "Technical Specification for Fiber Concrete Structures" (CECS38: 2004) has been modified, and the results from the adjusted formula correspond well with experimental findings.

The numerical simulation results of the loading closely match the experimental results. The distribution of surface cracks in the numerically simulated beam failure is similar to the experimental results.

Data availability statement

The original contributions presented in the study are included in the article/Supplementary material, further inquiries can be directed to the corresponding author.

Author contributions

XY: Writing–original draft, Writing–review and editing. RH: Writing–review and editing. XZ: Writing–review and editing.

Funding

The author(s) declare that no financial support was received for the research, authorship, and/or publication of this article.

Conflict of interest

The authors declare that the research was conducted in the absence of any commercial or financial relationships that could be construed as a potential conflict of interest.

Publisher's note

References

1. Zhao HT, Liu Y, Li XQ, Hao LW. Research progress on low-carbon technologies and assessment methods in cement industry. *Mater Sci Forum* (2021) 1035:933–43. doi:10.4028/www.scientific.net/msf.1035.933

2. Kumar A, Lakhani R, Mishra R, Khan RK, Khan S. Utilization of solid waste in the production of autoclaved aerated concrete and their effects on its physio-mechanical and microstructural properties: alternative sources, characterization, and performance insights. *Int J Concrete Structures Mater* (2023) 17(1):6. doi:10.1186/s40069-022-00569-x

3. Guo YY, Luo L, Liu TT, Hao LW, Li YM, Liu PF, et al. A review of low-carbon technologies and projects for the global cement industry. *J Environ Sci (China)* (2023) 136:682–97. doi:10.1016/j.jes.2023.01.021

4. Saha S, Rajasekaran C. Strength and shrinkage properties of heat-cured fly ash-based geopolymer mortars containing fine recycled concrete aggregate. *J Test Eval* (2020) 48(6):20180799. doi:10.1520/jte20180799

5. Öztürk ZB, Çam T. Performance of eco-friendly fly ash-based geopolymer mortars with stone-cutting waste. *Mater Chem Phys* (2023) 307:128112. doi:10.1016/j.matchemphys.2023.128112

6. Nazari A, Torgal FP, Cevik A, Sanjayan JG. Compressive strength of tungsten mine waste- and metakaolin-based geopolymers. *Ceramics Int* (2014) 40(4):6053–62. doi:10.1016/j.ceramint.2013.11.055

7. Van LS, Pławecka K. Geopolymer composites: manufacturing of sandwich steel and geopolymer structures with spray Technology without formwork. *Materials* (2023). doi:10.20944/preprints202308.1782.v2

8. Dacić A, Kopecskó K, Fenyvesi O, Merta I. The obstacles to a broader application of alkali-activated binders as a sustainable alternative-A review. *Materials* (2023) 16(8):3121. doi:10.3390/ma16083121

9. Jamalimoghadam M, Ajalloeian R, Saffarzadeh A. Sustainable alkali-activated materials. *Handbook Sust Concrete Ind Waste Manag* (2022) 489–508. doi:10.1016/b978-0-12-821730-6.00030-9

10. Mucsi G, Szenczi Á, Nagy S. Fiber reinforced geopolymer from synergetic utilization of fly ash and waste tire. *J Clean Prod* (2018) 178:429–40. doi:10.1016/j.jclepro.2018.01.018

11. Rostami M, Behfarnia K. The effect of silica fume on durability of alkali activated slag concrete. *Construction building Mater* (2017) 134:262–8. doi:10.1016/j.conbuildmat.2016.12.072

12. Runci A, Serdar M. Effect of curing time on the chloride diffusion of alkali-activated slag. *Case Stud Construction Mater* (2022) 16:e00927. doi:10.1016/j.cscm.2022.e00927

13. Bakharev T, Sanjayan JG, Cheng YB. Resistance of alkali-activated slag concrete to carbonation. *Cement Concrete Res* (2001) 31(9):1277–83. doi:10.1016/s0008-8846(01)00574-9

14. Wang W, Noguchi T. Alkali-silica reaction (ASR) in the alkali-activated cement (AAC) system: a state-of-the-art review. *Construction Building Mater* (2020) 252:119105. doi:10.1016/j.conbuildmat.2020.119105

15. Collins FG, Sanjayan JG. Effect of pore size distribution on drying shrinking of alkali-activated slag concrete. *Cement Concrete Res* (2000) 30(9):1401–6. doi:10.1016/s0008-8846(00)00327-6

16. Ou ZH, Feng RP, Li FT, Liu GL. Development of drying shrinkage model for alkali-activated slag concrete. *Construction Building Mater* (2022) 323:126556. doi:10.1016/j.conbuildmat.2022.126556

17. Zhang LF, Wang DF, Yue Y. Research progress of fiber reinforced alkali-activated cement-based composites. *J Mater Sci Eng* (2019) 37(02):325–30. doi:10.14136/j.cnki.issn1673-2812.2019.02.029

18. Eskandarinia M, Esmailzade M, Hojatkashani A, Rahmani A, Jahandar SS. Optimized alkali-activated slag-based concrete reinforced with recycled tire steel fiber. *Mater* (2022) 15(19):6623. doi:10.3390/ma15196623

19. Khaloo A, Raisi EM, Hosseini P, Tahsiri H. Mechanical performance of self-compacting concrete reinforced with steel fibers. *Construction Building Mater* (2014) 51:179–86. doi:10.1016/j.conbuildmat.2013.10.054

20. Gencel O, Brostow W, Datashvili T, Thedford M. Workability and mechanical performance of steel fiber-reinforced self-compacting concrete with fly ash. *Compos Inter* (2011) 18(2):169–84. doi:10.1163/092764411x567567

21. Qin LL, Yan JH, Zhou MY, Liu H, Wang AG, Zhang W, et al. Mechanical properties and durability of fiber reinforced geopolymer composites: a review on recent progress. *Eng Rep* (2022) 12(5):e12708. doi:10.1002/eng2.12708

22. Aydın S, Baradan B. The effect of fiber properties on high performance alkali-activated slag/silica fume mortars. *Composites B: Eng* (2013) 45(1):63–9. doi:10.1016/j.compositesb.2012.09.080

23. Gülşan ME, Alzeebaree R, Rasheed AA, Niş A, Kurtoğlu AE. Development of fly ash/slag based self-compacting geopolymer concrete using nano-silica and steel fiber. *Construction Building Mater* (2019) 211:271–83. doi:10.1016/j.conbuildmat.2019.03.228

24. Xu C, Yuan Y, Zhang YM, Xue YD. Peridynamic modeling of prefabricated beams post-cast with steelfiber reinforced high-strength concrete. *Struct Concrete* (2021) 22(1): 445–56. doi:10.1002/suco.202000113

25. Yang K, Tang Z, Cheng Z, Zhao H, Feng RP, Long GC. Mechanical properties of ultra-high strength cement-based materials (UHSC) incorporating metal powders and steel fibers. *Construction Building Mater* (2022) 318:125926. doi:10.1016/j.conbuildmat.2021.125926

26. Gao D, Zhang L. Flexural performance and evaluation method of steel fiber reinforced recycled coarse aggregate concrete. *Construction Building Mater* (2018) 159: 126–36. doi:10.1016/j.conbuildmat.2017.10.073

27. Ferdosian I, Camões A. Mechanical performance and post-cracking behavior of self-compacting steel-fiber reinforced eco-efficient ultra-high performance concrete. *Cement and Concrete Composites* (2021) 121:104050. doi:10.1016/j.cemconcomp.2021.104050

28. Zhang T, Pan D. Mechanical properties of steel-polypropylene hybrid fiber reinforced concrete in building structure. *Stavební obzor-Civil Eng J* (2021) 30(2). doi:10.14311/cej.2021.02.0037

29. Liu YZ, Dai KS, Li DS, Luo MY, Liu Y, Shi Y, et al. Structural performance assessment of concrete components based on fractal information of cracks. *J Building Eng* (2021) 43:103177. doi:10.1016/j.jobe.2021.103177

30. Yuan XH, Guan HT, Shi YY. Stress-strain relationship of steel fiber reinforced alkali activated slag concrete under static compression. *Adv Civil Eng* (2021) 2021:1–12. doi:10.1155/2021/7951646

31. Chen LL, Lian H, Xu Y, Li SZ, Liu ZW, Atroshchenko E, et al. Generalized isogeometric boundary element method for uncertainty analysis of time-harmonic wave propagation in infinite domains. *Appl Math Model* (2023) 114:360–78. doi:10.1016/j.apm.2022.09.030

32. Chen LL, Zhao J, Lian H, Yu B, Atroshchenko E, Li P. A BEM broadband topology optimization strategy based on Taylor expansion and SOAR method-Application to 2D acoustic scattering problems. *Int J Numer Methods Eng* (2023) 124(23):5151–82. doi:10.1002/nme.7345

33. Sasidharan N, Johny B. Finite element analysis and parametric study of curved concrete box girder using Abaqus software. *Int J Res Enginnering Tech* (2015) 4(10): 425–9. doi:10.15623/ijret.2015.0410069

34. Chen LL, Lian H, Liu Z, Gong Y, Zheng CJ, Bordas SPA. Bi-material topology optimization for fully coupled structural-acoustic systems with isogeometric FEM-BEM. *Eng Anal Boundary Elem* (2022) 135:182–95. doi:10.1016/j.enganabound.2021.11.005

35. Chen LL, Wang ZW, Lian H, Ma YJ, Meng ZX, Li P, et al. Reduced order isogeometric boundary element methods for CAD-integrated shape optimization in electromagnetic scattering. *Comp Methods Appl Mech Eng* (2024) 419:116654. doi:10.1016/j.cma.2023.116654

frontiers | Frontiers in Physics

TYPE Original Research
PUBLISHED 27 March 2024
DOI 10.3389/fphy.2024.1390321

OPEN ACCESS

EDITED BY
Pei Li,
Xi'an Jiaotong University, China

REVIEWED BY
Jian Deng,
Nanjing University of Aeronautics and Astronautics, China
Chunlei Li,
South China University of Technology, China

*CORRESPONDENCE
Guihong Wei,
2110302085@st.gxu.edu.cn

RECEIVED 23 February 2024
ACCEPTED 15 March 2024
PUBLISHED 27 March 2024

CITATION
Wu G, Wei G, Huang S, Zhang Q, Zeng S, Feng J, Zeng B and Yu P (2024), Study on the biomechanical properties of 3D printed blended esophageal stents with different structural parameters based on patient CT. *Front. Phys.* 12:1390321. doi: 10.3389/fphy.2024.1390321

Study on the biomechanical properties of 3D printed blended esophageal stents with different structural parameters based on patient CT

Guilin Wu[1,2], Guihong Wei[1]*, Shenghua Huang[1], Qilin Zhang[3], Shuai Zeng[2], Jun Feng[3], Bo Zeng[4] and Peng Yu[1]

[1]Key Laboratory of Disaster Prevention and Structural Safety of Ministry of Education, Guangxi Key Laboratory of Disaster Prevention and Structural Safety, College of Civil Engineering and Architecture, Scientific Research Center of Engineering Mechanics, Guangxi University, Nanning, China, [2]The 923th Hospital of PLA Joint Logistic Support Force, Nanning, China, [3]Guangxi Nanning Ruifeng Medical Devices Co., Ltd., Nanning, China, [4]Department of Thoracic Surgery, The First Affiliated Hospital, Sun Yat-sen University, Guangzhou, China

Introduction: Esophageal stenting is a widely used treatment for esophageal diseases, which can also be used for adjuvant therapy and feeding after chemotherapy for esophageal cancer. The structural parameters of the stent have a significant impact on its mechanical properties and patient comfort.

Methods: In the present work, we reconstructed the esophagus model based on the patient's computed tomography (CT) data, and designed stents with different structural parameters. We used 3D printing technology to achieve rapid production of the designed stents by using Thermoplastic polyurethane (TPU)/Poly-ε-caprolactone (PCL) blends as the materials. The mechanical properties and effects on the esophagus of polymer stents with four different structural parameters of diameter, wall thickness, length and flaring were investigated by in vitro tests of radial compression and migration of the stents, as well as by finite element simulations of the stent implantation process in the esophagus and of the stent migration process. An artificial neural network model was established to predict the radial force of the stent and the maximum equivalent stress of the esophagus during implantation based on these four structural parameters.

Results: The results show that wall thickness was the structural parameter that had the greatest impact on the radial force of the stent (statistically significant, $p < 0.01$), and flaring was the structural parameter that had the greatest impact on the maximum equivalent stress of the esophageal wall after stent implantation (statistically significant, $p < 0.01$). No. 6 stent had a maximum radial force of 18.07 N, which exceeded that of commercial esophageal stents and had good mechanical properties. And the maximum equivalent force on the esophagus caused by its implantation was only 30.39 kPa, which can improve patient comfort. The predicted values of the constructed back propagation (BP) neural network model had an error of less than 10% from the true values, and the overall prediction accuracies were both above 97%, which can provide guidance for optimizing the design of the stent and for clinical research.

Discussion: 3D printing technology presents a wide range of applications for the rapid fabrication of personalized TPU/PCL blend stents that are more suitable for individual patients.

KEYWORDS

3D printing, esophageal stent, CT, biomechanics, TPU/PCL, reverse modeling, artificial neural network

1 Introduction

Esophageal cancer is one of the most common malignant tumors worldwide, with extremely high morbidity and mortality. It is rarely cured in the advanced or terminal stage [1–3]. Esophageal stricture is a common symptom of esophageal cancer patients. Due to cancer cells, the local wall of the esophagus of patients will be unevenly thickened, causing esophageal stenosis and difficulty in swallowing, seriously affecting the quality of life of patients [4]. Despite surgical treatment or chemotherapy, the incidence of secondary esophageal stricture is still high [5, 6].

Esophageal stenting is an effective palliative treatment for esophageal disease, that can help patients with advanced esophageal cancer to relieve the esophageal obstruction and improve the swallowing function [7, 8]. After surgery or chemotherapy, esophageal stenting can be used to protect the treated area of the esophagus in feeding, and reduce the likelihood of secondary strictures for adjunctive treatment [9]. Esophageal stents include self-expanding metal stents (SEMS) and self-expanding plastic stents (SEPS) [10]. Currently, SEMS are widely used in clinical treatment of esophageal diseases due to their excellent shape memory properties and mechanical properties [11, 12]. However, metal stents can cause complications such as tumor tissue growth, perforation, bleeding, stent fall, and secondary strictures to varying degrees [13]. SEPS are effective in reducing esophageal injury and reducing the risk of esophageal restenosis, as well as being easy to remove from the esophagus [14]. However, it has been demonstrated that the migration rate of SEPS is significantly higher than that of SEMS [15]. Moreover, the sizes of commercial esophageal stents circulating are fixed and cannot be fully adapted to the patient, which will reduce the patient's comfort and affect the therapeutic effect. This puts forward higher demands for esophageal stents in terms of materials, structure and humanized design.

3D printing is a technology that uses layers of discrete materials to print three-dimensional objects based on three-dimensional digital models. The products manufactured by 3D printing technology have a short cycle and can save costs. More importantly, 3D printing is not only independent of product complexity and size limitations, but also allows for innovative and personalized autonomous production. With the development of 3D printing technology, 3D printing has shown advantages in the field of biomaterials and medical devices [16, 17]. For example, Farzin et al. fabricated of sugar-based stents with ideal geometry and size for facilitating arterial surgical anastomosis by 3D printing [18]. And Matheus et al. developed 3D printed bioresorbable nitric oxide-releasing vascular stents [19]. Currently, an increasing number of scholars have begun to use 3D printing technology to develop blend esophageal stents that are more suitable for patients and have excellent mechanical properties [20]. For example, Lin et al. developed a new 3D-printed flexible PLA/TPU tubular polymeric stent with spirals that exhibits excellent self-expansion and anti-migration properties, and the performance is modulated by changing the ratio of PLA to TPU [21].

The structure and mechanical properties of esophageal stents are the most important factors in determining the interaction between the stent and the esophageal wall. At the same time, the structure of the stent also influences on its mechanical properties. Therefore, it is necessary to study the impact of esophageal stent implantation with different structural parameters on the individual esophagus of specific patients. However, it is impossible to test stent implantation into the human esophagus in the clinic, which in turn makes it difficult to accurately predict the effects of stent implantation.

Finite element method (FEM) is widely used in the biomedical field as an important and effective research method [22, 23]. For instance, Alkentar et al. investigated the performance of Ti6Al4V lattice structures designed for biomedical implants by using the FEM [24]. FEM is not be limited by environment and cost as experiments. It can also well solve various nonlinear problems encountered in the biomedical field, and achieve results very similar to the real situation. The accuracy of FEM can be improved through model reconstruction of medical cases [25]. Therefore, it is necessary to perform inverse modeling of the patient's esophagus and FEM of the process of stent implantation into the esophagus with different structural parameters, so as to provide physicians with important guidance in designing stents and treating patients.

In this paper, we extracted the esophageal model from the computed tomography (CT) images and 3D printed it with thermoplastic elastomer (TPE). TPE is a new polymer material between rubber and resin, so it has the dual properties of rubber and plastic: high strength, high elasticity and injection molding [26, 27]. At the same time, TPE is an environmentally friendly, non-toxic and safe material with excellent weather resistance, fatigue resistance and temperature resistance. It also has a wide range of hardness from ultra-soft to 90A, which can meet the hardness needs of different products [28, 29]. Therefore, TPE is not only used in the manufacture of daily necessities and industrial products, but also in the manufacture of medical devices, such as tourniquets, nebulizer hoses, human tissue anatomy models, etc. [30]. Wu et al. used TPE to prepare high sensitivity capacitive pressure sensor of medical devices [31]. Fischenich et al. discovered that TPE hydrogels have elastic and viscous components that make them ideal for soft tissue replacements [32]. Esophageal model materials need to be as close as possible to the biomechanical properties of the human esophagus. In existing research, thermoplastic elastomers have been used for artificial blood vessels and artificial esophagus [33, 34]. TPE can be used to make artificial blood vessels [35]. Similarly, TPE can meet this basic requirement by adjusting its hardness, and as a

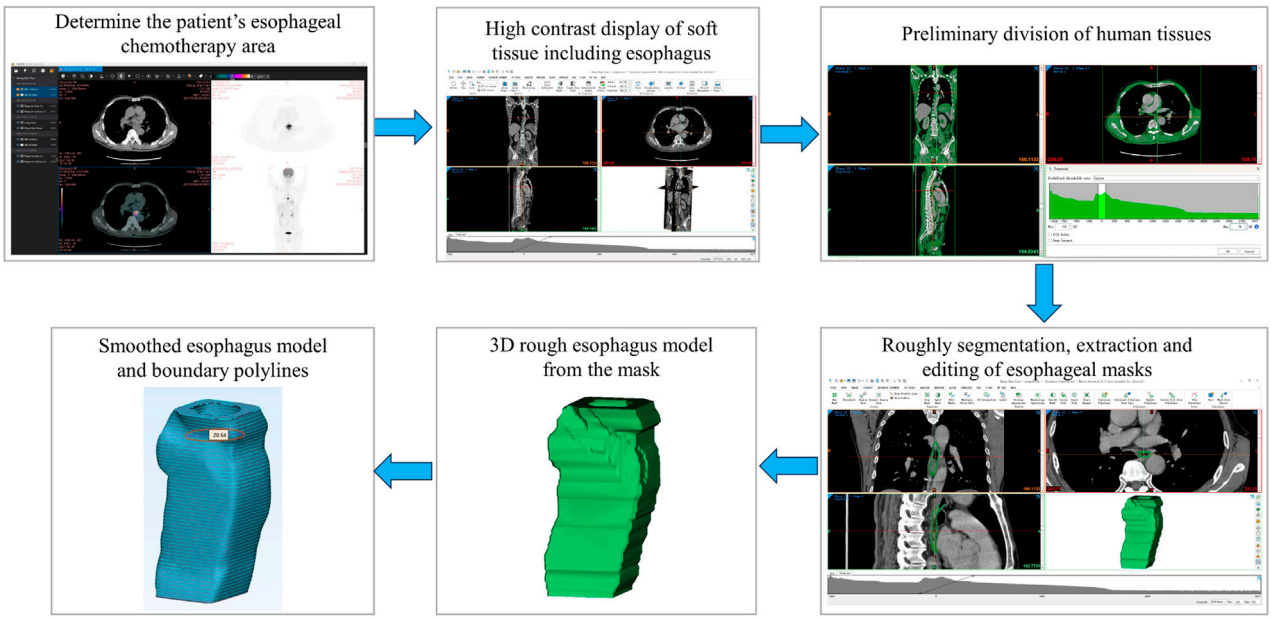

FIGURE 1
Esophageal model acquisition process.

commonly used soft material for 3D printing, it allows esophageal models to be molded quickly.

The stent designed in this paper consists of thermoplastic polyurethane (TPU) and poly-ε-caprolactone (PCL). TPU is a biocompatible polymer with high tensile strength, abrasion resistance, tear resistance, and low-temperature flexibility, enables provides the feasibility of designing elastic products with potential applications in medicine and tissue engineering [36–38]. PCL is a biodegradable polyester with the advantages of high availability and tensile strength, degradability and biocompatibility, and thus has been used in the field of tissue engineering [39, 40]. Some scholars used TPU and PCL blend materials for the manufacturing of various medical equipment, such as Pinto et al. prepared TPU/PCL blend for biomedical application [41]. Thus, TPU/PCL blends make it easier to manufacture flexible esophageal stents that are better suited to individual patients.

Back propagation (BP) neural network is a multilayer feedforward neural network trained according to the error back propagation algorithm. BP neural network has strong nonlinear mapping ability and flexible network structure, no need to determine the mathematical equation of the mapping relationship between the input and output in advance. It only learns a certain rule through its own training and gets the closest result to the desired output value when the input value is given [42–44]. Using BP neural network to predict the structural parameters of 3D printed esophageal stents can quickly and accurately obtain the index values of unknown combinations of structural parameters based on historical data and influencing factors, which can be fed back into the optimized design of esophageal stents for individual patients.

Based on the patient's CT scan data, we reversed model, optimized and simplified the patient's esophageal geometric model through medical software, and designed 12 esophageal stents with different structural parameters. By conducting *in vitro* tests and FEM on the 3D printed simulated esophagus and 12 esophageal stents, we analyzed the characteristics of structural parameters affecting the support performance, safety and comfort of 3D printed blend esophageal stents from a mechanical perspective. We established an artificial neural network model to predict the radial force of the stent and the maximum equivalent stress in the esophagus after stent implantation, and optimized the structural parameters of the esophageal stent for a specific patient. It provided physicians with a reference for the selection and design of esophageal stents, as well as the prediction and selection of auxiliary treatment with stent implantation after chemotherapy.

2 Materials and methods

2.1 CT reverse modeling and simplification of the esophagus

The main flowchart of esophageal model acquisition is shown in Figure 1.

2.1.1 Extraction of esophageal model

The esophageal model was extracted from CT scans of a patient with esophageal cancer who underwent chemotherapy. The purpose of the extraction was to design a stent that could improve the patient's comfort by covering the chemotherapy area and extending slightly beyond it. The chemotherapy area was determined by positron emission computed tomography (PET)-CT fusion imaging, which showed the metabolic activity of the tumor cells. The extracted esophagus included the chemotherapy area and 8 additional tomograms (each 1.25 mm thick) at both ends of the chemotherapy area.

The raw data of the esophageal model in this paper comes from the PET-CT enhancement scan images of the patient. The patient is an elderly male diagnosed with esophageal cancer in a hospital in Zhongshan, Guangdong Province, based on the provided medical imaging data in digital image and communication on medicine (DICOM) format.

The patient's DICOM data file before chemotherapy was imported into a medical image reading software called Xiaosaikankan DICOM Viewer, and PET-CT fusion browsing was used to obtain the metabolic information of each cell in the body. Based on the principle that tumor cells are metabolically active and their ability to uptake contrast agent is 2–10 times higher than normal cells, the location of the patient's esophageal tumor and the CT section range of the chemotherapy area were accurately and rapidly determined.

The DICOM data file of the patient's post-chemotherapy review was identified and imported by the medical image processing software called Mimics. After self-processing of the data by the software, three views of the patient's CT-enhanced scan data were obtained. The Soft tissue scale was selected in the Grayscale of the Contrast workspace below, so that the soft tissues including the esophagus could be displayed in high contrast, which facilitated the segmentation of the human body tissues.

In Mimics, the extraction method for esophagus was mainly divided into the following steps:

1. After the DICOM data file was successfully imported, a new two-dimensional mask was created using the New Mask in the SEGMENT function area, and the Threshold gray value range was adjusted to separate the esophagus from other tissues in the image, resulting in a preliminary segmentation of the human body tissues.
2. Since the gray value range of the esophagus also included other tissues within this range, such as liver, kidney, and stomach. The Crop Mask was used to roughly segment the desired extraction region of the esophagus after the gray value segmentation. The Edit Masks mask editing tool was used to extract the roughly segmented esophagus to obtain a relatively complete esophagus model.
3. Due to the software's inability to accurately distinguish more complex content during the gray value segmentation stage, there are still some problems with the esophageal model at this point, such as voids at the borders. The details of the model were refined using 2D mask editing. The Edit Masks and Multiple Slice Edit 2D editing tools were used to repair the details of the esophagus layer by layer in the 2D mask. The Mask 3D Preview function was used to preview the entire extraction process in the 3D view box and generate a 3D esophagus model from the mask. Finally, the Calculate Part tool was used to generate a 3D solid model of the esophagus from the edited mask.

2.1.2 Smoothing and simplification of the esophagus model

The extracted esophageal model had a complex and rough surface structure. To improve the 3D printing quality and reduce the computational complexity and time of the FEM, the model needed to be smoothed and simplified. The Smooth tool in the 3D TOOLS function area of Mimics software was not sufficient to achieve a satisfactory smoothing effect, so the model was further optimized in detail in a digital auxiliary design software called 3-Matic, while preserving the integrity of the inner wall boundary of the esophageal model.

The esophageal model data extracted from Mimics were transferred to 3-Matic. The Smooth tool in the Fix function area was used for surface processing, and then the Local Smoothing tool in the Finish function area was used to paint and smooth the local unevenness, abnormally raised areas, and the areas with serious granularity of the model, resulting in a smooth esophagus model. To accurately capture the boundary lines of the inner and outer walls of the esophagus, the Calculate Polylines tool was used to generate the boundary polylines of the inner and outer walls of the esophagus from the smooth esophageal model.

To ensure the convergence of the FEM and avoid the problems of numerical instability and long calculation time during the simulation process, the complex boundary polylines were fitted into circles one by one using the Radius tool in the Measure function area. By placing the centers of all circles on the same axis without changing their relative positions in the axial direction, the extracted esophagus was simplified to a slightly narrower cylinders in the middle, with a length of 64 mm, an inner diameter of 22 mm at both ends, and 18 mm in the middle, and an outer diameter of 28 mm at both ends and in the middle. The wall thickness of the esophageal cylinder was 3 mm at both ends and 5 mm in the middle, which was consistent with the results and analysis of the images on the patient's post-chemotherapy examination report.

The two ends of the simplified esophageal cylinder were extended 30 mm and 50 mm up and down the axis respectively as the esophageal non-chemotherapy area. As shown in Figure 2A, the non-chemotherapy zone was simplified to a uniform cylinder with an inner diameter of 22 mm and a wall thickness of 3 mm, in order to facilitate the simulation of stent implantation, anti-migration test and simulation. The simplified entire esophageal cylinder was modeled in SolidWorks software for subsequent 3D printing.

2.2 Stent design with different structural parameters

The biomechanical performance of the interaction between the stent and the esophagus after implantation depends on the structural parameters of the stent. The stent was designed based on four structural parameters by SolidWorks: 1) outer diameter; 2) wall thickness; 3) length; 4) presence of flares at both ends.

Based on the variation of the inner diameter of the middle section of the simplified cylindrical esophagus model, three different outer diameters of stents with a slightly narrower middle were designed (Figure 2B). For each outer diameter, the stents were designed different varying in wall thickness, length and presence of flares at both ends. The flare was designed as a bell mouth with a length of 4 mm and a slope of 0.5. To facilitate the subsequent training of the BP neural network, three more stents with different structural parameters were added to the orthogonal experimental design scheme. The structural parameters of the 12 different stents are shown in Table 1. The outer diameters of the stents are recorded on the diameter of the narrowest point in the center.

10.3389/fphy.2024.1390321

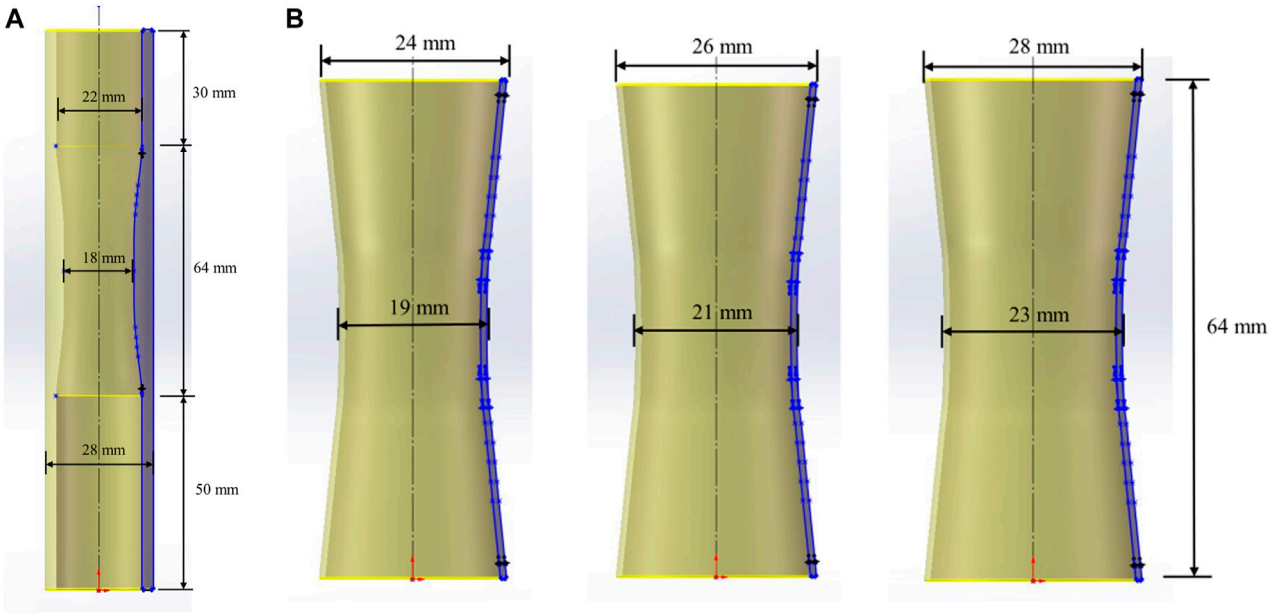

FIGURE 2
(A) Simplified esophageal model, **(B)** Three different outer diameters of stents.

TABLE 1 Structural parameters of esophageal stents.

No.	Outer diameters (mm)	Wall thickness (mm)	Length (mm)	Presence of flares at both ends
1	19	0.08	64	no
2	19	0.12	74	no
3	19	0.16	84	yes
4	21	0.08	84	yes
5	21	0.12	64	yes
6	21	0.16	74	no
7	23	0.08	74	yes
8	23	0.12	84	no
9	23	0.16	64	no
10	19	0.08	74	yes
11	21	0.12	64	no
12	23	0.16	84	no

2.3 3D printed esophageal and stents

The esophagus material was TPE and the stent material was TPU/PCL blend.

TPE with shore hardness of 30A was purchased from Jie Jia Plastic Technology Co., Ltd. (Dongguan, China). TPU with a specific gravity of 1.14–1.18 g/cm3 and shore hardness of 60A was purchased from De Chuang Co., Ltd. (Dongguan, China). PCL 600C (Mn = 65,000) was purchased from Shenzhen eSUN Industrial Co., Ltd. (Shenzhen, China). All materials were commercially available and were not further purified.

Materials with 80%TPU/20%PCL component ratios were prepared using a co-rotating twin-screw extruder (Nanjing Hass Extrusion Equipment Co., Ltd. China, diameter of screw = 2 cm, length/diameter ratio = 40/1). The process and details of TPU/PCL blend preparation can be found in Ref. [45].

The esophagus model and the designed stents in SolidWorks were exported as STL format files, and were sliced in Creality Print (Version3.5.9.0) slicing software. Then the G5 screw extrusion 3D printer from Shenzhen Creality 3D Technology Co., Ltd. (Shenzhen, China) was used for 3D printing (Figure 3). The printing parameters for different materials are presented in Table 2.

FIGURE 3
3D printed esophageal model and designed stent (from left to right are the esophagus and No. 1-No. 12 stents).

TABLE 2 Printing parameters for different materials.

Material	Nozzle temperature (°C)	Build plate temperature (°C)	Printing speed (mm/s)	Layer height (mm)
TPE	230	35	20	0.1
80%TPU/20%PCL	210	35	20	0.1

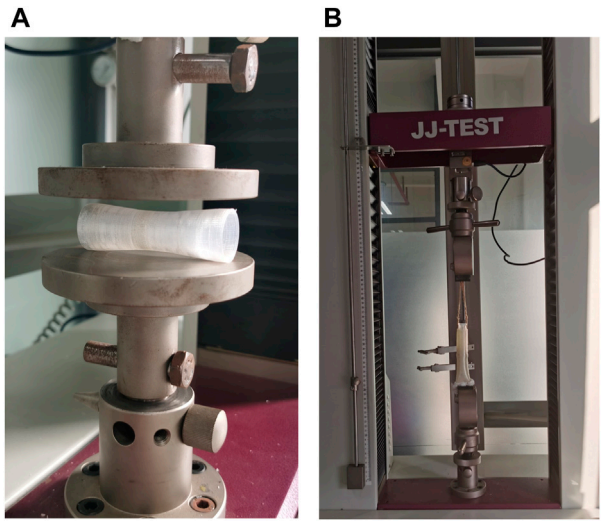

FIGURE 4
(A) Radial force test, **(B)** Migration resistance force test.

2.4 Radial behavior and migration resistance of the stent

2.4.1 Radial force test

The radial performance of esophageal stents was evaluated using a universal testing machine (JJ UTM-1422, Jin Jian Testing Instrument Co., Ltd., Chengde, China). Three samples of each stent were tested. As shown in Figure 4A, the stents were placed between two circular platens and compressed at a rate of 10 mm/min until the stents reached 50% strain, and the force was recorded.

2.4.2 Migration resistance force test

The migration resistance of the esophageal stents in the 3D printed simplified esophageal model was tested. As shown in Figure 4B, the lower end of the esophageal model was clamped, and then the esophageal stent was implanted into the corresponding position of the chemotherapy area of the esophageal model. Holes were perforated at the upper end of the esophageal stent and tied to the universal tensile machine with a rope to ensure the same placement position each time. Use the universal testing machine to pull out the esophageal stent from the esophageal model at a constant speed, and set the end distance to 35 mm. The force-distance curve and maximum peak force during the uniform traction process of the stent along the esophageal axis were recorded.

2.5 Finite element method of esophagus and stents

2.5.1 Modeling and material parameters of esophagus and stents

Modeling of the simplified esophagus and stents were completed in Abaqus, a finite element software for engineering simulation. A rigid cylinder with a diameter slightly larger than the maximum diameter of the esophagus and stent was built to assist in the contraction surface.

TABLE 3 Mooney-Rivlin parameters of esophagus and stent material.

Material	c_{10} (MPa)	c_{01} (MPa)	c_{11} (MPa)	c_{20} (MPa)	c_{02} (MPa)
Esophagus (TPE)	−0.027	0.048	−1.723	0.812	0.982
80%TPU/20%PCL	−10.600	15.180	−0.271	3.089E-02	3.492

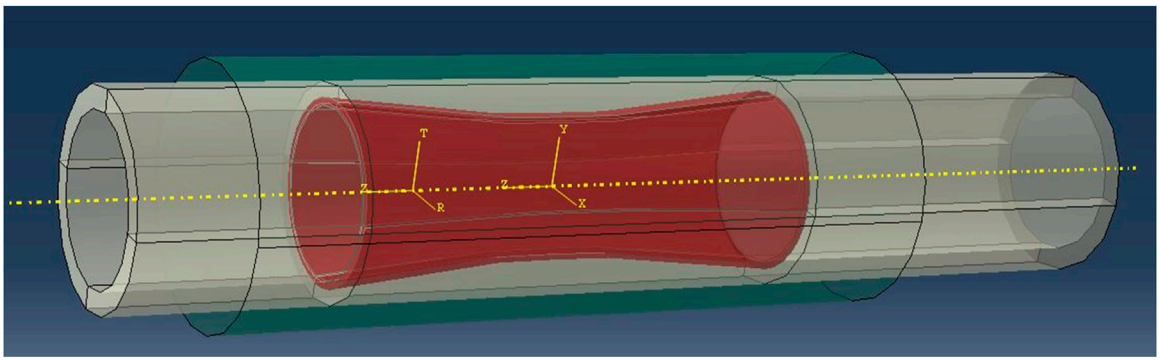

FIGURE 5
Assemble the esophagus, stent, and auxiliary constriction surface.

The esophagus was manufactured using TPE, a highly elastic material that had mechanical properties close to those of the human esophagus. The stent material was 80%TPU/20%PCL hyperelastic blend, so the Mooney-Rivlin hyperelastic model was used for finite element calculations.

The strain energy density function of the Mooney-Rivlin model is:

$$W = c_{10}(\overline{I_1} - 3) + c_{01}(\overline{I_2} - 3) + c_{20}(\overline{I_2} - 3)^2 + c_{11}(\overline{I_1} - 3)(\overline{I_2} - 3) + c_{02}(\overline{I_2} - 3)^2 + \frac{1}{D_1}(J - 1)^2$$

Where I_1 and I_2 are strain invariants, W is the strain energy density function, and c_{10}, c_{01}, c_{11}, c_{20}, c_{02}, and D_1 are the hyperelastic constants. The subscripts of the constants indicate different strain invariants. c_{10} denotes the linear term coefficient of the first strain invariant I_1, c_{01} denotes the linear term coefficient of the second strain invariant I_2, c_{11} denotes the cross-term coefficient of I_1 and I_2, c_{20} denotes the quadratic term coefficient of I_1, and c_{02} denotes the quadratic term coefficient of I_2.

The Mooney-Rivlin hyperelastic constants were automatically generated by uniaxial tensile tests (n = 5) in combination with Abaqus software to fit the stress-strain curves. The simulation curves of the experimental stress-strain curves fitted to the Mooney-Rivlin model can be found in ref. [46]. The hyperelastic constants of esophagus and 80%TPU/20%PCL hyperelastic materials are listed in Table 3 [47].

2.5.2 Assembly and interaction of esophageal-stent

The esophagus, stent, and auxiliary constriction surface were assembled as follows: As shown in Figure 5, the plane center point of the narrowest position of the simplified esophageal chemotherapy area as the coordinate origin. Then the stent was moved so that the center point of the plane at the narrowest position in the middle section of the stent and the axis of the cylinder coincided with the coordinate origin and the axis of the esophagus. Similarly, the auxiliary contraction surface was moved so that the center of mass and axis of the auxiliary surface coincide with the coordinate origin and the esophageal axis.

Simulation of stenting for esophageal treatment: A cylindrical coordinate system was established with the axis as the Z-axis and the radial direction of the stent as the T-axis. The esophagus was fixed in the Z-axis direction, and a uniform displacement was applied to the entire auxiliary contraction surface in the radial direction. After contraction, the auxiliary surface contacted the outer surface of the stent, and the stent was pressed into the simplified esophagus. Then the constraints between the auxiliary surface and the stent were released, allowing the stent to self-expand and interact with the inner wall of the esophageal model until equilibrium was reached.

Stent migration simulation in the esophagus: After the stent was implanted in the esophagus, the esophagus was kept fixed in the Z-axis direction, while a distance in the negative Z-axis direction was applied to the stent. The stent moved at a constant speed along the negative direction of the Z-axis in the esophagus. The friction coefficient between the outer surface of the stent and the surface of the inner wall of the esophagus was set to be 0.1, and the termination distance was 40 mm.

2.6 Artificial neural network design

2.6.1 Selection of input and output parameters

We established a simple single-output artificial neural network model to train the structural parameter combinations and performance metrics of existing esophageal stents, which could quickly predict the stent performance metrics of other structural

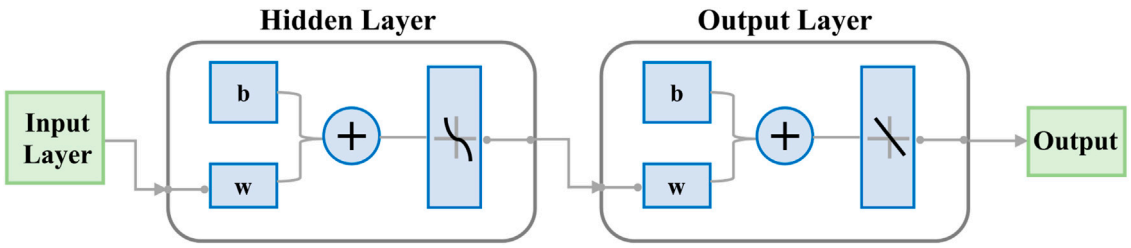

FIGURE 6
BP neural network topology.

parameter combinations. The most common BP neural network topology includes input layer, hidden layer, and output layer, as shown in Figure 6. The number of nodes in the input layer was set to 4, representing the four structural parameters of the designed stent: outer diameter, wall thickness, length and flare width. The number of nodes in the output layer was set to 1, which represented the performance index value of the designed stent.

The radial force of the stent determines the effect of supporting the esophageal treatment area, facilitating eating and assisting treatment after implantation. However, excessive radial force not only affects the patient's comfort, but can also lead to bleeding and other complications. In contrast, the maximum equivalent force in the esophagus after stent implantation can largely reflect the patient's comfort. Therefore, we used the stent radial force and the maximum equivalent stress of the esophagus after implantation as the performance indicators of the stent for training and prediction.

The characteristic parameters of the training set and test set of the BP neural network model are shown in Table 1, while the performance index values were obtained from the results *in vitro* test and FEM result. Common neural networks require 70% of the data as the training set and 30% of the data as the test set, and the amount of data will directly affect the prediction results. Therefore, all the data in the first 9 groups of the 12 sets of stents data were repeatedly trained as the training set, and the last 3 groups were used as the test set.

2.6.2 BP neural network modeling

The amount of data in this study was small and the calculation was simple, so the BP neural network model can be designed with a single hidden layer. The number of nodes in the hidden layer can be set according to the following empirical formula:

$$l = \sqrt{n + m} + a$$

where n is the number of input nodes, m is the number of output nodes, and a is a constant value from 1 to 10.

Since the number of hidden layer nodes is the main determinant of the accuracy of the neural network model, we set a to 1–10 in turn and plugged it into the formula to get the number of hidden layer nodes for the function training, after completing the design of the training function and data normalization. In this way, we obtained the number of hidden layer nodes that minimized mean square error (MSE) of the training set, and set it as the optimal number of hidden layer nodes to update the training function parameters.

The trainlm of Levenberg-Marquardt (L-M) optimization algorithm was adopted as the training function. Considering that the different magnitudes of the input parameters would interfere with the accuracy and performance of the network structure when training the neural network, all data were normalized through the mapminmax function so that the values of all magnitudes converge between 0 and 1. The maximum number of training times of the network was set to 1,000, the learning rate was 0.01, and the minimum error of the training target was 1e-6. After completing the training and testing of the network, denormalization was performed through the mapminmax function to obtain the actual predicted value of the output index value. Finally, the plot function and the bar function were used respectively to complete the plotting of the actual value, predicted value and error of the output indicator value.

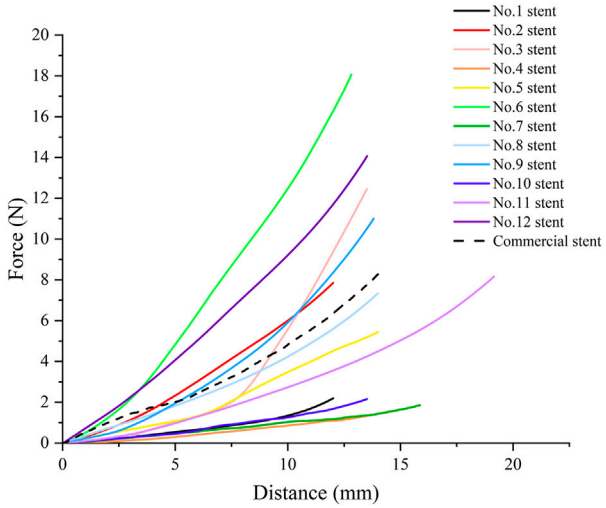

FIGURE 7
Radial force-distance curves of stents (n = 3).

3 Results and discussion

3.1 Results of radial compression test and migration test

3.1.1 Radial force of the stents

Figure 7 shows the radial force-distance curves of stents with different structural parameters and a commercial stent. The radial force of No.4 stent was the smallest, 1.64 N. The radial force of No.6 stent was the largest, 18.07 N. The radial force of commercial stent was 8.28 N,

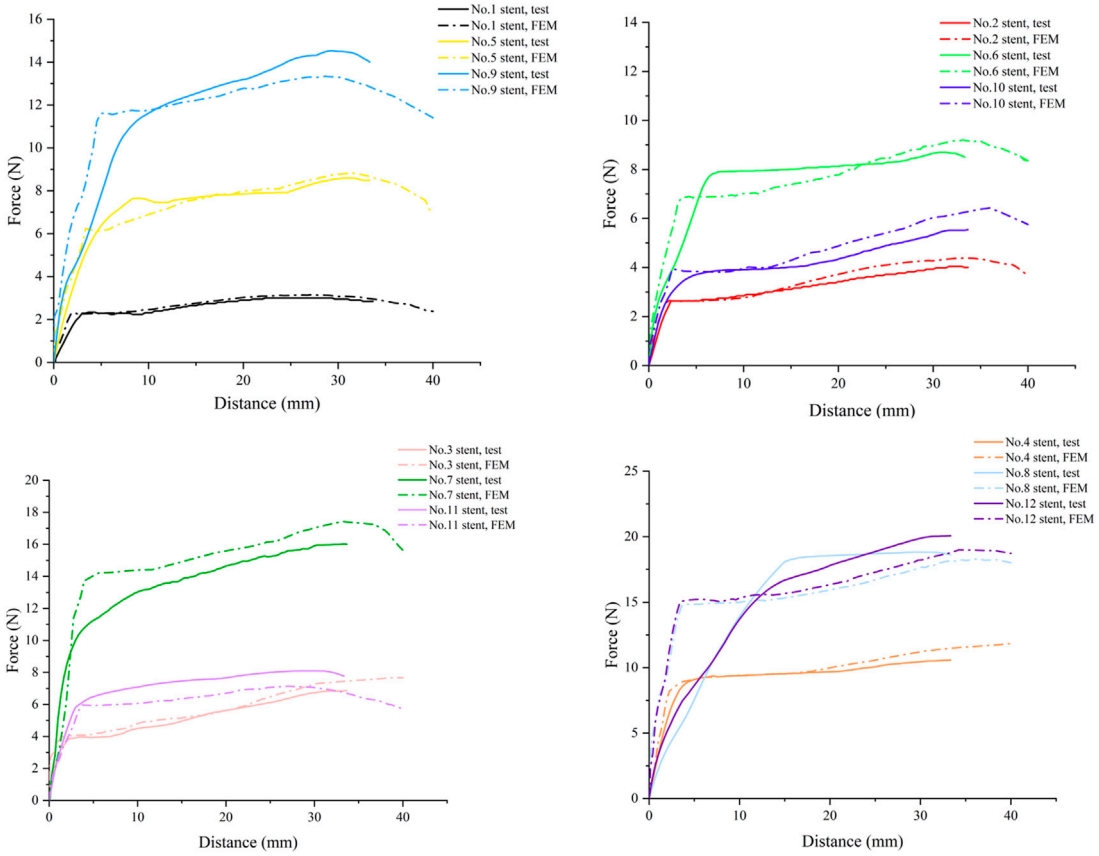

FIGURE 8
The force-distance curves of the stent migration test (n = 3) and simulation.

which lay between No.3 stent and No.11 stent. This suggests that the 3D printed polymer stent could provide the same radial support force as the commercial esophageal stent by adjusting the structural parameters, thereby supporting the chemotherapy area to assist with feeding.

By analysis of range and analysis of variance (ANOVA) on the maximum radial force obtained from the stents. We found that all the four structural parameters studied in the tests had significant influence (statistically significant, $p < 0.01$) and main effect on the stent radial force. Among them, wall thickness was the structural parameter with the greatest impact, which could greatly improve the stiffness of the stent. This was followed by flare and length in that order, while the outer diameter had the least effect. The optimum level of structural parameters for the maximum radial force were: 21 mm for the outer diameter, 0.16 mm for the wall thickness and 74 mm for the length without flare.

3.1.2 Migration resistance force of the stents

Since the FEM often has some differences with the actual situation, we performed *in vitro* tests to verify the accuracy of the model by comparing the test results with the finite element analysis results. The force-distance curves of the stent migration test and simulation are shown in Figure 8. From the figure, it could be seen that the force-distance curve shows a rapid upward trend in the initial stage. Then the upward trend gradually slowed down, became relatively flat, and finally decreased after passing the peak point. No. 1 stent had the lowest peak resistance to migration of 3.00 N, while No. 12 stent had the highest peak resistance to migration of 20.07 N. Increasing the diameter, wall thickness, length, as well as designing the flare of the stent can improve migration resistance. Among them, the outer diameter had the most significant effect on the migration resistance. Improving the migration resistance can reduce the probability of migration or even fall of the stent.

3.2 Finite element simulation of stent implantation and self-expansion

The stress distribution of the esophageal wall after the stent with different structural parameters is implanted into the esophagus is shown in Figure 9. The smallest maximum equivalent force on the esophageal wall after implantation was caused by stent 1 with 12.04 kPa. The largest maximum equivalent force caused was caused by stent 7 with 103.2 kPa. It could be seen that the maximum equivalent stress on the esophageal wall caused by the esophageal stent occurs at both ends of the stent, because the diameter of the stent is largest at both ends of the stent, which stretches the esophagus and causes greater deformation of the esophagus. This is most obvious in stents with flares at both ends. The stent without flares exerted a greater equivalent force on the esophageal wall at 10 mm from the origin because the rate of change of the stent diameter became greater here, resulting in a concentration of stress in the esophageal wall.

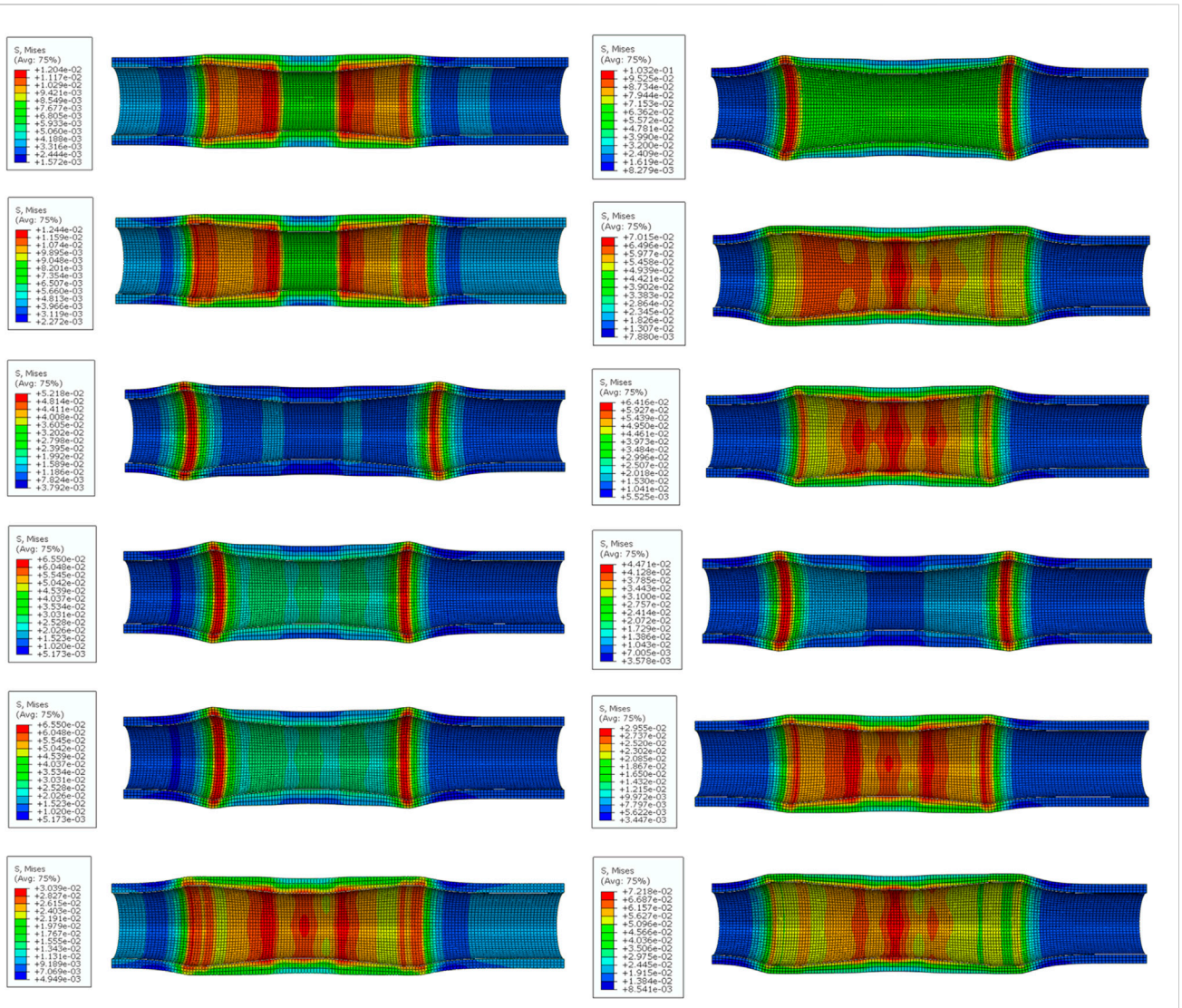

FIGURE 9
The stress distribution of the esophageal wall after stenting. (From top to bottom on the left are No.1 stent to No. 6 stent, and on the right are No. 7 stent to No.12 stent).

By performing range and ANOVA on the simulated maximum equivalent stress of the esophagus, it could be found that the outer diameter and dilation had a significant impact on the maximum equivalent stress (statistically significant, $p < 0.01$), and there was a main effect. Flare was the structural parameter that had the greatest impact, causing convex deformation of the esophageal wall and stress concentration at the contact point with the esophagus. Then followed the order of diameter, length and wall thickness. When the equivalent stress of the esophagus wall was minimum, the optimal levels of structural parameters were: outer diameter 19 mm, wall thickness 0.16 mm, length 64 mm, and without flare.

3.3 Finite element simulation of stent migration

The process of stent migration was investigated by applying displacement to the completed implanted stent in the esophagus. Comparing the force-distance curves of the migration test and the simulation in Figure 9, it was easy to find that the trends of the migration resistance of the stents with different structural parameters obtained by FEM were similar to those of the test results, and the peaks of the two were very close to each other. The peaks of the anti-migration force approximately occurred at the displacement point where the end of the stent passes through the narrowest area in the middle of the esophagus. Although the force-distance curves have errors due to the differences in the boundary conditions and load settings of the finite element simulation and the real test, this does not affect our analysis of the anti-migration ability of the stents through FEM.

When the maximum equivalent stress is exerted on the esophageal wall during dynamic migration of blended stents with different structural parameters, the stress distribution of the esophageal wall is shown in Figure 10. Obviously, the dynamic stress on the esophageal wall caused by dynamic

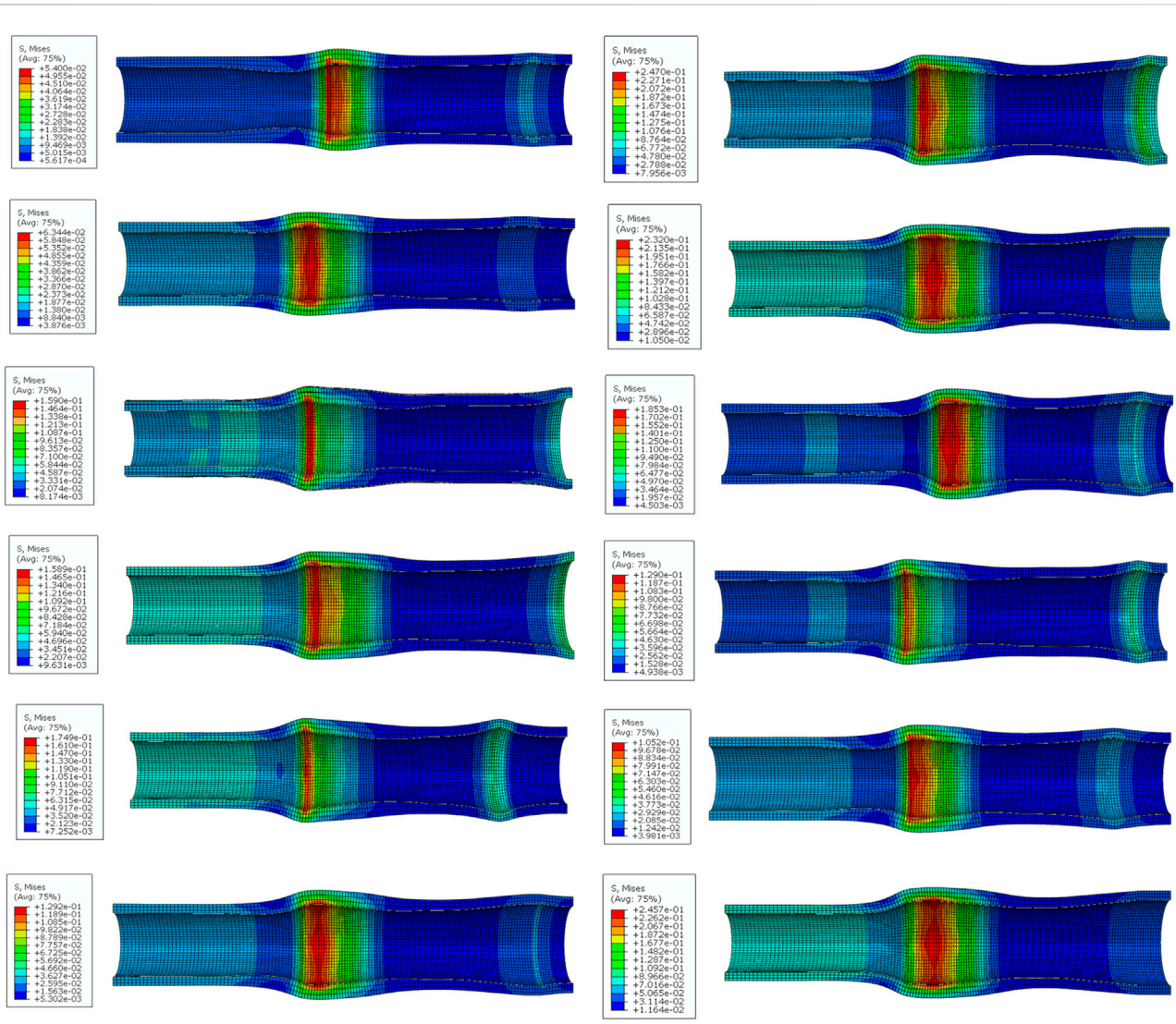

FIGURE 10
The stress distribution of the esophageal wall when the dynamic migration of the stent produces the maximum equivalent stress on the esophageal wall. (From top to bottom on the left are No. 1 stent to No. 6 stent, and on the right are No. 7 stent to No. 12 stent).

migration of the stent was higher than the static stress at the completion of implantation. This is due to the fact that in order to make the stent fit better into the esophagus to improve patient comfort, the esophageal stent was designed as a cylindrical model with a slightly narrower middle like the simplified esophagus model. Even the rate of change of the stent's outer diameter was basically the same as that of the esophagus's inner diameter. Therefore, when migration of the stent occurs to the point where its end passes through the narrowest region in the middle of the esophagus, the deformation of the narrowest region is the greatest, and the dynamic maximum equivalent stress caused by the stent to the esophagus is also the largest during the migration process. Therefore, when increasing the stent migration resistance, it is important to avoid excessive migration resistance that may cause secondary damage to the mucosa of the esophageal inner wall during stent migration [48].

3.4 Comparative analysis of neural network model predictions

3.4.1 Stent radial force prediction

When cyclically training and predicting the radial force of the stent through the BP neural network, the optimal number of hidden layer nodes was 9, and the corresponding MSE was 0.00019. The standard BP neural network was constructed with 9 hidden layer nodes, and the trend of MSE during the training process is shown in Figure 11A. As can be seen from the figure, the best verification performance occurred in the 6th round with MSE of 0.0004. The performance of the BP neural network at this point is shown in Figure 11B. It is evident that the constructed BP neural network model fitted the test data excellently, and the correlation coefficients R were all above 0.998. By analyzing the true and predicted values of the radial force of the last three groups of stents listed in Table 4, we found that the error between them was less than 10%, and the overall

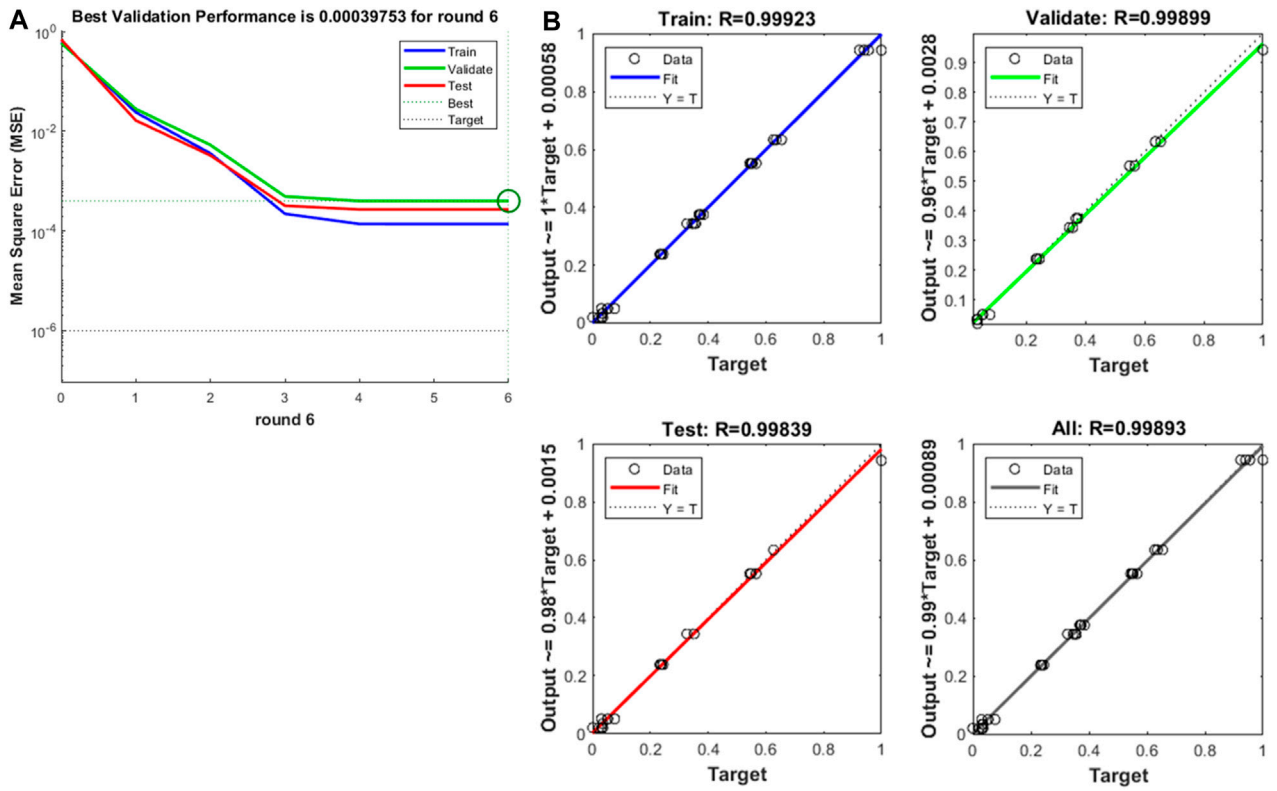

FIGURE 11
(A) Training mean squared error curve, **(B)** The curve fitting of BP neural network on training and predicting the radial force.

TABLE 4 Comparison of actual and predicted values of stent radial force.

No.	Actual (N)	Predicted (N)	Absolute (N)	Relative (%)
10	2.16	1.95	0.21	9.72
11	8.16	8.36	0.20	2.45
12	14.07	14.51	0.44	3.13

prediction accuracy was as high as 97.5%, which indicated that the BP neural network predicted the radial force of stents very well.

3.4.2 Prediction of maximum equivalent stress of esophagus

Similarly, the optimal number of hidden layer nodes was 6 and the corresponding MSE was 1.75e-05 when the maximum equivalent force of esophagus after stent implantation was trained and predicted cyclically by BP neural network. The standard BP neural network was constructed with 6 hidden layer nodes, and the trend of MSE was obtained during the training process as shown in Figure 12A. The figure shows that the best validation performance occurred in round 5 with MSE of 2.60e-05, at which time the performance of the BP neural network is shown in Figure 12B. It is also clear that the established BP neural network model fitted the finite element simulation data excellently, with correlation coefficients R above 0.999. Table 5 lists the true and predicted values of the maximal equivalent stress of the esophagus after stent implantation in the last three groups, and we could find that the errors between them are all less than 10%, and the overall prediction accuracy was as high as 99.91%, showing that the BP neural network also predicted the maximum equivalent stress of the esophagus very well.

3.5 Discussion

From the overall results of the *in vitro* tests and FEM, it can be seen that among the 12 designed stents, No. 6 stent has the best mechanical properties. Its radial force is the largest at 18.07 N, which can effectively stretch the middle section of the esophagus that is still somewhat stenotic after treatment and prevent the occurrence of secondary narrow. The maximum equivalent stress on the inner wall of the esophageal stent after its implantation is only 30.39 kPa, which improves patient comfort to a large extent. However, in the clinic, it is necessary to select the appropriate stent according to the complex actual situation and needs of the patient.

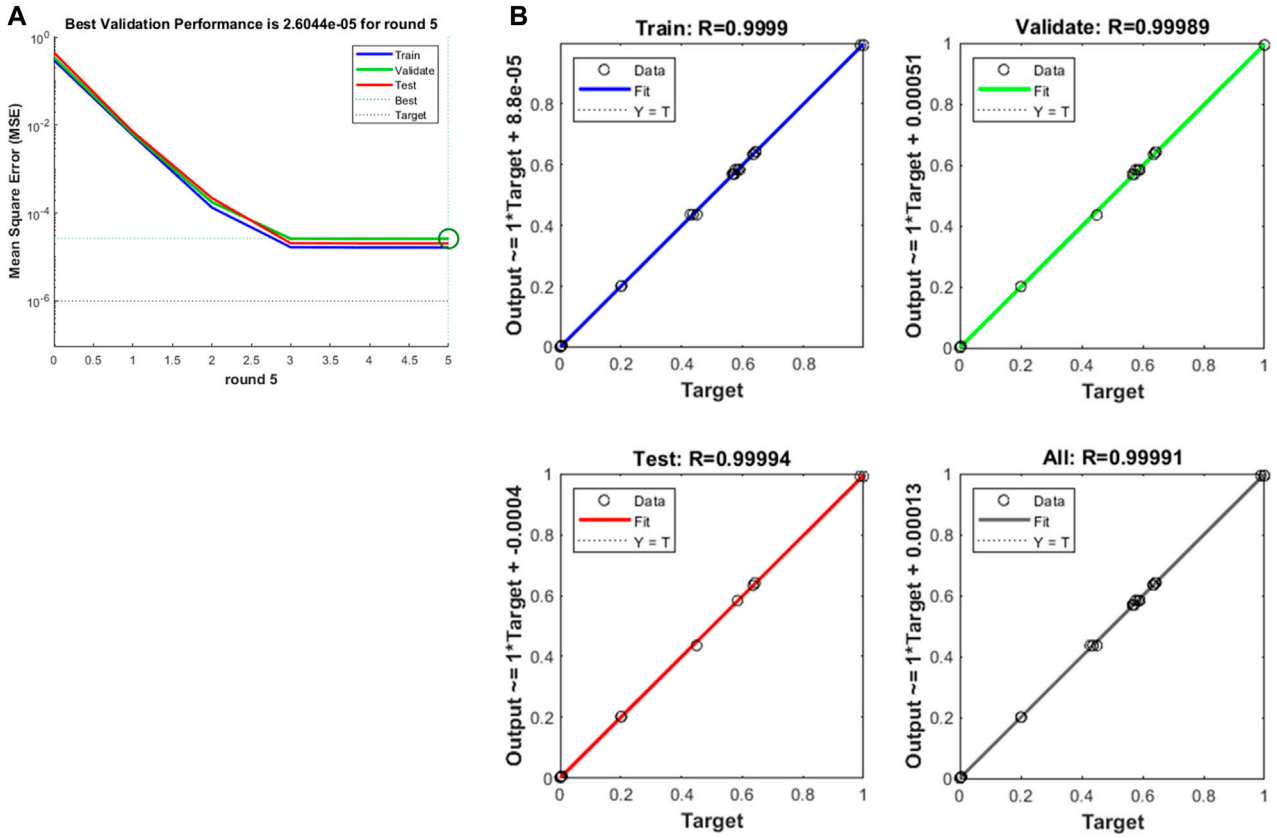

FIGURE 12
(A) Training mean squared error curve, **(B)** The curve fitting of BP neural network on training and predicting the maximum equivalent force of esophagus after stenting.

TABLE 5 Comparison of actual and predicted values of esophagus maximum equivalent force.

No.	Actual (kPa)	Predicted (kPa)	Absolute (kPa)	Relative (%)
10	44.71	49.15	4.44	9.93
11	29.55	29.92	0.37	1.25
12	72.18	68.91	3.27	4.53

In the current study, we obtained a simplified esophageal reconstruction model of the patient by processing the patient's CT scan images using Mimics software and 3-Matic software. Based on this, esophageal stents with different structural parameters were designed. Using a twin-screw extruder, we melt blended two polymers with different flexibility, TPU and PCL, in a ratio of 8:2 for 3D printing of flexible esophageal stents.

In this study, quasi-static finite element simulations of the stent implantation process were performed using Abaqus software to obtain the biomechanical interactions between the stent and the esophagus after stent implantation, which is important for assessing patient comfort and the likelihood of bleeding from esophageal injury after stent implantation. On this basis, finite element simulations of dynamic migration occurring after completion of stent implantation were performed to assess the effectiveness of stent-assisted therapy and the possibility of complications, such as stent displacement, after stent implantation. Therefore, FEM plays a vital role in the design of esophageal stent and can provide a reference for optimizing the structural parameters of the esophagus.

However, the simulation in this article used a simplified patient esophageal model, which ignored the weight of the stent itself, the complex environment in the esophagus, and the impact of the patient's eating and esophageal physiological swallowing on the stent. It also does not consider the possible changes in the esophageal characteristics due to chemotherapy [49]. Follow-up studies should explore the impact of patient feeding on the stent and the fatigue of the stent under cyclic swallowing stress [50].

The esophagus model used in the test was 3D printed by TPE, which can quickly obtain an esophagus model with physical properties close to those of the real human esophagus, but it cannot achieve a complete simulation of the real esophagus. In the study, we extracted and simplified the esophageal model as an

unstratified homogeneous structure, which was uniformly printed with TPE of the same properties. The entire esophageal model was given the same material properties during finite element analysis. However, based on the histology, the real esophagus consists of five layers from inside to outside are: mucosa, the submucosa, the virtual interfacial layer, the circumferential inner and the longitudinal outer muscle layer [51]. There may be differences in properties between the different histologic layers. Moreover, the tests were conducted *in vitro*, ignoring the influence of the *in vivo* environment on the stent, which may not be able to directly and accurately reflect the effect of stent implantation on the human body. Therefore, it is necessary to consider animal tests or even clinical tests in future studies to further evaluate the performance of stents.

The constructed BP neural network can be trained according to the performance index values derived from existing experiments or simulations, and can rapidly and well predict the radial force of other stents and the maximum equivalent force of the esophagus after stent implantation, so as to provide a reference for the design of structural parameters of stents. But the amount of data in the training set was not very large. In the future, the accuracy of prediction can be further improved by increasing the amount of data in the training set and optimizing the BP neural network by using genetic algorithm according to the influence of structural parameters on the performance index.

Using 3D printing technology, we can rapidly design and manufacture customized esophageal stents based on patients' CT and therapeutic needs, which can improve patient comfort and assist therapeutic effects.

4 Conclusion

In this study, the esophagus was inversely modeled based on CT images of the patient's esophagus, and stents with different structural parameters were designed. TPU/PCL blend and TPE were selected as materials to 3D print the stent and simplified esophageal model. The results indicated that the 3D printed esophageal stent designed based on the CT of the patient's esophagus exhibits good radial properties and anti-migration ability. Compared with 3D esophageal stents with fixed dimensions, it is able to ensure the required mechanical properties while generating less isotropic force on the esophageal wall, which can reduce the patient's discomfort. We can adjust the mechanical properties of the stent and its effect on the esophagus by adjusting the structural parameters of the stent. In addition, a BP neural network was established in this paper to predict the radial force of the stent and the maximum equivalent stress of the esophagus after implantation. The results showed that the mechanical properties of the stent can be quickly and relatively accurately obtained by finite element simulation and BP neural network prediction, and fed back into the design of the stent, providing scientific guidance to further improve the comfort and clinical selection of the stent. Of course, further studies are needed regarding the fatigue performance of the stent to cope with physiological swallowing of the esophagus after implantation, more accurate finite element simulation, and optimization of the BP neural network.

Data availability statement

The original contributions presented in the study are included in the article/supplementary material, further inquiries can be directed to the corresponding author.

Author contributions

GlW: Formal Analysis, Methodology, Validation, Writing–review and editing. GhW: Conceptualization, Investigation, Methodology, Software, Writing–original draft, Writing–review and editing. SH: Conceptualization, Investigation, Methodology, Resources, Writing–review and editing. QZ: Formal Analysis, Investigation, Supervision, Writing–original draft. SZ: Data curation, Formal Analysis, Investigation, Writing–original draft. JF: Formal Analysis, Investigation, Supervision, Writing–original draft. BZ: Conceptualization, Resources, Validation, Writing–review and editing. PY: Conceptualization, Methodology, Project administration, Validation, Writing–review and editing.

Funding

The author(s) declare that financial support was received for the research, authorship, and/or publication of this article. This work was financially supported by Nanning Technology and Innovation Special Program (20204122) and Research grant for 100 Talents of Guangxi Plan.

Conflict of interest

Authors QZ and JF were employed by Guangxi Nanning Ruifeng Medical Devices Co., Ltd.

The remaining authors declare that the research was conducted in the absence of any commercial or financial relationships that could be construed as a potential conflict of interest.

Publisher's note

References

1. Santucci C, Mignozzi S, Malvezzi M, Collatuzzo G, Levi F, La Vecchia C, et al. Global trends in esophageal cancer mortality with predictions to 2025, and in incidence by histotype. *Cancer Epidemiol* (2023) 87:102486. doi:10.1016/j.canep.2023.102486

2. Collaboration GBOD, Abate D, Abbasi N, Abbastabar H, Abd-Allah F, Abdel-Rahman O, et al. Global, regional, and national cancer incidence, mortality, years of life lost, years lived with disability, and disability-adjusted life-years for 29 cancer groups, 1990 to 2017: a systematic analysis for the global burden of disease study. *Jama Oncol* (2019) 5:1749–68. doi:10.1001/jamaoncol.2019.2996

3. Goense L, van Rossum P, Kandioler D, Ruurda JP, Goh KL, Luyer MD, et al. Stage-directed individualized therapy in esophageal cancer. *Ann N Y Acad Sci* (2016) 1381: 50–65. doi:10.1111/nyas.13113

4. Qi L, He W, Yang J, Gao Y, Chen J. Endoscopic balloon dilation and submucosal injection of triamcinolone acetonide in the treatment of esophageal stricture: a single-center retrospective study. *Exp Ther Med* (2018) 16:5248–52. doi:10.3892/etm.2018.6858

5. Yamasaki T, Tomita T, Takimoto M, Ohda Y, Oshima T, Fukui H, et al. Esophageal stricture after endoscopic submucosal dissection treated successfully by temporary stent placement. *Clin J Gastroenterol* (2016) 9:337–40. doi:10.1007/s12328-016-0685-0

6. Zhang Y, Zhang BZ, Wang YD, Zhang JJ, Wu YF, Xiao TY, et al. Advances in the prevention and treatment of esophageal stricture after endoscopic submucosal dissection of early esophageal cancer. *J Transl Int Med* (2020) 8:135–45. doi:10.2478/jtim-2020-0022

7. Wlodarczyk JR, Kuzdzal J. Stenting in palliation of unresectable esophageal cancer. *World J Surg* (2018) 42:3988–96. doi:10.1007/s00268-018-4722-7

8. Bi YH, Ren JZ, Chen HM, Bai LL, Han XW, Wu G. Combined airway and esophageal stents implantation for malignant tracheobronchial and esophageal disease a strobe-compliant article. *Medicine (Baltimore)* (2019) 98:e14169. doi:10.1097/MD.0000000000014169

9. Wen J, Yang YS, Liu QS, Yang J, Wang SF, Wang XD, et al. Preventing stricture formation by covered esophageal stent placement after endoscopic submucosal dissection for early esophageal cancer. *Dig Dis Sci* (2014) 59:658–63. doi:10.1007/s10620-013-2958-5

10. Kang Y. A review of self-expanding esophageal stents for the palliation therapy of inoperable esophageal malignancies. *Biomed Res Int* (2019) 2019:1–11. doi:10.1155/2019/9265017

11. Kim KY, Tsauo J, Song HY, Kim PH, Park JH. Self-expandable metallic stent placement for the palliation of esophageal cancer. *J Korean Med Sci* (2017) 32:1062–71. doi:10.3346/jkms.2017.32.7.1062

12. Herskovic AM, Rivard M, Rothstein RI, Hussein Z, Saunders J, Corcoran K, et al. Radiation esophageal stent. *J Clin Oncol* (2017) 35:e15514. doi:10.1200/JCO.2017.35.15_suppl.e15514

13. Singla V, Arora A, Khare S, Kumar A, Sharma P, Bansal N, et al. A novel technique to prevent migration of esophageal stent. *Endoscopy* (2020) 52:1040–1. doi:10.1055/a-1149-1084

14. Verschuur EM, Repici A, Kuipers EJ, Steyerberg EW, Siersema PD. New design esophageal stents for the palliation of dysphagia from esophageal or gastric cardia cancer: a randomized trial. *Am J Gastroenterol* (2008) 103:304–12. doi:10.1111/j.1572-0241.2007.01542.x

15. Oh YS, Kochman ML, Ahmad NA, Ginsberg GG. Clinical outcomes after self-expanding plastic stent placement for refractory benign esophageal strictures. *Dig Dis Sci* (2010) 55:1344–8. doi:10.1007/s10620-010-1134-4

16. Wang ZZ, Yang Y. Application of 3d printing in implantable medical devices. *Biomed Res Int* (2021) 2021:1–13. doi:10.1155/2021/6653967

17. Kalyan B, Kumar L. 3d printing: applications in tissue engineering, medical devices, and drug delivery. *Aaps Pharmscitech* (2022) 23:92. doi:10.1208/s12249-022-02242-8

18. Farzin A, Miri AK, Sharifi F, Faramarzi N, Jaberi A, Mostafavi A, et al. 3d-printed sugar-based stents facilitating vascular anastomosis. *Adv Healthc Mater* (2018) 7: e1800702. doi:10.1002/adhm.201800702

19. de Oliveira MF, Da Silva L, Catori DM, Lorevice M, Galvao K, Millás A, et al. Photocurable nitric oxide-releasing copolyester for the 3d printing of bioresorbable vascular stents. *Macromol Biosci* (2023) 23:e2200448. doi:10.1002/mabi.202200448

20. Ha DH, Chae S, Lee JY, Kim JY, Yoon J, Sen T, et al. Therapeutic effect of decellularized extracellular matrix-based hydrogel for radiation esophagitis by 3d printed esophageal stent. *Biomaterials* (2021) 266:120477. doi:10.1016/j.biomaterials.2020.120477

21. Lin M, Firoozi N, Tsai CT, Wallace MB, Kang Y. 3d-printed flexible polymer stents for potential applications in inoperable esophageal malignancies. *Acta Biomater* (2019) 83:119–29. doi:10.1016/j.actbio.2018.10.035

22. Wysocki MA, Doyle S. Enhancing biomedical data validity with standardized segmentation finite element analysis. *Sci Rep* (2022) 12:9860. doi:10.1038/s41598-022-13961-0

23. Mousavi SR, Khalaji I, Naini AS, Raahemifar K, Samani A. Statistical finite element method for real-time tissue mechanics analysis. *Comput Methods Biomech Biomed Engin* (2012) 15:595–608. doi:10.1080/10255842.2010.550889

24. Alkentar R, Máté F, Mankovits T. Investigation of the performance of ti6al4v lattice structures designed for biomedical implants using the finite element method. *Materials (Basel)* (2022) 15:6335. doi:10.3390/ma15186335

25. Ciklacandir S, Mihcin S, Isler Y. Detailed investigation of three-dimensional modeling and printing technologies from medical images to analyze femoral head fractures using finite element analysis. *Ing Rech Biomed* (2022) 43:604–13. doi:10.1016/j.irbm.2022.04.005

26. Liu X, Liu H, Wang D, Wang EP, Liu WJ, Yao KF, et al. Metallic glass-strengthened thermoplastic elastomer composites. *Physica E Low Dimens Syst Nanostruct* (2017) 90:37–41. doi:10.1016/j.physe.2017.02.020

27. Huang YC, Zheng Y, Sarkar A, Xu YM, Stefik M, Benicewicz BC. Matrix-free polymer nanocomposite thermoplastic elastomers. *Macromolecules* (2017) 50:4742–53. doi:10.1021/acs.macromol.7b00873

28. Mars WV, Ellul MD. Fatigue characterization of a thermoplastic elastomer. *Rubber Chem Technol* (2017) 90:367–80. doi:10.5254/rct.17.83780

29. Weerasekera N, Ajjarapu K, Sudan K, Sumanasekera G, Kate K, Bhatia B. Barocaloric properties of thermoplastic elastomers. *Front Energ Res* (2022) 10. doi:10.3389/fenrg.2022.887006

30. Wu YY, Liu CR, Lapiere M, Ciatti JL, Yang DS, Berkovich J, et al. Thermoplastic elastomers for wireless, skin-interfaced electronic, and microfluidic devices. *Adv Mater Technol* (2023) 8. doi:10.1002/admt.202300732

31. Wu GZ, Li SM, Hu JY, Dong MC, Dong K, Hou XL, et al. A capacitive sensor using resin thermoplastic elastomer and carbon fibers for monitoring pressure distribution. *Pigm Resin Technol* (2021) 50:437–43. doi:10.1108/PRT-10-2019-0098

32. Fischenich KM, Lewis JT, Bailey TS, Donahue T. Mechanical viability of a thermoplastic elastomer hydrogel as a soft tissue replacement material. *J Mech Behav Biomed Mater* (2018) 79:341–7. doi:10.1016/j.jmbbm.2018.01.010

33. Esmaeili S, Shahali M, Kordjamshidi A, Torkpoor Z, Namdari F, Saber-Samandari S, et al. An artificial blood vessel fabricated by 3d printing for pharmaceutical application. *Nanomed J* (2019) 6:183–94. doi:10.22038/nmj.2019.06.00005

34. Jiang H, Cui Y, Ma K, Gong M, Chang D, Wang T. Experimental reconstruction of cervical esophageal defect with artificial esophagus made of polyurethane in a dog model. *Dis Esophagus* (2016) 29:62–9. doi:10.1111/dote.12258

35. Wen XL, Sun ST, Wu PY. Dynamic wrinkling of a hydrogel-elastomer hybrid microtube enables blood vessel-like hydraulic pressure sensing and flow regulation. *Mater Horiz* (2020) 7:2150–7. doi:10.1039/d0mh00089b

36. RodríguezParada L, de la Rosa S, Mayuet PF. Influence of 3d-printed tpu properties for the design of elastic products. *Polymers (Basel)* (2021) 13:2519. doi:10.3390/polym13152519

37. Rigotti D, Dorigato A, Pegoretti A. 3d printable thermoplastic polyurethane blends with thermal energy storage/release capabilities. *Mater Today Commun* (2018) 15:228–35. doi:10.1016/j.mtcomm.2018.03.009

38. Lee H, Eom RI, Lee Y. Evaluation of the mechanical properties of porous thermoplastic polyurethane obtained by 3d printing for protective gear. *Adv Mater Sci Eng* (2019) 2019:1–10. doi:10.1155/2019/5838361

39. Tardajos MG, Cama G, Dash M, Misseeuw L, Gheysens T, Gorzelanny C, et al. Chitosan functionalized poly-ε-caprolactone electrospun fibers and 3d printed scaffolds as antibacterial materials for tissue engineering applications. *Carbohydr Polym* (2018) 191:127–35. doi:10.1016/j.carbpol.2018.02.060

40. Lin YH, Chiu YC, Shen YF, Wu Y, Shie MY. Bioactive calcium silicate/poly-ε-caprolactone composite scaffolds 3d printed under mild conditions for bone tissue engineering. *J Mater Sci Mater Med* (2018) 29:11. doi:10.1007/s10856-017-6020-6

41. Pinto LA, Backes EH, Harb SV, Pinto GM, Da Cunha D, Andrade R, et al. Shape memory thermoplastic polyurethane/polycaprolactone blend and composite with hydroxyapatite for biomedical application. *J Mater Res* (2023) 39:90–106. doi:10.1557/s43578-023-01172-w

42. Yang ST, Luo LN, Tan BH. Research on sports performance prediction based on bp neural network. *Mob Inf Syst* (2021) 2021:1–8. doi:10.1155/2021/5578871

43. Wang ZH, Chen QQ, Wang ZY, Xiong J. The investigation into the failure criteria of concrete based on the bp neural network. *Eng Fract Mech* (2022) 275:108835. doi:10.1016/j.engfracmech.2022.108835

44. Sun HL. Prediction of building energy consumption based on bp neural network. *Wirel Commun Mob Comput* (2022) 2022:1–10. doi:10.1155/2022/7876013

45. Yu P, Huang S, Yang Z, Liu T, Qilin Z, Feng J, et al. Biomechanical properties of a customizable tpu/pcl blended esophageal stent fabricated by 3d printing. *Mater Today Commun* (2023) 34:105196. doi:10.1016/j.mtcomm.2022.105196

46. Wu G, Huang S, Liu T, Yang Z, Wu Y, Wei G, et al. Numerical study of the biomechanical behavior of a 3d printed polymer esophageal stent in the esophagus by bp neural network algorithm. *Comp Model Eng Sci* (2024) 138:2709–25. doi:10.32604/cmes.2023.031399

47. Mozafari H, Dong PF, Zhao SJ, Bi YH, Han XW, Gu LX. Migration resistance of esophageal stents: the role of stent design. *Comput Biol Med* (2018) 100:43–9. doi:10.1016/j.compbiomed.2018.06.031

48. Garbey M, Salmon R, Fikfak V, Clerc CO. Esophageal stent migration: testing few hypothesis with a simplified mathematical model. *Comput Biol Med* (2016) 79:259–65. doi:10.1016/j.compbiomed.2016.10.024

49. Conklin JL. Evaluation of esophageal motor function with high-resolution manometry. *J Neurogastroenterol Motil* (2013) 19:281–94. doi:10.5056/jnm.2013.19.3.281

50. Li Y, Li J, Mao M, Yin H, Ni X, Pan C. Investigation on the design and application of hydraulic loading fatigue test device for non-vascular stent. *Exp Tech* (2023). doi:10.1007/s40799-023-00685-7

51. Peirlinck M, Debusschere N, Iannaccone F, Siersema PD, Verhegghe B, Segers P, et al. An *in silico* biomechanical analysis of the stent–esophagus interaction. *Biomech Model Mechanobiol* (2018) 17:111–31. doi:10.1007/s10237-017-0948-9

frontiers | Frontiers in Physics

TYPE Original Research
PUBLISHED 14 June 2024
DOI 10.3389/fphy.2024.1401538

OPEN ACCESS

EDITED BY
Yilin Qu,
Northwestern Polytechnical University, China

REVIEWED BY
Yanming Xu,
Huanghuai University, China
Gongye Zhang,
Southeast University, China

*CORRESPONDENCE
Peng Liu,
njustca@njust.edu.cn

RECEIVED 15 March 2024
ACCEPTED 13 May 2024
PUBLISHED 14 June 2024

CITATION
Zhang A, Liu P and Zhang H (2024), Analysis and experiment of stress concentration in penetration fuze buffer materials under stress wave incursion.
Front. Phys. 12:1401538.
doi: 10.3389/fphy.2024.1401538

Analysis and experiment of stress concentration in penetration fuze buffer materials under stress wave incursion

An Zhang, Peng Liu* and He Zhang

Ministerial Key Laboratory of ZNDY, Nanjing University of Science and Technology, Nanjing, Jiangsu, China

To enhance the impact resistance of penetration fuze, this paper investigates the response of fuze buffer materials to stress waves and develops a model for stress wave transmission inside the fuze. The stress concentration impacts of different cell structures of Imitation Bamboo Type Penetration Fuze Buffer Protection Structure (IBS) under stress wave action are compared and analyzed. The paper elucidates the impact of different cell parameters on stress concentration impacts, establishes nonlinear fitting functions of Stress Concentration Factor (SCF) and cell parameters, and solves the prediction error. Based on the wave function expansion method, an expression for Dynamic Stress Concentration Factor (DSCF) when stress waves interact with the potting material is derived, and numerical results of DSCF around bubbles under different physical parameters are provided. Finally, dynamic impact tests are conducted on the combined buffer scheme of penetration fuze. Impact test results show that, under an initial velocity impact of 50 m/s, the overload peak attenuation rate is 39.42%, and under an initial velocity impact of 70 m/s, the overload peak attenuation rate is 32.87%. IBS can effectively protect the electronic components inside the fuze.

KEYWORDS

stress wave, fuze, stress concentration, wave function, dynamic impact

1 Introduction

During the high-speed penetration process, both the projectile and the fuze are subjected to strong dynamic loads, and the stresses generated are transmitted in various forms of waves to different parts [1–3]. The phenomenon of stress waves is widely present in the lives and has been extensively studied by experts and scholars in various fields, mainly in engineering, military technology, and scientific theoretical research [4]. The most typical examples of stress wave phenomena are various explosive and impact load problems in the military field [5]. Under the dynamic response of impact loads, the response of objects often differs significantly from that under static loads [6]. For example, when glass is subjected to the impact of a stone, the back of the glass often fractures and collapses first. When a static load is applied to one end of a metal rod, an experimental phenomenon opposite to that of applying a dynamic load occurs: the deformation of the metal rod under static load is basically uniformly distributed along the metal rod, while under impact load, the deformation is concentrated more at the two ends of the metal rod [7, 8].

This article focuses on the study of buffer materials for penetration fuze and proposes an IBS. Establish a theoretical model for stress wave propagation inside the fuze and derive the

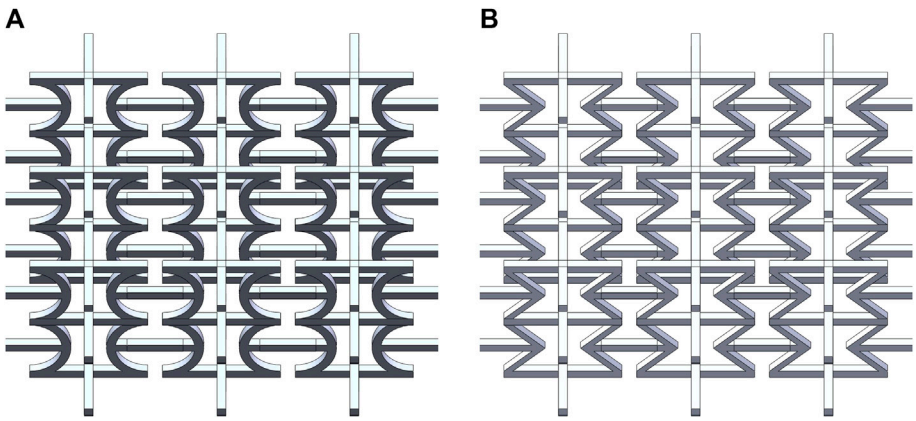

FIGURE 1
Honeycomb structure models of Penetration Fuze buffer. **(A)** IBS. **(B)** Traditional straight-edge structure.

energy absorption mechanism of IBS under axial impact load. By using finite element method to analyze the SCF of different cell structures under penetration overload, and exploring the influence of cell geometric parameters on SCF, a semi analytical solution of the nonlinear fitting function for predicting SCF is obtained. In addition, theoretical analysis and numerical calculation were conducted on the DSCF around the bubbles in the sealing material, and the distribution curve of the DSCF in the fuze sealing material was solved. Finally, the optimal structure of IBS is prepared through additive manufacturing technology, select the sealing material with the best buffering performance. Conduct dynamic impact tests on the optimized buffer scheme to verify that IBS can effectively reduce overload peaks and minimize damage to the electronic device structure of the fuze caused by stress waves.

2 Design of penetration fuze buffer structure model

2.1 Design of biomimetic cell geometry

Biomimetics is the study of the principles of structure and function of biological organisms, and based on these principles, new equipment, tools, and technologies are invented to create advanced techniques applicable to production, learning, and life. For example, in architecture, large-span thin-shell buildings are constructed by mimicking the structure of shells, and pillars are built by mimicking the structure of bones, which not only eliminates regions of stress concentration but also allows for the use of minimal building materials to withstand maximum loads. Zhang et al. [9] referred to the hierarchical structure of loofah sponge and the stiffening behavior of sea cucumber and proposed a new strategy for achieving multi-physical field protection through biomimetic structure design. This biomimetic structure effectively enhances the stiffness of polyurethane foam. Additionally, the stiffness of this biomimetic structure increases with increasing compressive strain rate, exhibiting excellent impact resistance under dynamic loads. Compared to polyurethane foam, the impact force of this biomimetic structure is reduced by 57.6%, and energy absorption is increased by 25.7%. This study provides an innovative means for the development of intelligent multi-physical field protection. Li [10] found that the arc-shaped structure of natural organisms can provide a reference for the design of impact-resistant structures. Most existing biomimetic arc-shaped impact-resistant structures are directly formed using 3D printing technology, and samples cannot dynamically adjust their impact resistance performance in various applications. This method uses 4D printing technology based on fuzed filament fabrication, dynamically adjusts process parameters, and incorporates them into the printing program to create flat structures with different design shapes. Through dynamic thermal stimulus processing, these structures can undergo deformation and transform into biomimetic arc-shaped structures. Thermal stimulus processing can drive the dynamic transformation of 2D planar structures into 3D structures. Under the same experimental conditions, the higher the thermal stimulus temperature, the more pronounced the deformation impact, and the higher the structural density. There is a certain positive correlation between the thermal stimulus temperature and the mechanical properties of biomimetic structure specimens. Additionally, designing different cyclic unit patterns has different compressive mechanical properties, with a greater number of cyclic units resulting in more prominent energy absorption characteristics. 3D models of Imitation Bamboo Type Penetration Fuze Buffer Protection Structure (IBS) and traditional concave hexagonal honeycomb structure are shown in Figure 1.

2.2 Stress wave transmission law of fuze rigid-flexible coupled system

During the penetration process of hard targets, when the projectile impacts the target plate at high speed due to strong dynamic loads, the stresses and deformations generated are propagated in the form of stress waves in the projectile-fuze structure. When the stress generated by the load reaches or far exceeds the yield strength of the projectile material, irreversible plastic deformation occurs in the material, resulting in the generation of plastic waves between the projectile and the fuze. Since the velocity of elastic waves is much faster than that of plastic waves, elastic waves precede plastic waves. Under uniaxial

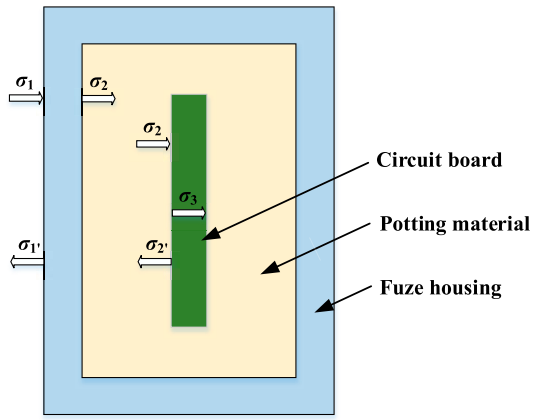

FIGURE 2
1D analysis model of fuze.

strain conditions, the velocity of elastic waves in the material is given by Eq. 2.1:

$$C = \sqrt{\frac{E}{\rho}} \tag{2.1}$$

where C is the velocity of longitudinal elastic waves in the medium, determined by the material's elastic modulus E and density ρ; and ρC is the impedance of longitudinal elastic waves. According to the theory of stress wave propagation, during the penetration of the projectile into the target plate, the impact is transmitted from the projectile to the buffer pad. When the elastic wave reaches the interface between two different media in the projectile-fuze structure, reflection and transmission of elastic waves occur. The reflected tensile elastic wave propagates to the left, unloading the elastic compression wave and the plastic loading wave successively. The transmitted elastic wave continues to propagate to the right, entering the cushioning and isolating material. Subsequently, the impact-resistant cushion is transmitted to the fuze casing, and the impact on the fuze casing passes through the potting layer before reaching the electronic device. Due to the different materials of the fuze casing, potting material, and circuit board, reflection and transmission of stress waves occur again during the internal propagation of stress waves in the fuze. In this paper, a 1D analysis of stress wave transmission is performed on the fuze casing, potting material, and circuit board, as shown in Figure 2.

At the interface between the fuze casing and the potting material, and between the potting material and the circuit board, the equation can be expressed as Eq. 2.2:

$$\begin{aligned} \sigma_2 &= T_1\sigma_1 \\ \sigma_3 &= T_2\sigma_2 \\ T_1 &= \frac{2(\rho C)_2}{(\rho C)_2 + (\rho C)_1} \\ T_2 &= \frac{2(\rho C)_3}{(\rho C)_3 + (\rho C)_2} \end{aligned} \tag{2.2}$$

where σ_1 is the stress of the fuze casing; σ_2 is the stress inside the potting material; σ_3 is the stress on the circuit board; and ρC is the wave impedance of the material. Substituting the above values into the equation, the stress relationship between the potting material and the fuze body and PCB board is obtained as follows:

$$\text{Polyurethane: } \sigma_1 = 0.12\sigma_2, \sigma_2 = 1.72\sigma_3$$
$$\text{Epoxy resin: } \sigma_1 = 0.20\sigma_2, \sigma_2 = 1.55\sigma_3$$

Through the above analysis of the potting material, in engineering applications, potting materials with low transmission coefficients should be selected to reinforce the circuit components and reduce the transmission of stress in the projectile.

2.3 Energy absorption characteristics of buffer honeycomb structure under penetration overload

The energy absorption behavior of honeycomb structures is described by the principle of energy conservation, which delineates the energy conversion process from intact to failure under in-plane loading conditions. It develops a nonlinear relationship between stress-strain and external work done by the load, which provides a solution closer to reality than directly solving boundary value problems of partial differential equations. Taking the elastoplastic energy absorption of honeycomb structures as an example, the strain energy density per unit volume is expressed as Eq. 2.3:

$$W_y = \int \sigma_{ij} d\varepsilon_{ij} \left(i, j = x, y, z\right) \tag{2.3}$$

where W_Y is the strain energy density and ε_{ij} is the strain component. Therefore, the total strain energy of elastoplastic deformation in honeycomb structures is given as Eq. 2.4:

$$Q_y = \int W_y dV = \frac{1}{2}\int \sigma_{ij}\varepsilon_{ij} dV \left(i, j = x, y, z\right) \tag{2.4}$$

If there is no energy loss during the crushing process of the honeycomb structure, then the strain energy inside the honeycomb structure numerically equals the work done by the surface load during the crushing displacement. According to the principle of virtual displacement, if the honeycomb structure is in a stable state under external loads, virtual displacements occur at various reference points inside the honeycomb structure. Likewise, the work done by external loads on virtual displacement numerically equals the virtual strain energy of the honeycomb structure under virtual displacement expressed as Eq. 2.5:

$$\delta Q_e = \int f_i \delta u_i dV + \int P_i \delta u_i ds \tag{2.5}$$

where δQ_e is the virtual work; f_i is the volume force; P_i is the surface force; and δU_i is the virtual displacement. Thus, the virtual strain energy caused by virtual displacement is Eq. 2.6:

$$\delta U_y = \int \sigma_{ij} \delta\varepsilon_{ij} dV \left(i, j = x, y, z\right) \tag{2.6}$$

If the external force is a time-varying load, it can be dominated by the potential function, then the variational equation can be expressed as Eq. 2.7:

$$\begin{aligned} \delta H &= \delta u + \delta V = 0 \\ H = U_y + V_y - Q_e &= \int W_y dV - \left(\int f_i u_i dV + \int P_i u_i ds\right) \end{aligned} \tag{2.7}$$

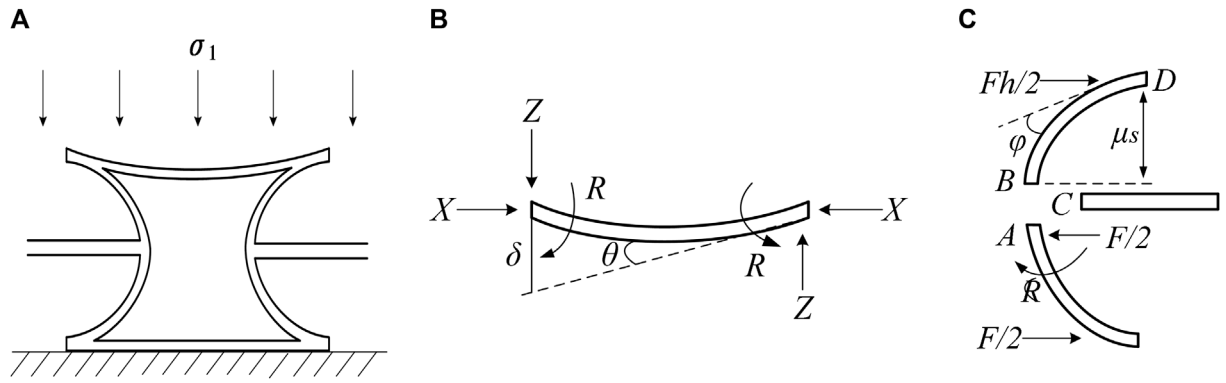

FIGURE 3
Schematic of uniaxial loading on cell face. **(A)** Representative cell deformation effect. **(B)** Upper crossbeam force diagram. **(C)** Internal concave curved edge force diagram.

where H is the total potential energy of the elastoplastic body. For the buffering honeycomb structure subjected to axial impact, initial deformation only results in local deformation bands. However, when the penetration overload exceeds tens of thousands of g-forces, the buffering honeycomb structure undergoes fracture and significant deformation, and energy is dissipated in other forms. Therefore, the honeycomb structure follows the principle of energy conservation under penetration conditions expressed as Eq. 2.8:

$$E_{TEA} = E_b + E_m + E_{fri} + E_{fra} + ... \tag{2.8}$$

where the terms on the right-hand side represent energy dissipation due to bending, torsion, friction, and fracture, respectively. Generally, porous honeycomb structures exhibit strong energy absorption characteristics and can serve as ideal energy absorption structures. Under low-speed impacts (around 2000g), the energy absorption structure only undergoes elastic deformation. However, in the load conditions experienced by penetration fuze, as the projectile penetrates defensive structures and the overload exceeds 50000g, the energy absorption structure is crushed and compacted, exhibiting structural fracture and failure under such instantaneous high dynamic loading conditions.

2.4 Uniaxial loading behavior of penetration fuze buffer honeycomb structure

The IBS designed in this article can effectively attenuate the impact amplitude when penetrating a reinforced concrete target, and improve the impact resistance of the internal circuit board of the fuze. In the project, the diameter of the projectile is 105–155mm, the strength of the target plate is C35-C60, and the buffer material is installed between the fuze and the projectile. The reserved thickness of the projectile in the buffer area is not more than 4 mm. Under ultra-high-speed penetration overload, the buffer protective structure for penetration fuze mainly undergoes linear elastic deformation, elastic buckling, plastic collapse, and fracture failure.

2.4.1 Linear elastic deformation

Under quasi-static compressive loads, honeycomb structures undergo linear elastic deformation and plastic collapse deformation. This section mainly studies the deformation under uniaxial loading in the plane, as shown in Figure 3.

Where (a) represents the deformation impact of a representative cell under axial stress σ_1; (b) represents the force diagram on the upper beam; and (c) represents the force diagram on the concave curved edge. The honeycomb structure initially enters the linear elastic region under initial compression displacement, where elastic deformation predominates. The equilibrium equation is given as Eq. 2.9:

$$\begin{aligned} X &= \sigma_1 (h + l \sin\theta) t_s \\ R &= \frac{Xl \sin\theta}{2} \end{aligned} \tag{2.9}$$

where t_s is the thickness of the thin wall in the axial direction; R is the bending moment; and X is the horizontal load. The deflection of the line is expressed as Eq. 2.10:

$$\begin{aligned} \delta &= \frac{Xl^3 \sin\theta}{12 E_s I} \\ I &= \frac{t_s e^3}{12} \end{aligned} \tag{2.10}$$

where Es is Young's modulus; I is the second moment of inertia of the line; and the deflection component is parallel to the load direction. The expression for cell strain can be derived as Eq. 2.11:

$$\varepsilon_1 = \frac{\delta \sin\theta}{l \cos\theta} = \frac{\sigma_1 (h + l \sin\theta) t_s l^2 \sin^2\theta}{12 E_s I \cos\theta} \tag{2.11}$$

Therefore, the elastic modulus of the cell in the axial direction is shown as Eq. 2.12:

$$E_1^* = \left(\frac{e}{l}\right)^3 \frac{E_s \cos\theta}{\left(\frac{h}{l} + \sin\theta\right) \sin^2\theta} \tag{2.12}$$

Similarly, analyzing the stress deformation on the curved edge, the honeycomb structure's curved edge undergoes shear deformation under penetration overload. Due to the symmetry of

the cell, the analysis shows that points A, B, and C of the 1/4 cell unit do not experience relative displacement under shear load, and the shear deflection is caused by compression of the upper beam and rotation around point B. The rotation angle is φ, as shown in Figure 3C, which represents the schematic diagram of force deformation of a representative honeycomb cell upper beam, curved edge, and support under penetration load. The resultant moment at point B can be expressed as Eq. 2.13:

$$M = \frac{Fh}{4} \tag{2.13}$$

Similarly, based on the previous analysis of deflection and moment of inertia, the expression for the rotation angle can be obtained as Eq. 2.14:

$$\varphi = \frac{Fhl}{24E_sI} \tag{2.14}$$

Therefore, the expression for the shear deflection at the right vertex D of the upper beam is determined as Eq. 2.15:

$$r_s = \frac{h}{2}\varphi + \frac{F}{8E_sI}\left(\frac{h}{2}\right)^3 \tag{2.15}$$

The shear strain on the curved edge can be expressed as Eq. 2.16:

$$\tau = \frac{2r_s}{h + l\sin\theta} \tag{2.16}$$

Using the same derivation method as the analysis of beam deformation under load, the shear modulus of the biomimetic honeycomb structure is obtained as Eq. 2.17:

$$G_1^* = \frac{E_s\left(\frac{h}{l} + \sin\theta\right)\left(\frac{t}{l}\right)^3}{\left(\frac{h}{l}\right)^2\left(1 + \frac{16h}{l}\right)\cos\theta} \tag{2.17}$$

2.4.2 Elastic buckling

When the honeycomb structure is in the initial stage of penetration load, linear elastic deformation predominates. The honeycomb structure can be analyzed as an elastic body. When the compressive load in the axial direction exceeds the Euler buckling load, elastic buckling occurs. The expression is given as Eq. 2.18:

$$Q_{cri} = \left(\frac{\varpi\pi}{h}\right)^2 E_sI \tag{2.18}$$

where ϖ is the endpoint constraint factor, representing the rotational stiffness at the connection between the curved edge of the representative honeycomb cell and the support rod; I is the second moment of inertia of the straight line. Similarly, the relationship between the curved edge bearing the penetration load and the impact stress can be expressed as Eq. 2.19:

$$Q = 2\sigma_2 l r_s \cos\theta \tag{2.19}$$

When P=P_{cri}, the honeycomb buffer honeycomb absorbs penetration overload energy through elastic collapse, and its collapse stress is determined as Eq. 2.20:

$$\sigma_2^* = \frac{(\varpi\pi)^2 t^3 E_s}{36\cos\theta l h^2} \tag{2.20}$$

where ϖ is impacted by the cell line diameter on the rotation stiffness at the connection between the curved edge and the support rod. The larger the value, the greater the suppression of the rotational impact of the cell, with a maximum value of 1.7. The smaller the value, the less inhibition of the rotational impact of the cell, with a minimum value of 0.3, at which point the cell rotates freely.

2.4.3 Plastic collapse

As the penetration overload increases gradually, when the axial load stress borne by the buffer honeycomb exceeds the critical load, plastic collapse of the honeycomb structure begins, and the pores are gradually filled. At this point, due to 3D structure of the buffer honeycomb and the negative Poisson's ratio impact, the honeycomb structure as a whole is in a state of being squeezed towards the geometric center from all sides. Therefore, this section analyzes from both the axial and radial directions. The plastic collapse of the honeycomb structure in the axial direction is shown in Figure 3. Under this condition, the equilibrium equation is shown as Eq. 2.21:

$$X = \sigma_1 (h + l\sin\theta) r_s \tag{2.21}$$

During the process of the projectile penetrating the target, the kinetic energy of the internal components of the fuze is mainly absorbed by the plastic deformation of the honeycomb structure. Let the cellular structure compress the energy absorption per unit volume as η, according to the law of conservation of energy, the plastic deformation energy of honeycomb materials ΔE is Eq. 2.22:

$$\Delta E = \eta \cdot \Delta L \cdot S \tag{2.22}$$

In the formula: ΔL is the compression stroke; S is the number of cells. Only when $\Delta E > E_f + E_i$ can the system kinetic energy be fully absorbed. Therefore, there are Eq. 2.23:

$$\eta \cdot \Delta L \cdot S > E_f + E_i \tag{2.23}$$

By combining (2.21), (2.22) and (2.23), it can be concluded that when plastic shear torsion occurs at each connection point of the honeycomb structure, the plastic work done at the connection point is Eq. 2.24:

$$4M_p\varphi \geq 2\sigma_1 r_s (h + l\sin\theta)\varphi l\sin\theta \tag{2.24}$$

Where M_P represents the plastic moment during plastic shear twisting. Based on the empirical equation of moment, the critical value of plastic collapse stress for the buffer honeycomb can be derived as Eq. 2.25:

$$\sigma_{p1}^* = \frac{\sigma_0 t^2}{2l^2\left(\frac{h}{l} + \sin\theta\right)\sin\theta} \tag{2.25}$$

Similarly, based on the expression of plastic moment and the critical value of plastic collapse stress, the maximum moment of the buffer honeycomb can be obtained as Eq. 2.26:

$$(M_{\max})_1 = \frac{1}{2}\sigma_1 (h + l\sin\theta) r_s l\sin\theta \tag{2.26}$$

In the radial direction, the buffer honeycomb cell is mainly subjected to compression from adjacent cells. By equating the plastic work required for compression deformation to the work done by the

penetration overload stress, the relationship between the maximum moment of the buffer honeycomb and the plastic moment is expressed as Eq. 2.27:

$$(M_{\max})_2 = \frac{1}{2}\sigma_2 l^2 r_s \cos^2\theta \tag{2.27}$$

By analyzing the radial plastic shear situation using a method similar to that of axial loading, in the early stages of collapse, the cells surrounding the representative cell undergo shear loading in the radial direction, causing plastic shear of the buffer honeycomb. The critical shear strength is calculated as Eq. 2.28:

$$\left(\tau^*_{p1}\right)_{12} = \frac{\sigma_0 t^2}{6(h/l)\cos\theta} \tag{2.28}$$

In the early to mid-stages of collapse, elastic buckling is insufficient to support the strength of the buffer honeycomb, leading to plastic collapse. At this point, the equilibrium equation is given as Eq. 2.29:

$$\left(\sigma^*_{e1}\right)_2 = \left(\sigma^*_{p1}\right)_2 \tag{2.29}$$

Existing research results show that for 3D printed metal structures, the magnitude of the elastic modulus is relatively low. When the relative density is small, the buffer honeycomb undergoes plastic collapse under penetration load.

2.4.4 Fracture failure

As the penetration overload further increases, the buffer honeycomb enters the final stage of protective work: fracture failure. At this point, the cells begin to collapse on a large scale, and the pores are gradually filled. The compressive stress borne by the buffer honeycomb under the action of the moment M_{max} is determined as Eq. 2.30:

$$\sigma_{\max} = \frac{8M_{\max}}{r_s t^2} \tag{2.30}$$

When the compressive stress equals the fracture strength of the buffer honeycomb, the structure undergoes fracture failure, and the fracture moment is expressed as Eq. 2.31:

$$M_f = \frac{\sigma_{fs} r_s t^2}{8} \tag{2.31}$$

By substituting the fracture moment into the equation for the maximum moment of the buffer honeycomb, the fracture strength of the biomimetic structure is obtained as Eq. 2.32:

$$\sigma^*_r = \frac{\sigma_{fs} t^2}{4l^2 \sin\theta\left(\frac{h}{l} + \sin\theta\right)} \tag{2.32}$$

2.5 Finite element analysis of stress concentration

The maximum local stress at the irregularities of the outer shape of the buffering structure is denoted as σ_{max}, and it can be obtained through solid elastoplastic deformation theory and structural mechanics calculations. During the process of projectile penetration through the target, the theoretical Stress Concentration Factor (SCF) is represented by the ratio of the maximum local stress σ_{max} to the nominal stress σ_{nom} approximately uniformly distributed on the cross-section of the buffering structure can be represented as Eq. 2.33:

$$SCF = \frac{\sigma_{\max}}{\sigma_{nom}} \tag{2.33}$$

From the equation above, the more abrupt the external shape mutations of the buffering structure, the more severe the stress concentration. In the case of penetration fuze with buffering structures made of metal, under the action of penetration overload, as the maximum local stress reaches the yield limit of the buffering structure, and with the continued increase in penetration overload, the nominal strain continues to increase while the nominal stress no longer increases. The additional overload will be borne by the remaining parts until the nominal stress at all section nodal points of the entire honeycomb structure approaches the yield strength. At this point, the energy absorption process of the buffering structure concludes.

IBS finite element model is imported into SolidWorks Simulation, with the biomimetic cell model being 6 mm in length and 4 mm in height. The structure is made of 7,075 aluminum alloy with elastic modulus of 7.2×10^{10}N/m^2, shear modulus of 2.69×10^{10}N/m^2, yield strength of 4.35×10^8N/m^2, density of 2830 kg/m^3, and Poisson's ratio of 0.33. The bottom of the cell is fixed, and a uniaxial compression load is applied to the top surface. To ensure the intuitiveness and efficiency of the finite element simulation, based on Saint-Venant principle, a 1:100 equivalent reduction model is selected for static analysis. Under actual penetration conditions, the penetration overload experienced by the projectile ranges from 0 to 50000 g. Compression loads of 20000g, 35000g, and 50000 g are respectively applied for in-plane axial loading to simulate the mechanical response behavior of IBS during penetration, and to compare it with traditional concave hexagonal structures to analyze the stress concentration impacts of different structures.

Considering the central symmetry characteristics of IBS, as well as the load and constraint conditions, and ensuring the accuracy of the calculation results, the number of meshes is minimized to ensure calculation accuracy and efficiency. One edge of the buffering structure model is selected for analysis. Using the partition meshing method, the cell model is divided into different regions according to the accuracy requirements of the calculation results. Finer meshes are applied to critical areas prone to stress concentration, while relatively sparse meshes are used in areas away from critical areas to improve computational efficiency.

In summary, the mesh size in non-critical areas is set to 0.2mm, and the mesh in critical areas is appropriately refined to four times the size of non-critical areas (0.05 mm). The transition ratio of the mesh is set to 1: 1.2. The final mesh division of the model is shown in Figure 4.

3 Analysis of stress concentration in different cell structures

3.1 Stress concentration analysis under 20000 g overload

The penetration process of the projectile can be divided into the pit opening stage, the tunneling stage, and the target back collapse

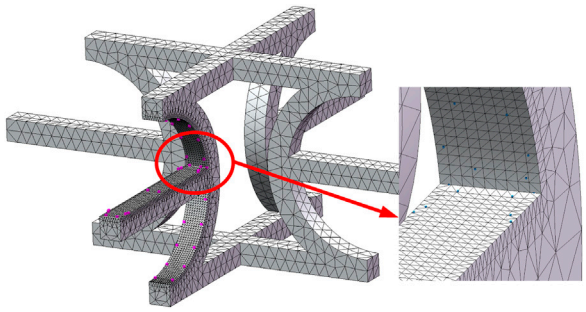

FIGURE 4
Finite element mesh model of buffer structure.

stage (exit stage). To explore the stress concentration impacts of different buffering structures at various stages of the penetration process, different overload values are applied. First, the stress situation of the buffering structure under the condition of 20000 g projectile penetration overload is analyzed, at which point the fuze is in the pit opening stage. Using the pre-compression node height h as a reference baseline, the stress-node curve is obtained as shown in Figure 5.

Figure 5 shows the stress-node curves of different cell structures under 20000 g overload. The red solid line represents the traditional concave hexagonal structure, while the black solid line represents IBS. On the inner wall of the cell, the protective performance of IBS is significantly better, with stress values at each node lower than those of the traditional structure. The peak stress is 13.09MPa, occurring in the middle section, with slight oscillations in stress values stabilizing at around 10 MPa. For the traditional structure, the peak stress is 64.17MPa, occurring at the contact position between the inclined surface and the upper beam. Stress values are smaller in the middle section but exhibit greater oscillations. On the outer wall of the cell, the stress values at each node of IBS are generally lower than those of the traditional structure, except at 1.2mm and 3.2 mm where they exceed. The peak stress is 29.79MPa, occurring in the middle section, with larger oscillations compared to the inner wall. For the traditional structure, the peak stress is 69.83MPa, occurring in the middle section. The stress concentration impact is significant at the contact position between the support frame and the inclined surface, leading to considerable stress oscillations, which could have adverse impacts on the energy absorption of the penetration fuze buffering structure.

3.2 Stress concentration analysis under 35000 g overload

The stress situation of the buffering structure under the condition of 35000 g projectile penetration overload is analyzed, at which point the fuze enters the tunneling stage, generating the stress-node curve as shown in Figure 6.

From the graph, it can be seen that under an overload of 35000g, On the inner wall of the cell, the degree of stress concentration in IBS is significantly lower than that in the traditional structure, with a peak stress of 26.14 MPa occurring below the support frame position, and stress values oscillating around 20 MPa. For the traditional structure, the peak stress is 101.73MPa, occurring above the support frame position, with smaller stress at non-contact areas but larger stress oscillations. On the outer wall of the cell, the degree of stress concentration in IBS is still lower than that in the traditional structure, with a peak stress of 59.49 MPa occurring in the middle section, and stress values oscillating more than on the inner wall of the cell. For the traditional structure, the peak stress is 139.66MPa, occurring in the middle section, with significant stress concentration at the corner of the straight edge, leading to larger stress oscillations.

3.3 Stress concentration analysis under 50000 g overload

The stress situation of the buffering structure under the condition of 50000 g projectile penetration overload is analyzed, at which point the fuze reaches its overload peak, generating the stress-node curve as shown in Figure 7.

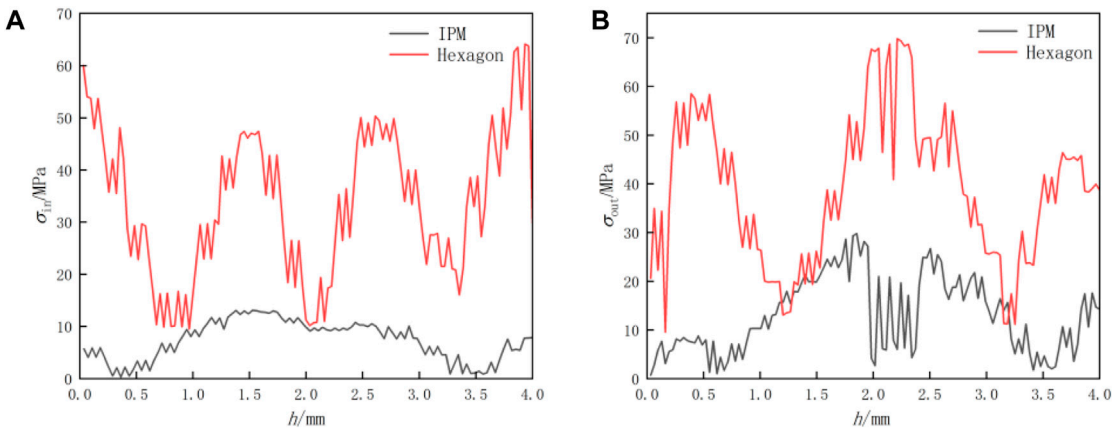

FIGURE 5
Stress distribution on inclined surface under 20000 g overload. **(A)** Inner wall of cell. **(B)** Outer wall of cell.

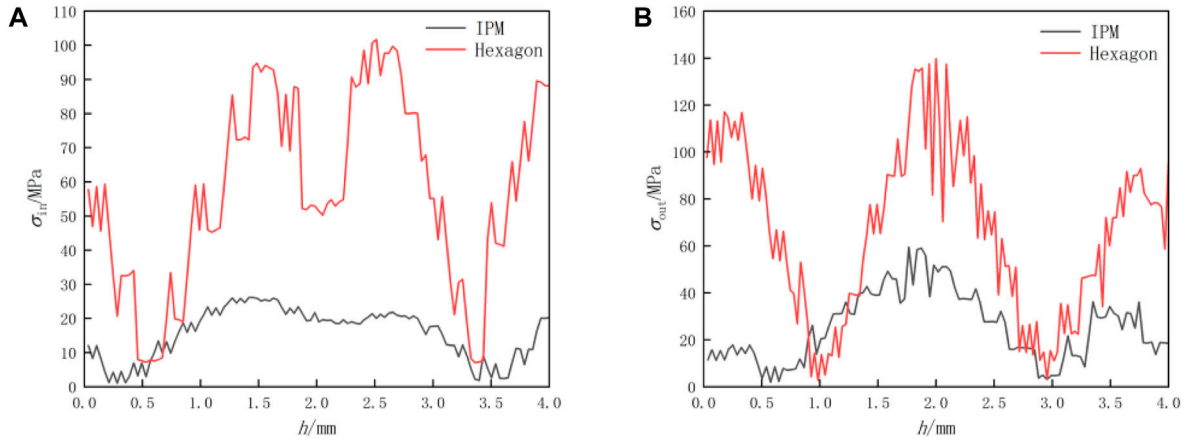

FIGURE 6
Stress distribution on inclined surface under 35000 g overload. **(A)** Inner wall of cell. **(B)** Outer wall of cell.

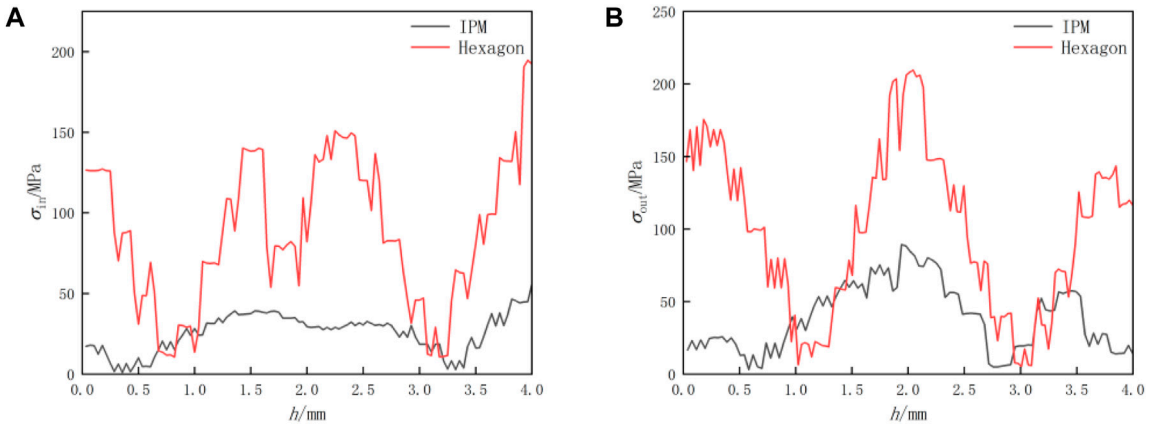

FIGURE 7
Stress distribution on inclined surface under 50000 g overload. **(A)** Inner wall of cell. **(B)** Outer wall of cell.

From the graph, it can be seen that under an overload of 50000g, On the inner wall of the cell, the stress distribution in IBS is uniform, and the degree of stress concentration is lower than that in the traditional structure, with a peak stress of 55.63 MPa occurring at the contact position between the curved edge and the upper beam, and stress values oscillating around 40 MPa. For the traditional structure, the peak stress is 194.63MPa, occurring at the contact position between the curved edge and the upper beam, with smaller stress at non-contact areas but larger stress oscillations. On the outer wall of the cell, the degree of stress concentration in IBS is still lower than that in the traditional structure, with a peak stress of 89.37 MPa occurring in the middle section, and stress values oscillating more significantly. For the traditional structure, the peak stress is 209.49MPa, occurring in the middle section, with significant stress concentration at the corner of the straight edge.

Overall, during various stages of the penetration process, the degree of stress concentration in the traditional structure is greater than that in IBS, indicating that IBS provides better buffering protection for the fuze. This is because of the presence of initial curvature, which makes bending the predominant mode of deformation in IBS, resulting in an increase in the equivalent modulus of the honeycomb structure. In general, the energy absorption of specialized energy absorption structures refers to the plastic energy dissipated under compression loads. Both structures undergo consistent impact loads and plastic deformation. IBS has a higher elastic modulus; therefore, it can absorb more kinetic energy during the penetration process.

4 Impact of cell geometry parameters on SCF

4.1 Impact of wall thickness on SCF

From the finite element simulation results, under the same penetration conditions, IBS can better eliminate stress concentration compared to the traditional concave hexagonal structure. Additionally, during the penetration process, the microstructural geometric parameters of the cell will also affect the stress concentration impact. Based on the calculated results of the developed IBS finite element model, stress concentration in IBS mainly occurs at the center of the curved edge. Therefore, the impact of cell geometric parameters

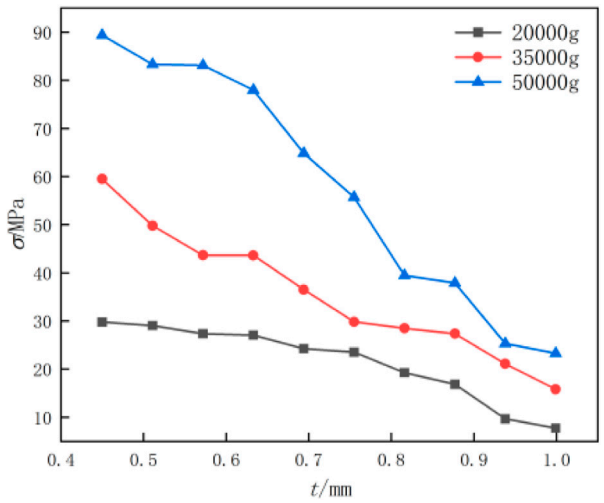

FIGURE 8
Relationship between peak stress and wall thickness.

on the distribution of SCF at the midpoint of the curved edge is studied. Figure 8 illustrates the peak stress of IBS with different wall thicknesses under various penetration overloads.

The impact of wall thickness on peak stress is significant, as depicted in Figure 8. For the same penetration overload, the peak stress decreases with the increase of wall thickness. For cells with the same wall thickness, the peak stress increases with the increase in penetration overload, and cells with smaller wall thickness exhibit a more pronounced response to overload. According to the material properties of metal and the national standard GB/T 3190-2018, combined with the evaluation equation for stress concentration degree, SCF at the center of the curved edge for different wall thicknesses under each condition is calculated, as shown in Table 1. SCF at the center of the curved edge decreases with increasing wall thickness. When the wall thickness reaches 1mm, the minimum SCF at an overload of 50000 g is 1.004.

4.2 Impact of side length on SCF

Figure 9 presents the peak stress of IBS with different side lengths under various penetration overloads. The impact of side length on peak stress is minimal, almost negligible, for the same penetration overload. For cells with the same side length, the peak stress increases with the increase in penetration overload. SCF at the center of the curved edge for different side lengths under each condition is calculated, as shown in Table 2. As the side length increases, SCF at the center of the curved edge slightly increases. However, this change has almost no impact on the stress concentration impact. When the side length reaches 7.8mm, the maximum SCF under an overload of 50000 g is 2.854.

4.3 Impact of curvature on SCF

In addition to wall thickness and side length, curvature also has a significant impact on stress concentration impacts. Figure 10 illustrates the peak stress of IBS with different curvatures under various penetration overloads. The impact of curvature on peak stress is significant. For the same penetration overload, the peak stress increases with the increase of curvature. For cells with the same curvature, the peak stress increases with the increase in penetration overload. Furthermore, cells with larger curvature exhibit a more pronounced response to overload. SCF at the center of the curved edge for different curvatures under each condition is calculated, as shown in Table 3. SCF at the center of the curved edge increases with the increase in curvature. When the curvature reaches 2.4, the maximum SCF under an overload of 50000 g is 3.907.

5 SCF nonlinear fitting functions

5.1 Fitting model of SCF with wall thickness

In the reliability assessment of penetration fuze buffer structures, to address the inefficiency of calculating SCF for each node individually, this study develops a fitting equation for SCF with cell geometric parameters to predict SCF under different cell structures. Under the premise of meeting the engineering design error requirements, only an approximate value of SCF is needed. Therefore, based on the aforementioned SCF calculation results, a nonlinear fitting method is used to establish a fitting function for SCF at the center of the curved edge of IBS during the penetration process. The sinusoidal fitting function model of SCF at the center of the curved edge of IBS under an overload of 20000 g with respect to wall thickness is as Eq. 5.1:

$$SCF(t) = \frac{y_1 + A_1 \sin\left(\pi \frac{t - t_{c1}}{w_1}\right)}{\sigma_{nom}} \tag{5.1}$$

where SCF(t) represents the data to be fitted; y_1 is the initial phase; t_{c1} is the fitting interval length; A_1 is the amplitude; and w_1 is the sampling frequency. According to the principle of least squares, the above equation can be transformed into Eq. 5.2:

$$f(t_{c1}, A_1, w_1) = \sum \left[y_1 + A_1 \sin \pi \frac{t - t_{c1}}{w_1} \right] \tag{5.2}$$

Taking the first partial derivatives with respect to t_{c1}, A_1, and w_1, the expression can be given as Eq. 5.3:

$$\begin{bmatrix} t_{c1} \\ A_1 \\ w_1 \end{bmatrix} = \begin{bmatrix} \sum \cos^2 t_i & \sum \sin t_i \cos t_i & \sum \cos t_i \\ \sum \sin A_i \cos A_i & \sum \sin^2 A_i & \sum \sin A_i \\ \sum \cos w_i & \sum \sin w_i & \sum \sin w_i \cos w_i \end{bmatrix}^{-1} \begin{bmatrix} \sum t_i \cos t_i \\ \sum t_i \sin A_i \\ \sum t_i w_i \end{bmatrix} \tag{5.3}$$

According to the trigonometric function equation derivation, it can be expressed as Eq. 5.4:

$$SCF(t) = \begin{bmatrix} \cos t_i & \sin t_i & \cos t_i \\ \sin t_i & \cos t_i & \sin t_i \\ \cos t_i & \sin t_i & \sin \cos t_i \end{bmatrix} y_i + \begin{bmatrix} \cos t_{ci} & \sin t_{ci} & \cos t_{ci} \\ \sin A_i & \cos A_i & \sin A_i \\ \cos w_i & \sin w_i & \sin \cos w_i \end{bmatrix} \tag{5.4}$$

By solving Eq. 5.1, the range of values for y_1, t_{c1}, A_1, and w_1 can be determined, with y_1 ranging from −7,219.95 ± 48.88, t_{c1} ranging from −10.63 ± 37.9, A_1 ranging from 7,249 ± 488.34, and w_1 ranging from 22.17 ± 75.62. After adjustment, the fitting goodness is 0.97778.

TABLE 1 Curved center SCFs for different wall thicknesses.

t/mm (g)	0.45	0.51	0.57	0.63	0.69	0.76	0.82	0.88	0.94	1
20,000	1.992	1.968	1.842	1.796	1.783	1.714	1.435	1.305	1.121	1.08
35,000	2.316	2.151	2.132	1.864	1.811	1.661	1.647	1.429	1.034	1.006
50,000	2.755	2.752	2.253	2.113	2.093	1.986	1.887	1.456	1.389	1.004

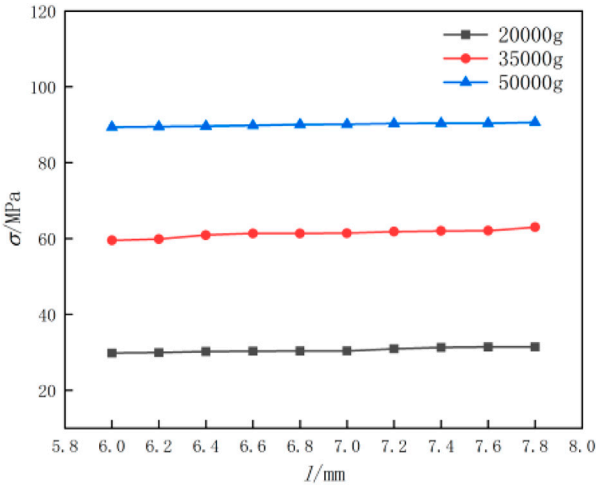

FIGURE 9
Relationship between peak stress and side length.

Gaussian fitting function model for SCF at the center of the curved edge of IBS under an overload of 35000 g with respect to wall thickness is as Eq. 5.5:

$$SCF(t) = \frac{y_2 + A_2 e^{-\frac{(t-t_{c2})^2}{2w_2^2}}}{\sigma_{nom}} \tag{5.5}$$

where SCF(t) represents the distribution function of stress concentration coefficient with respect to wall thickness; y_2 is the initial deviation; t_{c2} is the fitting interval length; A_2 is the loss factor; and w_2 is the normalized frequency. The purpose of this step is to predict the trend of the curve. Taking the logarithmic transformation of both sides of Gaussian curve, it can be expressed as Eq. 5.6:

$$\sigma_{nom} \ln SCF(t) = \ln y_2 - \frac{(t-t_{c2})^2}{2w_2^2} \tag{5.6}$$

The model in the above equation resembles a parabolic equation $y = at^2 + bt + c$ with respect to t. Therefore, by solving for the fitting parabolic coefficients, the expression for the Gaussian curve function can be determined. Using the principle of least squares, the parameters a_i, b_i, and c_i are obtained to minimize the sum of squared errors (S) is Eq. 5.7:

$$S = \sum_{i=1}^{n} (y_i - a_i t_i^2 - b_i t - c_i)^2 \tag{5.7}$$

Taking the first partial derivatives of the above equation and setting them equal to 0, the equation can be given as Eq. 5.8:

$$\begin{cases} a_i = \dfrac{A_2(t-t_{c2})}{w} \\ b_i = \dfrac{y_2 - t_{c2}}{w} \\ c_i = \dfrac{\left(\sum_{i=1}^{n} y_i - a_i \sum_{i=1}^{n} t_i^2 - b_i \sum_{i=1}^{n} t_i\right)}{n} \end{cases} \tag{5.8}$$

where the coefficient is expressed as Eq. 5.9:

$$\begin{cases} y_2 = n\sum_{i=1}^{n} t_i^2 - n\sum_{i=1}^{n} t_i \sum_{i=1}^{n} t_i \\ t_{c2} = n\sum_{i=1}^{n} t_i^2 y_i - \sum_{i=1}^{n} t_i^2 \sum_{i=1}^{n} y_i \\ A_2 = n\sum_{i=1}^{n} t_i y_i - \sum_{i=1}^{n} t_i \sum_{i=1}^{n} y_i \\ w_2 = n\sum_{i=1}^{n} t_i^3 - n\sum_{i=1}^{n} t_i^2 \sum_{i=1}^{n} t_i^2 \end{cases} \tag{5.9}$$

TABLE 2 Curved center SCFs for different side lengths.

L/mm (g)	6	6.2	6.4	6.6	6.8	7	7.2	7.4	7.6	7.8
20,000	1.992	1.993	1.995	1.996	1.997	1.997	1.997	1.999	2	2
35,000	2.316	2.317	2.318	2.319	2.322	2.324	2.341	2.344	2.35	2.387
50,000	2.755	2.773	2.781	2.801	2.821	2.83	2.845	2.847	2.853	2.854

TABLE 3 Curved center SCFs for different curvatures.

k (g)	1.5	1.6	1.7	1.8	1.9	2	2.1	2.2	2.3	2.4
20,000	1.992	2.01	2.14	2.183	2.224	2.232	2.274	2.32	2.457	2.47
35,000	2.316	2.441	2.635	3.711	2.75	2.812	3.129	3.167	3.23	3.498
50,000	2.755	2.767	3.066	3.093	3.096	3.306	3.567	3.628	3.646	3.907

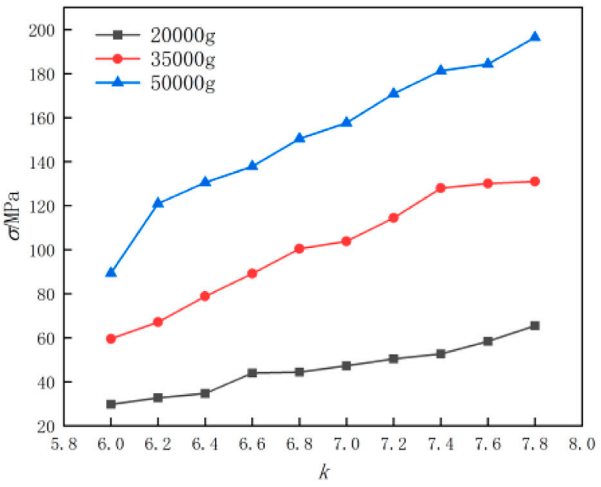

FIGURE 10
Relationship between peak stress and curvature.

It should be noted that the solution to this equation is obtained by taking the logarithm of the original Gaussian curve function, meaning that the predicted values of SCF are logarithmically transformed to satisfy the parabolic equation, and thus, y_2 ranges from 268.54 ± 4.16, t_{c2} ranges from 1.59 ± 3.15, A_2 ranges from −268.51 ± 4.16, and w_2 ranges from 17.9 ± 139.98. After adjustment, the fitting goodness is 0.96397. The Lorentz fitting function model for SCF at the center of the curved edge of IBS under an overload of 50000 g with respect to wall thickness is determined as Eq. 5.10:

$$SCF(t) = y_3 + \frac{2A_3}{\pi\sigma_{nom}} \bullet \frac{w_3}{4(t - t_{c3})^2 + {w_3}^2} \tag{5.10}$$

where SCF(t) represents the quadratic polynomial Lorentz fitting function; y_3 is the equivalent error; t_{c3} is the fitting interval length; A_3 is Gini coefficient; and w_3 is the composite weight. By dividing the wall thickness into n groups from small to large and setting the wall thickness of each group as ti and the corresponding SCF as y_i, SCF value of the i th group can be represented as Eq. 5.11:

$$SCF_i(t) = \frac{\sum_{i=1}^{n} t_i}{t_i} (i = 1, 2, ..., n) \tag{5.11}$$

The fitting error of the ith group SCF can be expressed as Eq. 5.12:

$$R_i = \frac{y_i}{\sum_{i=1}^{n} y_i} (i = 1, 2, ..., n) \tag{5.12}$$

By solving the above equation and plotting the cumulative percentage of wall thickness and the cumulative percentage of error on XOY plane, the follows expression can be given as Eq. 5.13:

$$0(0,0), p_1(SCF_1, R_1), p_2(SCF_1 + SCF_2, R_1 + R_2), ..., p_k\left(\sum_{i=1}^{k} SCF_i, \sum_{i=1}^{k} R_i\right), ..., p_n\left(\sum_{i=1}^{k} SCF_i, \sum_{i=1}^{k} R_i\right) = (t_i, y_i) \tag{5.13}$$

The sequences of the abscissa and ordinate of the above points are both monotonically increasing sequences. By fitting the above n+1 points with a smooth curve, Lorentz curve of SCF with respect to wall thickness at the center of the curved edge can be obtained, and thus, y_3 ranges from −18.04 ± 19.31, t_{c3} ranges from 0.49 ± 0.03, A_3 ranges from 131.44 ± 57.29, and w_3 ranges from 0.79 ± 0.2. After adjustment, the fitting goodness is 0.98085.

5.2 Fitting model of SCF with edge length

According to the analysis of the impact of edge length on SCF, the relationship between SCF at the center of the curved edge and the edge length tends to be linear overall. Therefore, this study adopts a linear function for fitting. The linear function fitting model of SCF at the center of the curved edge of IBS under an overload of 20000 g with respect to edge length is as Eq. 5.14:

$$SCF(l) = \frac{a_1 l + b_1}{\sigma_{nom}} \tag{5.14}$$

where SCF(l) represents the stress concentration coefficient to be fitted; a_1 is the slope, with a range of 0.97 ± 0.1; and b_1 is the intercept, with a range of 23.9 ± 0.6. After adjustment, the fitting goodness is 0.93139. The linear function fitting model of SCF at the center of the curved edge of IBS under an overload of 35000g with respect to edge length is as Eq. 5.15:

$$SCF(l) = \frac{a_2 l + b_2}{\sigma_{nom}} \tag{5.15}$$

where SCF(l) represents the stress concentration coefficient to be fitted; a_2 is the slope, with a range of 1.63 ± 0.19; and b_2 is the intercept, with a range of 50 ± 1.29. After adjustment, the fitting goodness is 0.91594. The linear function fitting model of SCF at the center of the curved edge of IBS under an overload of 50000g with respect to edge length is as follows:

Where SCF(l) represents the stress concentration coefficient to be fitted; a_3 is the slope, with a range of 0.69 ± 0.04; and b_3 is the intercept, with a range of 85.26 ± 0.26. After adjustment, the fitting goodness is 0.97465. The relationship between SCF and edge length is Eq. 5.16:

$$SCF(l) = \frac{a_3 l + b_3}{\sigma_{nom}} \tag{5.16}$$

5.3 Fitting model of SCF with curvature

In Figure 1, under an overload of 20000g, the relationship between SCF at the center of the curved edge of IBS and the curvature tends to rise in an approximately upward-opening parabolic trend. The quadratic function fitting model of the relationship between SCF at the center of the curved edge of IBS and the curvature is as Eq. 5.17:

$$SCF(k) = \frac{a_4 k^2 + b_4 k + c_4}{\sigma_{nom}} \tag{5.17}$$

Selecting n unit nodes (k_i, y_i), after m iterations, the equation can be expressed as Eq. 5.18:

$$SCF(k) = a_0 + a_1 + a_2k^2 + ... + a_mk^m = \sum_{j=0}^{m} a_jk^j \tag{5.18}$$

To determine the coefficients in the above equation, substitute the nodes into the polynomial to obtain the error equation as Eq. 5.19:

$$\begin{cases} a_0 + a_1k_1 + a_2k_1^2 + ... + a_mk_1^m - y_1 = R_1 \\ a_0 + a_1k_2 + a_2k_2^2 + ... + a_mk_2^m - y_2 = R_2 \\ ... \\ a_0 + a_1k_n + a_2k_n^2 + ... + a_mk_n^m - y_n = R_n \end{cases} \tag{5.19}$$

Minimizing the sum of squared errors provides as Eq. 5.20:

$$\sum_{i=1}^{n} R_i^2 = \sum_{i=1}^{n} \left[\sum_{j=0}^{m} a_ik^2 + b_ik + c_i \right]^2 = \delta \tag{5.20}$$

Taking the first partial derivative of both sides of the equation to determine as Eq. 5.21:

$$\frac{\partial \delta}{\partial a_i^k} = 2\sum_{i=1}^{n} \left[\sum_{j=0}^{m} a_ik^2 + b_ik + c_i \right] k_i^k = 0 \tag{5.21}$$

Thus, the solution coefficients can be obtained as Eq. 5.22:

$$\begin{cases} a_i = \sum_{j=0}^{m} a_jS_{n+j} \\ b_i = \sum_{j=0}^{m} k_i^n \\ c_i = \sum_{j=0}^{m} y_ik_i^n \end{cases} \tag{5.22}$$

Simultaneous equation (5.17)–(5.21), the quadratic term coefficient a_4 for the parabolic fitting equation is in the range of 1.56 ± 2.31, the linear term coefficient b_4 is in the range of −2.89 ± 31.95, and the constant term c_4 is in the range of −8.66 ± 1.1. After adjustment, the fitting goodness is 0.96529. Under an overload of 35000g, the relationship between SCF and curvature approximately follows a logarithmic growth trend. Therefore, a quadratic logarithmic polynomial is used to approximate the curve, and the coefficients of this polynomial equation are determined by logarithmic functions. The logarithmic fitting function model of the relationship between SCF at the center of the curved edge of IBS and the curvature is given as Eq. 5.23:

$$SCF(k) = \frac{B_2}{\sqrt{2\pi}v_2k\sigma_{nom}} e^{\frac{-\left[\ln \frac{k}{k_{c2}}\right]^2}{2v_2^2}} \tag{5.23}$$

where k_{c2}, v_2, and B_2 are constants. Taking the logarithm of both sides of the equation provides as Eq. 5.24:

$$N = -\frac{2V_2^2\sqrt{2\pi}v_2k\sigma_{nom}\ln y}{B2\left[\ln \frac{k}{k_{c2}}\right]^2} \tag{5.24}$$

After straightening n unit nodes, the equation can be expressed as Eq. 5.25:

$$2V_2^2\sqrt{2\pi}v_2k\sigma_{nom}\ln y = -\frac{(k_{n+1} - k_n)\left(\frac{\ln y_{n+1}}{\ln x_{n+1}} - \frac{\ln y_n}{\ln x_n}\right)}{(k_n - k_{n-1})\left(\frac{\ln y_n}{\ln x_n} - \frac{\ln y_{n-1}}{\ln x_{n-1}}\right)} \tag{5.25}$$

Therefore, the straightening coefficient N can be calculated as Eq. 5.26:

$$N = N_1 - k_1\tan\beta + k\tan\beta \tag{5.26}$$

Substituting the value of N into the original equation, u_2 can be solved, which ranges from 96.7 ± 11.72, k_{c2} ranges from 5.87 ± 0.48, v_2 ranges from 0.31 ± 0.6, and B_2 ranges from −315.58 ± 55.46. After adjustment, the fitting goodness is 0.97812. In general, increasing the order of the fitting polynomial can effectively improve the fitting accuracy. To accurately predict the relationship between SCF at the center of the curved edge of IBS and the curvature under an overload of 50000g, a cubic polynomial is used to fit the data. The fitting function model is expressed as Eq. 5.27:

$$SCF(k) = \frac{a_5k^3 + b_5k^2 + c_5k + d_5}{\sigma_{nom}} \tag{5.27}$$

where a_3, b_3, c_3, and d_3 are parameter values. To ensure that the predicted values are closer to the true calculated data, the sum of squared errors for all reference points needs to be minimized as Eq. 5.28:

$$\sum_i^n \left[SCF(k_i) - y_i\right]^3 \to 0 \tag{5.28}$$

Expressed in the form of a cubic polynomial function as Eq. 5.29:

$$d_3N + c_3\sum_{i=1}^{N} k_i + b_3\sum_{i=1}^{N} k_i^2 + a_3\sum_{i=1}^{N} k_i^3 = \sum_{i=1}^{N} SCF_i \tag{5.29}$$

After matrix transformation, it can be expressed as Eq. 5.30:

$$\begin{Bmatrix} N & \sum_{i=1}^{N} k_i & \sum_{i=1}^{N} k_i^2 & \sum_{i=1}^{N} k_i^3 \\ \sum_{i=1}^{N} k_i & \sum_{i=1}^{N} k_i^2 & \sum_{i=1}^{N} k_i^3 & \sum_{i=1}^{N} k_i^4 \\ \sum_{i=1}^{N} k_i^2 & \sum_{i=1}^{N} k_i^3 & \sum_{i=1}^{N} k_i^4 & \sum_{i=1}^{N} k_i^5 \\ \sum_{i=1}^{N} k_i^3 & \sum_{i=1}^{N} k_i^4 & \sum_{i=1}^{N} k_i^5 & \sum_{i=1}^{N} k_i^6 \end{Bmatrix} \begin{Bmatrix} d_3 \\ c_3 \\ b_3 \\ a_3 \end{Bmatrix} = \begin{Bmatrix} \sum_{i=1}^{N} SCF_i \\ \sum_{i=1}^{N} k_iSCF_i \\ \sum_{i=1}^{N} k_i^2SCF_i \\ \sum_{i=1}^{N} k_i^3SCF_i \end{Bmatrix} \tag{5.30}$$

where a_3 ranges from 17.6 ± 10.5; b_3 ranges from −378.71 ± 21.73; c_3 ranges from 2,750.46 ± 1.5; and d_3 ranges from −6,584 ± 36.13. After adjustment, the fitting goodness is 0.98668.

5.4 SCFAnalysis of SCF prediction errors

To meet engineering design requirements, it is necessary to verify the accuracy of SCF fitting function predictions. In practical applications of penetrating projectile engineering, project technical specifications require that the error in SCF predictions be within 15%. Therefore, Matlab's numerical computation and functions can be utilized to solve the error level of SCF fitting in complex engineering problems involving penetrating projectiles, and to visualize the results of the calculations. The 'assume' function in Matlab's Symbolic Math Toolbox is used to specify the properties of the coefficients, and the 'constraint' function is used to define the

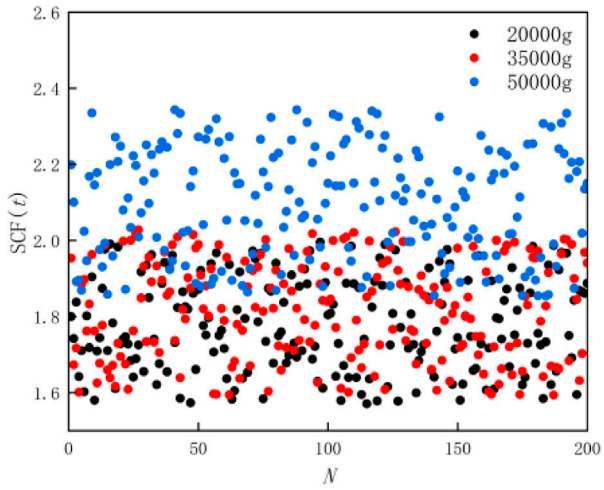

FIGURE 11
Predicted values of SCF for wall thickness.

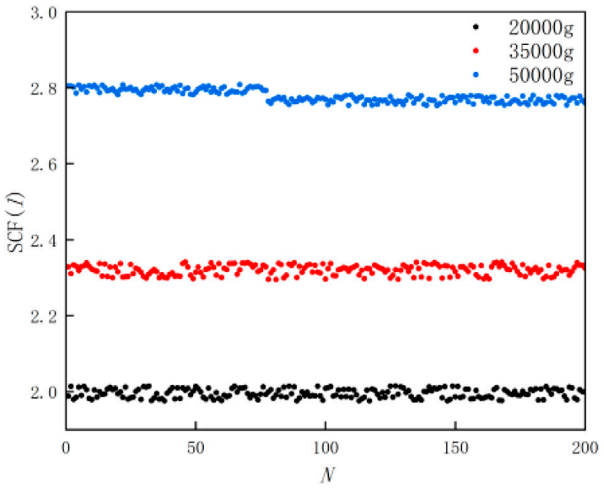

FIGURE 12
Predicted values of SCF for side length.

range of coefficient values obtained from the previous solution. Taking the wall thickness $t = 0.69$, the output SCF prediction error analysis results are shown in Figure 11.

In Figure 11, N represents the number of iterations, i.e., the number of samples. The black dots represent the predicted values of SCF at the center of the curved edge under 20000 g overload, the red dots represent the predicted values under 35000 g overload, and the blue dots represent the predicted values under 50000 g overload. As calculated earlier, when the wall thickness $t = 0.69$, the corresponding SCF values are 1.783, 1.811, and 2.093 respectively. The maximum deviation under 20000 g overload is 1.96, with an error of 9.97%; under 35000 g overload, the maximum deviation is 1.695, with an error of 6.4%; under 50000 g overload, the maximum deviation is 2.493, with an error of 11.94%. By organizing the data, it was found that the prediction error under overload of 35000 g was the smallest, and the SCF prediction values under overload of 20000g and 36000 g were relatively close. This is because there is a non-linear relationship between the maximum deviation and overload during high-speed penetration. As the overload increases, the buffer material approaches the yield limit faster, and plastic collapse energy absorption is more efficient. Taking the edge length $l = 6.4$, the output SCF prediction error analysis results are shown in Figure 12.

As calculated earlier, when the edge length $l = 6.4$, the corresponding SCF values are 1.995, 2.318, and 2.781 respectively. The maximum deviation under 20000 g overload is 1.975, with an error of 0.98%; under 35000 g overload, the maximum deviation is 2.341, with an error of 0.99%; under 50000 g overload, the maximum deviation is 2.753, with an error of 1.02%. The calculation found that the SCF prediction value about the edge length is the most accurate, because SCF is least affected by the edge length, and stress concentration mainly occurs in the vertical direction of the cell, that is, parallel to the loading direction. Taking the curvature $k = 2.2$, the output SCF prediction error analysis results are shown in Figure 13.

As calculated earlier, when the curvature $k = 2.2$, the corresponding SCF values are 2.32, 3.167, and 3.628 respectively. The maximum deviation under 20000 g overload is 2.098, with an error of 9.57%; under 35000 g overload, the maximum deviation is 2.885, with an error of 8.89%; under 50000 g overload, the maximum deviation is 3.978, with an error of 9.64%. The prediction errors of SCF for curvature are all less than 10%, with SCF prediction values closer under overload of 35000g and 50000 g. Unlike traditional concave hexagonal honeycomb structures, the deformation of IBS is dominated by bending due to the presence of initial curvature, which can increase the equivalent modulus of honeycomb structures. The predicted results all meet engineering technical specifications. Therefore, the nonlinear fitting curves of SCF proposed in this paper can meet the practical application requirements of penetrating projectile engineering.

6 Dynamic stress concentration in potting material under stress wave incidence

6.1 Wave function model

To ensure the reliable operation of explosive devices in ultra-high-speed penetration environments, they are typically sealed with materials such as epoxy resin and polyurethane to enhance their impact resistance. However, during the sealing process, defects such as bubbles and cracks may occur due to poor colloidal flow or insufficient mixing. These defects can lead to dynamic stress concentration under stress wave action, causing uneven stress distribution in the sealed body's circuit board. Consequently, the electronic components of the explosive device may become detached, and in more severe cases, the circuit board may fracture, resulting in device failure. Therefore, investigating the problem of dynamic stress concentration in sealed materials containing defects is of significant theoretical and engineering importance. The model of stress wave incidence during penetration is illustrated in Figure 14.

Assuming the radius of bubbles in the potting material is r, the primary stress wave during penetration is predominantly

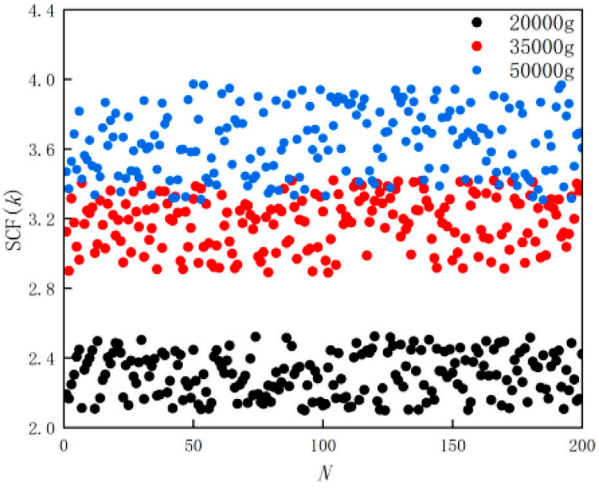

FIGURE 13
Predicted values of SCF for curvature.

longitudinal, with the incident direction along the positive X-axis. Its wave velocity is given as Eq. 6.1:

$$c = \sqrt{\frac{\lambda + 2\mu}{\rho}} \tag{6.1}$$

where λ and μ are Lamé constants; ρ is the density of the potting material; and a and b are the distances from the bubble center to the upper and lower boundaries, respectively. In the theory of elastic wave motion, the expression for the spatial displacement component u of a particle's motion equation is presented as Eq. 6.2:

$$\mu\nabla^2 u + (\lambda + \mu)\delta u = \rho\ddot{u} \tag{6.2}$$

The wave propagation equation inside the elastic body can be expressed as Eq. 6.3:

$$\begin{aligned} &\mu_m\nabla^2 u + (\lambda_m + \mu_m)\nabla_0(\nabla_0 u) = \rho\frac{\partial^2 u}{\partial t^2} \\ &\lambda_m = \frac{Ev}{(1+v)(1-2v)} \\ &\mu_m = \frac{Ea^2}{18(2-v^2)} \\ &\nabla_0 = \frac{\partial^2 u}{\partial x^2} + \frac{\partial^2 u}{\partial y^2} + \frac{\partial^2 u}{\partial t^2} \end{aligned} \tag{6.3}$$

where λ_m and μ_m are Lamé constants of the potting material; ∇ is Laplace operator; E is the elastic modulus of the potting material; and v is Poisson's ratio of the potting material. The stress on the sealed material's plane transmitted is given as Eq. 6.4:

$$\begin{aligned} \sigma_{xt} &= \lambda\left(\frac{\partial u_x}{\partial t} + \frac{\partial u_y}{\partial \vec{t}}\right) = \lambda\left(\frac{\partial u_x}{\partial t}e^{i\alpha} + \frac{\partial u_x}{\partial \vec{t}}e^{\alpha}\right) \\ \sigma_{yt} &= \lambda\left(\frac{\partial u_x}{\partial t} - \frac{\partial u_y}{\partial \vec{t}}\right) = \lambda\left(\frac{\partial u_x}{\partial t}e^{i\alpha} + \frac{\partial u_x}{\partial \vec{t}}e^{-\alpha}\right) \end{aligned} \tag{6.4}$$

This study does not consider the displacement situation of the explosive device boundary, which belongs to a stress boundary value problem. It requires solving the unknown coefficients in the displacement expression. The stress boundary conditions can be solved by utilizing the continuity conditions at the interface between the potting material and the explosive device. The boundary condition expression is obtained as Eq. 6.5:

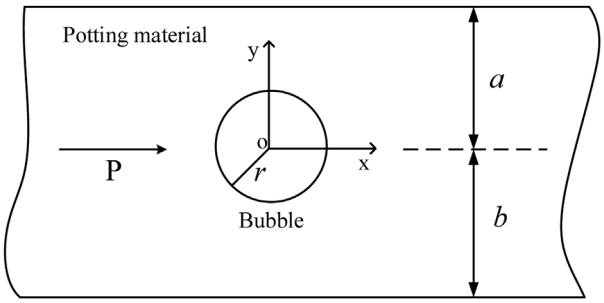

FIGURE 14
Bubble model of potting material under stress wave action.

$$\begin{cases} u_{x'} + iu_{y'} = u_{x''} + iu_{y''} \\ u_{x'} - iu_{y'} = u_{x''} - iu_{y''} \\ \sigma_{x'} + i\sigma_{xy'} = \sigma_{x''} + i\sigma_{xy''} \\ \sigma_{x'} - i\sigma_{xy'} = \sigma_{x''} - i\sigma_{xy''} \end{cases} \tag{6.5}$$

where σ_x and σ_y are the radial and tangential stresses of the potting material, respectively. At the internal interface of the potting material, considering the contact surface model between the potting material and the explosive device as ideal contact, the unknown coefficients can be solved by using the interface continuity condition and the stress-free condition on the inner surface of the potting material.

6.2 Dynamic stress concentration factor (DSCF)

When a stress wave enters a potting material containing bubbles, it encounters scattering due to bubbles, cracks, and indentations, generating new wave sources that spread outwards. Due to the combined action of the explosive device interface and bubbles, there is a significant increase in stress in the local area around the bubbles, leading to the rupture of the explosive device interface and the inner surface of the bubbles. Therefore, DSCF is used to characterize the scattering of stress waves. The form of stress wave scattering is given as Eq. 6.6:

$$P_{xy}^{(s)} = \sum_{n=0}^{k} C_n\left\{W_n\left(\frac{\tau_x}{|\tau_x|}\right)^n + \left(\frac{\tau_y}{|\tau_y|}\right)^{-n}\right\} \tag{6.6}$$

where C_n is an undetermined coefficient, which can be obtained by solving the boundary conditions of the bubble. At this time, the boundary condition is that the stress in the positive X-axis direction is 0. To obtain a steady-state solution, a variable is introduced, defined as Eq. 6.7:

$$\begin{cases} W = k_n e^{\left[t_x(1-i\omega)+t_y(1+i\omega)\right]} \\ F = k_n e^{\left[t_x(1-i\bar{\omega})+t_y(1+i\bar{\omega})\right]} \\ f = k_n e^{-i\omega t} \end{cases} \tag{6.7}$$

where ω is the oscillation frequency of the stress wave. It can be derived that the wave number of the scattered wave satisfies the equation as Eq. 6.8:

$$\alpha_{xy}^{n} = \frac{1}{2}\left[(2-\nu)k_n^2 + \sqrt{(4-\nu)^2 k_n^2 + 12(1-\nu)k_n^3\left(\frac{2}{k_n^2 a^2} - \frac{1-6\nu}{(1+\nu)(1-\nu)}\right)}\right] \tag{6.8}$$

By combining the particle displacement function and the displacement potential function, the general solution of 2D wave equation in the potting material can be obtained as Eq. 6.9:

$$\begin{cases} W = \sum_{m=1}^{k}\sum_{n=1}^{2} G_{mn} H_n^i(\alpha_m r)e^{i\omega} \\ F = \sum_{m=1}^{k}\sum_{n=1}^{2} G_{mn} H_n^i(\alpha_m r)e^{i\omega} \\ f = \sum_{m=1}^{k} G_n K_n^i(\beta_m r)e^{i\omega} \end{cases} \tag{6.9}$$

where G represents the scattering coefficient of the n th bubble. Based on the obtained incident wave field and scattered wave field of the stress wave in the bubble, the total displacement field and total stress field in the potting material can be obtained as Eq. 6.10:

$$\begin{aligned} u_t &= \int_{r_1}^{r_n} \tau_{\alpha i}^{i}\big|_{r=r_0} p(r,\alpha)\, d\vec{r}_0 \\ \sigma &= \int_{r_1}^{r_n} \tau_{\alpha i}^{i}\big|_{r=r_0} \mu \frac{\partial p(r,\alpha)}{\partial r}\, d\vec{r}_0 \end{aligned} \tag{6.10}$$

DSCF under stress wave scattering is defined as Eq. 6.11:

$$DSCF = \int_{r_1}^{r_2} r_{i\alpha}^{t}\big|_{r=r_0} \mu \frac{\partial P}{\partial \alpha}\Big|_{r=r_0} dr_0 \tag{6.11}$$

The formula for calculating the dynamic stress concentration coefficient in the presence of bubbles is as Eq. 6.12:

$$DSCF = \left|\frac{\sigma_{i\alpha}}{\sigma_{i0}}\right| \tag{6.12}$$

In the formula, the numerator represents the stress around the bubble, and the denominator represents the maximum amplitude of stress caused by the incident stress wave.

6.3 DSCF case analysis

Based on the theoretical wave function model derived in this paper, taking circular bubbles in the potting material as an example, programming calculations were performed using Matlab. The bubble radius ranges from r = 0.5–0.9mm, the incident angle is α, the density of the potting material for the penetrating detonator ρ is 1119 kg/m^3, the elastic modulus E is 3.02 × 103MPa, the Poisson's ratio ν is 0.37, and the dimensionless wave number Ka = 0.5-3.5. The bubble depth ratio a/h is dimensionless, with parameters k_1/k_2 = 0.2 and μ_1/μ_2 = 1.5. The distribution curve of the dimensionless DSCF on the surface of circular bubble cavities under the action of penetrating stress waves is shown in Figure 15.

Figure 15A illustrates the variation of DSCF around the bubble with the dimensionless wave number Ka. DSCF is significantly impacted by the wave number. DSCF is symmetrically distributed along the X-axis and increases with the increase of wave number. When Ka = 2, the maximum value of DSCF is 2.91, occurring at positions 118° and 242°.

Figure 15B shows the variation of DSCF around the bubble with the bubble radius r. DSCF does not change significantly with the bubble radius, and stress concentration phenomena mainly occur at the 90° and 270° directions. When the bubble radius is 0.7, the maximum value of DSCF is 3.48.

Figure 15C depicts the variation of DSCF around the bubble with the bubble depth ratio a/h. When the bubble depth ratio is 0.2 and 0.4, the maximum value of DSCF occurs at positions 220° and 230°, respectively, while for a/h = 0.6, the maximum value of DSCF occurs at position 210°. This is due to the increased oscillations near the tail of the projectile when it contacts the top end and the target plate.

Figure 15D presents the variation of DSCF around the bubble with the incident frequency f. The highest DSCF values appear on the side opposite to the projectile impact. As the incident frequency of stress waves increases, the noise in the curve increases, and DSCF gradually decreases. When f = 50Hz, the maximum value of DSCF is 2.22, occurring at 135°.

Based on the above analysis, in the process of structural optimization, attention should be paid to the strength and stability of the projectile tail, and solid materials should be filled around the contact between the projectile tail and the fuze. In addition, exhaust holes should be designed during the sealing process to allow gas to be fully discharged and reduce the presence of bubbles in the sealing material.

7 Dynamic impact testing of optimal buffering scheme

This article uses a single impact table (device impact overload>50,000 g, impact pulse width ≥231) μ s) Conduct experimental research on the protective characteristics of penetration fuze buffer materials. When the test projectile launched by the air gun comes into contact with the cutting board, it will generate an instantaneous peak value shock overload, which is transmitted in the form of stress waves from the contact point between the projectile and the cutting board to the interior of the projectile. This is used as the system input shock to excite the test device installed inside the test projectile. The shock table device is shown in Figure 16.

Combined with the calculated results from earlier sections, the optimal cell geometry parameters are shown in Table 4. IBS solid materials were manufactured using 3D printing technology, as depicted in Figure 17.

The impact wave-related parameters of the detonator casing, potting material reinforcement layer, and circuit board are shown in Table 5.

The pressure inside the chamber is controlled by the intake volume, thereby controlling the launch speed. The sensitivity of the pressure resistance sensor used in the overload signal recovery

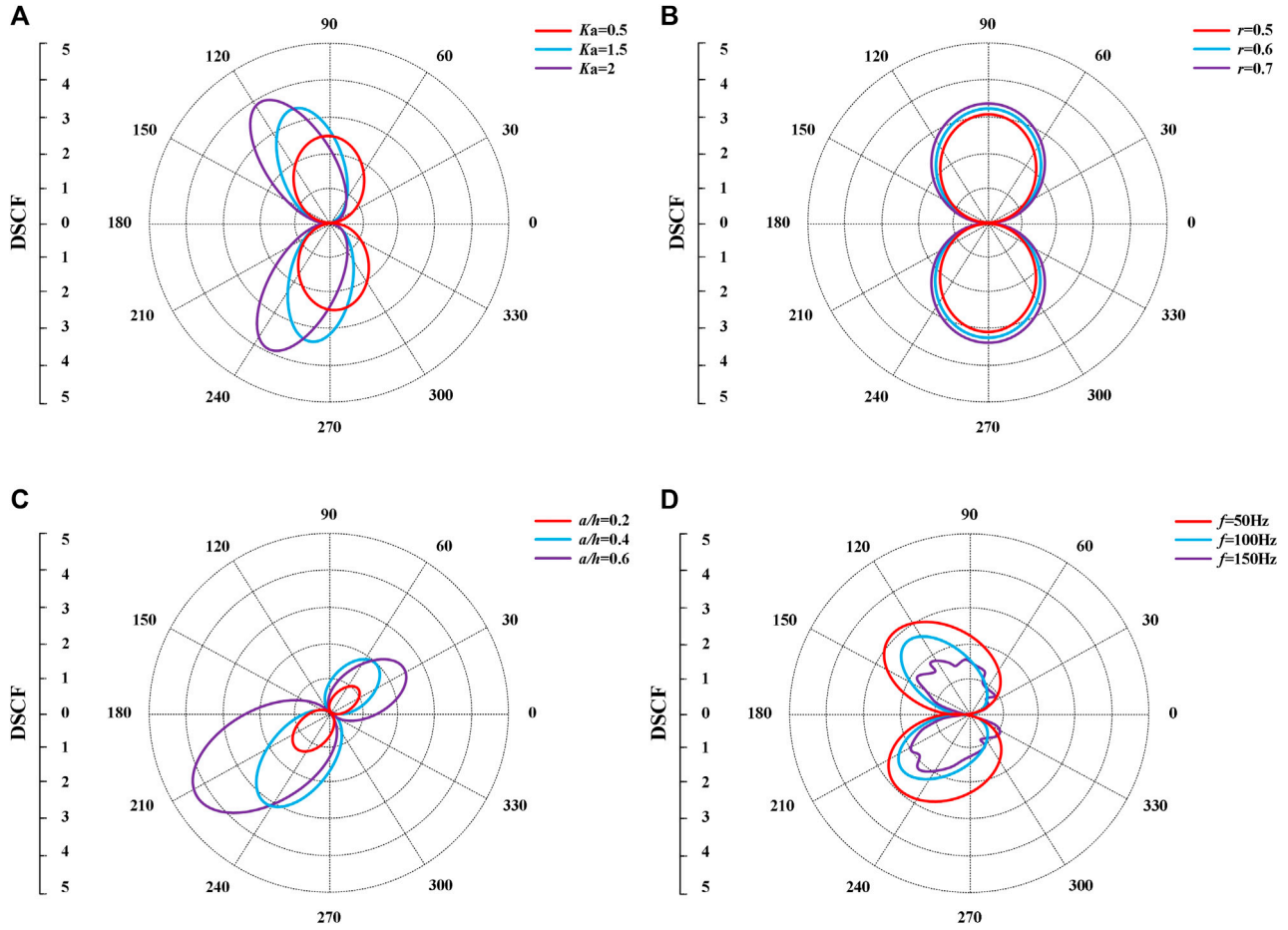

FIGURE 15
Distribution of DSCF in fuze potting material. **(A)** Relationship between DSCF and wave number. **(B)** Relationship between DSCF and radius. **(C)** Relationship between DSCF and depth. **(D)** Relationship between DSCF and frequency.

device is 0.8 μ V/g, with a magnification of 30 times. Conduct impact tests at different initial velocities, and the measured acceleration overload signal is shown in Figure 18.

In Figure 18, at an initial velocity of 50 m/s, the peak acceleration overload of the detonator without IBS buffering protection is 38,560g, while with IBS protection, the overload peak is 23,360g, resulting in a reduction rate of 39.42%. At an initial velocity of 70 m/s, the overload peak without IBS is 51,668g, while with IBS protection, the overload peak is 34,685g, resulting in a reduction rate of 32.87%. This reduction is attributed to the fact that when the stress wave reaches the interface between the base and the buffering structure, the plastic collapse of the buffering structure absorbs a large amount of kinetic energy from the detonator, resulting in a decrease in overload peak. The high wave impedance of the detonator potting material causes the transmitted wave to be weaker than the incident wave, thereby attenuating the stress wave and protecting the internal electronic components of the detonator, allowing them to record experimental data intact. Reference [11] used a conventional rubber buffer gasket with an overload peak of 470,000 g under the same working condition, and the combined buffer scheme in this paper reduced the maximum overload by 12315 g compared to it. The experimental data indicate that the combined buffering protection impact of IBS and potting material is significant. The effectiveness and scalability of this method have been demonstrated, and the missile storage system has survived well with normal data recovery. It can be correctly recorded and read back, meeting the design requirements of fast response, high tracking accuracy, and good stability of the fuze control system. It can be used as a buffer protection for fuze in typical penetration environments, high overload, and strong impact. The dynamic impact test further verifies the engineering applicability of this method.

8 Conclusion

This study calculated the basic mechanical properties of IBS, elucidated the energy absorption mechanism of IBS penetration process, and developed a theoretical mechanical model for in-plane uniaxial loading. Through finite element analysis, a comparison was made between IBS and traditional concave hexagonal structures, and the stress distribution in key areas of both was analyzed. SCFs of IBS curved edges under different penetration overloads were calculated, and the impact of geometric parameters such as cell wall thickness, aspect ratio, and curvature on SCF was further analyzed. A nonlinear fitting function for SCF was established, and a method for predicting

FIGURE 16
Single impact platform.

TABLE 4 Cell geometric parameters.

Parameter	Value
Thickness t/mm	0.6
Inclination angle θ/(°)	45
Curvature k	1.5
Height h/mm	1.4
Side length L/mm	6

SCF at peak stress locations in IBS was proposed, with the accuracy of SCF fitting function predictions being validated. To more precisely explain the phenomenon of stress wave propagation and scattering, and to accurately determine the location of dynamic stress concentration in the potting material, numerical results of DSCF around the bubbles under different physical parameters were provided. Finally, dynamic impact testing was conducted on the combined buffering protection scheme. The main conclusions are outlined as follows:

1) Throughout the stages of the penetration process, the degree of stress concentration in traditional structures is greater than that in IBS, indicating that IBS provides better buffering protection for fuze.

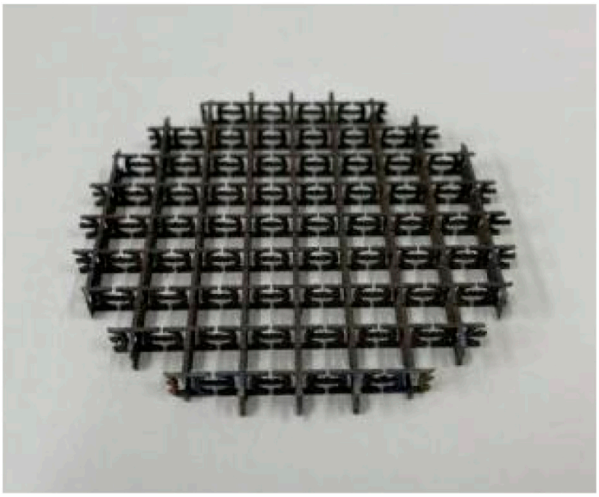

FIGURE 17
IBS solid material.

TABLE 5 Material impedance parameters.

Material	ρ/g·cm^{-3}	$C/10^3$ ms	ρC (10^6Pa)·m^{-1}·s^{-1}
Fuze casing	2.77	5.09	14.10
Polyurethane	1.20	0.75	0.90
Epoxy resin	1.20	1.35	1.62
Circuit board	1.80	3.05	5.49

2) In the context of the same penetration overload, the peak stress decreases with the increase of wall thickness. For cells with the same wall thickness, as the penetration overload increases, the peak stress also increases. Additionally, cells with smaller wall thickness show a more pronounced response to overload. The impact of side length on peak stress is negligible. The peak stress increases with the increase of curvature. Cells with larger curvature exhibit a more pronounced response to overload.
3) DSCF around the bubbles in the potting material is significantly impacted by the dimensionless wave number, showing symmetrical distribution along the X-axis and increases with the increase of wave number. The change in DSCF with bubble radius (r) is not significant. With increasing bubble depth, DSCF also increases, emphasizing the importance of the strength and stability of the projectile tail section. Low-frequency stress wave incidence has a more severe impact on bubble DSCF.
4) The overload peak attenuation rates are 39.42% at an initial velocity of 50 m/s and 32.87% at an initial velocity of 70 m/s. IBS effectively protects the internal electronic components of fuze, demonstrating significant buffering protection effectiveness.

With the strengthening of future construction projects, fuze will face more severe tests. Future fuze buffer materials should have the characteristics of lightweight, higher specific energy absorption, better filtering performance, easy processing, easy installation, and high forming accuracy.

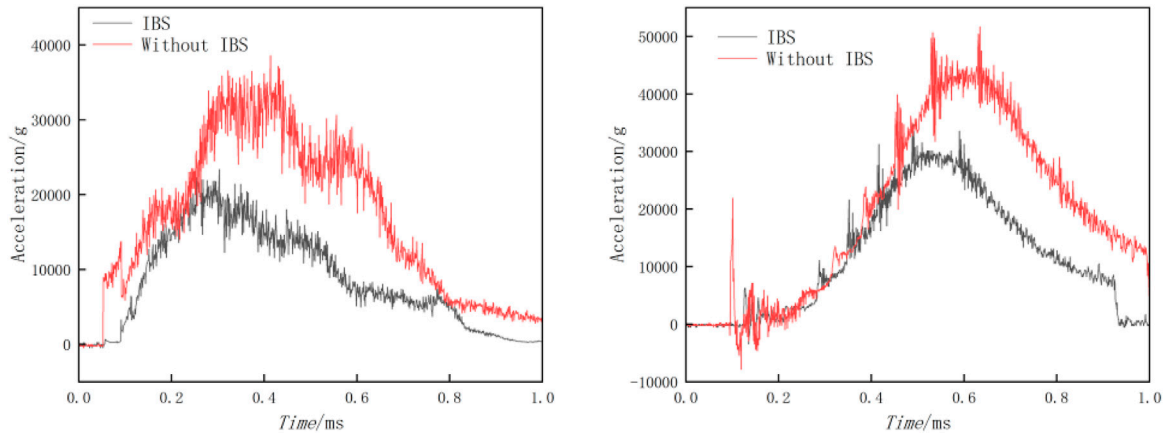

FIGURE 18
Impact signal measured through accelerometer. **(A)** V0 = 50 m/s. **(B)** V0 = 70 m/s.

Data availability statement

The original contributions presented in the study are included in the article/supplementary material, further inquiries can be directed to the corresponding author.

Author contributions

AZ: Data curation, Visualization, Writing–original draft, Writing–review and editing. PL: Methodology, Software, Writing–review and editing. HZ: Funding acquisition, Project administration, Supervision, Writing–review and editing.

Funding

The author(s) declare that financial support was received for the research, authorship, and/or publication of this article. This study has received support from the National Natural Science Foundation of China, with the Project No. 61403201.

Conflict of interest

The authors declare that the research was conducted in the absence of any commercial or financial relationships that could be construed as a potential conflict of interest.

Publisher's note

All claims expressed in this article are solely those of the authors and do not necessarily represent those of their affiliated organizations, or those of the publisher, the editors and the reviewers. Any product that may be evaluated in this article, or claim that may be made by its manufacturer, is not guaranteed or endorsed by the publisher.

References

1. Ding C, Chen B, Li WA, Gao D, Chen Y, Feng J. A numerical study on projectile penetration into underwater Torpedo warhead. *J Phys Conf Ser* (2023) 2478:072043. doi:10.1088/1742-6596/2478/7/072043

2. Li XL, Zhao EL, Liu ZT, Liu Y, Feng X, Gu Z. Experimental study on multiple propagation characteristics of stress wave and surface displacement behavior in coal based on SHPB and DIC. *Bull Eng Geology Environ* (2023) 82:246. doi:10.1007/s10064-023-03272-7

3. Ma HR, Sun H, Li CS, Penetration overload prediction method based on a deep neural network with multiple inputs. *Appl Sciences-Basel* (2023) 13:2351. doi:10.3390/app13042351

4. Mei L, Song XM, Wang WB. Study on the dimensionless model of high-speed penetration efficiency. *Appl Mech Mater* (2015) 789:362–7. doi:10.4028/www.scientific.net/AMM.789-790.362

5. Poonam Malik S, Antil A, Kumar K, Nautiyal RC. Impact of initial stress on wave propagation in exponentially graded isotropic nonlocal generalized thermoelastic solid medium. *Mech Sol* (2023) 58(3):939–60. doi:10.3103/s0025654423600320

6. Surana KS, Abboud E. Deviatoric stress waves due to rheology in incompressible thermoviscoelastic solid medium with small strain, small deformation physics. *Meccanica* (2023) 58(4):755–79. doi:10.1007/s11012-023-01646-5

7. Xiao Y, Li C, Miao C. Analysis of overload response characteristics of high-speed penetration of composite heterogeneous warhead. *Proc SPIE* (2023). doi:10.1117/12.2680731

8. Zhang H, Niu S, Analysis the influence of projectile penetration velocity and length - diameter ratio on fuze overload signal adhesion. *J Phys Conf Ser* (2023) 2478:072035. doi:10.1088/1742-6596/2478/7/072035

9. Zhang JS, Wang Y, Wu JP, Zhou J, Wang W, Liu S, et al. STF-filled biomimetic variable stiffness hierarchic porous material with impact resistance, thermal insulation, and sensing. *Chem Eng J* (2023) 477:146939. doi:10.1016/j.cej.2023.146939

10. Li GW, Tan LC, Ren LQ, Zheng A, Li Y, He Z, et al. Biomimetic 4D printing of dome-shaped dynamic mechanical metamaterials. *J Mater Res Tech* (2023) 24:4047–59. doi:10.1016/j.jmrt.2023.04.039

11. Ding LB, Zhang A, Peng JW, Li CS. The protective performance of rubber pads for penetration fuze. *Front Mater* (2023) 10:1284738. doi:10.3389/fmats.2023.1284738

frontiers | Frontiers in Physics

TYPE Original Research
PUBLISHED 19 June 2024
DOI 10.3389/fphy.2024.1428875

OPEN ACCESS

EDITED BY
Pei Li,
University of Southern Denmark, Denmark

REVIEWED BY
Zhe Liu,
Xi'an Jiaotong University, China
Lu Meng,
Taiyuan University of Technology, China

*CORRESPONDENCE
Yanming Xu,
xuyanming@ustc.edu

RECEIVED 07 May 2024
ACCEPTED 28 May 2024
PUBLISHED 19 June 2024

CITATION
Xu Y and Yang S (2024), Sensitivity analysis of non-uniform rational B-splines–based finite element/boundary element coupling in structural-acoustic design.
Front. Phys. 12:1428875.
doi: 10.3389/fphy.2024.1428875

Sensitivity analysis of non-uniform rational B-splines–based finite element/boundary element coupling in structural-acoustic design

Yanming Xu[1]* and Sen Yang[1,2]

[1]Henan International Joint Laboratory of Structural Mechanics and Computational Simulation, College of Architectural and Civil Engineering, Huanghuai University, Zhumadian, China, [2]College of Architecture and Civil Engineering, Xinyang Normal University, Xinyang, China

For the purpose of modeling the acoustic fluid-structure interaction using direct differentiation method and conducting a structural-acoustic sensitivity analysis, a coupling approach based on the finite element method and the fast multipole boundary element method is suggested. Non-uniform rational B-splines isogeometric analysis bypasses the difficult volume parameterization procedure in the isogeometric finite element method and the time-consuming meshing process in classical finite element/boundary element method, allowing numerical analysis on computer-aided design models to be completed directly. The finite element/fast multipole boundary element method based on non-uniform rational B-splines isogeometric analysis enables the numerical prediction of the effects of arbitrarily formed vibrating structures on the sound field. Several numerical examples are shown to demonstrate the usefulness and efficiency of the proposed method.

KEYWORDS

FEM, FMBEM, NURBS, structural-acoustic coupling, sensitivity analysis

1 Introduction

The investigation of acoustic radiation or scattering from elastic objects in fluid is a common topic. Acoustic fluid-structure interaction problems Junger and Feit [1] can only be analytically solved when the structure has simple geometry and boundary conditions. More complex geometries in real life make analytical solutions unfeasible; thus, effective numerical techniques need to be developed.

The finite element method (FEM) has been widely used to study the dynamic behavior of issues including acoustics, fracture mechanics, electromagnetics, and fluid-structure interactions. However, when modeling infinite domains, there are several issues with the FEM. As is well known, because BEM provides excellent accuracy and simple mesh creation, it has been employed successfully to solve acoustic problems. The Sommerfeld radiation condition at infinity is quickly met, especially for external acoustic issues SOMMERFELD [2]. Using the Galerkin technique for BEM implementation, the boundary integral problem has been quantitatively addressed Engleder [3]; Chen et al. [4]. Nonetheless, the collocation approach has always been preferred by the technical community. As a result, the coupling FEM/BEM technique is appropriate for examining fluid-structure interaction issues Everstine and Henderson [5]; Fritze et al. [6]; Chen et al. [7].

However, coupling analysis of underwater structural-acoustic problems remains the bottleneck of high computational cost because CBEM generates a dense and non-symmetric coefficient matrix that requires $O(N^3)$ arithmetic operations to directly resolve the equation system, for example, when employing the Gauss elimination approach. Many techniques have been used to speed up the resolution of the integral problem, including the fast multipole method (FMM), the fast direct solver, and the adaptive cross approximation approach. Martinsson and Rokhlin [8,9] created the fast direct solver. It works well for issues requiring somewhat ill-conditioned matrices and rapidly produces a simplified factorization of the matrix's inverse. The adaptive cross approximation technique developed by Bebendorf and Rjasanow [10] generates blockwise low-rank approximants from the BEM matrices for situations requiring a large number of repetitions.

Since FMM was developed, it is now possible to solve the CBEM system of equations more rapidly Greengard and Rokhlin [11]; Coifman et al. [12]; Rokhlin [13]. Therefore, large-scale fluid-structure interaction issues may be handled by employing a coupling technique based on FEM/fast multipole boundary element method (FEM/FMBEM) Schneider [14]. The coupling method FEM/FMBEM is also suggested by this work to address the difficult fluid-structure interaction challenges.

Increasingly, architects and designers are considering noise control through structural geometry modifications. This structural-acoustic optimization offers a significant deal of potential to reduce radiated noise Kim and Dong [15]; Chen et al. [16]; Qu et al. [17]. Acoustic design sensitivity analysis is a crucial step in the processes of acoustic design and optimization since it can show how a geometry change affects the structure's acoustic performance. A summary of the development of structural-acoustic optimization for noise removal is provided by Marburg [18]. Due to its ease of use, the finite difference method (FDM) has been widely applied in structural-acoustic optimization Lamancusa [19]; Hambric [20]; Marburg and Hardtke [21]. However, this method performs poorly, particularly when several design parameters are taken into account simultaneously. Use the direct differentiation method (DDM) Zheng et al. [22]; Liu et al. [23] or the adjoint variable method (AVM) Choi et al. [24]; Wang [25] to solve this issue. It is well knowledge that the most time-consuming part of the gradient-based optimization process is the sensitivity analysis for the fluid-structure interaction issue. This study subjects the coupling technique FEM/FMBEM to the structural-acoustic sensitivity analysis based on DDM to expedite the analysis.

FEM and BEM may be used in computer-aided engineering (CAE), with the aid of appropriate software. However, as part of the preprocessing stage, modern CAE demands that the models created by CAD software be transformed into simulation-ready models. Geometry mistakes are caused by the CAE's transmission of geometric model data. The combination of BEM with geometric modeling and numerical simulation using isogeometric analysis (IGA) Hughes et al. [26]; Chen et al. [27]; Shen et al. [28] is one suggested solution to this issue Simpson et al. [29,30]. Thanks to IGABEM, geometric mistakes and time-consuming preprocessing procedures may be avoided, and numerical simulation may be carried out straight from the precise models. Since its inception, IGABEM has been used to address a wide range of issues, including elastic mechanics Scott et al. [31], potential problems Takahashi and Matsumoto [32]; Chen et al. [7]; Zhang et al. [33], heat transfer problems Cao et al. [34], wave propagation Ginnis et al. [35]; Chen et al. [36]; Zhang et al. [37–40], fracture mechanics Shen et al. [41], electromagnetics Simpson et al. [42]; Xu et al. [43]; Chen et al. [44]; Li et al. [45]; Qu et al. [46–48], and structural optimization Chen et al. [49]; Xu et al. [50]; Li et al. [51]; Chen et al. [52]; Lian et al. [53]; Chen et al. [54]; Lu et al. [55]; Chen et al. [56]. In this work, the non-uniform rational B-splines (NURBS) IGABEM is employed.

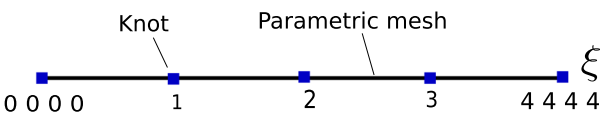

FIGURE 1
The one-dimensional parametric space for a knot vector.

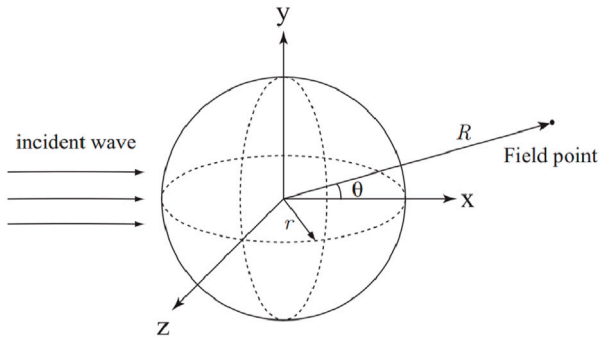

FIGURE 2
Diagram of the spherical shell model with incoming wave.

In this study, NURBS IGA is utilized in model constructing to eliminate geometric mistakes and increase calculation accuracy. FEM and BEM are combined to form structural-acoustic coupling sensitivity analysis. FMM is applied to speed up the calculation procedure. For problems requiring fluid-structure interaction and structural acoustic sensitivity evaluations, coupling FEM/FMBEM is advised. Numerical examples illustrate the accuracy and efficiency of this approach.

2 Derivation of the non-uniform rational B-splines (NURBS)

This section gives the basic NURBS concepts that form the foundation of the isogeometric analysis. For further details, the readers are referred to Hughes et al. [26]. A fundamental concept in NURBS is the knot vector, which is composed of a set of non-decreasing real integers expressed as in Eq. 1.

$$\Xi = \left[\xi_1, \xi_2, \ldots, \xi_{n+p+1}\right], \quad \xi_a \in \mathbb{R}, \tag{1}$$

where ξ_i is the real integer, a is the knot index, p is the polynomial order, and n is the total number of basis functions. A knot vector

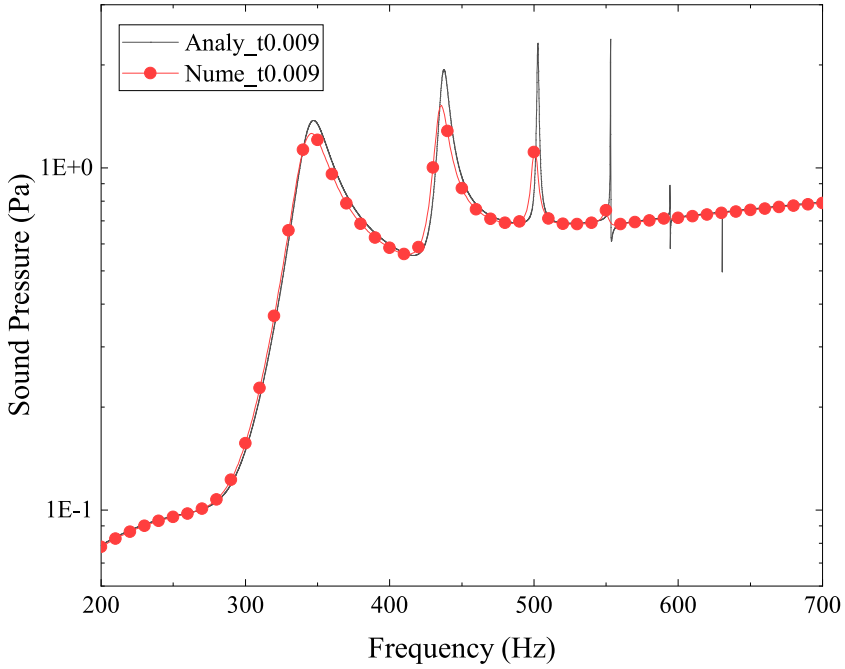

FIGURE 3
Sound pressure at location (3, 0, 0) for spherical shell model, numerical result vs. analytical result. The radius r = 0.9 m, shell thichness t = 0.009 m.

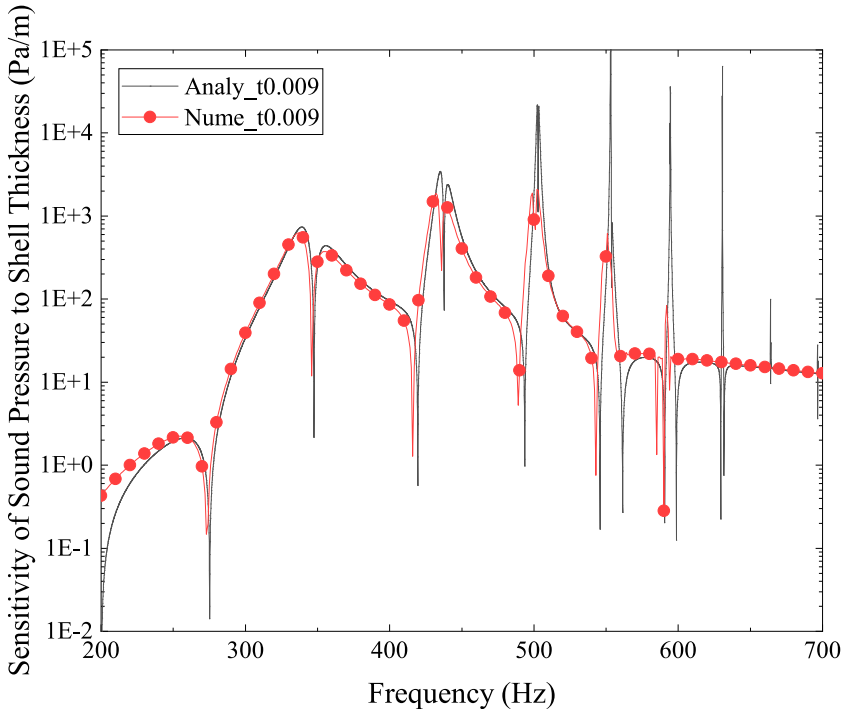

FIGURE 4
Sensitivity of sound pressure to shell thickness at location (3, 0, 0) for spherical shell model, numerical result vs. analytical result. The radius r = 0.9 m, shell thichness t = 0.009 m.

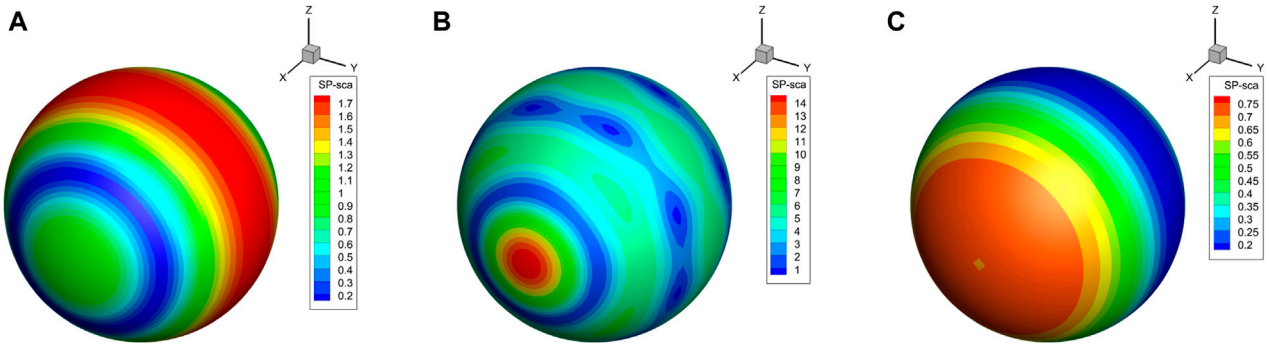

FIGURE 5
(A) Sound pressure on the spherical shell surface at frequency of 300 Hz. **(B)** Sound pressure on the spherical shell surface at frequency of 500 Hz. **(C)** Sound pressure on the spherical shell surface at frequency of 700 Hz. Sound pressure at frequencies of 300 Hz, 500 Hz, and 700 Hz on the spherical shell surface. The radius r = 0.9 m, shell thickness t = 0.009 m.

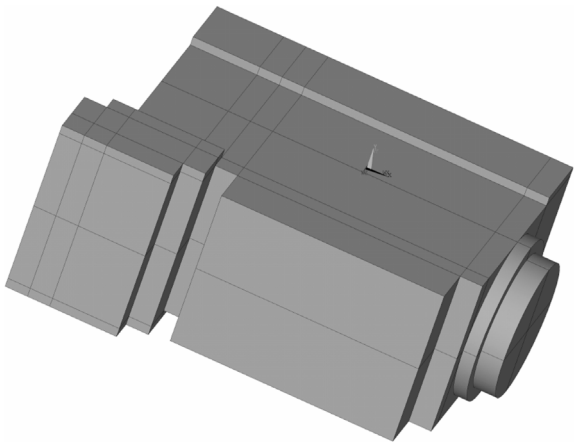

FIGURE 6
Diagram of the diesel engine box model.

may be conceptualized as a one-dimensional parametric space, as Figure 1 illustrates.

The B-spline basis functions for a particular knot vector are expressed using the Cox-de Boor recursion formula. For $p = 0$, we have Eq. 2. And we have Eq. 3 for $p \geq 1$.

$$N_{a,0}(\xi) = \begin{cases} 1 & \text{if} \quad \xi_a \leq \xi < \xi_{a+1}, \\ 0 & \text{otherwise}, \end{cases} \tag{2}$$

$$N_{a,p}(\xi) = \frac{\xi - \xi_a}{\xi_{a+p} - \xi_a} N_{a,p-1}(\xi) + \frac{\xi_{a+p+1} - \xi}{\xi_{a+p+1} - \xi_{a+1}} N_{a+1,p-1}(\xi). \tag{3}$$

B-spline basis functions are well-suited for numerical analysis due to their many beneficial properties, such as linear independence. The B-spline curve may be produced by linearly mixing B-spline basis functions and control points, as shown in Eq. 4.

$$\mathbf{x}(\xi) = \sum_{i=1}^{n} N_{a,p}(\xi) \mathbf{P}_{a,p}, \tag{4}$$

where $\mathbf{x}$ is the B-spline curve, and the coefficient $\mathbf{P}_{a,p}$ denotes the coordinates of the control point. This means that the basis function of a B-spline curve is the translation of a parametric one-dimensional space into real space. The following two-dimensional parametric spaces have a knot vector in each dimension, as shown in Eqs 5, 6.

$$\left[\xi_1, \xi_2, \ldots, \xi_{n+p+1}\right], \quad \xi_a \in \mathbb{R}, \tag{5}$$

$$\left[\eta_1, \eta_2, \ldots, \eta_{m+l+1}\right], \quad \xi_b \in \mathbb{R}. \tag{6}$$

The B-spline surface may be constructed using the tensor product property, as shown in Eq. 7.

$$\mathbf{x}(\xi, \eta) = \sum_{a=1}^{n} \sum_{b=1}^{m} N_{a,p}(\xi) N_{b,l}(\eta) \mathbf{P}_{a,b}, \tag{7}$$

where the matching number of the basis function in each dimension is denoted by n and m. It should be noted that the lack of the Kronecker delta characteristic means that B-spline control points are typically not on the surface.

NURBS is used to expand B-splines by associating a weight coefficient with each control point. With NURBS, designers may accurately represent a variety of curves with conic segments, such as circles and ellipses, and increase control over the curves without increasing the number or degree of control points. Eqs 8, 9 represent the B-spline basis functions in two dimensions, from which the NURBS basis functions are generated.

$$R_{a,b}(\xi, \eta) = \frac{N_{b,p}(\xi) N_{b,l}(\eta) w_{a,b}}{W(\xi, \eta)}, \tag{8}$$

$$W(\xi, \eta) = \sum_{a=1}^{n} \sum_{b=1}^{m} N_{a,p}(\xi) N_{b,l}(\eta) w_{a,b}. \tag{9}$$

in which w is the weight coefficient.

NURBS surfaces are defined using NURBS basis functions and control points, as shown in Eq. 10, in a manner akin to that of B-spline surfaces. We may recast Eq. 10 as Eq. 11 by utilizing the global index A to iterate between basis functions or control points.

$$\mathbf{x}(\xi, \eta) = \sum_{a=1}^{n} \sum_{b=1}^{m} R_{a,p}(\xi) R_{b,l}(\eta) \mathbf{P}_{a,b}. \tag{10}$$

$$\mathbf{x}(\xi, \eta) = \sum_{A=1}^{N_A} R_A(\xi, \eta) \mathbf{P}_A. \tag{11}$$

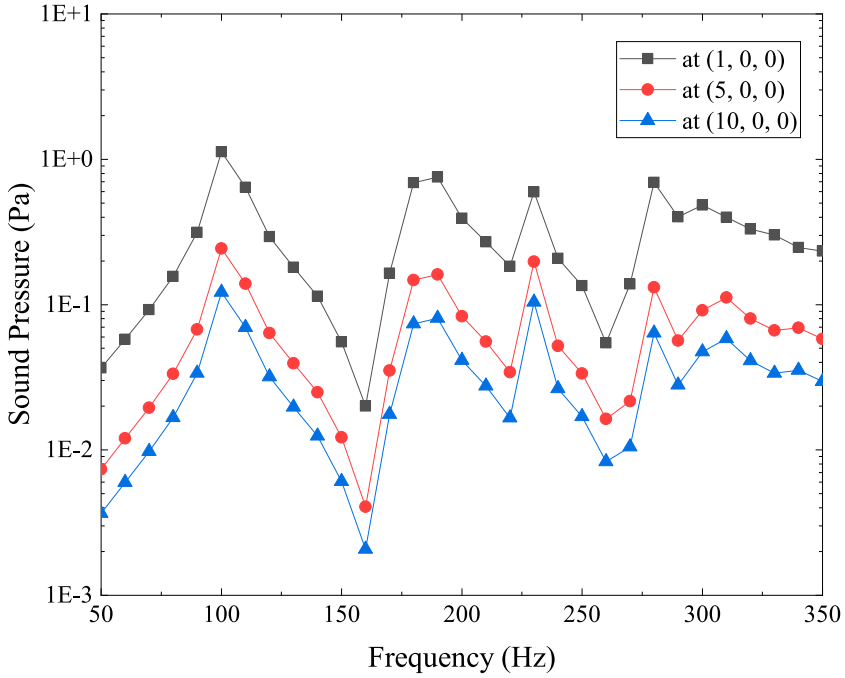

FIGURE 7
Sound pressure at location (1, 0, 0), (5, 0, 0) and (10, 0, 0) for diesel engine box model. The shell thichness t = 0.01 m.

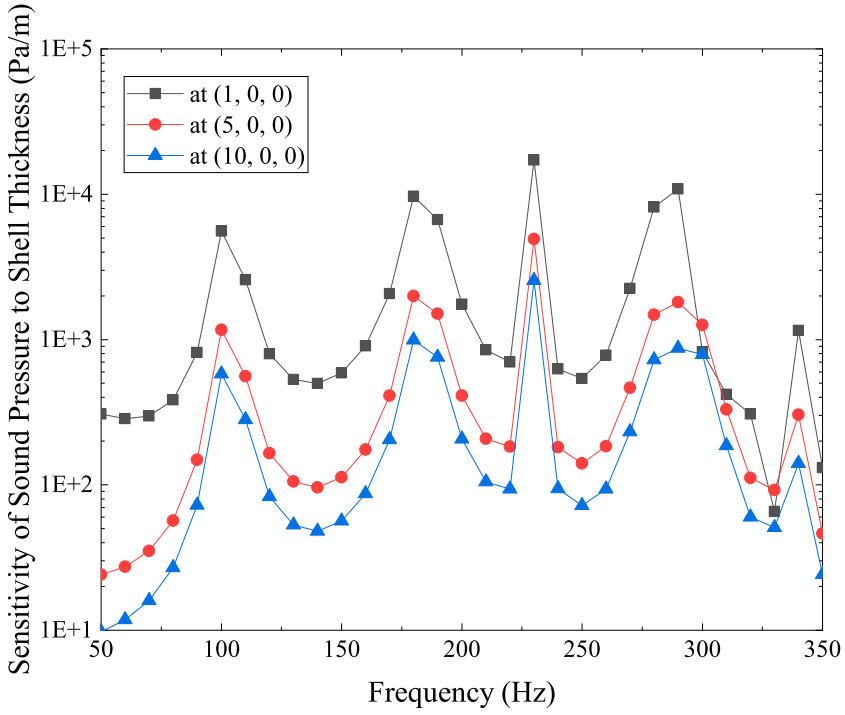

FIGURE 8
Sensitivity of sound pressure to shell thickness at location (1, 0, 0), (5, 0, 0) and (10, 0, 0) for diesel engine box model. The shell thichness t = 0.01 m.

The knot insertion operator can be used to add more control points without changing the structural shape. This feature contributes to improving the accuracy of predicting physical fields while preserving geometric correctness by using the *h*-refinement approach.

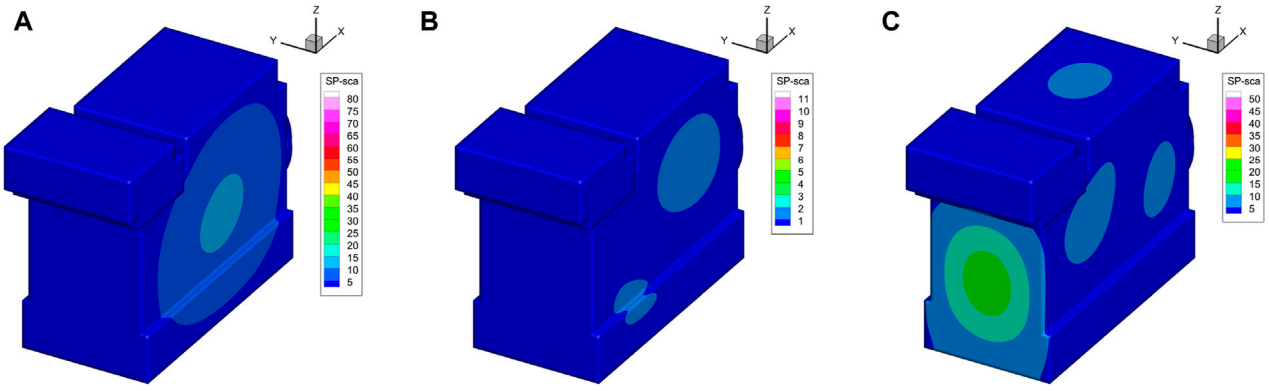

FIGURE 9
(A) Sound pressure on the diesel engine's surface at frequency of 100 Hz **(B)** Sound pressure on the diesel engine's surface at frequency of 200 Hz. **(C)** Sound pressure on the diesel engine's surface at frequency of 300 Hz. Sound pressure at frequencies of 100 Hz, 200 Hz, and 300 Hz on the diesel engine's surface. The thichness t = 0.01 m.

3 Derivation of structural-acoustic interaction analysis

3.1 Derivation of boundary element method

The time-harmonic wave field of sound in the Helmholtz equation is described by Eq. 12.

$$\nabla^2 p(x) + k^2 p(x) = 0, \tag{12}$$

in which the wave number is k and the sound pressure is p.

A boundary integral equation unique to the structural boundary Γ may be constructed from Eq. 12 to Eq. 13.

$$c(x)p(x) + \int_\Gamma F(x,y)p(y)\,d\Gamma(y) = \int_\Gamma G(x,y)q(y)\,d\Gamma(y), \quad x, y \in \Gamma, \tag{13}$$

where the source point is x, the field point is y, the Green's function is G (x, y), the intensity of the incoming wave is p, the normal derivative of p is q, $q(y) = \mathrm{i}\rho\omega v(y)$, the structure material's density is ρ, the frequency of incoming wave is ω, the normal velocity is v, and the normal derivative of G is F. If the boundary Γ is smooth near the source point x, then $c(x) = 1/2$.

In three-dimensional situations, the Green's function G (x, y) may be expressed using Eq. 14 for acoustic concerns.

$$G(x,y) = \frac{e^{ikr}}{4\pi r}, \tag{14}$$

in which $r = |y - x|$ is the distance between x and y.

The derivative of the integral representation in Eq. 13 with respect to the outer normal at point x may be represented as Eq. 15 in situations when the source point x has a smooth border Γ.

$$\frac{1}{2}q(x) + \int_\Gamma \frac{\partial F(x,y)}{\partial n(x)} p(y)\,d\Gamma(y) = \int_\Gamma \frac{\partial G(x,y)}{\partial n(x)} q(y)\,d\Gamma(y). \tag{15}$$

It is generally known that applying a single Helmholtz boundary integral equation to issues needing external boundary values is challenging due to nonuniqueness. The nonuniqueness problem is effectively handled in this work by utilizing the Burton-Miller technique Burton and Miller [57], which combines the linear Eqs 13, 15. The singular boundary integrals caused by Eqs 13, 15 may also be directly and effectively computed using the Cauchy principal value and the Hadamard finite part integral technique Zheng et al. [22].

One can get the system of linear algebraic equations represented in Eq. 16, if the border Γ is split up into elements by combining all of the center-of-element collocation point equations and displaying them using matrix representations Ciskowski and Brebbia [58].

$$\mathbf{Hp} = \mathbf{Gq} + \mathbf{p_i}, \tag{16}$$

in which the coefficient matrices are **H** and **G**, the nodal pressure caused by the incoming wave is $\mathbf{p_i}$.

3.2 Derivation of finite element method

This section contains expressions related to the structural-acoustic analysis as described in detail by researchers Fritze et al. [6]; Chen et al. [59]. The steady-state reaction of the structure may be deduced from the frequency-response analysis if it is subjected to a harmonic load. Eq. 17 derives the linear system of the structural-acoustic equation.

$$\begin{aligned} (\mathbf{K} + \mathrm{i}\omega\mathbf{C} - \omega^2\mathbf{M})\mathbf{u}(\omega) &= \mathbf{Au} = \mathbf{f}, \\ \mathbf{A} &= \mathbf{K} + \mathrm{i}\omega\mathbf{C} - \omega^2\mathbf{M}, \end{aligned} \tag{17}$$

where the stiffness matrix is **K**, the damping matrix is **C**, the mass matrix is **M**, the nodal displacement vector is **u**, the imaginary unit is $\mathrm{i} = \sqrt{-1}$, the excitation frequency is ω, and the complete excitation is **f**.

It should be noted that damping may result in a noticeable phase angle in the steady-state response, even though it keeps the same frequency with the applied load. If the load is not harmonic, Eq. 17 can still be applied by decomposing the time-dependent impulses into the frequency domain. In order to take into account the effects of the acoustic pressure applied to structural surfaces

on various aspects, a coupling matrix is included to move the structural nodal load from the fluid effect to fluid nodal pressure. Eq. 18 might thus be used to define the whole excitation, which combines the structural load and the acoustic load.

$$\begin{aligned}\mathbf{Au} &= \mathbf{C_{sf}p} + \mathbf{f_s} = \mathbf{f},\\ \mathbf{C_{sf}} &= \int_{\Gamma_{int}} \mathbf{N_s^T n N_f} d\Gamma,\end{aligned} \tag{18}$$

where $\mathbf{N_s}$ is the interpolation function in structure, $\mathbf{n}$ is the structural surface's outward normal direction, $\mathbf{N_f}$ is the interpolation function in fluid, Γ is the interaction surface, $\mathbf{C_{sf}}$ is the coupling matrix, $\mathbf{p}$ is the fluid nodal pressure, and $\mathbf{f_s}$ is the structural load.

The structural nodal load is directed from the fluid effect to the fluid nodal pressure via the coupling matrix $\mathbf{C_{sf}}$. The nodal displacement may then be determined using Eq. 19.

$$\mathbf{u} = \mathbf{A}^{-1}\mathbf{f}. \tag{19}$$

3.3 Derivation of FEM/BEM interaction analysis

The exact formulae for FEM/BEM modeling were published by Fritze et al. [6], and this section contains related equations. The continuity constraint over the interaction surface connects the governing equations from the previous section, as shown in Eq. 20. Next, it makes sense to express the normal velocity $\mathbf{v}$ as a function of the displacement $\mathbf{u}$, in line with Eq. 21.

$$\mathbf{q} = -\mathrm{i}\omega\rho\mathbf{v}, \tag{20}$$

$$\begin{aligned}\mathbf{v} &= \mathrm{i}\omega\mathbf{S}^{-1}\mathbf{C_{fs}u},\\ \mathbf{S} &= \int_{\Gamma_{int}} \mathbf{N_f^T N_f} d\Gamma,\\ \mathbf{C_{fs}} &= \mathbf{C_{sf}^T}.\end{aligned} \tag{21}$$

We can get Eq. 22 by combining Eqs 16, 20, 21. Eqs 17, 22 may be combined to form an equation system, as demonstrated in Eq. 23.

$$\mathbf{Hp} = \omega^2\rho\mathbf{GS}^{-1}\mathbf{C_{fs}u} + \mathbf{p_i}. \tag{22}$$

$$\begin{bmatrix}\mathbf{A} & -\mathbf{C_{sf}}\\ -\omega^2\rho\mathbf{GS}^{-1}\mathbf{C_{fs}} & \mathbf{H}\end{bmatrix}\begin{Bmatrix}\mathbf{u}\\ \mathbf{p}\end{Bmatrix} = \begin{Bmatrix}\mathbf{f_s}\\ \mathbf{p_i}\end{Bmatrix}. \tag{23}$$

Since the direct iterations on Eq. 23 converge slowly, solving the system equation directly would need a lot more computing power and storage. Moreover, obtaining extremely accurate numerical findings is challenging. We present the following technique for solving the aforementioned non-symmetric linear system without the need for an iterative solution. It is possible to get the coupled boundary element equation Fritze et al. [6] by replacing Eq. 19 in Eq. 22, as shown in Eq. 24. The solution of the linear equations in Eq. 24 may be performed using a sparse direct solver. To speed up the solution, FMM and the Generalized Minimum Residual (GMRES) iterative solver are used.

$$\begin{aligned}\mathbf{Hp} - \mathbf{GWC_{sf}p} &= \mathbf{GWf_s} + \mathbf{p_i},\\ \mathbf{W} &= \omega^2\rho\mathbf{S}^{-1}\mathbf{C_{fs}A}^{-1}.\end{aligned} \tag{24}$$

4 Derivation of sensitivity analysis in shape design

The goal of shape optimization is to identify, within predetermined bounds, the ideal design parameters that characterize the intended form of the given structure. Gradients of given cost functions can be found by applying shape design sensitivity analysis. The obtained gradients may then be used to select which way to search for the optimal ranges of the design variables. Therefore, the acoustic shape sensitivity research Zheng et al. [22]; Chen et al. [60] is frequently the first and most important phase in the process of creating and optimizing acoustic shapes. The chain rule of differentiation is used in the direct approach to compute the sensitivity of the function after determining the sensitivity of the variables. Because this method is so intimately associated with the analytical process, it is quite successful.

Eq. 25 can be generated by differentiating Eq. 17 with respect to the design variable in the shape design sensitivity computation using FEM.

$$\left(\dot{\mathbf{K}} + i\omega\dot{\mathbf{C}} - \omega^2\dot{\mathbf{M}}\right)\mathbf{u} + \left(\mathbf{K} + i\omega\mathbf{C} - \omega^2\mathbf{M}\right)\dot{\mathbf{u}} = \dot{\mathbf{A}}\mathbf{u} + \mathbf{A}\dot{\mathbf{u}}. \tag{25}$$

To get Eqs. 13, 15, 26, 27, are differentiated with respect to the design variable in the case when the source point x is surrounded by a smooth border Γ.

$$\begin{aligned}\frac{1}{2}\dot{p}(x) = &\int_\Gamma \left[\dot{G}(x,y)q(y) - \dot{F}(x,y)p(y)\right]d\Gamma(y)\\ &+\int_\Gamma \left[G(x,y)\dot{q}(y) - F(x,y)\dot{p}(y)\right]d\Gamma(y)\\ &+\int_\Gamma \left[G(x,y)q(y) - F(x,y)p(y)\right]d\dot{\Gamma}(y).\end{aligned} \tag{26}$$

$$\begin{aligned}\frac{1}{2}\dot{q}(x) = &\int_\Gamma \left[\frac{\partial \dot{G}(x,y)}{\partial n(x)}q(y) - \frac{\partial \dot{F}(x,y)}{\partial n(x)}p(y)\right]d\Gamma(y)\\ &+\int_\Gamma \left[\frac{\partial G(x,y)}{\partial n(x)}\dot{q}(y) - \frac{\partial F(x,y)}{\partial n(x)}\dot{p}(y)\right]d\Gamma(y)\\ &+\int_\Gamma \left[\frac{\partial G(x,y)}{\partial n(x)}q(y) - \frac{\partial F(x,y)}{\partial n(x)}p(y)\right]d\dot{\Gamma}(y).\end{aligned} \tag{27}$$

For three-dimensional problems, we have Eq. 28

$$\begin{aligned}\dot{G}(x,y) &= -\frac{e^{ikr}}{4\pi r^2}(1-ikr)\frac{\partial r}{\partial y_i}\left(\dot{y}_i - \dot{x}_i\right),\\ \dot{F}(x,y) &= \frac{e^{ikr}}{4\pi r^3}\left[\left(3-3ikr-k^2r^2\right)\frac{\partial r}{\partial n(y)}\frac{\partial r}{\partial y_j} - (1-ikr)n_j(y)\right]\left(\dot{y}_j - \dot{x}_j\right)\\ &\quad -\frac{e^{ikr}}{4\pi r^2}(1-ikr)\frac{\partial r}{\partial y_i}\dot{n}_i(y),\\ \dot{r} &= r_{,j}\left(\dot{y}_j - \dot{x}_j\right).\end{aligned} \tag{28}$$

The singular boundary integrals introduced by Eqs 26, 27 may be computed directly and efficiently using the Cauchy principal value and the Hadamard finite part integral technique Zheng et al. [22].

Applying Eq. 22 and differentiating Eq. 24 with respect to the design variable will result in Eq. 29 for the sensitivity analysis for shape design using coupling FEM/BEM. Since the matrices are full and asymmetric, solving Eq. 29 directly with normal BEM requires a significant amount of computational work. FMM and GMRES, on the other hand, can be utilized to speed up computation. Eqs 24, 29 use FMM to accelerate the matrix-vector combinations. GMRES is

used to solve the associated sensitivity equation and the formula for the FEM/BEM coupling.

$$\begin{aligned} \mathbf{H}\dot{\mathbf{p}} - \mathbf{G}\mathbf{W}\mathbf{C}_{sf}\dot{\mathbf{p}} &= \dot{\mathbf{G}}\mathbf{X} + \mathbf{G}\mathbf{Y} - \dot{\mathbf{H}}\mathbf{p}, \\ \mathbf{X} &= \mathbf{W}\left(\mathbf{C}_{sf}\mathbf{p} + \mathbf{f}_s\right), \\ \mathbf{Y} &= \dot{\mathbf{W}}\left(\mathbf{C}_{sf}\mathbf{p} + \mathbf{f}_s\right) + \mathbf{W}\left(\dot{\mathbf{C}}_{sf}\mathbf{p} + \dot{\mathbf{f}}_s\right), \\ \dot{\mathbf{W}} &= \omega^2\rho\left(\dot{\mathbf{S}^{-1}}\mathbf{C}_{fs}\mathbf{A}^{-1} + \mathbf{S}^{-1}\dot{\mathbf{C}}_{fs}\mathbf{A}^{-1} + \mathbf{S}^{-1}\mathbf{C}_{fs}\dot{\mathbf{A}^{-1}}\right). \end{aligned} \tag{29}$$

5 Numerical examples

In this part, numerical examples for real-world engineering problems illustrate the effectiveness of the proposed method. The method for doing the numerical analysis is built using our in-house Fortran code.

5.1 Spherical shell model

This subsection makes use of Figure 2's concept of a thin underwater spherical shell exposed to plane wave incidence. With an amplitude of 1, the plane wave is incident in the x-direction. The sound pressure and sensitivity at point (3, 0, 0) are examined, and the coordinate origin (0, 0, 0) is located in the center of the spherical shell. The radius of the spherical shell is r = 0.9 m and the shell thickness is t = 0.009 m. Water has a density of $\rho_f = 1.0 \times 10^3$ kg/m^3, and sound waves travel at a speed of c = 1,482 m/s in this fluid.

For the model in Figure 2, the sound pressure values at the point (3, 0, 0) are analyzed. Figure 3 gives the numerical and analytical results of the sound pressure. The GMRES implementation uses the FMM approach to accelerate the linear solution. The considerable agreement between the analytical and numerical results in Figure 3 indicates that the FMM approach maintains the extraordinary accuracy of the conventional BEM.

Sensitivity analysis plays a crucial role in shape optimization. In this example, the objective function is the sound pressure at position (3,0,0), the design variable is the spherical shell's thickness t. Figure 4 displays the sound pressure sensitivity. As can be seen from Figure 4, the numerical solution agrees well with the analytical solution. In addition, Figures 3, 4 show how both sound pressure and sensitivity increase significantly at peak resonance. Furthermore, in Figure 4, the location of the sharp increase in sound pressure sensitivity does not always correspond to the resonance peak in Figure 3. At computed frequencies where the sound pressure curve is generally flat, there may also be a significant sensitivity to sound pressure. This highlights how crucial it is to investigate sound pressure and sensitivity within a frequency range.

The sound pressure on the boundary surface of the spherical shell at 300 Hz, 500 Hz, and 700 Hz frequencies is depicted in Figure 5. The $x-y$ and $x-z$ planes exhibit symmetrical feature in these figures, while the sound pressure exhibits a phase difference along the x-axis. These results make sense as the plane wave happens along the x-axis.

5.2 Diesel engine box model

In this section, a simplified diesel engine box shell model (as shown in Figure 6) is used for sound field analysis under the action of incident waves. As in Section 5.1, the plane wave is incident along the x-direction with an amplitude of 1. Water is the fluid. The model is located within the coordinate range where $x \in [-0.5, 0.48]$, $y \in [-0.2, 0.2]$, and $z \in [0, 0.69]$. The thickness of the shell is 0.01 m. Analysis is done on the sound pressure and sensitivity at positions (1, 0, 0), (5, 0, 0), and (10, 0, 0).

Figure 7 shows the sound pressure at positions (1, 0, 0), (5, 0, 0), and (10, 0, 0), while Figure 8 shows how sensitive the sound pressure is to shell thickness at the same places.

The sound pressure trend at various calculation locations in relation to the computation frequency is similar in Figure 7. The diesel engine model's eigenfrequency is where the peak is located. For various calculation sites, the sensitivity of sound pressure to shell thickness is shown in Figure 8 in a similar trend. The peaks on both sides emerge at comparable computational frequency when comparing Figures 7, 8. Take note that the sensitivity in Figure 8 peaks at 340 Hz, while Figure 7 does not show this peak. As was concluded in Section 5.1, at computed frequencies where the sound pressure is rather flat, it is possible to have substantial sound pressure sensitivity. This emphasizes once more how crucial it is to examine sound pressure and sensitivity over a band of frequencies. Furthermore, in Figures 7, 8, the sound pressure and its sensitivity decrease as the distance between the model and the computation point increases [computation point from (1, 0, 0) to (10, 0, 0)]. This result is reasonable considering the attenuation of energy.

The sound pressure on the model's boundary surface in Figure 6 is displayed in Figure 9 at the frequency of 100 Hz, 200 Hz, and 300 Hz. As seen by Figure 9, the sound pressure peaks on the diesel engine model's surface often emerge on both sides of the structure when stimulated by a plane incident wave in the x-direction. Additionally, when the computational frequency exceeds a certain threshold, (e.g., 300 Hz), the acoustic pressure peak appears on the plane that meets the incident wave. This phenomena may be investigated in greater detail for various material properties, geometrical factors, and incident wave frequencies in further studies.

The fluid effect must be taken into account while studying the vibro-acoustic coupling problem for thin-shell designs, as the numerical simulations unequivocally demonstrate. Consequently, the coupling analysis must be performed. Since the mesh quality directly affects the computational accuracy of the coupling analysis, defining high-quality meshes is essential. This indicates that both engineering and academics stand to gain much from the use of IGA, such as NURBS, to improve computational accuracy.

6 Conclusion

Utilizing a coupling approach based on BEM and FEM, sensitivity analysis and the modeling of the acoustic-structure coupling are completed. FEM is used to simulate the problem's structural components. The boundary of the structure under study, which is also the boundary of the acoustic domain, is discretized using BEM in order to obviate the need to mesh the acoustic space. FMM is used to accelerate the matrix-vector output. By eliminating the need for meshing and utilizing CAD models to directly examine the sensitivity of the structural-acoustic interaction, NURBS IGABEM eliminates geometric errors. Sound pressure sensitivity equations are developed for connecting structural-acoustic systems.

To illustrate the precision and usefulness of the suggested approach, numerical examples are shown. The suggested technique might be used to quantitatively estimate the effect of design features on the sound field in real-world circumstances.

Data availability statement

The original contributions presented in the study are included in the article/Supplementary material, further inquiries can be directed to the corresponding author.

Author contributions

YX: Conceptualization, Investigation, Methodology, Project administration, Resources, Software, Supervision, Writing–original draft. SY: Data curation, Formal Analysis, Funding acquisition, Validation, Visualization, Writing–review and editing.

Funding

The author(s) declare that financial support was received for the research, authorship, and/or publication of this article. Sponsored by the Henan Provincial Key R&D and Promotion Project under Grant No. 232102220033, the Zhumadian 2023 Major Science and Technology Special Project under Grant No. ZMDSZDZX2023002, the Natural Science Foundation of Henan under Grant No. 222300420498, and the Postgraduate Education Reform and Quality Improvement Project of Henan Province under Grant No. YJS2023JD52.

Conflict of interest

The authors declare that the research was conducted in the absence of any commercial or financial relationships that could be construed as a potential conflict of interest.

Publisher's note

All claims expressed in this article are solely those of the authors and do not necessarily represent those of their affiliated organizations, or those of the publisher, the editors and the reviewers. Any product that may be evaluated in this article, or claim that may be made by its manufacturer, is not guaranteed or endorsed by the publisher.

References

1. Junger MC, Feit D. *Sound, structures, and their interaction*, 225. MA: MIT press Cambridge (1986).

2. Sommerfeld A. *Partial differential equations in Physics*. Academic Press (1949). doi:10.1016/B978-0-12-654658-3.50003-3

3. Engleder OSS. Stabilized boundary element methods for exterior Helmholtz problems. *Numerische Mathematik* (2008) 110:145–60. doi:10.1007/s00211-008-0161-y

4. Chen L, Zhang Y, Lian H, Atroshchenko E, Ding C, Bordas S. Seamless integration of computer-aided geometric modeling and acoustic simulation: isogeometric boundary element methods based on catmull-clark subdivision surfaces. *Adv Eng Softw* (2020) 149:102879. doi:10.1016/j.advengsoft.2020.102879

5. Everstine GC, Henderson FM. Coupled finite element/boundary element approach for fluid-structure interaction. *The J Acoust Soc America* (1990) 87:1938–47. doi:10.1121/1.399320

6. Fritze D, Marburg S, Hardtke HJ. FEM-BEM-coupling and structural-acoustic sensitivity analysis for shell geometries. *Comput Structures* (2005) 83:143–54. doi:10.1016/j.compstruc.2004.05.019

7. Chen L, Cheng R, Li S, Lian H, Zheng C, Bordas S. A sample-efficient deep learning method for multivariate uncertainty qualification of acoustic-vibration interaction problems. *Comput Methods Appl Mech Eng* (2022) 393:114784. doi:10.1016/j.cma.2022.114784

8. Martinsson P, Rokhlin V. A fast direct solver for boundary integral equations in two dimensions. *J Comput Phys* (2005) 205:1–23. doi:10.1016/j.jcp.2004.10.033

9. Martinsson P, Rokhlin V. A fast direct solver for scattering problems involving elongated structures. *J Comput Phys* (2007) 221:288–302. doi:10.1016/j.jcp.2006.06.037

10. Bebendorf SMR. Adaptive low-rank approximation of collocation matrices. *Computing* (2003) 70:1–24. doi:10.1007/s00607-002-1469-6

11. Greengard L, Rokhlin V. A fast algorithm for particle simulations. *J Comput Phys* (1987) 73:325–48. doi:10.1016/0021-9991(87)90140-9

12. Coifman R, Rokhlin V, Wandzura S. The fast multipole method for the wave equation: a pedestrian prescription. *IEEE Antennas Propagation Mag* (1993) 35:7–12. doi:10.1109/74.250128

13. Rokhlin V. Diagonal forms of translation operators for the Helmholtz equation in three dimensions. *Appl Comput Harmonic Anal* (1993) 1:82–93. doi:10.1006/acha.1993.1006

14. Schneider S. FE/FMBE coupling to model fluid-structure interaction. *Int J Numer Methods Eng* (2008) 76:2137–56. doi:10.1002/nme.2399

15. Kim NH, Dong J. Shape sensitivity analysis of sequential structural-acoustic problems using FEM and BEM. *J Sound Vibration* (2006) 290:192–208. doi:10.1016/j.jsv.2005.03.013

16. Chen L, Zhao J, Lian H, Yu B, Atroshchenko E, Li P. A BEM broadband topology optimization strategy based on Taylor expansion and SOAR method-Application to 2D acoustic scattering problems. *Int J Numer Methods Eng* (2023) 124:5151–82. doi:10.1002/nme.7345

17. Qu Y, Zhou Z, Chen L, Lian H, Li X, Hu Z, et al. Uncertainty quantification of vibro-acoustic coupling problems for robotic manta ray models based on deep learning. *Ocean Eng* (2024) 299:117388. doi:10.1016/j.oceaneng.2024.117388

18. Marburg S. Developments in structural-acoustic optimization for passive noise control. *Arch Comput Methods Eng* (2002) 9:291–370. doi:10.1007/BF03041465

19. Lamancusa J. Numerical optimization techniques for structural-acoustic design of rectangular panels. *Comput Structures* (1993) 48:661–75. doi:10.1016/0045-7949(93)90260-K

20. Hambric SA. Sensitivity calculations for broad-band acoustic radiated noise design optimization problems. *J Vibration Acoust* (1996) 118:529–32. doi:10.1115/1.2888219

21. Marburg S, Hardtke HJ. Shape optimization of a vehicle hat-shelf: improving acoustic properties for different load cases by maximizing first eigenfrequency. *Comput Structures* (2001) 79:1943–57. doi:10.1016/S0045-7949(01)00107-9

22. Zheng C, Matsumoto T, Takahashi T, Chen H. Explicit evaluation of hypersingular boundary integral equations for acoustic sensitivity analysis based on direct differentiation method. *Eng Anal Boundary Elem* (2011) 35:1225–35. doi:10.1016/j.enganabound.2011.05.004

23. Liu Z, Bian P, Qu Y, Huang W, Chen L, Chen J, et al. A galerkin approach for analysing coupling effects in the piezoelectric semiconducting beams. *Eur J Mechanics-A/Solids* (2024) 103:105145. doi:10.1016/j.euromechsol.2023.105145

24. Choi K, Shim I, Wang S. Design sensitivity analysis of structure-induced noise and vibration. *J Vibration Acoust* (1997) 119:173–9. doi:10.1115/1.2889699

25. Wang S. Design sensitivity analysis of noise, vibration, and harshness of vehicle body structure. *Mech Structures Machines* (1999) 27:317–35. doi:10.1080/08905459908915701

26. Hughes T, Cottrell J, Bazilevs Y. Isogeometric analysis: CAD, finite elements, NURBS, exact geometry and mesh refinement. *Comput Methods Appl Mech Eng* (2005) 194:4135–95. doi:10.1016/j.cma.2004.10.008

27. Chen L, Lu C, Lian H, Liu Z, Zhao W, Li S, et al. Acoustic topology optimization of sound absorbing materials directly from subdivision surfaces with isogeometric boundary element methods. *Comput Methods Appl Mech Eng* (2020) 362:112806. doi:10.1016/j.cma.2019.112806

28. Shen X, Du C, Jiang S, Sun L, Chen L. Enhancing deep neural networks for multivariate uncertainty analysis of cracked structures by POD-RBF. *Theor Appl Fracture Mech* (2023) 125:103925. doi:10.1016/j.tafmec.2023.103925

29. Simpson R, Bordas S, Trevelyan J, Rabczuk T. A two-dimensional isogeometric boundary element method for elastostatic analysis. *Comput Methods Appl Mech Eng* (2012) 209-212:87–100. doi:10.1016/j.cma.2011.08.008

30. Simpson R, Bordas S, Lian H, Trevelyan J. An isogeometric boundary element method for elastostatic analysis: 2D implementation aspects. *Comput Structures* (2013) 118:2–12. Special Issue: UK Association for Computational Mechanics in Engineering. doi:10.1016/j.compstruc.2012.12.021

31. Scott M, Simpson R, Evans J, Lipton S, Bordas S, Hughes T, et al. Isogeometric boundary element analysis using unstructured T-splines. *Comput Methods Appl Mech Eng* (2013) 254:197–221. doi:10.1016/j.cma.2012.11.001

32. Takahashi T, Matsumoto T. An application of fast multipole method to isogeometric boundary element method for Laplace equation in two dimensions. *Eng Anal Boundary Elem* (2012) 36:1766–75. doi:10.1016/j.enganabound.2012.06.0042012.06.004

33. Zhang S, Yu B, Chen L. Non-iterative reconstruction of time-domain sound pressure and rapid prediction of large-scale sound field based on ig-drbem and pod-rbf. *J Sound Vibration* (2024) 573:118226. doi:10.1016/j.jsv.2023.118226

34. Cao G, Yu B, Chen L, Yao W. Isogeometric dual reciprocity bem for solving non-fourier transient heat transfer problems in fgms with uncertainty analysis. *Int J Heat Mass Transfer* (2023) 203:123783. doi:10.1016/j.ijheatmasstransfer.2022.123783

35. Ginnis A, Kostas K, Politis C, Kaklis P, Belibassakis K, Gerostathis T, et al. Isogeometric boundary-element analysis for the wave-resistance problem using T-splines. *Comput Methods Appl Mech Eng* (2014) 279:425–39. doi:10.1016/j.cma.2014.07.001

36. Chen L, Lian H, Xu Y, Li S, Liu Z, Atroshchenko E, et al. Generalized isogeometric boundary element method for uncertainty analysis of time-harmonic wave propagation in infinite domains. *Appl Math Model* (2023) 114:360–78. doi:10.1016/j.apm.2022.09.030

37. Zhang G, He Z, Qin J, Hong J. Magnetically tunable bandgaps in phononic crystal nanobeams incorporating microstructure and flexoelectric effects. *Appl Math Model* (2022) 111:554–66. doi:10.1016/j.apm.2022.07.005

38. Zhang G, He Z, Gao XL, Zhou H. Band gaps in a periodic electro-elastic composite beam structure incorporating microstructure and flexoelectric effects. *Archive Appl Mech* (2023) 93:245–60. doi:10.1007/s00419-021-02088-9

39. Zhang G, Gao X, Wang S, Hong J. Bandgap and its defect band analysis of flexoelectric effect in phononic crystal plates. *Eur J Mechanics-A/Solids* (2024) 104:105192. doi:10.1016/j.euromechsol.2023.105192

40. Zhang G, He Z, Wang S, Hong J, Cong Y, Gu S. Elastic foundation-introduced defective phononic crystals for tunable energy harvesting. *Mech Mater* (2024) 191:104909. doi:10.1016/j.mechmat.2024.104909

41. Shen X, Du C, Jiang S, Zhang P, Chen L. Multivariate uncertainty analysis of fracture problems through model order reduction accelerated SBFEM. *Appl Math Model* (2024) 125:218–40. doi:10.1016/j.apm.2023.08.040

42. Simpson R, Liu Z, Vázquez R, Evans J. An isogeometric boundary element method for electromagnetic scattering with compatible B-spline discretizations. *J Comput Phys* (2018) 362:264–89. doi:10.1016/j.jcp.2018.01.025

43. Xu Y, Li H, Chen L, Zhao J, Zhang X. Monte Carlo based isogeometric stochastic finite element method for uncertainty quantization in vibration analysis of piezoelectric materials. *Mathematics* (2022) 10:1840. doi:10.3390/math10111840

44. Chen L, Wang Z, Lian H, Ma Y, Meng Z, Li P, et al. Reduced order isogeometric boundary element methods for CAD-integrated shape optimization in electromagnetic scattering. *Comput Methods Appl Mech Eng* (2024) 419:116654. doi:10.1016/j.cma.2023.116654

45. Li H, Chen L, Zhi G, Meng L, Lian H, Liu Z, et al. A direct fe2 method for concurrent multilevel modeling of piezoelectric materials and structures. *Comput Methods Appl Mech Eng* (2024) 420:116696. doi:10.1016/j.cma.2023.116696

46. Qu Y, Pan E, Zhu F, Jin F, Roy A. Modeling thermoelectric effects in piezoelectric semiconductors: new fully coupled mechanisms for mechanically manipulated heat flux and refrigeration. *Int J Eng Sci* (2023) 182:103775. doi:10.1016/j.ijengsci.2022.103775

47. Qu Y, Zhang G, Gao X, Jin F. A new model for thermally induced redistributions of free carriers in centrosymmetric flexoelectric semiconductor beams. *Mech Mater* (2022) 171:104328. doi:10.1016/j.mechmat.2022.104328

48. Qu Y, Jin F, Yang J. Temperature effects on mobile charges in thermopiezoelectric semiconductor plates. *Int J Appl Mech* (2021) 13:2150037. doi:10.1142/s175882512150037x

49. Chen L, Liu C, Zhao W, Liu L. An isogeometric approach of two dimensional acoustic design sensitivity analysis and topology optimization analysis for absorbing material distribution. *Comput Methods Appl Mech Eng* (2018) 336:507–32. doi:10.1016/j.cma.2018.03.025

50. Xu G, Li M, Mourrain B, Rabczuk T, Xu J, Bordas SP. Constructing IGA-suitable planar parameterization from complex CAD boundary by domain partition and global/local optimization. *Comput Methods Appl Mech Eng* (2018) 328:175–200. doi:10.1016/j.cma.2017.08.052

51. Li S, Trevelyan J, Wu Z, Lian H, Wang D, Zhang W. An adaptive SVD-Krylov reduced order model for surrogate based structural shape optimization through isogeometric boundary element method. *Comput Methods Appl Mech Eng* (2019) 349:312–38. doi:10.1016/j.cma.2019.02.023

52. Chen L, Lian H, Liu Z, Chen H, Atroshchenko E, Bordas S. Structural shape optimization of three dimensional acoustic problems with isogeometric boundary element methods. *Comput Methods Appl Mech Eng* (2019) 355:926–51. doi:10.1016/j.cma.2019.06.012

53. Lian H, Chen L, Lin X, Zhao W, Bordas SPA, Zhou M. Noise pollution reduction through a novel optimization procedure in passive control methods. *Comput Model Eng Sci* (2022) 131:1–18. doi:10.32604/cmes.2022.019705

54. Chen L, Lian H, Natarajan S, Zhao W, Chen X, Bordas S. Multi-frequency acoustic topology optimization of sound-absorption materials with isogeometric boundary element methods accelerated by frequency-decoupling and model order reduction techniques. *Comput Methods Appl Mech Eng* (2022) 395:114997. doi:10.1016/j.cma.2022.114997

55. Lu C, Chen L, Luo J, Chen H. Acoustic shape optimization based on isogeometric boundary element method with subdivision surfaces. *Eng Anal Boundary Elem* (2023) 146:951–65. doi:10.1016/j.enganabound.2022.11.010

56. Chen L, Lian H, Dong H, Yu P, Jiang S, Bordas S. Broadband topology optimization of three-dimensional structural-acoustic interaction with reduced order isogeometric fem/bem. *J Comput Phys* (2024) 509:113051. doi:10.1016/j.jcp.2024.113051

57. Burton AJ, Miller GF. The application of integral equation methods to the numerical solution of some exterior boundary-value problems. *Proc R Soc Lond* (1971) 323:201–10. doi:10.1098/rspa.1971.0097

58. Ciskowski RD, Brebbia CA. *Boundary element methods in acoustics*. Springer (1991).

59. Chen L, Li H, Guo Y, Chen P, Atroshchenko E, Lian H. Uncertainty quantification of mechanical property of piezoelectric materials based on isogeometric stochastic fem with generalized n th-order perturbation. *Eng Comput* (2023) 1–21. doi:10.1007/s00366-023-01788-w

60. Chen L, Lian H, Liu Z, Gong Y, Zheng C, Bordas S. Bi-material topology optimization for fully coupled structural-acoustic systems with isogeometric FEM-BEM. *Eng Anal Boundary Elem* (2022) 135:182–95. doi:10.1016/j.enganabound.2021.11.005enganabound.2021.11.005

frontiers | Frontiers in Physics

TYPE Original Research
PUBLISHED 15 July 2024
DOI 10.3389/fphy.2024.1420874

OPEN ACCESS

EDITED BY
Pei Li,
University of Southern Denmark, Denmark

REVIEWED BY
Kui Liu,
Harbin Institute of Technology, China
Lu Meng,
Taiyuan University of Technology, China

*CORRESPONDENCE
Yanming Xu,
xuyanming@ustc.edu

RECEIVED 21 April 2024
ACCEPTED 10 June 2024
PUBLISHED 15 July 2024

CITATION
Yang Y, Lei G, Yang S and Xu Y (2024), Two-dimensional acoustic analysis using Taylor expansion-based boundary element method. *Front. Phys.* 12:1420874.
doi: 10.3389/fphy.2024.1420874

Two-dimensional acoustic analysis using Taylor expansion-based boundary element method

Yan Yang[1], Guang Lei[1,2], Sen Yang[1,2] and Yanming Xu[1]*

[1]Henan International Joint Laboratory of Structural Mechanics and Computational Simulation, College of Architectural and Civil Engineering, Huanghuai University, Zhumadian, China, [2]College of Architecture and Civil Engineering, Xinyang Normal University, Xinyang, China

The use of boundary elements in two-dimensional acoustic analysis is presented in this study, along with a detailed explanation of how to derive the final discrete equations from the fundamental fluctuation equations. In order to overcome the fictitious eigenfrequency problem that might arise during the examination of the external sound field, this work employs the Burton-Miller approach. Additionally, this work uses the Taylor expansion to extract the frequency-dependent component from the BEM function, which speeds up the computation and removes the frequency dependency of the system coefficient matrix. The effect of the radiated acoustic field generated by underwater structures' on thin-walled structures such as submarines and ships is inspected in this work. Numerical examples verify the accuracy of the proposed method and the efficiency improvement.

KEYWORDS

boundary element method, Burton-Miller method, Taylor expansion, singular integral, Helmholtz equation

1 Introduction

Water, as another common acoustic medium, has a much higher acoustic impedance than air, and the difference between it and the mechanical impedance of common structures is not so large as to be directly negligible. Therefore, the effect of the radiated acoustic field generated by the vibration of underwater structures on structures in general and on thin-walled structures such as submarines and ships in particular is usually difficult to be directly ignored. These structures are subject to significant vibration during underwater navigation. Structural vibration causes noise [1–5], which in turn affects [6] the surrounding environment, thus triggering the engineering requirements for noise reduction. The analysis of the noise problem is actually the acoustic analysis [7, 8]. In the past research, the acoustic problems are divided into the finite sound field problems (also called the internal sound field problems) [9–12] and the infinite sound field problems (also called the external sound field problems) [13–15]. For finite sound field or internal sound field problems, the finite element method (FEM) [16–18] has been effective in solving such problems and has been widely used in practical analysis. The analysis of the outer sound field problem is much more complex than the inner sound field, and the analysis of the infinite sound field [19, 20] leads to a drastic increase in the computational volume, which is difficult to bear. The boundary element method (BEM) [21–26], on the other hand, only needing to discretize the model on the boundary, while automatically satisfying the

radiation conditions at infinity, is widely used in the analysis of external acoustic problems [27, 28]. Moreover, BEM is a semi-analytic method constructed on the basis of the basic solution, leading to a higher accuracy.

Although BEM has many advantages in acoustic analysis, it also has some drawbacks. The first one is the singularity problem, which leads to poor accuracy or even wrong results. Chen et al. [29–32] successfully applied the singular phase elimination technique to the discontinuous higher-order element and compared the accuracy performance of different elements. The second one is the fictitious eigenfrequency problem [33–36], and the main solutions to this problem are CHIEF method and Burton-Miller method [37–40]. In this paper, Burton-Miller is used to solve the fictitious eigenfrequency problem. The third one is the high memory requirement problem. The coefficient matrix formed using BEM [41–43] is a dense matrix with high memory requirement, which limits the application of BEM in large-scale problems. However, although the boundary element coefficient matrix is dense, it has the property of low rank. A series of fast methods [44–46] using low-rank decomposition have been proposed, including fast multipole method, H-matrix, adaptive cross approximation and some other fast algorithms, which could successfully reduce the computational volume and memory usage, making it possible to apply BEM on complex engineering problems [47–49]. The fourth one is the frequency dependent problem. Unlike FEM, the kernel function of BEM is frequency-dependent. The discrete formation of the coefficient matrix is influenced by frequency, necessitating its recalculation under each distinct frequency [50–52], leading to a sharp increase in the computational volume of the boundary element under frequency band analysis. In acoustic wideband analysis, researchers have developed some fast algorithms to enhance the efficiency of solving large-scale problems. The frequency-dependent terms are separated from the integration kernel using Taylor series expansions of sine and cosine functions [53–59], which reduces the workload and computational time of numerical integration. To mitigate the frequency dependence of the system coefficient matrix, this study uses the Taylor expansion to extract the frequency-dependent terms embedded within the product function of BEM. This approach is undertaken to eliminate the influence of frequency variations on the matrix, thereby enhancing the accuracy and versatility of BEM [60–63] in diverse engineering applications.

In this paper, we introduce the Burton-Miller method and the Taylor expansion technique through two examples of circular and airfoil models. These two techniques solve the problem of spurious peaks present in the boundary element method and eliminate the influence of frequency variations on the matrix, thereby enhancing the accuracy and versatility of BEM. This provides a reference value for the study of underwater noise problems. In the course of this study we found that no spurious peaks occur when the radius of the circle is small. In the process of Taylor expansion, the magnitude of the error in the analytical solution and Taylor expansion is related to the number of expansion terms.

The following is the article's remaining content: Using the Burton-Miller approach and the Taylor expansion series, the two-dimensional acoustic boundary element method is introduced in Section 2. Sections 3 offers numerical examples to back up the recommended method. Section 4 brings the text's conclusions to a close.

2 Two-dimensional acoustic boundary element method

Suppose there exists a circular region Ω_y, whose boundary is L. If the domain is filled with a homogeneous ideal fluid medium, the fluctuation equation for the sound pressure in this circular region is

$$\nabla^2 P(x,t) - \frac{1}{c_f^2}\frac{\partial^2 P(x,t)}{\partial t^2} = 0, \forall x \in \Omega_y \tag{1}$$

in which ∇^2 represents the Laplace operator, $P(x,t)$ signifies the sound pressure at a specific point x within the sound field at a particular time t, and c_f denotes the wave speed. Assuming a simple harmonic sound field, the sound pressure can be formulated as

$$P(x,t) = p(x)e^{-i\omega t} \tag{2}$$

where $p(x)$ denotes the time-independent sound pressure value in imaginary units $i = \sqrt{-1}$, and the angular frequencies $\omega = 2\pi f$, $e^{-i\omega t}$ are time-dependent terms. Since sound waves exist in simple harmonic form in many cases, and since the Fourier transform can be used to convert the time-domain data into the result of superposition of different simple harmonic wave components, in this paper we only consider the steady-state simple harmonic sound field. Substituting Eq. 1 into Eq. 2, the Helmholtz control differential equation based on sound pressure is obtained as

$$\nabla^2 p(x) + k^2 p(x) = 0, \forall x \in \Omega_y \tag{3}$$

where $k = \frac{\omega}{c_f}$ denotes the wave number. Ultimately the two-dimensional sound field problem transforms into a problem of solving the partial differential Eq. 3, and therefore boundary conditions need to be considered. For the 2D sound field problem, there are three types of boundary conditions that are usually considered, as shown in Figure 1:

Dirichlet boundary conditions, also known as Type I boundary conditions, where the sound pressure is known as Eq. 4

$$p(x) = \bar{p}(x), \forall x \in L_D \tag{4}$$

where $\overline{()}$ indicates that the value is known.

Neumann boundary conditions, also known as Type II boundary conditions, where the normal derivative of the sound pressure or the normal speed of vibration is known as Eq. 5

$$q(x) = \frac{\partial p(x)}{\partial n(x)} = i\rho_y \omega \overline{v_y}(x), \forall x \in L_N \tag{5}$$

in which q represents the acoustic flux, $n(x)$ signifies the external normal vector at point x, ρ_y denotes the density of the acoustic medium, and v_y represents the normal vibrational velocity of the acoustic medium at the boundary Ω_y, and the relationship between the acoustic flux and the normal vibrational velocity can be deduced from the Euler equation.

Robin boundary conditions, also known as Type III boundary conditions, where there is a certain linear relationship between the

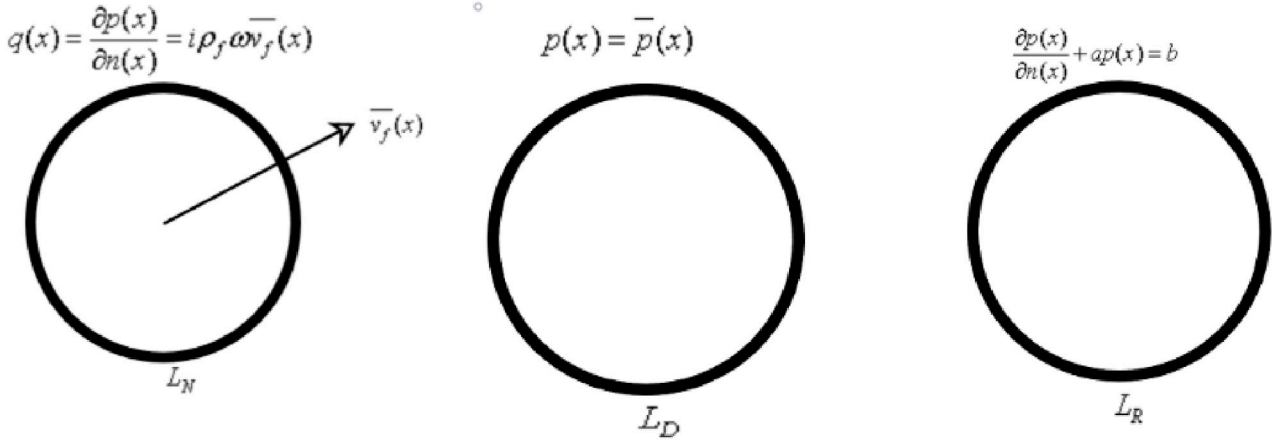

FIGURE 1
Schematic representation of the three boundary conditions.

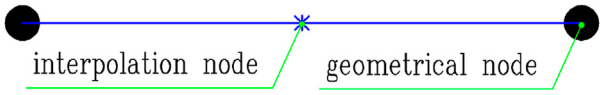

FIGURE 2
Schematic diagram of CBE21 element.

sound pressure and the derivative of sound pressure, as shown in Eq. 6

$$\frac{\partial p(x)}{\partial n(x)}+ap(x)=b,\forall x\in L_R \tag{6}$$

where a and b are known coefficients.

2.1 Boundary integral equation

BEM is centered on the derivation of the boundary integral equation. By multiplying both ends of the Helmholtz equation by the weight function $A(x,y)$ and integrating over the sound field Ω_y, we get

$$\int_{\Omega_y}[\nabla^2 p(x)+k^2 p(x)]A(x,y)d\Omega(y)=0 \tag{7}$$

Let the weight function $A(x,y)$ satisfy

$$\nabla^2 \mathrm{A}(\mathrm{x},\mathrm{y})+\mathrm{k}^2\mathrm{A}(\mathrm{x},\mathrm{y})=-\delta(x-y) \tag{8}$$

when $x\in\Omega_y$ and $x\notin L$, according to Eqs 7, 8, we get

$$\int_{\Omega_y}p(y)\left[\nabla^2\mathrm{A}(\mathrm{x},\mathrm{y})+\mathrm{k}^2\mathrm{A}(\mathrm{x},\mathrm{y})\right]d\Omega(y)$$
$$=-\int_{\Omega_y}p(y)\delta(x-y)d\Omega(y)=-p(x) \tag{9}$$

Equation 7 is transformed by Green's second constant, and then Eq. 9 can be substituted to obtain the integral equation:

$$p(x)+\int_L B(x,y)p(y)dL(y)=\int_L A(x,y)q(y)dL(y) \tag{10}$$

where $q(y)=\frac{\partial p(y)}{\partial n(y)}$ denotes the sound flux. According to the above equation, the sound pressure at point x can be regarded as the result of the superposition of the sound pressure and sound flux generated by the sound source point y. If the field point x is approximated to the integration boundary L, $x\in L$, Eq. 10 can be written as

$$c(x)p(x)+\int_L B(x,y)p(y)dL(y)=\int_L A(x,y)q(y)dL(y) \tag{11}$$

where the coefficient $c(x)$ depends on the geometric features at point x. Eq. 11 is known as the conventional boundary integral equation (CBIE). If the boundary at point x is smooth, then $c(x)=1/2$. Derivation to the outer normal $n(x)$ yields the normal derivative boundary integral equation (NDBIE), as shown as

$$c(x)q(x)+\int_L D(x,y)p(y)dL(y)=\int_L E(x,y)q(y)dL(y) \tag{12}$$

The kernel function of each order in Eqs 11, 12 can be expressed as Eq. 13

$$A(x,y)=\frac{\mathrm{i}}{4}H_0^{(1)}(kr)$$
$$B(x,y)=\frac{\partial A(x,y)}{\partial n(x)}=-\frac{\mathrm{ik}}{4}H_1^{(1)}(kr)\frac{\partial r}{\partial n(x)}$$
$$E(x,y)=\frac{\partial A(x,y)}{\partial n(x)}=-\frac{\mathrm{ik}}{4}H_1^{(1)}(kr)\frac{\partial r}{\partial n(x)}$$
$$D(x,y)=\frac{\partial^2 A(x,y)}{\partial n(x)\partial n(y)}=\frac{\mathrm{ik}}{4r}H_1^{(1)}(kr)n_j(x)n_j(y)$$
$$-\frac{\mathrm{ik}^2}{4}H_2^{(1)}(kr)\frac{\partial r}{\partial n(x)}\frac{\partial r}{\partial n(y)} \tag{13}$$

where $r=|x-y|$ denotes the Euclidean distance between the field point and the source point, and $H_n^{(1)}$ denotes the nth order first class Hankel function.

When solving a two-dimensional sound field problem using Eq. 11 or Eq. 12 alone, there are some special frequencies where the computed results will deviate significantly from the analytical solution. However, these are only mathematical problems brought about by the use of boundary integral equations for

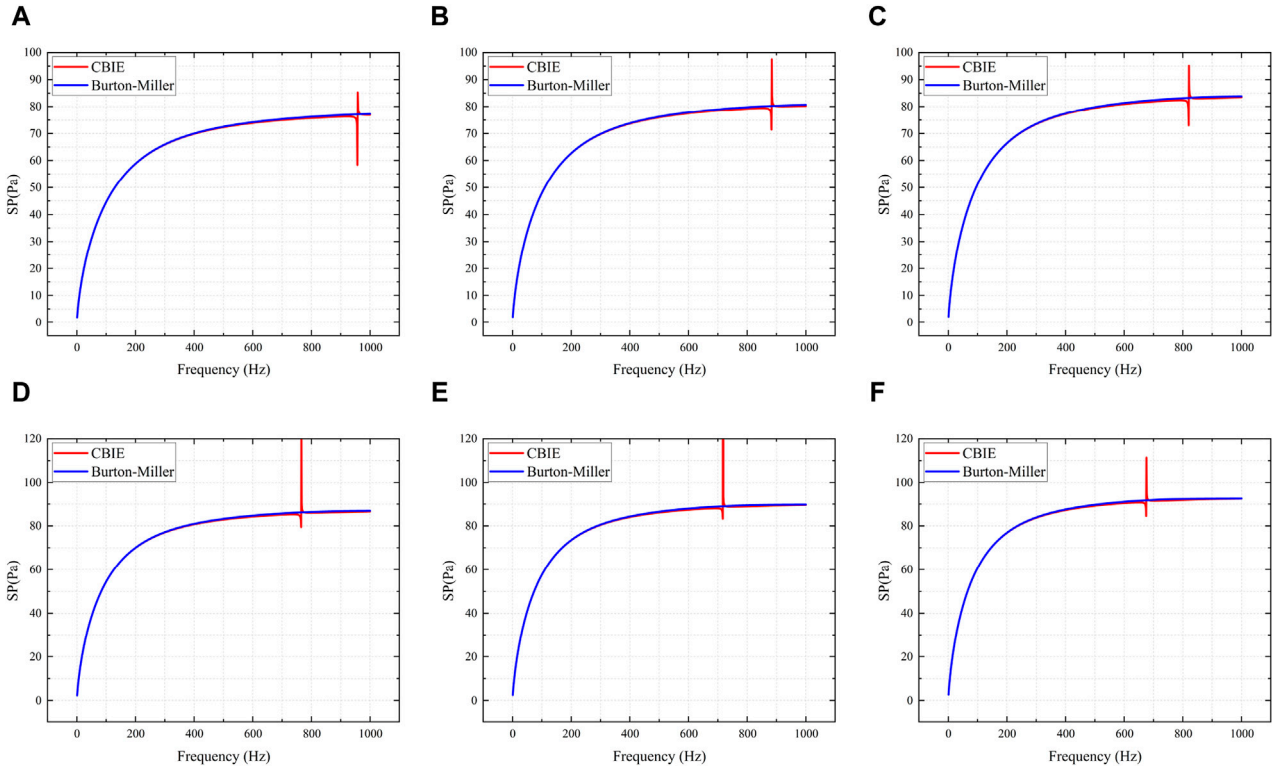

FIGURE 3
Sound pressure obtained using CBIE and Burton-Miller for different radius. **(A)**: r_0 = 0.60 m, **(B)**: r_0 = 0.65 m, **(C)**: r_0 = 0.70 m, **(D)**: r_0 = 0.75 m, **(E)**: r_0 = 0.80 m, **(F)**: r_0 = 0.85 m.

solving the problem and do not have any real physical significance, and these frequencies are called fictitious eigenfrequencies. Although using either boundary integral equation alone may fail to obtain the correct solution at a particular frequency, a linear combination of Eqs 11, 12 gets an exact and unique solution, which is known as the Burton-Miller method. The combined form can be expressed as

$$CBIE + \alpha NDBIE = 0 \tag{14}$$

where α denotes the coupling coefficient, $\alpha = i/k$ when the wave number $k \geq 1$, and *vice versa* $\alpha = i$.

Different element types can be used to discretize the boundary, and in order to facilitate the representation of the element types, a convention is adopted for the representation of the element types: CBEmn denotes a continuous element, m denotes m geometric interpolation points, and n denotes n physical interpolation points. The boundary is now discretized into a number of constant elements CBE21 since there is only one interpolation point in the element. A schematic diagram of the this element is shown in Figure 2.

The boundary is now discretized into N constant elements, and the values of the physical quantities p and q on the elements are equal to the values of the interpolated nodes. For the integral of the i node over the j element, Eq. 11 can be discretized into the following form

$$c(x)p^i + \sum_{j=1}^{N} \int_{L_j} B(x,y)dL(y)p^j = \sum_{j=1}^{N} \int_{L_j} A(x,y)dL(y)q^j \tag{15}$$

in which $\int_{L_j} A(x,y)q(y)dL(y)$ and $\int_{L_j} B(x,y)p(y)dL(y)$ are both directly computable. Introducing the coefficient matrices **G** and **H**, we have Eqs 16, 17

$$\hat{H}^{ij} = \int_{L_j} B(x,y)p(y)dL(y) \tag{16}$$

and

$$G^{ij} = \int_{L_j} A(x,y)q(y)dL(y) \tag{17}$$

Then Eq. 15 can be rewritten as

$$\sum_{j=1}^{N} H^{ij}p^j = \sum_{j=1}^{N} G^{ij}q^j \tag{18}$$

If we assume that the boundary is smooth, then c(x) = 1/2, and H^{ij} in Eq. 18 can be expressed as Eq. 19

$$H^{ij} = \begin{cases} \hat{H}^{ij}, i \neq j \\ \hat{H}^{ij} + \frac{1}{2}, i = j \end{cases} \tag{19}$$

The same discretization can be performed on Eq. 12, and then according to Eq. 14 the matrix form of the linear system equations can be obtained as Eq. 20

$$\mathbf{Hp} = \mathbf{Gq} \tag{20}$$

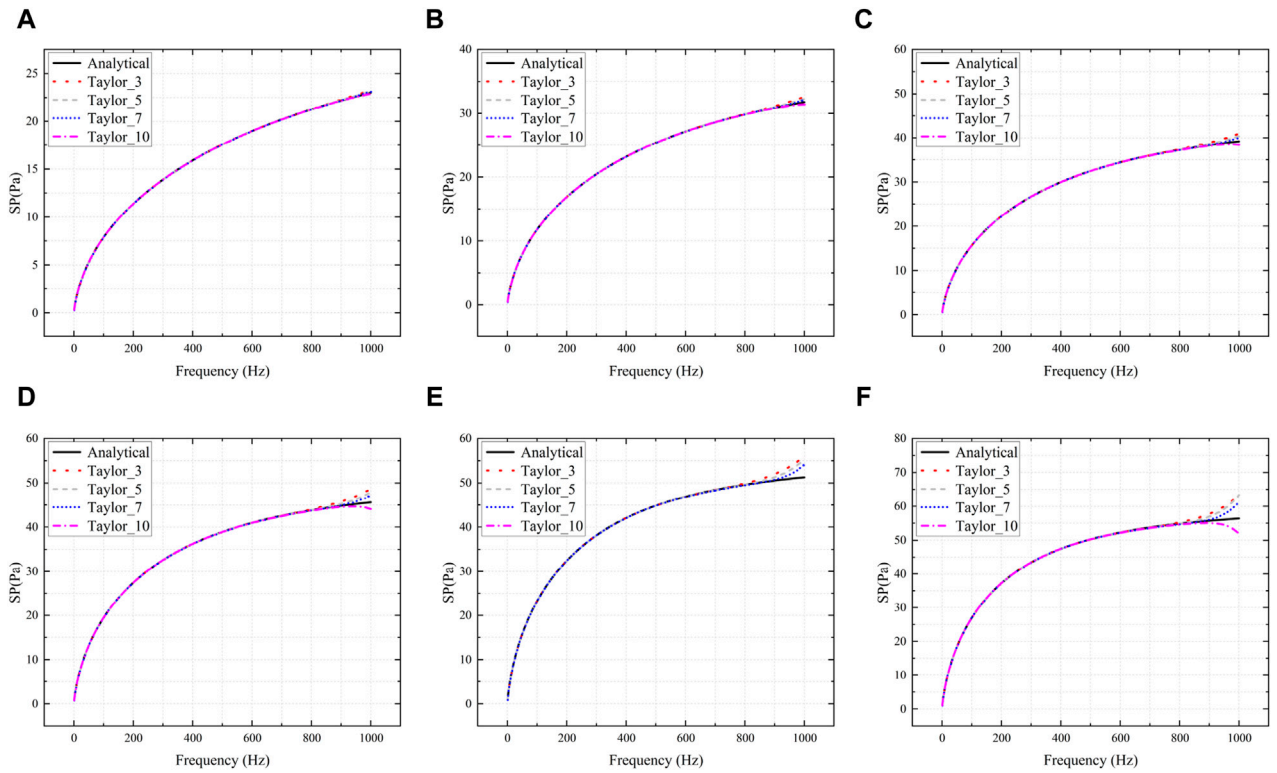

FIGURE 4
Sound pressure calculated with different number of Taylor expansion terms. **(A)**: r_0 = 0.10 m, **(B)**: r_0 = 0.15 m, **(C)**: r_0 = 0.20 m, **(D)**: r_0 = 0.25 m, **(E)**: r_0 = 0.30 m, **(F)**: r_0 = 0.35 m.

Reassembling Eq. 20 by moving all the unknowns to the left side of the equation and transferring all the knowns to the right side of the equation yields Eq. 21

$$\mathbf{Ax} = \mathbf{b} \tag{21}$$

where $\mathbf{A}$ represents the asymmetric full-rank coefficient matrix, $\mathbf{x}$ denotes the unknown vector associated with the boundary nodes, and $\mathbf{b}$ signifies the known vector. By solving this equation, the unknown values at all nodes can be determined. Subsequently, the sound pressure $\mathbf{P}_y$ at any point within the domain can be calculated by substituting the obtained results into Eq. 22.

$$\mathbf{P}_y = \mathbf{G}_y\mathbf{q} - \mathbf{H}_y\mathbf{p} \tag{22}$$

where $\mathbf{H}_y$ and $\mathbf{G}_y$ are the coefficient matrices when the field point y is in the outer acoustic domain.

2.2 Wideband analysis based on Taylor theory

The Green's function $A(x, y)$ incorporates the n-th order Hankel function of the first kind, which exhibits an explicit dependence on the wave number k. The Taylor expansion of this Hankel function, centered at a designated frequency expansion point $z_0 = k_0 r$, can be formulated as Eq. 23

$$H_n^{(1)}(z) = \sum_{m=0}^{\infty} \frac{(z - z_0)^m}{m!} \left[H_n^{(1)}(z)\right]_{z=z_0}^{(m)} \tag{23}$$

where we have Eq. 24

$$\left[H_n^{(1)}(z)\right]_{z=z_0}^{(m)} = \frac{\mathrm{d}^m H_n^{(1)}(z)}{\mathrm{d}z^m}\Big|_{z=z_0} \tag{24}$$

The Taylor expansion of the kernel functions presented in Eq. 23 can be analogously derived by substituting z and z_0 with kr and $k_0 r$, respectively.

Note the considerable challenge in deriving an explicit expression for the m-th order derivative of the n-th order Hankel function, as presented in Eq. 23. To overcome this difficulty, a recursive formulation for the Hankel function is introduced as

$$\frac{\mathrm{d}H_n^{(1)}(z)}{\mathrm{d}z} = \frac{n}{z} H_n^{(1)}(z) - H_{n+1}^{(1)}(z) \tag{25}$$

The recursive expression for the m-th order derivative of the n-th order Hankel function can be obtained through iterative differentiation of Eq. 25 with respect to the variable z. Specifically, this involves repeatedly applying the differentiation operator to obtain the desired derivative order, as shown in Eq. 26.

$$\left[H_n^{(1)}(z)\right]^{(m)} = \sum_{i=1}^{m} \left[H_n^{(1)}(z)\right]^{(m-i)} \frac{(-1)^{i+1}(m-1)!}{z^i (m-i)!} - \left[H_{n+1}^{(1)}(z)\right]^{(m-1)} \tag{26}$$

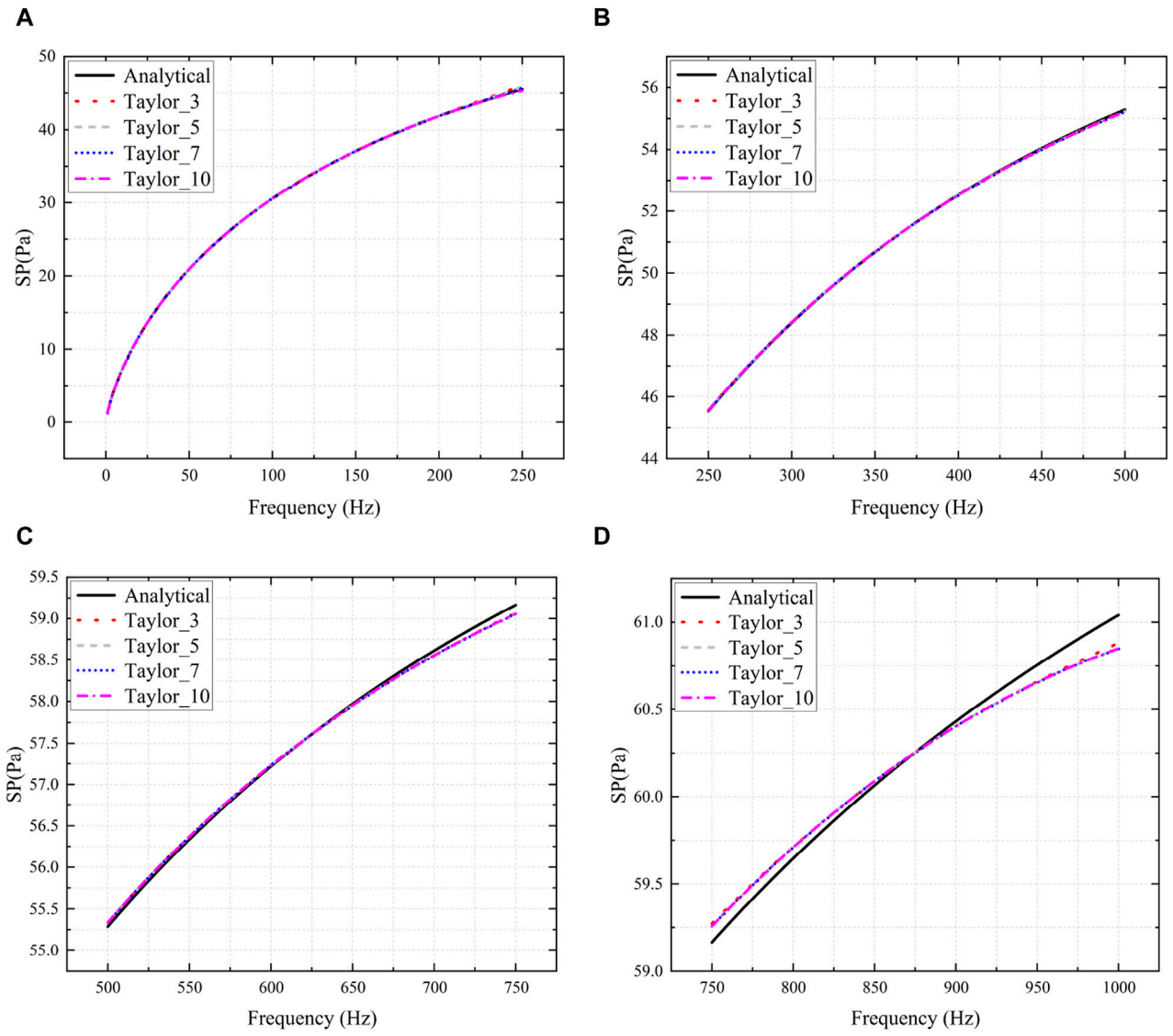

FIGURE 5
Sound pressure calculated with different number of Taylor expansion terms. r_0 = 0.40 m. **(A)**: 1–250 Hz, **(B)**: 250–500 Hz, **(C)**: 500–750 Hz, **(D)**: 750–1000 Hz.

By substituting Eq. 23 into Eqs 11, 12, then incorporating the impedance boundary condition $q(x) = i\rho_y \omega \overline{v_y}(x)$ to represent the sound absorption properties, the integrals in Eqs 11, 12 can be reformulated into an expansion form tailored to the fixed frequency point k_0:

$$\begin{aligned}
\int_L B(x,y)p(y)dL(y) &= \sum_{m=0}^{\infty} \frac{(k-k_0)^m}{m!} I_1^m \\
\int_L A(x,y)q(y)dL(y) &= \sum_{m=0}^{\infty} \frac{(k-k_0)^m}{m!} I_2^m \\
\alpha \int_L D(x,y)p(y)dL(y) &= \sum_{m=0}^{\infty} \frac{(k-k_0)^m}{m!} \left(kI_3^m + k^2 I_4^m\right) \\
\alpha \int_L E(x,y)q(y)dL(y) &= \sum_{m=0}^{\infty} \frac{(k-k_0)^m}{m!} kI_5^m
\end{aligned} \tag{27}$$

where

$$\begin{aligned}
I_1^m &= -\int_L \frac{\mathrm{i}r^{m-1}}{4} \left[zH_1^{(1)}(z)\right]_{z=k_0 r}^{(m)} \frac{\partial r}{\partial n(y)} p(y)d(y) \\
I_2^m &= \int_L \frac{ir^m}{4} \left[H_0^{(1)}(z)\right]_{z=k_0 r}^{(m)} q(y)dL(y) \\
I_3^m &= \int_L \frac{\alpha \mathrm{i}r^{m-1}}{4} \left[H_1^{(1)}(z)\right]_{z=k_0 r}^{(m)} n_j(x)n_j(y)p(y)dL(y) \\
I_4^m &= \int_L \frac{\alpha \mathrm{i}r^m}{4} \left[H_2^{(1)}(z)\right]_{z=k_0 r}^{(m)} \frac{\partial r}{\partial n(x)} \frac{\partial r}{\partial n(y)} p(y)dL(y) \\
I_5^m &= -\int_L \frac{\alpha \mathrm{i}r^m}{4} \left[H_1^{(1)}(z)\right]_{z=k_0 r}^{(m)} \frac{\partial r}{\partial n(y)} q(y)dL(y)
\end{aligned} \tag{28}$$

wherein, the m-th derivative of the function $zH_1^{(1)}(z)$ appearing in the integral I_1^m can be calculated as Eq. 29

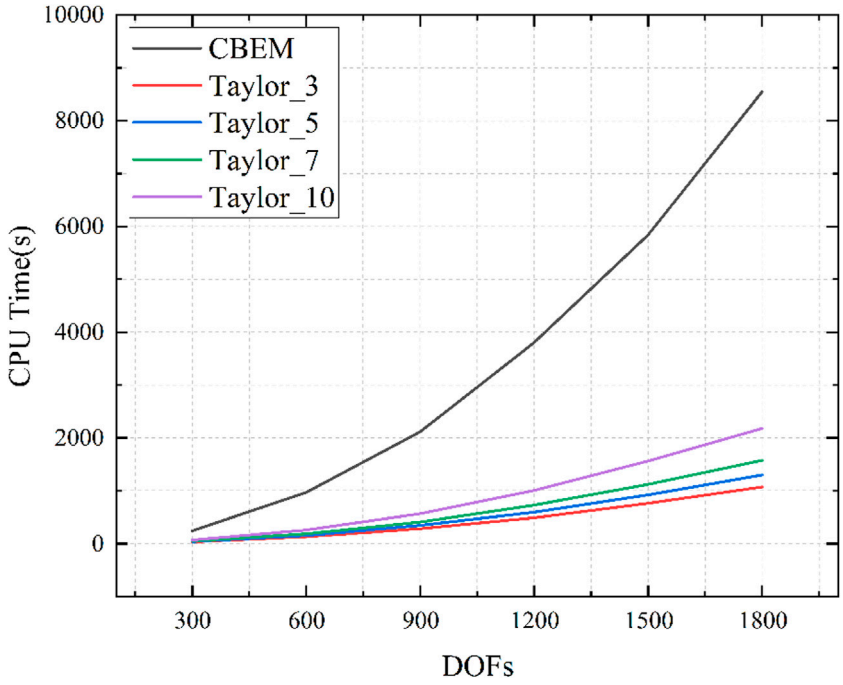

FIGURE 6
CPU time for different number of expansion terms.

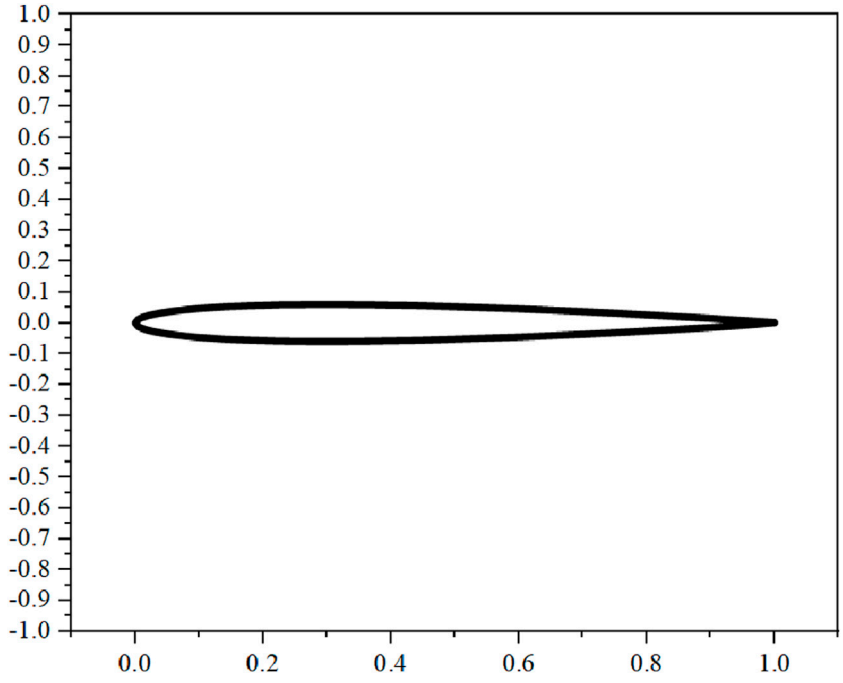

FIGURE 7
The airfoil Model.

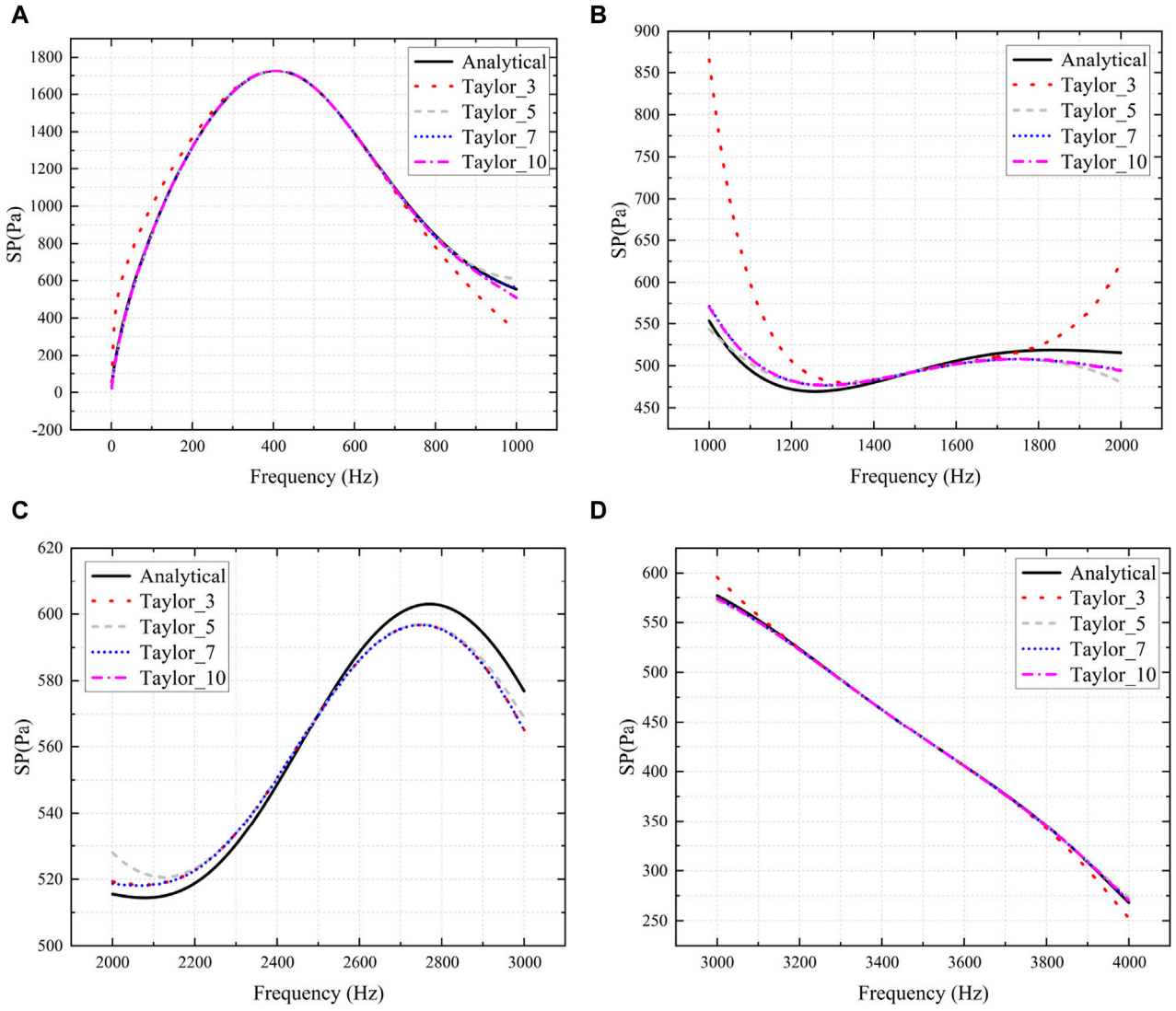

FIGURE 8
Sound pressure obtained using the analytical method and the boundary element method based on Taylor expansion. **(A)**: 1–1000 Hz, **(B)**: 1000–2000 Hz, **(C)**: 2000–3000 Hz, **(D)**: 3000–4000 Hz.

$$\left[zH_1^{(1)}(z)\right]^{(m)} = m\left[H_1^{(1)}(z)\right]^{(m-1)} + z\left[H_1^{(1)}(z)\right]^{(m)} \tag{29}$$

Substituting Eq. 27 into Eqs 11, 12 then simultaneously applying the impedance boundary condition $q(x) = i\rho_y\omega\overline{v_y}(x)$ yields the following result:

$$C(x)[p(x) - q(x)] + \sum_{m=0}^{\infty} \frac{(k-k_0)^m}{m!}\left[(I_1^m - I_2^m) + (I_3^m - I_5^m)k + I_4^m k^2\right] = 0 \tag{30}$$

Owing to the presence of singular kernel functions and their normal derivatives in Eq. 14, the boundary integrals containing a sequence of expansion expressions in Eq. 28 exhibit singularities as well. These integrals are evaluated by employing the Cauchy principal value and the Hadamard finite part integral technique [64].

The discretization of Eq. 30 is achieved through the application of the collocation method, employing constant elements, which results in:

$$\left[\mathbf{C} + \sum_{m=0}^{\infty} \frac{(k-k_0)^m}{m!}\left(\mathbf{I}_1^m + k\mathbf{I}_3^m + k^2\mathbf{I}_4^m\right)\right]\mathbf{p} = \left[\alpha\mathbf{C} + \sum_{m=0}^{\infty} \frac{(k-k_0)^m}{m!}\left(\mathbf{I}_2^m + k\mathbf{I}_5^m\right)\right]\mathbf{q} \tag{31}$$

where we have Eq. 32

$$\mathbf{C} = \begin{bmatrix} C_1 & & \mathbf{0} \\ & \ddots & \\ \mathbf{0} & & C_N \end{bmatrix} \tag{32}$$

In the present study, we employ the Taylor expansion technique to decompose the frequency-dependent system matrix given in Eqs 11, 12 into a summation of frequency-dependent scalar functions multiplied by frequency-independent system matrices. Upon examination of Eq. 31, it becomes evident that the coefficients $\mathbf{I}_1^m, \mathbf{I}_2^m, \mathbf{I}_3^m, \mathbf{I}_4^m, \mathbf{I}_5^m$ exhibit no frequency dependence. Consequently, these coefficients need to be computed only once for multi-frequency problems, thereby eliminating the need for repeated computations. As a result, the coefficient matrix remains frequency-independent.

2.3 Symbols

The following symbols are used in the formulas:

p	is sound pressure
k	is wave number
n	is external normal direction of the boundary
q	is normal derivative of p
i	is imaginary unit, $i = \sqrt{-1}$
ρ_y	is structural density
ω	is frequency of the incoming force
v_y	is normal velocity
r	is the Euclidean distance between the field point and the source point
c_f	is wave velocity
L	is the integration boundary
∇^2	is the Laplace operator
x	is source point
y	is field point
$\mathbf{H}$	is the coefficient matrix of the vector $\mathbf{p}$
$\mathbf{G}$	is the coefficient matrix of the vector $\mathbf{q}$
$c(x)$	is 1/2 if the boundary Γ is smooth in the vicinity of the source point x
$p(x)$	is intensity of the incoming wave at source point x
$p(y)$	is sound pressure at field point y
$q(y)$	is normal derivative of $p(y)$
$\overline{()}$	is known function given on the border

3 Numerical example

3.1 Cylindrical Shell's 2-D cross section

Considering a infinitely long cylindrical shell pipe model, in which the radius is r_0, and the center of the circle is at (0, 0). Take the cross section of this cylindrical shell, then it is a two-dimensional problem. The normal velocity v_0 at the boundary of the cross section is randomly set to be a constant, 9.6×10^{-5} m/s. The boundary conditions are $q = i\rho_y \omega v_0$. The cross section is uniformly discretized into 100 constant elements. When the pipe radius r_0 is taken as 0.60 m . . .. . . 0.85 m, and the frequency f is taken as 0–1,000 Hz (in step of 1 Hz), the sound pressure at point (2, 0) m is calculated here using CBIE and Burton-Miller, respectively. The results of sound pressure calculated using these two methods are shown in Figure 3.

Several conclusions can be inferred from Figure 3. As the radius of the pipe increases, the sound pressure also increases. The results obtained using the conventional boundary element method (CBEM) and Burton-Miller exhibit a high degree of similarity. However, when the radius exceeds 0.60 m, CBEM tends to produce fictitious engenfrwquencies, whereas the Burton-Miller method proves effective in mitigating this issue.

The sound pressure results obtained using BEM based on Taylor expansion are presented in Figure 4. A frequency step of 1 Hz is utilized, and the width of each frequency band is set to z. The notation $Taylor\_3$ refers to the numerical solution derived using Taylor expansion with three expansion terms (TM = 3). Similarly, $Taylor\_5$, $Taylor\_7$, and $Taylor\_10$ represent the numerical solutions employing five, seven, and ten expansion terms, respectively.

It becomes evident that sound pressure values exhibit variations across different frequency bands, as shown in Figure 4. Furthermore, within the same frequency band, the sound pressure values determined through the numerical method closely align with those obtained analytically. However, as the distance from the expansion point increases, the error also increases. Among the considered Taylor expansion terms, $Taylor\_10$ demonstrates the closest agreement with the sound pressure values obtained analytically. This implies that increasing the number of Taylor expansion terms leads to a numerical solution that more closely approximates the analytical solution.

As depicted in Figure 4, the numerical results exhibit general concordance with the analytical solution across various numbers of expansion terms. However, notable discrepancies arise at the extremities of the frequency band range. The observed agreement between the numerical and analytical solutions is primarily evident in the central region of the frequency spectrum. The discrepancies observed at the lower and upper ends of the frequency range primarily arise from the positioning of the fixed frequency expansion point at the midpoint of the range. As a result, as the distance from this fixed expansion point increases, the accuracy of the numerical results tends to deteriorate. To mitigate these deviations, the original frequency range of [1, 1,000] Hz has been subdivided into four distinct subranges: [1, 250] Hz, [250, 500] Hz, [500, 750] Hz, and [750, 1,000] Hz. Subsequent numerical simulations have been conducted within these refined subranges. As an illustrative example, consider the case where $r_0 = 0.40\ m$. As can be seen from Figure 5, by adopting this segmented approach, the accuracy and reliability of the numerical results are improved, particularly at the extremities of the frequency spectrum.

The CPU time consumed using CBIE and Taylor expansion is demonstrated in Figure 6. We can see that the former method takes

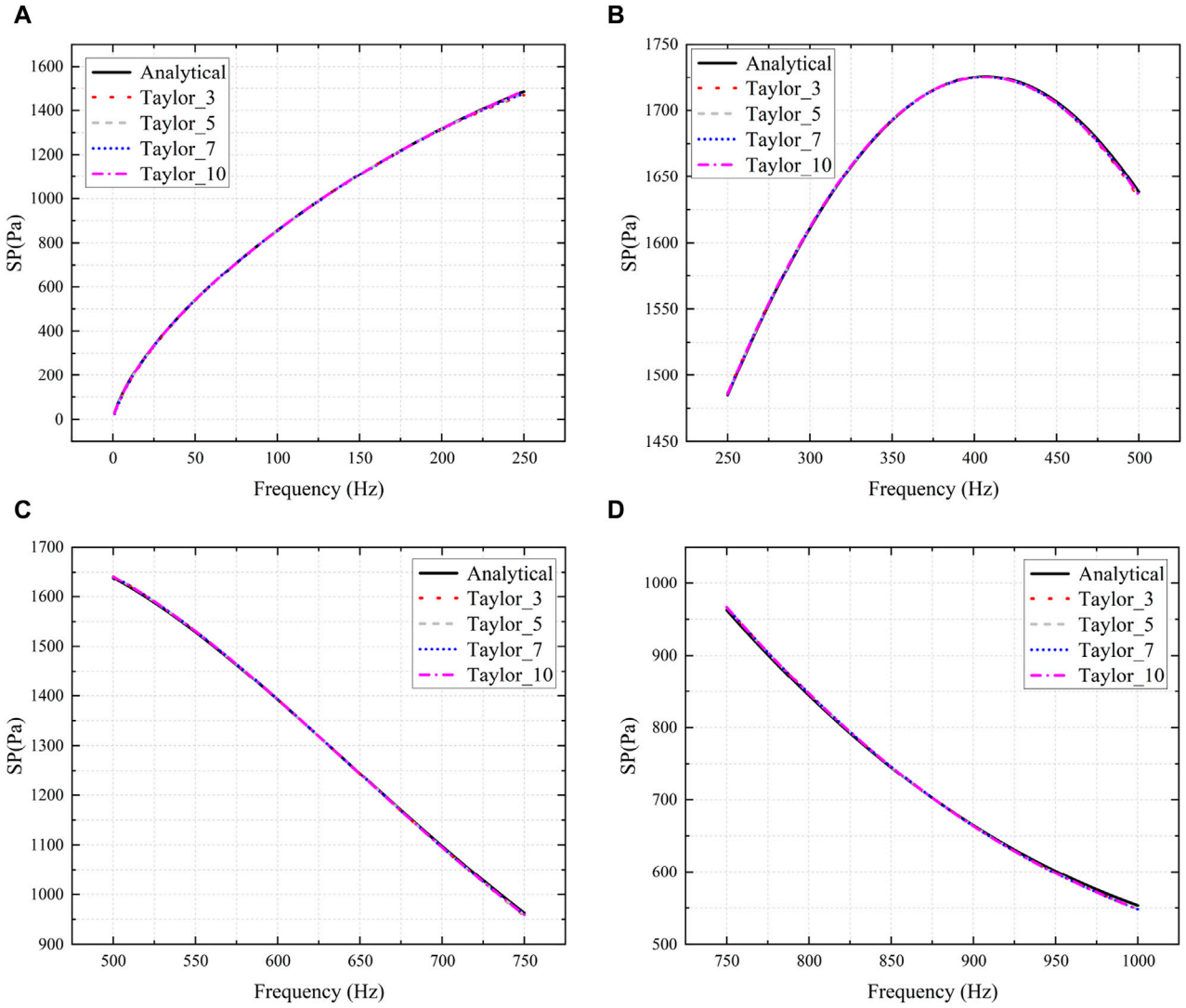

FIGURE 9
Sound pressure obtained using analytical solution and Taylor expansion methods. **(A)**: 1–250 Hz, **(B)**: 250–500 Hz, **(C)**: 500–750 Hz, **(D)**: 750–1000 Hz.

much more time than the latter. Therefore, The decoupling method represented by Taylor expansion effectively reduces the time for wideband computation.

3.2 Airfoil model

Due to the continuous development of artificial intelligence, bionic technology is becoming more and more sophisticated. Now we are working on the fins of an underwater bionic fish, which we can simplify into a wing-shaped model. For the airfoil model shown in Figure 7, CBIE and Taylor expansion is used to calculate the sound pressure at (2, 0) in the four frequency bands of [1–1,000] Hz, [1,000–2,000] Hz, [2,000–3,000] Hz and [3,000–4,000] Hz, respectively, as shown in Figure 8. It can be seen that the analytical solution bears a substantial resemblance to the solution derived using Taylor expansion across various frequency bands. Notably, the outcome at the Taylor expansion point precisely aligns with the analytical solution. However, as one moves further away from the expansion point, the divergence between the two solutions gradually increases.

To minimize the errors arising from the calculation, we will continue to subdivide [1–1,000] Hz into [1–250] Hz, [250–500] Hz, [500–750] Hz and [750–1,000] Hz, as shown in Figure 9. It can be seen that as the frequency band decreases, the solution based on Taylor expansion results in smaller errors. Therefore, we can conclude that the smaller the frequency band of the expansion, the closer the result of the Taylor expansion is to the real solution.

3.3 Sound barrier model

The acoustic analysis of a half-Y-shaped sound barrier (Figure 10) is carried out in this subsection. Figure 11 gives the real part, the imaginary part and the amplitude of the sound pressure

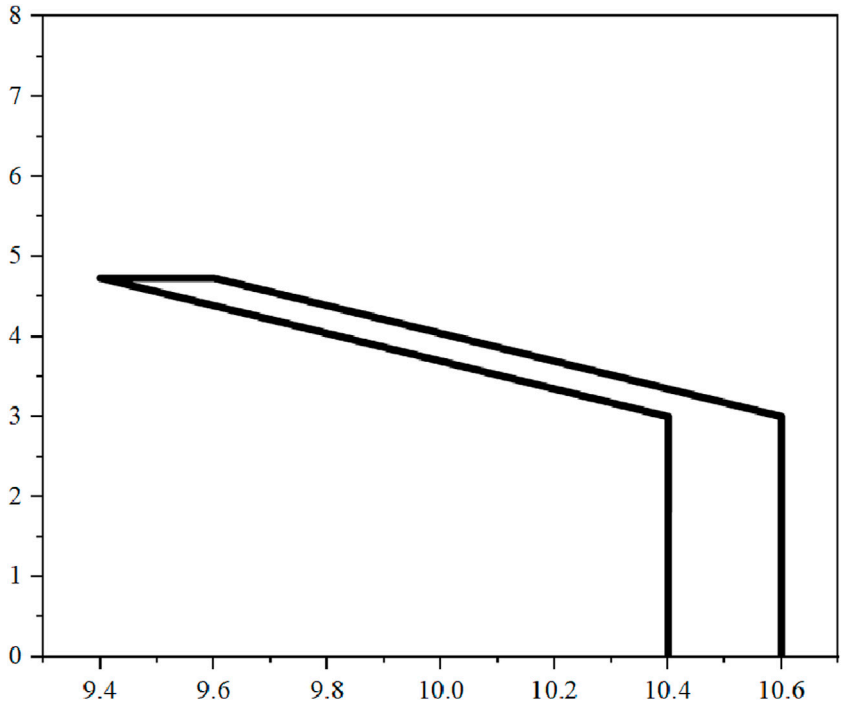

FIGURE 10
Half-Y-shaped sound barrier model.

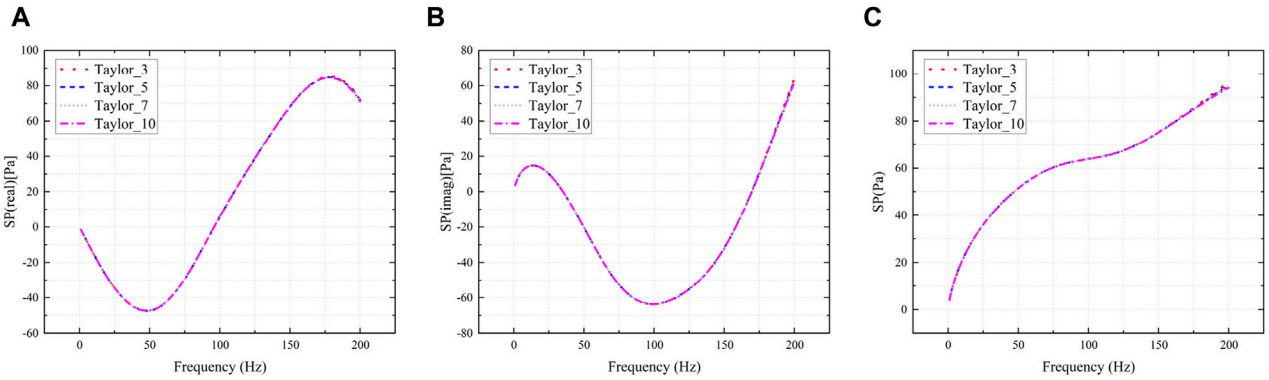

FIGURE 11
Sound pressure results at (16, 2) for the half-Y-shaped model. **(A)**: the real part, **(B)**: the imaginary part, **(C)**: the amplitude.

at point (16, 2). It can be seen that the sound pressure exhibits variation among the different expansion terms, particularly at the extremities of the frequency range. Consequently, in this subsection, an adaptive band segmentation technique is employed to partition the frequency range of [1, 200] Hz into two sub-intervals. The sound pressure results of the two sub-intervals are shown in Figure 12. It can be seen that the results obtained demonstrate a remarkable consistency, irrespective of the number of expansion terms employed. This result just validates the effectiveness of the proposed adaptive band segmentation technique.

Figure 13 compares the CPU time spent on the proposed method and CBEM for two different frequency settings. It can be seen that the proposed method exhibits a substantial decrease in CPU time when compared to CBEM. Although the CPU time escalates with an augmentation in the number of Taylor expansion terms, using Taylor expansion will still greatly reduce the CPU time used for wideband computation using the proposed method.

4 Conclusion

This paper focuses on the two-dimensional acoustic problems. The Burton-Miller method is used to solve the fictitious eigenfrequency

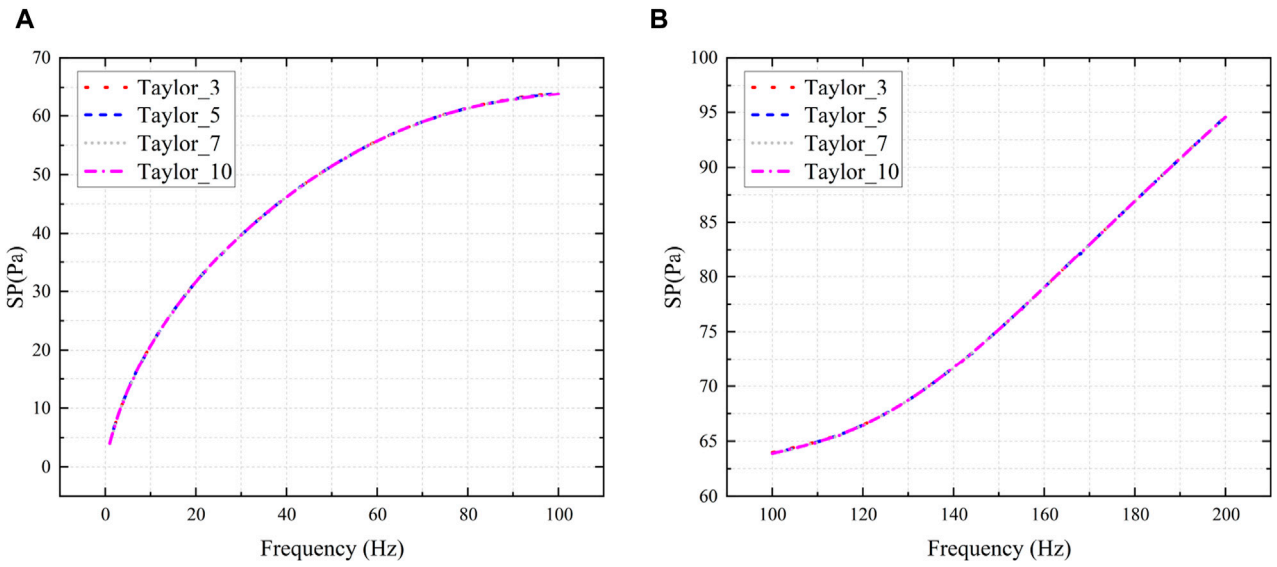

FIGURE 12
Sound pressure at (16, 2). **(A)**: 1–100 Hz, **(B)**: 100–200 Hz.

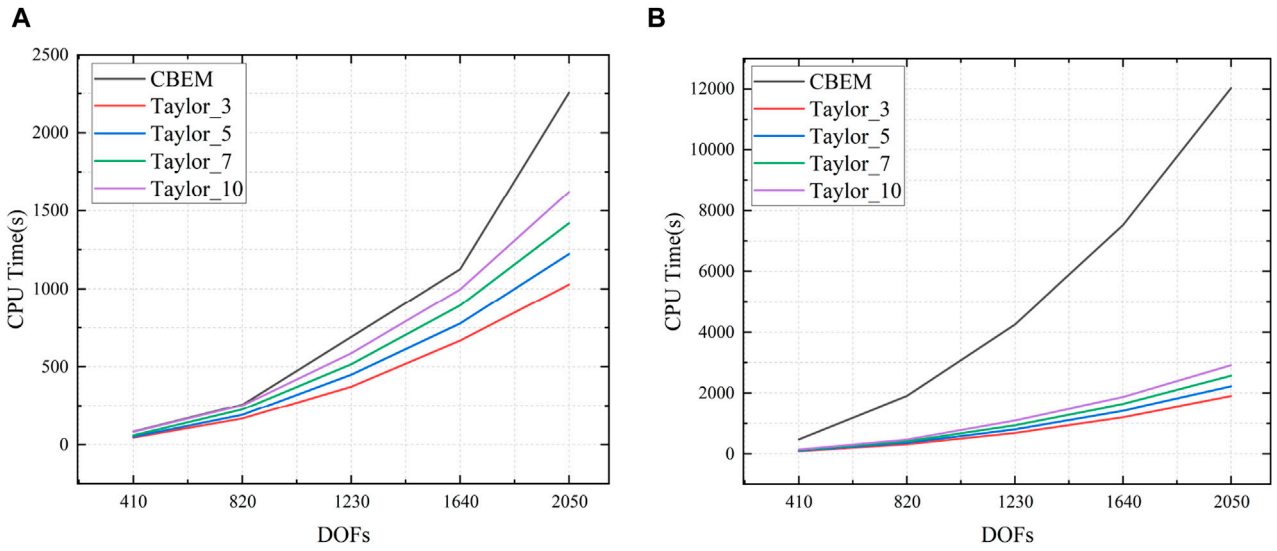

FIGURE 13
CPU time spent on numerical simulations using CBEM and Taylor expansion. **(A)**: Frequency band (1, 100) Hz, step 1 Hz. **(B)**: Frequency band (1, 100) Hz, step 0.1 Hz.

problem. The Taylor expansion method is used to solve the problem of frequency dependence and low computational efficiency in wideband analysis, showing the time requirement advantage of the Taylor expansion over CBEM. The error in Taylor expansion-based analysis is reduced by narrowing the frequency bands. The validity of the adaptive frequency band segmentation technique is verified by comparing the sound pressure of each expansion term. The necessity of Taylor expansion is illustrated by comparing the CPU time. In practical engineering applications, the circular and airfoil arithmetic examples in this paper provide a reference for studying the noise problem of underwater vehicles. The Burton-Miller method and the Taylor expansion technique introduced in the paper are also able to be applied to other areas of acoustics.

Data availability statement

The original contributions presented in the study are included in the article/supplementary material, further inquiries can be directed to the corresponding author.

Author contributions

YY: Conceptualization, Funding acquisition, Investigation, Methodology, Project administration, Writing–original draft. GL: Conceptualization, Data curation, Visualization, Writing–original draft. SY: Validation, Writing–original draft. YX: Formal Analysis, Resources, Software, Supervision, Writing–review and editing.

Funding

The authors declare that financial support was received for the research, authorship, and/or publication of this article. Sponsored by the Henan Provincial Key R&D and Promotion Project under Grant No. 232102220033, the Henan Province science and technology research project under Grant No. 242102321031, the Youth Backbone Teacher Training Program of Henan Province under Grant No. 2019GGJS232, the Zhumadian 2023 Major Science and Technology Special Project under Grant No. ZMDSZDZX2023002, the Natural Science Foundation of Henan under Grant No. 222300420498, and the Postgraduate Education Reform and Quality Improvement Project of Henan Province under Grant No. YJS2023JD52.

Conflict of interest

The authors declare that the research was conducted in the absence of any commercial or financial relationships that could be construed as a potential conflict of interest.

Publisher's note

References

1. Lian H, Chen L, Lin X, Zhao W, Bordas SPA, Zhou M. Noise pollution reduction through a novel optimization procedure in passive control methods. *Comput Model Eng Sci* (2022) 131:1–18. doi:10.32604/cmes.2022.019705

2. Ding C, Tamma K, Cui X, Ding Y, Li G, Bordas S. An nth high order perturbation-based stochastic isogeometric method and implementation for quantifying geometric uncertainty in shell structures. *Adv Eng Softw* (2020) 148:102866. doi:10.1016/j.advengsoft.2020.102866

3. Marburg S. Developments in structural-acoustic optimization for passive noise control. *Arch Comput Methods Eng* (2002) 9:291–370. doi:10.1007/BF03041465

4. Xu Y, Li H, Chen L, Zhao J, Zhang X. Monte Carlo based isogeometric stochastic finite element method for uncertainty quantization in vibration analysis of piezoelectric materials. *Mathematics* (2022) 10:1840. doi:10.3390/math10111840

5. Chen L, Cheng R, Li S, Lian H, Zheng C, Bordas SP. A sample-efficient deep learning method for multivariate uncertainty qualification of acoustic–vibration interaction problems. *Comput Methods Appl Mech Eng* (2022) 393:114784. doi:10.1016/j.cma.2022.114784

6. Zhao W, Chen L, Chen H, Marburg S. Topology optimization of exterior acoustic-structure interaction systems using the coupled fem-bem method. *Int J Numer Methods Eng* (2019) 119:404–31. doi:10.1002/nme.6055

7. Zhao W, Chen L, Chen H, Marburg S. An effective approach for topological design to the acoustic-structure interaction systems with infinite acoustic domain. *Struct Multidisciplinary Optimization* (2020) 62:1253–73. doi:10.1007/s00158-020-02550-2

8. Venås JV, Kvamsdal T. Isogeometric boundary element method for acoustic scattering by a submarine. *Comput Methods Appl Mech Eng* (2020) 359:112670. doi:10.1016/j.cma.2019.112670

9. Shen X, Du C, Jiang S, Zhang P, Chen L. Multivariate uncertainty analysis of fracture problems through model order reduction accelerated sbfem. *Appl Math Model* (2024) 125:218–40. doi:10.1016/j.apm.2023.08.040

10. Zhang G, Qu Y, Gao XL, Jin F. A transversely isotropic magneto-electro-elastic timoshenko beam model incorporating microstructure and foundation effects. *Mech Mater* (2020) 149:103412. doi:10.1016/j.mechmat.2020.103412

11. Zhang GY, Guo ZW, Qu YL, Gao XL, Jin F. A new model for thermal buckling of an anisotropic elastic composite beam incorporating piezoelectric, flexoelectric and semiconducting effects. *Acta Mechanica* (2022) 233:1719–38. doi:10.1007/s00707-022-03186-7

12. Shen X, Du C, Jiang S, Sun L, Chen L. Enhancing deep neural networks for multivariate uncertainty analysis of cracked structures by pod-rbf. *Theor Appl Fracture Mech* (2023) 125:103925. doi:10.1016/j.tafmec.2023.103925

13. Coox L, Atak O, Vandepitte D, Desmet W. An isogeometric indirect boundary element method for solving acoustic problems in open-boundary domains. *Comput Methods Appl Mech Eng* (2017) 316:186–208. Special Issue on Isogeometric Analysis: Progress and Challenges. doi:10.1016/j.cma.2016.05.039

14. Chen L, Lian H, Xu Y, Li S, Liu Z, Atroshchenko E, et al. Generalized isogeometric boundary element method for uncertainty analysis of time-harmonic wave propagation in infinite domains. *Appl Math Model* (2023) 114:360–78. doi:10.1016/j.apm.2022.09.030

15. Zhang J, Zhou J, Wang S, Wang H, Lu F. Research on dynamic characteristics and radiation noise of a helicopter main reducer based on finite element and boundary element method. *J Mech Sci Technol* (2023) 37:4489–505. doi:10.1007/s12206-023-0807-9

16. Zhang S, Yu B, Chen L. Non-iterative reconstruction of time-domain sound pressure and rapid prediction of large-scale sound field based on ig-drbem and pod-rbf. *J Sound Vibration* (2024) 573:118226. doi:10.1016/j.jsv.2023.118226

17. Chen L, Chen H, Zheng C, Marburg S. Structural–acoustic sensitivity analysis of radiated sound power using a finite element/discontinuous fast multipole boundary element scheme. *Int J Numer Methods Fluids* (2016) 82:858–78. doi:10.1002/fld.4244

18. Qu YL, Guo ZW, Zhang GY, Gao XL, Jin F. A new model for circular cylindrical Kirchhoff–love shells incorporating microstructure and flexoelectric effects. *J Appl Mech* (2022) 89:121010. doi:10.1115/1.4055658

19. Liu Z, Bian PL, Qu Y, Huang W, Chen L, Chen J, et al. A galerkin approach for analysing coupling effects in the piezoelectric semiconducting beams. *Eur J Mech - A/Solids* (2024) 103:105145. doi:10.1016/j.euromechsol.2023.105145

20. Marburg S The burton and miller method: unlocking another mystery of its coupling parameter. *J Comput Acoust* (2016) 24:1550016. doi:10.1142/s0218396x15500162

21. Lian H, Kerfriden P, Bordas S. Shape optimization directly from cad: an isogeometric boundary element approach using t-splines. *Comput Methods Appl Mech Eng* (2017) 317:1–41. doi:10.1016/j.cma.2016.11.012

22. Chen L, Marburg S, Zhao W, Liu C, Chen H. Implementation of isogeometric fast multipole boundary element methods for 2d half-space acoustic scattering problems with absorbing boundary condition. *J Theor Comput Acoust* (2018) 27:1850024. doi:10.1142/S259172851850024X

23. Chen L, Lu C, Lian H, Liu Z, Zhao W, Li S, et al. Acoustic topology optimization of sound absorbing materials directly from subdivision surfaces with isogeometric boundary element methods. *Comput Methods Appl Mech Eng* (2020) 362:112806. doi:10.1016/j.cma.2019.112806

24. Dölz J, Kurz S, Schöps S, Wolf F. Isogeometric boundary elements in electromagnetism: rigorous analysis, fast methods, and examples. *SIAM J Scientific Comput* (2019) 41:B983–B1010. doi:10.1137/18M1227251

25. Sumbatyan M, Martynova T, Musatova N. Boundary element methods in diffraction of a point-source acoustic wave by a rigid infinite wedge. *Eng Anal Boundary Elem* (2021) 125:157–67. doi:10.1016/j.enganabound.2021.01.017

26. Kurz S, Schöps S, Unger G, Wolf F. Solving maxwell's eigenvalue problem via isogeometric boundary elements and a contour integral method. *Math Methods Appl Sci* (2021) 44:10790–803. doi:10.1002/mma.7447

27. Cheng S, Wang F, Li PW, Qu W. Singular boundary method for 2d and 3d acoustic design sensitivity analysisimage 1. *Comput Maths Appl* (2022) 119:371–86. doi:10.1016/j.camwa.2022.06.009

28. Chen L, Li K, Peng X, Lian H, Lin X, Fu Z. Isogeometric boundary element analysis for 2d transient heat conduction problem with radial integration method. *CMES-Computer Model Eng Sci* (2021) 126:125–46. doi:10.32604/cmes.2021.012821

29. Chen L, Lian H, Liu Z, Gong Y, Zheng S. CJand Bordas. Bi-material topology optimization for fully coupled structural-acoustic systems with isogeometric fem–bem. *Eng Anal Boundary Elem* (2022) 135:182–95. doi:10.1016/j.enganabound.2021.11.005

30. Chen L, Zhang Y, Lian H, Atroshchenko E, Ding C, Bordas S. Seamless integration of computer-aided geometric modeling and acoustic simulation: isogeometric boundary element methods based on catmull-clark subdivision surfaces. *Adv Eng Softw* (2020) 149:102879. doi:10.1016/j.advengsoft.2020.102879

31. Chen L, Lian H, Dong H, Yu P, Jiang S, Bordas S. Broadband topology optimization of three-dimensional structural-acoustic interaction with reduced order isogeometric fem/bem. *J Comput Phys* (2024) 509:113051. doi:10.1016/j.jcp.2024.113051

32. Chen L, Lian H, Liu Z, Chen H, Atroshchenko E, Bordas S. Structural shape optimization of three dimensional acoustic problems with isogeometric boundary element methods. *Comput Methods Appl Mech Eng* (2019) 355:926–51. doi:10.1016/j.cma.2019.06.012

33. Qu Y, Jin F, Zhang G. Mechanically induced electric and magnetic fields in the bending and symmetric-shear deformations of a microstructure-dependent fg-mee composite beam. *Compos Structures* (2021) 278:114554. doi:10.1016/j.compstruct.2021.114554

34. Cao G, Yu B, Chen L, Yao W. Isogeometric dual reciprocity bem for solving non-fourier transient heat transfer problems in fgms with uncertainty analysis. *Int J Heat Mass Transfer* (2023) 203:123783. doi:10.1016/j.ijheatmasstransfer.2022.123783

35. Qu Y, Pan E, Zhu F, Jin F, Roy AK. Modeling thermoelectric effects in piezoelectric semiconductors: new fully coupled mechanisms for mechanically manipulated heat flux and refrigeration. *Int J Eng Sci* (2023) 182:103775. doi:10.1016/j.ijengsci.2022.103775

36. Zheng CJ, Bi CX, Zhang C, Zhang YB, Chen HB. Fictitious eigenfrequencies in the bem for interior acoustic problems. *Eng Anal Boundary Elem* (2019) 104:170–82. doi:10.1016/j.enganabound.2019.03.042

37. Toshimitsu R, Isakari H. A burton–miller-type boundary element method based on a hybrid integral representation and its application to cavity scattering. *Eng Anal Boundary Elem* (2024) 158:303–12. doi:10.1016/j.enganabound.2023.11.003

38. Fu ZJ, Chen W, Gu Y. Burton–miller-type singular boundary method for acoustic radiation and scattering. *J Sound Vibration* (2014) 333:3776–93. doi:10.1016/j.jsv.2014.04.025

39. Zheng CJ, Chen HB, Gao HF, Du L. Is the burton–miller formulation really free of fictitious eigenfrequencies? *Eng Anal Boundary Elem* (2015) 59:43–51. doi:10.1016/j.enganabound.2015.04.014

40. Zhang J, Lin W, Shu X, Zhong Y. A dual interpolation boundary face method for exterior acoustic problems based on the burton–miller formulation. *Eng Anal Boundary Elem* (2020) 113:219–31. doi:10.1016/j.enganabound.2020.01.005

41. Chen L, Marburg S, Chen H, Zhang H, Gao H. An adjoint operator approach for sensitivity analysis of radiated sound power in fully coupled structural-acoustic systems. *J Comput Acoust* (2017) 25:1750003. doi:10.1142/S0218396X17500035

42. Wu Y, Dong C, Yang H. Isogeometric indirect boundary element method for solving the 3d acoustic problems. *J Comput Appl Maths* (2020) 363:273–99. doi:10.1016/j.cam.2019.06.013

43. Chen L, Liu C, Zhao W, Liu L. An isogeometric approach of two dimensional acoustic design sensitivity analysis and topology optimization analysis for absorbing material distribution. *Comput Methods Appl Mech Eng* (2018) 336:507–32. doi:10.1016/j.cma.2018.03.025

44. Liu X, Xu J. A low-frequency fast multipole boundary element method for acoustic problems in a subsonic uniform flow. *Eng Anal Boundary Elem* (2024) 162:102–16. doi:10.1016/j.enganabound.2024.01.026

45. Liu B, Wang Q, Feng Y, Zhang ZS, Huang Q, Tian W, et al. The fast multipole method–accelerated line integration boundary element method for 3d heat conduction analysis with heat source. *Eng Computations* (2023) 40:1676–97. doi:10.1108/ec-03-2022-0157

46. Li Y, Atak O, Desmet W. Novel and efficient implementation of multi-level fast multipole indirect bem for industrial helmholtz problems. *Eng Anal Boundary Elem* (2024) 159:150–63. doi:10.1016/j.enganabound.2023.11.027

47. Zhang G, Gao X, Wang S, Hong J. Bandgap and its defect band analysis of flexoelectric effect in phononic crystal plates. *Eur J Mech - A/Solids* (2024) 104:105192. doi:10.1016/j.euromechsol.2023.105192

48. Zhang G, Gao XL. A non-classical model for first-ordershear deformation circular cylindrical thin shells incorporating microstructure and surface energy effects. *Maths Mech Sol* (2021) 26:1294–319. doi:10.1177/1081286520978488

49. Jin Q, Thompson DJ, Lurcock DE, Toward MG, Ntotsios E. A 2.5d finite element and boundary element model for the ground vibration from trains in tunnels and validation using measurement data. *J Sound Vibration* (2018) 422:373–89. doi:10.1016/j.jsv.2018.02.019

50. Li Z, Gao Z, Liu Y. Enriched constant elements in the boundary element method for solving 2d acoustic problems at higher frequencies. *Comput Model Eng Sci* (2024) 138:2159–75. doi:10.32604/cmes.2023.030920

51. Lei J, Shao C, Zhang C. Frequency-domain fundamental solutions and boundary element method for consistent couple stress elastodynamic problems. *Int J Numer Methods Eng* (2023) 124:4992–5019. doi:10.1002/nme.7335

52. Li Y, Atak O, Jonckheere S, Desmet W. Accelerating boundary element methods in wideband frequency sweep analysis by matrix-free model order reduction. *J Sound Vibration* (2022) 541:117323. doi:10.1016/j.jsv.2022.117323

53. Chen L, Lu C, Zhao W, Chen H, Zheng C. Subdivision surfaces—boundary element accelerated by fast multipole for the structural acoustic problem. *J Theor Comput Acoust* (2020) 28:2050011. doi:10.1142/s2591728520500115

54. Wang Z, Zhao Z, Liu Z, Huang Q. A method for multi-frequency calculation of boundary integral equation in acoustics based on series expansion. *Appl Acoust* (2009) 70:459–68. doi:10.1016/j.apacoust.2008.05.005

55. Ramzan M, Ahmad MO, Bashir MN, Asghar A, Shehzad SA. Development of numerical tools using boundary element method based on taylor series for nonlinear analysis. *Mod Phys Lett B* (2023) 37. doi:10.1142/s0217984923500501

56. Han Z, Pan W, Cheng C, Hu Z, Niu Z. A semi-analytical treatment for nearly singular integrals arising in the isogeometric boundary element method-based solutions of 3d potential problems. *Comput Methods Appl Mech Eng* (2022) 398:115179. doi:10.1016/j.cma.2022.115179

57. Riaz M, Hashmi MR, Pamucar D, Chu Y. Spherical linear diophantine fuzzy sets with modeling uncertainties in mcdm. *Comput Model Eng Sci* (2021) 126:1125–64. doi:10.32604/cmes.2021.013699

58. Chen L, Lian H, Natarajan S, Zhao W, Chen X, Bordas S. Multi-frequency acoustic topology optimization of sound-absorption materials with isogeometric boundary element methods accelerated by frequency-decoupling and model order reduction techniques. *Comput Methods Appl Mech Eng* (2022) 395:114997. doi:10.1016/j.cma.2022.114997

59. Chen L, Wang Z, Lian H, Ma Y, Meng Z, Li P, et al. Reduced order isogeometric boundary element methods for cad-integrated shape optimization in electromagnetic scattering. *Comput Methods Appl Mech Eng* (2024) 419:116654. doi:10.1016/j.cma.2023.116654

60. Liu Y. On the bem for acoustic wave problems. *Eng Anal Boundary Elem* (2019) 107:53–62. doi:10.1016/j.enganabound.2019.07.002

61. Zheng YT, Liu Y, Gao XW, Yang Y, Peng HF. Improved hole and tube elements in bem for elasticity problems. *Eng Anal Boundary Elem* (2024) 159:17–35. doi:10.1016/j.enganabound.2023.11.021

62. Qu Y, Zhou Z, Chen L, Lian H, Li X, Hu Z, et al. Uncertainty quantification of vibro-acoustic coupling problems for robotic manta ray models based on deep learning. *Ocean Eng* (2024) 299:117388. doi:10.1016/j.oceaneng.2024.117388

63. Dölz J, Harbrecht H, Kurz S, Schöps S, Wolf F. A fast isogeometric bem for the three dimensional laplace- and helmholtz problems. *Comput Methods Appl Mech Eng* (2018) 330:83–101. doi:10.1016/j.cma.2017.10.020

64. Chen L, Zhao J, Lian H, Yu B, Atroshchenko E, Li P. A bem broadband topology optimization strategy based on taylor expansion and soar method-application to 2d acoustic scattering problems. *Int J Numer Methods Eng* (2023) 124:5151–82. doi:10.1002/nme.7345

frontiers | Frontiers in Physics

TYPE Original Research
PUBLISHED 16 July 2024
DOI 10.3389/fphy.2024.1426846

OPEN ACCESS

EDITED BY
Pei Li,
University of Southern Denmark, Denmark

REVIEWED BY
Xiangsheng Gao,
Beijing University of Technology, China
Jinqiang Li,
Harbin Engineering University, China
Zhiwei Hao,
Harbin Institute of Technology, China

*CORRESPONDENCE
Haifeng Gao,
gaohaifeng@tyut.edu.cn

RECEIVED 02 May 2024
ACCEPTED 29 May 2024
PUBLISHED 16 July 2024

CITATION
Li H, Gao H, Liang J, Li Z, Xu H and Zheng C (2024), A level set based topology optimization for elastodynamic problems using BEM. *Front. Phys.* 12:1426846. doi: 10.3389/fphy.2024.1426846

A level set based topology optimization for elastodynamic problems using BEM

Huiwen Li[1,2], Haifeng Gao[1]*, Jianguo Liang[1], Zhiqiang Li[1], Huidong Xu[1] and Changjun Zheng[3]

[1]College of Mechanical and Vehicle Engineering, Taiyuan University of Technology, Taiyuan, China, [2]Shanxi-Zheda Institute of Advanced Materials and Chemical Engineering, Taiyuan, China, [3]Institute of Sound and Vibration Research, Hefei University of Technology, Hefei, Anhui, China

The paper presents a topology optimization methodology for 2D elastodynamic problems using the boundary element method (BEM). The topological derivative is derived based on the variation method and the adjoint variable method. The level set method is employed for the representation of the material domain and voids within a specified design domain. Thus, the boundaries can easily be generated, following the zero isocontour of the level set function. Numerical implementation is carried out to demonstrate the effectiveness of the proposed topology optimization methodology in wave isolation and waveguide problems.

KEYWORDS

boundary element method, topology optimization, level set method, elastodynamic problems, vibration control

1 Introduction

The problem of vibration control with artificial structures has been an important issue in aerospace [1,2], vehicle design [3], civil engineering [4], and vibration pollution [5]. The suppression, absorption, or waveguide of elastic waves are considered effective tools for the vibration problems which affect the safety, reliability, and stability of equipment. Passive vibration control approaches are widely applied in engineering problems due to their simple design and low cost. Various passive vibration control structures are designed and artificially manufactured to meet the requirements of vibration-related engineering problems. Phononic crystals and metamaterials are adopted for mechanical filters and vibration isolators due to their band gaps, which can strictly forbid the propagation of acoustic or elastic waves in a certain range of frequency [6]. An open trench and wave-impeding block-combined vibration isolation barrier is an effective way of protecting equipment or buildings from environmental vibration sources [7]. Waveguide absorbers are designed to extract elastic wave energy, dissipating it with artificial spiral acoustic black holes [8]. The narrow control frequency range, which is considered a drawback of passive systems, is improved by invoking nonlinear dynamic theories [9].

The numerical simulation method is an effective and efficient approach which can significantly reduce the cost of the design or analysis of vibration problems. Moreover, topology optimization methods based on numerical techniques are developed to acquire the desired structures with prescribed objectives and constraints. Early efforts on structural design through topology optimization methods include previous research works [10, 11]. Several widely used topology optimization algorithms, such as the homogenization method [12], the solid isotropic material with penalization (SIMP) method [13–16], the evolutionary structural optimization (ESO) method [17–20], the

moving morphable component (MMC) method [21–24], and level set-based methods [25–27], have gained great attraction in research investigations. Liu et al. carried out the topology optimization of attached piezoelectric actuators of thin-walled structures for both vibration control and manufacturing constraints using a K-means clustering method [28]. Liu et al. analyzed the topology optimization of high-frequency vibration of solid structures using the energy finite element method (EFEM), which allows less calculation and a clear distribution of the energy density [29]. Yan et al. optimized the distribution of damping material in shell structures to minimize the residual vibration using SIMP, and the sensitivity was obtained using the adjoint method [30]. For vibration isolation problems, Zhou et al. developed a multi-objective and multi-level optimization method for the design of supporting structures and loci of isolators [31]. The topology optimization of one-material structures for displacement antiresonances at frequencies of interest is carried out by Silva et al [32]. These techniques allow the evolution of the topology without the need to perform remeshing, and most of the topological numerical methods have been implemented relying on the finite element method (FEM), which usually easily leads to checkboard patterns and grayscale problems.

However, the quantities on the boundary of the analyzing domain are engineers' concern in most cases for vibration isolation or waveguide problems. Unlike the finite element method, which involves substantial computational and memory expenditure during mesh generation, the boundary element method merely discretizes the model boundaries. This method offers advantages such as dimension reduction, high computational accuracy, and constant elements for modeling. Thus, the combination of the LSM with the boundary element method (BEM) provides an easy numerical updating process for the topology evolution since the zero isosurface/isoline of the level set function (LSF), which represents the boundaries emerging in the design domain, has the same dimension as boundary elements'. The simplicity of the pre-process and post-process in the generation of boundary elements makes the combination approach a promising tool for topology optimization problems. Jing et al. presented topology optimization for maximizing the total potential energy of thermal problems with the level set method and BEM [33]. Chen et al. optimized the topology and shape of sound-absorbing materials through isogeometric BEM [34–37] and optimized the topology of vibrating structures that interacted with acoustic waves through isogeometric FEM–BEM [38, 39], which reduced the radiated sound power and improved optimization efficiency. Isakari et al. developed topology optimization for acoustic-elastic coupled problems by employing a fast BEM–FEM coupled solver [40]. Oliveira et al. extended the isogeometric BEM to topology optimization based on the LSM for elastic static problems [41]. Matsushima et al. solved the defect detection inverse problems using the BEM [42], and Tang et al. considered the objective function, which includes the tangential derivative of displacements for cavity detection [43]. The application of the BEM-based topology method to the design of vibration control structures, however, is not sufficiently investigated. The suppression or magnification of the vibration amplitudes at certain frequencies can effectively manipulate the elastic wave propagation.

In view of the aforementioned advantages of the proposed methodology, the present work aims to extend the BEM and level set-based topology optimization to elastodynamic problems for the design of vibration control structures. The paper first introduces the formulas for the boundary integral equation and its discretization, and then, the topology optimization algorithm, which includes the formulation of the topology derivative and evolution equation, is presented. Numerical implementations are finally shown to demonstrate the effectiveness of the method for vibration isolation and waveguide applications.

2 Boundary element method for 2D elastodynamic problems

The linear elastodynamic problems are governed by the equation written in the form of displacement [44]:

$$(C_1^2 - C_2^2)q_{j,jk}(\mathbf{y},t) + C_2^2 q_{k,jj}(\mathbf{y},t) = \ddot{q}_k(\mathbf{y},t) \qquad \mathbf{y} \in \Omega,\ t \in [0,\infty], \tag{1}$$

where $\mathbf{y}$ denotes a point in the medium domain Ω and q_j denotes the x_j component of the displacement vector in Eq. 1. C_1 and C_2 are the P wave speed and S wave speed, respectively, which are written as

$$C_1 = \sqrt{E(1-\nu)/\{\rho(1+\nu)(1-2\nu)\}}, \tag{2}$$

$$C_2 = \sqrt{E/\{2\rho(1+\nu)\}}, \tag{3}$$

where E is the Young's modulus, ν is the Poisson's ratio, and ρ is the density of the medium, as shown in Eqs 2, 3.

Let us rewrite the governing equation by removing the time-related terms due to the harmonic vibration of linear elastic structures. Then, we have

$$(C_1^2 - C_2^2)Q_{j,jk}(\mathbf{y},\omega) + C_2^2 Q_{k,jj}(\mathbf{y},\omega) + \omega^2 Q_k(\mathbf{y},\omega) = 0, \tag{4}$$

where ω is the circular frequency and Q is a complex number that denotes the vibration displacement, including amplitude and phase. The boundary integral equation (BIE) form of Eq. 4 is written as

$$\begin{aligned} &c_{kl}(\mathbf{y}_s)Q_k(\mathbf{y}_s,\omega) + \int_\Gamma \Phi_{kl}^{\star}(\mathbf{y},\mathbf{y}_s,\omega)Q_k(\mathbf{y},\omega)\mathrm{d}\Gamma(\mathbf{y}) \\ &-\int_\Gamma \Psi_{kl}^{\star}(\mathbf{y},\mathbf{y}_s,\omega)T_k(\mathbf{y},\omega)\mathrm{d}\Gamma(\mathbf{y}) = 0 \qquad \mathbf{y}_s \in \Gamma, \end{aligned} \tag{5}$$

where c_{kl} is the free term of the BIE and the kernels $\Psi_{ij}(\mathbf{y},\mathbf{y}_s,\omega)$ and $\Phi_{ij}(\mathbf{y},\mathbf{y}_s,\omega)$ are known as displacement and traction fundamental solutions for 2D elastodynamic problems, respectively:

$$\Psi_{ij}^{\star}(\mathbf{y},\mathbf{y}_s,\omega) = \frac{1}{2\pi\rho C_2^2}\left[\psi\delta_{ij} - \chi r_{,i}r_{,j}\right], \tag{6}$$

$$\begin{aligned} \Phi_{ij}^{\star}(\mathbf{y},\mathbf{y}_s,\omega) = \frac{1}{2\pi}\Bigg\{&\left(\frac{d\psi}{dr} - \frac{1}{r}\chi\right)\left(\delta_{i,j}\frac{\partial r}{\partial n} + r_{,j}n_i\right) \\ &-\frac{2}{r}\chi\left(n_j r_{,j} \quad -2r_{,i}r_{,j}\frac{\partial r}{\partial n}\right) - 2\frac{d\chi}{dr}r_{,i}r_{,j}\frac{\partial r}{\partial n} \\ &+\left(\frac{C_1^2}{C_2^2} - 2\right)\left(\frac{d\psi}{dr} - \frac{d\chi}{dr} - \frac{1}{r}\chi\right)r_{,i}n_j\Bigg\}, \end{aligned} \tag{7}$$

where δ_{ij} is Kronecker's delta, r is the distance between $\mathbf{y}_s$ and $\mathbf{y}$, and n_i is the unit outward normal vector to the boundary in Eqs 6, 7.

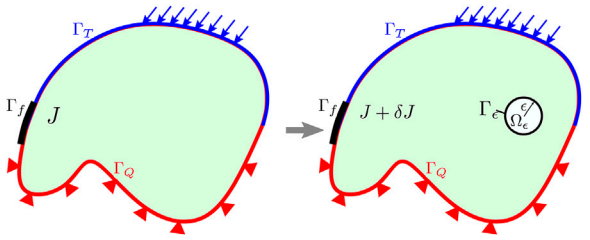

FIGURE 1
Variation in the objective function according to the removal of an infinitesimal cavity Ω_ϵ.

$$\psi = K_0\left(\frac{i\omega r}{C_2}\right) + \frac{C_2}{sr}\left[K_1\left(\frac{i\omega r}{C_2}\right) - \frac{C_2}{C_1}K_1\left(\frac{i\omega r}{C_1}\right)\right], \tag{8}$$

$$\chi = K_2\left(\frac{i\omega r}{C_2}\right) - \frac{C_2^2}{C_1^2}K_2\left(\frac{i\omega r}{C_1}\right), \tag{9}$$

where i is the imaginary unit and K_j denotes the modified Bessel functions of order j in Eqs 8, 9.

In order to evaluate the topological derivative, the expression of the stress is required:

$$\begin{aligned}\sigma_{ij}(\mathbf{y}_{\text{in}},\omega) = &\int_\Gamma T_k(\mathbf{y},\omega)D_{kij}(\mathbf{y}_{\text{in}},\mathbf{y},\omega)\mathrm{d}\Gamma(\mathbf{y})\\ &-\int_\Gamma Q_k(\mathbf{y},\omega)S_{kij}(\mathbf{y}_{\text{in}},\mathbf{y},\omega)\mathrm{d}\Gamma(\mathbf{y}),\end{aligned} \tag{10}$$

where $\mathbf{y}_{\text{in}}$ is a point in Ω and D_{kij} and S_{kij} are three-order tensors in Eq. 10.

Discretizing Eq. 5 with N constant boundary elements, we obtain a linear equation as follows:

$$\begin{aligned}&c_{kl}(\mathbf{y}_s)Q_k^j(\mathbf{y}_s,\omega) + \sum_{j=1}^{N}\left(\int_{\Gamma_j}\Phi_{kl}^\star(\mathbf{y},\mathbf{y}_s,\omega)\,\mathrm{d}\Gamma(\mathbf{y})\right)Q_k^j(\mathbf{y},\omega)\\ &-\sum_{j=1}^{N}\left(\int_{\Gamma_j}\Psi_{kl}^\star(\mathbf{y},\mathbf{y}_s,\omega)\,\mathrm{d}\Gamma(\mathbf{y})\right)T_k^j(\mathbf{y},\omega) = 0,\end{aligned} \tag{11}$$

where $c_{kl} = \frac{1}{2}\delta_{kl}$ when the boundary is smooth, $\mathbf{y}_s$ is a point on the boundary Γ, and $Q_k^j(\mathbf{y},\omega)$ and $T_k^j(\mathbf{y},\omega)$ denote the kth component of the displacement and traction of element Γ_j, respectively.

Let i in Eq. 11 vary from 1 to N; then, we obtain a system of $2N$ linear algebraic equations as shown in Eq. 12.

$$\mathbf{HQ} = \mathbf{GT}, \tag{12}$$

where $\mathbf{H}$ and $\mathbf{G}$ are $2N \times 2N$ matrices, respectively, and $\mathbf{Q}$ and $\mathbf{T} \in \mathbb{C}^{2N}$.

3 Topology optimization algorithm

3.1 Topological derivative

To carry out the topology optimization for a continuous medium, the sensitivity of the objective function with respect to the change in topology is needed. As shown in Figure 1, the objective function J is defined on Γ_f, which is a portion of the boundary of domain Ω_ϵ. The sensitivity can be considered the topological derivative $\mathcal{T}$, which can be formulated by computing the variation in the objective function δJ as a circular infinitesimal cavity Ω_ϵ with a radius ϵ being generated. Taking $\epsilon \to 0$, the topological derivative $\mathcal{T}$ at the center of the circular cavity is obtained.

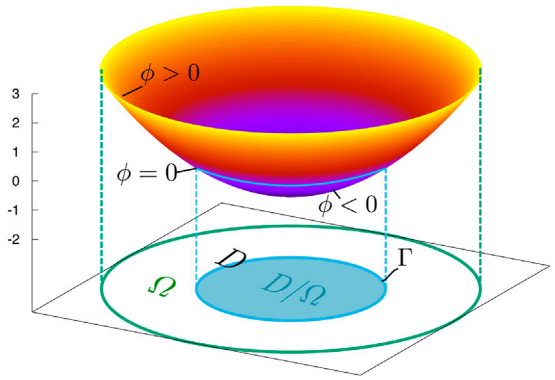

FIGURE 2
Medium domain Ω defined by the LSF implicitly.

Usually, the objective function is defined as a real value on the objective boundary Γ_f:

$$J = \int_{\Gamma_f} f(Q_k, T_k)d\Gamma. \tag{13}$$

As the cavity Ω_ϵ is generated, J changes to

$$J + \delta J = \mathrm{Re}\left[\int_{\Gamma_f}\left(f(Q_k,T_k) + \frac{\partial f}{\partial Q_k}\delta Q_k + \frac{\partial f}{\partial T_k}\delta T_k\right)d\Gamma\right]. \tag{14}$$

Subtracting Eq. 13 from Eq. 14, δJ is obtained as follows:

$$\delta J = \mathrm{Re}\left[\int_{\Gamma_f}\left(\frac{\partial f}{\partial Q_k}\delta Q_k + \frac{\partial f}{\partial T_k}\delta T_k\right)d\Gamma\right]. \tag{15}$$

To evaluate δJ in Eq. 15, we have to calculate δQ_k on Γ. However, the governing equation for δQ_k also governs the generated boundary Γ_ϵ and holds

$$\begin{aligned}(C_1^2 - C_2^2)\delta Q_{j,jk}(\mathbf{y},\omega) + C_2^2\delta Q_{k,jj}(\mathbf{y},\omega) + \omega^2\delta Q_k(\mathbf{y},\omega) = 0 \quad &\mathbf{y}\in\Omega\backslash\Omega_\epsilon,\\ \delta Q_k(\mathbf{y}) = 0 \quad &\mathbf{y}\in\Gamma_Q,\\ \delta T_k(\mathbf{y}) = 0 \quad &\mathbf{y}\in\Gamma_T,\\ \delta T_k(\mathbf{y}) = -T_k(\mathbf{y}) \quad &\mathbf{y}\in\Gamma_\epsilon,\end{aligned} \tag{16}$$

where δQ_k on Γ_ϵ cannot be acquired easily in Eq. 16. Thus, we introduce an adjoint field of $\tilde{Q}_k$ and $\tilde{T}_k$ using Betti's reciprocal theorem [45] to avoid the direct evaluation of δQ_k as follows:

$$\int_{\Gamma\cup\Gamma_\epsilon}\left(\tilde{T}_k\delta Q_i - \tilde{Q}_k\delta T_k\right)d\Gamma = 0, \tag{17}$$

and substituting the boundary conditions in Eq. 21 and 17, we have

$$-\int_{\Gamma_Q}\tilde{Q}_k\delta T_k d\Gamma + \int_{\Gamma_T}\tilde{T}_k\delta Q_k d\Gamma + \int_{\Gamma_\epsilon}\left(\tilde{T}_k\delta Q_k + \tilde{Q}_k T_k\right)d\Gamma = 0. \tag{18}$$

Assuming that Γ_f includes Γ_Q and Γ_T, δJ can be written as

$$\delta J = \mathrm{Re}\left[\int_{\Gamma_T}\frac{\partial f}{\partial Q_k}\delta Q_k d\Gamma + \int_{\Gamma_Q}\frac{\partial f}{\partial T_k}\delta T_k d\Gamma\right]. \tag{19}$$

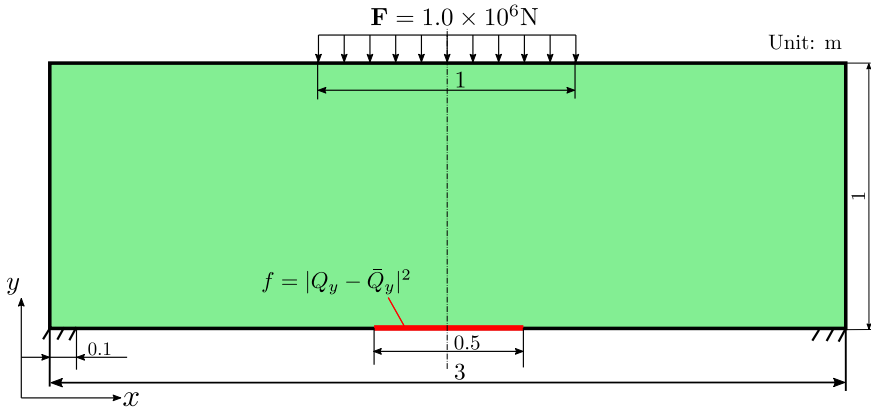

FIGURE 3
Definition of the boundary conditions for example 1.

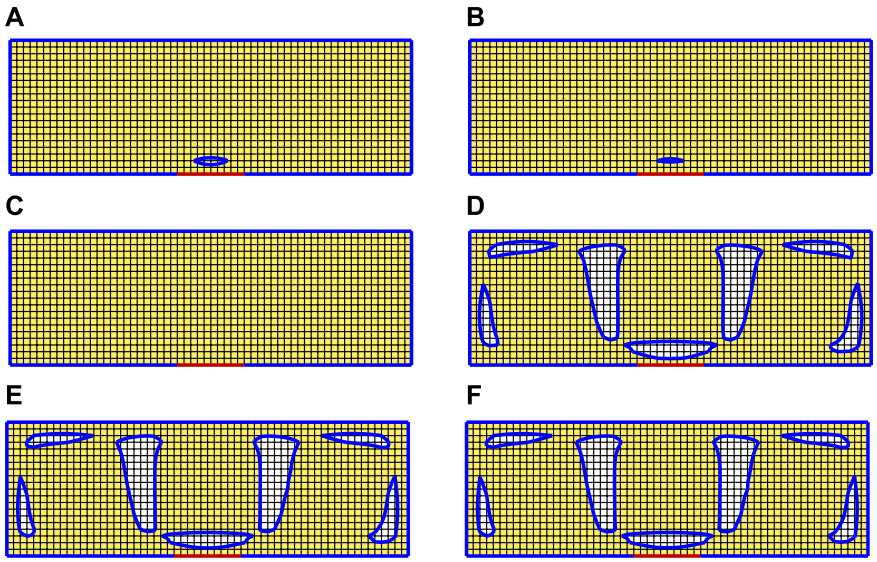

FIGURE 4
Intermediate optimized solutions during the iteration for example 1: a) Step 8, b) Step 10, c) Step 12, d) Step 13, e) Step 20, and f) Step 30.

Considering the adjoint field as the Lagrange multiplier, we obtained δJ by subtracting Eq. 18 from Eq. 19 as follows:

$$\delta J = \mathrm{Re}\left[\int_{\Gamma_T}\left(\frac{\partial f}{\partial Q_k} - \tilde{T}_k\right)\delta Q_k d\Gamma + \int_{\Gamma_Q}\left(\frac{\partial f}{\partial T_k} + \tilde{Q}_k\right)\delta T_k d\Gamma - \int_{\Gamma_\epsilon}\left(\tilde{T}_k \delta Q_k + \tilde{Q}_k T_k\right)d\Gamma\right]. \tag{20}$$

In order to avoid the evaluation of δQ_k, we can construct the adjoint field $\tilde{Q}_k$, which holds

$$\begin{aligned}(C_1^2 - C_2^2)\tilde{Q}_{j,jk}(\mathbf{y},\omega) + C_2^2\tilde{Q}_{k,jj}(\mathbf{y},\omega) + \omega^2\tilde{Q}_k(\mathbf{y},\omega) = 0 \quad & \mathbf{y} \in \Omega,\\ \tilde{Q}_k(\mathbf{y}) = -\frac{\partial f}{\partial T_k}(\mathbf{y}) \quad & \mathbf{y} \in \Gamma_Q,\\ \tilde{T}_k(\mathbf{y}) = \frac{\partial f}{\partial Q_k}(\mathbf{y}) \quad & \mathbf{y} \in \Gamma_T,\end{aligned} \tag{21}$$

and Eq. 20 becomes Eq. 22.

$$\delta J = \mathrm{Re}\left[-\int_{\Gamma_\epsilon}\left(\tilde{T}_k \delta Q_k + \tilde{Q}_k T_k\right)d\Gamma\right], \tag{22}$$

where the terms related to $\tilde{Q}_k$ and Q_k can be evaluated by taking the Taylor series expansions at the center of Ω_ϵ and the asymptotic expansion of δQ_k at the center of Ω_ϵ can be used for the evaluation of the terms, including δQ_k. The details of the evaluation can be found in [46], where δJ can be written in the form of Eq. 23.

$$\delta J = (\pi\epsilon^2)\mathcal{T} + o(\epsilon^3). \tag{23}$$

Let us consider the center of Ω_ϵ as point $\mathbf{y}$, and the topological derivative at the point $\mathbf{y}$ can be calculated by taking the limit, as shown in Eq. 24.

$$\mathcal{T}(\mathbf{y}) = \lim_{\varepsilon \to 0} \frac{\delta J}{\pi\varepsilon^2}. \tag{24}$$

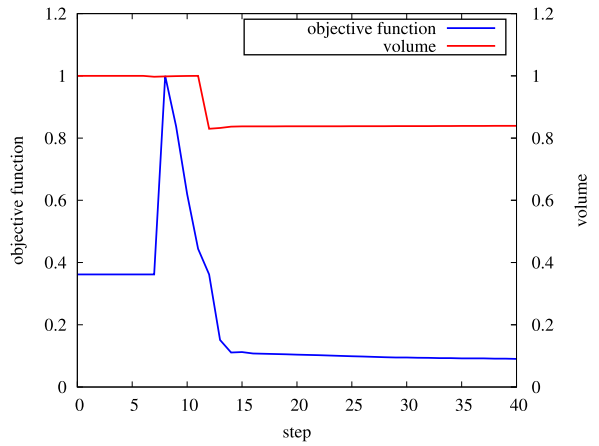

FIGURE 5
Convergence of the objective function and area for example 1.

The formula for $\mathcal{T}(\mathbf{y})$ is given in Eq. 25.

$$\mathcal{T}(\mathbf{y}) = \mathrm{Re}\left[\frac{\lambda+2\mu}{4\mu(\lambda+\mu)}\left(4\sigma_{jk}(\mathbf{y})\tilde{\sigma}_{jk}(\mathbf{y}) - \sigma_{jj}(\mathbf{y})\tilde{\sigma}_{kk}(\mathbf{y})\right) - \rho\omega^2 Q_j(\mathbf{y})\tilde{Q}_j(\mathbf{y})\right] \quad \mathbf{y} \in D, \tag{25}$$

where λ and μ are Lamé constants, which are given in Eq. 26.

$$\lambda = \frac{2\nu G}{1-2\nu}$$
$$\mu = \frac{E}{2(1+\nu)}. \tag{26}$$

3.2 LSM

The elastic material medium is defined by the LSF ϕ in the design domain D. As shown in Figure 2, for a point $\mathbf{y}$ in D, the medium and void are defined using the value of $\phi(\mathbf{y})$ as shown in Eq. 27.

$$\begin{cases} <\phi(\mathbf{y}) \le 1, & \mathbf{y} \in \Omega \\ \phi(\mathbf{y}) = 0, & \mathbf{y} \in \Gamma \\ -1 \le \phi(\mathbf{y}) < 0, & \mathbf{y} \in D\backslash\Omega \end{cases}. \tag{27}$$

The optimization problem for minimizing the objective function $J = \int_{\Gamma_f} f(Q_k, T_k)d\Gamma$ can be given in Eq. 28.

$$\inf_{\phi} \quad J(\chi_\phi) = \int_{\Gamma} f(Q_k, T_k)\chi_\phi d\Gamma, \tag{28}$$

subject to

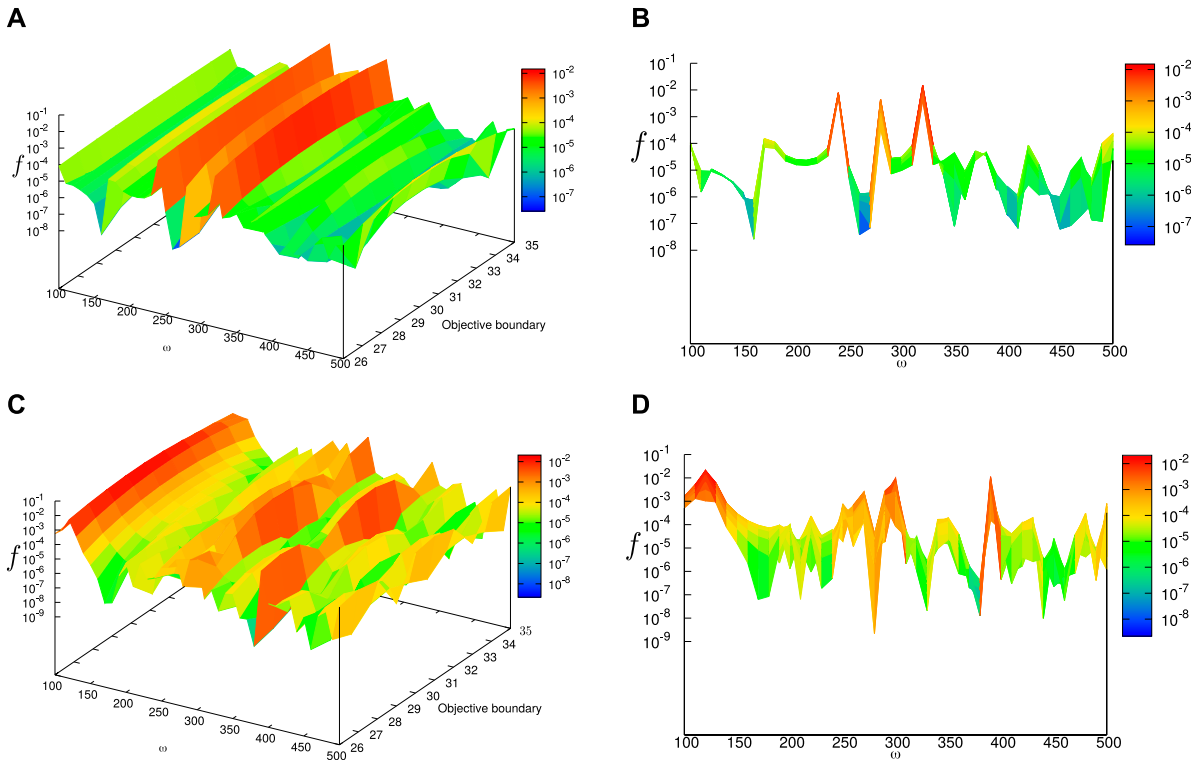

FIGURE 6
Objective function response of the structure before and after optimization for example 1 as ω varies from 100 Hz to 500 Hz: a) the vibration amplitude at objective boundary with frequency sweep from 100 Hz to 500 Hz before optimization. b) The vibration amplitude at objective boundary with frequency sweep from 100 Hz to 500 Hz before optimization (f−ω plane). c) The vibration amplitude at objective boundary with frequency sweep from 100 Hz to 500 Hz after optimization. d) The vibration amplitude at objective boundary with frequency sweep from 100 Hz to 500 Hz after optimization (f−ω plane).

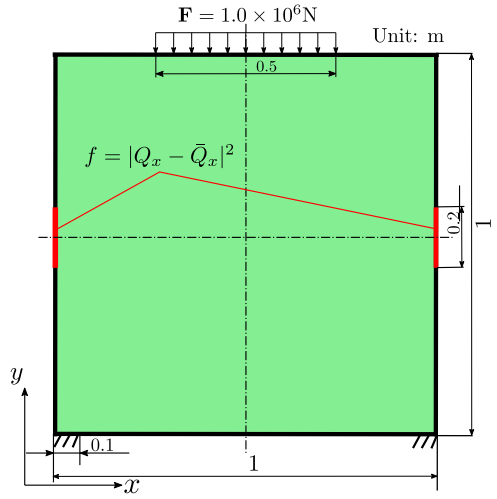

FIGURE 7
Definition of the boundary conditions for example 2.

$$I = \mathrm{Re}\left[\int_D \alpha\left[(C_1^2 - C_2^2)Q_{j,jk}(\mathbf{y},\omega) + C_2^2 Q_{k,jj}(\mathbf{y},\omega) + \omega^2 Q_k(\mathbf{y},\omega)\right]d\Omega\right] = 0, \tag{29}$$

where α is the Lagrange multiplier in Eq. 29.

$$G(\chi_\phi) = \int_D \chi_\phi d\Omega - G_{\max} \le 0, \tag{30}$$

where G is the volume constraint which controls the size of the material area, χ_ϕ is the characteristic function, and $G_{\max}$ is the admissible upper limit of the material area in Eq. 30.

Let us rewrite the objective function J using $\bar{J}$ as follows:

$$\bar{J} = F + I + \lambda G(\chi_\phi), \tag{31}$$

where λ is the Lagrange multiplier for the area constraint G in Eq. 31. According to the Karush–Kuhn–Tucker (KKT) condition, the optimal solution of the optimization problem is shown in Eq. 32.

$$\bar{J}' = F' + I' + \lambda = 0, \quad I = 0, \quad \lambda G(\chi_\phi) = 0, \quad \lambda \ge 0, \quad G(\chi_\phi) \le 0. \tag{32}$$

Let us introduce the reaction-diffusion equation:

$$\frac{\partial \phi(\mathbf{y})}{\partial t^\star} = K\left(\mathcal{T} - \lambda + \tau \nabla^2 \phi(\mathbf{y})\right), \tag{33}$$

where $\mathcal{T}$ is the topological derivative $F' + I'$ and K and τ are positive constants referred to as Tikhonov regularization parameters [47] in Eq. 33. K controls the updating speed, and τ decides the curvature of the LSF.

4 Numerical implementation

4.1 Example 1: vibration isolation at *y*-direction

Let us consider the structure depicted in Figure 3, where we can find the excitation force $\mathbf{F} = 1.0 \times 10^6$ N with the frequency at 230 Hz

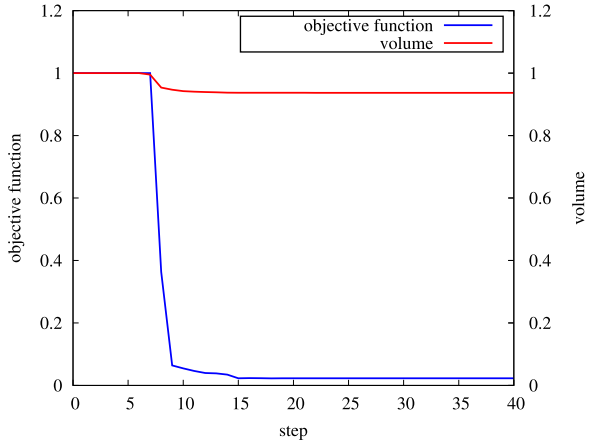

FIGURE 8
Convergence of the objective function and area for example 2.

and the objective function $f = |Q_y - \bar{Q}_y|^2$ with a given $\bar{Q}_y = 0$. The material constants are given as follows: Young's modulus $E = 1.248 \times 10^8$Pa, Poisson's ratio $\nu = 0.34$, and density $\rho = 1.6 \times 10^4$ kg/m^3. $\bar{Q}_y = 0$ implies that the purpose of the optimization is to decrease the vibration amplitude in the y-direction at the bottom of the rectangular design domain. The parameters for the evolution equation are specified as $K = 25$ and $\tau = 0.5$.

The intermediate results at steps 8, 10, 12, 13, 20, and 30 are presented in Figure 4. A small cavity is generated from step 8 and disappears at step 12; however, the cavities appear again at step 13 and reduce the vibration amplitude at the objective boundary. The convergence of the objective function and the area is shown in Figure 5. The convergence curve of the objective function shows the change in the vibration amplitude at the objective boundary, and it can be seen that the value of the objective function increases at step 8 and decreases rapidly from step 13. The increase in the objective function implies that the starting point of the topological derivative may just lose a solution and look for the next solution. Thus, one can find that the objective function increases first and then decreases rapidly. Finally, the objective function becomes smaller compared with it at the beginning. The optimal structure leads to a reduction in the vibration amplitude from 0.36 to 0.09 (normalized).

Let us consider the response problem of the optimized structure under the excitation frequency range [100, 500] Hz. As shown in Figure 6, the objective function, which implies the vibration amplitude at the objective boundary, presents a value of 10^{-2} at the optimizing frequency of 230 Hz before the optimization. However, the objective function decreases to approximately 10^{-7} after the optimization. The frequency sweep analysis implies that the optimized structure is effective for the isolation of vibration in the vicinity of 230 Hz, when the displacement response along the y-direction of the bottom of the rectangular structure is considered.

4.2 Example 2: vibration isolation at *x*-direction

In elastodynamic problems, when a structure is subjected to excitation forces, both longitudinal and transverse waves are

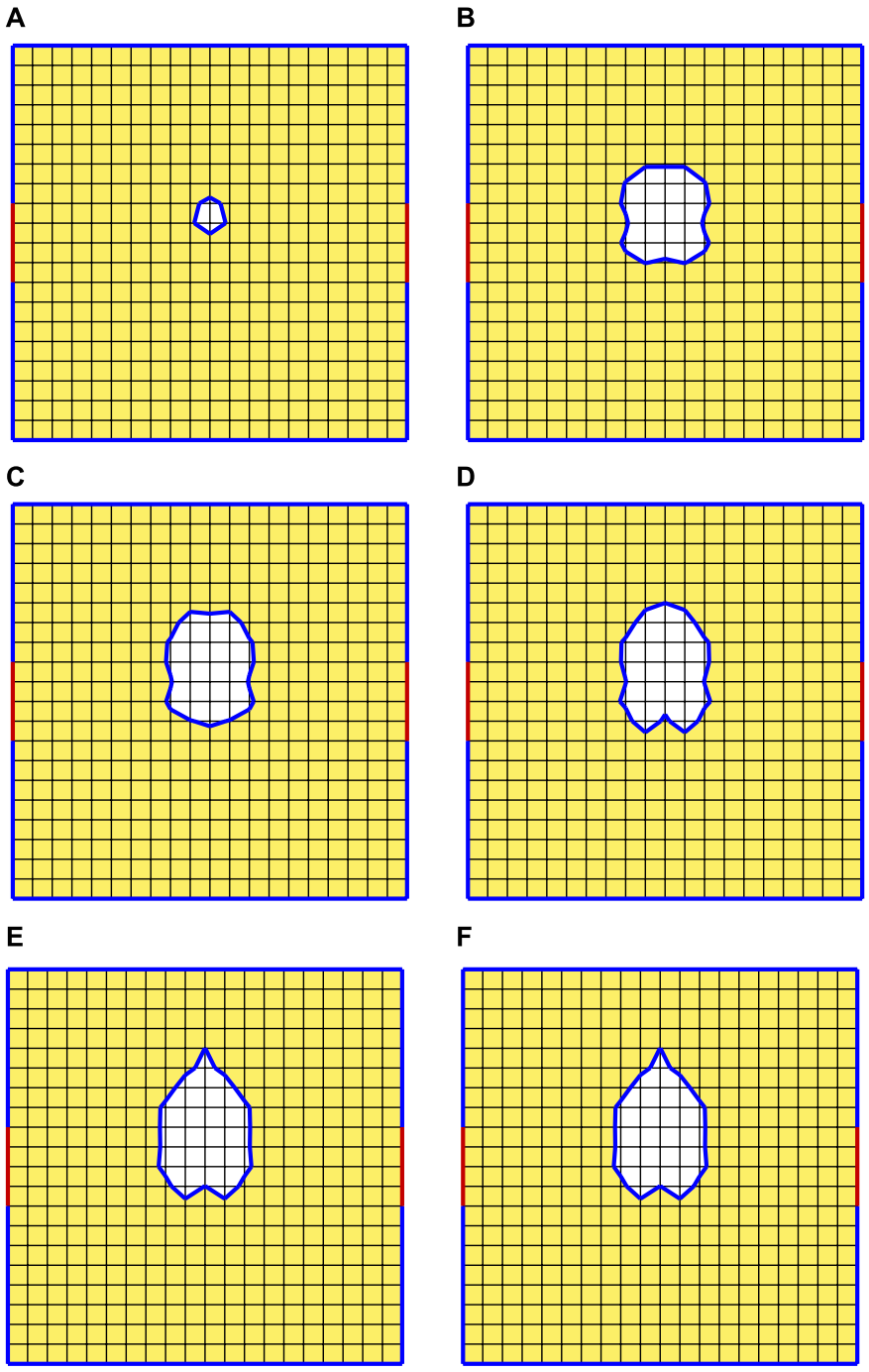

FIGURE 9
Intermediate optimized solutions during the iteration for example 2: a) Step 8, b) Step 9, c) Step 10, d) Step 11, e) Step 20, and f) Step 30.

generated inside the structure. At positions perpendicular to the direction of the excitation force, longitudinal waves in the structure are the main influencing factor of the magnitude of the external normal amplitude, while at positions parallel to them, transverse waves in the structure are the main influencing factor of the magnitude of the external normal amplitude. The model optimization in example 1 reduces the amplitude at the position perpendicular to the direction of the excitation force. Therefore, this example studies the amplitude magnitude at the position parallel to the excitation force in the structure.

Example 2 employs the model presented in Figure 7, where the objective boundaries are specified on the left and right sides of the square design domain uniformly. The material constants are given the same as those in example 1. The displacements along the x-direction are controlled through the definition of the objective function

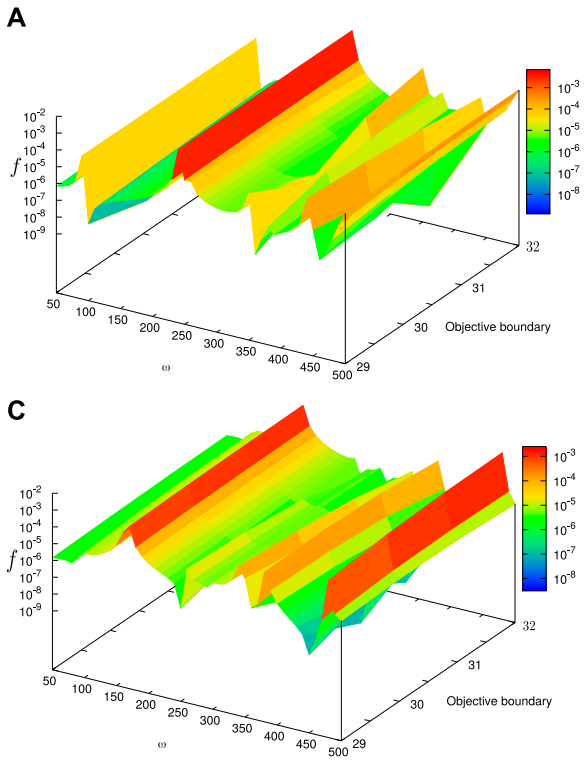

FIGURE 10
Objective function response of the structure before and after optimization for example 2 as ω varies from 50 Hz to 500 Hz: a) the vibration amplitude at objective boundary with frequency sweep from 50 Hz to 500 Hz before optimization. b) The vibration amplitude at objective boundary with frequency sweep from 50 Hz to 500 Hz before optimization (f−ω plane). c) The vibration amplitude at objective boundary with frequency sweep from 50 Hz to 500 Hz after optimization. d) The vibration amplitude at objective boundary with frequency sweep from 50 Hz to 500 Hz after optimization (f−ω plane).

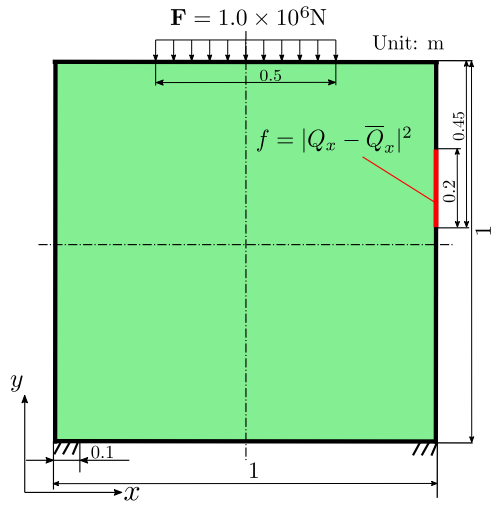

FIGURE 11
Definition of the boundary conditions for example 3.

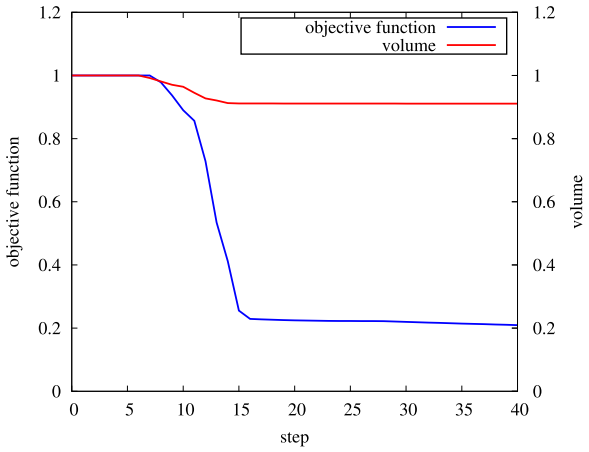

FIGURE 12
Convergence of the objective function and area for example 2.

$f = |Q_x - \bar{Q}_x|^2$ and $\bar{Q}_x = 0$. The constraints and harmonic loads are applied to the model with the excitation frequency at 250 Hz. Tikhonov's regularization parameters are specified as $K = 21$ and $\tau = 0.3$.

Figure 8 shows the convergence of the objective function and the area during the calculation. The objective function decreases to 0.029 from step 15 and converges to the vicinity of 0.027. A cavity is generated at step 8 and enlarged with the evolution of the LSF. Furthermore, from step 15, the generated cavity almost remains unchanged until step 40, and the results of steps 20 and 30 are also

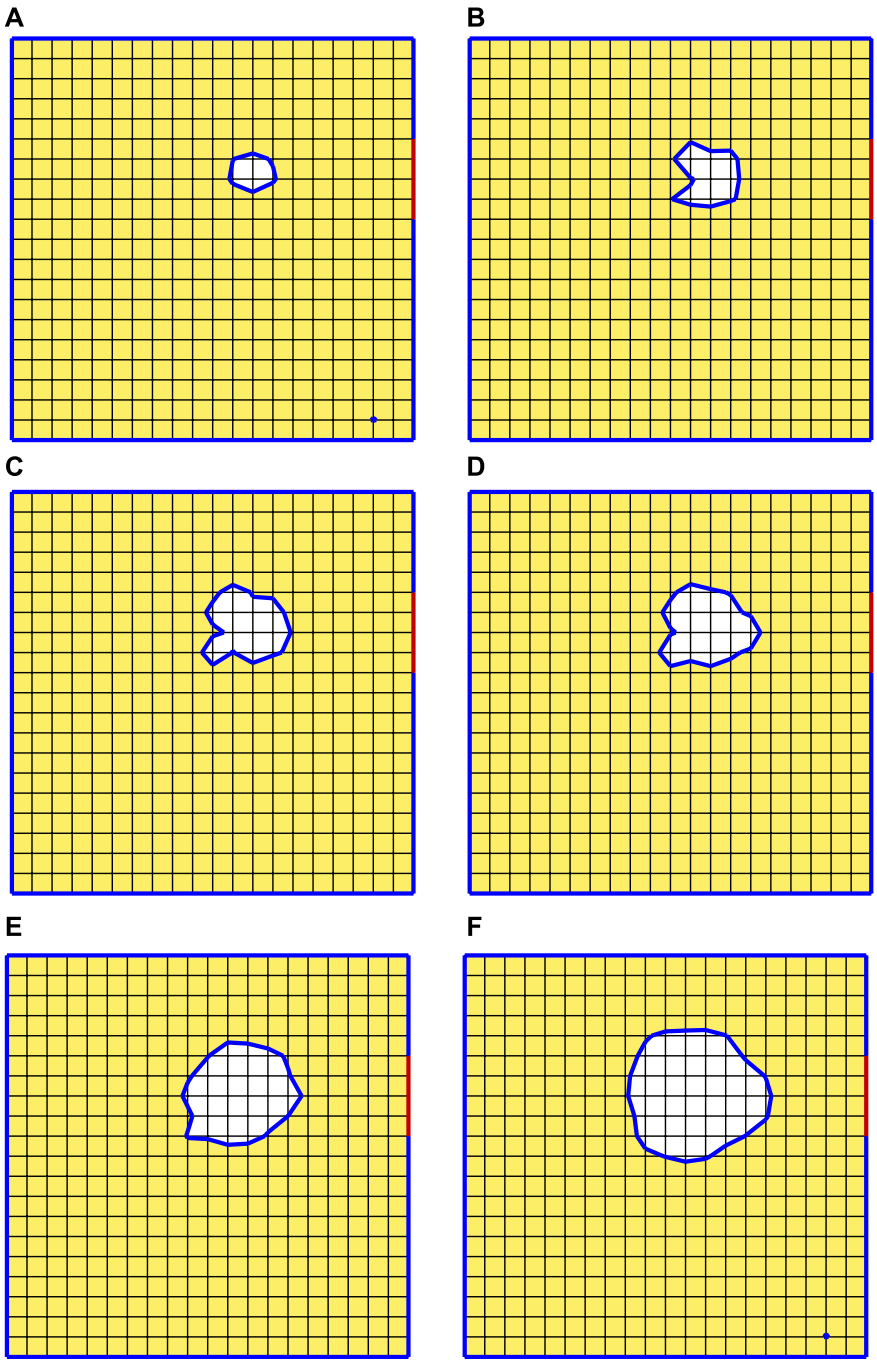

FIGURE 13
Intermediate optimized solutions during the iteration for example 3: a) Step 8, b) Step 9, c) Step 10, d) Step 11, e) Step 12, and f) Step 16.

presented in Figure 9. The reduction in the objective function demonstrates the effectiveness of the vibration suppression of the amplitude along the x-direction at the objective boundary. Moreover, the reduction in the vibration also happens at the neighborhood of 250 Hz according to the results of frequency sweep. The excitation frequency of 250 Hz is near the second natural frequency of the original design domain, and the peaks of the objective function in the frequency sweep analysis are shifted after optimization, as shown in Figure 10. The objective function with $\bar{Q}_x = 0$ changes along with the displacement's change, and the response presented in Figure 10B implies that not only the peak at 250 Hz is removed but also the first natural frequency is shifted.

4.3 Example 3: vibration enhanced at certain boundary

Another application of the proposed method is to enhance the vibration amplitude at a certain boundary. The model depicted in Figure 11 has the objective boundary defined on the right side of a

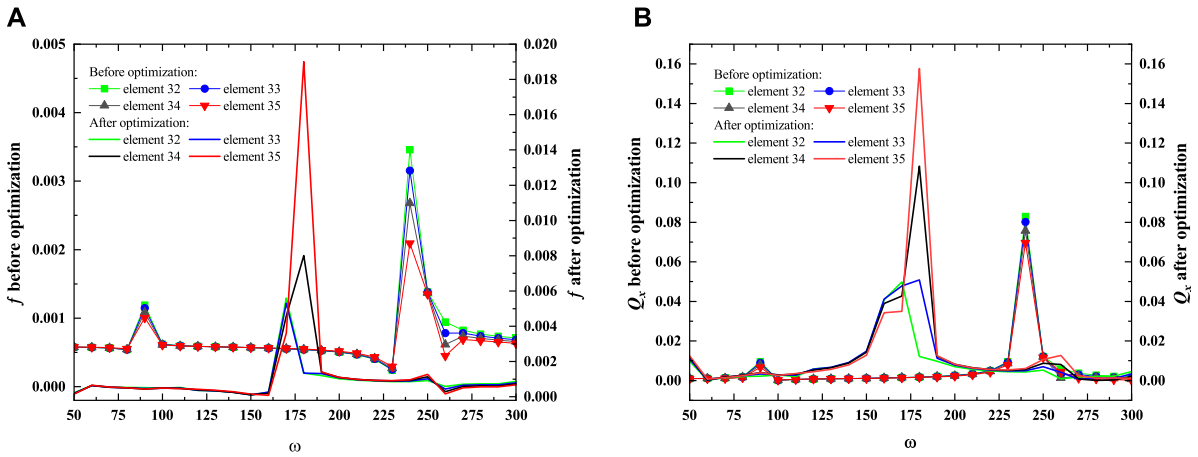

FIGURE 14
Responses of the objective function and vibration amplitude at the objective boundary of the structure before and after optimization for example 3 as ω varies from 50 Hz to 300 Hz: a) responses of the objective function and b)responses of the vibration amplitude.

TABLE 1 Values of f and Q_x at 150 Hz for example 3.

Element no.	f	f^*	Q_x(m)	Q_x^*m)
32	5.70×10^{-4}	1.10×10^{-4}	1.12×10^{-3}	1.45×10^{-2}
33	5.68×10^{-4}	1.03×10^{-4}	1.14×10^{-3}	1.48×10^{-2}
34	5.69×10^{-4}	1.15×10^{-4}	1.14×10^{-3}	1.42×10^{-2}
35	5.71×10^{-4}	1.50×10^{-4}	1.09×10^{-3}	1.27×10^{-2}

square design domain asymmetrically. The material constants are the same as in the previous examples,' and the excitation frequency is set at 150 Hz. The initial Q_x values at the objective boundary (from elements 32–35) lie between 1.09×10^{-3} m and 1.14×10^{-3} m. In order to guide the vibration energy to the objective boundary and strengthen the vibration amplitude, the objective function is defined as $f = |Q_x - \bar{Q}_x|^2$ with $\bar{Q}_x = 2.50 \times 10^{-2}$. The purpose is to reduce the objective function, and then, the amplitude can be enlarged due to the form of the defined f.

The reduction in the objective function can be observed in Figure 12, and it implies that the displacement is increasing. From step 16, the objective function decreases almost by 80%, and the cavity emerges from step 8, as shown in Figure 13. The cavity expands along with the iteration of LSF, which becomes steady from step 15. It can be seen that the generated cavity is located near the objective boundary, which leads to the strengthening of the vibration. The responses of both the objective function and displacement Q_x are displayed in Figure 14, where one can find that the order of the magnitude of the vibration amplitude along the x-direction is enlarged from 10^{-3} to 10^{-2}. Figure 14 also shows that the natural frequencies are modified by the change in topology. The detail of the vibration amplitude change at 150 Hz is presented in Table 1, where one can also find the change in the objective function.

Example 3 shows that the proposed topology optimization method can also be applied to vibration-enhancing problems, and the elastic wave can be guided to a certain portion of the boundary. Furthermore, τ affects the final optimized results, as shown in Figure 15, where the results at step 40 with $\tau = 0.1$, $\tau = 0.3$, $\tau = 0.7$, and $\tau = 0.9$ are presented, and it is found that the results can be manipulated by changing the curvature of LSF by defining different values of τ. The manufacturing requirement can be satisfied by choosing an appropriate value of τ.

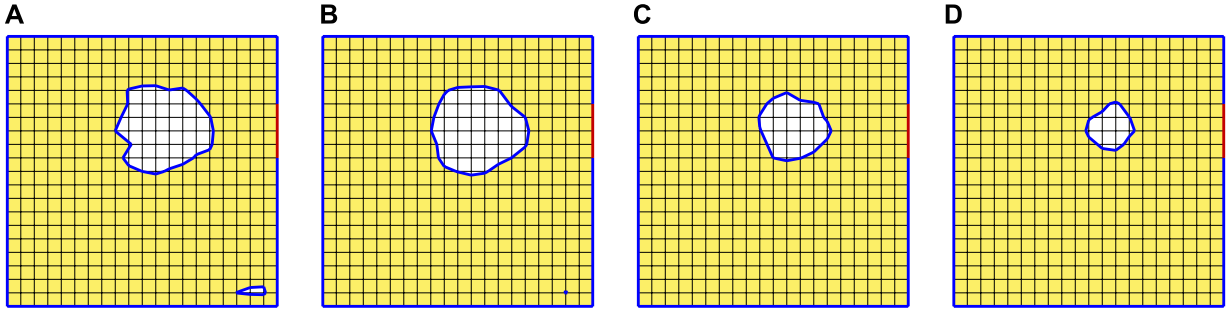

FIGURE 15
Optimized results with different τ values for example 3: a) τ = 0.1, b) τ = 0.3, c) τ = 0.7, and d) τ = 0.9.

5 Conclusion

The work is undertaken to propose a topology optimization methodology for 2D elastodynamic problems using BEM. The topological derivative obtained using the adjoint viable method includes the stress tensors of both the original and adjoint fields. The topology optimization methodology can generate clear boundaries due to the implicit expression of the voids by the LSF. Fortunately, the boundary-only discretization, which is one of the features of the BEM, leads to an easy rebuild of the numerical models in the iteration process. Several numerical examples with different optimization purposes are presented. The results of the simulations show that the proposed methodology is effective for structure topology design in the application of vibration isolation and waveguide problems.

Data availability statement

The original contributions presented in the study are included in the article/Supplementary material; further inquiries can be directed to the corresponding author.

Author contributions

HL: writing–original draft and writing–review and editing. HG: writing–original draft and writing–review and editing. JL: writing–review and editing. ZL: writing–review and editing. HX: writing–review and editing. CZ: writing–review and editing.

Funding

The author(s) declare that financial support was received for the research, authorship, and/or publication of this article. This work was supported by the Fundamental Research Program of Shanxi Province (grant no. 202203021221053), the National Natural Science Foundation of China (grant nos. 12272117 and 52075361), the Shanxi-Zheda Institute of Advanced Materials and Chemical Engineering (grant no. 2022SX-TD021), the Lvliang Science and Technology Guidance Special Key R&D Project (grant no. 2022XDHZ08), the Major Science and Technology Project of Shanxi Province (grant no. 20201102003), and the Key Research and Development Projects in Shanxi Province (grant no. 201903D421030).

Acknowledgments

The authors wish to express their appreciation to the reviewers for their helpful suggestions, which greatly improved the presentation of this paper.

Conflict of interest

The authors declare that the research was conducted in the absence of any commercial or financial relationships that could be construed as a potential conflict of interest.

Publisher's note

References

1. Kamesh D, Pandiyan R, Ghosal A Modeling, design and analysis of low frequency platform for attenuating micro-vibration in spacecraft. *J Sound Vibration* (2010) 329: 3431–50. doi:10.1016/j.jsv.2010.03.008

2. Yan B, Wang K, Kang C-X, Zhang X-N, Wu C-Y Self-sensing electromagnetic transducer for vibration control of space antenna reflector. *IEEE/ASME Trans Mechatronics* (2017) 22:1944–51. doi:10.1109/TMECH.2017.2712718

3. Huang P, Yao Y, Xiu W, Wu J, Geng D, Yang Z, et al. Vibration modelling and testing of off-road vehicle incorporating coupled roll and pitch vibrations. *Biosyst Eng* (2024) 240:111–22. doi:10.1016/j.biosystemseng.2024.02.006

4. Xiao P, Miao L, Zheng H, Lei L Low frequency vibration reduction bandgap characteristics and engineering application of phononic-like crystal metaconcrete material. *Construction Building Mater* (2024) 411:134734. doi:10.1016/j.conbuildmat.2023.134734

5. Fan X, Li L, Zhao L, He H, Zhang D, Ren Z, et al. Environmental noise pollution control of substation by passive vibration and acoustic reduction strategies. *Appl Acoust* (2020) 165:107305. doi:10.1016/j.apacoust.2020.107305

6. Rifaie MA, Abdulhadi H, Mian A Advances in mechanical metamaterials for vibration isolation: a review. *Adv Mech Eng* (2022) 14:168781322210828. doi:10.1177/16878132221082872

7. Cao X, Zhou F, Liu J, Ma Q Experimental study and numerical analysis for vibration isolation performance on open trench and wave impeding block combined vibration isolation barrier. *Soil Dyn Earthquake Eng* (2024) 177:108418. doi:10.1016/j.soildyn.2023.108418

8. Park S, Lee JY, Jeon W Vibration damping of plates using waveguide absorbers based on spiral acoustic black holes. *J Sound Vibration* (2022) 521:116685. doi:10.1016/j.jsv.2021.116685

9. Xu X, Barnhart MV, Fang X, Wen J, Chen Y, Huang G A nonlinear dissipative elastic metamaterial for broadband wave mitigation. *Int J Mech Sci* (2019) 164:105159. doi:10.1016/j.ijmecsci.2019.105159

10. Sigmund O, Maute K Topology optimization approaches:a comparative review. *Struct Multidisciplinary Optimization* (2013) 48:1031–55. doi:10.1007/s00158-013-0978-6

11. Huang X, Xie Y-M A further review of eso type methods for topology optimization. *Struct multidisciplinary optimization* (2010) 41:671–83. doi:10.1007/s00158-010-0487-9

12. Bendsøe MP, Kikuchi N Generating optimal topologies in structural design using a homogenization method. *Computer Methods Appl Mech Eng* (1988) 71:197–224. doi:10.1016/0045-7825(88)90086-2

13. Bendsøe MP Optimal shape design as a material distribution problem. *Struct optimization* (1989) 1:193–202. doi:10.1007/BF01650949

14. Rozvany GIN, Zhou M, Birker T Generalized shape optimization without homogenization. *Struct optimization* (1992) 4:250–2. doi:10.1007/BF01742754

15. Bendsøe MP, Sigmund O Material interpolation schemes in topology optimization. *Archive Appl Mech* (1999) 69:635–54. doi:10.1007/s004190050248

16. Groen JP, Langelaar M, Sigmund O, Ruess M Higher-order multi-resolution topology optimization using the finite cell method. *Int J Numer Methods Eng* (2017) 110: 903–20. doi:10.1002/nme.5432

17. Xie Y, Steven G A simple evolutionary procedure for structural optimization. *Comput Structures* (1993) 49:885–96. doi:10.1016/0045-7949(93)90035-C

18. Querin O, Steven G, Xie Y Evolutionary structural optimisation (eso) using a bidirectional algorithm. *Eng Computations* (1998) 15:1031–48. doi:10.1108/02644409810244129

19. Huang X, Xie Y Convergent and mesh-independent solutions for the bi-directional evolutionary structural optimization method. *Finite Elem Anal Des* (2007) 43:1039–49. doi:10.1016/j.finel.2007.06.006

20. Li Y Topology optimization of compliant mechanisms based on the beso method. Melbourne (Australia): Royal Melbourne Institute of Technology University (2014). Dissertation.

21. Guo X, Zhang W, Zhong W Doing topology optimization explicitly and geometrically - a new moving morphable components based framework. *J Appl Mech* (2014) 81:081009. doi:10.1115/1.4027609

22. Zhang W, Chen J, Zhu X, Zhou J, Xue D, Lei X, et al. Explicit three dimensional topology optimization via moving morphable void (mmv) approach. *Computer Methods Appl Mech Eng* (2017) 322:590–614. doi:10.1016/j.cma.2017.05.002

23. Zhang W, Song J, Zhou J, Du Z, Zhu Y, Sun Z, et al. Topology optimization with multiple materials via moving morphable component (mmc) method. *Int J Numer Methods Eng* (2018) 113:1653–75. doi:10.1002/nme.5714

24. Zhang W, Li D, Kang P, Guo X, Youn S-K Explicit topology optimization using iga-based moving morphable void (mmv) approach. *Computer Methods Appl Mech Eng* (2020) 360:112685. doi:10.1016/j.cma.2019.112685

25. Wang MY, Wang X, Guo D A level set method for structural topology optimization. *Computer Methods Appl Mech Eng* (2003) 192:227–46. doi:10.1016/S0045-7825(02)00559-5

26. Liu J, Ma YS 3d level-set topology optimization: a machining feature-based approach. *Struct Multidisciplinary Optimization* (2015) 52:563–82. doi:10.1007/s00158-015-1263-7

27. Chung H, Amir O, Kim HA Level-set topology optimization considering nonlinear thermoelasticity. *Computer Methods Appl Mech Eng* (2020) 361:112735. doi:10.1016/j.cma.2019.112735

28. Liu Y, Xiao D Shape feature controlled topology optimization of attached piezoelectric actuators for vibration control of thin-walled smart structures. *Appl Math Model* (2023) 120:575–94. doi:10.1016/j.apm.2023.03.018

29. Liu H, Zhang Z, Li B, Xie M, Hong J, Zheng S Topology optimization of high frequency vibration problems using the efem-based approach. *Thin-Walled Structures* (2021) 160:107324. doi:10.1016/j.tws.2020.107324

30. Yan K, Cheng GD, Wang BP Topology optimization of damping layers in shell structures subject to impact loads for minimum residual vibration. *J Sound Vibration* (2018) 431:226–47. doi:10.1016/j.jsv.2018.06.003

31. Zhou P, Du J, Lü Z Simultaneous topology optimization of supporting structure and loci of isolators in an active vibration isolation system. *Comput Structures* (2018) 194:74–85. doi:10.1016/j.compstruc.2017.09.006

32. Silva OM, Neves MM, Lenzi A On the use of active and reactive input power in topology optimization of one-material structures considering steady-state forced vibration problems. *J Sound Vibration* (2020) 464:114989. doi:10.1016/j.jsv.2019.114989

33. Jing G, Jia J, Xiang J Level set-based bem topology optimization method for maximizing total potential energy of thermal problems. *Int J Heat Mass Transfer* (2022) 182:121921. doi:10.1016/j.ijheatmasstransfer.2021.121921

34. Chen L, Lu C, Lian H, Liu Z, Zhao W, Li S, et al. Acoustic topology optimization of sound absorbing materials directly from subdivision surfaces with isogeometric boundary element methods. *Computer Methods Appl Mech Eng* (2020) 362:112806. doi:10.1016/j.cma.2019.112806

35. Chen L, Lian H, Natarajan S, Zhao W, Chen X, Bordas S Multi-frequency acoustic topology optimization of sound-absorption materials with isogeometric boundary element methods accelerated by frequency-decoupling and model order reduction techniques. *Computer Methods Appl Mech Eng* (2022) 395:114997. doi:10.1016/j.cma.2022.114997

36. Lu C, Chen L, Luo J, Chen H Acoustic shape optimization based on isogeometric boundary element method with subdivision surfaces. *Eng Anal Boundary Elem* (2023) 146:951–65. doi:10.1016/j.enganabound.2022.11.010

37. Chen L, Lian H, Liu Z, Chen H, Atroshchenko E, Bordas S Structural shape optimization of three dimensional acoustic problems with isogeometric boundary element methods. *Computer Methods Appl Mech Eng* (2019) 355:926–51. doi:10.1016/j.cma.2019.06.012

38. Chen L, Lian H, Dong H-W, Yu P, Jiang S, Bordas SP Broadband topology optimization of three-dimensional structural-acoustic interaction with reduced order isogeometric fem/bem. *J Comput Phys* (2024) 509:113051. doi:10.1016/j.jcp.2024.113051

39. Chen L, Lian H, Liu Z, Gong Y, Zheng C, Bordas S Bi-material topology optimization for fully coupled structural-acoustic systems with isogeometric fem–bem. *Eng Anal Boundary Elem* (2022) 135:182–95. doi:10.1016/j.enganabound.2021.11.005

40. Isakari H, Kondo T, Takahashi T, Matsumoto T A level-set-based topology optimisation for acoustic-elastic coupled problems with a fast bem-fem solver. *Computer Methods Appl Mech Eng* (2017) 315:501–21. doi:10.1016/j.cma.2016.11.006

41. Oliveira HL, de Castro e Andrade H, Leonel ED An isogeometric boundary element approach for topology optimization using the level set method. *Appl Math Model* (2020) 84:536–53. doi:10.1016/j.apm.2020.03.047

42. Matsumoto KMIT An application of topology optimisation to defect identification in two-dimensional elastodynamics with the bem and h-matrix method. *Int J Comput Methods Exp Measurements* (2018) 6:73. doi:10.2495/CMEN-V6-N6-1033-1042

43. Tang P, Matsushima K, Isakari H, Takahshi T, Matsumoto T An adjoint variable method for the topological derivative of the tangent derivative of boundary data. *Trans JASCOME* (2020) 20:19–201219.

44. Gao H, Matsumoto T, Takahashi T, Isakari H Investigation of finite/infinite unidirectional elastic phononic plates by bem. *Eng Anal Boundary Elem* (2014) 40:93–103. doi:10.1016/j.enganabound.2013.12.003

45. Barber JR *The reciprocal theorem*. Netherlands: Springer (1992).

46. Tang P *Level-set based topology optimization with objective functional of tangential derivatives of boundary displacement for two-dimensional elastodynamics problem*. Dissertation. Nagoya (Japan): Nagoya University (2021).

47. Tikhonov A, Arsenin VY *Solutions of ill-posed problems*. Washington, D.C: Winston and Sons (1997).

frontiers | Frontiers in Physics

TYPE Original Research
PUBLISHED 24 July 2024
DOI 10.3389/fphy.2024.1424995

OPEN ACCESS

EDITED BY
Pei Li,
University of Southern Denmark, Denmark

REVIEWED BY
Ang Zhao,
Shanghai Civil Aviation College, China
Heng Zhang,
Xi'an Jiaotong University, in collaboration with reviewer AZ
Kui Liu,
Harbin Institute of Technology, China
Cheng Ruhui,
Nanjing University of Aeronautics and Astronautics, in collaboration with reviewer KL

*CORRESPONDENCE
Chengmiao Liu,
lcm15139350198@163.com

RECEIVED 29 April 2024
ACCEPTED 28 May 2024
PUBLISHED 24 July 2024

CITATION
Hu Q and Liu C (2024), Two-dimensional electromagnetic scattering analysis based on the boundary element method.
Front. Phys. 12:1424995.
doi: 10.3389/fphy.2024.1424995

Two-dimensional electromagnetic scattering analysis based on the boundary element method

Qian Hu[1] and Chengmiao Liu[2]*

[1]Henan International Joint Laboratory of Structural Mechanics and Computational Simulation, College of Architecture and Civil Engineering, Huanghuai University, Zhumadian, China, [2]College of Architecture and Civil Engineering, Xinyang Normal University, Xinyang, China

An effective formula for the shape-sensitivity analysis of electromagnetic scattering is presented in this paper. First, based on the boundary element method, a new electromagnetic scattering formula is derived by combining the traditional electromagnetic scattering formula with the non-uniform rational B-spline (NURBS) curve, and the geometric model is represented by NURBS, which ensures the geometric accuracy, avoids the heavy grid division in the optimization process, and realizes the fast calculation of high-fidelity numerical solutions. Second, by deducing the sensitivity variables, the electromagnetic scattering equation of shape optimization is obtained, which can provide reliable data references for shape optimization. Finally, the effectiveness and accuracy of the algorithm are demonstrated by an example, and the sensitivity data of some examples are given.

KEYWORDS

two-dimensional, electromagnetic scattering, isogeometric boundary element method, non-uniform rational B-spline, deformation circle model

1 Introduction

At present, the field of radar detection and target stealth design has become a research hotspot, and electromagnetic simulation technology [1] as an indispensable tool in this field is also very important. Commonly used computational electromagnetic methods include finite element method (FEM) [2, 3], boundary element method (BEM) (or method of moment) [4], and finite difference time domain method (FDTD) [5] [6–8]. Among them, the boundary element method is more favored in solving electromagnetic problems because it is only discretized on the surface of the structure and naturally satisfies the radiation condition at infinity. Compared with other domain discretization methods, the boundary element method has higher computational accuracy and smaller degrees of freedom.

Electromagnetic scattering sensitivity analysis has gradually become a hot field with the development of computational electromagnetism. Sensitivity analysis is a statistical method used to observe the behavior or changes in a model by varying its variables within a specific range. It enables the identification and evaluation of relationships between data, systems, or models in order to optimize the model efficiently [9–11]. In the context of electromagnetic scattering, sensitivity analysis aims to explore and analyze how an object or system responds and performs under such conditions. This analysis provides valuable guidance for evaluating object performance and optimizing system design through parameter adjustments [12-14]. Commonly employed methods for electromagnetic scattering

sensitivity analysis include derivative-based local approach [15, 16], linear-regression analysis [17-19], and variogram analysis [20, 21] of response surfaces. In this study, we adopted the derivative-based local approach and derived the corresponding shape sensitivity analysis equation through partial differentiation with respect to shape variables. However, the traditional boundary element method employs low-order Lagrange polynomials as basis functions (e.g., Raviart–Thomas [22] or RWG [1] basis functions), which leads to certain limitations: 1) inability to capture intricate details in complex models, resulting in reduced geometric accuracy and 2) utilization of low-order basis functions for approximating physical fields diminishes both the accuracy and sensitivity of the objective function.

The isogeometric analysis (IGA) [23, 24] proposed by Hughes et al. provides a new way to solve the above problems. The key point of IGA is to approximate the physical field by spline function. The use of IGA can avoid repeated mesh division, realize the interaction between Computer Aided Design and Computer Aided Engineering, improve the accuracy of the objective function, and avoid the secondary machining of the model. Isogeometric analysis was first introduced into the finite element method and then quickly generalized to other methods such as the boundary element method. IGA received very wide attention as soon as it was proposed and was quickly applied to elasticity [25–29], fracture mechanics [8, 30–33], acoustic [34–43], fluid mechanics [44–46], flexible composites [9, 47–51], heat conduction [52–55], etc., [56, 57]. However, IGA has not been used in electromagnetism because it needs to meet the divergence and curl coincidence conditions. [58], who proposed B-spline-compatible vector and other geometric finite elements to construct discrete de Rham sequences, made significant achievements in solving this problem [59, 60]. The introduction of compatible B-splines into the boundary element method [61] by Simpson et al. is an important step in the application of the isogeometric boundary element method (IGABEM) in electromagnetics. [62] used the IGABEM to solve the three-dimensional double periodic multilayer structure of electromagnetic scattering problems. [63–65], using the IGABEM combined with the nth-order perturbation method, quantitatively analyzed the uncertainty of the electromagnetic scattering incidence frequency of an antenna array structure. All these have promoted the development of the IGABEM in electromagnetism. In this paper, non-uniform rational B-spline (NURBS) is used as the basis function, and the electromagnetic scattering analysis equation is obtained by combining equal geometry and boundary elements. On this basis, the electromagnetic scattering sensitivity analysis equation for shape sensitivity analysis is derived. To sum up, the innovations of this paper are as follows:

- The formula for electromagnetic scattering analysis is obtained by using the NURBS curve as the basis function
- The IGABEM is used for shape design sensitivity for 2D electromagnetic scattering.

The remainder of this paper is organized as follows: Section 2 gives the IGABEM formula for solving the electromagnetic scattering analysis problem with NURBS as the basis function;

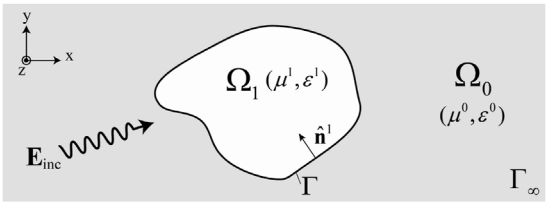

FIGURE 1
A target structure residing within an infinite domain impinged by an electromagnetic plane wave Ω_0 is the unbounded exterior region to which the free space parameters are assigned (μ^0,ε^0); $\hat{n}^1$ denotes the boundary of Ω_1. The normal vector $\hat{n}^1$ points toward the interior of Ω_1 from its interface.

Section 3 introduces the shape sensitivity analysis formula with shape design as variables; Section 4 presents two models to verify the accuracy and effectiveness of the IGABEM, and some shape sensitivity data of the models are also given; and Section 5 provides a summary of the paper.

2 Electromagnetic scattering analysis with the Galerkin IGABEM under transverse electric polarization

This section uses the IGABEM. First, the surface current is obtained by solving the surface integral equation, and then the scattering field is obtained by combining the obtained current with the two-dimensional electric field radiation equation. Finally, the two-dimensional radar cross-section is solved by the scattering field and incident field.

2.1 Boundary integral equations

We first assume a bounded field Ω_1 whose connected boundary Γ is in the unbounded field Ω_0 and whose permittivity and permeability are the scalars ε^0 and μ^0, respectively. An electromagnetic plane wave $\mathbf{E}_{\text{inc}}$ with angular frequency ω is applied to an object with wave number $k = \omega\sqrt{\varepsilon^0\mu^0}$, as shown in Figure 1.

The surface integral equations on Ω are as follows:

$$\left[\mathrm{i}\omega\mu\left(\mathcal{L}\mathbf{J}\right)(\tilde{\mathbf{r}}) + \left(\mathcal{K}\mathbf{M}\right)(\tilde{\mathbf{r}})\right]_{\tan} + \frac{1}{2}\hat{\mathbf{n}}(\tilde{\mathbf{r}}) \times \mathbf{M}(\tilde{\mathbf{r}}) = \left[\mathbf{E}_{\text{inc}}(\tilde{\mathbf{r}})\right]_{\tan}, \quad (1)$$

$$\hat{\mathbf{n}}(\tilde{\mathbf{r}}) \times \left[\mathrm{i}\omega\varepsilon\left(\mathcal{L}\mathbf{M}\right)(\tilde{\mathbf{r}}) - \left(\mathcal{K}\mathbf{J}\right)(\tilde{\mathbf{r}})\right]_{\tan} + \mathbf{J}(\tilde{\mathbf{r}}) = \hat{\mathbf{n}}(\tilde{\mathbf{r}}) \times \left[\mathbf{H}_{\text{inc}}(\tilde{\mathbf{r}})\right]_{\tan}, \quad (2)$$

where $\mathbf{J}$ and $\mathbf{M}$ represent surface current and surface magnetic flow, respectively, and $(\cdot)_{\tan}$ denotes tangential components of the vector. The operators $\mathcal{L}$ (Eq. 4) and $\mathcal{K}$ (Eq. 3) are

$$\left(\mathcal{L}\mathbf{J}\right)(\tilde{\mathbf{r}}) = \left[1 + \frac{1}{k^2}\nabla\nabla\cdot\right]\int_{\Gamma(\mathbf{r})} G(\tilde{\mathbf{r}},\mathbf{r})\mathbf{J}(\mathbf{r})d\Gamma(\mathbf{r}) \quad (3)$$

$$\left(\mathcal{K}\mathbf{M}\right)(\tilde{\mathbf{r}}) = \nabla \times \int_{\Gamma(\mathbf{r})} G(\tilde{\mathbf{r}},\mathbf{r})\mathbf{M}(\mathbf{r})d\Gamma^{l}(\mathbf{r}), \quad (4)$$

where $\mathbf{E}_{\text{inc}}(\tilde{\mathbf{r}})$ and $\mathbf{H}_{\text{inc}}(\tilde{\mathbf{r}})$ represent the electric and magnetic fields, respectively, generated by the incident wave, which exist only in Ω_0. $G(\tilde{\mathbf{r}},\mathbf{r})$ denotes Green's function. Green's function for 2D problems (Eq. 5) can be written as

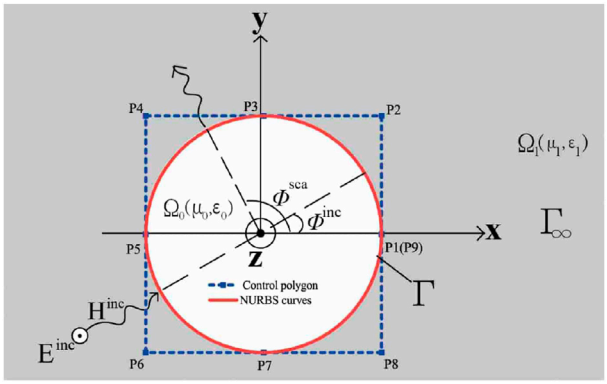

FIGURE 2
Sectional model boundary NURBS curve and control point.

$$G(\tilde{\mathbf{r}},\mathbf{r}) = -\frac{\mathrm{i}}{4}H_0^{(2)}(kr), \quad \text{with} \quad r = |\tilde{\mathbf{r}} - \mathbf{r}|, \tag{5}$$

where $H_0^{(2)}$ denotes the Hankel functions of the second kinds of order zero.

Eqs 1, 2 are the surface electric field integral equation (EFIE) and surface magnetic field integral equation (MFIE), respectively. When dealing with closed conductors, the internal resonance phenomenon is easy to occur, resulting in non-unique solutions for the EFIE and MFIE. The most common way to deal with this problem is to combine the MFIE with EFIE to obtain a combined integral equation called the combined field integral equation (CFIE) (Eq. 6), which is expressed as follows:

$$\alpha\mathbf{EFIE} + (1-\alpha)\eta\mathbf{MFIE}, \tag{6}$$

where $\eta = \sqrt{\mu^0/\varepsilon^0}$ and $0 \leqslant \alpha \leqslant 1$, and $\alpha = 0.5$ is commonly used.

When the incident wave is TE polarized, the incident electric field and magnetic field are

$$\mathbf{E}_{\mathrm{inc}}(\mathbf{x}) = e^{ik\left(x_1\cos\left(\phi_{\mathrm{inc}}\right)+x_2\sin\left(\phi_{\mathrm{inc}}\right)\right)}\hat{\mathbf{z}}, \tag{7}$$

and

$$\mathbf{H}_{\mathrm{inc}}(\mathbf{x}) = \frac{1}{\eta}\left[-\sin\left(\phi_{\mathrm{inc}}\right)\hat{\mathbf{x}} + \cos\left(\phi_{\mathrm{inc}}\right)\hat{\mathbf{y}}\right]\cdot e^{ik\left(x_1\cos\left(\phi_{\mathrm{inc}}\right)+x_2\sin\left(\phi_{\mathrm{inc}}\right)\right)}. \tag{8}$$

The TE polarizes with only a $\hat{\mathbf{z}}$ component, so Eqs 6, 7 can be written as

$$\frac{\omega\mu}{4}\int_{\Gamma(\mathbf{y})}\mathbf{J}(\mathbf{y})H_0^{(2)}(kr)d\Gamma(\mathbf{y}) = \mathbf{E}_{\mathrm{inc}}(\mathbf{x}) \tag{9}$$

and Eq. 10

$$\frac{1}{2}\mathbf{J}(\mathbf{x}) + \frac{\mathrm{i}k}{4}\int_{\Gamma(\mathbf{y})}\mathbf{J}(\mathbf{y})\left[\hat{\mathbf{n}}(\mathbf{x})\cdot\hat{\mathbf{r}}\right]H_1^{(2)}(kr)d\Gamma(\mathbf{y}) = \hat{\mathbf{n}}(\mathbf{x})\times\mathbf{H}_{\mathrm{inc}}(\mathbf{x}), \tag{10}$$

where Eq. 11

$$\hat{\mathbf{n}}(\mathbf{x})\cdot\hat{\mathbf{r}} = \frac{\partial r}{\partial n(\mathbf{x})} = r_{,\ell}n_\ell(\mathbf{x}), \qquad \ell = 1,2 \tag{11}$$

and Eq. 12

$$\hat{\mathbf{n}}(\mathbf{x})\times\mathbf{H}_{\mathrm{inc}}(\mathbf{x}) = \mathbf{H}_{\mathrm{inc}}^{n}(\mathbf{x}) = \frac{1}{\eta}\left[n_1(\mathbf{x})\cos\left(\phi_{\mathrm{inc}}\right) + n_2(\mathbf{x})\sin\left(\phi_{\mathrm{inc}}\right)\right]e^{ik\left(x_1\cos\left(\phi_{\mathrm{inc}}\right)+x_2\sin\left(\phi_{\mathrm{inc}}\right)\right)}\hat{\mathbf{z}}. \tag{12}$$

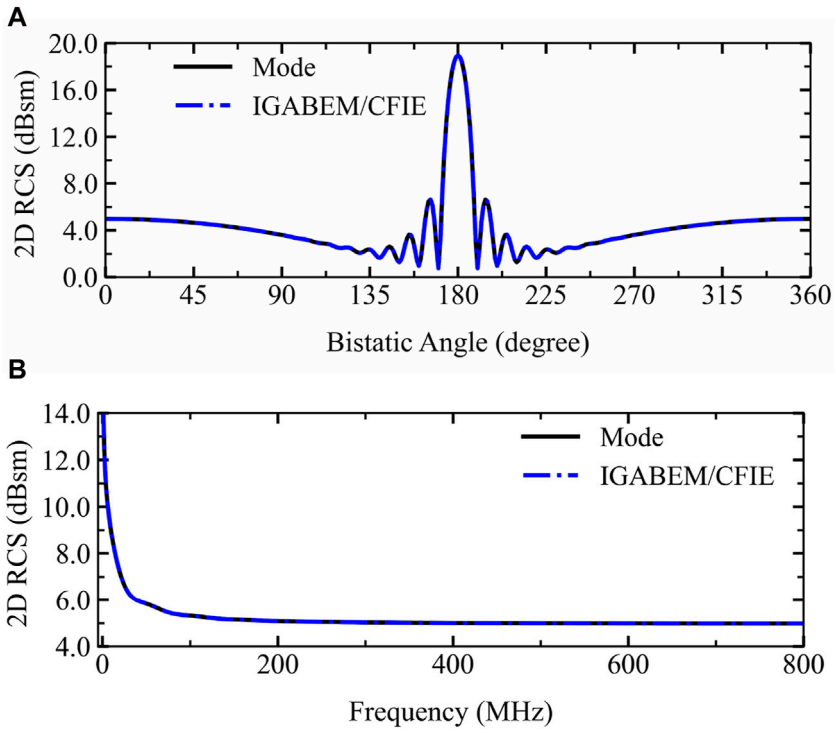

FIGURE 3
The RCS for PEC cylinder. **(A)** The RCS at 800 MHz under back-scattering. **(B)** The RCS at $\phi^{\mathrm{inc}} = 0$ at different frequency.

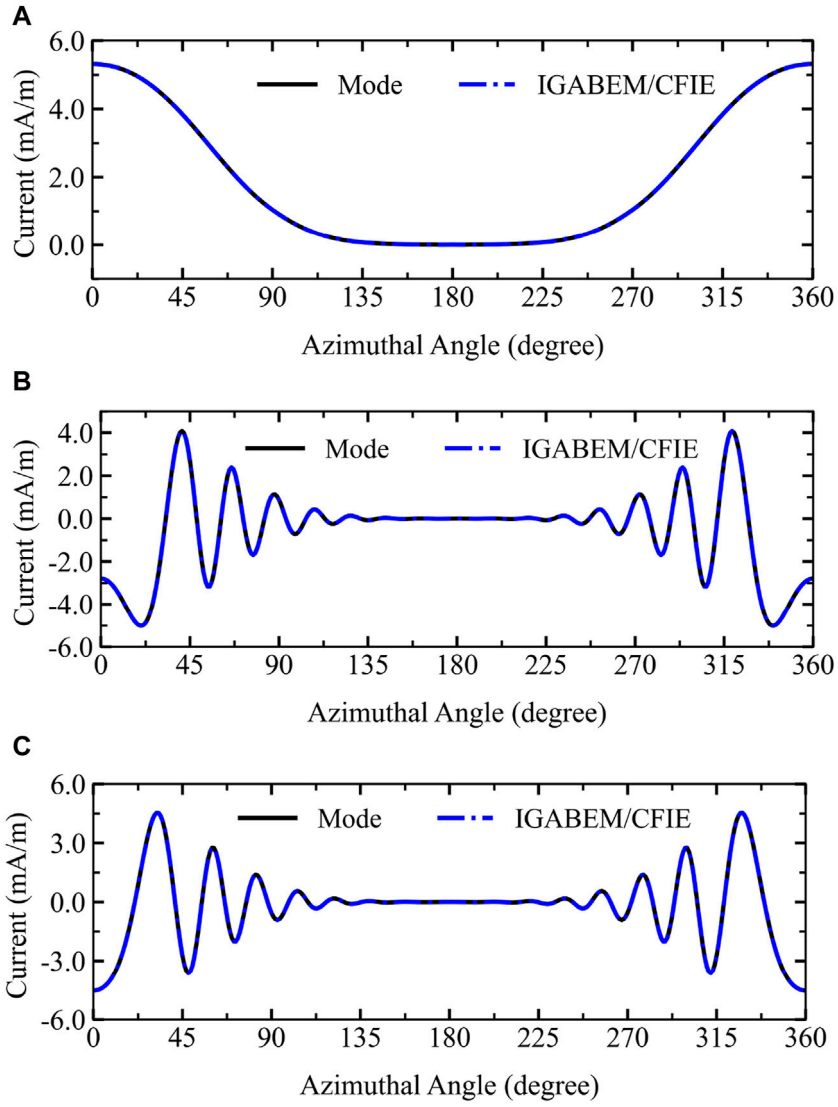

FIGURE 4
Current for the cylinder at 800 MHz with $\phi^{inc} = 0$. **(A)** |Jz(ϕ a)|; **(B)** Re Jz(ϕ a); and **(C)** Im Jz (ϕ a).

In IGA, NURBS is used for constructing geometry and discretizing physical field. A point with Cartesian coordinate $\mathbf{x}$ at a NURBS (Eq. 13) curve is expressed by

$$\mathbf{x}(\xi) = \sum_{i=1}^{N_f} R_i(\xi)\mathbf{P}_i, \tag{13}$$

where $\mathbf{P}_i$ denotes the ith control point. $R_i^z(\xi)$ is the NURBS basis function with order p and ξ parametric coordinates. The electric and magnetic currents in Ω_0 are discretized with NURBS basis functions as Eq. 14

$$\mathbf{J}(\mathbf{y}) = \sum_{i=1}^{N_f} \mathbf{R}_i^z(\mathbf{y})X_i^J, \quad \mathbf{J}(\mathbf{x}) = \sum_{i=1}^{N_f} \mathbf{R}_i^z(\mathbf{x})X_i^J. \tag{14}$$

Using the weighted basis function and the test function to expand Eqs 8, 9, the matrix elements of Eqs 8, 9 can be obtained as Eq. 15

$$\begin{aligned} A_E^J(j,i) &= \frac{\omega\mu}{4}\int_{\Gamma(\mathbf{x})} \mathbf{R}_j^z(\mathbf{x}) \cdot \int_{\Gamma(\mathbf{y})} \mathbf{R}_i^z(\mathbf{y}) H_0^{(2)}(kr) d\Gamma(\mathbf{y}) d\Gamma(\mathbf{x}) \\ &= \frac{\omega\mu}{4}\sum_{\tilde{e}=1}^{N_e}\sum_{e=1}^{N_e}\int_{\Gamma_{\tilde{e}}} \mathbf{R}_j^z(\mathbf{x}(\xi)) \cdot \int_{\Gamma_e} \mathbf{R}_i^z(\mathbf{y}(\xi)) H_0^{(2)}(kr(\xi)) \\ &\quad \times d\Gamma(\mathbf{y}(\xi)) d\Gamma(\mathbf{x}(\xi)) \end{aligned} \tag{15}$$

and Eq. 16

$$\begin{aligned} A_H^J(j,i) &= \frac{1}{2}\int_{\Gamma(\mathbf{x})} \mathbf{R}_j^z(\mathbf{x}) \cdot \mathbf{R}_i^z(\mathbf{x}) d\Gamma(\mathbf{x}) + \frac{ik}{4}\int_{\Gamma(\mathbf{x})} \mathbf{R}_j^z(\mathbf{x}) \cdot \int_{\Gamma(\mathbf{y})} \mathbf{R}_i^z(\mathbf{y}) \\ &\quad \times [\hat{\mathbf{n}}(\mathbf{x}) \cdot \hat{\mathbf{r}}] H_1^{(2)}(kr) d\Gamma(\mathbf{y}) d\Gamma(\mathbf{x}) \\ &= \frac{1}{2}\sum_{\tilde{e}=1}^{N_e}\int_{\Gamma_{\tilde{e}}} \mathbf{R}_j^z(\mathbf{x}(\xi)) \cdot \mathbf{R}_i^z(\mathbf{x}(\xi)) d\Gamma(\mathbf{x}(\xi)) + \frac{ik}{4}\sum_{\tilde{e}=1}^{N_e} \\ &\quad \times \sum_{e=1}^{N_e}\int_{\Gamma_{\tilde{e}}} \mathbf{R}_j^z(\mathbf{x}(\xi)) \cdot \int_{\Gamma_e} \mathbf{R}_i^z(\mathbf{y}(\xi)) \\ &\quad \times [\hat{\mathbf{n}}(\mathbf{x}(\xi)) \cdot \hat{\mathbf{r}}(\xi)] H_1^{(2)}(kr(\xi)) d\Gamma(\mathbf{y}(\xi)) d\Gamma(\mathbf{x}(\xi)), \end{aligned} \tag{16}$$

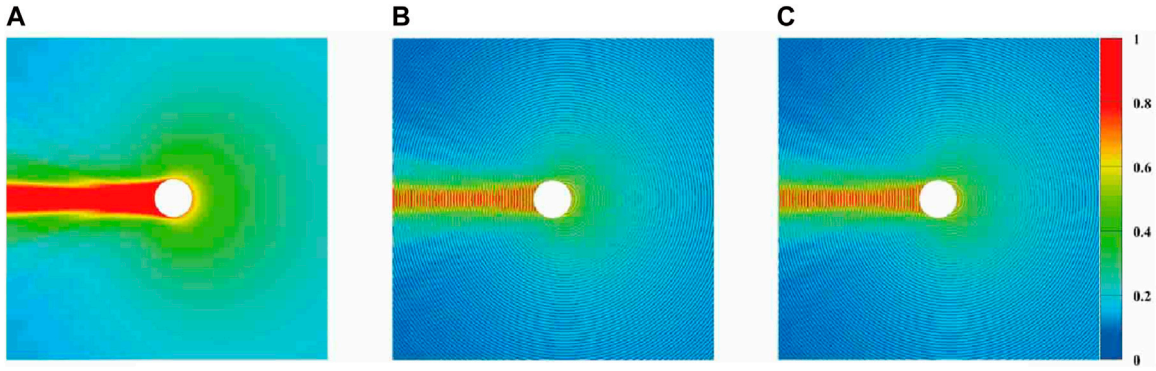

FIGURE 5
Electric field distribution around the PEC cylinder at 800 MHz: **(A)** ABS (Ez); **(B)** |Re(Ez)|; and **(C)** |Im(Ez)|.

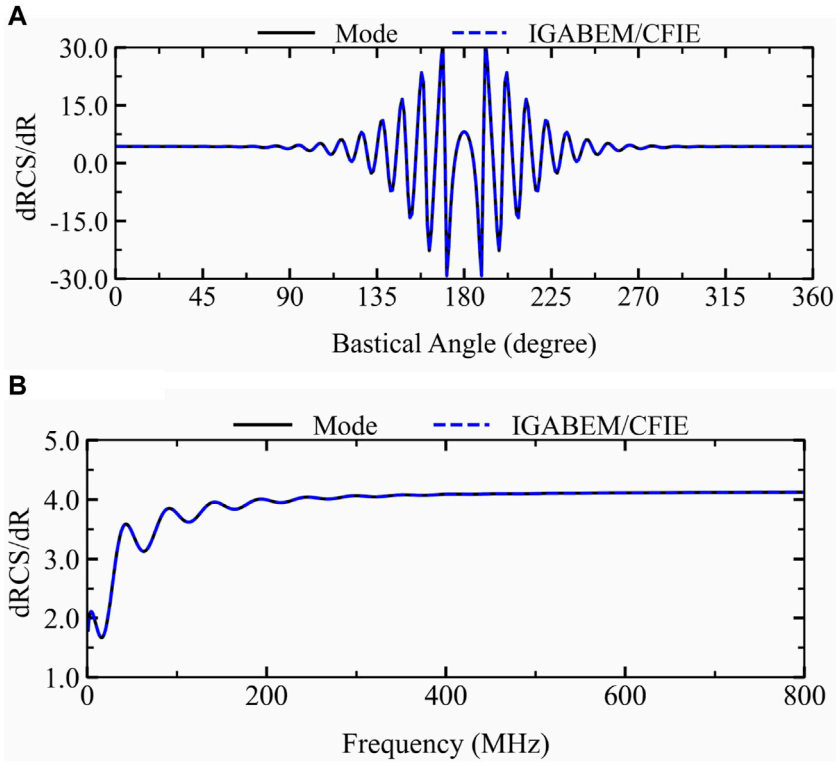

FIGURE 6
Sensitivity of RCS for the PEC cylinder to shape change: **(A)** RCS sensitivity at 800 MHz with $\phi^{inc} = 0$. **(B)** RCS sensitivity with $\phi^{inc} = 0$ at different frequencies.

where N_e is the number of NURBS elements and $d\Gamma = J(\xi)d\xi$ with the Jacobian matrix $J(\xi)$.

The vector elements on the right side of Eqs 8, 9 can be expressed as follows Eq. 17:

$$B_E(j) = \int_{\Gamma(\mathbf{x})} \mathbf{R}_j^z(\mathbf{x}) \cdot \mathbf{E}_{\text{inc}}(\mathbf{x}) d\Gamma(\mathbf{x}) = \sum_{\tilde{e}=1}^{N_e} \int_{\Gamma_{\tilde{e}}} \mathbf{R}_j^z(\mathbf{x}(\xi)) \cdot \mathbf{E}_{\text{inc}}(\mathbf{x}(\xi)) d\Gamma(\mathbf{x}(\xi)) \quad (17)$$

and Eq. 18

$$B_H(j) = \int_{\Gamma(\mathbf{x})} \mathbf{R}_j^z(\mathbf{x}) \cdot [\hat{\mathbf{n}}(\mathbf{x}) \times \mathbf{H}_{\text{inc}}(\mathbf{x})] d\Gamma(\mathbf{x}) = \sum_{\tilde{e}=1}^{N_e} \int_{\Gamma_{\tilde{e}}} \mathbf{R}_j^z(\mathbf{x}(\xi)) \cdot [\hat{\mathbf{n}}(\mathbf{x}(\xi)) \times \mathbf{H}_{\text{inc}}(\mathbf{x}(\xi))] d\Gamma(\mathbf{x}(\xi)). \quad (18)$$

The discretized formulations of Eqs 8, 9 are given by Eq. 19

$$\mathbf{A}_E^J \mathbf{X}^J = \mathbf{B}_E \quad (19)$$

and Eq. 20

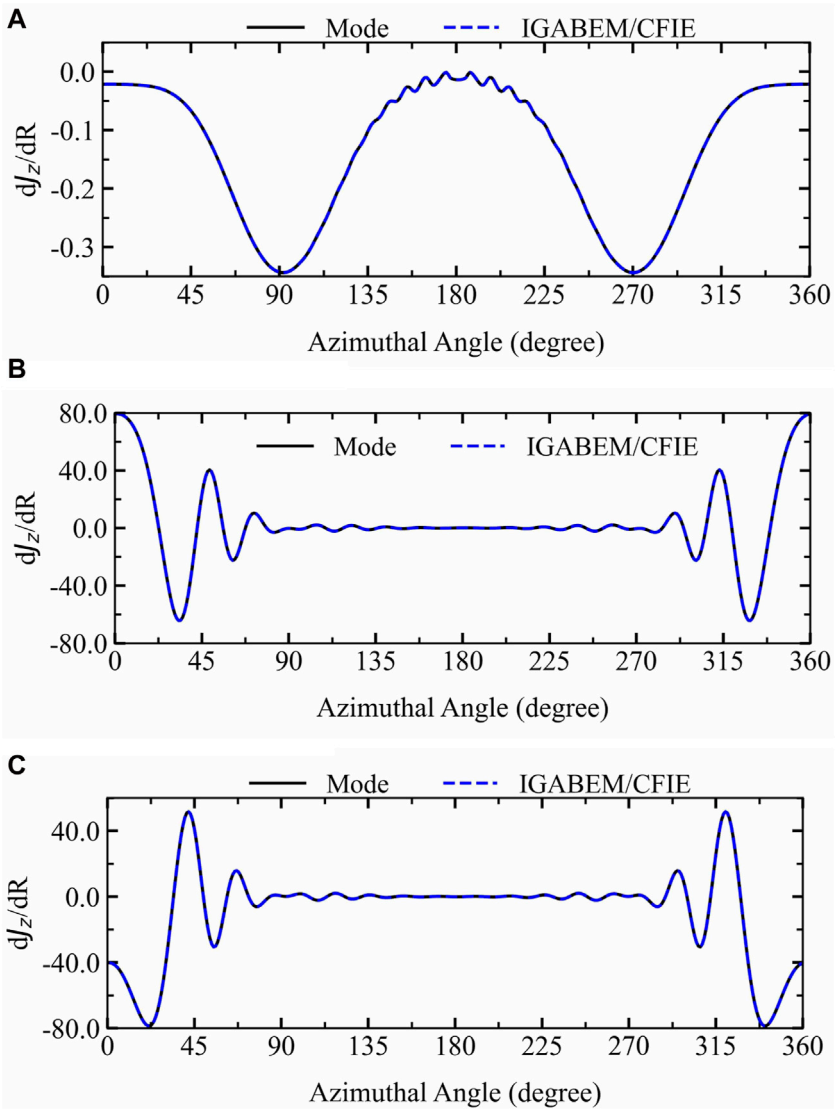

FIGURE 7
Sensitivity of the current for the PEC cylinder to shape change: **(A)** |Jz(ϕ a)|; **(B)** Re Jz(ϕ a); and **(C)** Im Jz (ϕ a).

$$\mathbf{A}_H^J \mathbf{X}^J = \mathbf{B}_H. \tag{20}$$

In addition, combining the EFIE with the nMFIE yields the CFIE as Eq. 21

$$\underbrace{\left[\alpha \mathbf{A}_E^J + (1-\alpha)\eta \mathbf{A}_H^J\right]}_{\mathbf{A}=[A(j,i)]} \mathbf{X}^J = \underbrace{\alpha \mathbf{B}_E + (1-\alpha)\eta \mathbf{B}_H}_{\mathbf{B}=[B(j)]}. \tag{21}$$

Hence, we can obtain the following linear system of equations Eq. 22:

$$\mathbf{A}\mathbf{X}^J = \mathbf{B}. \tag{22}$$

By solving the above equation, we can obtain the surface current **J**, scattered electric field, and magnetic field. In addition, the value of the 2D radar scattering cross-section RCS_{2D} that we require can be obtained from the obtained scattered electric field, as shown below:

$$RCS_{2D} = 2\pi\rho \frac{|E_{\text{sca}}|^2}{|E_{\text{inc}}|^2}. \tag{23}$$

In general, we convert Eq. 22 to the following expression when using it, as Eq. 24:

$$RCS_{dbsm} = 10 \times \lg(RCS_{2D}). \tag{24}$$

3 Sensitivity analysis of electromagnetic scattering problems

By differentiating Eq. 8 with respect to an arbitrary shape design variable, one can obtain the following formulations for electromagnetic shape design sensitivity analysis:

$$\begin{aligned}&\frac{\omega\mu}{4}\int_{\Gamma(\mathbf{y})} \dot{\mathbf{j}}(\mathbf{y}) H_0^{(2)}(kr) d\Gamma(\mathbf{y}) + \frac{\omega\mu}{4}\int_{\Gamma(\mathbf{y})} \mathbf{J}(\mathbf{y}) \dot{H}_0^{(2)}(kr) d\Gamma(\mathbf{y}) \\ &+\frac{\omega\mu}{4}\int_{\Gamma(\mathbf{y})} \mathbf{J}(\mathbf{y}) H_0^{(2)}(kr) d\dot{\Gamma}(\mathbf{y}) = \dot{\mathbf{E}}_{\text{inc}}(\mathbf{x}).\end{aligned} \tag{25}$$

The dot $\dot{(\,)}$ above represents the differentiation of the shape design variable. The formula of $\dot{H}_0^{(2)}(kr)$ and $\dot{\mathbf{E}}_{\text{inc}}(\mathbf{x})$ Eq. 26:

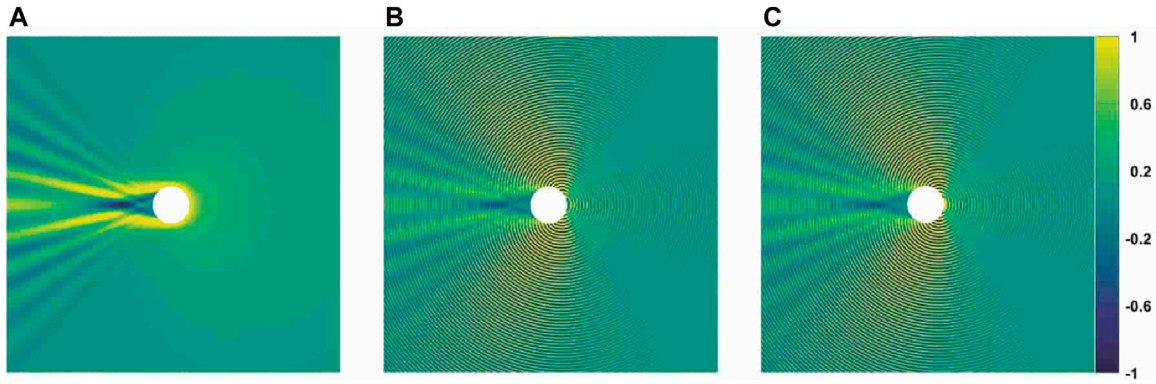

FIGURE 8
Sensitivity of the electric field around the cylinder to shape changes at 800 MHz $\phi^{inc} = 0$ TE polarization: **(A)** Abs(Ez)/dR; **(B)** |Re(Ez)|/dR; and **(C)** |Im(Ez)|/dR.

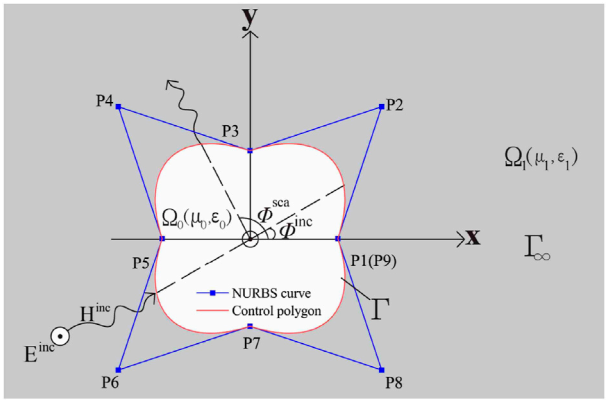

FIGURE 9
NURBS curve and control points of a deformation circle model.

$$\dot{H}_0^{(2)}(kr) = -kH_1^{(2)}(kr)\dot{r} \tag{26}$$

and Eq. 27

$$\dot{\mathbf{E}}_{inc}(\mathbf{x}) = ik[\dot{x}_1\cos(\phi_{inc}) + \dot{x}_2\sin(\phi_{inc})]e^{ik(x_1\cos(\phi_{inc})+x_2\sin(\phi_{inc}))}\hat{\mathbf{z}}, \tag{27}$$

where Eq. 28

$$\dot{r} = r_{,\ell}(\dot{x}_\ell - \dot{y}_\ell), \tag{28}$$

where x_ℓ and y_ℓ and $\ell = 1$ or 2 are, respectively, the coordinate points **x** and **y** of Cartesian components. The index after the comma indicates the partial derivative with respect to the coordinate component. Einstein's summation convention is used throughout this article, so the repeated indicators in this article represent summations within their ranges. $\dot{n}_\ell(\mathbf{y})$ and $d\dot{\Gamma}(\mathbf{y})$ can be written as Eq. 29

$$\dot{n}_\ell(\mathbf{y}) = -\dot{y}_{\kappa,\ell}n_\kappa(\mathbf{y}) + \dot{y}_{\kappa,m}n_\kappa(\mathbf{y})n_m(\mathbf{y})n_\ell(\mathbf{y}) \tag{29}$$

and Eq. 30

$$d\dot{\Gamma}(\mathbf{y}) = [\dot{y}_{\ell,\ell} - \dot{y}_{\ell,\kappa}n_\ell(\mathbf{y})n_\kappa(\mathbf{y})]d\Gamma(\mathbf{y}), \tag{30}$$

where an index after a comma denotes the partial derivative with respect to the coordinate component and $\dot{y}_{k,m} = \partial\dot{y}_k/\partial y_m$.

By differentiating Eq. 9 with respect to an arbitrary shape design variable, one can obtain the sensitivity formulations for the nMFIE, which is expressed as Eq. 31

$$\begin{aligned}\frac{1}{2}\dot{\mathbf{J}}(\mathbf{x}) &+ \frac{ik}{4}\int_{\Gamma(\mathbf{y})}\dot{\mathbf{J}}(\mathbf{y})[r_{,\ell}n_\ell(\mathbf{x})]H_1^{(2)}(kr)d\Gamma(\mathbf{y}) + \frac{ik}{4}\int_{\Gamma(\mathbf{y})}\mathbf{J}(\mathbf{y})\\ &\times[\dot{r}_{,\ell}n_\ell(\mathbf{x}) + r_{,\ell}\dot{n}_\ell(\mathbf{x})]H_1^{(2)}(kr)d\Gamma(\mathbf{y}) + \frac{ik}{4}\int_{\Gamma(\mathbf{y})}\mathbf{J}(\mathbf{y})\\ &\times[r_{,\ell}n_\ell(\mathbf{x})]\dot{H}_1^{(2)}(kr)d\Gamma(\mathbf{y}) + \frac{ik}{4}\int_{\Gamma(\mathbf{y})}\mathbf{J}(\mathbf{y})\\ &\times[r_{,\ell}n_\ell(\mathbf{x})]H_1^{(2)}(kr)d\dot{\Gamma}(\mathbf{y}) = \dot{\mathbf{H}}_{inc}^n(\mathbf{x}),\end{aligned} \tag{31}$$

where Eqs 32–34

$$\dot{H}_1^{(2)}(kr) = H_1^{(2)}(kr)\frac{\dot{r}}{r} - H_2^{(2)}(kr)k\dot{r}, \tag{32}$$

$$\dot{r}_{,\ell} = \frac{(\dot{x}_\ell - \dot{y}_\ell)n_\ell(\mathbf{x})}{r} - \frac{\dot{r}r_{,\ell}n_\ell(\mathbf{x})}{r}, \tag{33}$$

$$\dot{n}_\ell(\mathbf{x}) = -\dot{x}_{\kappa,\ell}n_\kappa(\mathbf{x}) + \dot{x}_{\kappa,m}n_\kappa(\mathbf{x})n_m(\mathbf{x})n_\ell(\mathbf{x}), \tag{34}$$

and Eq. 35

$$\begin{aligned}\dot{\mathbf{H}}_{inc}^n(\mathbf{x}) = \frac{1}{\eta}e^{ik(x_1\cos(\phi_{inc})+x_2\sin(\phi_{inc}))}&\{\dot{n}_1(\mathbf{x})\cos(\phi_{inc}) + \dot{n}_2(\mathbf{x})\sin(\phi_{inc})\\ &+ ik\cdot[n_1(\mathbf{x})\cos(\phi_{inc}) + n_2(\mathbf{x})\sin(\phi_{inc})]\cdot[\dot{x}_1\cos(\phi_{inc})\\ &+\dot{x}_2\sin(\phi_{inc})]\}\hat{\mathbf{z}}.\end{aligned} \tag{35}$$

Discretizing the sensitivity of the electric current in the domain using the sum of weighted basis functions yields Eq. 36

$$\dot{\mathbf{J}}(\mathbf{y}) = \sum_{i=1}^{N_f}\mathbf{R}_i^z(\mathbf{y})\dot{X}_i^J, \quad \dot{\mathbf{J}}(\mathbf{x}) = \sum_{i=1}^{N_f}\mathbf{R}_i^z(\mathbf{x})\dot{X}_i^J. \tag{36}$$

By using the weighted basis function and the test function to discretize Eq. 24, the matrix elements of Eq. 24 can be obtained as Eq. 37

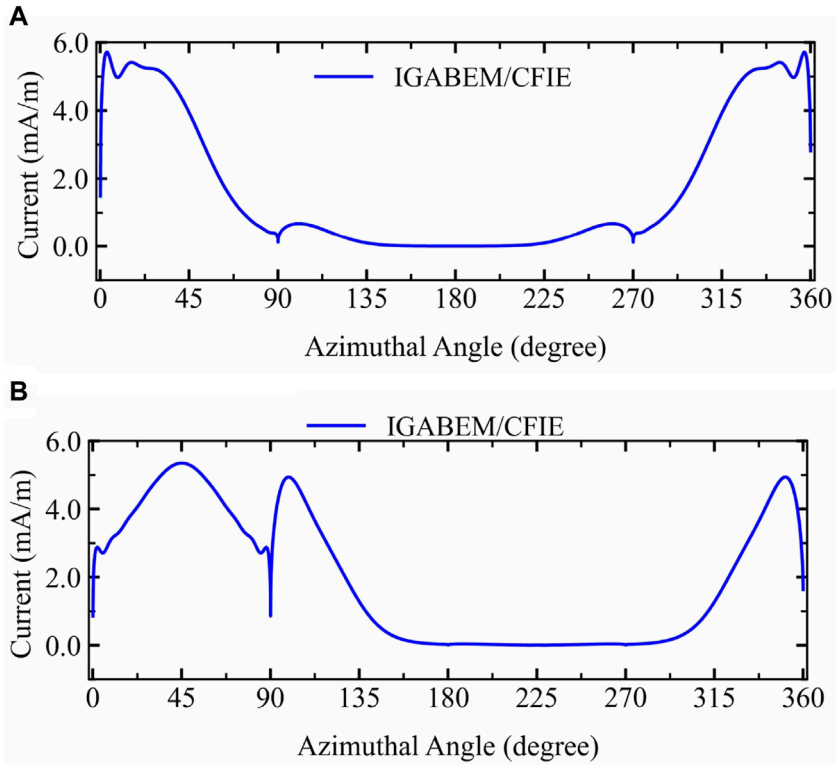

FIGURE 10
Current for the deformation circle model: **(A)** current at $\phi^{inc} = 0$. **(B)** Current at $\phi^{inc} = 45$. **(A)** |Jz(ϕ a)| and **(B)** | Jz(ϕ a)|.

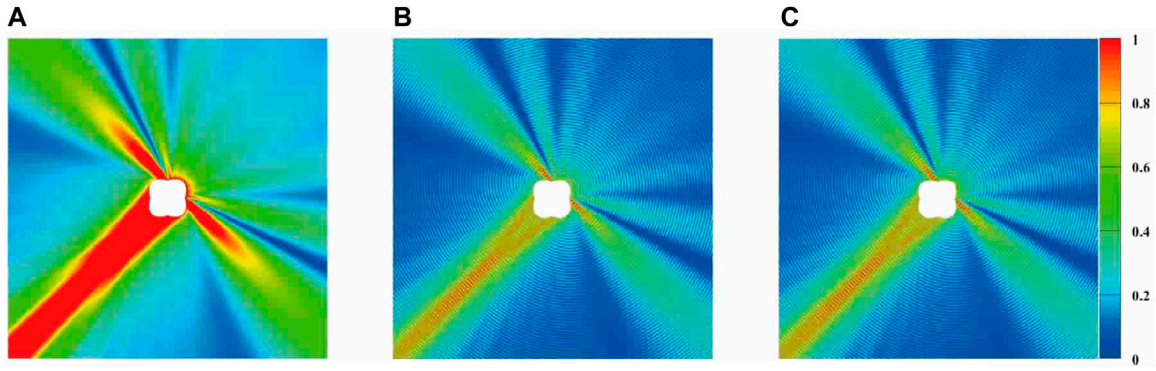

FIGURE 11
Electric field distribution around the PEC cylinder at 800 MHz: **(A)** ABS (Ez); **(B)** |Re(*Ez*)|; and **(C)** |Im(Ez)|.

$$\begin{cases} A_E^J(j,i) = \dfrac{\omega\mu}{4}\displaystyle\int_{\Gamma(\mathbf{x})} \mathbf{R}_j^z(\mathbf{x}) \cdot \int_{\Gamma(\mathbf{y})} \mathbf{R}_i^z(\mathbf{y}) H_0^{(2)}(kr) d\Gamma(\mathbf{y}) d\Gamma(\mathbf{x}) \\ \dot{A}_E^J(j,i) = \dfrac{\omega\mu}{4}\displaystyle\int_{\Gamma(\mathbf{x})} \mathbf{R}_j^z(\mathbf{x}) \cdot \int_{\Gamma(\mathbf{y})} \mathbf{R}_i^z(\mathbf{y}) \dot{H}_0^{(2)}(kr) d\Gamma(\mathbf{y}) d\Gamma(\mathbf{x}) + \\ \qquad \dfrac{\omega\mu}{4}\displaystyle\int_{\Gamma(\mathbf{x})} \mathbf{R}_j^z(\mathbf{x}) \cdot \int_{\Gamma(\mathbf{y})} \mathbf{R}_i^z(\mathbf{y}) H_0^{(2)}(kr) \left[\dot{y}_{\ell,\ell} - \dot{y}_{\ell,\kappa} n_\ell(\mathbf{y}) n_\kappa(\mathbf{y})\right] \\ \qquad \times d\Gamma(\mathbf{y}) d\Gamma(\mathbf{x}) \\ \dot{B}_E(j) = \displaystyle\int_{\Gamma(\mathbf{x})} \mathbf{R}_j^z(\mathbf{x}) \cdot \dot{\mathbf{E}}_{\text{inc}}(\mathbf{x}) d\Gamma(\mathbf{x}) \end{cases} \tag{37}$$

Similarly, by using the weighted basis function and the test function to discretize Eq. 30, the matrix elements of Eq. 30 can be obtained as Eq. 38

$$\begin{cases} A_H^I(j,i) = \dfrac{1}{2}\displaystyle\int_{\Gamma(\mathbf{x})} \mathbf{R}_j^z(\mathbf{x}) \cdot \mathbf{R}_i^z(\mathbf{x}) d\Gamma(\mathbf{x}) + \dfrac{ik}{4}\displaystyle\int_{\Gamma(\mathbf{x})} \mathbf{R}_j^z(\mathbf{x}) \cdot \int_{\Gamma(\mathbf{y})} \mathbf{R}_i^z(\mathbf{y}) [r_{,\ell} n_\ell(\mathbf{x})] H_1^{(2)}(kr) d\Gamma(\mathbf{y}) d\Gamma(\mathbf{x}) \\ \dot{A}_H^I(j,i) = \dfrac{ik}{4}\displaystyle\int_{\Gamma(\mathbf{x})} \mathbf{R}_j^z(\mathbf{x}) \cdot \int_{\Gamma(\mathbf{y})} \mathbf{R}_i^z(\mathbf{y}) [\dot{r}_{,\ell} n_\ell(\mathbf{x}) + r_{,\ell} \dot{n}_\ell(\mathbf{x})] H_1^{(2)}(kr) d\Gamma(\mathbf{y}) d\Gamma(\mathbf{x}) + \\ \qquad \dfrac{ik}{4}\displaystyle\int_{\Gamma(\mathbf{x})} \mathbf{R}_j^z(\mathbf{x}) \cdot \int_{\Gamma(\mathbf{y})} \mathbf{R}_i^z(\mathbf{y}) [r_{,\ell} n_\ell(\mathbf{x})] \dot{H}_1^{(2)}(kr) d\Gamma(\mathbf{y}) d\Gamma(\mathbf{x}) + \\ \qquad \dfrac{ik}{4}\displaystyle\int_{\Gamma(\mathbf{x})} \mathbf{R}_j^z(\mathbf{x}) \cdot \int_{\Gamma(\mathbf{y})} \mathbf{R}_i^z(\mathbf{y}) [r_{,\ell} n_\ell(\mathbf{x})] H_1^{(2)}(kr) \left[\dot{y}_{\ell,\ell} - \dot{y}_{\ell,\kappa} n_\ell(\mathbf{y}) n_\kappa(\mathbf{y})\right] d\Gamma(\mathbf{y}) d\Gamma(\mathbf{x}) \\ \dot{B}_H(j) = \displaystyle\int_{\Gamma(\mathbf{x})} \mathbf{R}_j^z(\mathbf{x}) \cdot \dot{\mathbf{H}}_{\text{inc}}^n(\mathbf{x}) d\Gamma(\mathbf{x}) \end{cases} \tag{38}$$

The discretized formulations of Eqs 24, 30 based on Galerkin's IGABEM with B-spline basis functions are given by Eq. 39

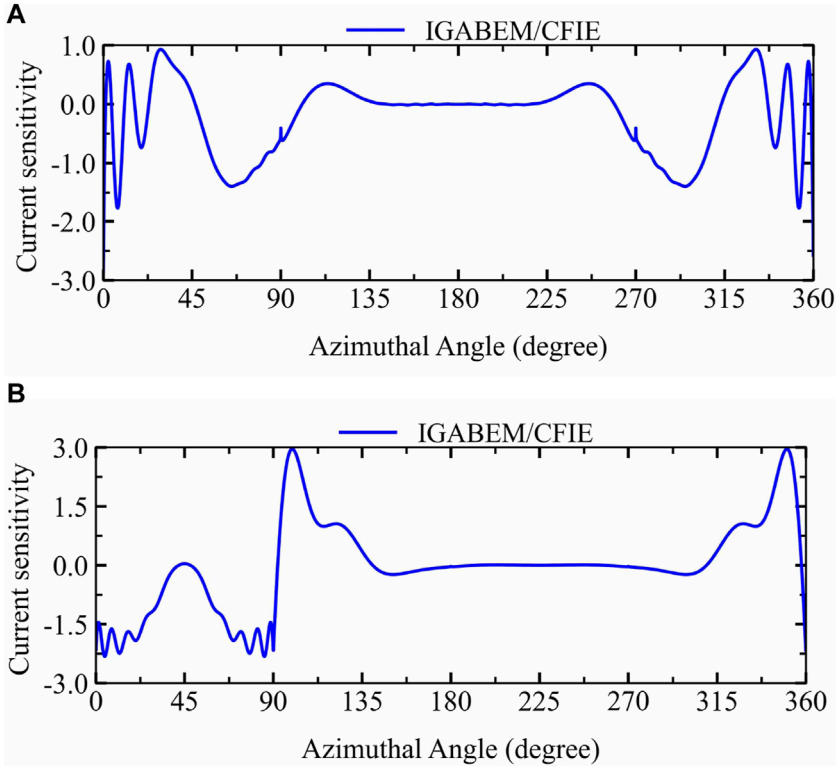

FIGURE 12
Sensitivity of the current to shape change: **(A)** current sensitivity with $\phi^{inc} = 0$. **(B)** Current sensitivity with $\phi^{inc} = 45$. **(A)** | (ϕ a)| sensitivity and **(B)** |Jz (ϕ a)| sensitivity.

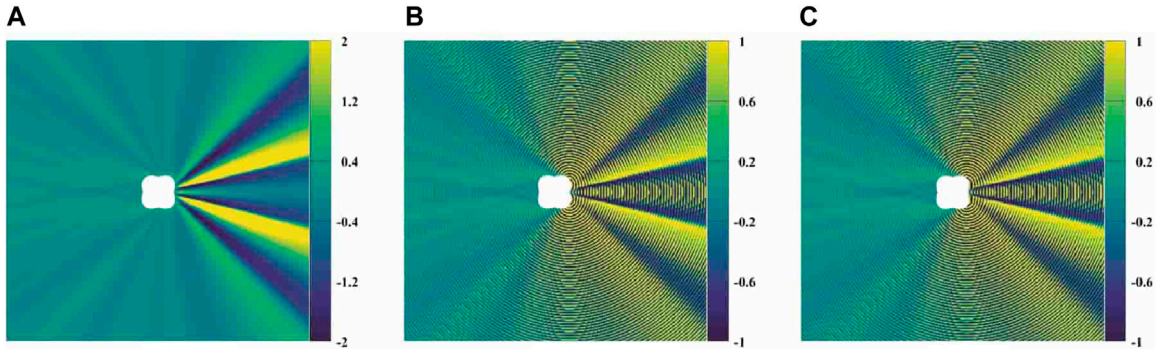

FIGURE 13
Sensitivity of the electric field around the model to shape change at 800 MHz: **(A)** Abs (Ez) sensitivity; **(B)** |Re (Ez)| sensitivity; and **(C)** |Im (Ez)| sensitivity.

$$\mathbf{A}_E^J \dot{\mathbf{X}}^J + \dot{\mathbf{A}}_E^J \mathbf{X}^J = \dot{\mathbf{B}}_E \tag{39}$$

and Eq. 40

$$\mathbf{A}_H^J \dot{\mathbf{X}}^J + \dot{\mathbf{A}}_H^J \mathbf{X}^J = \dot{\mathbf{B}}_H. \tag{40}$$

Thus, the sensitivity formulation of the CFIE is formed by combining the sensitivity formulation of the EFIE and nMFIE, which is expressed as Eq. 41

$$\underbrace{\left[\alpha \mathbf{A}_E^J + (1-\alpha)\eta \mathbf{A}_H^J\right]}_{\mathbf{A}=[A(j,i)]} \dot{\mathbf{X}}^J + \underbrace{\left[\alpha \dot{\mathbf{A}}_E^J + (1-\alpha)\eta \dot{\mathbf{A}}_H^J\right]}_{\dot{\mathbf{A}}=[\dot{A}(j,i)]} \mathbf{X}^J = \underbrace{\alpha \dot{\mathbf{B}}_E + (1-\alpha)\eta \dot{\mathbf{B}}_H}_{\dot{\mathbf{B}}=[\dot{B}(j)]}. \tag{41}$$

Hence, we can obtain the following linear system of equations Eq. 42:

$$\mathbf{A}\dot{\mathbf{X}}^{J} + \dot{\mathbf{A}}\mathbf{X}^{J} = \dot{\mathbf{B}}. \tag{42}$$

By solving the above equation, the sensitivity of the surface current $\dot{\mathbf{J}}$ can be obtained. In addition, the sensitivity of the scattered electric field and magnetic field can also be obtained. In addition, the sensitivity of RCS_{2D} in Eq. 22 will be solved by differentiating Eq. 22 with respect to the design variable.

4 Numerical results

In this section, the framework is written in Fortran 90 language, and the correctness and effectiveness of the IGABEM are verified by perfect electric conductor (PEC) circular examples. In addition, the sensitivity analysis of the two important parameters of the model shape and the incident wave is also be carried out.

4.1 Numerical verification using the PEC cylinder model

In the first example, a PEC cylinder of radius 1 is geometrically modeled using NURBS curves, as shown in Figure 2. The object is hit by an incident TE-polarized plane wave.

First, we use the IGABEM/CFIE to calculate the RCS value at 800 MHz, $0 < \phi^{sca} < 2\pi$, and back-scattering ($\phi^{inc} = 0$). The comparison between the result and the analytical solution is shown in Figure 3A. The figure shows that the analytical solution is very consistent with that of the IGABEM/CFIE. In addition, the RCS value begins to fluctuate when the scattering angle reaches 135° and reaches a maximum when the scattering angle reaches 180°.

In addition, because of the symmetry of the example itself, its RCS is also symmetric at approximately 180°. Then, the IGABEM/CFIE is used to calculate the RCS value of the back-scattering at different frequencies. Figure 3B shows that its RCS gradually decreases with the change in frequency, and the final region is stable.In addition, the current at $\phi^{inc} = 0$ at 800 MHz is also calculated, and its absolute value, real part, and imaginary part are compared with the analytical solution, as shown in Figure 4. As can be seen, the IGABEM/CFIE is still in good agreement with the analytic solution. Furthermore, it can be seen that the current fluctuates greatly on both sides, and the fluctuation is small near $\phi^{a} = \pi$ degrees, and the current is almost zero.

Finally, in order to observe the distribution of the electric field around the cylinder, we calculated the electric field near 20 × 20 m around the cylinder with $\phi^{inc} = 0$ at 800 MHz, as shown in Figure 5. It can be seen that the electric field is mainly distributed in the direction of the incident angle, and the direction of the incident angle is symmetrical.

In order to explore the sensitivity of the cylinder to shape change, we first calculated the sensitivity of the RCS scattered by the back-scattering at 800 MHz, $0 \leqslant \phi^{sca} \leqslant 2\pi$, and compared the result with the analytical solution in Figure 6A; it can be seen that the IGABEM/CFIE still maintains a high coincidence. In addition, its RCS fluctuates more when $\phi^{sca} = \pi$ but less on both sides. In addition, the sensitivity of RCS to shape change under back-scattering at different frequencies was calculated, as shown in Figure 6B. It can be seen that with the change in frequency, the RCS sensitivity gradually increases and eventually becomes stable.

In addition, the IGABEM/CFIE was used to calculate the sensitivity of the current to shape change at 800 MHz with $\phi^{inc} = 0$. The comparison results of the absolute value, real part, and imaginary part with the analytic solution are shown in Figure 7. It can be seen that the analytical solution is still very consistent with the IGABEM/CFIE. In addition, the current fluctuates greatly on both sides, and the sensitivity of the current is symmetric about $\phi^{a} = \pi$.

Finally, in order to observe the sensitivity distribution of the electric field to shape change within the range of 20 × 20 around the cylinder, the sensitivity of the electric field to shape change under back-scattering at 800 MHz was calculated, as shown in Figure 8. It can be seen that the electric field is more sensitive to the shape change in the direction of the incident angle, and the remaining regions are almost zero. In addition, the direction of the incidence angle is symmetrical.

4.2 Deformation circle model

The deformation circle model is suitable for studying the shape change of objects under the action of external forces and is usually used in structural mechanics and civil engineering fields. In this section, we construct a deformation circle model by changing the location of control points $p2$, $p4$, $p6$, and $p8$ in Figure 2, as shown in Figure 9. Due to the particularity of the deformation circle, we explore the model from two perspectives $\phi^{inc} = 0$ and $\phi^{inc} = 45$.

First, we calculate the current at $\phi^{inc} = 0$ and $\phi^{inc} = 45$ at 800 MHz using the IGABEM/CFIE. As shown in Figure 10, when $\phi^{inc} = 0$, the current fluctuates greatly on both sides and is smaller when $90 < \phi^{a} < 270$. When $\phi^{inc} = 45$, the current also fluctuates greatly on both sides, and it fluctuates less when $150 < \phi^{a} < 300$.

In order to clearly observe the electric field distribution in the 20 × 20 region around the deformation circle model, the electric field distribution under $\phi^{inc} = 45$ at 800 MHz was also calculated, as shown in Figure 11. It can be seen that the electric field is more densely distributed in the direction of the incident angle and smaller in the other regions.

In addition, in order to explore the current sensitivity to shape change, we also calculated the current sensitivity to shape change at 800 MHz, $\phi^{inc} = 0$, and $\phi^{inc} = 45$. As shown in Figure 12, when $\phi^{inc} = 0$, the current fluctuates greatly on both sides, while the current fluctuates slightly when $120 < \phi^{a} < 250$. In addition, due to the unique symmetry of the model, its current sensitivity is also symmetric about $\phi^{a} = \pi$. When $\phi^{inc} = 45$, the current fluctuates more on both sides and less at $150 < \phi^{a} < 290$. In addition, due to the unique symmetry of the example, $0 < \phi^{a} < 90$ is symmetric with respect to $\phi^{a} = 45$. $90 < \phi^{a} < 360$ is symmetric between $\phi^{a} = 225$.

Finally, in order to better observe the sensitivity of the electric field around the deformation circle model to shape change, we calculated the sensitivity of the electric field to shape change at 800 MHz when $\phi^{inc} = 0$ in the surrounding 20 × 20 region, as shown in Figure 13. As shown in the figure, the electric field

is relatively dense at the rear of the model, and because of the inherent symmetry of the deformation circle model, its electric field distribution is symmetrical with respect to the incident angle.

5 Conclusion

In this paper, a formula that can be used to calculate two-dimensional electromagnetic scattering analysis is proposed by combining equal geometry and boundary elements, and then, a formula for electromagnetic scattering shape sensitivity analysis is proposed on the basis of the formula, which can provide reliable data guidance for sensitivity analysis and model optimization. Finally, two calculation columns are used to verify the effectiveness of the proposed method.

In future studies, we will extend the proposed algorithm to solve three-dimensional electromagnetic problems, thereby further enhancing its generality and applicability in various engineering fields.

Data availability statement

The original contributions presented in the study are included in the article/Supplementary Material; further inquiries can be directed to the corresponding author.

Author contributions

QH: writing–review and editing. CL: writing–original draft.

Funding

The author(s) declare that no financial support was received for the research, authorship, and/or publication of this article.

Conflict of interest

The authors declare that the research was conducted in the absence of any commercial or financial relationships that could be construed as a potential conflict of interest.

Publisher's note

All claims expressed in this article are solely those of the authors and do not necessarily represent those of their affiliated organizations, or those of the publisher, the editors, and the reviewers. Any product that may be evaluated in this article, or claim that may be made by its manufacturer, is not guaranteed or endorsed by the publisher.

References

1. Rao S, Wilton D, Glisson A. Electromagnetic scattering by surfaces of arbitrary shape. *IEEE Trans Antennas Propagation* (1982) 30:409–18. doi:10.1109/tap.1982.1142818

2. Jin JM *The finite element method in electromagnetics*. John Wiley and Sons (2015).

3. Zhang G, He Z, Qin J, Hong J. Magnetically tunable bandgaps in phononic crystal nanobeams incorporating microstructure and flexoelectric effects. *Appl Math Model* (2022) 111:554–66. doi:10.1016/j.apm.2022.07.005

4. Gibson WC *The method of moments in electromagnetics*. Chapman and Hall: CRC Press (2021).

5. Taflove A, Hagness SC, Piket-May M *Computational electromagnetics: the finite-difference time-domain method, vol. 3*. Amsterdam, The Netherlands: Elsevier (2005).

6. Chen J, Qu Y, Guo Z, Li D, Zhang G. A one-dimensional model for mechanical coupling metamaterials using couple stress theory. *Math Mech Sol* (2023) 28:2732–55. doi:10.1177/10812865231177670

7. Qu Y, Pan E, Zhu FRAK, Jin F, Roy AK. Modeling thermoelectric effects in piezoelectric semiconductors: new fully coupled mechanisms for mechanically manipulated heat flux and refrigeration. *Int J Eng Sci* (2023) 182:103775. doi:10.1016/j.ijengsci.2022.103775

8. Shen X, Du C, Jiang S, Zhang P, Chen L. Multivariate uncertainty analysis of fracture problems through model order reduction accelerated sbfem. *Appl Math Model* (2024) 125:218–40. doi:10.1016/j.apm.2023.08.040

9. Liu Z, Bian P, Qu Y, Huang W, Chen L, Chen J, et al. A galerkin approach for analysing coupling effects in the piezoelectric semiconducting beams. *Eur J Mech/A Sol* (2024) 103:105145. doi:10.1016/j.euromechsol.2023.105145

10. Chen L, Liu C, Zhao W, Liu L. An isogeometric approach of two dimensional acoustic design sensitivity analysis and topology optimization analysis for absorbing material distribution. *Comput Methods Appl Mech Eng* (2018) 336:507–32. doi:10.1016/j.cma.2018.03.025

11. Chen L, Lian H, Dong H, Yu P, Jiang S, Bordas S. Broadband topology optimization of three-dimensional structural-acoustic interaction with reduced order isogeometric fem/bem. *J Comput Phys* (2024) 113051. doi:10.1016/j.jcp.2024.113051

12. Nikolova NK, Li Y, Li Y, Bakr MH. Sensitivity analysis of scattering parameters with electromagnetic time-domain simulators. *IEEE Trans microwave Theor Tech* (2006) 54:1598–610. doi:10.1109/TMTT.2006.871350

13. Sargheini S *Shape sensitivity analysis of electromagnetic scattering problems*. Ph.D. thesis. ETH Zurich (2016).

14. Spies BR, Habashy TM. Sensitivity analysis of crosswell electromagnetics. *Geophysics* (1995) 60:834–45. doi:10.1190/1.1443821

15. Kucherenko S, Rodriguez-Fernandez M, Pantelides C, Shah N. Monte Carlo evaluation of derivative-based global sensitivity measures. *Reliability Eng Syst Saf* (2009) 94:1135–48. doi:10.1016/j.ress.2008.05.006

16. Jumabekova A, Berger J, Foucquier A. An efficient sensitivity analysis for energy performance of building envelope: a continuous derivative based approach. *Building Simulation* (2021) 14:909–30. doi:10.1007/s12273-020-0712-4

17. Prabhakar Y. A combinatorial approach to the variable selection in multiple linear regression: Analysis of selwood et al. data set – a case study. *Qsar Comb Sci* (2010) 22:583–95. doi:10.1002/qsar.200330814

18. Montgomery DC, Peck EA, Vining GG *Introduction to linear regression analysis*. John Wiley and Sons (2021).

19. Seber GA, Lee AJ *Linear regression analysis*. John Wiley and Sons (2012).

20. Maus S. Variogram analysis of magnetic and gravity data. *Geophysics* (2012) 64:776–84. doi:10.1190/1.1444587

21. Bohling G. Introduction to geostatistics and variogram analysis. *Kans Geol Surv* (2005) 1:1–20.

22. Raviart P-A, Thomas JM. A mixed finite element method for 2-nd order elliptic problems. In: *Mathematical aspects of finite element methods* (2006).

23. Nguyen VP, Anitescu C, Bordas SP, Rabczuk T. Isogeometric analysis: an overview and computer implementation aspects. *Mathematics Comput Simulation* (2015) 117:89–116. doi:10.1016/j.matcom.2015.05.008

24. Cottrell JA, Hughes TJ, Bazilevs Y *Isogeometric analysis: toward integration of CAD and FEA*. John Wiley and Sons (2009).

25. Cottrell J, Hughes T, Reali A. Studies of refinement and continuity in isogeometric structural analysis. *Comput Methods Appl Mech Eng* (2007) 196:4160–83. doi:10.1016/j.cma.2007.04.007

26. Fischer P, Klassen M, Mergheim J, Steinmann P, Müller R. Isogeometric analysis of 2d gradient elasticity. *Comput Mech* (2011) 47:325–34. doi:10.1007/s00466-010-0543-8

27. Makvandi R, Reiher JC, Bertram A, Juhre D. Isogeometric analysis of first and second strain gradient elasticity. *Comput Mech* (2018) 61:351–63. doi:10.1007/s00466-017-1462-8

28. Qu Y, Zhang G, Gao X-L, Jin F. A new model for thermally induced redistributions of free carriers in centrosymmetric flexoelectric semiconductor beams. *Mech Mater* (2022) 171:104328. doi:10.1016/j.mechmat.2022.104328

29. Zhang G, Qu Y, Gao X-L, Jin F. A transversely isotropic magneto-electro-elastic timoshenko beam model incorporating microstructure and foundation effects. *Mech Mater* (2020) 149:103412. doi:10.1016/j.mechmat.2020.103412

30. Li W, Ambati M, Nguyen-Thanh N, Du H, Zhou K. Adaptive fourth-order phase-field modeling of ductile fracture using an isogeometric-meshfree approach. *Comput Methods Appl Mech Eng* (2023) 406:115861. doi:10.1016/j.cma.2022.115861

31. Shen X, Du C, Jiang S, Sun L, Chen L. Enhancing deep neural networks for multivariate uncertainty analysis of cracked structures by pod-rbf. *Theor Appl Fracture Mech* (2023) 125:103925. doi:10.1016/j.tafmec.2023.103925

32. De Luycker E, Benson DJ, Belytschko T, Bazilevs Y, Hsu MC. X-fem in isogeometric analysis for linear fracture mechanics. *Int J Numer Methods Eng* (2011) 87:541–65. doi:10.1002/nme.3121

33. Sun F, Dong C, Yang H. Isogeometric boundary element method for crack propagation based on bézier extraction of nurbs. *Eng Anal Boundary Elem* (2019) 99: 76–88. doi:10.1016/j.enganabound.2018.11.010

34. Khajah T, Antoine X, Bordas S *Isogeometric finite element analysis of time-harmonic exterior acoustic scattering problems* (2016). arXiv preprint arXiv:1610.01694.

35. Chen L, Cheng R, Li S, Lian H, Zheng C, Bordas SPA. A sample-efficient deep learning method for multivariate uncertainty qualification of acoustic–vibration interaction problems. *Comput Methods Appl Mech Eng* (2022) 393:114784. doi:10.1016/j.cma.2022.114784

36. Lu C, Chen L, Luo J, Chen H. Acoustic shape optimization based on isogeometric boundary element method with subdivision surfaces. *Eng Anal Boundary Elem* (2023) 146:951–65. doi:10.1016/j.enganabound.2022.11.010

37. Zhang S, Yu B, Chen L. Non-iterative reconstruction of time-domain sound pressure and rapid prediction of large-scale sound field based on ig-drbem and pod-rbf. *J Sound Vibration* (2024) 573:118226. doi:10.1016/j.jsv.2023.118226

38. Chen L, Zhang Y, Lian H, Atroshchenko E, Ding C, Bordas SP. Seamless integration of computer-aided geometric modeling and acoustic simulation: isogeometric boundary element methods based on catmull-clark subdivision surfaces. *Adv Eng Softw* (2020) 149:102879. doi:10.1016/j.advengsoft.2020.102879

39. Chen L, Lian H, Liu Z, Chen H, Atroshchenko E, Bordas S. Structural shape optimization of three dimensional acoustic problems with isogeometric boundary element methods. *Comput Methods Appl Mech Eng* (2019) 355:926–51. doi:10.1016/j.cma.2019.06.012

40. Chen L, Zhao J, Lian H, Yu B, Atroshchenko E, Pei L. A bem broadband topology optimization strategy based on taylor expansion and soar method—application to 2d acoustic scattering problems. *Int J Numer Methods Eng* (2023) 124:5151–82. doi:10.1002/nme.7345

41. Chen L, Lian H, Liu Z, Gong Y, Zheng C, Bordas S. Bi-material topology optimization for fully coupled structural-acoustic systems with isogeometric fem–bem. *Eng Anal Boundary Elem* (2022) 135:182–95. doi:10.1016/j.enganabound.2021.11.005

42. Chen L, Lian H, Natarajan S, Zhao W, Chen X, Bordas S. Multi-frequency acoustic topology optimization of sound-absorption materials with isogeometric boundary element methods accelerated by frequency-decoupling and model order reduction techniques. *Comput Methods Appl Mech Eng* (2022) 395:114997. doi:10.1016/j.cma.2022.114997

43. Chen L, Lu C, Lian H, Liu Z, Zhao W, Li S, et al. Acoustic topology optimization of sound absorbing materials directly from subdivision surfaces with isogeometric boundary element methods. *Comput Methods Appl Mech Eng* (2020) 362:112806. doi:10.1016/j.cma.2019.112806

44. Zhang M, Sun J, Chen W. An interface tracking method of coupled youngs-vof and level set based on geometric reconstruction. *Chin J Theor Appl Mech* (2019) 51:775–86.

45. Takizawa K, Bazilevs Y, Tezduyar TE. Isogeometric discretization methods in computational fluid mechanics. *Math Models Methods Appl Sci* (2022) 32:2359–70. doi:10.1142/s0218202522020018

46. Nørtoft P, Gravesen J. Isogeometric shape optimization in fluid mechanics. *Struct Multidisciplinary Optimization* (2013) 48:909–25. doi:10.1007/s00158-013-0931-8

47. Hamdia KM, Ghasemi H, Zhuang X, Rabczuk T. Multilevel Monte Carlo method for topology optimization of flexoelectric composites with uncertain material properties. *Eng Anal Boundary Elem* (2022) 134:412–8. doi:10.1016/j.enganabound.2021.10.008

48. Chen L, Li H, Guo Y, Chen P, Elena A, Lian H. Uncertainty quantification of mechanical property of piezoelectric materials based on isogeometric stochastic fem with generalized nth-order perturbation. *Eng Comput* (2023) 40:257–77. doi:10.1007/s00366-023-01788-w

49. Qu Y, Zhu F, Pan E, Jin F, Hirakata H. Analysis of wave-particle drag effect in flexoelectric semiconductor plates via mindlin method. *Appl Math Model* (2023) 118: 541–55. doi:10.1016/j.apm.2023.01.040

50. Zhang G, Guo Z, Qu Y, Mi C. Global and local flexotronic effects induced by external magnetic fields in warping of a semiconducting composite fiber. *Compos Structures* (2022) 295:115711. doi:10.1016/j.compstruct.2022.115711

51. Li H, Chen L, Zhi G, Meng L, Lian H, Liu Z, et al. A direct fe2 method for concurrent multilevel modeling of piezoelectric materials and structures. *Comput Methods Appl Mech Eng* (2024) 420:116696. doi:10.1016/j.cma.2023.116696

52. Zang Q, Liu J, Ye W, Lin G. Isogeometric boundary element for analyzing steady-state heat conduction problems under spatially varying conductivity and internal heat source. *Comput Math Appl* (2020) 80:1767–92. doi:10.1016/j.camwa.2020.08.009

53. Jahangiry HA, Jahangiri A. Combination of isogeometric analysis and level-set method in topology optimization of heat-conduction systems. *Appl Therm Eng* (2019) 161:114134. doi:10.1016/j.applthermaleng.2019.114134

54. Yoon M, Ha S-H, Cho S. Isogeometric shape design optimization of heat conduction problems. *Int J Heat Mass Transfer* (2013) 62:272–85. doi:10.1016/j.ijheatmasstransfer.2013.02.077

55. Cao G, Yu B, Chen L, Yao W. Isogeometric dual reciprocity BEM for solving non-Fourier transient heat transfer problems in FGMs with uncertainty analysis. *Int J Heat Mass Transfer* (2023) 203:123783. doi:10.1016/j.ijheatmasstransfer.2022.123783

56. Qu Y, Jin F, Yang J. Effects of mechanical fields on mobile charges in a composite beam of flexoelectric dielectrics and semiconductors. *J Appl Phys* (2020) 127. doi:10.1063/5.0005124

57. Qu Y, Zhou Z, Chen L, Lian H, Li X, Hu Z, et al. Uncertainty quantification of vibro-acoustic coupling problems for robotic manta ray models based on deep learning. *Ocean Eng* (2024) 299:117388. doi:10.1016/j.oceaneng.2024.117388

58. Buffa A, Sangalli G, Vázquez R. Isogeometric analysis in electromagnetics: B-splines approximation. *Comput Methods Appl Mech Eng* (2010) 199:1143–52. doi:10.1016/j.cma.2009.12.002

59. Buffa A, Sangalli G, Vázquez R. Isogeometric methods for computational electromagnetics: B-spline and t-spline discretizations. *J Comput Phys* (2014) 257: 1291–320. doi:10.1016/j.jcp.2013.08.015

60. Evans JA, Hughes TJ. Isogeometric divergence-conforming b-splines for the Darcy–Stokes–brinkman equations. *Math Models Methods Appl Sci* (2013) 23:671–741. doi:10.1142/s0218202512500583

61. Simpson RN, Liu Z, Vazquez R, Evans JA. An isogeometric boundary element method for electromagnetic scattering with compatible b-spline discretizations. *J Comput Phys* (2018) 362:264–89. doi:10.1016/j.jcp.2018.01.025

62. Takahashi T, Hirai T, Isakari H, Matsumoto T. An isogeometric boundary element method for three-dimensional doubly-periodic layered structures in electromagnetics. *Eng Anal Boundary Elem* (2022) 136:37–54. doi:10.1016/j.enganabound.2021.11.020

63. Chen L, Lian H, Xu Y, Li S, Liu Z, Atroshchenko E, et al. Generalized isogeometric boundary element method for uncertainty analysis of time-harmonic wave propagation in infinite domains. *Appl Math Model* (2023) 114:360–78. doi:10.1016/j.apm.2022.09.030

64. Takahashi T, Matsumoto T. An application of fast multipole method to isogeometric boundary element method for laplace equation in two dimensions. *Eng Anal boundary Elem* (2012) 36:1766–75. doi:10.1016/j.enganabound.2012.06.004

65. Chen L, Wang Z, Lian H, Ma Y, Meng Z, Li P, et al. Reduced order isogeometric boundary element methods for cad-integrated shape optimization in electromagnetic scattering. *Comput Methods Appl Mech Eng* (2024) 419:116654. doi:10.1016/j.cma.2023.116654

Appendix A: Analytical solution

The analytical solution for the scattered electric field of an infinite perfectly electric cylinder with TE-polarized incident waves is

$$E_z^s(\rho,\phi_{sca}) = \sum_{n=0}^{\infty} j^n c_n A_n H_n^{(2)}(k_0\rho)\cos(n\phi_{sca}), \tag{A1}$$

where $|E_z^i| = 1$ for convenience, ϕ_{sca} is the bistatic scattering angle, and $c_n = 1$ for $n = 0$, and $c_n = 2$ otherwise. For the conducting cylinder, the coefficient A_n is

$$A_n = -\frac{J_n(k_0\alpha)}{H_n^{(2)}(k_0\alpha)}, \tag{A2}$$

where α is the radius of the cylinder. The scattered far electric field is

$$E_z^s(\rho,\phi_{sca}) = \sqrt{\frac{2}{\pi}}\frac{e^{-j(k_0\rho-\pi/4)}}{\sqrt{k_0\rho}}\sum_{n=0}^{\infty}(-1)^n c_n A_n \cos n\phi_{sca}. \tag{A3}$$

The induced electric current $J_z(\phi_\alpha)$ is

$$J_z(\phi_\alpha) = \frac{2}{\pi\eta^0 k_0 a}\sum_{n=0}^{\infty}\frac{(j)^n c_n \cos n\phi_\alpha}{H_n^{(2)}(k_0 a)}, \tag{A4}$$

where ϕ_α is the azimuthal angle on the surface of the cylinder. The above formula is the analytical solution of the scattered electric field of the PEC under TE polarization.

frontiers | Frontiers in Physics

TYPE Original Research
PUBLISHED 01 August 2024
DOI 10.3389/fphy.2024.1432527

OPEN ACCESS

EDITED BY
Pei Li,
University of Southern Denmark, Denmark

REVIEWED BY
Jian Zhang,
Wenzhou University, China
Qiang Liu,
Chengdu University of Information Technology, China

*CORRESPONDENCE
Ning Zhao,
moj6302@163.com

RECEIVED 14 May 2024
ACCEPTED 19 June 2024
PUBLISHED 01 August 2024

CITATION
Zhao N, Duan Z, Li Q, Guo K, Zhang Z and Liu B (2024), A cable insulation defect classification method based on CNN-transformer.
Front. Phys. 12:1432527.
doi: 10.3389/fphy.2024.1432527

A cable insulation defect classification method based on CNN-transformer

Ning Zhao*, Zhiguo Duan, Qian Li, Kang Guo, Ziguang Zhang and Baoan Liu

State Grid Shijiazhuang Electric Power Supply Company, Shijiazhuang, Hebei, China

Cable insulation defect detection ensures electrical safety, prevents accidents, extends equipment life and guarantees stable system operation. For the traditional cable insulation defect detection and identification of difficult problems, this paper proposes the use of ultrasonic cable insulation defect detection and combined with the Convolutional Neural Network (CNN)-transformer model of cable insulation defect classification method. Firstly, the ultrasonic probe is used to obtain different cable insulation defect signals, and then the CNN-transformer model is used to classify different cable insulation defects. The CNN is used to initially extract the characteristics of the cable insulation defects from the input signals, and then the multi-attention mechanism in the time series Transformer is used to extract the transient local and periodic global characteristics of the cable insulation defect signals. The deeper transient local features and periodic global features of the cable insulation defect signal are extracted by the multi-attention mechanism in the time series Transformer; finally, the recognition results are outputted by the fully connected layer and softmax classifier. The results show that ultrasonic reflection and transmission phenomena occur at the defects, and different defects can be accurately reflected by the defect echo time and amplitude, and the accuracy of cable insulation defect recognition using the CNN-transformer model reaches 100%, with good generalization ability.

KEYWORDS

cable, insulation defect, ultrasonic reflection, defect recognition, CNN-transformer

1 Introduction

Cable insulation defect detection is a crucial step in ensuring the normal operation and safe use of cables. A good insulation state can effectively prevent faults such as cable short circuits and leakage, ensuring the safety of equipment and personnel [1, 2]. Regular inspection and maintenance can improve the reliability and service life of cables, reducing power outages and maintenance costs [3, 4]. In addition, meeting legal and regulatory requirements is also a manifestation of corporate social responsibility. Therefore, cable insulation defect detection is not only a technical activity but also a responsibility and commitment to the enterprise and society. By accurately classifying defects, engineers can assess the condition of power cables, identify potential risks, and prevent catastrophic failures [5]. This classification process allows for targeted interventions, such as repair or replacement, based on the specific nature of the detected defects. In addition, effective defect classification facilitates online monitoring to ensure the continuous operation of the power system without affecting reliability. Moreover, understanding the root cause of insulation

failures is crucial for implementing preventive measures and optimizing the performance of power cables in various applications in electrical engineering [6, 7].

In order to ensure the safe and stable operation of the cable body and its accessories, and to grasp whether there are defects in the interior of the high-voltage cable and the type and size of the defects, it is urgent to develop an effective method that can quickly and accurately detect internal defects in insulated cables [8]. Currently, commonly used detection methods include AC superposition method, capacitive coupling method, directional coupling method, electromagnetic coupling method, leakage current test method, and detection method using oscillating wave voltage [9].

The literature [10] for the cable detection technology problems, proposed a power cable insulation defect detection method based on oscillating waves. This method dynamically generates a cable insulation defect detection benchmark database through the application of oscillating waves and signal sources in the field, identifies the fault mode corresponding to the maximum function value, and detects the type, location, and severity of cable insulation defects. In order to accurately determine the insulation status of power cables and ensure the safe and stable operation of the system, literature [11] conducted a simulation study on the detection of insulation defects in power cables based on electrical capacitance tomography technology. Using Landweber image reconstruction algorithm combined with optimized capacitance sensors and sensitivity fields, four typical cable insulation defects, including air gap defects, water tree defects, wedge scratch defects, and composite defects, were reconstructed, achieving the detection of insulation defects in power cables. To address the problem of difficulty in detecting the edges of scratches and stains on the surface of the main insulation of 10 kV cables, a method for identifying defects on the main insulation surface of 10 kV cables based on the Canny algorithm was proposed in the literature [12]. The method uses the scale-invariant feature transform (SIFT) method to complete the stitching of images of the main insulation of the cable and then uses the Canny algorithm to calculate the gradient and amplitude of the edges of defects on the main insulation surface, suppress maximum information points, remove false edges, and obtain information about the edges of defects caused by scratches and stains. The literature [13] studies the detection of defects in the insulation of aviation cables through infrared technology. Through numerical simulation, the temperature distribution and time variation of the insulated surface of the tested cable under different thermal excitations are analyzed. Meanwhile, experimental testing shows that the temperature variation range in the curve can successfully reflect the size and location of insulation defects. A new method for detecting insulation defects is proposed in the literature [14], which uses terahertz equipment to detect defects in cables, obtains terahertz images containing defects, and uses morphological algorithms to denoise and enhance the blurred images to obtain high-quality defect images to determine the location and size of the defects.

However, the actual cable structure is complex, and the methods in the above literature have problems such as complex operation, long detection time, and low detection accuracy, which cannot be effectively applied to the detection of insulation cable defects. Ultrasonic defect detection methods have the outstanding advantages of convenient operation, low cost, fast detection speed, and accurate defect location, and have been widely used in the detection of defects in insulators, pipelines, plate-like components, etc., and have achieved good detection results. The literature [15] uses conventional ultrasonic nondestructive testing methods to detect internal porosity defects in composite insulators, which can detect small porosity defects and verify the feasibility of ultrasonic detection of internal defects in complex structural objects. However, this method cannot achieve good coupling between the ultrasonic probe and objects with large curvature. The literature [16] uses ultrasonic pulse echo method to detect internal defects of composite insulators immersed in water, which can detect small defects in the umbrella skirt. This method can achieve ultrasonic detection of objects with large curvature, but requires immersing the object to be detected in water, which affects the later use of the detected object. Due to the special internal environment of aircraft, cable damage is inevitable, usually starting from defects in the insulation layer, which may cause significant economic losses and even pose a serious threat to the lives and safety of people on board. The literature [17] proposes a four-class defect classification method based on the deep forest method, which requires a small sample size and is not affected by network structure and parameters. The method has high recognition accuracy and avoids the problems of traditional deep learning classification that rely on large samples and require parameter adjustment. Due to the wide application and special nature of materials, the feasibility of using ultrasonic detection technology to achieve defect detection in insulated cables needs urgent research.

The reflection signals of different types of cable insulation defects are extremely similar and difficult to distinguish directly, so the identification and classification of cable insulation defects are very important. Traditional cable insulation defect classification mostly includes two stages: cable insulation defect feature extraction and cable insulation defect classification [18]. In the feature extraction of cable insulation defects, traditional methods have developed relatively mature, such as short-time Fourier transform, wavelet transform, S transform, empirical mode decomposition, Hilbert-Huang transform, etc. After feature extraction, the cable insulation defect signal needs to be input into a classifier for recognition [19]. The principle of existing classifiers is mostly based on machine learning algorithms, such as artificial neural networks, support vector machines, random forests, extreme learning machines, etc. Traditional machine learning algorithms generally perform poorly in the identification of cable insulation defects, and the accuracy is greatly affected by the feature extraction algorithm. It requires manual adjustment to make the dimension of feature extraction compatible with the required input of the classifier, which has certain limitations.

In the 21st century, deep learning has gradually developed and matured. Given that traditional machine learning methods have difficulty in efficiently and accurately processing time series data, adopting deep learning methods to mine useful information from time series data has become a key focus of many scholars. The results prove that it can effectively perform online monitoring and accurately classify defect types. In literature [20], in response to the problem that the statistical features of traditional partial discharge (PD) pattern recognition rely on expert experience and lack certain generalization, a partial discharge pattern recognition

method based on CNN and long-short term features was developed. The results showed that CNN-LSTM has better overall recognition accuracy. Literature [21] developed a deep learning method based on CNN for pattern recognition of high-voltage cable insulation defects. The results showed that the performance of the CNN method was improved compared to traditional methods such as BPNN and SVM.

Transformer is a deep learning model that has emerged in recent years [22]. After its first improvement in 2019, it was applied to time series prediction and achieved good results [23]. With the widespread application of Transformer in the field of computer vision, target detection algorithms based on Transformer have also made significant progress, such as DETR [24], VIT-FRCNN [25], and Deformable DETR [26]. However, the high computational cost of the Transformer method makes it difficult to deploy in practical tasks. Therefore, this paper introduces the Transformer to construct a cable insulation defect classification model. To overcome the problems that a single deep learning method may have in classification, such as poor prediction accuracy during a certain period of time and sensitivity to feature selection, a CNN-Transformer composite cable insulation defect classification model is proposed by combining CNN. The proposed CNN-transformer model excels in accuracy by combining CNN feature extraction with Transformer's capability for long-range dependency modeling. It is designed for high computational efficiency, optimizing training and inference speeds. The model also exhibits robustness to data variations and noise, making it a strong contender among current state-of-the-art methods.

The innovations of this study are as follows:

(1) The introduction of ultrasonic testing technology, which is non-invasive, highly sensitive, capable of quickly and accurately locating defects, and offers strong environmental adaptability and data visualization characteristics.
(2) The proposal of a CNN-Transformer composite model for the first time in cable insulation defect classification, addressing the challenge of distinguishing between the extremely similar reflection signals from different types of cable insulation defects.

2 Classification model

Unlike traditional methods, the CNN Transformer proposed in this paper takes the original one-dimensional signal for cable defect detection as input, without the need for any complex preprocessing operations. It integrates feature extraction and disturbance recognition, and directly outputs classification results. To ensure the model's reliability in power systems and prevent harm from misclassification, a multi-faceted approach is implemented. This includes extensive testing, validation through diverse datasets, integration of operational environment understanding, and a feedback mechanism for continuous learning. Additionally, safety protocols are in place to prioritize system integrity in cases of uncertainty, collectively reinforcing the model's dependability and the safety of power systems.

2.1 Transformer

Transformer consists of an encoder and a decoder, completely abandoning the basic architecture of recurrent neural networks and convolutional neural networks, and using attention mechanisms to complete network construction. The multi-head attention mechanism is the biggest highlight of the Transformer. The Transformer module is the core part of cable defect detection, used for feature extraction and representation. In the entire cable defect detection, the Transformer module is composed of multiple stacked Transformer basic modules, and the depth of the network is the number of Transformer basic modules. A Transformer basic module consists of a multi-head self-attention (MSA) module, a Multi-layer Perception (MLP) module, two residual modules, and two normalization modules.

2.1.1 MSA layer

The MSA layer is the core of the Transformer module. The attention mechanism can be seen as a mapping from a query matrix Query (Q) and a set of key-value matrices Key (K)-Value (V) to the output, represented by Eq. 1.

$$Attention(Q,K,V) = softmax\left(\frac{Q\cdot K^T}{\sqrt{d_k}}\right)\cdot V \tag{1}$$

where d_k is the dimension of Q and K. Q. K and V are essentially a set of linear mappings of the input time series. The attention mechanism enables each embedded subsequence in the input time series to obtain information from all other subsequences, which is very effective in solving the long-term dependencies of the time series. However, a set of Q, K, and V cannot obtain information from all subspaces, so multiple attention heads are concatenated into a new attention module called multi-head attention, represented by Eq. 2.

$$\begin{aligned} H_i &= Attention\left(QW_Q^i, KW_K^i, VW_V^i\right) \\ MSA(Q,K,V) &= concat(H_1,H_2,\ldots,H_h)W_0 \end{aligned} \tag{2}$$

where the attention weight matrix $W_0 \in R^{hd_v\times dim}$, $W_Q^i, W_K^i \in R^{dim\times d_k}, W_V^i \in R^{dim\times d_v}$. The three matrices Q, K, and V of a normal self-attention mechanism come from the same input $X = [x_1, x_2, x_3, \ldots, x_n]$, represented by Eqs 3–5.

$$Q = W_q\cdot X \tag{3}$$

$$K = W_k\cdot X \tag{4}$$

$$V = W_v\cdot X \tag{5}$$

where W_q, W_k, and W_v are three trainable parameter matrices.

The multi-head attention mechanism performs the self-attention process h times, combines the outputs, and performs normalization through residual connection to obtain the output of the attention layer. The process is shown in Figure 1.

2.1.2 MLP layer

In order to enhance the non-linear feature extraction capability of the Transformer, a multi-layer perceptron module is introduced.

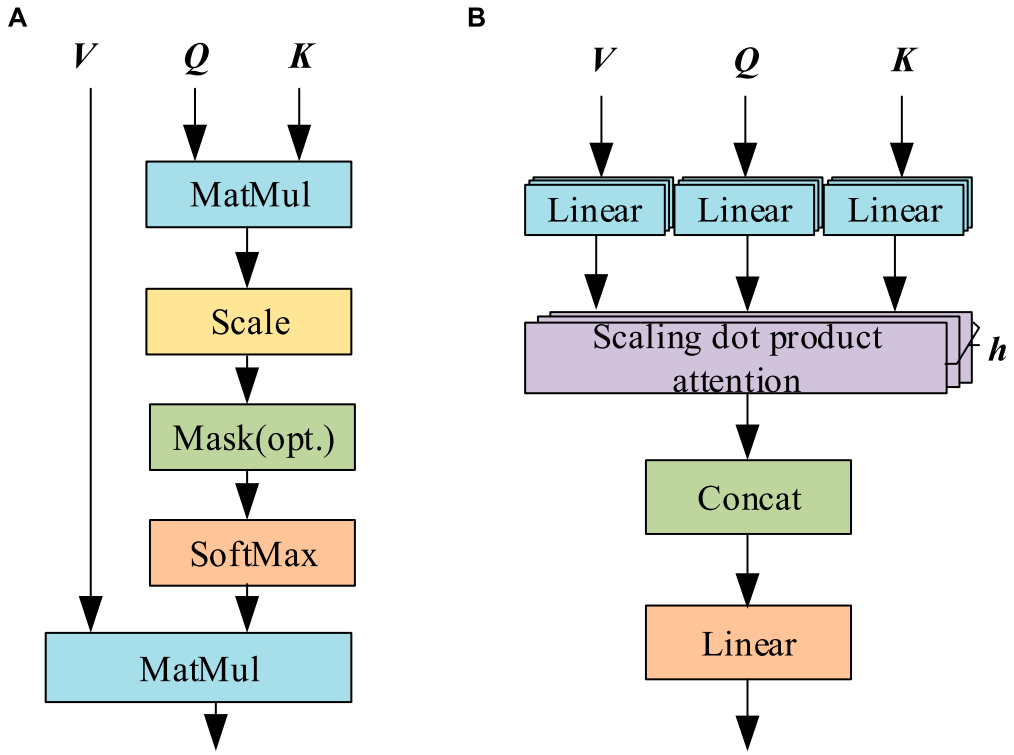

FIGURE 1
Scaling dot product attention and multi-head attention process diagram. **(A)** Scaling dot product attention. **(B)** Multiple headed attention.

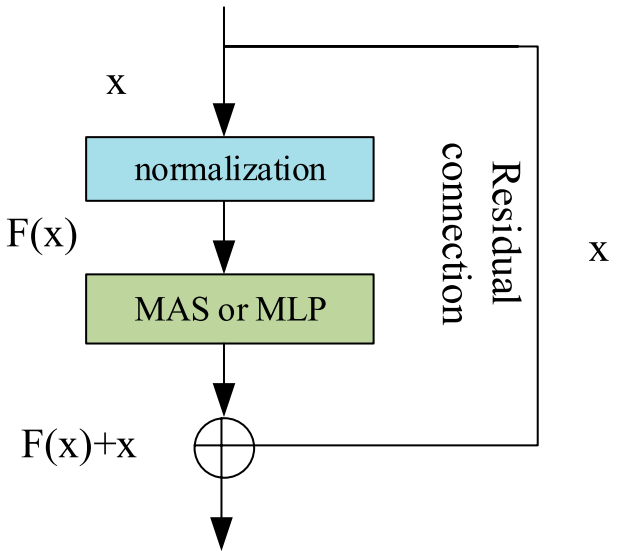

FIGURE 2
Residual block structure.

MLP first uses a nonlinear activation function to increase the dimensionality of the input, and then uses a linear transformation to reduce the dimensionality. For input x, MLP(x) can be represented by Eq. 6.

$$MLP(x) = \sigma\left(xW_1^l + b_1^l\right)W_2^l + b_2^l \tag{6}$$

Linear transformation weight matrix $W_1^1 \in R^{dim \times dim_{MLP}}$, $b_1^1 \in R^{dim_{MLP}}$, $W_2^1 \in R^{dim_{MLP} \times dim}$, $b_2^1 \in R^{dim}$. DimMLP is a linear transformation mapping dimension that is generally larger than the input dimension dim. σ (•) represents the activation function, using the GeLU function as the activation function, which can be expressed as Eq. 7.

$$\begin{aligned} GeLU(x) &= xP(X \le x) = x\phi(x) = x\left[1 + erf\left(x/\sqrt{2}\right)\right]/2 \\ &\approx 0.5x\left(1 + \tanh\left[\sqrt{\frac{2}{\pi}}\left(x + 0.045x^3\right)\right]\right) \end{aligned} \tag{7}$$

where $\phi(x)$ is the standard Gaussian distribution function. The GeLU function is a smooth version of the RuLU function, which avoids the discontinuity of the derivative at 0 and introduces random regularization, making feature extraction more versatile.

2.1.3 Residual and normalization modules

As the number of layers in the network deepens, nonlinear activation functions lead to data being mapped to more discrete spaces, making it increasingly difficult to fit the mapping function. Multilayer backpropagation may lead to gradient explosion and vanishing. The residual module is essentially a superposition operation between the nonlinear transformations of input and output, as shown in Figure 2. Among them, x is the input, and the mapping function that needs to be fitted in the network can be reconstructed as $F(x)+x$ through residual connections. The residual connection path of the side branches makes the mapping function easier to fit when the network layers are deeper. Therefore,

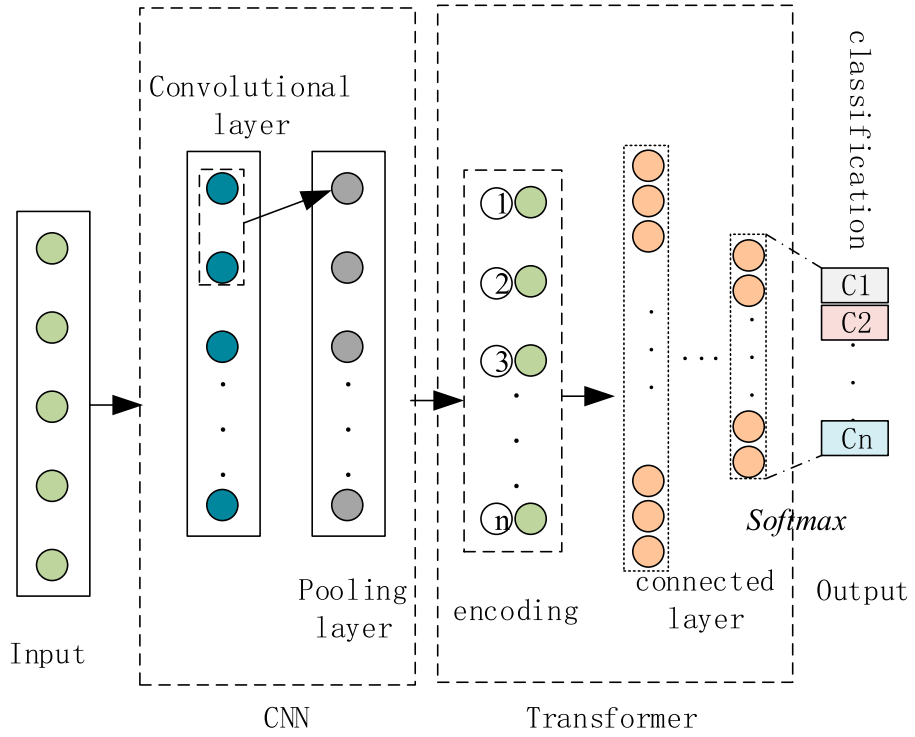

FIGURE 3
CNN transformer network model structure diagram.

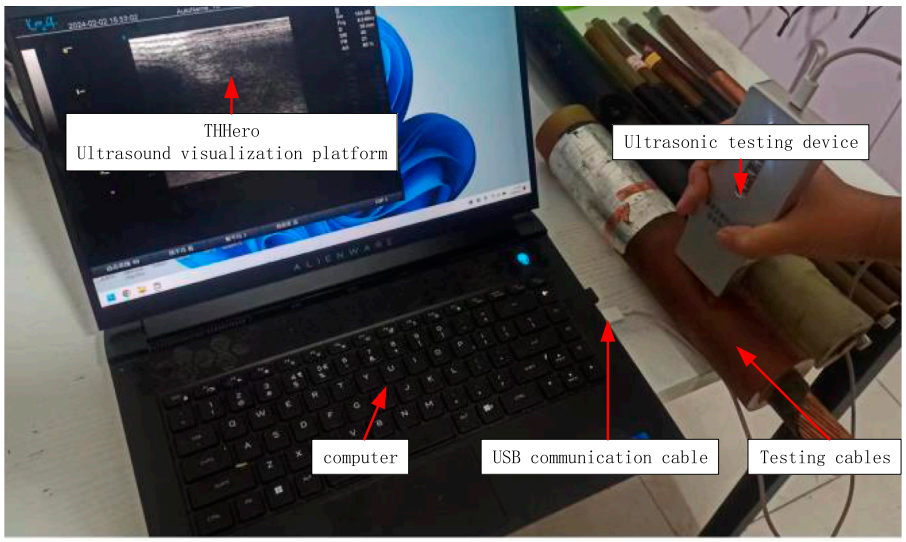

FIGURE 4
Cable insulation defect detection test device.

introducing residual modules in the MSA and MLP layers can greatly alleviate the problem of gradient vanishing and exploding as the network layers deepen.

In order to ensure the consistency of data distribution and accelerate the convergence speed of the model, a normalization module is introduced before the MSA and MLP layers. The commonly used normalization modules include Batch Normalization (BN) [27] and Layer Normalization (LN) [28]. BN standardizes the features of each batch, while LN standardizes all features of hidden layers in the network, regardless of the input batch

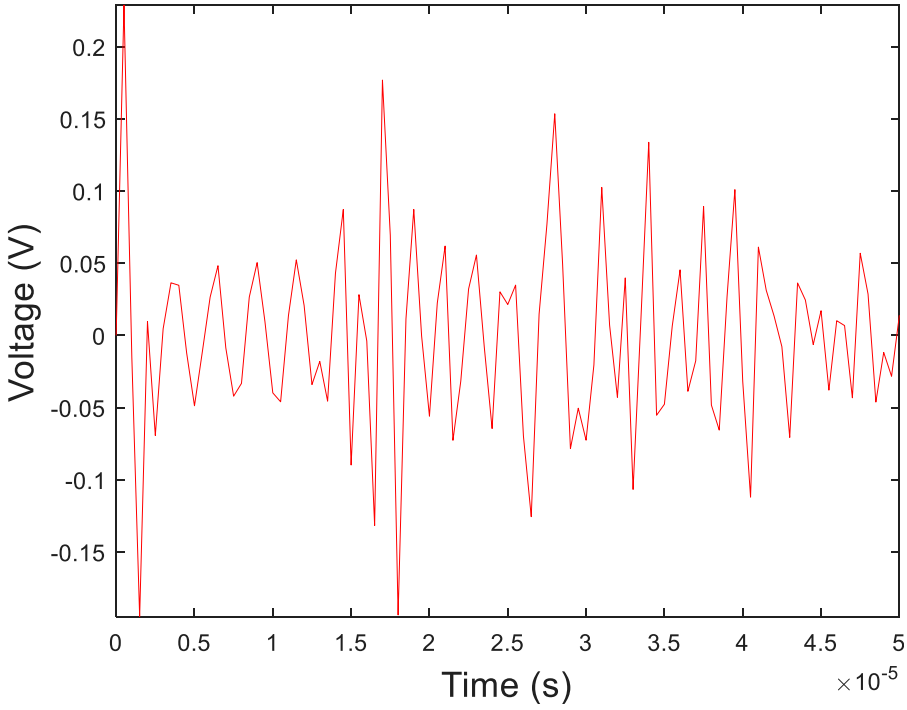

FIGURE 5
Internal echoes of cables under normal conditions.

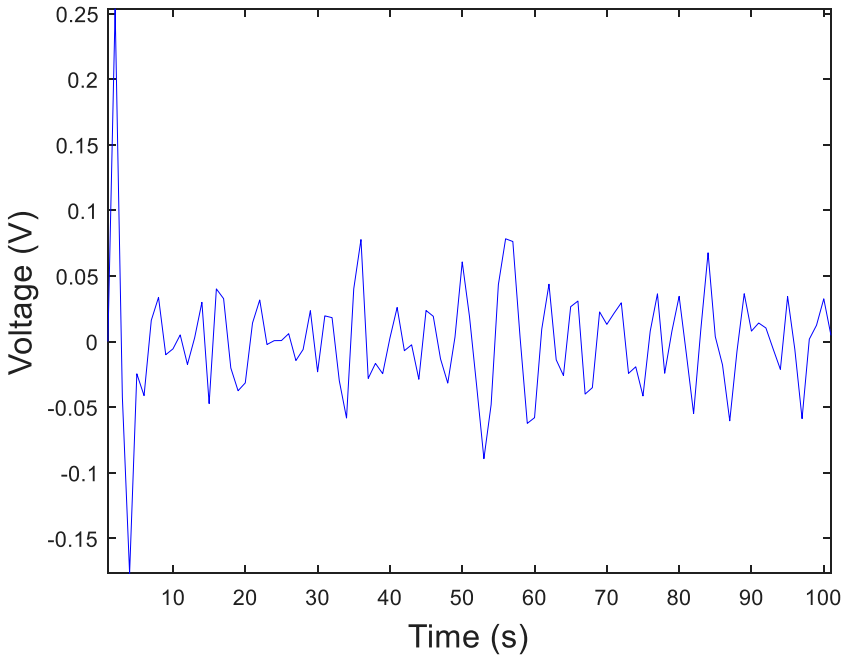

FIGURE 6
Echo of internal crack defects in cables.

size. In the Transformer model, the input is a one-dimensional time-series signal with a long length. To save hardware costs, small batch data is used for training. Compared to BN, LN can make the model converge faster in small-batch training. Therefore, this paper uses LN for normalization processing.

2.2 CNN-transformer

In the CNN-Transformer model, the Convolutional Neural Network component initially processes the input data. It extracts local features through convolutional layers and

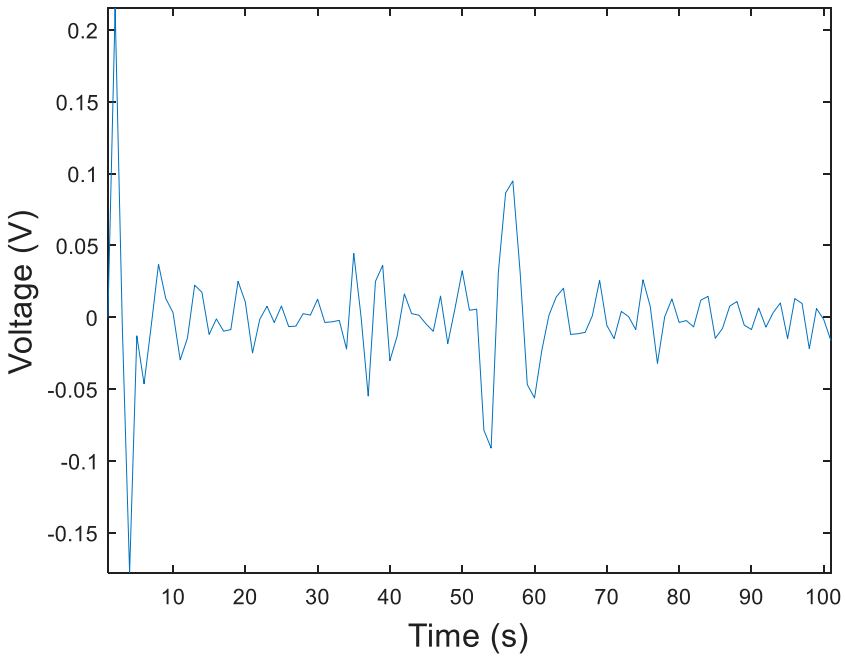

FIGURE 7
Echo of internal water droplet defects in cables.

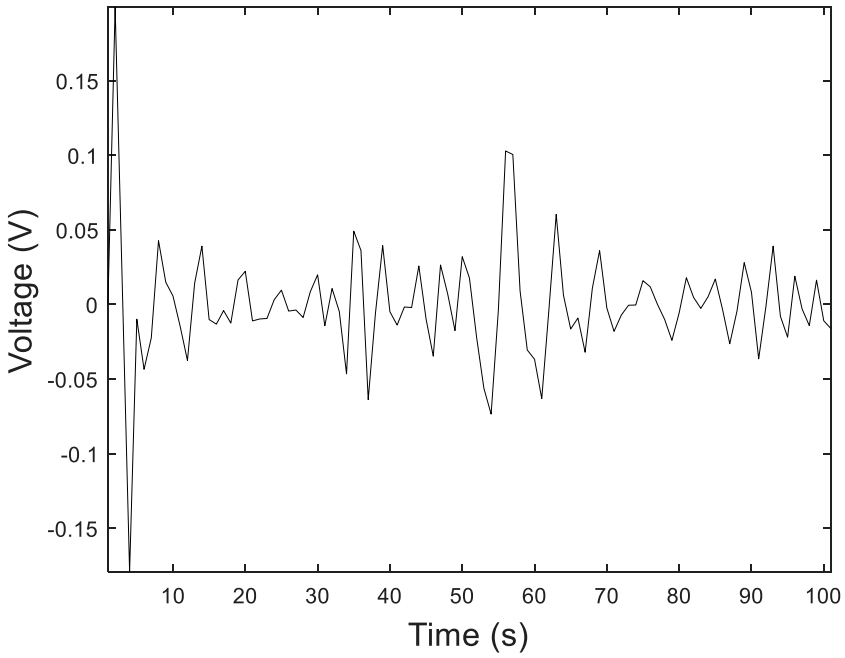

FIGURE 8
Echo of internal bubble defects in cables.

introduces non-linearity through activation layers such as ReLU to enhance the model's expressive power. Pooling layers may then reduce the spatial dimensions of the features, decreasing the number of parameters. Following this, the Transformer component captures global dependencies through self-attention mechanisms and expands this capability with multi-head attention to focus on different parts of the sequence. Each self-attention layer is typically followed by a feed-forward network to further refine the feature representation. Layer normalization and residual connections are used to stabilize

TABLE 1 Software and hardware parameters.

Hardware/Software	Environmental parameters
Operating System	Windows10 (64) 21H2
CPU	Intel Core i5-10400 @2.90Hz
GPU	NVIDIA GeForce RTX 2060
Random Access Memory	DDR4 32GB
Python	3.9
PyTorch	1.12.0
Cuda	11.6

During training, we choose the cross-entropy function commonly used in classification problems as the loss function, which is expressed as follows.

the training process and prevent the vanishing gradient problem. By combining the CNN's ability to extract local features with the Transformer's capacity to capture global dependencies, the CNN-Transformer model excels in tasks involving image processing, sequence data, and other complex pattern recognition challenges. In the direction of time series prediction, CNN is used to extract spatial features between different feature values in the sequence. It is to upscale the original signal into a two-dimensional image, and then extract deep features using CNN and other networks. To better adapt to the task of cable fault classification, convolutional layers and global average pooling structures are added, and the results are output through a fully connected layer. The improved method can better utilize the feature information of time series data and adapt to the characteristics of cable fault classification tasks. The method structure is shown in Figure 3. The CNN-Transformer model approaches the feature extraction process differently from traditional methods. While traditional CNNs are adept at capturing local features through convolutional operations, the integration with the Transformer component allows the model to not only focus on local patterns but also to leverage the Transformer's strength in capturing long-range dependencies and contextual information across the entire input data. This

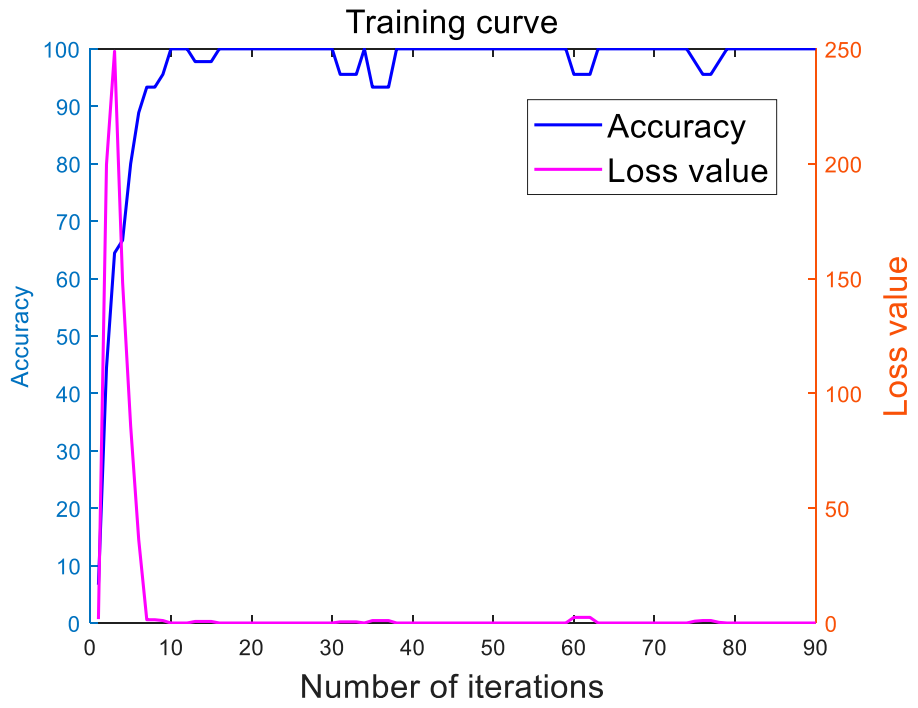

FIGURE 9
Model training process.

TABLE 2 Recognition accuracy of CNN-Transformer cable insulation defects.

Number	Cable insulation defect category	Recognition accuracy/%
1	normal	100
2	internal crack	100
3	Internal water droplet defect	100
4	Internal Bubble Defect	100

TABLE 3 Comparison of recognition accuracy of different models.

Model	Classification and identification accuracy of cable insulation defects/%			
	Normal	Internal crack	Internal water droplet defect	Internal bubble defect
CNN-LSTM	97.68	98.21	31.35	85.32
SVM	91.25	75.25	90.64	64.13
RF	98.38	87.21	35.34	86.32
CNN	99.21	100	96.18	52.51
Transformer	100	82.92	98.11	87.39
Proposed methodology	100	100	100	100

fusion enables a more comprehensive feature representation, where the CNN extracts detailed spatial hierarchies and the Transformer processes these features to understand broader relationships and sequences, leading to potentially more accurate and robust models in various tasks such as image classification, natural language processing, and beyond.

The model is inherently scalable and adaptable, designed to manage larger datasets efficiently. Its architecture allows for flexibility in handling various cable insulation materials and a diverse range of defect types, with the potential for further enhancement through additional training and parameter tuning as needed.

The specific steps are described as follows:

1) Conduct preliminary feature extraction on the input one-dimensional time series signal through convolution to obtain feature information of the cable insulation defect signal at different time scales.
2) The convolutional features extracted are sent to a time series Transformer, which embeds the category and location information of the original signal for encoding. The multi-head attention mechanism captures deeper transient local features and periodic global features of the cable insulation defect signal, and the multilayer perceptron module improves the model's nonlinear feature extraction ability. The residual

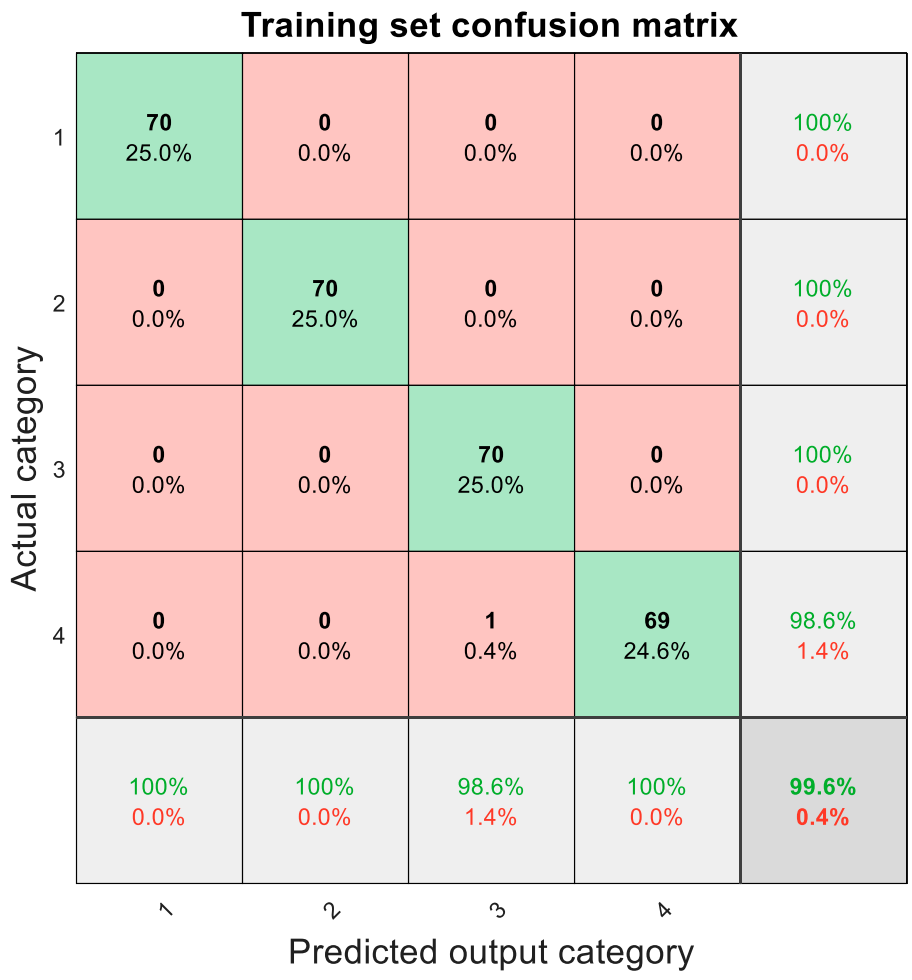

FIGURE 10
Training set mixing matrix.

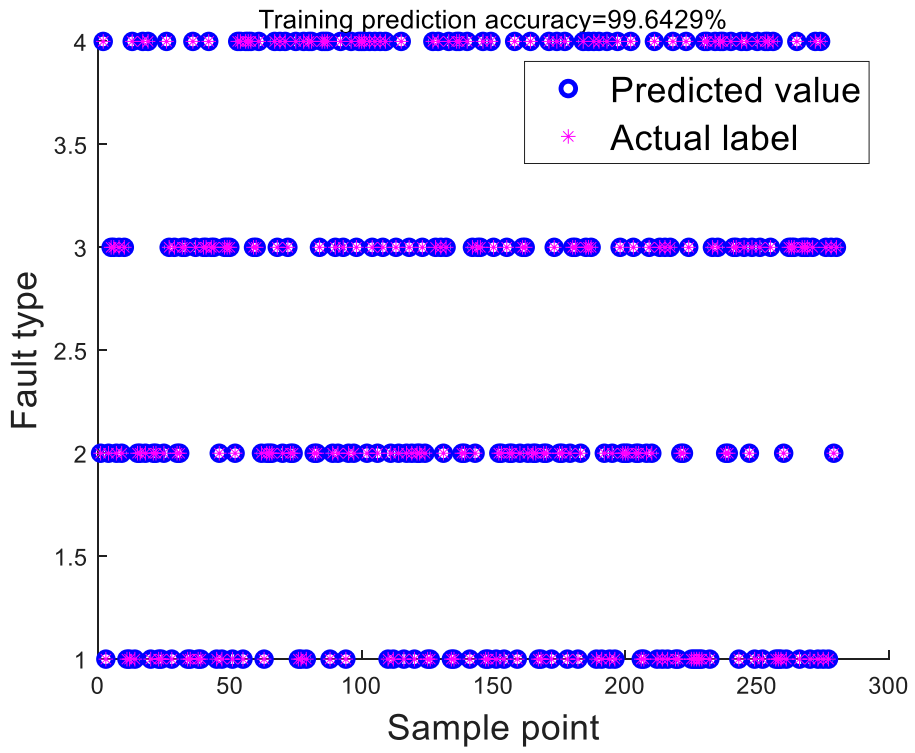

FIGURE 11
Comparison between predicted values and true values on the training set.

connection module is used to avoid gradient explosion and vanishing gradient network degradation problems, and extracts effective features required for classification.

3) Input the features to the fully connected layer and softmax classifier to obtain the fault signal category label recognized by the model.

The model's performance in real-world scenarios is enhanced through the integration of noise reduction techniques and robust feature extraction methods. Its architecture and training process are specifically tailored to improve generalization, allowing it to adapt to real-world data deviations. Despite these measures, ongoing adjustments and optimizations are essential to address unknown noise and variability. Implementing the CNN-transformer model in industrial environments involves challenges such as ensuring data quality and quantity, securing sufficient computational resources, integrating with existing systems, meeting real-time processing demands, maintaining robustness to environmental variability, achieving scalability, complying with regulatory standards, and managing ongoing model maintenance and updates. These factors can significantly influence the practical application and effectiveness of the model in industrial settings. The model is slated for enhancement with a roadmap that includes adding features to boost its adaptability across various cable types and environmental settings. This strategy involves broadening the training dataset and possibly integrating self-adaptive algorithms for *in-situ* learning. The architecture will undergo refinement to manage material and defect variances more adeptly, with a commitment to uphold efficiency and efficacy in a spectrum of industrial environments. The development cycle is designed to be iterative, allowing for regular updates informed by practical deployment and feedback.

3 Ultrasonic testing results

3.1 Test platform

The cable insulation defect detection test device is shown in Figure 4 and consists mainly of a cable termination sample, an ultrasonic probe, a power supply, an ultrasonic visualization platform, and a USB communication cable. The steps for cable insulation defect detection are as follows. First, an ultrasonic probe makes direct contact with the cable insulation surface, and ultrasonic waves are transmitted into the interior of the cable insulation sample through a coupling agent. Then, the reflected signals are processed by a digital controller and converted into waveforms displayed on the display system interface. The specific steps used in the experiment include sample preparation, the transmission and reception of ultrasonic signals, and signal processing and analysis. During the detection process, the ultrasonic probe is directly in contact with the cable insulation surface through a couplant, and the ultrasonic wave is transmitted into the interior of the cable insulation sample under the action of the couplant. The reflected signal is processed by a digital controller and converted into a waveform that is displayed on the display system interface. The dataset consists of 400 samples, which are divided into training, validation, and testing sets for the model's training, tuning, and performance evaluation, respectively. The

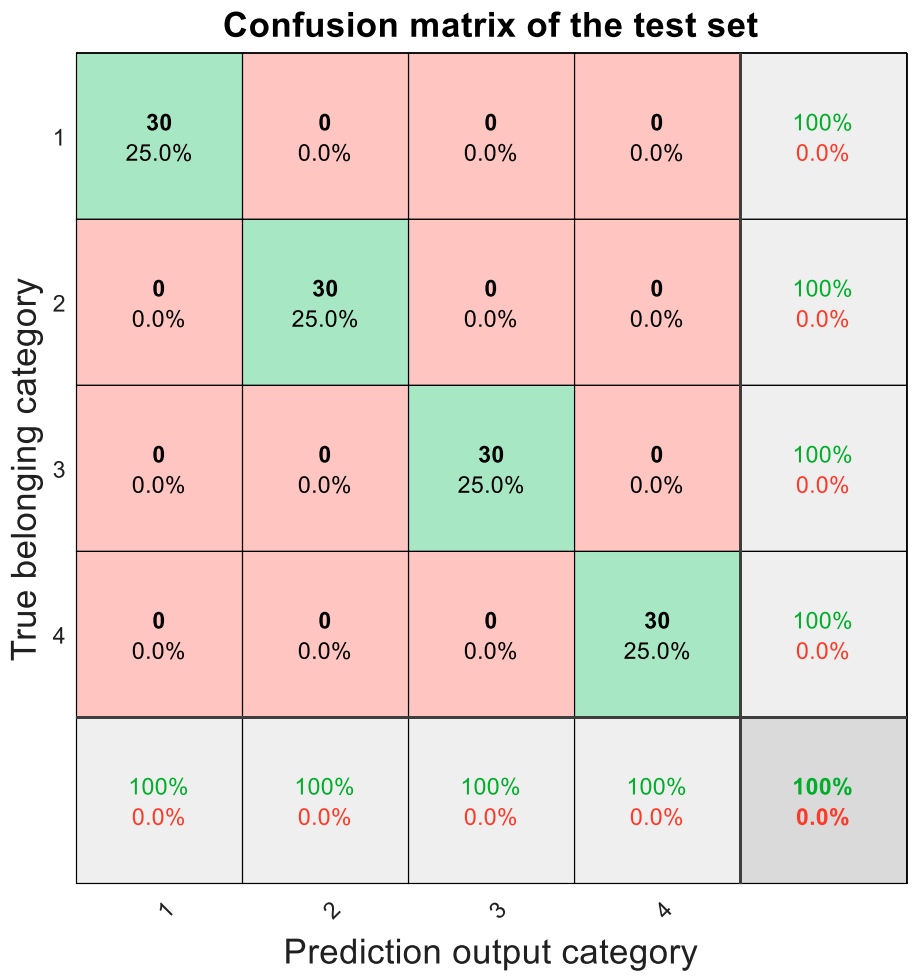

FIGURE 12
Test set confusion matrix.

collection method of the samples adheres to standardized ultrasonic detection procedures, ensuring the consistency and reliability of the data. All data were collected in a controlled laboratory environment to minimize the impact of environmental factors on signal acquisition.

3.2 Monitoring results

Figures 5–8 are internal echoes detected by the cable insulation defect detection test device under different conditions. From the figure, the echo signal characteristics of the cable under different conditions are not particularly obvious, with the same voltage fluctuation amplitude.

4 Classification results and analysis

4.1 Model parameters and training results

This article conducts the verification of the CNN-Transformer classification model based on ultrasound detection data. The MCF-TST model proposed in this article is built on the PyTorch deep learning framework and Python. The hardware and software parameters of the training environment are shown in Table 1. The preset CNN node number (32, 64, 128), Dropout value (0.1, 0.2, 0.3, 0.4, 0.5), Encoder layer number (4, 5, 6), and time step (4, 6, 8, 10). There are 600 groups of each signal, and they are divided into training set, validation set and test set according to 4:1:1. The dataset for the CNN-transformer model was assembled with a blend of simulated and real-world data to ensure a broad representation of defect scenarios. It includes a significant number of samples necessary for effective model training and validation, with a focus on high data quality and precise labeling. The exact dataset size is tailored to the task's demands, but it is sufficiently large to enable the model to generalize well across various conditions. The cross-entropy function commonly used in classification problems is chosen as the loss function for training, represented by Eq. 8.

$$Loss = -\frac{1}{B}\sum_{p=1}^{B}\sum_{q=1}^{N_{cls}} y_{pq}\log\left(\hat{y}_{pq}\right) \tag{8}$$

where B is the size of the training batch, N_{cls} is the number of cable insulation defect categories, y_{pq} and $\hat{y}_{py}$ are the true label and predicted probability of the pth input in the qth cable insulation defect category,

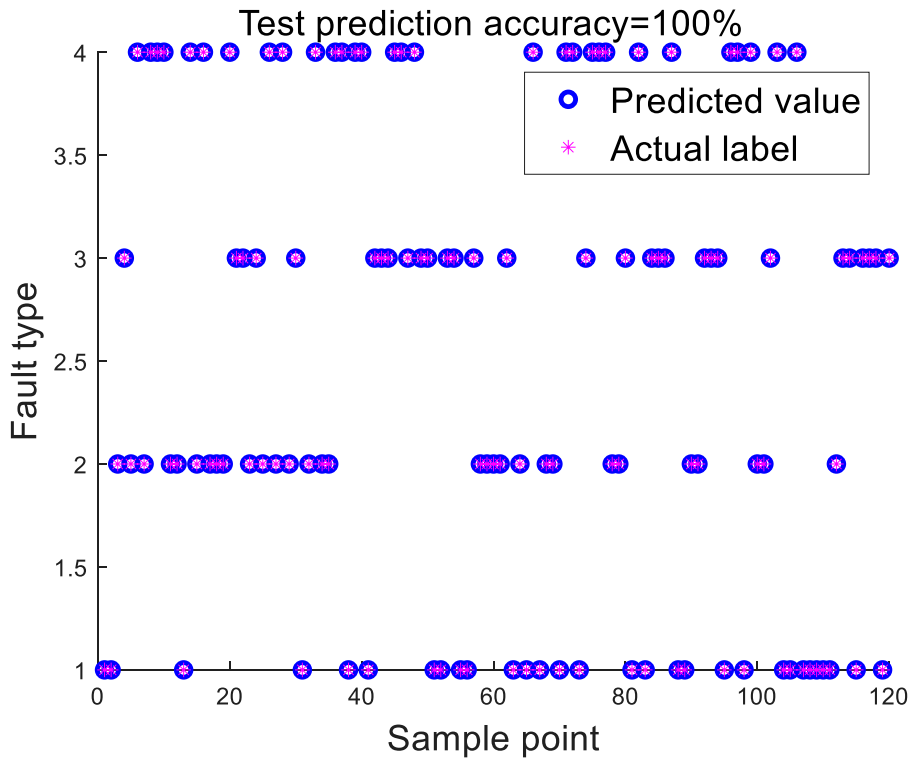

FIGURE 13
Comparison between predicted and true values on the test set.

respectively. The recognition accuracy Acc and loss value Loss of the training set and test set during model training are shown in Figure 9.

Figure 6 shows that the model proposed in this article can achieve high accuracy after training, and maintains high accuracy and low loss throughout. The model converges quickly and does not exhibit overfitting. The recognition accuracy of various cable insulation defects is shown in Table 2. To assess the model's performance under varying conditions, a series of experiments were conducted in this paper, simulating the impact of various environmental factors and signal disturbances on the model's capabilities. These experiments included classification tests under conditions with added noise at different signal-to-noise ratio levels, altered positions of the ultrasonic probe, and cable samples of varying degrees of aging. The results indicate that while the model performs exceptionally well under high signal-to-noise ratio conditions, its accuracy declines in the presence of high noise levels or when signal characteristics are not distinct.

4.2 Verification of model recognition accuracy

To verify the performance of the model in this article, the accuracy of recognition compared with other machine models is shown in Table 3. The experiments utilized several different types of cable samples, each with unique physical properties and signal characteristics. The model's performance on these samples was evaluated by comparing it with its performance on the original dataset. Furthermore, to further explore the model's generalization ability, tests were conducted under various signal-to-noise ratio conditions, simulating the diverse noisy environments that might be encountered in field applications. The results indicated that while the model achieved high accuracy on the original dataset, its performance declined on certain types of cable samples. This revealed potential limitations of the model when generalizing to data that significantly deviates from the training data. To address this issue, strategies such as data augmentation, transfer learning, or multi-task learning are considered for future work to enhance the model's generalization capability across different types of cables.

To enhance the rigor and verifiability of comparative experiments, this paper provides a detailed description of the implementation parameters for the traditional methods involved. Here are example parameters for each method:

1) Support Vector Machine (SVM): The kernel function is set to the Radial Basis Function (RBF), the penalty parameter (C) is chosen as 10, and the gamma parameter for the kernel function is set to 0.1, selected based on cross-validation results.
2) Random Forest (RF): The number of decision trees in the forest is set to 100, and the maximum number of features considered for the split in each tree is set to the square root of the total number of features. The splitting criterion uses Gini impurity.
3) Convolutional Neural Network (CNN): The network includes two convolutional layers, each followed by a max-pooling layer. The first convolutional layer uses 32 filters of size 3×3, and the second convolutional layer uses 64 filters of size 3×3. A ReLU activation function follows all convolutional layers, and a fully connected layer at the end performs classification.

From the data in Table 3, it can be seen that compared to traditional machine learning model classifiers and neural networks, the model proposed in this paper has the highest accuracy in identifying four types of cable insulation defects. The comparison results demonstrate the superiority of the Transformer model over other models in Transformer cable insulation defect recognition.

To further verify the confusion of the model for different types of cable insulation defects, we used a test set with 30dB noise, with 100 data points per type of cable insulation defect. We drew a confusion matrix for the four types of cable insulation defects, as shown in Figures 10, 11. The horizontal and vertical coordinates represent the true label and predicted label of the cable insulation defect signal, respectively. During the assessment of the proposed CNN-Transformer model, the focus was on its computational efficiency, a critical determinant for practical deployment. The model's training time, measured from the start of initialization until the point of convergence where the loss plateaued, was around 1 h, highlighting the duration necessary for it to adeptly learn the nuances of cable insulation defects. Furthermore, the inference time for the model to classify a single instance was benchmarked at approximately 0.1 s, demonstrating its capability to perform prediction tasks efficiently and suggesting its suitability for real-time applications.

As shown in Figures 12, 13, all types of cable insulation defects can be accurately identified by the model when identifying composite cable insulation defects. In this paper, the calculated 100% accuracy rate is based on experimental results under specific conditions. This outcome was measured on a carefully selected and balanced dataset, targeting a range of predefined defect types and severity levels. The evaluation process employed standardized metrics, including precision, recall, and the F1 score, and utilized cross-validation and an independent test set to ensure the accuracy and reproducibility of the results. Moreover, the model considered various potential defect scenarios during both training and testing phases to enhance its generalization capabilities. However, it should be noted that this accuracy rate may be subject to the constraints of the experimental conditions, and the complexities encountered in real-world applications may impact the model's performance.

5 Conclusion

Considering that the detection of cable insulation defects is a key step to ensure the normal operation and safe use of cables, there are certain limitations in common detection and identification methods. Therefore, it is proposed to adopt ultrasonic detection technology combined with CNN-Transformer for cable insulation defect classification. Through simulation experiments and hardware experiments, the following conclusions are drawn:

1) Ultrasonic testing method is used to detect defects in insulated cables, which can detect the defect signals of insulated cables and provide clear echoes of defects.
2) Proposed CNN-Transformer, which captures the local transient features and periodic steady-state global features of cable insulation defect signals through multi-head attention mechanism, and exhibits excellent performance in cable insulation defect recognition.
3) Through various comparative experiments, the model with the optimal parameters is determined to identify the signal of cable insulation defects, and the recognition accuracy reaches 100% in the absence of noise.

The dataset used in this article is still not comprehensive enough. In the future, it may be considered to further improve the experiment and validate the model with live measurement data to meet application requirements.

Data availability statement

The original contributions presented in the study are included in the article/Supplementary Material, further inquiries can be directed to the corresponding authors.

Author contributions

NZ: Writing–original draft, Writing–review and editing. ZD: Writing–original draft, Writing–review and editing. QL: Conceptualization, Data curation, Methodology, Writing–original draft. KG: Conceptualization, Investigation, Software, Writing–review and editing. ZZ: Data curation, Methodology, Supervision, Writing–original draft. BL: Data curation, Formal Analysis, Writing–review and editing.

Funding

The author(s) declare that financial support was received for the research, authorship, and/or publication of this article.

Conflict of interest

Authors NZ, ZD, QL, KG, ZZ, and BL were employed by State Grid Shijiazhuang Electric Power Supply Company.

The authors declare that this study received funding from State Grid Hebei Electric Power Co., Ltd. (No. KJ2022-016). The funder was involved in the study design, collection, analysis, interpretation of data, the writing of this article, and the decision to submit it for publication.

Publisher's note

References

1. Ren G, Wang Y, Cao J. Overview of early insulation fault detection methods for power cables. *J Chongqing Univ* (2023) 46(11):1–12. doi:10.11835/j.issn.1000-582X.2022.212

2. Hua X, Wang L, Yang S. Lifetime prediction of aviation cables based on an improved electromagnetic–thermal coupling model. *IEEE Trans Dielectr Electr Insul* (2023) 30(6):2788–97. doi:10.1109/tdei.2023.3295347

3. Shen XW, Du CB, Jiang SY, Zhang P, Chen LL. Multivariate uncertainty analysis of fracture problems through model order reduction accelerated SBFEM. *Appl Math Model* (2024) 125:218–40. doi:10.1016/j.apm.2023.08.040

4. Hua X, Wang L, Yang S. Multiscale analysis of the aging process of cable insulation. *IEEE Trans Dielectr Electr Insul* (2022) 30(1):238–46. doi:10.1109/tdei.2022.3217425

5. Shen XW, Du CB, Jiang SY, Sun LG, Chen LL. Enhancing deep neural networks for multivariate uncertainty analysis of cracked structures by POD-RBF. *Theor Appl Fract Mech* (2023) 125:103925. doi:10.1016/j.tafmec.2023.103925

6. Hua X, Wang L, Zhang Y. Analysis and diagnosis of shielded cable faults based on FEM and time-reversal time-frequency domain reflectometry. *IEEE Trans Ind Electron* (2021) 64(4):4205–14. doi:10.1109/TIE.2021.3071685

7. Chen LL, Wang ZW, Lian HJ, Ma YJ, Meng ZX, Li P, et al. Reduced order isogeometric boundary element methods for CAD-integrated shape optimization in electromagnetic scattering. *Comput Methods Appl Mech Eng* (2024) 419:116654. doi:10.1016/j.cma.2023.116654

8. Hua X, Xu W, Wang L, Zhang Y, Temperature mapping model of cables considering the coupling of electromagnetic and thermal fields. *Digit Twin* (2023) 3(2):1–16. doi:10.12688/digitaltwin.17718.2

9. Dong YG. Detection method for insulation defects in power cables. *Era Agr Mach* (2015) 42(10):19–20.

10. Quan YS, Wang DJ, Chen G, Zhang ZC. Study on the methodology of detection for power cable insulation defects based on oscillatory wave. *Adv Mater Res* (2013) 805-806:880–3. doi:10.4028/www.scientific.net/amr.805-806.880

11. Lin YB, Chen A, Jin YX Simulation study on cable insulation defect detection based on capacitance tomography imaging. *J Electr Eng* (2023) 18(3):54–62.

12. Fang CH, Zhang F, Dang WJ A method for identifying surface defects in the main insulation of 10 kV cables based on the Canny algorithm. *Optoelectron Lasers* (2021) 32(11):1188–95.

13. Wen F, Jin J. Detection of superficial defects in the insulation layers of aviation cables by infrared thermographic technique. *Coatings* (2022) 12(6):745. doi:10.3390/coatings12060745

14. Luo G, Lu Q, Huang H, Chen H, Han J, Chen X. Research on cable insulation layer defect detection based on terahertz technology. *J Phys Conf Ser* (2023) 2662(1):012024–248. doi:10.1088/1742-6596/2662/1/012024

15. Xie CZ, Zhang Y, Hao YP Application of ultrasonic flaw detector to detect internal defects of composite insulators. *High Voltage Engineering* (2009) 35(10):2464–9. doi:10.1016/S1003-6326(09)60084-4

16. Gao Y, Li XD, Xue JQ Research on ultrasonic pulse detection of internal defects in silicone rubber. *High Voltage Engineering* (1997) 23(2):17–19.

17. Wang Q, Huang M, Wang X, Zhang Y, Zhang Q, An Y, et al. Defect detection and identification for aircraft cable insulation layer based on deep forest. *Ultrasonics* (2023) 135:107128. doi:10.1016/j.ultras.2023.107128

18. Zhou X, Wu X, Ding P, Li X, He N, Zhang G, et al. Research on transformer partial discharge UHF pattern recognition based on CNN-LSTM. *Energies* (2020) 13:61. doi:10.3390/en13010061

19. Howard R, Cegla F. On the probability of detecting wall thinning defects with dispersive circumferential guided waves. *NDT E Int* (2017) 86:73–82. doi:10.1016/j.ndteint.2016.11.011

20. Peng X, Yang F, Wang G, Wu Y, Li L, Li Z, et al. A convolutional neural network-based deep learning methodology for recognition of partial discharge patterns from high-voltage cables. *IEEE Trans Power Deliv* (2019) 34(4):1460–9. doi:10.1109/tpwrd.2019.2906086

21. Uckol HI, Ilhan S, Ozdemir A. Workmanship defect classification in medium voltage cable terminations with convolutional neural network. *Electr Power Syst Res* (2021) 194:107105. doi:10.1016/j.epsr.2021.107105

22. Liang H, Liu S, Du J A review of deep learning applications in time series prediction research. *Comput Sci Explor* (2023) 17(6):1285–1300.

23. Vaswani A, Shazeer N, Parmar N *Attention is all you need*. arXiv (2017). doi:10.48550/arXiv.1706.03762

24. Carion N, Massa F, Synnaeve G End-to-end object detection with transformers. In: *2020 European conference on computer vision (ECCV)* (2020). p. 213–29.

25. Beal J, Kim E, Tzeng E *Toward transformer-based object detection* (2020). doi:10.48550/arXiv.2012.09958

26. Chen LL, Cheng RH, Li SZ, Lian HJ, Zheng CJ, Bordas SPA. A sample-efficient deep learning method for multivariate uncertainty qualification of acoustic–vibration interaction problems. *Comput Methods Appl Mech Eng* (2022) 393:114784. doi:10.1016/j.cma.2022.114784

27. Chen LL, Li HZ, Guo YY, Chen P, Atroshchenko E, Lian HJ. Uncertainty quantification of mechanical property of piezoelectric materials based on isogeometric stochastic FEM with generalized Nth-order perturbation. *Eng Comput* (2023) 40(1):257–77. doi:10.1007/s00366-023-01788-w

28. Lu C, Chen LL, Luo JL, Chen HB. Acoustic shape optimization based on isogeometric boundary element method with subdivision surfaces. *Eng Anal Bound Elem* (2023) 146:951–65. doi:10.1016/j.enganabound.2022.11.010

frontiers | Frontiers in Physics

TYPE Original Research
PUBLISHED 02 August 2024
DOI 10.3389/fphy.2024.1432783

OPEN ACCESS

EDITED BY
Pei Li,
University of Southern Denmark, Denmark

REVIEWED BY
Fuhong Min,
Nanjing Normal University, China
Fan Zhang,
Sichuan University, China

*CORRESPONDENCE
Ning Zhao,
moj6302@163.com

RECEIVED 14 May 2024
ACCEPTED 19 July 2024
PUBLISHED 02 August 2024

CITATION
Zhao N, Fang Y, Wang S, Li Q, Wang X and Feng C (2024), Research on the identification method of cable insulation defects based on Markov transition fields and transformer networks.
Front. Phys. 12:1432783.
doi: 10.3389/fphy.2024.1432783

Research on the identification method of cable insulation defects based on Markov transition fields and transformer networks

Ning Zhao*, Yongyi Fang, Siying Wang, Qian Li, Xiaonan Wang and Chi Feng

State Grid Shijiazhuang Electric Power Supply Company, Shijiazhuang, Hebei, China

Identifying cable insulation defects is crucial for preventing system failures and ensuring the reliability of electrical infrastructure. This paper introduces a novel method leveraging the Markov transition field (MTF) and Transformer network to improve the precision of cable insulation defect identification and enhance the algorithm's noise resistance. Firstly, the algorithm performs modal transformation on the time series data acquired by the ultrasonic probe through MTF, generating corresponding images. Following this, the image data are input into a pre-trained Transformer network to achieve automated feature extraction. Subsequently, a multi-head attention mechanism is introduced, which assigns weights to the features extracted by the Transformer network, thereby emphasizing the most critical information for the identification task. Finally, more accurate defect identification is achieved based on the weighted features. The results demonstrate that this method achieves higher accuracy and stronger noise resistance compared to traditional image processing and recognition methods, making it a robust solution for cable insulation defect identification.

KEYWORDS

cable, insulation defect, Markov transition field, transformer networks, multi-head attention mechanism

1 Introduction

In the safe operation of power systems, the detection of cable insulation defects plays a crucial role, and its importance cannot be overlooked [1]. Currently, the analysis process of cable insulation defects mostly employs numerical computation methods [2]. These methods primarily involve numerically solving the physical processes and mathematical models of cable insulation defects to predict and analyze the characteristics of insulation defects [3]. In the identification of cable insulation defects, commonly used numerical computation methods include the finite element method, the finite difference method, and the boundary element method [4, 5]. In modern industry and daily life, as the primary medium for transmitting electrical energy, the stability and reliability of cables have a crucial impact on ensuring the continuity and safety of the power supply [6, 7]. Therefore, conducting accurate and effective detection of cable insulation defects is a key component of the maintenance and operation of power systems [8, 9]. In the field of cable insulation defect detection for power systems, due to the combined effects of external environmental factors,

material aging, and construction quality issues, the insulation layer of the cable may exhibit various types of defects such as cracks, holes, and water trees [10, 11]. If these defects are not detected and addressed in a timely manner, they may cause cable failures and could even lead to serious power system accidents [12, 13]. Therefore, conducting systematic research to enhance the accuracy and efficiency of detection technology is of great significance for preventing and reducing the occurrence of power accidents.

With the advancement of technology, the detection technology for cable insulation defects is also continuously improving. Reference [14] proposes a new method for detecting and locating defects in cross-linked grounded configuration cable sheaths. Through simulation and actual case validation, this method can effectively identify and locate various types of defects, and it enhances the stability of detection under low load currents by using an improved capacitive current subtraction method. Reference [15] addresses the issue of cable defect localization by proposing a method for selecting the upper limit scanning frequency based on short-time Fourier transform. Through simulation and experimental validation, this method can effectively reduce the impact of high-frequency signal attenuation on defect localization and improve the accuracy of localization. Research results indicate that compared with traditional frequency domain reflectometry, the proposed method has higher performance in both single-point and multi-point defect localization. Reference [16] addresses the issue of internal defect detection in cable terminals by proposing a non-destructive testing technology based on the microwave reflection method. By establishing a theoretical model and simulating with CST software, the impact of defect type, size, silicone rubber thickness, and detection distance on the reflection coefficient was analyzed. Experiments confirmed the feasibility of the theoretical model and simulation results, successfully detecting a tiny defect of two square millimeters, proving the efficiency and practicality of the method. Reference [17] addresses the analysis and diagnosis of shielded cable faults by establishing a two-dimensional model of a cable with defects using the finite element method and calculating its characteristic impedance. Reference [18] conducts experimental research on single-ended partial discharge (PD) measurements using a high-frequency current transformer to address the issue of simultaneous activity of multiple PD defects in medium-voltage underground power cables. By analyzing the reflected pulses with time-domain reflectometry, two PD sources at different locations were successfully identified and located. The research results indicate that the proposed method can effectively distinguish signals from different PD sources and accurately determine the location of the PD sources, which is of great significance for the detection and maintenance of PD defects in actual cable networks. The deficiency of current cable insulation defect detection techniques lies in the fact that, although various methods can effectively identify and locate defects, they often fail to accurately identify the type of insulation defects. This leads to a lack of targeted detection and analysis methods for different types of defects in practical applications, thereby affecting the accuracy of the detection results and the specificity of maintenance work. Therefore, enhancing the accuracy of defect identification and developing technologies capable of recognizing and differentiating various types of defects are directions that current research needs to focus on and improve.

Research on intelligent classification methods for cable insulation defects is crucial for enhancing the reliability and safety of power systems [19, 20], as it ensures precise identification and effective management of various defects, thereby preventing potential power failures and accidents. Reference [21] addresses the issue of insulation defect identification in direct current cross-linked polyethylene (DC XLPE) cables by conducting research on a new method based on Contourlet transform and Tsallis entropy feature extraction, and employs a corrected output code classifier optimized by an adaptive cuckoo search algorithm for defect identification. The results indicate that this method has a high classification accuracy rate in identifying typical insulation defects of cables and provides a new approach for the identification of insulation defect types in DC XLPE cables. Reference [22] proposes a diagnostic method based on the time-frequency domain reflectometry for fault classification in multi-core cables. By converting the reflected signals into images and utilizing advanced image processing algorithms, combined with artificial neural networks for fault classification. Experimental results show that this method can improve the accuracy and reliability of fault diagnosis in multi-core cable systems, especially suitable for fault classification of terminal block faults in cables of varying lengths. Reference [23] addresses the issue of internal defects in the insulation of power cables by proposing a machine learning diagnostic scheme based on PD pattern analysis. Through waveform analysis and feature extraction, the method employs support vector machine (SVM) and ensemble tree algorithms to identify and classify internal sources of PD of various shapes and sizes. Experimental results demonstrate that the proposed method can effectively identify and classify defects in the insulation of cables, with an accuracy rate ranging from 96% to 92%. Reference [24] introduces a novel method for fault classification in power distribution cables based on the detection of the DC component using magneto sensitivity. The method reconstructs the current using a stochastic optimization algorithm, extracts the DC component with mathematical morphology, and identifies the type of fault accordingly. Experiments have proven that this method can effectively classify faults, is robust, and does not require pre-calibration. However, existing intelligent classification methods rely on specific technologies, are sensitive to noise, and require extensive preprocessing for practical application.

The principal contributions encapsulated within this paper are delineated as follows:

(1) The paper presents a groundbreaking integration of the Markov transition field (MTF) with Transformer network architecture, facilitating the conversion of time series data, as captured by ultrasonic probing, into image modalities through a process of modality transformation. This innovative step significantly enriches the data's representational capacity, thereby yielding a more comprehensive informational substrate that is instrumental for downstream tasks of feature extraction and defect recognition.
(2) The paper employs a pre-trained Transformer network for the automated extraction of features, complemented by the introduction of a multi-head attention mechanism that assigns weights to these features. This strategic enhancement ensures that the information critical for the recognition task is

effectively brought into prominence. Consequently, the approach not only bolsters the precision of defect recognition but also fortifies the algorithm's resilience to noise. It distinguishes itself particularly in the context of identifying insulation defects within cables, showcasing exceptional performance in this niche yet critical domain.

2 Fundamental theory

2.1 Markov transition field

MTF is a method for transforming temporal data into spatial image data. This method extends the Markov state transition matrix, fully preserves the discretized temporal dynamic information by sequentially expressing the state transition matrix, and ultimately generates a two-dimensional image through fuzzy kernel aggregation. Given a time series signal $X = \{x_1, x_2, \cdots, x_n\}$, composed of n sampled signals x at different timestamps. The MTF method first divides the time series signal into Z regions based on amplitude, each region represented as g ($i = 1, 2, \cdots, Z$), with each sampled signal mapped to the region g. The division strategies include: uniform division, quantile division, and normal distribution division. Uniform division refers to the division where each region in each sample has the same amplitude width; Quantile division refers to the division where each region in the sample contains an equal number of sampled points; Normal distribution division refers to the division where the number of sampled points contained in each region follows a normal distribution. Then, the probabilities of transitions from region q_i to q_j for the sampled signals x_{i-1} and x_i at consecutive moments are calculated. Each calculated probability P is taken as the element w_{ij} to construct a $Z \times Z$ dimensional Markov state transition matrix $\boldsymbol{W}$ as shown in Eq. 1. From Eq. 1, it can be seen that the Markov state transition matrix only calculates the transition probabilities between consecutive moments, without considering the dynamic probability transitions of the time series data. To address this limitation, MTF makes improvements by generating a dynamic probability transition matrix M across time scales based on the Markov state transition matrix, as shown in Eq. 2. The MTF innovates the identification of cable insulation defects by transforming time series data into spatial image data. Through modal transformation, MTF retains the discretized temporal dynamics of the data and generates two-dimensional images using fuzzy kernel aggregation. These images provide a richer representation and more intuitive information for feature extraction and recognition. Moreover, the image data generated by MTF can be integrated with advanced machine learning techniques, such as Transformer networks and multi-head attention mechanisms, to enhance the accuracy and robustness of the identification algorithm against noise. The dynamic probability transition matrix of MTF and the fuzzy kernel averaging method further improve the ability to capture the dynamic characteristics of time series data, significantly increasing the efficiency of cable insulation defect identification.

$$\boldsymbol{W} = \begin{bmatrix} w_{11} & w_{12} & \cdots & w_{1z} \\ w_{21} & w_{22} & \cdots & w_{2Z} \\ \vdots & \vdots & & \vdots \\ w_{z1} & w_{z2} & \cdots & w_{zz} \end{bmatrix} \tag{1}$$

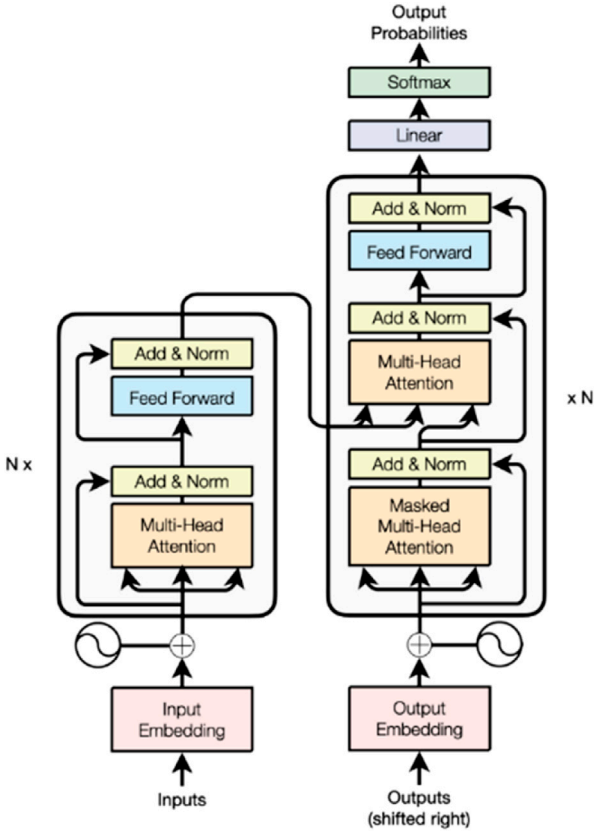

FIGURE 1
Schematic diagram of the transformer network architecture.

$$\boldsymbol{M} = \begin{bmatrix} M_{11} & M_{12} & \cdots & M_{1n} \\ M_{21} & M_{22} & \cdots & M_{2n} \\ \vdots & \vdots & \ddots & \vdots \\ M_{n1} & M_{n2} & \cdots & M_{nn} \end{bmatrix} \tag{2}$$

Each element w_{ij} in the MTF represents the transition probability between points separated by a time interval of $|i\text{-}j|$, $w_{ij|i-j|=1}$ indicates that there is only one interval in the transition process along the time axis, w_{ij} for a time interval of 0 is a special case, representing the probability of each quantile transitioning to itself. Considering that when n is large, using the original MTF to directly generate an image would result in an excessively large image, which occupies more computer storage space and is not conducive to rapid calculation and analysis by on-site intelligent devices or power grid back-end systems. To address this, a fuzzy kernel$\{1/m^2\}_{m\times m}$ is used to average each non-overlapping pixel to obtain a two-dimensional image of the aggregated $m\times m$ dimensional MTF.

2.2 Transformer network

In recent years, the Chat Generative Pre-trained Transformer has garnered widespread attention due to its powerful creativity and logical reasoning capabilities. The model employs a Transformer as its underlying architecture, which, through the introduction of a self-attention mechanism, enables the network to process positional

information in the input sequence in parallel, better understands the interdependencies between input sequences, thereby significantly improving training and inference speeds. Therefore, in Generative Adversarial Networks, using the Transformer as the generator's architecture can endow the model with stronger expressive and generalization capabilities. Compared to Convolutional Neural Networks, the Transformer can establish global dependencies within images, thereby capturing more global image information. To adapt to image tasks, the model in this paper has been adjusted from the traditional structure by removing the decoder and retaining only the encoder. The structure of the Transformer network is shown in Figure 1. The Transformer network used in this paper is pre-trained through self-supervised learning on an ultrasonic detection dataset, utilizing modal transformation technology to convert time series data into images, and combining a multi-head attention mechanism to extract and weight features, thereby enhancing the accuracy and robustness of cable insulation defect identification.

The encoder mainly consists of a multi-head attention mechanism and a multi-layer perceptron. A single attention mechanism involves each input containing three different vectors, namely, the *Query* vector ($\boldsymbol{Q}$), *Key* vector ($\boldsymbol{K}$), and Value vector ($\boldsymbol{V}$). Their results are obtained by performing matrix multiplications of the input feature map $\boldsymbol{X}$ with three weight matrices $\boldsymbol{W}_q$, $\boldsymbol{W}_{\mathrm{k}}$, and $\boldsymbol{W}_{\mathrm{v}}$, respectively, as shown in Eq 3.

$$\left\{\begin{array}{l}\boldsymbol{Q}=\boldsymbol{X}\times\boldsymbol{W}_q\\ \boldsymbol{K}=\boldsymbol{X}\times\boldsymbol{W}_k\\ \boldsymbol{V}=\boldsymbol{X}\times\boldsymbol{W}_v\end{array}\right\} \tag{3}$$

Attention scores for each input vector are then calculated using the softmax function, as shown in Eq. 4:

$$Attention=\mathrm{softmax}\left(\frac{QK^{\mathrm{T}}}{\sqrt{d_k}}\right)\mathbf{V} \tag{4}$$

In the equation: d_k represents the dimensionality of either the Query ($\boldsymbol{Q}$) or the Key ($\boldsymbol{K}$) vectors, with the understanding that the dimensionality of $\boldsymbol{Q}$ and $\boldsymbol{K}$ is equal.

The multi-head attention mechanism, denoted as MultiHead, is shown in Eq. 5:

$$MltiHead=Concat\left(head_1,...,head_h\right)\boldsymbol{W}_o \tag{5}$$

Concat denotes the concatenation operation, $head_h$ represents the output of the h attention head, $\boldsymbol{W}_o$ is the weight matrix.

2.3 Multi-head attention mechanism

The multi-head attention mechanism, by simulating human visual attention, allows the model to focus on the most critical parts of the input data. This mechanism not only enhances the model's ability to express features but also improves the accuracy of defect identification by parallel processing of high-dimensional features. Specifically, the multi-head attention mechanism enables the model to receive information from different subspaces, thereby more effectively capturing and distinguishing various defect characteristics during the feature extraction and classification process. By assigning different weights to the features extracted by the Transformer network, this mechanism emphasizes information that is vital for the identification task, significantly enhancing the accuracy of cable insulation defect identification and the algorithm's robustness to noise. At any given moment, out of a large amount of input data, only a small fraction of features are typically important. The attention mechanism allows the model to focus more on these critical parts, thereby improving the overall performance of the model.

The field of deep learning typically employs soft attention mechanisms for computation, which fuse the various input vectors by weighting and summing them according to an attention distribution. Assuming a set of extracted features, denoted as $H = [h_1, h_2, h_k]$, is given as input, along with a task-related query vector β, the relevance between β and each input h_i is calculated using the attention scoring function s (h_i,β), which is then followed by the normalization of the obtained scores using the Softmax function, resulting in an attention distribution $A = [a_1, a_2, a_k]$ that corresponds to the input features, and ultimately, the input information is weighted and summed according to the attention distribution to produce the output result $\boldsymbol{Y}$. As shown in Eqs 6-7.

$$a_i=\frac{\exp\left[s\left(\boldsymbol{h}_i,\boldsymbol{\beta}\right)\right]}{\sum_{j=1}^{k}\exp\left[s\left(\boldsymbol{h}_j,\boldsymbol{\beta}\right)\right]} \tag{6}$$

$$\boldsymbol{Y}=\sum_{i=1}^{k}a_i\cdot\boldsymbol{h}_i \tag{7}$$

The attention scoring function s (h_i, β) typically includes four forms: additive model, dot product model, scaled dot product model, and bilinear model. As shown in Eqs 8-11.

$$s_1\left(\boldsymbol{h},\boldsymbol{\beta}\right)=\boldsymbol{v}^{\mathrm{T}}f_{\tanh}\left(\boldsymbol{W}_0\boldsymbol{h}+\boldsymbol{U}\boldsymbol{\beta}\right) \tag{8}$$

$$s_2\left(\boldsymbol{h},\boldsymbol{\beta}\right)=\boldsymbol{h}^{\mathrm{T}}\boldsymbol{\beta} \tag{9}$$

$$s_3\left(\boldsymbol{h},\boldsymbol{\beta}\right)=\frac{\boldsymbol{h}^{1}\boldsymbol{\beta}}{\sqrt{D}} \tag{10}$$

$$s_4\left(\boldsymbol{h},\boldsymbol{\beta}\right)=\boldsymbol{h}^{\mathrm{T}}\boldsymbol{W}_{\mathrm{o}}\boldsymbol{\beta} \tag{11}$$

where $\boldsymbol{W}_0$, U, and $\boldsymbol{v}$ are all learnable parameter matrices or vectors, D is the dimension of the input vector; $f$tanh () is the hyperbolic tangent activation function.

Multi-head attention is the cornerstone of the Transformer model [25], Compared to the standard attention mechanism, multi-head attention allows the output of the attention layer to contain representational information from different subspaces, thereby enhancing the model's expressive power. It utilizes different query vectors β_i to focus on different parts of the input information, to achieve the goal of analyzing the current input information from different perspectives, as shown in Figure 2. It mainly consists of three steps: First, the input features extracted are represented as $H = [h_1,h_2, \ldots,h_k]$, Then, a linear transformation is applied to H, mapping it to the query space Q, key space K, and value space V; Subsequently, the scaled dot product and the Softmax function are used to calculate the attention distribution for each, and the attention distributions are summed with weights to obtain the corresponding output Y_i; Finally, the multiple output results are concatenated. As shown in Eqs 12–16.

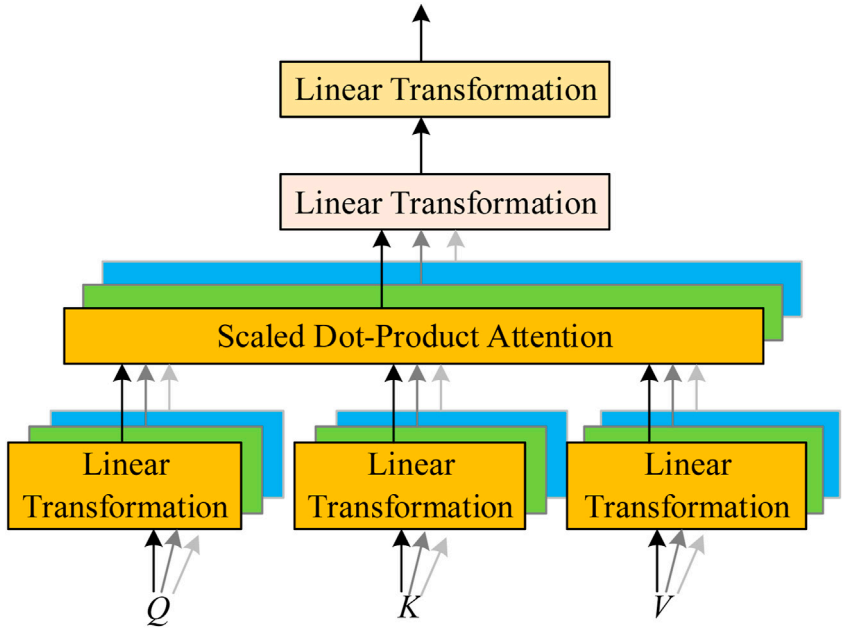

FIGURE 2
Multi-head attention structure.

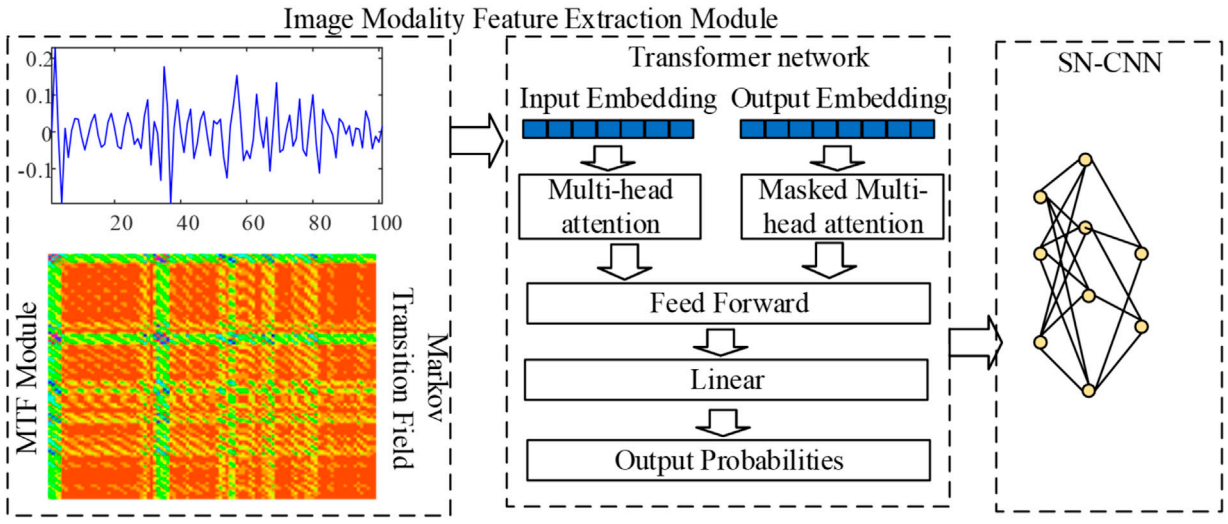

FIGURE 3
MTF and transformer network fusion recognition algorithm.

$$\boldsymbol{Q} = \boldsymbol{H}\boldsymbol{W}_{\mathrm{Q}} = \left[\boldsymbol{\beta}_1, \boldsymbol{\beta}_2, \cdots, \boldsymbol{\beta}_{\lambda}\right] \tag{12}$$

$$\boldsymbol{K} = \boldsymbol{H}\boldsymbol{W}_{\mathrm{K}} = \left[\boldsymbol{k}_1, \boldsymbol{k}_2, \cdots, \boldsymbol{k}_{\mu}\right] \tag{13}$$

$$\boldsymbol{V} = \boldsymbol{H}\boldsymbol{W}_{\mathrm{V}} = \left[\boldsymbol{v}_1, \boldsymbol{v}_2, \cdots, \boldsymbol{v}_{\mu}\right] \tag{14}$$

$$\boldsymbol{Y}_i = \sum_{j=1}^{\mu} f_{\mathrm{Softmax}}\left[s_3\left(\boldsymbol{\beta}_i, \boldsymbol{k}_j\right)\right] \cdot \boldsymbol{v}_j = f_{\mathrm{Softmax}}\left(\frac{\boldsymbol{Q}\boldsymbol{K}^{\mathrm{T}}}{\sqrt{\boldsymbol{D}_k}}\right) \cdot \boldsymbol{V} \tag{15}$$

$$\mathbf{Y} = f_{\mathrm{Concat}}\left(\mathbf{Y}_1, \mathbf{Y}_2, \cdots, \mathbf{Y}_{\lambda}\right) \tag{16}$$

Where W_Q, WK, WV are the linear transformation parameters for the query, key, and value spaces, respectively; Dk is the matrix composed of the dimensionality of each key; k is the element vector in the key space; v is the element vector in the value space; T is the transpose transformation; λ is the number of query vectors; $f_{\mathrm{Concat}}(\,)$ is the feature concatenation function; μ is the dimensionality after the linear transformation.

2.4 Recognition algorithm based on the integration of MTF and transformer network

This paper proposes an integrated recognition algorithm of MTF and Transformer network, as shown in Figure 3. A

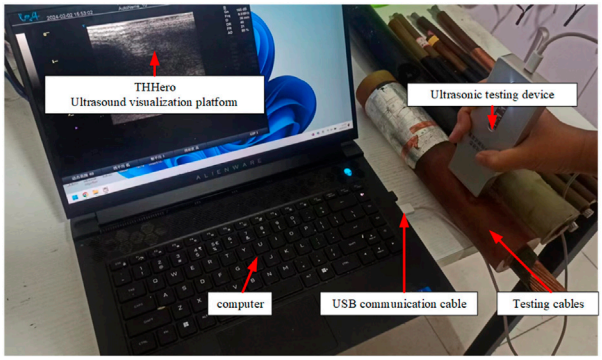

FIGURE 4
Cable insulation defect detection test platform.

Transformer network with greater expressive power is used as the generator, and a Spectral Normalization Convolutional Neural Network (SN-CNN) that meets the Lipschitz continuity constraint is designed as the discriminator. The multi-head attention mechanism of the Transformer generator endows the model with superior expressive power; the concisely structured SN-CNN discriminator reduces the computational complexity of the image generation model and performs well. The method is highly noise-resistant, utilizing a pre-trained Transformer network and multi-head attention mechanism to focus on critical identification information while suppressing noise. It incorporates a denoising process through in-depth median filtering, ensuring accurate defect detection even with noisy ultrasonic signal data. The model's predictions transform complex data into intuitive images, automatically extract key features, and use a multi-head attention mechanism to highlight important information, explaining the identification results of cable insulation defects in a user-friendly manner, thereby enhancing the end-users' understanding of the model's decision-making logic.

3 Ultrasound-based cable insulation defect detection

3.1 Test platform construction

The experimental platform for cable insulation defect detection based on ultrasonic technology is shown in Figure 4. Its core components include a cable terminal sample, an ultrasonic probe, a power supply, an ultrasonic visualization platform, and a USB communication cable. During the cable insulation defect detection process, the ultrasonic probe is coated with a coupling agent to ensure direct contact with the cable insulation surface. The role of the coupling agent is to reduce the acoustic impedance loss as the ultrasonic waves travel from the probe into the cable insulation material, thereby enhancing the signal transmission efficiency. Once the ultrasonic waves successfully penetrate the interior of the cable insulation sample, they interact with the internal structure and produce reflections upon encountering defects or material interfaces. These reflected signals are then captured by the ultrasonic probe and transmitted to a digital controller. The digital controller is responsible for processing and analyzing the echo signals, including operations such as signal amplification, filtering, and conversion. The processed signals are then presented in waveform on the display interface of the ultrasonic visualization platform, allowing for a direct observation of the internal structural characteristics and potential defect locations within the cable insulation. Additionally, the USB communication cable of the experimental platform is responsible for the fast and stable transmission of data between the ultrasonic probe and the digital controller, ensuring the efficiency and accuracy of the entire detection process.

3.2 Insulation defect detection results

Figure 5A shows the echo signal within the cable insulation under normal conditions. Figure 5B shows the echo signal caused by crack defects within the cable insulation. Figure 5C shows the echo signal caused by water droplet defects within the cable insulation. Figure 5D shows the echo signal caused by bubble defects within the cable insulation. Comparing the echo signals under the four types of insulation defects, it can be observed that there are no significant differences in the characteristics of the echo signals across different conditions. Among them, the amplitude of the echo signal within the insulation under normal conditions is significantly greater than that when there are defects within the insulation. Furthermore, when there are different defects within the cable insulation, the echo signals under each defect are difficult to directly observe through temporal characteristics. Therefore, it is necessary to rely on the intelligent recognition algorithm proposed above for identification.

4 Cable insulation defect recognition based on intelligent recognition algorithms

4.1 Model parameters and training results

Based on the aforementioned ultrasonic detection data, this section is dedicated to the verification of an integrated recognition algorithm of MTF and Transformer network. The proposed recognition algorithm is constructed using the PyTorch deep learning framework and the Python programming language. PyTorch is an open-source machine learning library, widely used in applications in fields such as computer vision and natural language processing [26]. Python, as a high-level programming language, provides convenience for rapid algorithm development and prototype design with its concise syntax and rich library support [27]. The specific training environment configuration is shown in Table 1. In the algorithm training phase, the cross-entropy loss function was selected, which is a widely used loss function in classification problems. The cross-entropy loss function measures the difference between the model's predicted probability distribution and the true label distribution, with the mathematical expression as shown in Eq 17. The method proposed in this paper can process a data point within 100 milliseconds and demonstrates a high degree of stability and reliability, which is sufficient to meet the needs of

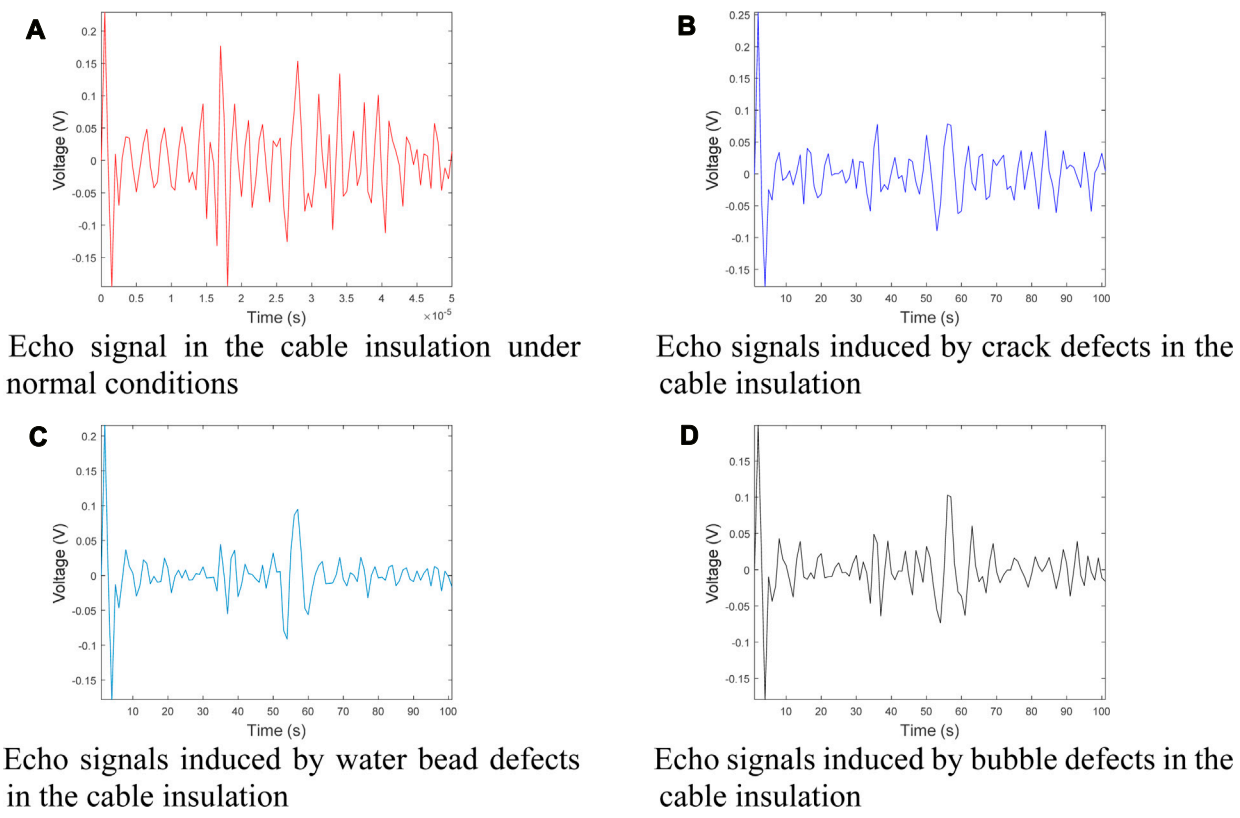

FIGURE 5
The echo signal in the cable insulation layer under different defects. **(A)** Echo signal in the cable insulation under normal conditions. **(B)** Echo signals induced by crack defects in the cable insulation. **(C)** Echo signals induced by water bead defects in the cable insulation. **(D)** Echo signals induced by bubble defects in the cable insulation.

TABLE 1 Parameters of Hardware and software.

Hardware/Software	System environment parameters
Operating System	Windows10 (64) 21H2
CPU	Intel Core i5-10400 @2.90Hz
GPU	NVIDIA GeForce RTX 2060
Random Access Memory	DDR4 32 GB
Python	3.9
PyTorch	1.12.0
Cuda	11.6

online real-time monitoring. Moreover, the method also has good scalability and can adapt to monitoring tasks of different scales, ensuring efficient detection of cable insulation defects in a variety of practical application scenarios.

$$L = -\sum_{i=1}^{N} y_i \log(p_i) \tag{17}$$

Where N is the number of samples, yi is the true label of the ith sample, typically represented by one-hot encoding, pi is the probability that the model predicts sample i belongs to a certain class. The goal of the loss function is to minimize the difference between the predicted probability distribution and the true label distribution.

Utilizing the MTF module to process the four types of echo signals mentioned above and convert them into an image modality. The MTF module is capable of assessing the imaging system's response to details of different spatial frequencies, through which the signals obtained from ultrasonic detection can be transformed into image data, facilitating subsequent image analysis and machine learning classification tasks. The transformed image modalities are displayed in Figures 6A–D, these image modalities clearly reflect the characteristics of different echo signals, providing richer and more intuitive information for the subsequent recognition algorithm. During the training process of the recognition algorithm, the training set and the test set were strictly divided, to ensure the model's generalization ability and to evaluate its performance. Figure 7 shows the variation of recognition accuracy and loss values during the training process for both the training and test sets. Figure 7 illustrates the variation in recognition accuracy and loss values during the training process of the identification algorithm. It can be observed that as training progresses, the recognition accuracy gradually increases while the loss values decrease. Initially, the accuracy level is relatively high, indicating that the algorithm is capable of quickly learning data characteristics and performing effective recognition. With more training iterations, the accuracy

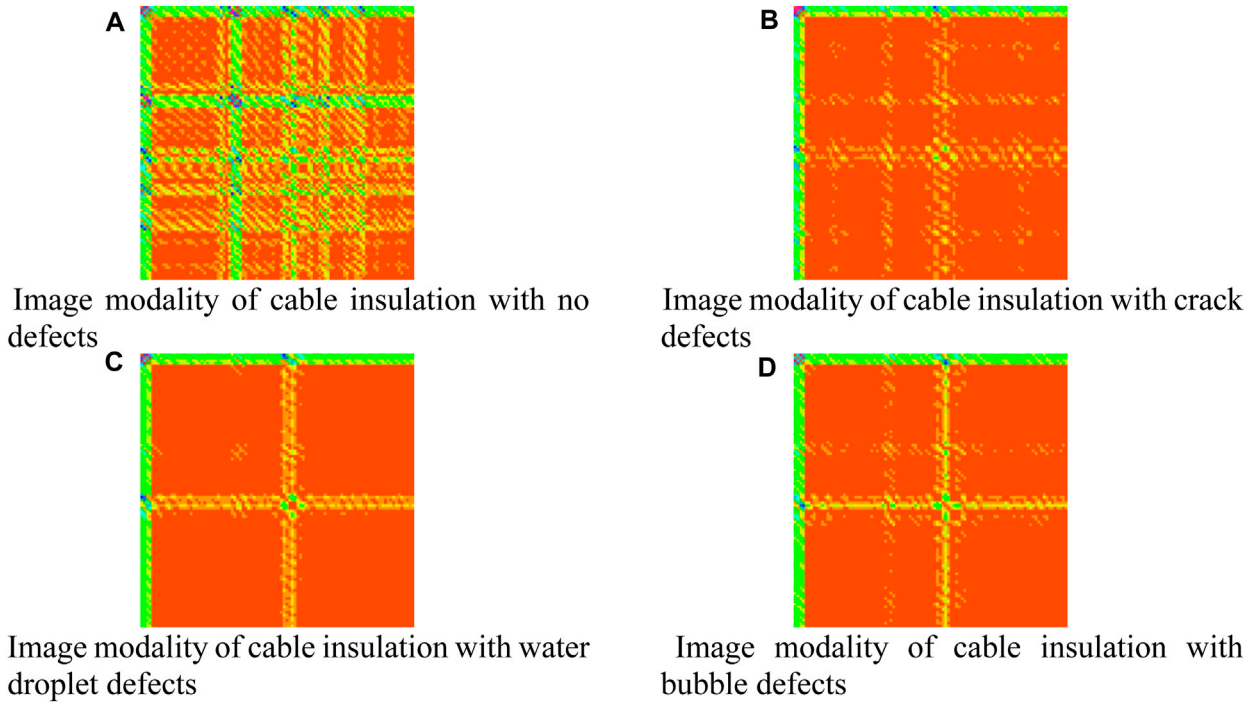

FIGURE 6
Image modality of cable insulation with different defects. **(A)** Image modality of cable insulation with no defects. **(B)** Image modality of cable insulation with crack defects. **(C)** Image modality of cable insulation with water droplet defects. **(D)** Image modality of cable insulation with bubble defects.

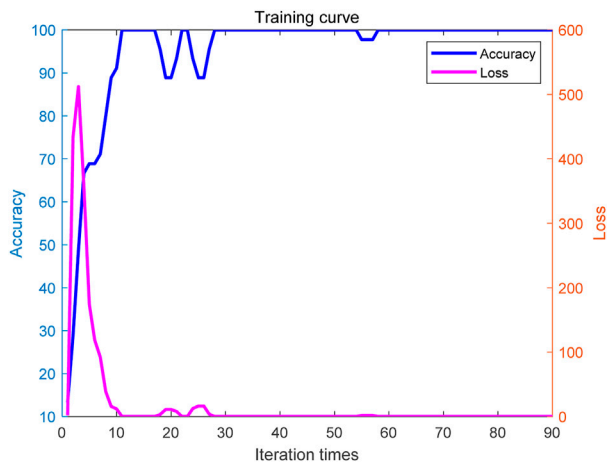

FIGURE 7
Recognition algorithm training process.

continues to improve and tends to stabilize, demonstrating the algorithm's good convergence performance. Concurrently, the loss values continue to decrease, eventually maintaining at a low level, reflecting the reduction in the discrepancy between the model's predictions and the actual labels, thereby enhancing the model's generalization ability. Specifically, at the beginning of the training, the recognition accuracy might start at around 70% or 80%. As training proceeds, the accuracy steadily rises, potentially reaching over 90% after several hundred iterations, and may approach or achieve 100% with further training. Meanwhile, the loss value, which might initially be high such as 1.0 or higher, gradually descends to 0.2, 0.1, or even lower, indicating a reduction in the model's error on the training data. Furthermore, the shape of the curves can reflect certain characteristics of the algorithm. For instance, if the accuracy curve shows a smooth upward trend, it may indicate that the training process of the algorithm is stable without signs of overfitting. If the loss curve fluctuates after decreasing to a certain level, it could be due to the learning rate settings or uneven data distribution.

The confusion matrix is a statistical tool used to evaluate the performance of recognition algorithms [28]. It compares the actual categories with the predicted by the algorithm, allowing for the demonstration of the of the algorithm and potential classification errors. Therefore, in order to comprehensively evaluate the performance of the proposed recognition, the confusion matrix is used as a tool to visually show the classification performance of the algorithm on the training and test set. Figure 8 shows the confusion matrix of the training set, and Figure 9 shows the between the predicted values and actual values on the training set. Figure 10 shows the confusion matrix of the set, and Figure 16 shows the comparison between the predicted values and actual values on the test set. From the classification results presented in Figures 8–11, it can be observed that the proposed recognition algorithm excellent performance on both the set and test set, achieving 100% classification. This high performance, coupled with the advanced machine learning techniques employed, suggests that the method is well-suited for application across different types of cables, including

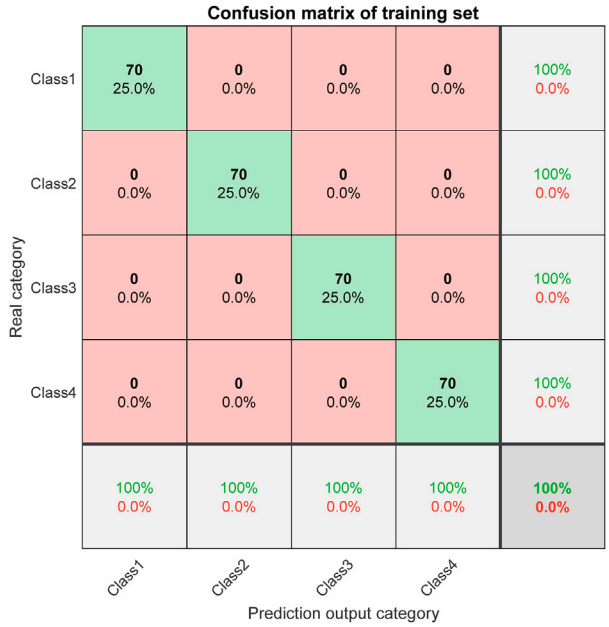

FIGURE 8
Confusion matrix of the training set.

FIGURE 10
Confusion matrix of the test set.

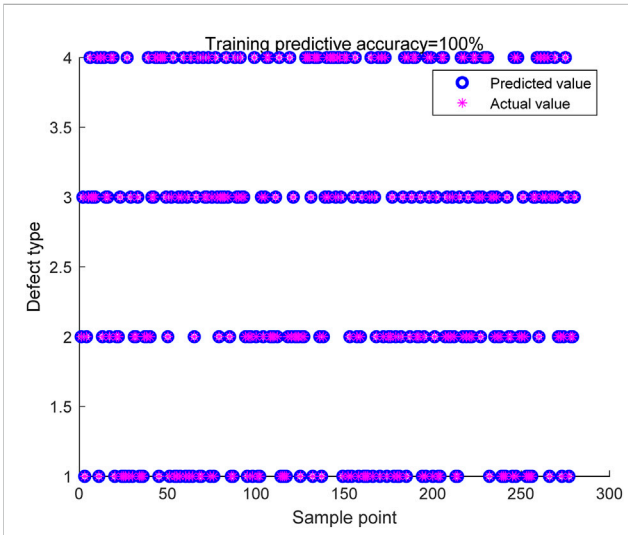

FIGURE 9
Comparison between predicted values and actual values on the training set.

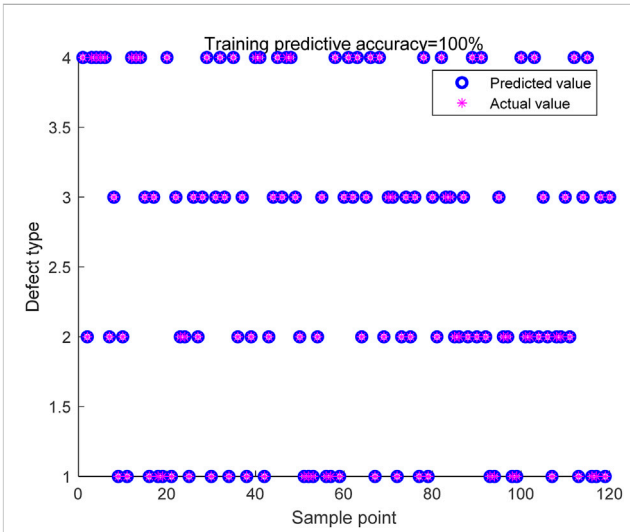

FIGURE 11
Comparison between predicted values and actual values on the test.

both high voltage and low voltage cables. The use of a pre-trained Transformer network and a multi-head attention mechanism further supports the method's potential for robust and generalized detection capabilities, making it applicable to a wide range of cable insulation defect scenarios.

4.2 Algorithm accuracy comparison

To comprehensively evaluate the performance of the proposed MTF and Transformer fusion recognition algorithm in the field of cable insulation defect recognition, a series of experimental comparisons were conducted. These experiments included comparing the recognition accuracy of the proposed algorithm with several widely recognized traditional recognition algorithms. The specific comparison results have been detailed in Table 2, which displays the performance differences of different algorithms on the same test set. Table 2 presents a comparative analysis of recognition accuracy among various models, revealing the superiority of the proposed method. The proposed integration of the MTF with the Transformer network, as demonstrated in our experiments, achieves a remarkable 100% accuracy rate across all categories of cable insulation

TABLE 2 Comparison of recognition accuracy among different models.

Models	Cable insulation defect category and recognition accuracy/%			
	Normal	Internal cracks	Internal water droplet defects	Internal bubble defect
SVM	96.62	97.69	90.55	94.70
RF	92.28	94.51	91.63	93.54
CNN	97.46	98.02	96.19	89.92
Transformer	99.85	100	95.64	93.31
CNN-Transformer	100	93.87	97.85	96.34
The proposed recognition algorithm	100	100	100	100

defects. This performance significantly exceeds that of traditional algorithms such as the SVM, Random Forest (RF), CNN, and the standalone Transformer model. The distinct advantage of our method lies in its ability to capture intricate patterns and relationships within the data through the synergistic application of MTF and the Transformer network. The modality transformation provided by MTF enriches the data representation, while the Transformer network, with its multi-head attention mechanism, adeptly captures the nuanced features essential for accurate defect classification. However, it is also crucial to consider potential limitations. The complexity of the model may lead to increased computational requirements compared to simpler algorithms. Additionally, while the model has shown excellent performance on the tested dataset, its generalizability to other datasets or environments with different noise characteristics and defect types should be further validated.

5 Conclusion

This study proposes an identification algorithm based on the fusion of MTF and Transformer network for the intelligent classification of cable insulation defects. By utilizing the MTF module, the time series data acquired by the ultrasonic probe is transformed into images, enhancing the representation of the data and providing richer information for subsequent feature extraction and classification. By integrating a pre-trained CNN and a multi-head attention mechanism, the algorithm can effectively extract key features and perform precise classification, significantly improving the accuracy and robustness of cable insulation defect identification.

Through comparative experiments with various traditional recognition algorithms, the results demonstrate that the proposed recognition algorithm has achieved a 100% accuracy rate in the identification task of cable insulation defects, significantly outperforming traditional methods such as SVM, RF, CNN, and Transformer. This significant performance improvement confirms the effectiveness and superiority of the fusion recognition algorithm combining MTF with the Transformer network in the identification of cable insulation defects.

Additionally, the recognition algorithm proposed in this study has demonstrated outstanding performance on both the training and testing sets, achieving 100% classification accuracy, indicating that the algorithm has strong learning and generalization capabilities. This outcome provides a novel technical approach for the detection of cable insulation defects, which is of significant importance for enhancing the reliability and safety of power systems.

Future research will focus on enhancing the environmental adaptability of the cable insulation defect identification method. This will be achieved by assessing the impact of environmental factors, optimizing algorithm parameters, integrating environmental compensation mechanisms, and verifying the method in various practical scenarios to ensure stable operation under different conditions. This will provide more reliable detection technology for power systems.

Data availability statement

The original contributions presented in the study are included in the article/Supplementary Material, further inquiries can be directed to the corresponding author.

Author contributions

NZ: Writing–original draft, Writing–review and editing, Methodology. YF: Supervision, Writing–review and editing. SW: Methodology, Project administration, Writing–review and editing. QL: Conceptualization, Formal Analysis, Writing–original draft. XW: Project administration, Resources, Writing–original draft. CF: Formal Analysis, Project administration, Writing–review and editing.

Funding

The author(s) declare that financial support was received for the research, authorship, and/or publication of this article.

Conflict of interest

Authors NZ, YF, SW, QL, XW, and CF were employed by State Grid Shijiazhuang Electric Power Supply Company.

The authors declare that this study received funding from State Grid Hebei Electric Power Co., Ltd. (No. KJ2022-016). The funder was involved in the study design, collection, analysis, interpretation of data, the writing of this article, and the decision to submit it for publication.

Publisher's note

References

1. Hu Y, Chen L, Liu Y, Xu Y. Principle and verification of an improved algorithm for cable fault location based on complex reflection coefficient spectrum. *IEEE Trans Dielect Elect Insul* (2023) 30(1):308–16. doi:10.1109/tdei.2022.3224700

2. Liu ZW, Bian PL, Qu YL, Huang WC, Chen LL, Chen JB, et al. A galerkin approach for analysing coupling effects in the piezoelectric semiconducting beams. *Eur J Mech A Sol* (2024) 103:105145. doi:10.1016/j.euromechsol.2023.105145

3. Chen LL, Lian HJ, Xu YM, Li SZ, Liu ZW, Atroshchenko E, et al. Generalized isogeometric boundary element method for uncertainty analysis of time-harmonic wave propagation in infinite domains. *Appl Math Model* (2023) 114:360–78. doi:10.1016/j.apm.2022.09.030

4. Li HZ, Chen LL, Zhi G, Meng L, Lian HJ, Liu ZW, et al. A direct fe2 method for concurrent multilevel modeling of piezoelectric materials and structures. *Computer Methods Appl Mech Eng* (2024) 420:116696. doi:10.1016/j.cma.2023.116696

5. Chen LL, Lian HJ, Dong HW, Yu P, Jiang SJ, Bordas SPA. Broadband topology optimization of three-dimensional structural acoustic interaction with reduced order isogeometric fem/bem. *J Comput Phys* (2024) 509:113051. doi:10.1016/j.jcp.2024.113051

6. Li Z, Zheng Z, Wu Y, Du B. Space charge and electric field dependent on polarity reversal of HVDC cable insulation. *IEEE Trans Dielect Elect Insul* (2024) 31(1):58–65. doi:10.1109/tdei.2023.3335189

7. Chen LL, Wang ZW, Lian HJ, Ma YJ, Meng ZX, Li P, et al. Reduced order isogeometric boundary element methods for CAD-integrated shape optimization in electromagnetic scattering. *Comput Methods Appl Mech Eng* (2024) 419:116654. doi:10.1016/j.cma.2023.116654

8. Hua X, Wang L, Yang S, Zhang S. Temperature mapping model of cables considering the coupling of electromagnetic and thermal field. *Digital Twin* (2023) 3(2):2. doi:10.12688/digitaltwin.17718.1

9. Shen XW, Du CB, Jiang SY, Zhang P, Chen LL. Multivariate uncertainty analysis of fracture problems through model order reduction accelerated SBFEM. *Appl Math Model* (2024) 125:218–40. doi:10.1016/j.apm.2023.08.040

10. Li X, Guo Y, Li Y. Particle swarm optimization-based SVM for classification of cable surface defects of the cable-stayed bridges. *IEEE Access* (2020) 8:44485–92. doi:10.1109/access.2019.2961755

11. Hua X, Wang L, Yang S. Lifetime prediction of aviation cables based on an improved electromagnetic–thermal coupling model. *IEEE Trans Dielectr Electr Insul* (2023) 30(6):2788–97. doi:10.1109/tdei.2023.3295347

12. Chen LL, Li HZ, Guo YY, Chen P, Atroshchenko E, Lian HJ. Uncertainty quantification of mechanical property of piezoelectric materials based on isogeometric stochastic FEM with generalized Nth-order perturbation. *Eng Comput* (2023) 40(1):257–77. doi:10.1007/s00366-023-01788-w

13. Hua X, Wang L, Yang S. Multiscale analysis of the aging process of cable insulation. *IEEE Trans Dielectr Electr Insul* (2023) 30(1):238–46. doi:10.1109/tdei.2022.3217425

14. Shokry MA, Khamlichi A, Garnacho F, Malo JM, Álvarez F. Detection and localization of defects in cable sheath of cross-bonding configuration by sheath currents. *IEEE Trans Power Deliv* (2019) 34(4):1401–11. doi:10.1109/tpwrd.2019.2903329

15. Huang J, Zhou K, Xu Y, Meng P, Tang Z, Liang Z. Upper sweeping frequency selection for cable defect location based on STFT. *IEEE Trans Instrum Meas* (2023) 72:1–9. doi:10.1109/tim.2023.3271718

16. Cheng L, Xu W, Wang X, Yang L, Liao R, Ni Y. Defect detection of cable termination based on the microwave reflection method. *IEEE Trans Dielectr Electr Insul* (2024) 31(1):111–20. doi:10.1109/tdei.2023.3309930

17. Hua X, Wang L, Zhang Y. Analysis and diagnosis of shielded cable faults based on finite-element method and time-reversal time-frequency domain reflectometry. *IEEE Trans Ind Electron* (2022) 69(4):4205–14. doi:10.1109/tie.2021.3071685

18. Shafiq M, Kiitam I, Taklaja P, Kütt L, Kauhaniemi K, Palu I. Identification and location of PD defects in medium voltage underground power cables using high frequency current transformer. *IEEE Access* (2019) 7:103608–18. doi:10.1109/access.2019.2930704

19. Chen LL, Cheng RH, Li SZ, Lian HJ, Zheng CJ, Bordas SPA. A sample-efficient deep learning method for multivariate uncertainty qualification of acoustic–vibration interaction problems. *Comput Methods Appl Mech Eng* (2022) 393:114784. doi:10.1016/j.cma.2022.114784

20. Shen XW, Du CB, Jiang SY, Sun LG, Chen LL. Enhancing deep neural networks for multivariate uncertainty analysis of cracked structures by POD-RBF. *Theor Appl Fract Mech* (2023) 125:103925. doi:10.1016/j.tafmec.2023.103925

21. Xu Y, Sheng G, Yang F, Chen X, Qian Y, Jiang X. Classification of partial discharge images within DC XLPE cables in contourlet domain. *IEEE Trans Dielectr Electr Insul* (2018) 25(2):486–93. doi:10.1109/tdei.2017.006752

22. Bang SS, Shin YJ. Classification of faults in multicore cable via time–frequency domain reflectometry. *IEEE Trans Ind Electron* (2020) 67(5):4163–71. doi:10.1109/tie.2019.2920606

23. Abu-Rub OH, Khan Q, Refaat SS, Nounou H. Cable insulation fault identification using partial discharge patterns analysis. *IEEE Can J Electr Comput Eng* (2022) 45(1):31–41. doi:10.1109/icjece.2021.3119465

24. Zhu K, Pong PWT. Fault classification of power distribution cables by detecting decaying DC components with magnetic sensing. *IEEE Trans Instrum Meas* (2016) 69(5):2016–27. doi:10.1109/tim.2019.2922514

25. Wu D, Zheng Y, Cheng P. Triple channel feature fusion few-shot intent recognition with orthogonality constrained multi-head attention. *IEEE Access* (2024) 12:31685–96. doi:10.1109/access.2024.3369902

26. Tian X, Shi L, Luo Y, Zhang X. Garbage classification algorithm based on improved MobileNetV3. *IEEE Access* (2024) 12:44799–807. doi:10.1109/access.2024.3381533

27. Begum SSA, Syed H. GSAtt-CMNetV3: pepper leaf disease classification using osprey optimization. *IEEE Access* (2024) 12:32493–506. doi:10.1109/access.2024.3358833

28. Heydarian M, Doyle TE, Samavi R. MLCM: multi-label confusion matrix. *IEEE Access* (2022) 10:19083–95. doi:10.1109/access.2022.3151048

Frontiers in Physics

Investigates complex questions in physics to understand the nature of the physical world

Addresses the biggest questions in physics, from macro to micro, and from theoretical to experimental and applied physics.

Discover the latest Research Topics

See more →

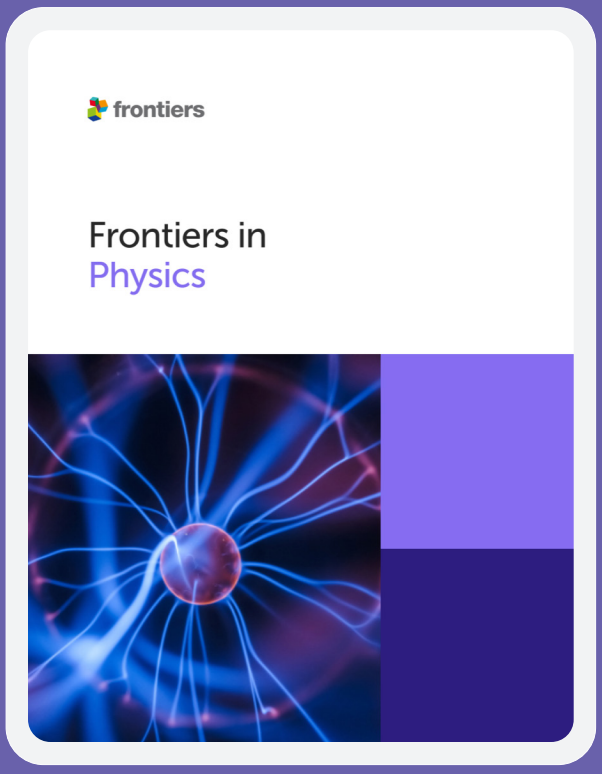

Frontiers

Avenue du Tribunal-Fédéral 34
1005 Lausanne, Switzerland
frontiersin.org

Contact us

+41 (0)21 510 17 00
frontiersin.org/about/contact